Springer Atmospheric Sciences

John J. Qu
Alfred M. Powell, Jr.
M.V.K. Sivakumar *Editors*

Satellite-based Applications on Climate Change

Springer

Satellite-based Applications on Climate Change

John J. Qu • Alfred M. Powell, Jr.
M.V.K. Sivakumar
Editors

Satellite-based Applications on Climate Change

Springer

Editors
John J. Qu
Environmental Science and Technology
George Mason University
Fairfax, VA, USA

Alfred M. Powell, Jr.
Administration, NOAA/NESDIS,
Center for Satellite Application and Res
National Oceanic and Atmospheric
Camp Springs, MD, USA

M.V.K. Sivakumar
Climate Prediction and Adaptation Branch
Climate and Water Programme
World Meteorological Organization
Geneva, Switzerland

ISBN 978-94-007-5871-1 ISBN 978-94-007-5872-8 (eBook)
DOI 10.1007/978-94-007-5872-8
Springer Dordrecht Heidelberg New York London

Library of Congress Control Number: 2013934717

Printed on acid-free paper

Springer is part of Springer Science+Business Media (www.springer.com)

Foreward

Global climate change has become an urgent and important issue because of its significant impact on our lives and the environment. In fact, to a great extent, climate change is the bellwether of our environment and reflects our ability and commitment to manage human activities in such a way as to support a sustainable Earth environment for the benefit of present and future generations. A sustainable future depends on our success in the race to develop far greater understanding of climate change both natural and anthropogenic.

Changes in the north polar ice coverage, the number of wildfires, which is one measure of the increasing frequency of severe weather events, and the ever growing number of temperature records being broken annually attest to the fact that climate change is real. Our understanding of climate change and its effects on the Earth and its chain of life are directly dependent on our ability to observe all facets of Earth systems, physical, chemical, and biological. Certainly in situ or Earth-based local observations remain critical to understanding our planet, but only satellites can provide complete coverage of the globe to allow scientists to monitor changes of the Earth whether they occur in the tropics, over the oceans, within the continents, or in the polar ice caps.

Satellite-based remote sensing measurements with their 24×7 large data streams are critical for understanding the complicated global changes of the Earth system of systems. The environmental satellites operated by the National Oceanic and Atmospheric Administration (NOAA), National Aeronautics and Space Administration (NASA), and our partner international space agencies have been collecting information about the Earth's atmosphere and environment for decades. These satellite systems although relatively new and revolutionary in applications to the Earth sciences have already led to enormous advances in our understanding of the atmosphere, ocean, and land cover, as well as the significant improvement of weather and climate forecasts in the past several decades. Satellite observations are proving to be essential for global climate change study because they provide the global, regional, and local context about how change in one area of the planet is related to change in another region. This information helps scientists determine the

cause and effect relationships to improve our ability to understand and model the impacts.

This book presents recent advances in satellite-based remote sensing applications related to the issue of climate change. Research results and applications on a range of climate topics that touch upon key specialization areas such as atmospheric sciences, hydrology, oceanography, phenology, and ecology are presented in a logical and useful format for answering today's urgent questions. This volume will be a valuable reference for researchers and graduate students interested in recent findings derived from remote sensing measurements that have been applied to the climate sciences.

The imaginative and intricate techniques presented herein are indicative of the kind of investigation and scientific development that is urgently needed now and in the future to develop our understanding of climate change. Greater understanding is needed now to provide for more accurate forecasting that will lead to the prudent use of our precious resources, allowing us to live in harmony with our environment. I applaud the authors for their hard work in bringing together the most recent and valuable of satellite-based climate science techniques and hope that careful study of the material contained herein will inspire the next generation of climate scientists and Earth observation developers. A sustainable future depends on it!

Conrad C. Lautenbacher Jr.,
VADM U.S. Navy (ret), PhD
Administrator, National Oceanic and Atmospheric Administration (NOAA), and Undersecretary of Commerce 2001–2008
August 2012

Preface

Climate and other environmental changes are drawing unprecedented concern and attention from national governments, international organizations, and local communities. Global warming is leading to noticeable impacts on the environment, ecosystems, and human livelihoods, all of which carry important implications for sustainable economic and social development in the future. Satellite observations of climate and environmental change have become an increasingly important tool in recent years for helping to shape the response of international communities to this critical global challenge.

This book includes 21 chapters which present the latest advances in satellite-based remote sensing of the Earth's environment ranging from applications and research in climate, atmospheric science, hydrology, oceanography, geomorphology, ecology, and fire studies. Introductory chapters also cover key technical aspects such as instrumentation, calibration, data analysis, and GIS tools for decision-making.

We convey our thanks to all the authors who spent their valuable time to contribute chapters to this book. We also wish to extend our appreciation to the anonymous reviewers for their critical and constructive comments and suggestions. The support from the Center for Satellite Applications and Research (STAR) of the National Oceanic and Atmospheric Administration (NOAA) and Environmental Science and Technology Center (ESTC) of George Mason University (GMU) is gratefully acknowledged. Special recognition is given to Dr. Xianjun Hao, Dr. Lilong Zhao, and Mr. Weijie Fu who helped us to edit this book.

We sincerely hope that the contents of this book provide the readers with a better understanding of climate change monitoring from space and that this book will serve the needs of scientists and graduate students who are interested in satellite remote sensing and its applications.

John J. Qu
Alfred M. Powell, Jr.
Mannava V.K. Sivakumar

Contents

Chapter 1
An Introduction to Satellite-Based Applications and Research for Understanding Climate Change

Alfred M. Powell Jr., John J. Qu, and Mannava V.K. Sivakumar

Abstract The use of satellite data in applications has changed as the environmental community has become more sophisticated deriving products from the remotely sensed measurements. This introduction summarizes the changes from the first satellites where the images were used to improve cloud forecasts to the international coordination groups that have formed to improve collaboration and data sharing of satellite observations. This introduction also addresses some of the key challenges associated with using satellite data for both weather and climate; the challenges include calibration, derived products, trend uncertainty, and measurement quality. A short discussion of subsequent future issues is briefly discussed as satellite measurement calibration reaches maturity.

Keywords Satellite • Applications • Research • Calibration • Collaboration • Climate • Trend • Uncertainty

A.M. Powell Jr. (✉)
Center for Satellite Applications and Research (STAR) in the National Oceanic and Atmospheric Administration (NOAA) located at the NOAA Center for Weather and Climate Prediction (NCWCP), 5830 University Research Court, College Park, MD 20746, USA
e-mail: Al.Powell@noaa.gov

J.J. Qu
Department of GGS/College Of Science (COS), Environmental Science and Technology Center (ESTC), George Mason University (GMU), MS 6A2, Fairfax, VA 22030, USA

M.V.K. Sivakumar
Climate Prediction and Adaptation Branch (CLPA), Climate and Water Department (CLW), World Meteorological Organization, 7 bis Avenue de la Paix, Case Postale No. 2300, Geneva 2 CH-1211, Switzerland

J.J. Qu et al. (eds.), *Satellite-based Applications on Climate Change*,
DOI 10.1007/978-94-007-5872-8_1,

1.1 Introduction

Climate change is one of most important issues facing the world today. With the Arctic polar ice extent at near record minimums and new temperature records being set in many regions of the world, the need to understand how our planet is responding to environmental change is critical for society. Although some progress was made toward understanding the changes in weather, the understanding of changes in oceans and land over time is still in a formative stage. A description of climate observations in support of the Global Climate Observing System can be found in Thomas R. Karl's (ed) (1996) book: *Long-Term Climate Monitoring by the Global Climate Observing System*. As better quality global observations of the Earth are collected from satellites, the opportunity to gain insight into the dynamic processes driving our planet and the long-term trends will improve. Even though there are thousands of surface observations, rawinsondes, buoys, and other in situ measurements from ships and aircraft, the observations are limited in global coverage, particularly over the oceans and the polar caps. Measurements over the sparsely observed oceans and polar caps are needed to understand how the various regions of our planet are connected. The land regions where we live are impacted by changes in the oceans and the polar caps. For example, if the polar caps continue to melt, sea level rise will affect islands and coastlines – inundating some to such an extent that the inhabitants must live elsewhere. Changes in temperature will affect precipitation, evaporation, and crop growth, leading to economic impacts and potential disruptions in global food supply. It is vital that a fundamental understanding of how our planet works be developed so accurate predictions of environmental change can be provided. This will allow the world's decision makers to make tough choices relative to both global and regional consequences. To garner an improved understanding about how our environment functions, a comprehensive set of global observations are required. Satellites can help provide those observations and eliminate the data sparse coverage in many regions of the world like the oceans, deserts, and polar caps.

1.2 Satellites and Changes over Time

Satellite observations play a crucial role filling the gaps in the data sparse regions and helping to understand the connections between different regions of the world. The observations will provide information about how the Earth exchanges energy between the tropics and the poles and how the heat exchange impacts global atmospheric circulation patterns as well as the weather and climate trends around the globe. Satellites are relatively new on the global monitoring scene with only about 30 years of modern observations. Progress is being made in understanding the spaceborne observations, how they relate to our collection of in situ observations, and how they can be used to predict changes in our environment.

In the early years, the first satellites were successful if the imagery had sufficient contrast and clarity to be used for cloud pattern analysis. One of the first publications on satellite data applications was the *Environmental Science Services*

Administration (ESSA) Technical Report, from the *National Environmental Satellite Center* (NESC) on the Application of Meteorological Satellite Data in Analysis and Forecasting (Anderson et al. 1969). In the introductory chapter, the wisdom of the early satellite scientist pioneers was captured in the following quotes on page 1:

> Since the advent of the operational ESSA weather satellites in 1966, routine use of satellite cloud photographs has increased steadily. Meteorologists worldwide now depend on these data to supplement conventional observations and rely completely on satellite cloud observations where other data are not available. The problem of "sparse data" areas has been greatly alleviated since weather satellites now provide analysts with a timely view of the cloud conditions over all parts of the earth. Even so, the advantages of the satellite data are not limited to isolated areas but also provide additional intelligence over areas where the conventional observations are dense.
>
> If the maximum value of these data is to be realized, correct interpretation of the cloud photographs is essential. This technical report furnishes guidance in the interpretation of satellite cloud photographs and presents the latest relationships as determined by research and study in this field.

The ESSA Technical Report authors further comment:

> Future research with improved satellite data will undoubtedly result in the determination of new concepts and a better understanding of the relationships between the satellite data and the dynamics of the atmosphere.

The pioneers of environmental satellite applications had a vision for the use of satellite data and understood the value of training and educating others in the use of the new satellite data. By training others, the value of the satellite data and its benefits to society would be recognized. Twenty-five years after the Anderson publication, similar issues of training and educating users as well as gaining an improved understanding of the satellite measurements were identified by Stanley Kidder and Thomas VonderHaar in their 1995 book entitled *Satellite Meteorology: An Introduction* (Kidder and Vonder Haar 1995). In the preface to their book, they write:

> We place special emphasis on the physical understanding of measurements from space because it is this understanding which will allow both the useful application of current techniques and the development of future techniques. We also tend to emphasize operational techniques over experimental techniques. We do this in the belief that most readers will not do their own information or parameter retrievals from raw satellite data; they will use parameters retrieved by others. Most often these parameters will be retrieved using operational, near real-time methods. A thorough exploration of the operational techniques is therefore important.

Note the shift in approach from the first scientists who were involved in all aspects of the satellite program and its development – a team of scientific jack-of-all-trades. The early scientists helped in the instrument design, worked closely with the instrument engineers, and performed their own data analysis which led to developing "operational products" for the community of users. From their scientific analyses, the scientists taught others how to use the information to monitor the Earth to make better weather forecasts. As the use of satellites for monitoring the Earth became more routine, a core group of scientific specialists was developed who also train users on the benefits of the routine operational products. By 1995, the field of satellite meteorology had grown dramatically, and the value of satellite data had proven its worth to multiple communities eager to take advantage of the satellite measurements and the information derived from them.

1.3 International Satellite Collaboration and Coordination

The complexity of the world's satellite systems and programs led to the development of coordinating groups to better leverage satellite resources and share their data. The Group on Earth Observations (GEO) was formed from a call to action by the 2002 World Summit on Sustainable Development. The World Summit recognized that international collaboration was critical for exploiting the growing potential of Earth observations to support decision making in an increasingly complex world. GEO is a voluntary partnership of governments and international organizations. It provides a framework where partners can develop new strategies and projects and coordinate their investments.

To improve efforts to apply satellite observations, GEO coordinates efforts to build a Global Earth Observation System of Systems (GEOSS). GEOSS will provide a broad range of societal benefits including reducing the loss of life and property, improving human health, managing energy resources, adapting to climate variability and change, improving water resource management and weather forecasts, protecting coastal marine and marine ecosystems, supporting sustainable agriculture, and monitoring and conserving biodiversity. GEOSS coordinates numerous complex issues. This crosscutting approach avoids duplication, encourages synergies between systems, and ensures substantial economic, societal, and environmental benefits.

GEOSS provides decision-support tools to a wide variety of users. GEOSS is a global and flexible network of content providers allowing decision makers to access an extraordinary range of information at their desk. This "system of systems" links together observing systems around the world. It promotes common technical standards, so satellite data from the numerous instruments can be fused into integrated data sets. The "GEOPortal" offers users a single Internet access point for data, imagery, and analytical software packages. It connects users to existing databases of observations, tools, and software. It provides reliable, up-to-date information critical for the work of decision makers, planners, and emergency managers. Users with limited or no access to the Internet will be able to use satellite information available via the "GEONETCast" telecommunication satellite network where data is broadcast to field systems with small portable antennas (information on GEO and GEOSS is derived from http://www.earthobservations.org/about_geo.shtml).

Another key satellite group, the Committee on Earth Observation Satellites (CEOS), was established in 1984. CEOS coordinates civil spaceborne Earth observations. Members enhance international coordination and data exchange for societal benefit and represent space agencies as well as national and international organizations. Members participate in planning and related CEOS activities through a variety of working groups; one is related to climate applications.

CEOS established a Working Group on Climate (WGClimate) to coordinate and encourage collaborative climate monitoring activities between the world's major space agencies. The Working Group's mandate is to facilitate the implementation and exploitation of the Essential Climate Variable (ECV) time series through coordination of CEOS member activities (information on CEOS is derived from http://www.ceos.org).

Using the satellite observations and coordinating the satellite constellation is fundamental to managing the Earth observations. However, the use of the observations is impacted by the data formats and communications pathways and extends to various user communities. The World Meteorological Organization (WMO) is a specialized agency of the United Nations which helps facilitate international coordination. It originated from the International Meteorological Organization (IMO), founded in 1873. The WMO was established in 1950. It became the specialized agency of the United Nations (UN) in 1951 for meteorology (weather and climate), operational hydrology, and related geophysical sciences. The WMO is the UN system's authoritative voice on the state and behavior of the Earth's atmosphere, its interaction with the oceans, the climate, and the distribution of water resources. WMO provides the framework for international cooperation and collaboration.

As weather, climate, and the water cycle recognize no country boundaries, global level international cooperation is essential for developing meteorological and hydrological applications to reap the observational benefits. WMO membership consists of 189 member states and territories. WMO facilitates the free and unrestricted exchange of data and information. It also promotes products and services relating to the safety and security of society, economic welfare, and the protection of the environment. WMO contributes to policy formulation at national and international levels. For weather, climate, and water-related hazards, which account for nearly 90% of all natural disasters, WMO's programs provide information for advance warnings that save lives and reduce property and environmental damage (information on WMO is derived from www.wmo.int).

Studies show that every dollar invested in meteorological and hydrological services produces an economic return many times greater. The world of satellite observations has come a long way from the first observations taken nearly 50 years ago.

Systems for the routine collection of data on the state of the climate system are the bedrock for generating climate services. The requirements and standards for observing systems and their component instruments for measuring the state of the climate system are described fully in the relevant WMO manuals and in a range of documents developed by the Global Climate Observing System (GCOS). The needs for climate data are not the same across all applications. Climate change detection and attribution need high-quality, homogeneous, long-term data. For this purpose, the GCOS baseline systems, especially the GCOS Surface Network (GSN) and the GCOS Upper-Air Network (GUAN), are the essential benchmarks for ensuring the overall homogeneity of the global/regional databases. The GCOS Climate Monitoring Principles provide the "Gold Standard Rules" for planning, developing and operating observing systems. WMO is now implementing the WMO Integrated Global Observing System (WIGOS) as an all-encompassing approach to the improvement and evolution of meteorological and related observing systems.

Given the change in emphasis of satellite programs, their coordination internationally, and the expanding satellite constellation coordination, it is no surprise that the satellite research and applications community has changed substantially. This book discusses selected analyses and research findings in application areas of interest to the environmental satellite community and its users. The wide range of

satellite products, the need for specialization in specific areas of endeavor, and the expanding interest in new or improved satellite and model forecast capabilities mean that today's satellite scientists, product specialists, and the climate community are collaborating more than any point in the past. Future expectations include a greater and more rapid information exchange.

Partnerships similar to ones described in the various coordinating organizations foster the continuation of the original principles listed in the two publications cited earlier, for example, to train and educate others about the satellite measurements and the products with the result being (a) the development of new satellite-based concepts and (b) a better understanding of the dynamics of our planet as reflected in the atmosphere, the oceans, on the land, and in space.

1.4 Modern Satellite Era

Twenty-five years after the first environmental satellites, the scientific roles changed. Kidder and VonderHaar emphasized providing satellite-derived "operational products" to users over the research or experimental products. The community of users had expanded greatly thanks to a plethora of satellite-based products and services that provided capabilities which had become routinely used.

Today, approximately 45 years after the first ESSA satellites, one can see animating loops of satellite images routinely on the television weather broadcasts. Users can obtain specialized satellite-derived products that display the cloud patterns, vegetation indices, sea surface temperatures, cloud track winds, snow cover, precipitation, and over 450 other specialized satellite-based products that help decision makers mitigate the impacts of the weather and climate on the economy. Users can obtain these satellite products freely from the National Oceanic and Atmospheric Administration (NOAA), National Environmental Satellite Data and Information Service (NESDIS), and other international centers around the globe. Near real-time updates about the status of instruments used by NOAA operationally can be found at http://www.star.nesdis.noaa.gov/icvs/.

The modern satellite and environmental scientists are becoming specialists in particular niche areas like winds, precipitation, vegetation, crop yields, drought identification, satellite data assimilation into the forecast models, and satellite calibration. As the satellite capabilities advanced, ensuring the stability of the instruments and tracking their individual calibration contributed to the higher-fidelity satellite products developed by the mid-1990s. Today, the problem of satellite calibration continues to evolve and has become more complex. It involves not only the United States constellation of operational environmental satellites but the environmental satellite data from our international partner's satellites as well as the National Aeronautics and Space Administration's (NASA) environmental research satellites. Satellite calibration has grown into a specialized field where the calibration is no longer ensuring the accuracy of individual satellite instruments but a calibrated constellation of satellites and their instruments. To support our understanding of climate, instrument stability and cross-satellite calibration have become essential components for

developing products capable of supporting climate services including monitoring climate trends. Accurate calibration is required to meet the needs of today's users, and access to this more accurate data has expanded the user community to include climate scientists. To support new requirements for more tailored products and services, an international Global Space-based Inter-Calibration System (GSICS) working group coordinates the activities of participating nations to improve the overall calibration of all the satellites in the international constellation. The GSICS Working Group was established in 2005 by the WMO and the Coordinating Group for Meteorological Satellites (CGMS) for the purpose of monitoring, improving, and harmonizing the quality of observations from operational weather and environmental satellites of the Global Observing System (GOS). The goal is to provide consistent accuracy among space-based observations worldwide for climate monitoring and weather forecasting. (Information about the US GSICS Coordination Center and its international role was derived from http://www.star.nesdis.noaa.gov/smcd/GCC/index.php and http://gsics.wmo.int/).

1.5 Using Satellite Data to Understand Climate

With the intercalibrated satellite data as the global foundation data source, an improved understanding of the environment can be derived from the information. Understanding the movement of water in the Earth system is important for many applications of satellite data. Passive microwave observations and the products derived from them are routinely available and widely used in meteorological analyses and forecasting applications requiring rainfall, total precipitable water (TPW), and snowfall rate products, for example. These measurements and products form the foundation for initializing satellite and climate models. Ferraro et al. (2010) provides a summary of example applications within NOAA. However, simply generating satellite-based products is not sufficient. For climate purposes, the measurements must be stable and consistent across the period of the observations. For snow and snow cover, Romanov (2011) shows how the tools developed for monitoring global snow cover could be used to support agricultural applications with specific application in Ukraine to assess crop yield impacts.

To address the needs of the climate community, improved calibration is the essential stepping stone. Intercalibration techniques were the first step and compared a reference satellite instrument with another satellite instrument. In Yang et al. (2011), intercalibration was accomplished between the Defense Meteorological Satellite Program Special Sensor Microwave Imagers (SSM/I) on F13 and F15 and the Tropical Rainfall Monitoring Mission (TRMM). The reduced biases for total precipitable water (TPW) products were significant. Intersensor TPW biases were reduced by 75% over the global ocean and 20% over the tropical ocean. In addition, intersensor calibration reduced biases by 20.6, 15.7, and 6.5% for oceanic, land, and global precipitation, respectively (Yang et al. 2011). The removal of biases between measuring systems is extremely important for assessing accurate climate trends and establishing measurement uncertainties.

Global climate change signals as small as a few percent per decade critically depend on accurately calibrated level 1B (L1B) data and the derived Fundamental Climate Data Records (FCDRs). Detecting small climate changes over decades is a major challenge and also impacts the retrieval of geophysical parameters from satellite observations. Without dependable FCDRs and their derivative Thematic Climate Data Records (TCDRs), the trends calculated from the measurements will be questioned. Cao et al. (2008) analyzed the consistency of calibrated reflectance from the operational L1B data between AVHRR on NOAA-16 and NOAA-17 and between NOAA-16/AVHRR and Aqua/MODIS, based on the recent Simultaneous Nadir Overpass (SNO) observation time series. The SNO approach advanced the science of satellite calibration to a higher level of accuracy and reliability and now includes the intercalibration between polar and geostationary measurements. Even so, the measurement uncertainty is still too high relative to the trends being monitored. As a consequence, a more stable calibration source has been sought: the Moon. The Moon is thought to be a reliable and stable calibration reference for studying climate change from satellites (Cao et al. 2009). However, having a quality FCDR does not guarantee the same or equivalent quality TCDR or derived trend.

To calculate confident trends, Zou et al. (2009) developed a calibrated data set based on the SNO approach for the Microwave Sounding Units (MSU) on NOAA satellites 10 through 14 over the period from 1987 to 2006. This intercalibrated data set reduced intersatellite biases by an order of magnitude compared to prelaunch calibration and resulted in a well-merged time series for the MSU channels 2, 3, and 4, which represent the deep layer temperature of the mid-troposphere (T2), tropopause (T3), and the lower stratosphere (T4). From Zou et al.'s (2009) data set, the trend patterns revealed the tropical mid-troposphere warmed at a rate of 0.28 $\pm$ 0.19 K per decade, while the Arctic atmosphere warmed two to three times faster than the global average. Even with this improved trend calculation, there is appreciable regional variability not demonstrated in this single number.

Liu and Weng (2009) also reported findings about the warming trend in the troposphere and the cooling trend in the stratosphere. However, Liu and Weng's (2009) analysis presents evidence that the lower stratosphere has warmed slightly since 1996 and the warming trend in the lower stratosphere may be related to a possible recovery of stratospheric ozone concentration. This points out that even with highly calibrated data, the debate over climate trends will likely change from data quality to one of improving our understanding of the dynamic effects. In this regard, Qin et al. (2012) analyzed MSU brightness temperatures to estimate the global climate trend in the troposphere and stratosphere using a new adaptive and temporally local data analysis method – Ensemble Empirical Mode Decomposition (EEMD). Using EEMD, a nonstationary time series is decomposed into a sequence of amplitude-frequency-modulated oscillatory components and a time-varying trend. The data from the NOAA-15 satellite over the time period from October 26, 1998 to August 7, 2010 shows that most trends derived from microwave channels are nonlinear in the Northern Hemisphere with a few channel exceptions. Although the decadal trend variation of the global average brightness temperature is no more than 0.2 K, the regional decadal trend variation could be different by plus or minus 3 K in the high latitudes and over high terrain.

While the calibration is improving for the core measurements, Cao et al. (2009) pointed out there are still significant uncertainties in determining the long-term climate trends using indices such as the Normalized Difference Vegetation Index (NDVI). This is partly due to the lack of stability in measurements required for climate change detection and partly due to the nonphysical derivation of the NDVI from measured radiances. Using calibrated AVHRR (Advanced Very High Resolution Radiometer) data from 1982 to 2007, complex trends in both the growing season amplitude and seasonally integrated vegetation greenness in southwestern North America can be observed. Zhang et al. (2010) show greenness measurements from 1982 to 2007 with an increasing trend in grasslands but a decreasing trend in shrublands. Also, vegetation growth appears to be a function of both the rainfall amount and the dry season length. The average global temperature over the past 100 years increased 0.74°C according to the 2007 Intergovernmental Panel on Climate Change Report. The period after 2000 was the warmest and includes the two warmest years (2007 and 2010) since the 1880s. A warmer world is expected to have tendencies toward higher temperature variability increasing the risk of summer droughts, which should affect larger areas, last longer, be more intense and produce more devastating impacts on the environment and economy. Due to data sparse ground observing stations, the assessment of agricultural impacts has been performed using satellite data. Drought affects the largest number of people in the world and has the largest economic impacts. The Vegetation Health Index has both a temperature and moisture component to distinguish the effects of the dominant variables (temperature and moisture/rainfall) for a particular region. Using the new indices, drought intensity and the area covered appear to be increasing as the temperature warms (Kogan et al. 2013). During the most recent decade, the global drought analysis indicates that 17–35% of the world experienced droughts from moderate to exceptional intensity, 7–15% severe to exceptional, and 2–6% the most exceptional droughts, an increase over earlier periods. Two droughts, 2010 in Russia and 2011 in the USA, stand out by their intensity, affected area, and substantial economic consequences (Kogan et al. 2013).

Climate products will continue to evolve with time. They will incorporate a greater variety of both satellite and in situ data. The combined use of the most modern measurements to understand current trends while leveraging our knowledge and understanding of the older in situ observations combined with modeled physics to allow an improved assessment of past climate changes is the future trend. An example of this type of project is the monthly reconstruction of precipitation project (Smith et al. 2010) which covers 1900 until the present. This reconstruction attempts to resolve interannual and longer time scales as well as spatial scales larger than 5° over the entire globe using both direct and indirect correlations. A key advantage for this type reconstruction is that it evaluates global precipitation variations for periods much longer than the satellite period of record, which begins in 1979 for routine use in NOAA operational models. In the future, the multisource fusion of the in situ observations with remotely sensed measurements and detailed model physics will allow the investigation of climate change to a level well beyond today's capability. However, the unfolding debate over whether the model physics is

accurate will become the central scientific debate as the observations become more reliable with lower uncertainties through better calibration. Since models have many physical pathways with differing and complex physics, it will take a substantial period of time to assess which model physics components should be used. As the environmental research community successfully achieves their goals by improving the satellite data and its applications, the climate trends will not only be a debate about the observations but also the model-dependent physics used to facilitate understanding the climate as well. The question of climate trends will shift in the level of detail along with our understanding of the climate.

1.6 Book Overview

With the goal of adding an incremental improvement to our climate understanding, the chapters in this text have been grouped into the following four areas:

1.6.1 Part I Overview of Satellite-Based Measurements and Applications

This section addresses the vitally important calibration of satellite instruments and their data since accurate calibration is the key to high-quality climate products and services. With high-quality calibration, the data can be used to support climate change studies and large-scale atmospheric trends and improve our understanding of the forcings that drive the global atmospheric systems. As one looks to the future, the development of new instruments and their potential value to society need to be addressed. Calibration will be essential for using the satellite observations effectively.

1.6.2 Part II Atmospheric and Climate Applications

Precipitation and temperature are two very important measurements for understanding how our climate will change and how it will affect different regions. Using the microwave and precipitation measurements, a set of papers addresses global precipitation monitoring, the development of a historical precipitation record, and suitable methods for developing atmospheric temperature climate data records for better monitoring climate trends.

1.6.3 Part III Hydrological and Cryospheric Applications

The movement of water and variations in the ice caps are critical to understanding how our planet is changing. Given the dramatic decline in the Northern Hemisphere ice extent over the last decade, it is important to understand changes in the Arctic. With global warming as a contributor to the declining ice extent, it may also impact the intensity of hurricanes and the amount of tropical rainfall. Changes in the sea surface temperatures influence the development of hurricanes and evaporation and precipitation patterns around the globe. These important topics are covered in this section recognizing their potential for significant impacts globally and on coastal communities.

1.6.4 Part IV Land Surface and Ecological Applications

With changes in global temperature and precipitation as key drivers, their impacts are investigated using satellite data to develop products and analyses for monitoring climate trends. The impacts of temperature and precipitation on vegetation growth, health, and trends will be paramount. As temperatures increase, a global migration of plants, animals, and sea creatures is expected. A relatively recent ecological related development is the pioneering work to detect sentinel species migration and change from satellites.

This suite of chapters discusses key topics and findings that those interested in satellite remote sensing will find appealing. The chapters touch on the most pressing problem areas for helping to make effective decisions about sustaining our environment and mitigating the consequences of climate change.

Acknowledgements This work was supported by the National Oceanic and Atmospheric Administration (NOAA); National Environmental Satellite, Data, and Information Service (NESDIS); and the Center for Satellite Applications and Research (STAR).
The views, opinions, and findings contained in this publication are those of the authors and should not be considered as an official NOAA or US government position, policy, or decision.

References

Anderson RK, Ashman JP, Bittner F, Farr GR, Ferguson EW, Oliver VJ, Smith AH (1969) ESSA technical report NESC 51, application of meteorological satellite data in analysis and forecasting (including supplement, Nov 1971 and supplement #2, Mar 1973), re-published 1974 by Superintendent of Documents. U.S. Government Printing Office, Washington, D.C. 20402

Cao C, Xiong X, A W, Wu X (2008) Assessing the consistency of AVHRR and MODIS L1B reflectance for generating fundamental climate data records. J Geophys Res 113:D09114. doi:10.1029/2007JD009363

Cao C, Vermote E, Xiong X (2009) Using AVHRR lunar observations for NDVI long-term climate change detection. J Geophys Res 114:D20105. doi:10.1029/2009JD012179

Ferraro R, Kusselson S, Kidder S, Zhao L, Meng H (2010) Application of AMSU-based products to support NOAA's mission goals. Natl Weather Dig 34(1):1–16

Karl T (ed) (1996) Long-term climate monitoring by the global climate observing system. Kluwer Academic, Dordrecht/Boston, 518pp

Kidder SQ, Vonder Haar TH (1995) Satellite meteorology: an introduction. Academic, San Diego, CA

Kogan F, Adamenko T, Guo W (2013) Global and regional drought dynamics in the climate warming era. Remote Sens Lett 4(4):364–372. doi:10.1080/2150704X.2012.736033

Liu Q, Weng F (2009) Recent stratospheric temperature observed from satellite measurements. Sci Online Lett Atmos 5:53–56. doi:10.2151/sola.2009–014

Qin Z, Zou X, Weng F (2012) Comparison between linear and nonlinear trends in NOAA-15. Clim Dyn. doi:10.1007/s00382-012-1296-1

Romanov P (2011) Satellite-derived information on snow cover for agriculture applications in Ukraine. In: Kogan F, Powell AM, Federov O (eds) (2011) Use of satellite and in-situ data to improve sustainability, The NATO science for peace and security programme, Proceedings of the NATO advanced research workshop on using satellite and in-situ data to improve sustainability, Kiev, 9–12 June 2009, Springer, Dordrecht, p 313.

Smith T, Arkin PA, Sapiano MRP, Chang CY (2010) Merged statistical analyses of historical monthly precipitation anomalies beginning 1900. J Climate 23:5755–5770. doi:10.1175/2010JCLI3530.1

Yang S, Weng F, Yan B, Sun N, Goldberg M (2011) Special Sensor Microwave Imager (SSM/I) intersensor calibration using a simultaneous conical overpass technique. J Appl Meteorol Climatol 50:77–95

Zhang X, Goldberg M, Tarpley D, Friedl MA, Morisette J, Kogan F, Yu Y (2010) Drought-induced vegetation stress in southwestern North America. Environ Res Lett 5. doi:10.1088/1748-9326/5/2/024008, 024008 (11pp)

Zou CZ, Gao M, Goldberg MD (2009) Error structure and atmospheric temperature trends in observations from the microwave sounding unit. J Climate 22. doi:10.1175/2008JCLI2233.1

Chapter 2
Calibrating a System of Satellite Instruments

Changyong Cao, Ruiyue Chen, and Sirish Uprety

Abstract Satellite instrument calibration is the essential and fundamental process to convert the Earth view sensor response in voltage and counts to radiance and reflectance. Calibration accuracy directly affects the quality of the satellite Level 1b data used for numerical weather prediction and climate change detection. Therefore, ideally all calibration should be made traceable to the International System of Units (SI). However, since each satellite instrument is calibrated separately with different methodologies and at different times in history, there is often disagreement between satellite measurements which could cause errors in both weather and climate applications. This chapter provides an overview of the fundamentals of satellite instrument calibration and reviews some of the challenges in establishing consistent satellite measurements across a system of satellites. Examples are used to demonstrate the progress made in inter-satellite calibration in recent years to support climate change detection studies and to contribute to the Global Earth Observation System of Systems (GEOSS).

Keywords Satellite instrument • Calibration • Accuracy • Consistency

C. Cao (✉)
Satellite Meteorology and Climatology Division (SMCD), Center for Satellite Applications and Research (STAR), NOAA/NESDIS
e-mail: changyong.cao@noaa.gov

R. Chen
IMSG Inc., Rockville, MD

S. Uprety
Cooperative Institute for Research in the Atmosphere (CIRA), Colorado State University, Fort Collins, CO.

J.J. Qu et al. (eds.), *Satellite-based Applications on Climate Change*,
DOI 10.1007/978-94-007-5872-8_2,

2.1 Introduction

Climate change detection and numerical weather prediction (NWP) critically depend on accurate, reliable, and consistent radiance data from multiple sensors onboard a constellation of satellites. The calibration consistency across international satellites is further challenged in the implementation of GEOSS (Global Earth Observation System of Systems). As a result, establishing on-orbit calibration links among operational satellite radiometers is receiving increasing attention. According to the CEOS (Committee on Earth Observation Satellites), which consists of the majority of the space agencies worldwide, its member agencies are operating or planning about 240 satellites with Earth observation missions over the next 15 years, carrying over 385 different instruments (http://www.eohandbook.com). Unfortunately, not all satellite observations can be put into productive use because the data quality varies from one instrument to another significantly and the measurements may not be consistent even for satellites within the same agency due to different calibration methodologies and techniques used. This chapter presents the fundamental issues in satellite instrument calibration for climate applications and provides an overview of the current status, challenges, and latest developments in the calibration of operational satellite radiometers with specific examples.

For climate change detection, calibration accuracy and consistency are essential since the signal of climate change can be very small, such as 0.1 K per decade in sea surface temperature. Given a satellite radiometer's typical design life of about 5 years, the detection of decadal climate change relies on observations from a series of satellites. It is well known that despite the best effort in prelaunch and postlaunch calibration, the same series of radiometers on different satellites, such as the AVHRR (Advanced Very High Resolution Radiometer), HIRS (High Resolution Infrared Radiation Sounder), and AMSU (Advanced Microwave Sounding Unit)/MSU(Microwave Sounding Unit) on NOAA satellites, do not necessarily produce consistent measurements. This leads to the inter-satellite biases which have become major concerns in constructing time series for climate change detection. Current satellite systems are significantly challenged to meet these application requirements. Sensors and onboard calibration sources may degrade in orbit; measurements may not be traceable to international standards; long-term data sets must be stitched together from a series of overlapping satellite observations; and orbital drift can introduce artifacts into long-term time series. As demonstrated in the tropospheric temperature trend study using MSU channel 2 observations, the inter-satellite biases can become so critical that depending on how the biases are treated may lead to different conclusions about the tropospheric warming (e.g., compare results from Zou et al. 2006; Vinnikov and Grody 2003; Christy et al. 1998).

Clearly, satellite detection of the global climate change signals critically depends on consistent and accurately calibrated Level 1b data or FCDRs (fundamental climate data records). Without dependable FCDRs, the derived TCDRs (thematic climate data records) may produce false trends with questionable scientific value. This has been increasingly recognized by more and more users of

satellite data. The logical approach to achieve satellite measurement consistency is to perform rigorous cross-calibration intercomparisons, which are needed to establish traceability.

As the technology of satellite observations of the Earth matured, user requirements and expectations for satellite data have also evolved not only for climate but also for weather applications. Although qualitative applications of satellite data, such as generating cloud maps, have less stringent requirement for calibration accuracy, most quantitative applications require accurately calibrated satellite data, and this need has rapidly evolved in the last decade. For example, in the early days of meteorological satellites, numerical weather prediction (NWP) required retrieved quantities of vertical temperature, moisture, and water vapor profiles from satellite data. In the past decade, NWP has witnessed the greatest evolution of direct radiance assimilation from satellite measurements into numerical weather prediction models. As a result, resolving the observation versus model differences, aka, the biases, becomes a prerequisite for direct radiance assimilation. Satellite observations with unresolvable biases will be rejected by the NWP models.

Therefore, the importance of instrument calibration for satellite applications cannot be overstated. Calibrated radiances are the fundamental building blocks for all satellite products, including the radiances for data assimilation in NWP, reanalysis, and fundamental climate data records for climate change detection. Calibration is the centerpiece of data quality assurance in satellite data processing, distribution, and archive and is part of the core competency of any satellite program.

2.2 Satellite Instrument Calibration Methodologies

Calibration is the process of quantitatively defining the sensor responses to known and controlled signal inputs. These signals should ideally be traceable to established reference standards. Traceability requires the establishment of an unbroken chain of comparisons to stated references each with a stated uncertainty. It should be noted for satellite sensors on-orbit, the calibration signals may become neither well known nor controllable. Also, operationally, calibration is the process of converting the Earth observation raw signals to physical quantities to generate SDR (sensor data records) or Level 1b data.

Calibration is generally divided into three areas: radiometric, spectral, and spatial calibration. Radiometric calibration focuses on the accuracy and traceability of the radiometric quantity of the measurement. Spectral calibration ensures that the spectral responses of the system are accurate at the operating conditions and changes over time are well known. Spatial calibration ensures the geometric distortion is well characterized by a number of metrics including the point spread function or modulation transfer function. Spatial calibration also ensures the band-to-band co-registration and geo-location/navigation for each pixel. The radiometric, spectral, and spatial calibrations go hand in hand (Fig. 2.1). A problem in either the spectral or spatial calibration introduces uncertainties in the radiometric calibration.

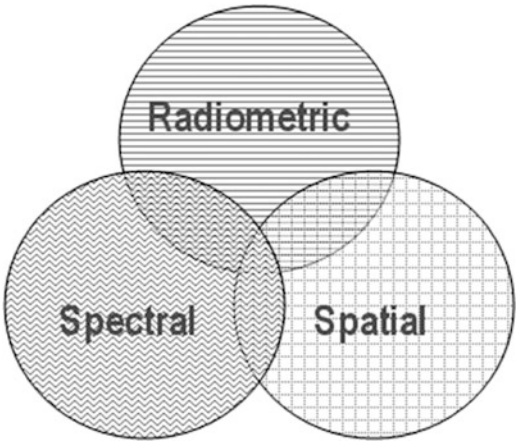

Fig. 2.1 Three areas of calibration: radiometric, spectral, and spatial

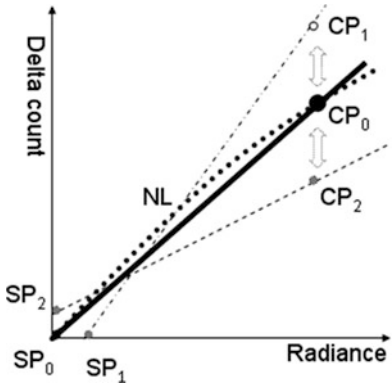

Fig. 2.2 Basic concept of radiometric calibration common to most satellite systems

Nevertheless, the word "calibration" often refers to radiometric calibration, unless specified otherwise.

In radiometric calibration, a satellite instrument calibration system often uses two relatively well-known calibration points, one is typically the space view, or SP_0 in Fig. 2.2, and the other is an onboard calibration device or calibration point CP_0. This device is typically a blackbody for the infrared and microwave instruments, while it is a solar diffuser or lamp for the solar bands. Other calibration systems are also used for satellite radiometers, such as noise diodes for some microwave radiometers as a calibration source. Assuming that the system has a linear response to incoming radiance, this two-point calibration is sufficient to calibrate all observations to sensor data records, or Level 1b data. For a nonlinear system, a quadratic equation is typically used where the quadratic term is determined prelaunch and additional uncertainties may be introduced.

While the deep space SP_0 in the two-point calibration is believed to be stable, the stability of neither a solar diffuser nor the blackbody for CP_0 can be assumed. In fact, the stability of this calibration point has become a critical issue in the on-orbit

calibration of satellite instruments. For example, the blackbodies used for the heritage infrared radiometers such as AVHRR (Advanced Very High Resolution Radiometer) and HIRS (High Resolution Infrared Radiation Sounder) have an emissivity on the order of 0.98, which makes the CP_0 fluctuates with the ambient temperature. Modern instruments such as infrared atmospheric sounders IASI (Infrared Atmospheric Sounding Interferometer) and AIRS (Atmospheric Infrared Sounder) use cavity blackbodies where the emissivity are high which makes the calibration point more robust than those for the heritage instruments.

For spectral calibration, few broadband satellite instruments have onboard spectral calibration devices, and therefore prelaunch measurements of instrument spectral response are critical. Unfortunately, the prelaunch measurements of the spectral response are often performed at ambient conditions and then extrapolated to operating temperature based on the known behavior of spectral shift, which introduces uncertainties. Spectral uncertainties often lead to spectrally induced biases that are difficult to be separated from radiometric biases. This is especially important for atmospheric sounding instruments where an error in the spectral response often leads to the observation of a different atmospheric layer at a different altitude. The advent of the hyperspectral systems significantly reduced the spectral uncertainties which led to their use as a reference standard to calibrate broadband instruments.

2.3 Challenges in Calibrating Heritage Satellite Instruments for Climate Change Detection

It is recognized that heritage operational satellite instruments were designed for traditional weather applications with no stringent requirement for calibration accuracy, which is reflected in the mission requirement documents. On the other hand, there is a need to recalibrate the long-term data records for climate applications. An important science question is what it would take to recalibrate the operational instruments for climate studies. Unfortunately, there is no easy answer to this simple question.

It is necessary to review the past calibration performance of the heritage instruments in the context of the challenges in establishing calibration consistency for climate change detection. Figure 2.3 shows the relative observation biases for AVHRR channel 2 between successive NOAA satellites from 1984 to 2003. Apparently, the discrepancies between satellite measurements can be very large (a ratio of 1.85 equals to a difference of 85%). This is due to several factors: (a) AVHRR has no onboard calibration and therefore relies on using prelaunch and vicarious calibration, and (b) the instrument degradation was not well characterized for some of the NOAA satellites over their history and therefore causes a trend in the inter-satellite bias. Obviously, the operational data, which have a large

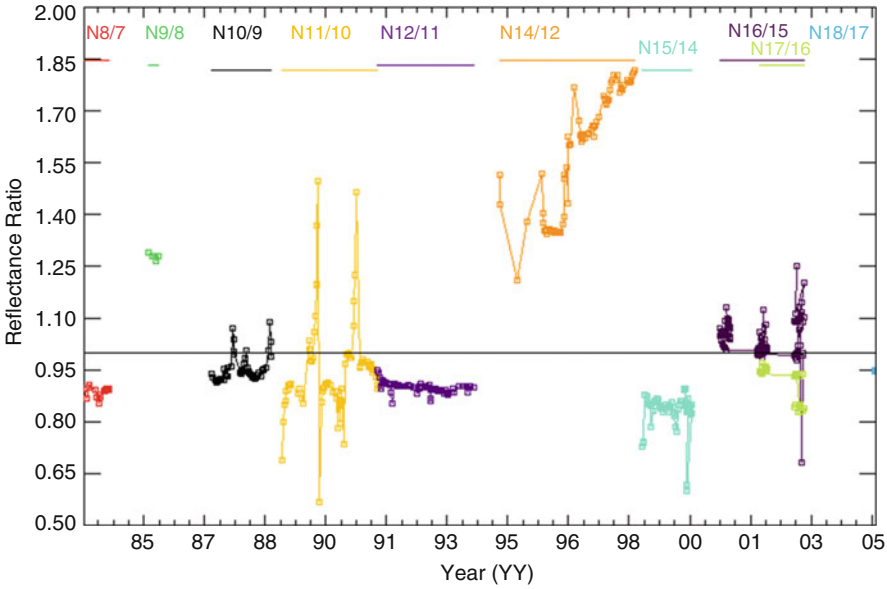

Fig. 2.3 AVHRR channel 2 inter-satellite biases between successive satellites showing large discrepancies between satellites when not well calibrated

Table 2.1 Instrument performance specification, and climate requirements

	Specification	Performance achieved	Climate requirements
AVHRR VIS/NIR	±5% absolute	−10% relative to MODIS	1% per decade for albedo
AVHRR IR	±0.5 K absolute per mission requirement	±0.5 K relative to IASI on MetOp	±0.1 K per decade for SST
HIRS	Not well defined	±0.2 K relative to IASI on MetOp	±0.1 K per decade for temperature trend
AMSU	1.5–2 K	±0.2 K relative to each other on different satellites	±0.1 K per decade for temperature trend

uncertainty in the measurement accuracy and consistency, are not good enough for climate change detection without recalibration and/or recharacterization.

Table 2.1 compares the current instrument performance specification, performance achieved, and climate change detection requirements. For example, for albedo, the stability requirement is 1% per decade, while the current estimate is no better than 5%. For the IR bands of AVHRR, the requirement is 0.1 K per decade, but a 0.5 K variation is found from orbital variation alone.

Therefore, although the calibration system presented earlier appears to be very simple, to achieve very accurate and consistent calibration that meets the needs of climate change detection, it is not so straightforward. There are many science questions to be answered, which ultimately determines the reliability of the data.

Here are some of the questions with respect to Fig. 2.2 in the context of climate change detection: How well do we know about the calibration points? Is the CP_0 point stable for the lifetime of the instrument? Do we have the same CP_0 points across satellites? How well do we know about the nonlinearity and on-orbit behavior? Each question requires extensive studies, and the results would be very significant.

First of all, the onboard calibration device (CP_0), as one of the pivotal points in this calibration system, is neither necessarily stable over its lifetime nor consistent with other calibration points on other satellites. This creates inconsistencies between satellites. In fact, the calibration point can fluctuate up and down during its lifetime as shown in Fig. 2.2 (CP_0–CP_1 or CP_2). Similarly, although the deep space itself is stable, the instrument response to it may not be stable or could be contaminated by stray light, lunar intrusion in the field of view, or the satellite bus in case of sidelobe effects in the microwave instruments. This causes major uncertainties in the calibration which affects all the data records produced. For example, in the SP_1-CP_1 calibration curve in Fig. 2.2, the calibrated radiances would be too low at high radiance values while too high at low radiance values. Similarly, the SP_2-CP_2 calibration curve produces low-biased radiances at low radiances and high-biased radiances at high radiances. As a result, all data produced will have biases. If each satellite has its own bias, then a constellation of satellites will have biases relative to each other and make the observations inconsistent, which significantly limit our ability to detect climate change.

Many examples exist where the CP_0 is not stable, such as the blackbody calibration for the infrared channels of AVHRR, because the low emissivity of the blackbody makes the blackbody radiances deviate from what a true blackbody would emit. The lack of onboard calibration devices in the AVHRR solar bands effectively makes CP_0 nonexistent, and vicarious targets such as deserts have to be used which also introduce uncertainties as discussed later.

For the reflective solar bands, there are significant calibration challenges. Prelaunch calibration with an integrating sphere is mainly used for specification compliance and postlaunch comparisons, because the instrument may degrade during launch as well as over time in orbit. Although it is feasible to establish prelaunch SI (International System of Units) traceability, this traceability can be lost postlaunch. As a result, the on-orbit traceability relies on vicarious targets such as the desert sites for systems without onboard calibration.

The reflectance of vicarious targets can have large variability both short term and long term. In short term, the reflectance is affected by the presence of clouds, water vapor, ozone, and other atmospheric effects. In long term, the desert target may drift over time due to geomorphological processes or human activities. The Libyan target used for AVHRR, for example, has experienced significant expansion of irrigation farming which affects both the short- and long-term stability of the target. All vicarious targets have bidirectional reflectance effects which change with season and solar zenith/azimuth and view angles. The new generation of radiometers, such as MODIS (Moderate Resolution Imaging Spectroradiometer) on NASA's EOS (Earth Observing System) and VIIRS (Visible Infrared Imager Radiometer Suite) on

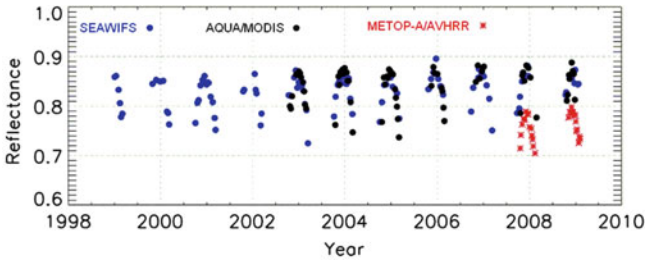

Fig. 2.4 Dome C time series comparisons between MODIS, MetOp/AVHRR, and SeaWiFS

JPSS (Joint Polar Satellite Systems), has onboard solar diffusers with improved calibration, but it is still desirable to verify their consistency relative to other satellites.

Calibration traceability issues often cause discrepancies between different instruments. For example, since MODIS calibration uses a solar diffuser, while AVHRR calibration is traceable to the Libyan Desert, a discrepancy is observed when comparing AVHRR and MODIS solar bands. Multiple independent studies suggest that a ~10% difference in measured reflectance values exists between MODIS and AVHRR 0.63 um band, and this difference cannot be accounted for by the differences in their spectral response functions (Cao et al. 2008a). This discrepancy is also observed at vicarious sites such as the Dome C site in Antarctica (Fig. 2.4), and it was found to be due to inaccurate characterization of the desert target in the early 1980s. Clearly on-orbit calibration traceability is causing uncertainties which will undoubtedly affect time series analysis using both AVHRR and MODIS. Similar issues exist when comparing data from international satellites for which not all calibration information is readily available to the international research community.

For the infrared and microwave instruments calibrated with blackbody and space view, prelaunch thermal vacuum tests are typically performed in the factory to ensure that the instrument meets specifications, but more work needs to be done to improve the calibration traceability. For example, in the case of AVHRR and HIRS on NOAA satellites, the "NIST traceability" simply meant that the blackbody PRTs (platinum resistance thermometers) are traceable to National Institute of Standards and Technology (NIST) standards, while the radiometric traceability has not been established. The postlaunch performance of the blackbodies for the legacy radiometers is generally good enough for traditional weather applications with an estimated accuracy of ± 0.5 K but may not be sufficiently accurate for climate applications and today's numerical weather predictions. On-orbit uncertainties are mainly caused by a combination of stray light in the scan-cavity and blackbody emissivity, especially in terminator orbits.

Nonlinearity is another major source of uncertainty which can introduce scene-dependent biases. For the silicon detectors in the visible/near-infrared, the relationship between incoming radiation and output counts is generally linear, the MCT (mercury cadmium telluride) detectors in the infrared in photoconductive mode, as well as the square law detectors in the microwave, are nonlinear between incoming radiation and output counts. The nonlinearity of these systems is tested in a thermal vacuum

chamber prelaunch at different target and instrument temperatures, but it was found that test artifacts often obscure the true nonlinearity of the system. Also, since there is no readily available method for verifying the nonlinearity postlaunch, uncertainty exists in using prelaunch determined nonlinearity in postlaunch calibration.

The new generation of instrument has significant improvements in both scan-cavity and blackbody designs. The high-quality blackbodies in some cases are made directly traceable to NIST radiometric standards. However, even with perfect traceability, it is still desirable to verify the calibration between satellites. Otherwise, the links between satellites are not known and may not be established.

2.4 Inter-satellite Instrument Calibration

Given the limited life span of a satellite for a typical mission, constructing a long-term time series for climate change detection requires accurate and consistent data from a series of satellites. It is well known that despite the best calibration efforts, biases and inconsistencies still exist for the same series of radiometers on different satellites. Unlike instrument noise which can be quantified precisely with on-orbit calibration targets, biases are very difficult to characterize due to the lack of commonly traceable on-orbit absolute calibration standards and the variable nature of biases both short term and long term in response to the spacecraft and instrument thermal dynamics. Several methods have been developed to address the inter-satellite calibration issue, and each has its advantages and limitations.

The SNO (Simultaneous Nadir Overpass) method (Cao et al. 2004, 2005a) was developed for quantifying inter-satellite biases initially for instrument performance monitoring and has been used by scientists in constructing time series for climate change detection. This method is relatively simple and robust and is based on the fact that any pair of polar-orbiting satellites with different altitudes can regularly observe the Earth at orbital intersections at nearly the same time and that these events are predictable with orbital perturbation models such as SGP4. The frequency of occurrence is a function of the altitude difference between the two satellites (typically once every 2–10 days). Observations from the two satellites at the SNOs can then be collocated pixel by pixel and the biases between them quantified. The uncertainties in the SNO analysis are further reduced in a SNO time series where the inter-satellite biases at the SNOs are studied as a function of time.

Using the SNO method, an on-orbit calibration reference network can be established. The network can keep track of the long-term time series of inter-satellite biases at the SNOs, GEO (Geostationary)/LEO (Low Earth Orbiting) satellites, and selected vicarious sites for all operational satellites. Even without an absolute scale, this will tie the calibration of all the satellites together to provide traceability of individual satellites to each other. It is difficult to know which radiometer produces the absolutely correct radiance in this scenario, but truth is likely to emerge from the long-term measurements by a multitude of satellites. In addition, airborne radiometers can be used as checkpoints for the long-term time series to provide calibration links to

the absolute standard. Also, further research on moon calibration may allow us to use it as an absolute calibration standard in the visible/near-infrared for the long-term time series according to NIST (http://www.nist.gov/physlab/div844/grp06/lusi.cfm).

Applications of the SNO method to microwave instruments have shown very promising results for climate change detection analysis. Several factors contributed to this success. First, the inter-satellite biases for microwave instruments appear to change little over the short term and slowly over the long term. Second, the microwave channel center frequencies are made to be stable and well known, which significantly reduces uncertainties related to spectral calibration. Third, each microwave instrument has its own onboard blackbody calibration, which keeps track of the instrument degradation independently. It is found that the SNO method works very well for microwave instruments sensing the mid-troposphere to upper stratosphere, where the uncertainty in the bias is much smaller than the instrument noise. For example, studies have demonstrates the excellent agreement on the order of 0.1 K for the 53.6 GHz channel of AMSU on NOAA-16 and -17 (Cao and Tobin 2008).

The application of the SNO method to the visible/near-infrared and infrared radiometers has great potential. Studies have shown that the SNO method is very effective in quantifying the inter-satellite biases for these channels. Since the biases are short-term invariant for the visible/near-infrared instruments, they can be used for intercalibrating the satellites for global data. The dry atmosphere and highly reflective surface for a broad range of solar zenith angles at the SNO sites in the polar regions are advantageous for calibrating these channels (Jaross et al. 1998; Masonis and Warren 2001). However, since the SNO method only provides a relative calibration between two satellites and none of the NOAA satellites has onboard calibration for the visible/near-infrared channels, the SNO calibration alone is not sufficient to produce a recalibrated long-term time series for these channels. This method would be more useful if one satellite can be relied on as a stable standard, such as in the intercalibration of MODIS and NOAA radiometers (Cao et al. 2008a; Heidinger et al. 2002), but the difference in the spectral response functions between them introduces uncertainties and makes the intercalibration difficult. Therefore, this spectral bias must be resolved in intercomparisons such as through hyperspectral analysis (Cao et al. 2010).

For infrared radiometers, studies have shown that the SNO method can quantify inter-satellite biases with uncertainties smaller than the instrument noise (Cao and Heidinger 2002). However, additional uncertainties exist when compared to that of the microwave and visible instruments. First, the calibration accuracy may vary over an orbit, as found for AVHRR (Wang and Cao 2008). Biases found at the SNOs may not be the same in other parts of the orbit, and the bias may be orbital and seasonal dependent. The inter-satellite bias can also depend on the scene radiance (Shi et al. 2008). The calibration accuracy may also change long term in response to a number of factors such as degradation and orbital drift. Second, for infrared sounders, small differences in spectral response functions may mean that a different layer of the atmosphere is observed, thus producing seasonal biases as the atmosphere changes over time.

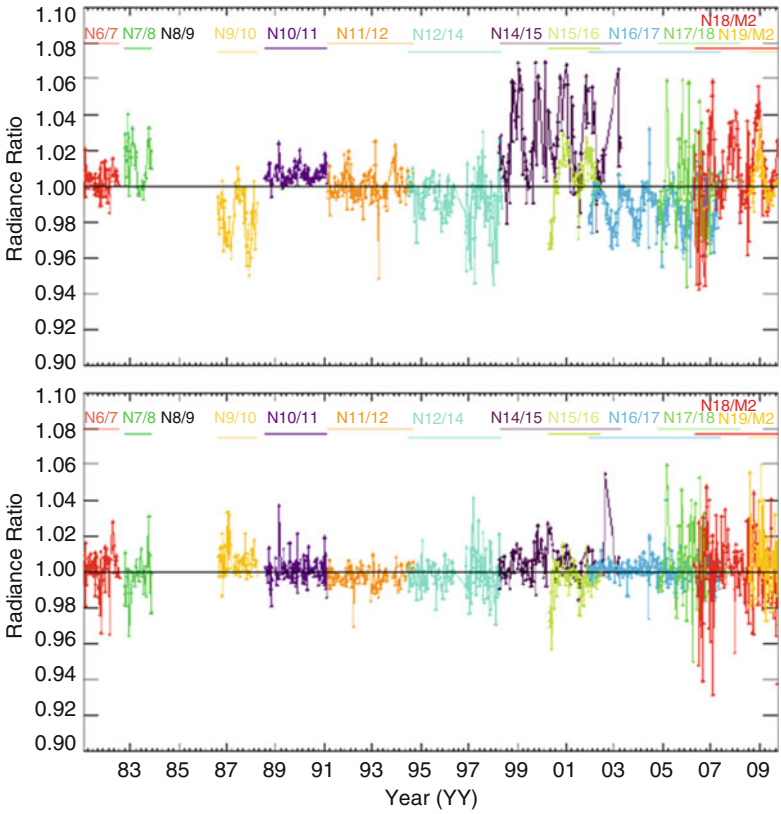

Fig. 2.5 HIRS SNO long-term time series for selected CO2 channels (channels 4 and 6)

An example of long-term SNO time series of HIRS is provided in Fig. 2.5 in the form of radiance ratios to show the inter-satellite biases. Among the 19 infrared channels of HIRS, channels 4 and 6 are shown here with a time span of 29 years. There are several observations that can be made from this figure. First, the inter-satellite biases for channel 4 vary much greater (as much as 6%) than those for channel 6. In fact, without comparing the time series of these two channels, the bias variability in channel 4 would lead us to believe that this may be due to major performance differences at the HIRS instrument level. On the other hand, analysis of channel 6 time series suggests that the inter-satellite biases are in fact small (mostly within 1%) for this channel during the same time period. Further investigation reveals that channel 6 is situated in a relatively flat spectral region of the atmospheric profile, while channel 4 is on a steeper gradient of this profile and is therefore more sensitive to spectral differences between satellites for this channel. Therefore, the large biases for channel 4 are likely due to spectral issues related to the spectral response functions, or spectrally induced biases (Cao et al. 2008b). This means in order to develop consistent long-term time series from HIRS, the spectral

differences and uncertainties have to be resolved in the recalibration. This type of problem is significantly reduced with hyperspectral sounders such as AIRS and IASI, which are both spectrally resolved and contributed to the excellent agreement between them (Wang 2009, personal communications).

The second feature from Fig. 2.5 is that the largest bias occurred between NOAA-14 and NOAA-15 HIRS which oscillates seasonally. This was further investigated in a study (Cao et al. 2008b) which demonstrated that spectral uncertainty in the HIRS on either NOAA-14 or NOAA-15 is likely the culprit, and a spectral shift is necessary to reproduce this large bias based on studies with IASI spectra. This also suggests that prelaunch characterization of spectral response functions is critical for postlaunch instrument performance.

Finally, it is evident that for both channels 4 and 6, the inter-satellite biases between HIRS on NOAA-18 and other satellites have large variability. This is due to the fact that NOAA-18 HIRS has a loose lens problem which introduces large noise for all long-wave channels. Apparently, instrument noise increases the uncertainty in SNO time series analysis.

On the other hand, given the relatively low noise for most of the operational instruments, in general, noise is not the major constraint in the inter-satellite analysis. Studies have shown that the SNO method can resolve inter-satellite biases on the order of 0.1 K in the sounding channels of the microwave and infrared instruments and 1% in the visible/near-infrared imagers (Cao et al. 2005a, b, 2008a). In both cases, the uncertainty is larger than the instrument noise levels.

The SNO method has its limitations. First, since the SNOs occur at many different locations in the polar regions, the spectral characteristics of the SNO sites are not yet well quantified and introduce uncertainties in the intercalibration of window channels. Second, while the SNO method works well for the sounding channels in the microwave and infrared, larger uncertainties are found for low-resolution surface channels where surface inhomogeneity and pointing accuracy become the limiting factors (Cao et al. 2005a, b, 2009; Zou et al. 2006). Third, for the infrared window channels (and some infrared sounding channels), the temperature at the SNO (below 280 K) is limited to a narrow range which does not cover the full range of the global surface temperature. Fourth, for the infrared instruments, inter-satellite biases at the SNO points may not be representative of the biases over an orbit due to orbital variations of calibration accuracy in response to fluctuations in instrument temperature and stray light in certain parts of the orbit (Cao et al. 2001, 2004; Trishchenko et al. 2002). Finally, the SNO method is very sensitive to geo-location and sampling errors, for example, the AVHRR 4 KM GAC (Global Area Coverage) data does not have an optimal match with the MODIS 1KM data due to the sampling scheme used in AVHRR, which introduces uncertainties in intercalibrating AVHRR and MODIS.

Significant progress has been made intercalibrating GOES and POES radiometers in recent years under the World Meteorological Organization's (WMO) Global Space-based Inter-calibration System (GSICS) program, extending the existing work in this area (Gunshor et al. 2004). Conceptually, since the GOES nadir is fixed at a given location and the POES satellites pass the GOES nadir point regularly, it would seem to be an ideal configuration for intercalibration. However, there are several challenges.

First, the GOES radiometers have a lower calibration accuracy than their polar counterparts. For example, the current GOES imager calibration accuracy is 1 K, compared to 0.5 K for AVHRR. The large diurnal variation in the GOES instrument temperature, on the order of nearly 30 K, presents a challenge in intercalibration with POES radiometers, which has an orbital temperature variation of 2–3 K. Second, although the GOES nadir has a fixed location on the Earth, it does not necessarily observe the nadir at the time of POES overpass because it takes ~30 min for GOES to perform a complete scan of the Earth. As a result, the simultaneity between POES and GOES is typically around 15 min, compared to 30 s in the SNO method. The fast scanning capability on future GOES-R/ABI will significantly improve the simultaneity which will reduce the uncertainties.

Earth targets such as the Libyan Desert, Antarctica, and deep convective clouds have been used for vicarious calibration of visible/near-infrared channels. However, this strategy for inter-satellite calibration is affected by observation time differences and uncertainties introduced by bidirectional reflectance factors of the surface and the intervening atmosphere. Vicarious calibration can achieve inter-sensor calibration with ~2% accuracy, but differences of 4–10% are not uncommon (Green and Pavri 2002; Thome, 2006, personal communication). An extensive inter-satellite calibration campaign using the Dome C site has been coordinated under the CEOS/Working Group on Calibration/Validation (Cao et al. 2010) using this approach.

It is possible to use the Moon for intercalibration of radiometers on different satellites, as demonstrated in studies with MODIS, SeaWiFS and other instruments (Barnes et al. 2004; Xiong et al. 2005). There are significant advantages with this approach. The Moon has a stable reflectance (Kieffer 1997), and inter-satellite calibration using the Moon is not affected by observation gaps between satellites if the Moon is used as an absolute calibration standard. Consistency at the 1% level has been demonstrated for intercalibration of the MODIS on Aqua and Terra using the Moon. However, instrument design can impose a potential limitation to using the Moon for calibration. For example, the AVHRR space clamp circuitry makes the lunar calibration approach difficult (Cao et al. 2009). Spacecraft maneuvers to view the Moon are possible for some missions but may be impractical for other missions. Currently, the Moon is only used for the calibration of the visible/near-infrared channels. There are significant challenges to using the Moon for calibrating infrared instruments, and the feasibility of lunar calibration for microwave instruments has yet to be investigated.

Satellite mission overlap is essential to most intercalibration techniques. This requires not only time overlap and consistency in local observation time but also assurance of spectral continuity in channel selection between satellites. For example, channel discontinuities were created when the HIRS channel 10 center wavenumbers were changed over the course of the NOAA satellite series. The small frequency change from MSU channel 2 to AMSU channel 5 also created problems in climate change detection (Iacovazzi and Cao 2007). Such changes should be avoided, if possible, in mission requirements.

2.5 Future Developments

It is a significant challenge to calibrate the operational satellite instruments for climate change detection. As a result, further developments in many areas are needed. First, in order to establish consistency through inter-satellite calibration, uncertainties in the SNO method should be further reduced with SNO site characterization using highly accurate spectral, spatial, BRDF (bidirectional reflectance distribution function), and elevation models. This will be especially helpful for the window or surface channels. The reduced uncertainty will allow us to better quantify the inter-satellite biases and small trends in the satellite measurements. Long-term observation of vicarious sites such as the Dome C, Libyan Desert, and other sites with stable instruments will provide independent site stability and calibration accuracy assessments. International collaboration under the WMO/GSICS and CEOS facilitate data sharing and allow us to intercalibrate radiometers globally to establish a calibration reference network and a quasi on-orbit standard.

Further improvements in onboard calibrators, that is, blackbody in the infrared and microwave, and multiple solar diffusers in the visible/near-infrared will reduce calibration uncertainties and facilitate the establishment of on-orbit calibration standard. For instruments with onboard calibration, not only the biases between satellites but also the root cause of the biases should be investigated. This is because bias correction without knowing the root cause can be unreliable. Once the root cause is identified, this information can be used as feedback to the instrument development process to improve the calibration of future models.

For the microwave instruments, further improvement in the prelaunch nonlinearity and sidelobe characterization is highly desirable. Knowledge of nonlinearity is critical for decadal climate change detection. Further improvements in instrument noise would significantly reduce the uncertainties in the SNO analysis, since sample size is relatively small at the SNOs for these instruments. Also, the possibility of long-term nonlinearity change, spectral response, and frequency drift should be investigated.

For infrared instruments, intercalibrations between sounders and imagers on the same satellite are very valuable. Since both types of instrument are on the same spacecraft and simultaneous Earth views are available globally, accurate intercalibration, both radiometrically and spectrally, is possible (Tobin et al. 2006; Wang and Cao 2008). Recent analysis of MetOp data show that the HIRS has a more stable calibration than that of AVHRR when both are compared to IASI on MetOp IASI. This will help us use HIRS to calibrate AVHRR historical data since both are on the same spacecraft. As more and more hyperspectral sounders become available, this type of inter-sensor calibration will become more valuable.

Uncertainties in the spectral response functions (SRF) have been a major issue for optical instruments, including the prelaunch measurement uncertainties, SRF differences between instruments, and SRF changes over time. The lack of stringent requirement in the prelaunch testing, the inability to make identical SRFs, and the lack of on-orbit spectral calibration devices are the root causes of these problems. It

is recognized that while this issue is being resolved with hyperspectral systems, it will remain to be an issue for broadband instruments, and new technologies are desirable to introduce fundamental changes in these areas. One such technology on the horizon is the quantum cascade laser (or tunable laser) calibration systems which potentially will allow us to perform on-orbit spectral and radiometric calibration. The use of such systems for vicarious calibration should also be explored in the future.

2.6 Concluding Remarks

It is essential to establish the on-orbit calibration consistency among all Earth-observing satellite radiometers for climate change detection, numerical weather prediction, reanalysis, and implementation of GEOSS. This presents a significant challenge to the current operational satellite radiometers in space, and therefore rigorous calibration and intercalibration are needed. On-orbit calibration traceability is required for all radiometers, which can be achieved by establishing the long-term time series of inter-satellite calibration at the SNOs, GEO/LEO nadir points, and selected vicarious sites for a constellation of operational satellites. This will tie all satellite radiometers together to provide traceability of individual satellites to a calibration reference network. The absolute accuracy can then be established through absolute on-orbit radiometers such as those on the CLARREO (Climate Absolute Radiance and Refractivity Observatory) and with the help of in situ and aircraft campaigns. The system will help us diagnose radiance biases for reanalysis, data assimilation, and time series analysis for climate change detection. It will also bring together a world of radiometers to facilitate the implementation of GEOSS.

Acknowledgements The authors would like to thank Drs. Pubu Ciren, Likun Wang, and Bob Iacovazzi for providing part of the data used in this chapter. We also thank Dr. Lawrence Flynn of NOAA/NESDIS/STAR and Dr. Shucai Guan of NOAA/NCEP/NCO for a critical review of the manuscript with constructive comments and suggestions. The manuscript contents are solely the opinions of the author and do not constitute a statement of policy, decision, or position on behalf of NOAA or the US government.

References

Barnes RA, Eplee RE, Patt FS, Kieffer HH, Stone TC, Meister G, Butler JJ, McClain CR (2004) Comparison of SeaWiFS measurements of the moon with the U.S. Geological survey lunar model. Appl Opt 43:5838–5854

Cao C, Heidinger A (2002) Inter-comparison of the longwave infrared channels of MODIS and AVHRR/NOAA-16 using simultaneous nadir observations at orbit intersections, Earth observing systems VII. In: Barnes W (ed) Proceedings of SPIE, vol 4814, Seattle, 2002, pp 306–316

Cao C, Tobin D (2008) Inter-calibration of instruments. In: Ohring G (ed) Achieving satellite instrument calibration for climate change. NOAA/NESDIS/STAR Publication, p 144

Cao C, Weinreb M, Sullivan J (2001) Solar contamination effects on the infrared channels of the AVHRR. J Geophys Res 106(D24):33463–33469

Cao C, Weinreb M, Xu H (2004) Predicting simultaneous nadir overpasses among polar-orbiting meteorological satellites for the inter-satellite calibration of radiometers. J Atmos Ocean Technol 21:537–542

Cao C, Ciren P, Goldberg M, Weng F, Zou C (2005a) Simultaneous nadir overpasses for NOAA-6 to NOAA-17 satellites from 1980 to 2003 for the inter-satellite calibration of radiometers. NOAA technical report NESDIS 118, p 74

Cao C, Xu H, Sullivan J, McMillin L, Ciren P, Hou Y (2005b) Inter-satellite radiance biases for the High-Resolution Infrared Radiation Sounders (HIRS) on board NOAA-15,-16 and -17 from simultaneous nadir observations. J Atmos Ocean Technol 22:381–395

Cao C, Xiong X, Wu A, Wu X (2008a) Assessing the consistency of AVHRR and MODIS L1B reflectance for generating fundamental climate data records. J Geophys Res 113:D09114. doi:10.1029/2007JD009363, 10 pp

Cao C, Goldberg M, Wang L (2008b) Spectral bias estimation of historical HIRS using IASI observations for improved fundamental climate data records. J Atmos Ocean Technol 26:1378–1387

Cao C, Vermote E, Xiong X (2009) Using AVHRR lunar observations for NDVI long-term climate change detection. J Geophys Res 114:D20105. doi:10.1029/2009JD012179, 9 pp

Cao C, Uprety S, Xiong X, Wu A, Jing P, Smith D, Chander G, Fox N, Ungar S (2010) Establishing the Antarctic Dome C community reference standard site towards consistent measurements from earth observation satellites. Can J Remote Sens 36:498–513

Christy JR, Spencer RW, Lobel ES (1998) Analysis of the merging procedure for the MSU daily temperature time series. J Climate 11:2016–2041

Green RO, Pavri B (2002) AVIRIS in-flight calibration experiment results for 2001. In: Green RO (ed) Proceedings of the 11th JPL airborne earth science workshop, JPL Pub. 03-4, Jet Propulsion Laboratory, Pasadena, pp 125–137

Gunshor MM, Schmit TJ, Menzel WP (2004) Inter-calibration of the infrared window and water vapor channels on operational geostationary environmental satellites using a single polar-orbiting satellite. J Atmos Ocean Technol 21:61–68

Heidinger A, Cao C, Sullivan J (2002) Using MODIS to calibrate AVHRR reflectance channels. J Geophys Res 107(D23):4702. doi:10.1029/2001JD002035, 10 pp

Iacovazzi R, Cao C (2007) Quantifying EOS-aqua and NOAA POES AMSU – a brightness temperature biases for weather and climate applications utilizing the SNO method. J Atmos Ocean Technol. doi:10.1175/JTECH2095.1

Jaross G, Krueger AJ, Flittner D (1998) Multispectral calibration of remote-sensing instruments over Antarctica. Metrologia 35:625–629

Kieffer HH (1997) Photometric stability of the lunar surface. Icarus 130(2):323–327

Masonis SJ, Warren SG (2001) Gain of the AVHRR visible channel as tracked using bidirectional reflectance of Antarctica and Greenland snow. Int J Remote Sens 22(8):1495–1520

Shi L, Bates J, Cao C (2008) Scene temperature dependent HIRS inter-satellite biases. J Atmos Ocean Technol 25:2219–2229

Tobin DC, Revercomb HE, Moeller CC, Pagano T (2006) Use of atmospheric infrared sounder high-spectral resolution spectra to assess the calibration of moderate resolution imaging spectroradiometer on EOS aqua. J Geophys Res 111:D09S05. doi:10.1029/2005JD006095, 15 pp

Trishchenko AP, Fedosejevs G, Li Z, Cihlar J (2002) Trends and uncertainties in thermal calibration of AVHRR radiometers onboard NOAA-9 to NOAA-16. J Geophys Res 107:4778. doi:10.1029/2002JD002353, 13 pp

Vinnikov KY, Grody NC (2003) Global warming trend of mean tropospheric temperature observed by satellites. Science 302(5643):269–272

Wang L, Cao C (2008) On-orbit calibration assessment of AVHRR longwave channels on MetOp–a using IASI. IEEE Trans Geosci Remote Sens 46(12):4005–4013

Xiong X, Che N, Barnes WL (2005) Terra MODIS on-orbit spatial characterization and performance. IEEE Trans Geosci Remote Sens 43:355–365

Zou C, Goldberg M, Cheng Z, Grody N, Sullivan J, Cao C, Tarpley D (2006) Recalibration of microwave sounding unit for climate studies using simultaneous nadir overpasses. J Geophys Res 111:D19114. doi:10.1029/2005JD006798, 24 pp

Chapter 3
MODIS Instrument Characteristics, Performance, and Data for Climate Studies

Vincent V. Salomonson and Xiaoxiong Xiong

Abstract The Moderate Resolution Imaging Spectroradiometer (MODIS) is an instrument designed for comprehensive studies of land, ocean, and atmosphere processes and trends. The first MODIS was launched on the NASA Terra spacecraft in December 1999 into a sun-synchronous orbit with an equator crossing time at 10:30 a.m. The second MODIS was launched on the NASA Aqua spacecraft in May 2002 into a sun-synchronous orbit with an equator crossing time at 1:30 p.m. This chapter describes the procedures leading to carefully calibrated, characterized, and consistent Level 1B observations that are subsequently being confidently used to produce higher-level products contributing to studies of climate change. Illustrative results achieved to date over the 10–12 years that MODIS has been operating are provided. With the successful launch and operation of a very similar instrument called the Visible and Infrared Imaging Radiometer Suite (VIIRS) on October 28, 2011 on the Suomi NPP (National Polar-orbiting Partnership) satellite, there is a firm commitment to obtain observations consistent with MODIS for the foreseeable future.

Keywords Moderate Resolution Imaging Spectroradiometer • MODIS • Calibration • Characterization • Climate data products • Visible Infrared Imager Radiometer Suite • VIIRS

V.V. Salomonson (✉)
Atmospheric Sciences, University of Utah, 135 S 1460 East Rm 819 (WBB), Salt Lake City, UT 84112-0110, USA
e-mail: vincesalomonson@msn.com

X. Xiong
Code 614.4, NASA/GSFC, Greenbelt, MD, USA
e-mail: Xiaoxiong.Xiong-1@nasa.gov

J.J. Qu et al. (eds.), *Satellite-based Applications on Climate Change*,
DOI 10.1007/978-94-007-5872-8_3,

3.1 Introduction

The Moderate Resolution Imaging Spectroradiometer (MODIS) is an instrument designed for comprehensive studies of land, ocean, and atmosphere processes and trends (Esaias 1986; Salomonson et al. 1989). It was launched on the Terra and Aqua spacecrafts that represent key missions of the NASA Earth Observing System (EOS) conceived originally as "System Z" in the 1970s and implemented progressively through launch of several, coordinated missions formally starting from 1997 to the present (Salomonson et al. 2011; Parkinson et al. 2006; http://eospso.gsfc.nasa.gov/eos_homepage/mission_profiles/index.php). The Terra spacecraft was launched in December 1999 into a sun-synchronous orbit with equator crossing time nominally at 10:30 a.m., and the first observations became available in February 2000. The Aqua spacecraft was launched in May 2002 into a sun-synchronous orbit with an equator crossing time nominally at 1:30 p.m., and the first observations became available in June 2002.

This chapter will describe characteristics of the total MODIS effort with emphasis on aspects that relate to the use of the MODIS instrument and attendant data products for studies of the climate of the Earth. The principal emphasis will be on describing procedures and results that have so far (as of early 2012) led to the data being calibrated and characterized so as to yield consistent Level 1B observations that subsequently can be reliably and confidently used to produce climate-related products. First, the characteristics of the MODIS instrument will be described along with the extensive efforts to calibrate the instrument and characterize its performance over more than a decade. In later sections, the availability of data products will provided along with examples illustrating the present and future potential for climate studies. Next, a brief description of the operational environmental follow-on instrument similar to MODIS called the Visible Infrared Imager Radiometer Suite (VIIRS) will be described. Lastly, concluding remarks describe some of the challenges foreseen as data from MODIS and VIIRS are acquired, checked, and studied for their integrity and continued use for climate studies.

3.2 MODIS Instrument Characterization and Performance

The MODIS instrument was developed with improvements over heritage sensors in terms of its spectral, spatial, and temporal resolutions and with rigorous, stringent calibration requirements. The heritage sensors include the Advanced Very High Resolution Radiometer (AVHRR) and the High Resolution Infrared Radiation Sounder (HIRS) that fly on National Oceanic and Atmospheric Administration (NOAA) environmental satellites, the Landsat Thematic Mapper (TM), the Coastal Zone Color Scanner (CZCS), and the Sea-viewing Wide Field-of-view Sensor (SeaWiFS). Band selection for the MODIS instrument was guided by the bands existing on all these sensors. The MODIS instrument, in particular, and in terms related to global, daily coverage, complements and enhances observations from the AVHRR (still operating) and the CZCS that dated back to 1978 and was followed

by the very successful SeaWiFS instrument that begin operation in 1997 and ceased operating in December 2010.

The MODIS is a cross-track, "whisk broom" radiometer that provides observations in 36 spectral bands (see Table 3.1 and Fig. 3.1) covering wavelengths from 0.41 to 14.4 μm and at three nadir spatial resolutions: 250 m, 500 m, and 1 km. Together Terra and Aqua MODIS have produced more than 10 years of global data sets that have significantly helped scientists worldwide to better understand the Earth as an interacting system and the impacts on this system due to human-related activities.

The calibration performance requirements for the instrument (at a typical radiance and within scan angles of ±45°) are 5% radiance absolute accuracy and 2% reflectance accuracy relative to the sun in the reflected solar radiation bands (RSB). For the thermal infrared bands (TIR), the requirements are ±1% radiance accuracy for the majority of the bands, but ±0.75% for band 20, ±10% for band 21, and ±0.5% for bands 31 and 31. A more detailed description of the MODIS instrument and on-orbit performance is provided by Xiong et al. (2009). Additionally the location of the observations ("pixels") on the Earth surface was required to be 150 m (rms) with a goal of 50 m (rms).

In order to maintain on-orbit calibration and data product quality expressed as the requirements noted previously, MODIS was built with a very capable set of onboard calibrators (OBCs), including a solar diffuser (SD), a solar diffuser stability monitor (SDSM), a blackbody (BB), a deep space view (SV) port, and a spectroradiometric calibration assembly (SRCA). These calibrators along with the monitoring of selected ground-based target areas, plus deep space and the moon as seen through the space view port, have been used to monitor and assess the performance of the instrument since launch. These calibration devices are very important and necessary because one cannot simply rely on the prelaunch instrument characterization (which was extensive) due to on-orbit degradation or change in the reflective optical surfaces, the emissive properties of instrument components, and the change in the properties of detectors and the calibration sources themselves (e.g., the solar diffuser), plus the possibility as seen prior to the launch of the Terra and Aqua missions that changes that could occur in the registration of the bands and included detectors relative to each other and spectral shifts in the bands on-orbit. Figures 3.1 and 3.2 depict the various calibration devices.

Both instruments have been shown to be operationally stable over the 10 or more years of operation (i.e., through to early 2012). The temperature variations of the warm focal plane assemblies of both instruments have been no more than 3.5° in the case of the Terra MODIS and 2° for the Aqua MODIS. The cold focal plane assemblies have shown a small temperature increase in recent years of less than 0.1 K/year. The temperature of the blackbody is nominally set at 285 K and has been relatively constant. The blackbody temperature of the Terra MODIS has only changed 30 m-K over 12 years and the Aqua MODIS effectively zero degrees over 10 years.

There, however, have been significant changes in other components that had to be accommodated. The visible spectral bands (VIS) have shown relatively large changes in detector responses (or gains). The changes are different at the varying

Table 3.1 Overall characteristics of the MODIS instrument on the NASA Earth Observing System (EOS) Aqua and Terra spacecrafts

Orbit:	705 km, 10:30 a.m. descending node or 1:30 p.m. ascending node, sun-synchronous, near-polar, circular
Scan rate:	20.3 rpm, cross track
Swath dimensions:	2,330 km (across track) by 10 km (along track at nadir)
Telescope:	17.78 cm diam. off-axis, afocal (collimated), with intermediate field stop
Size:	1.0 × 1.6 × 1.0 m
Weight:	250 kg
Power:	225 W (orbital average)
Data rate:	11 Mbps (peak daytime)
Quantization:	12 bits
Spatial resolution:	250 m (bands 1–2)
(at nadir):	500 m (bands 3–7), 1,000 m (bands 8–36)
Design life:	5 years

Primary use	Band	Bandwidth[a]	Spectral radiance[b]	Required SNR[c]
Land/cloud boundaries	1	620–670	21.8	128
	2	841–876	24.7	201
Land/cloud properties	3	459–479	35.3	243
	4	545–565	29.0	228
	5	1,230–1,250	5.4	74
	6	1,628–1,652	7.3	275
	7	2,105–2,155	1.0	110
Ocean color phytoplankton biogeochemistry	8	405–420	44.9	880
	9	438–448	41.9	838
	10	483–493	32.1	802
	11	526–536	27.9	754
	12	546–556	21.0	750
	13	662–672	9.5	910
	14	673–683	8.7	1,087
	15	743–753	10.2	586
	16	862–877	6.2	516
Atmospheric water vapor	17	890–920	10.0	167
	18	931–941	3.6	57
	19	915–965	15.0	250

Primary use	Band	Bandwidth[a]	Spectral radiance[b]	Required NEAT (K)[d]
Surface/cloud temperature	20	3.660–3.840	0.45	0.05
	21	3.929–3.989	2.38	2.00
	22	3.929–3.989	0.67	0.07
	23	4.020–4.080	0.79	0.07
Atmospheric temperature	24	4.433–4.498	0.17	0.25
	25	4.482–4.549	0.59	0.25
Cirrus clouds	26	1.360–1.390	6.00	150[e]
Water vapor	27	6.535–6.895	1.16	0.25
	28	7.175–7.475	2.18	0.25
	29	8.400–8.700	9.58	0.05

(continued)

Table 3.1 (continued)

Primary use	Band	Bandwidth[a]	Spectral radiance[b]	Required NEAT (K)[d]
Ozone	30	9.580–9.880	3.69	0.25
Surface/cloud temperature	31	10.780–11.280	9.55	0.05
	32	11.770–12.270	8.94	0.05
Cloud top altitude	33	13.185–13.485	4.52	0.25
	34	13.485–13.785	3.76	0.25
	35	13.785–14.085	3.11	0.25
	36	14.085–14.385	2.08	0.35

[a]Bands 1–19 nm; bands 20–36 μm
[b]W/m^2-μm-sr
[c]*SNR* signal-to-noise ratio
NEΔT noise-equivalent temperature difference: } performance goal is 30–40% better than required
[d]SNR

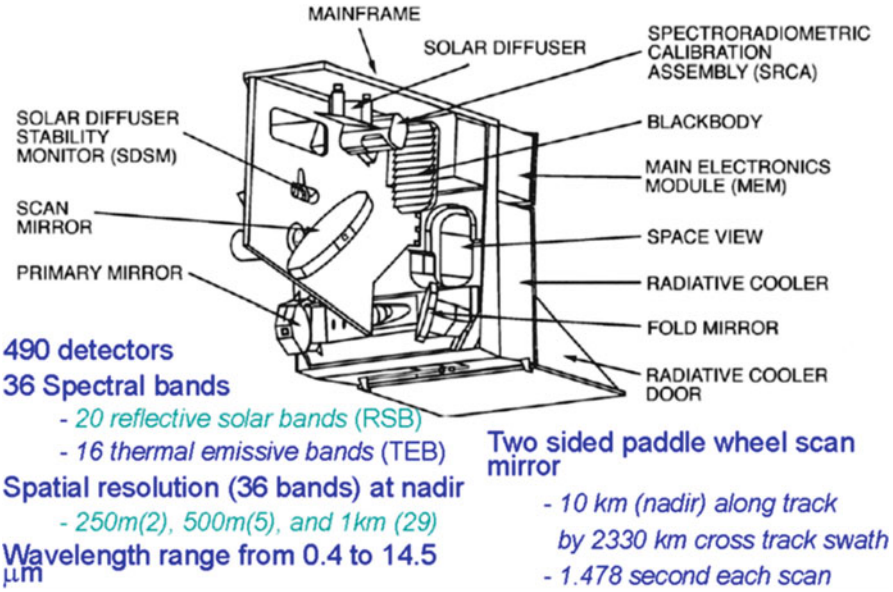

Fig. 3.1 MODIS instrument cavity and its onboard calibrators: solar diffuser (*SD*), solar diffuser stability monitor (*SDSM*), blackbody (*BB*), and spectroradiometric calibration assembly (*SRCA*). Other key characteristics of the MODIS are illustrated in this figure

angle of incidence of the reflected solar radiation on the MODIS scanning mirror, and, in the case of the Terra MODIS, it depends on which side of the mirror is involved, i.e., mirror side 1 (ms1) or mirror side 2 (ms2). This difference occurred due to a procedural anomaly that occurred during the prelaunch testing of the Terra MODIS. No such difference has to be accounted for in the case of the Aqua MODIS. Figure 3.3 depicts the changes in Terra MODIS detector responses. For the near-infrared (NIR), the short-wave infrared (SWIR), and thermal infrared emissive bands (TEB), the changes in detector responses have been generally small.

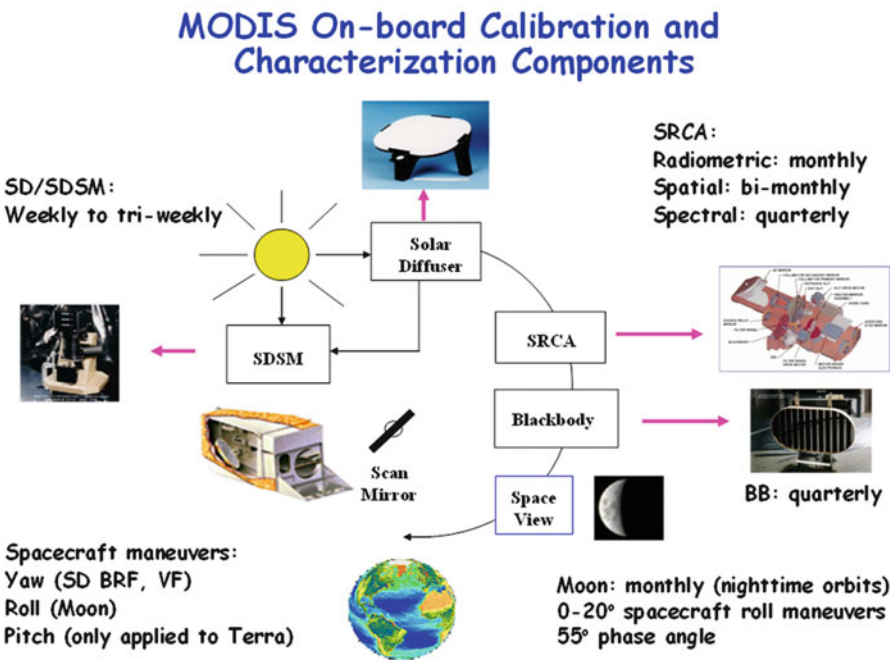

Fig. 3.2 Calibration and characterization components of the Aqua and Terra MODIS instruments including the frequency for their application

Additionally, the solar diffuser (SD) showed some degradation that was particularly significant at the shorter wavelengths (e.g., bands 3, 8, 9, and 10). Figure 3.4 shows the extent of the changes in the solar diffuser properties for both instruments. These changes were observed by the solar diffuser stability monitor (SDSM). The wavelengths of SDSM detectors (1–8) are as follows: 0.41, 0.47, 0.53, 0.55, 0.65, 0.75, 0.86, and 0.90 μm. The largest changes occurred at the shortest wavelengths and become progressively smaller as the wavelengths become larger. In the case of the Terra SD, the door covering the opening to the solar diffuse experienced difficulties and was left open to insure that proper measurements could be provided. Leaving the door caused much larger exposure of the solar diffuser to the sun and thus greater degradation in wavelength response over time. In the case of the Aqua SD, the SD/SDM calibration frequency has been gradually reduced at about 2,200 days into the mission to lengthen the lifetime of the SD door opening and closing mechanism and is now done every 6 weeks as compared to weekly at the beginning of the Aqua mission.

Most of the other MODIS components have been relatively stable and generally meet requirements. For instance, most of the detectors (475 out of 490) continue to meet sensor design signal-to-noise (SNR) requirements. The on-orbit spectral and spatial performance (e.g., band shifts or spatial registration of bands to each other) have largely remained quite stable and within specifications (0.1 km) over the

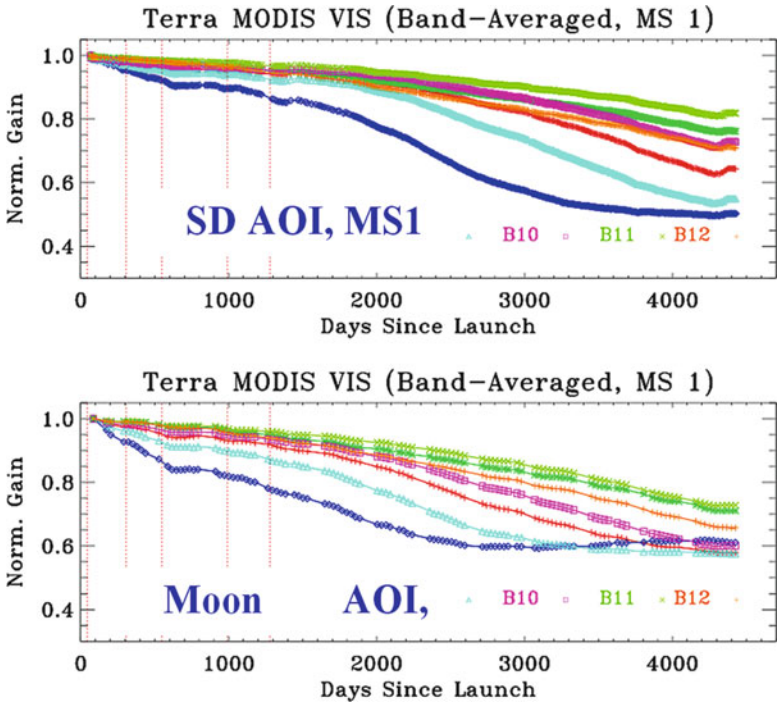

Fig. 3.3 Variation in detector response for the Terra MODIS (days since launch) for the angle of incidence (*AOI*) relative to the solar diffuser (SD—AOI = 50.2°) and when looking at the moon (AOI = 11.2°), showing the mirror side 1 (*MS-1*) example. Similar changes have occurred for the Aqua MODIS

lifetime of the instruments up through 2011. An exception is the registration of the cold focal plane bands relative to the warm focal plane bands for the Aqua MODIS instrument by 0.2–0.35 km. That this aspect did not meet specifications was known prior to launch, but approval to go back in and fix this problem was not approved due to budgetary considerations. The offset has remained constant during the operation of both instruments. In the vast majority of instances, this exception has not created insurmountable problems in the research accomplished using the MODIS data.

The calibration consistency of the MODIS instruments can also be validated using carefully selected "ground-truth sites" that are uniform and stable in their characteristics over time or for which there are good, independent data corroborating the MODIS observations. One area that has been used is located on the Antarctic Plateau and is called the Dome Concordia ("Dome C") site at 75.102° south and 12.395° east (see Wenny and Xiong 2008). Other sites include one in the Libyan Desert and selected deep convective clouds (see Doelling et al. 2011). An example is shown in Fig. 3.5 for surface temperature (band 31—see Table 3.1) observed over the Dome C site. The mean difference between the Aqua and Terra

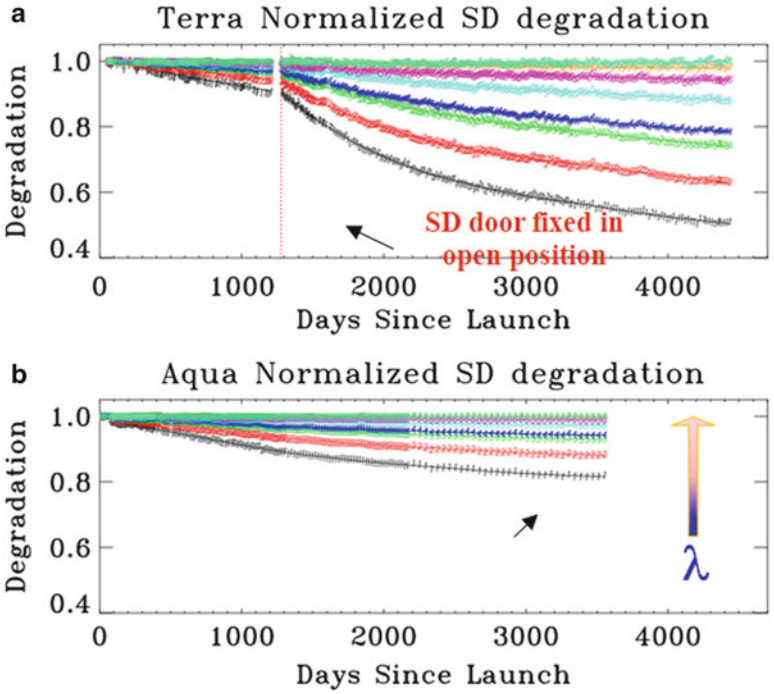

Fig. 3.4 Illustrations of the degradation in the solar diffuser (*SD*) surface over the operation of the Terra (**a**) and Aqua (**b**) MODIS instruments

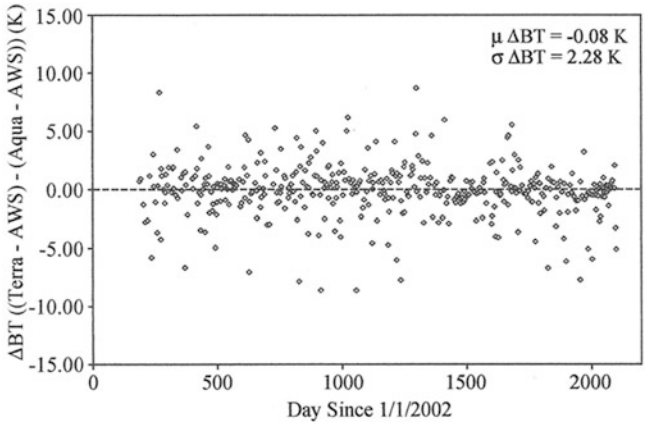

Fig. 3.5 Relative bias trend between the Terra and Aqua MODIS estimates of surface temperature (band 31) using the Automatic Weather Station data at Dome C (For more in-depth discussion of these results, see Wenny and Xiong (2008))

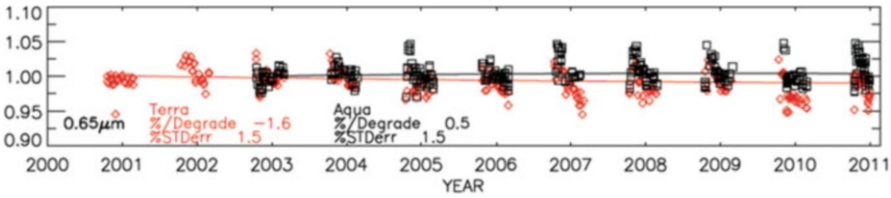

Fig. 3.6 Trends in the reflectance observed by the MODIS band 1 (0.620–0.670 μm) (see Doelling et al. (2011))

MODIS is only 0.08 K over more than 2,000 days. This is well within the calibration uncertainty for band 31.

Similarly using the "Dome C" site in Antarctica, along with other sites (deep convective clouds and the Libyan Desert), the trends in band 1 (0.620–0.670 μm) reflectance are also shown to be quite stable (see Fig. 3.6, Doelling et al. 2011).

As noted previously, the geolocation of MODIS observations was specified to be 150 m (rms) with a goal of 50 m (rms). Overall, the geolocation of MODIS observations has met the goal as illustrated in Fig. 3.7. An in-depth description of how the geolocation results have been obtained is given in Wolfe (2006).

3.3 MODIS Data Products

Relative to the use of MODIS observations, both for research (including climate research) and applications, the validity of the results fundamentally depends on the integrity of the radiances and reflectances provided from MODIS. All the aspects involved in the calibration and characterization of the MODIS in the previous section have to be accounted for and provided in the "Level 1B" products. Because of the many details involved, the processes are not described here, but they are fully described by Xiong et al. (2005a, b, 2006). These processes led to the results illustrated in Figs. 3.5 and 3.6 in the previous section.

In addition to the basic Level 1B products that serve as the basis for all subsequent MODIS products, there are nominally approximately 40 Level 2 and above products developed and maintained by the MODIS Science Team. A recent list of those products along with web locations for getting more information on these products follows below (see also http://modis.gsfc.nasa.gov/data/dataprod/index.php). The main facility producing MODIS products is the MODIS Adaptive Processing System (MODAPS) located at the NASA Goddard Space Flight Center. The data products for the Level 1B and atmosphere products are stored and distributed at the MODIS "Level 1 and Atmospheres Archive and Distribution System" (LAADS) also located at the NASA Goddard Space Flight Center in Maryland. The land products are stored and distributed at the Land Processes Distributed Active Archive Center (LPDAAC) located at the U.S. Geological Survey (USGS) Earth Resources Observation and Science (EROS) Center in

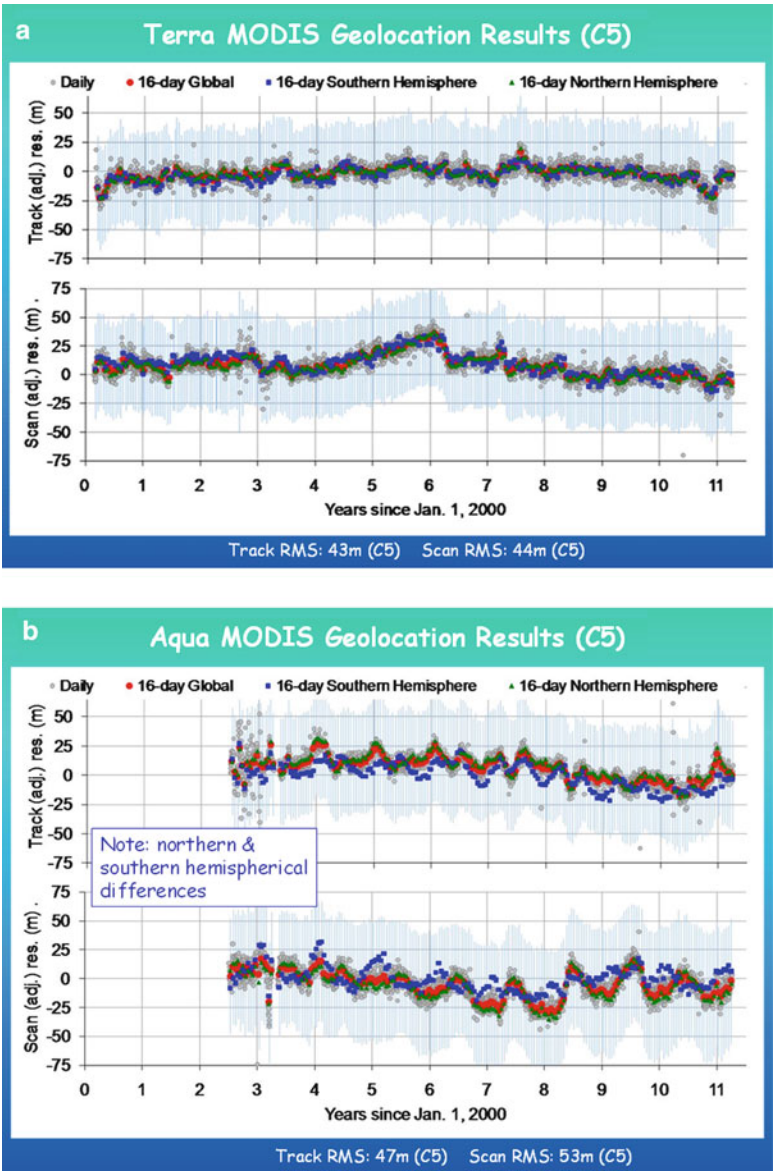

Fig. 3.7 Geolocation results for the Terra (**a**) and Aqua (**b**) MODIS as achieved in the "collection 5" (C5) reprocessing version

Sioux Falls, South Dakota. Cryosphere products are stored at the National Snow and Ice Data Center (NSIDC) in Boulder, Colorado. The MODIS ocean products are produced, archived, and distributed by the Ocean Color Data Processing System (OCDPS) located at NASA/Goddard Space Flight Center. As a note when one starts

retrieving specific products, one will find that the Terra MODIS products are designated by "MOD," and Aqua MODIS products are designated by "MYD." As of early 2012, there are in total several petabytes (10^{15} bytes) stored at the locations noted.

MODIS Calibration Products
(see also: http://mcst.gsfc.nasa.gov/)
MOD 01 – Level-1A Radiance Counts
MOD 02 – Level-1B Calibrated Geolocated Radiances
MOD 03 – Geolocation Data Set

MODIS Atmosphere Products
(see also: http://modis-atmos.gsfc.nasa.gov/)
MOD 04 – Aerosol Product
MOD 05 – Total Precipitable Water (Water Vapor)
MOD 06 – Cloud Products
MOD 07 – Atmospheric Profiles
MOD 08 – Gridded Atmospheric Product
MOD 35 – Cloud Mask

MODIS Land Products
(see also: http://edcdaac.usgs.gov/dataproducts.asp and http://modis-land.gsfc.nasa.gov/)
MOD 09 – Surface Reflectance
MOD 11 – Land Surface Temperature & Emissivity
MOD 12 – Land Cover/Land Cover Change
MOD 13 – Gridded Vegetation Indices (Max NDVI & Integrated MVI)
MOD 14 – Thermal Anomalies, Fires & Biomass Burning
MOD 15 – Leaf Area Index & FPAR
MOD 16 – Evapotranspiration
MOD 17 – Net Photosynthesis and Primary Productivity
MOD 43 – Surface Reflectance
MOD 44 – Vegetation Cover Conversion

MODIS Cryosphere Products
(see also: http://nsidc.org/daac/modis/index.html)
MOD 10 – Snow Cover
MOD 29 – Sea Ice Cover

MODIS Ocean Products
(Details about ocean products are best obtained by going to http://oceancolor.gsfc.nasa.gov/)
Angstrom Exponent
Aerosol Optical Thickness
Chlorophyll a
Downwelling diffuse attenuation coefficient at 490 nm
Photosynthetically Available Radiation
Particulate Inorganic Carbon

Particulate Organic Carbon
Remote Sensing Reflectance
Sea Surface Temperature (11 um daytime and nightime)
Sea Surface Temperature 4 um (nightime)

One essential aspect involved in the provision of the products from MODIS is the updating of the data to reflect new knowledge about the performance of the instrument and refinement of the algorithms as they are compared to ground truth and other information that show what improvements should and can be made. To date (early 2012) several "collections" or versions of the Level-1, land, and atmosphere data have been accomplished that have significantly improved the products. A "collection 6"/version 6 reprocessing is underway and will be largely completed in 2012. The ocean products have been reprocessed even more often so as to allow compatible observations with the SeaWiFS observations and Aqua MODIS observations in particular. MODIS Terra observations have also been reprocessed repeatedly to incorporate as much improvement as possible for use in biological oceanography studies. As noted above, the status of reprocessing for all MODIS products can be obtained by visiting the sites noted above in the products list.

A few examples of results using the MODIS data record with some key figures are noted below.

The first example (Fig. 3.8) shows the global, mean distribution of aerosol optical depth for 4 months derived from MODIS Aqua observations extending from 2002 to the present (2012). This information can be seen along with other MODIS atmosphere products at http://modis-atmos.gsfc.nasa.gov/products.html.

Another example from Hall et al. (2012) illustrates the use MODIS snow cover data over several years to evaluate the variability in depletion curves over several years on the Wind River Basin, Wyoming (see Fig. 3.9).

The third example comes from the processing of MODIS Aqua data for ocean products. The examples shown in Fig. 3.10 illustrate the annual concentration of chlorophyll-a concentration over the Aqua MODIS data record extending from 2002 to the present (2012). Several composites can be seen or obtained extending from daily composites to a composite of the entire mission.

3.4 The MODIS Operational Follow-On Instrument: VIIRS

From the point of view of continuing MODIS-like observations for climate studies, it is fortunate that the sensor called the Visible and Infrared Imaging Radiometer Suite (VIIRS) was launched successfully on October 28, 2011, on the Suomi NPP (National Polar-orbiting Partnership) satellite. The NPP mission is the first of the NASA/NOAA Joint Polar Satellite System (JPSS). By virtue of the JPSS being an "operational" system, there is a commitment to fly VIIRS on missions after NPP and thus obtain observations consistent with MODIS for the foreseeable future.

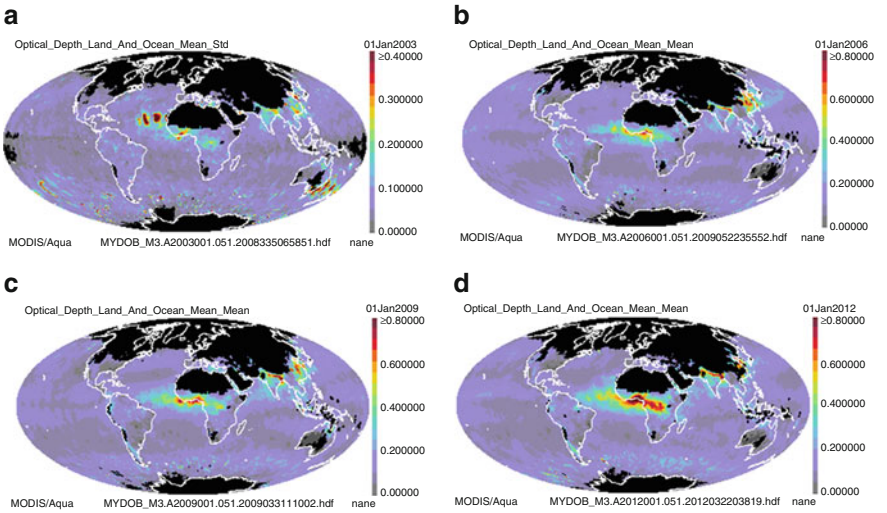

Fig. 3.8 Examples of Aqua MODIS monthly browse imagery: (**a**) mean aerosol optical depth for January 2003; (**b**) same for January 2006; (**c**) same for January 2009; (**d**) same for January 2012 (See for details: http://modis-atmos.gsfc.nasa.gov/MYD08_M3/browse_c51.html)

VIIRS is a derivative of the MODIS instruments on the Aqua and Terra missions with a large fraction of the capabilities found on MODIS along with some improvements in spatial resolution. A comparison of the MODIS and VIIRS is provided in Fig. 3.11 and Table 3.2 below.

The swath width of the VIIRS is 3,000 km, thereby providing total global daily coverage.

3.5 Summary and Concluding Remarks

In previous sections, it has been described that from launch to early 2012, the Aqua and MODIS instruments have been carefully calibrated and characterized, and adjustments made for instrument change over time. This has led to Level 1 and higher-level products that have been and can continue to be used reliably for research and applications including changes driven by climate change albeit the period of record is just a little over a decade.

As noted at the beginning of this chapter, MODIS observations extend and improve on observations provided by the AVHRR that begin in 1978. As of early 2012, that means some products (e.g., cloud cover, snow cover, normalized difference vegetation index (NDVI), sea surface temperature) derivable from both AVHRR and MODIS span over 30 years. Similarly Ocean Color products derived from the SeaWiFS starting in 1997, and now being extended by Aqua MODIS, cover nearly 15 years and perhaps a longer record depending on the utility of the

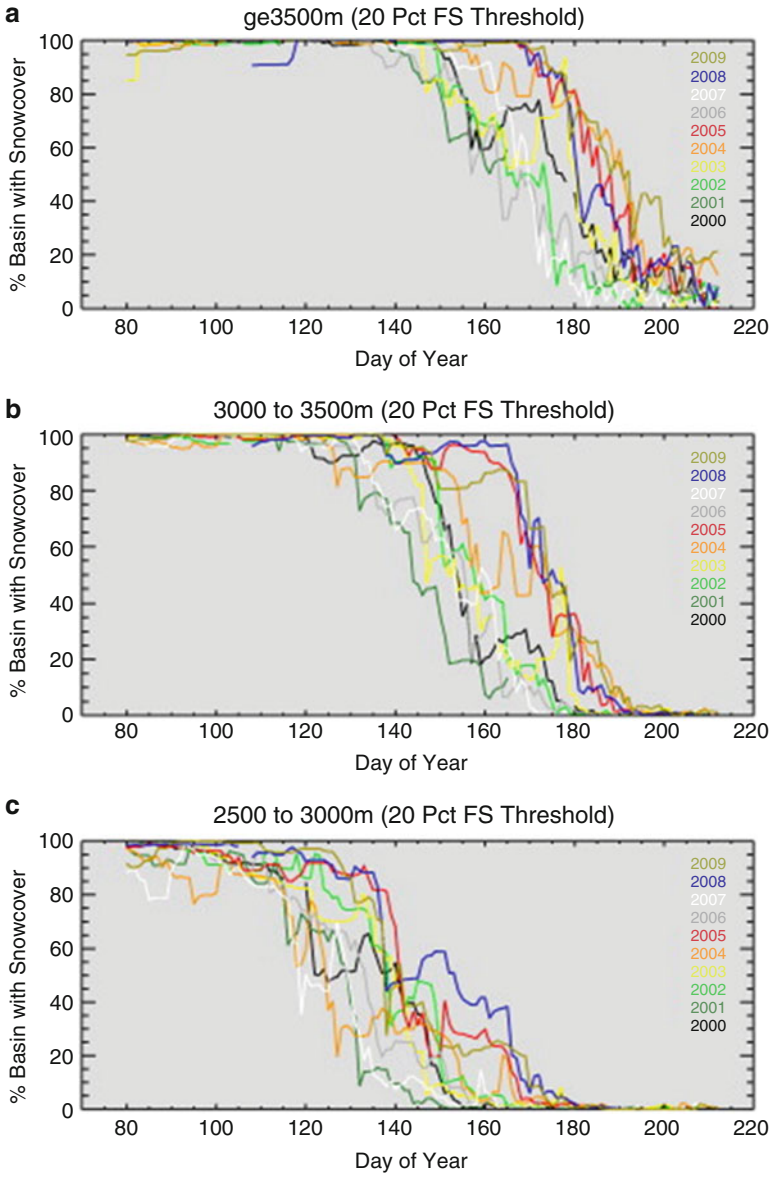

Fig. 3.9 Snow cover results from MODIS depletion of snow cover over several years. The curves are derived from the MODIS cloud-gap-filled (CGP) 500 m resolution product derived from the fractional snow cover product, MOD10A1, in the Wind River Range, Wyoming. Breaks are evident in the plots in some years due to sporadic mission MODIS data. (**a**) Elevation greater than or equal to 3,500 m; (**b**) Elevation from 3,000 to 3,500 m; (**c**) Elevation from 2,500 to 3,000 m (Figure 2 in Hall et al. 2012)

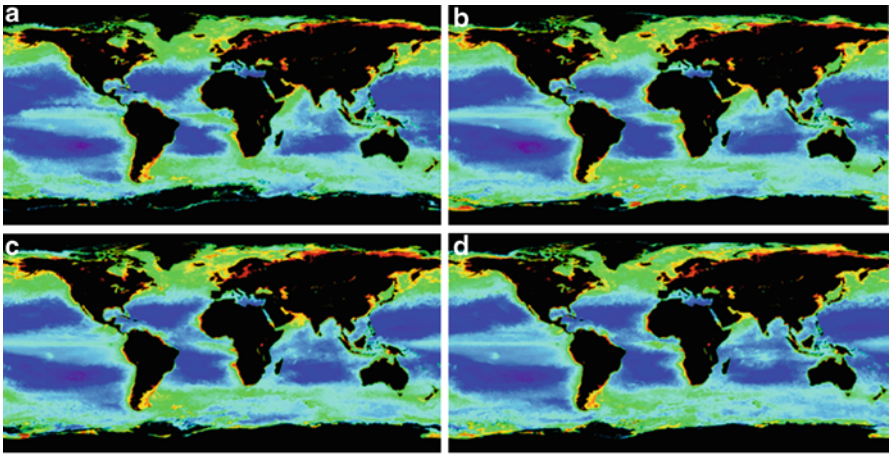

Fig. 3.10 MODIS Aqua annual composites of chlorophyll-a concentration: (**a**) 2002; (**b**) 2005; (**c**) 2008; (**d**) 2011. The details for the annual composites including the chlorophyll-a concentrations color scale that goes with these images can be found at http://oceancolor.gsfc.nasa.gov/cgi/l3

Fig. 3.11 Overall comparison of the MODIS and VIIRS instruments. VIIRS (*top*) and MODIS (*bottom*). VIIRS mass power and volume are 162 kg, 140 W, and 1.2 m^3. For MODIS, these are 230 kg, 147 W and 2.0 m^3

CZCS observations that begin in 1978. Success with the JPSS and the VIIRS offers the considerable potential that even longer data records increasingly useful for climate studies can be provided.

Table 3.2 Comparison of MODIS and VIIRS bands and spatial resolutions

MODIS		VIIRS	
Band #	λ	λ	Band ID
1	620–670	600–680	I-1
2	841–876	845–885	I-2
3	459–479		
4	545–565		
5	1,230–1,250	1,230–1,250	M-8
6	1,628–1,652	1,580–1,670	M-10
		1,580–1,610	I-3
7	2,105–2,155	2,225–2,275	M-11
8	405–420	402–422	M-1
9	438–448	436–454	M-2
10	483–493	478–498	M-3
11	526–536		
12	546–556	545–565	M-4
13	662–672	662–682	M-5
14	673–683		
15	743–753	739–754	M-6
16	862–877	846–885	M-7
17	890–920		
18	931–941		
19	915–965		
20	3.660–3.840	3.610–3.790	M-12
		3.550–3.930	I-4
21	3.929–3.989		
22	3.940–4.001		
23	4.020–4.080	3.973–4.128	M-13
24	4.433–4.498		
25	4.482–4.549		
26	1.360–1.390		M-9
27	6.535–6.895		
28	7.175–7.475		
29	8.400–8.700	8.400–8.700	M-14
30	9.580–9.880		
31	10.780–11.280	10.253–11.263	M-15
		10.050–12.400	I-5
32	11.770–12.270	11.538–12.488	M-16
33	13.185–13.485		
34	13.485–13.785		
35	13.785–14.085		
36	14.085–14.385		

MOD1S Bands l and 2 are 250 m at nadir
MOD1S Bands 3–7 are 500 m at nadir
MOD1S Bands 8–36 are 1,000 m at nadir
VIIRS Bands I-1 and I-2 are 371 m at nadir
VIIRS Band I-3 is 371 m at nadir
VIIRS Bands I-4 and I-5 are 371 m at nadir

Along with the real potential for providing observations nominally useful for climate studies, there, nevertheless, will be continuing challenges for the research and applications communities to utilize these observations successfully. A few examples are noted below.

The first set of challenges deals with updating with accommodating changes in instrument performance or updating of product algorithms. There must be resources not only to continue the calibration and instrument characterization of the instruments, but also quality assurance activities should be provided to look for anomalies or inconsistencies in the data. Additionally periodic reprocessing of the data sets should be considered mandatory in order to assure research and applications communities that "trends" seen in the data records are real (e.g., due to climate change) and not a quirk in the data set for which corrections have not been made properly.

The second set of challenges has to do with merging data sets and processing the large amounts of data involved. To do optimally do climate studies covering as many years as possible can involve fusing data records from the various instruments (e.g., AVHRR, MODIS, VIIRS, SeaWiFS, on US satellites and similar instruments on satellites operated by other countries and agencies) to provide quality data sets spanning many years. Furthermore, techniques to analyze or sample the large data volumes will have to be developed or improved so as to allow climate results from these data to be acquired. This could involve utilizing improved computing and storage technologies or approaches (e.g., "cloud" computing and storage) or selection of key indicator subsets of data such as "golden months" or other subsampling approaches.

Albeit there are challenges ahead such as those just noted, the fundamental nearly synoptic, global coverage by satellite instruments such as the MODIS makes the investments to allow the confident use of the data seem well justified. Given what has been accomplished to date, the promise for the future in obtaining better understanding of the processes and trends in the many parameters comprising the Earth-atmosphere system seems very exciting and real.

References

Doelling DR, Morstad D, Bhatt R, Scarino B, Xiong X, Wu A (2011) MODIS visible sensor radiometric performance with multiple approaches over various targets. In: Proceedings of the CALCON conference. Logan, Aug 29–Sept 1 2011

Esaias WE (1986) Moderate resolution imaging spectroradiometer (MODIS): MODIS instrument panel report, Earth observing system report, vol IIb, National Aeronautics and Space Administration

Hall DK, Foster JL, DiGirolamo NE, Riggs GA (2012) Snow cover, snowmelt timing and stream power in the Wind River Range. Wyoming. Geomorphology 137(1):87–93

Meynart R, Neeck SP, Shimoda H (eds) (2005) Sensors, systems, and next-generation satellites IX. In: Proceedings of SPIE, vol 5978, 59780V. 0277-786X/05/$15. doi:10.1117/12.627631

Parkinson CL, Ward A, King MD (eds) (2006) Earth science reference handbook: a guide to NASA's earth science program and earth observing satellite missions. National Aeronautics and Space Administration, Washington, D.C., 265 pp

Salomonson VV, Barnes WL, Maymon PW, Montgomery HE (1989) MODIS: advanced facility instrument for studies of the earth as a system. IEEE Trans Geosci Remote Sens 27(2):145–153

Salomonson VV, Abrams MJ, Kahle A, Barnes W, Xiong X, Yamaguchi Y (2011) Chapter 1: Evolution of NASA's earth observing system and development of the moderate-resolution imaging spectroradiometer and the advanced spaceborne thermal emission and reflection radiometer instruments. In: Ramachandran B, Abrams MJ, Justice C (eds) Land remote sensing and global environmental change. Springer Science + Business Media, LLC, New York, pp 3–34. ISBN 978-1-4419-6748-0

Wenny BN, Xiong X (2008) Using a cold earth surface target to characterize long-term stability of the MODIS thermal emissive bands. IEEE Geosci Remote Sens Lett 5(2):162–165

Wolfe RE (2006) Chapter 4: MODIS geolocation. In: Qu JJ, Gao W, Kafatos M, Murphy RE, Salomonson VV (eds) Earth science satellite remote sensing, vol 1, Science and instruments. Springer, Berlin/Heidelberg/New York, pp 50–73. ISBN 13 978-3-540-35606-6

Xiong X, Toller G, Chiang V, Sun J, Esposito J, Barnes W (2005a) MODIS level 1B algorithm theoretical basis document prepared for the National Aeronautics and Space Administration. see: http://mcst.gsfc.nasa.gov/uploads/files/documents/M1058.pdf

Xiong X, Sun J, Wu A, Chiang K, Esposito J, Barnes W (2005b) Terra and Aqua MODIS calibration algorithms and uncertainty analysis. In: Meynart R, Neeck SP, Shimoda H (eds) Sensors, systems, and next-generation satellites IX, proceedings of SPIE, vol 5978, 59780V, 0277-786X/05/$15, Brugge, 2005. doi: 10.1117/12.627631

Xiong X, Isaacman A, Barnes W (2006) Chapter 3: MODIS level-1B products. In: Qu JJ, Gao W, Kafatos M, Murphy RE, Salomonson VV (eds) Earth science satellite remote sensing, vol 1, Science and instruments. Springer, Berlin/Heidelberg/New York, pp 31–49. ISBN 13 978-3-540-35606-6

Xiong X, Chiang K, Sun J, Barnes W, Guenther B, Salomonson VV (2009) NASA EOS Terra and Aqua MODIS on-orbit performance. Adv Space Res 43(3):413–422. doi:10.1016/j.asr.2008.04.008

Chapter 4
Evaluation of the Temperature Trend and Climate Forcing in the Pre- and Post Periods of Satellite Data Assimilation

Alfred M. Powell Jr. and Jianjun Xu

Abstract Based on multiple linear regression analysis, three temperature datasets from two reanalyses and one set of satellite observations have been used to evaluate the different responses in the winter [December–February (DJF)] period in the pre- and post periods of satellite data assimilation as they relate to a selected set of climate forcings: solar, the stratospheric quasi-biennial oscillation (QBO), El Niño Southern Oscillation (ENSO), and stratospheric aerosol optical depth (AOD). The two periods are defined as 1958–1978 when no satellite data was available to be assimilated and the 1979–2002 period when satellite data was assimilated in the operational forecast models. The multiple regression analysis shows that the solar response of the DJF temperatures in the three datasets shows large-scale similarities although there are differences over the southern middle-high latitudes and some tropical areas. The stratospheric response showed the strongest DJF temperature anomalies related to solar variability occurring over the Arctic, but its sign is negative in 1979–2002 and positive in 1958–1978. The temperature features may be partially explained by the impacts of the solar cycle, El Niño Southern Oscillation, stratospheric quasi-biennial oscillation, stratospheric aerosols, and other factors. In contrast, the tropospheric response, with a dynamic wavelike structure, occurs over the middle latitudes. The tropospheric differences between the two periods are not clearly resolved and raise questions about the efficacy of the observations and our ability to use the observations effectively.

A.M. Powell Jr. (✉)
Center for Satellite Applications and Research (STAR) in the National Oceanic and Atmospheric Administration (NOAA) located at the NOAA Center for Weather and Climate Prediction (NCWCP), 5830 University Research Court, College Park, MD 20746, USA
e-mail: Al.Powell@noaa.gov

J. Xu
Department of GGS, Environmental Science and Technology Center (ESTC)/College of Science (COS), George Mason University (GMU), MS 6A2, Fairfax, VA 22030, USA

J.J. Qu et al. (eds.), *Satellite-based Applications on Climate Change*,
DOI 10.1007/978-94-007-5872-8_4,

4.1 Introduction

Many previous studies have revealed that changes in the stratosphere and troposphere are directly or indirectly associated with solar variability attributed to the decadal solar cycle (van Loon and Shea 1999; van Loon and Labitzke 2000; Balachandran et al. 1999; Gleisner and Thejll 2003; Haigh et al. 2005; Crooks and Gray 2005; Gray et al. 2005; Matthes et al. 2006; Kodera and Shibata 2006; IPCC 2007; Rind et al. 2008; Meehl and Arblaster 2009; Meehl et al. 2009 and many others). However, great uncertainty remains concerning the actual atmospheric response and differing conclusions in the various studies (Fröhlich and Lean 1998; Willson and Mordvinov 2003; Haigh 2003; Hood 2004; Keckhut et al. 2005; Scafetta and West 2005, 2006; Lean 2006) and other potential climate forcings (Hansen et al. 2005). In addition to solar forcing, other factors such as the QBO, El Nino Southern Oscillation, and stratospheric aerosol optical depth may impact the temperature fields.

The observational uncertainties are associated with the different data sources and other potential climate forcings. First, due to various combinations of the observation record used to represent the solar variability (Willson and Mordvinov 2003; Fröhlich and Lean 2004; Dewitte et al. 2005), there is disagreement over the solar forcing results (Scafetta and West 2006; Lean 2006). Based on the total solar irradiance (TSI) composite of the PMOD between solar cycles 21–23, Lean (2006) pointed out the solar contribution to global warming would be negligible. However, Scafetta and West (2006) relied on the ACRIM TSI composite concluding that the Sun contributed at least 10–30% of the 0.40 ± 0.04 K global surface warming. Second, the different atmospheric datasets and techniques used to compile and integrate the atmospheric data lead to results with different characteristics that have been questioned. The main atmospheric datasets used for current community studies include conventional surface and rawinsonde observations along with rocketsonde data (Dunkerton et al. 1998), lidar data (Keckhut et al. 2005), satellite data from the Stratospheric Sounding Unit (SSU) and Microwave Sounding Unit (MSU) instruments (Scaife et al. 2000; Keckhut et al. 2001; Hood 2004; Gray et al. 2009), and model assimilated datasets (ERA-40 and NCEP/NCAR reanalysis). We note that both assimilated datasets include the SSU/MSU assimilated observations since November 1978. Also, we note that the NCEP/NCAR reanalysis assimilated derived temperatures from the satellite data (Kalnay et al. 1996), while the ERA-40 reanalysis assimilated the satellite-measured radiance data directly (Uppala et al. 2005). These differences in approach could affect trend analyses. The differences in the reanalysis model physics could generate dynamic differences in the trends and anomaly comparisons (Mo et al. 1995). In addition to diverse data sources in the reanalyses, varying length data source periods can contribute to even more differences. Previous studies have employed a variety of data sources and observational periods (Pawson and Fiorino 1999; van Loon and Shea 2000; Labitzke et al. 2002; Haigh 2003; Keckhut et al. 2005; Crooks and Gray 2005; Xu and Powell 2010) that may have impacted their

conclusions. This analysis possibly suffers from the same issues. As the science becomes more complicated, it is difficult to understand the effects from a variety of data sources combined with models which may have many physical interactions contributing to a single outcome. Part of the purpose of this study is to resolve the similarities and differences between two recognized reanalyses that use different models and a direct satellite measurement to help resolve what is real and possibly what is not in terms of climate forcing impacts.

In the present work, the multiple linear regression analysis results for the lower stratospheric and the middle tropospheric temperature changes associated with the solar variability, ENSO, QBO, and stratospheric aerosols are reported for the two reanalyses datasets (NCEP/NCAR and ERA-40) for the two periods of 1979–2002 and 1958–1978. The satellite Microwave Sounding Unit (MSU) measurements are only reported in the period of 1979–2002 when it was used in the operational forecasting. The data and analysis techniques are described in the following section. The linear trend of the temperature and their differences in the two periods are offered in Sect. 4.3. Section 4.4 presents the multiple regression analyses for the temperature and the impacts of the selected set of climate forcings. Section 4.5 gives the final summary.

4.2 Data and Methodology

To understand the temperature trends and the climate forcings, the data used in this study include two reanalyses, one satellite retrieval dataset and climate forcing indices including solar F10.7-cm radio flux, ENSO, QBO, and stratospheric aerosol optical depth (AOD) data. A data period was chosen consistent with available data from both the NCEP/NCAR and ERA-40 reanalyses (1958–2002). All datasets except for the satellite-retrieved data spanned the two periods 1958–1978 and 1979–2002.

4.2.1 NCEP/NCAR Reanalysis

The monthly NCEP/NCAR reanalysis (Kalnay et al. 1996) with a 2.5° × 2.5° grid resolution is used for the two periods of 1979–2002 and 1958–1978. It should be noted that the reanalysis period of 1958–1978 has no satellite data. The Television Infrared Observation Satellite (TIROS) Operational Vertical Sounder (TOVS) data, the Microwave Sounding Unit (MSU), the High-Resolution Infrared Radiation Sounder (HIRS), and the Stratospheric Sounding Unit (SSU) information were not available before the end of 1978. The Special Sensor Microwave/Imager (SSM/I) data was assimilated in this system from 1993. The reanalysis has 17 pressure levels that range from 10 hPa to the surface (1,000 hPa).

4.2.2 ERA-40

The monthly ERA-40 reanalysis (Uppala et al. 2005) is employed for the same periods as the NCEP/NCAR reanalysis datasets. The ERA-40 reanalysis data uses the Integrated Forecasting System (IFS) developed jointly by ECMWF and Météo-France. Derived temperatures from the satellite data (Kalnay et al. 1996) were assimilated in the NCEP/NCAR reanalysis, while the satellite-measured radiances were assimilated directly in the ERA-40 reanalysis. The reanalysis has 23 pressure levels that range from 1 hPa to the surface (1,000 hPa).

4.2.3 MSU (Microwave Sounding Unit)

The MSU monthly temperature dataset between the end of 1978 and 2006 was created using the brightness temperature measurements derived from channels 2 and 4 from the TIROS-N, NOAA-10, 11, 12, and 14 satellites (Zou et al. 2009). The data were averaged over 2.5 × 2.5 latitude-longitude grids. To reduce the biases in the intersatellite MSU instruments, NESDIS scientists (Zou et al. 2006, 2009) developed an intercalibration method based on the simultaneous nadir overpass (SNO) matchups. Due to orbital geometry, the SNO matchups are confined to the polar region where the brightness temperature range is slightly smaller than the global range. Nevertheless, the resulting calibration coefficients are applied globally to the entire life cycle of an MSU satellite.

Such intercalibration reduces intersatellite biases by an order of magnitude compared to prelaunch calibration and, thus, results in a well-merged time series for the MSU channels 2 and 4, which respectively represent the deep layer temperature of the middle troposphere (~600 hPa) and lower stratosphere (~87 mb).

4.2.4 Climate Forcings: Solar, ENSO, QBO, and Stratospheric Aerosols

The solar variability proxies used in this, and in most studies, are the solar radio irradiance (the 10.7-cm radio flux). The solar radio irradiance spans the time period from 1947 to 2009 and can be found at http://www.ngdc.noaa.gov/stp/SOLAR. On the basis of previous studies that have tested different proxies (Keckhut et al. 1995), the 10.7-cm solar flux, which closely tracks the temporal behavior of the UV changes on daily, monthly, and 11-year time scales, is taken in our analysis to represent solar variability. The NINO3.4 is the ENSO index averaged sea-surface temperature in the equatorial Pacific (5°N–5°S, 170°W–120°W) provided by NOAA's Climate Prediction Center (CPC). QBO is the equatorial zonal wind at 30 hpa from Freie Universität Berlin provided by Labitzke, and aerosol impacts are represented by the global stratospheric aerosol optical depth (AOD) from NASA GISS climate model datasets (Hansen et al. 2005) which is indicative of volcanic influences.

4.2.5 Methodology

It is obvious that the two analysis periods have an important difference: the lack of satellite data prior to November 1978 and the use of assimilated satellite data after 1978. The MSU-retrieved temperature data is available for the period of 1978 through 2006. Based on the whole publicly available data from ERA-40 for 1958–2002, two data periods in the present study were chosen: 1979–2002 and 1958–1978. All three datasets will be used in the 1979–2002 period; the two reanalysis datasets used in the earlier period did not contain satellite data. The winter season was defined as December through February in this study. A multiple linear regression analysis was used in this study to ascertain the linear impacts for the selected set of forcing parameters.

4.2.5.1 Multiple Linear Regression Analysis

For a limited selection of atmospheric variables (Y), a multiple linear regression equation can be expressed as follows:

$$Y = a_0 + a_1\,\mathrm{TRD} + a_2\,\mathrm{F10.7} + a_3\,\mathrm{ENSO} + a_4\,\mathrm{QBO} + a_5\,\mathrm{AOD} + \epsilon \qquad (4.1)$$

where a_0 is the long-term mean for a particular variable (in this case, temperature), TRD is the linear trend, and F10.7 represents the solar forcing quantified by the solar 10.7-cm radio flux. ENSO is the El Niño index, QBO is the equatorial zonal wind at 30 hpa from the Free University of Berlin (K. Labitzke, 2009, private communication), AOD is the global stratospheric aerosol optical depth, and ϵ is a residual error term. The coefficients a_0, a_1, a_2, a_3, a_4, and a_5 are determined by least squares regression. Note that each forcing term index was normalized before the calculation.

This global analysis will be completed in steps. First, a reference baseline will be established by reviewing the trends in the global temperatures and the resulting pattern. This baseline provides insight into the consistency of the datasets prior to performing any additional analysis. Next a multiple regression analysis that accounts for the selected forcing factors is performed.

4.3 Trend of Global Temperature

Before discussing the impacts of climate forcing on the temperature anomalies, it is important to first review the preliminary features of the DJF temperature trends in the two periods as a baseline. The trend was calculated by the term a_1TRD in Eq. (4.1).

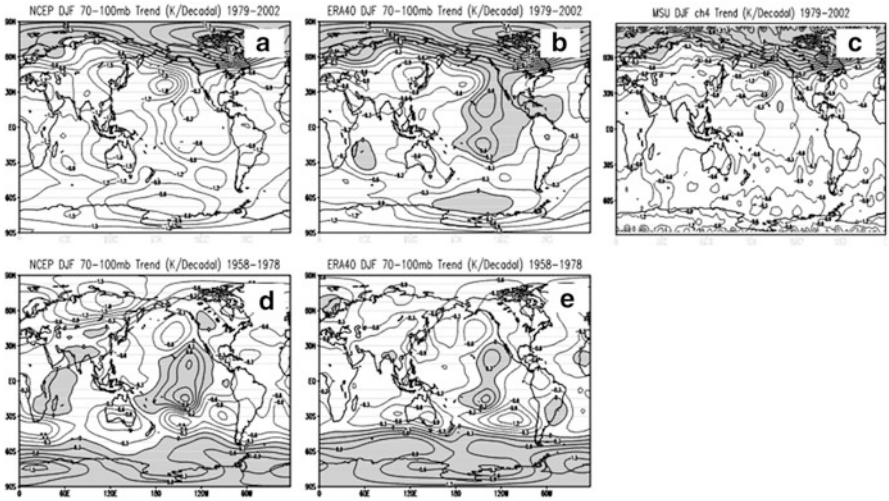

Fig. 4.1 Trend of December–February temperature (K/decade) in the lower stratosphere (70–100 hPa) in the three datasets. Shaded areas indicate a positive trend of temperature. For 1979–2002: (**a**) NCEP/NCAR reanalysis, (**b**) ERA-40 reanalysis, and (**c**) MSU Ch4 measurement; For 1958–1978: (**d**) NCEP/NCAR reanalysis and (**e**) ERA-40 reanalysis in 1958–1978 (Adapted from Powell and Xu (2011), Figure 2)

4.3.1 Stratosphere

Because the measurement from MSU channel 4 represents the lower stratosphere layer temperature with peak at 87 hPa (Zou et al. 2009), the layer mean temperature between 70 and 100 hPa was chosen to represent the lower stratospheric temperature in the NCEP/NCAR and the ERA-40 reanalyses.

In 1979–2002, the temperature tended to decrease over most of the global areas except for the area north of 60°N latitude where warming consistently occurred (Fig. 4.1a–c) in the three datasets. The basic pattern can be confirmed by visually comparing the analyses with each other. The largest warming with a rate of 2.1–2.7 K/decade was identified over the high latitudes of the North American continent. However, it is worth noting that the temperatures tended to increase over the tropical eastern Pacific in the ERA-40 reanalysis, which is different from the other two datasets.

The temperature trend in the 1958–1978 period (Fig. 4.1d, e) differs from its counterparts in the 1979–2002 period in the two reanalyses. The largest warming is observed south of 60°S, and the maximum rate was 1.5 K/decade. For the NCEP reanalysis (Fig. 4.1d), the largest cooling rate of −1.8 K/decade was observed over the high latitudes of the Eurasian continents. In contrast, the cooling rate is only −0.9 K/decade over the same location in the ERA-40 reanalysis (Fig. 4.1e). Note that a similar warming can be found over the tropical eastern Pacific in both reanalyses. The basic temperature patterns are confirmed in the polar regions of all three datasets and indicate the greatest positive change in the Arctic occurred

during 1979–2002. In addition, the two reanalyses are similar for the 1958–1978 period showing warming in the Antarctic – a reversal of the 1979–2002 pattern where the Arctic showed warming.

Three of the four panels from the ERA-40 and NCEP-NCAR reanalyses indicate an equatorial warming over the eastern Pacific and is a region to compare during the analysis.

4.3.2 Troposphere

The retrieved temperature from the MSU channel 2 (ch2) represents the layer temperature with a peak at 600 hPa (Zou et al. 2009); the mean temperature from 500 to 700 hPa is employed to represent the middle tropospheric temperature in the NCEP/NCAR and the ERA-40 reanalyses.

Compared to the stratospheric analysis, the tropospheric temperatures tended to increase in the two study periods. For the period of 1979–2002 (Fig. 4.2a–c), the main warming areas are found over the Eurasian continents, western Pacific, North American continents, and the southern middle latitudes. The temperature over the tropical Indian Ocean and Pacific Ocean decreased in the two reanalyses (Fig. 4.2a, b), but clear evidence is found that the MSU ch2 temperature tended to increase over these regions although its amplitude is small (Fig. 4.2c). In addition, the temperature over the Antarctic shows a strong cooling trend in the NCEP/NCAR reanalysis, while the temperature over some areas appears to have a warming trend in the ERA-40 reanalysis.

The main warming areas in 1958–1978 (Fig. 4.2d, e) appeared over most of the southern hemisphere and the Arctic zone in the two reanalyses. The biggest temperature trend difference between 1979–2002 and 1958–1978 occurred in the northern middle-high latitudes, where the trend is dominated by negative values. The largest warming is observed over the southern high latitudes, but the pattern shows a significant difference in the NCEP and ERA-40 reanalyses. It is worth noting that a negative trend can be found over the northern high latitudes of the Eurasian continent, North Pacific Ocean, and west coast of the North American continent in both periods.

Based on Table 4.1, the global mean temperature tended to increase in the troposphere and decrease in the stratosphere between the two periods of 1958–1978 and 1979–2002. Both the stratospheric and tropospheric temperature trends in the two periods are similar in the two reanalysis datasets and can also be confirmed in the MSU measurements for 1979–2002 although there is a different temperature trend between the two reanalyses and the MSU measurements over the Antarctic zone and tropical eastern Pacific. However, the variability and temperature trend patterns also show significant differences between the two periods in the temperature structure observed over the tropical and middle-high latitudes. Overall, the analyses show sufficient similarity to proceed with the multiple linear regression analyses to ascertain the contributions from solar forcing, aerosols, QBO, and El Niño.

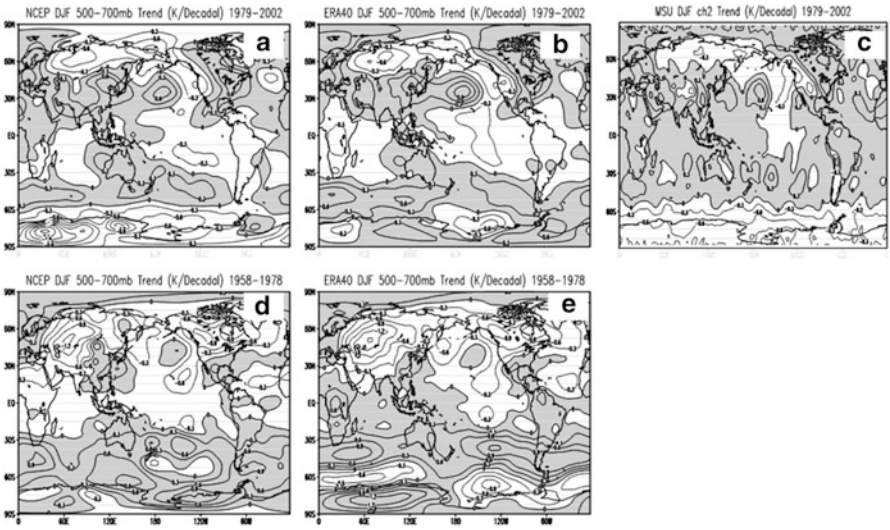

Fig. 4.2 Same as Fig. 4.1 except for the middle troposphere (500–700 hPa) (Adapted from Powell and Xu (2011), Figure 3)

Table 4.1 Trend of global mean temperature for December–February units: K/decade

	NCEP/NCAR	ERA40	MSU
100–70 mb (1979–2002)	−0.92	−0.16	−0.47
100–70 mb (1958–1978)	−0.24	−0.18	n/a
700–500 mb (1979–2002)	0.015	0.064	0.090
700–500 mb (1958–1978)	0.021	0.044	n/a

4.4 Multiple Linear Regression Analysis

Generally, three methods are used to assess the impact of climate forcing changes on the Earth: modeling, composite analysis, and statistical analysis. A previous composite analysis likely indicates nonlinear relationships in the stratosphere and troposphere (Powell and Xu 2010, 2011); however, for a complicated climate system, the composite analysis cannot identify which sources are contributing to the observed temperature anomaly (TA) signal. Fortunately, the multiple linear regression methodology is a good way to identify the linear signal from potential multiple sources (Haigh 2003). Although the regression methodology can typically only address linear relationships, it is a step to improve our understanding of the relative source contributions. In other words, the regression method will overcome to some degree the limitations in the composite analysis. However, one must keep in mind that the regression approach also cannot make attributions for cause and effect but only points to possible areas for investigation.

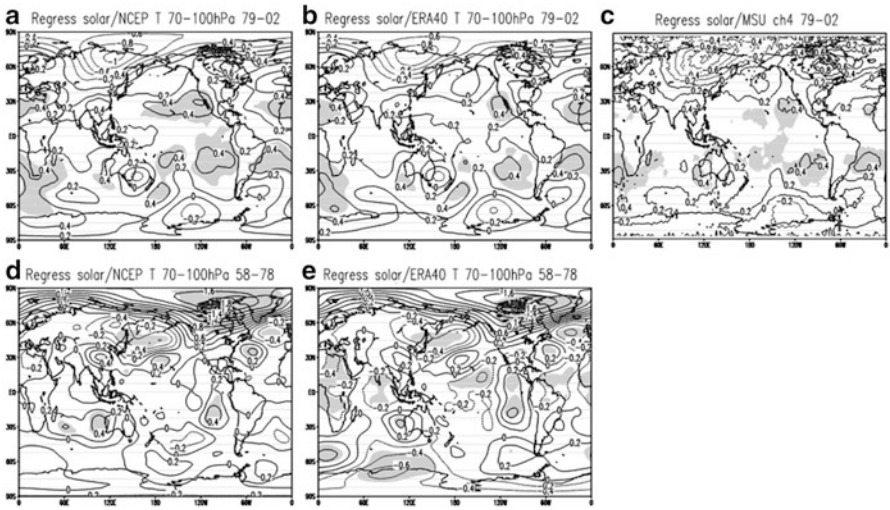

Fig. 4.3 Solar signal in the stratospheric (70–100 hpa) temperature anomalies (°C) from regression analysis of 1979–2002 (*upper*) and 1958–1978 (*bottom*): (**a**, **d**) NCEP/NCAR reanalysis, (**b**, **e**) ERA-40 reanalysis, and (**c**) MSU ch4 measurement. The *shaded areas* indicate the statistical significance at the 95% level (Adapted from Powell and Xu (2011), Figure 8)

4.4.1 Solar Response

For the stratosphere, the multiple linear regression analysis of temperature with the normalized 10.7-cm solar flux in 1979–2002 shows (Fig. 4.3a–c) a strong negative regression coefficient (cooling) in the Arctic zone with positive values (warming) in the tropical latitudes and a portion of the southern middle-high latitudes in the two reanalyses and MSU ch4 measurements. In contrast, the regressed temperature anomaly in 1958–1978 (Fig. 4.3d, e) has a large positive regression coefficient in the Arctic zone and negative value in the tropical latitudes. The strongest correlations occur over part of the Arctic zone and the Pacific. In these areas, the correlations exceed the statistical significance test at the 95% level. The opposite sign of the temperature response to solar variation in the two periods has been significantly reproduced in most areas, especially for the strong signal in the Arctic zone.

For the troposphere, the regression analysis for 1979–2002 shows a similar pattern in each of the three datasets except for the Antarctic zone (Fig. 4.4a–c). Negative regression coefficients tend to occur over the high latitudes (50–80°N), while positive values occur over the middle latitudes (20–50°N). The wavelike pattern alternating between positive and negative anomalies appears over both northern and southern middle latitudes. However, a large difference is found over the Antarctic zone in the three datasets. The MSU and NCEP data show weak positive anomalies, while the ERA-40 shows moderate negative anomalies over the eastern hemisphere of the Antarctic polar region. In 1958–1978, the temperature regression analysis corresponding with solar variability is similar to its counterpart

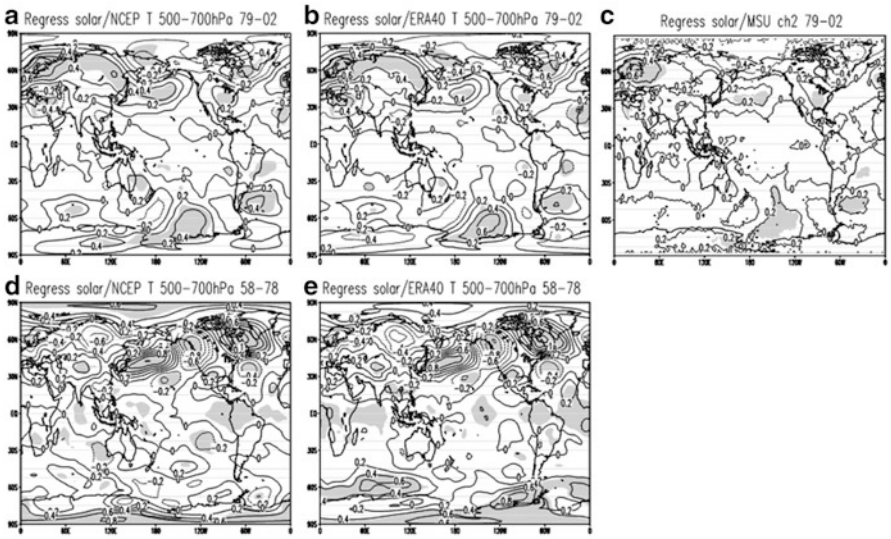

Fig. 4.4 Same as Fig. 4.3 except for the troposphere (500–700 hpa) (Adapted from Powell and Xu (2011), Figure 9)

in 1979–2002 over most areas (Fig. 4.4a vs. d and Fig. 4.4b vs. e). However, there is a significant wavelike pattern over the tropospheric northern middle latitudes.

To summarize, the regression analyses indicate the temperature responds to the solar variation in the stratosphere and troposphere quite differently. The anomaly is a reversal with the solar variation and can be identified over most areas in the two periods. However, the regression analysis cannot significantly reproduce the opposite solar signal in the troposphere; this result implies that solar variability is closely related to lower stratospheric temperature, but it only partially explains the temperature anomaly in the troposphere.

4.4.2 ENSO, QBO, and Stratospheric Aerosol Response

Given the solar forcing results, what other forcings could be responsible for the temperature anomalies? To address this question, the remaining, limited set of climate forcing terms in Eq. (4.1) were analyzed, and the ERA-40 dataset will only be used in this section.

The regression for the temperature variability for the three additional separate climate forcing terms (ENSO, QBO, and stratospheric aerosols) was completed. The results in the stratosphere are shown in Fig. 4.5. First, there is a zonally heterogeneous response to the ENSO forcing over the globe, and the pattern is quite different in the two periods (Fig. 4.5a, b) except both show negative responses observed in tropical eastern Pacific. In addition, an interesting result worth noting is that the ENSO forcing is symmetrical about the equator over most of the tropical/subtropical areas although the amplitude response is different in the two periods.

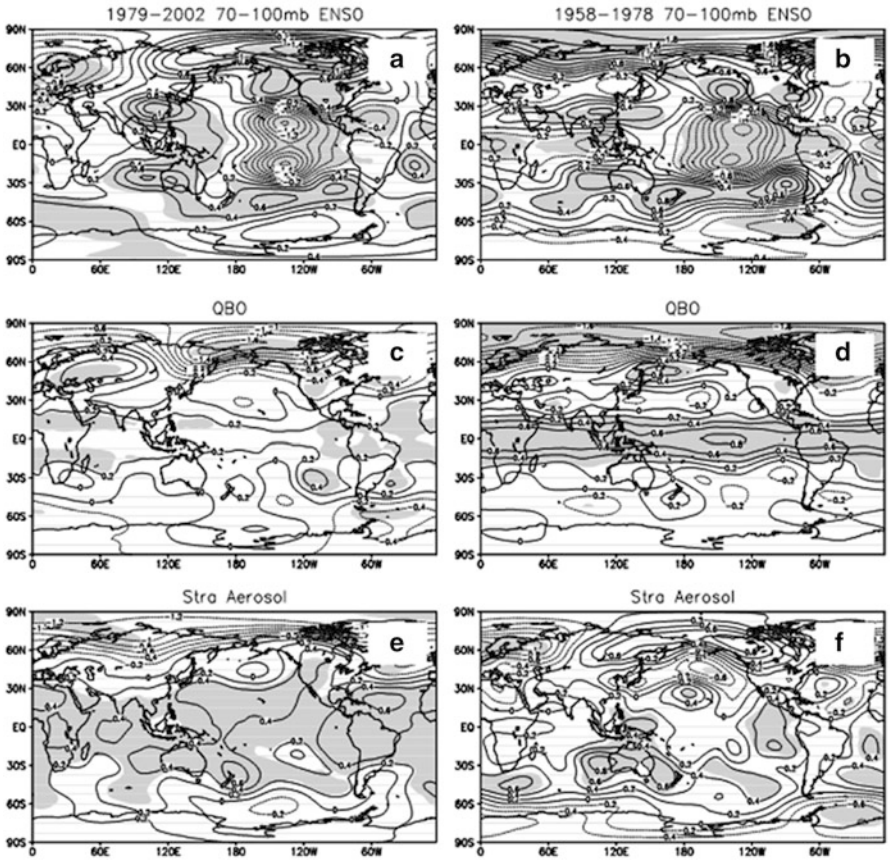

Fig. 4.5 Temperature response in the stratosphere (70–100 hpa) to the forcing in the two periods of 1979–2002 and 1958–1978: (**a**, **b**) ENSO; (**c**, **d**) QBO; (**e**, **f**) stratospheric aerosol. The *shaded areas* indicate the statistical significance at the 95% level

The shaded areas indicate that the temperature response to ENSO exceeds the statistical significance test at the 95% confidence level.

Second, the stronger signal response to the QBO forcing appeared over the tropical and Arctic zones. However, the amplitudes are different in the two periods (Fig. 4.5c, d). The result clearly reproduced the negative relationship between the QBO forcing and stratospheric temperature over the Arctic (Holton and Tan 1980) where the Arctic stratosphere is indeed warmer under easterly QBO conditions and colder under westerly QBO conditions. Moreover, a remarkable zonal homogeneous positive anomaly exceeding the 95% significance test is observed in the tropical areas, especially in the period of 1958–1978.

Third, the response to the stratospheric aerosols (Fig. 4.5e, f) has a similar pattern in the two periods with positive contributions in the tropical and subtropical areas. However, the response is significantly different over both polar regions in the

two periods. The Arctic was completely dominated by negative trends, and the Antarctic was partially dominated by positive trends in the period of 1978–2002, while the opposite was generally true in the period of 1958–1977 with the Arctic partially dominated by positive trends and the Antarctic completely dominated by negative trends.

For the troposphere, a pronounced positive response to ENSO is observed over the tropical eastern Pacific (Fig. 4.6a, b), which is opposite to its counterpart in the stratosphere. This positive ENSO response in the tropical troposphere is present in the two study periods, while the wavelike response occurs in both middle-high latitudes. But the structure of the wavelike response shows a significant difference in the two periods. It implies a different impact of the ENSO events on the temperature variability over the middle-high latitudes in the two periods.

Compared to the stratosphere, the tropospheric response to QBO was significantly reduced (Fig. 4.6c, d), especially in the tropical areas. The wavelike response is again identified over the middle-high latitudes although the area exceeding the statistical significance test at the 95% level is markedly compressed. In addition, the different responses in the two periods are observed over both middle-high latitudes.

Finally, the tropospheric response to the stratospheric aerosols shows (Fig. 4.6e, f) an opposing pattern to the one in the tropics (Fig. 4.5e, f). The stronger response appears over both middle-high latitudes. The amplitude of the response in the period of 1958–1977 is much higher than its counterpart in the period of 1978–2002. Note that the significant negative contribution from stratospheric aerosols, which are impacted via volcanic eruptions, was identified over most areas.

To summarize, the linear trend of the lower stratospheric temperature (Fig. 4.1) and the strongest temperature anomalies occur repeatedly over the Arctic, but its sign is positive in 1979–2002 and negative in 1958–1978. The opposite response to solar cycle forcing (Fig. 4.3) is only observed over the northern middle-high latitudes. The response to ENSO, QBO, and stratospheric aerosol forcing shows a similar pattern over the tropical areas in the two periods (Fig. 4.5). A stronger negative response to the ENSO forcing exists over the tropical eastern Pacific; this indicates a negative contribution to the stratospheric warming constrained over the same areas (Fig. 4.1b, d, e). The QBO forcing (Fig. 4.5c, d) always produces a negative anomaly over the northern high latitudes and a positive anomaly over the tropical areas in the two periods. In addition, stratospheric aerosols contribute negatively to the opposing anomalies over both polar areas in the two periods (Fig. 4.5e, f). In contrast, the tropospheric response to ENSO forcing shows an opposite distribution to the stratosphere over the tropical eastern Pacific (Fig. 4.6a, b). The wavelike pattern of temperature trend (Fig. 4.2) over the middle-high latitudes is connected jointly by the ENSO, QBO, and stratospheric aerosol forcing (Fig. 4.6). However, the wave structure shows significant differences in the two periods. The QBO contribution to tropospheric temperature was reduced dramatically (Fig. 4.6c, d), while stratospheric aerosols largely made a negative contribution to the temperature in the troposphere (Fig. 4.6e, f).

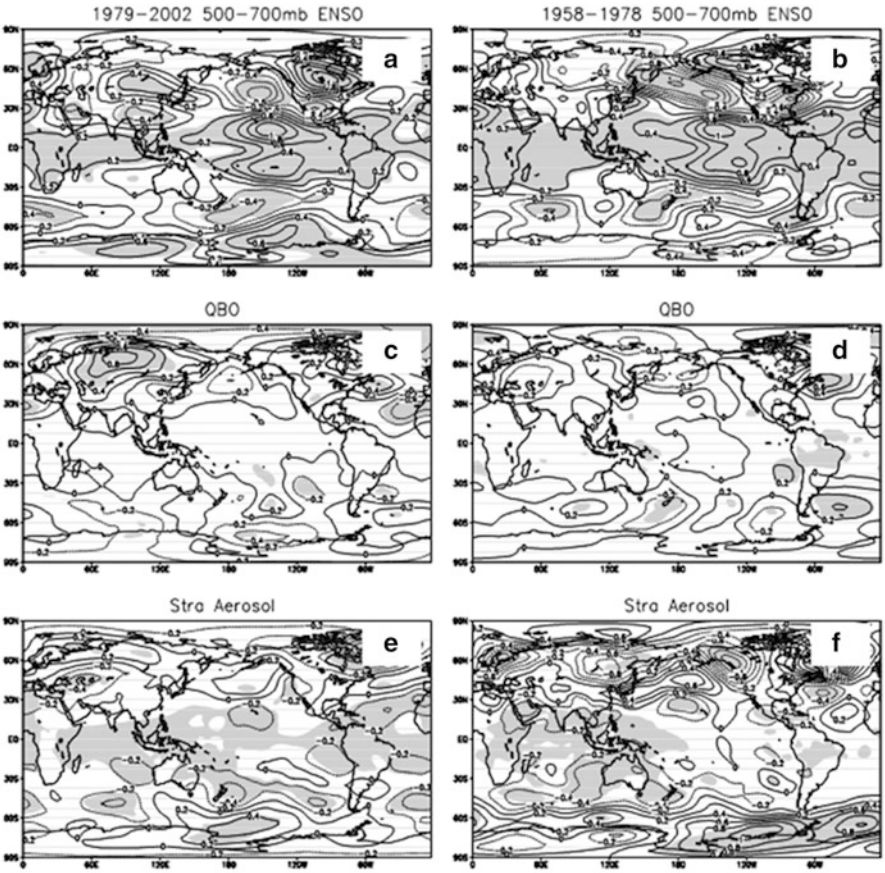

Fig. 4.6 Same as Fig. 4.5 except for the troposphere (500–700 hpa)

However, it is worth noting that the solar response in the regression analysis is not statistically significant in the Arctic region. The different temperature trends in the two periods can be reasonably explained jointly by solar, ENSO, QBO, and stratospheric aerosols.

4.5 Summary

Based on the multiple linear regressions for a selected set of forcing parameters computed from two reanalysis (NCAR/NCEP and ERA40) datasets and one satellite-retrieved temperature (MSU) dataset, the temperature responses to climate forcings in winter (December–February) are compared between the pre- (1958–1978) and post (1979–2002) periods of satellite data assimilation. The results show:

1. The global mean temperature tended to increase in the troposphere and decrease in stratosphere in the two periods of 1958–1978 and 1979–2002. However, the change rate and patterns of the temperature trends show significant differences between the two periods. A heterogeneous temperature structure is observed over the tropical and middle-high latitudes. Both stratospheric and tropospheric temperature trends in the two periods are similar in the two reanalysis datasets and were also confirmed in the MSU measurements for 1979–2002 although there are different temperature trend rates between the two reanalyses and the MSU measurements over the Antarctic zone and tropical eastern Pacific.
2. During the two periods, common features were observed showing the most sensitive areas of DJF TAs to solar forcing emerge over the Arctic, the northern high and middle latitudes, and the tropical-subtropical eastern Pacific. The patterns of DJF TAs associated with the solar forcing in the lower stratosphere and the middle troposphere were similar in each of the three datasets; the exception areas are located over the tropical oceans and most of the middle-high latitudes in the southern hemisphere. The TA response in DJF to solar forcing has a substantial spatial heterogeneity. The stratospheric TAs have more uniform values, while the tropospheric TAs have a wavelike pattern alternating between positive and negative values over both northern and southern middle latitudes.
3. Except for the possible impacts from the reanalysis datasets with and without the satellite data assimilation, the different temperature responses in the two periods can be reasonably explained by the solar, ENSO, QBO, and stratospheric aerosol forcing.

This analysis reaffirms the core forcing parameters for atmospheric temperature trends as solar, ENSO, QBO, and stratospheric aerosols. The analyses show many similar features and trends of approximately the same magnitude. However, there are many discrepancies that need to be explained. On the positive side, two independent reanalyses using different models, assimilation processes, and data ingest quality control demonstrate similar trends, regional changes, and anomalies. This is good news for both the weather and climate communities that are trying to converge on similar trends and improve the reliability of climate forcing estimates. However, there are some clear discrepancies between the pre- and post satellite era analyses. Coincidently, the inclusion of satellite data into the operational models started in late 1978 and aligns with a potential climate shift identified in the literature. This leaves open the question as to whether the reversal in the polar regions may have been due to the addition of satellite data or possibly an actual change in the climate near 1977–1978.

An updated set of global multi-satellite microwave measurements which includes the use of satellite intercalibration techniques as a method for obtaining improved temperature accuracy was used for comparison. This analysis shows that the satellite microwave measurements during the 1979–2002 period are very consistent with the reanalyses. It is acknowledged the satellite data is not a truly

independent set of observations when compared to the reanalyses since it was also assimilated in both the NCEP-NCAR and the ERA reanalyses. However, one of the goals was to verify the consistency of this dataset with the reanalyses and to compare the trends and anomalies against the improved calibration of this dataset. The result affirms similar trends and anomalies. However, more work is required to refine the trend amplitudes between the three datasets.

Acknowledgements The NCEP/NCAR monthly reanalysis data were obtained from NOAA/CDC Web site. The ERA-40 reanalysis data were obtained from the ECMWF Web site and the solar sunspot number from the NOAA/NGDC Web site. The authors would like to thank these agencies for providing the data. Special thanks to Dr. C. Zou from NOAA/NESDIS/STAR for many excellent discussions and the MSU temperature datasets that were provided.

This work was supported by the National Oceanic and Atmospheric Administration (NOAA), National Environmental Satellite, Data and Information Service (NESDIS), and Center for Satellite Applications and Research (STAR). The views, opinions, and findings contained in this publication are those of the authors and should not be considered an official NOAA or US Government position, policy, or decision.

References

Balachandran NK, Rind D, Lonergan P, Shindell DT (1999) Effects of solar cycle variability on the lower stratosphere and the troposphere. J Geophys Res 104:27321–27339. doi:10.1029/1999JD900924

Crooks SA, Gray LJ (2005) Characterization of the 11-year solar signal using a multiple regression analysis of the ERA-40 dataset. J Climate 18:996–1015. doi:10.1175/JCLI-3308.1

Dewitte S, Crommelynck D, Mekaoui S, Joukoff A (2005) Measurement and uncertainty of the long-term total solar irradiance trend. Sol Phys 224:209–216

Dunkerton TJ, Delisi DP, Baldwin MP (1998) Middle atmosphere cooling trend in historical rocketsonde data. Geophys Res Lett 25:3371–3374

Fröhlich C, Lean J (1998) Sun's total irradiance: cycles, trends and related climate change uncertainties since 1976. Geophys Res Lett 25:4377–4380

Fröhlich C, Lean J (2004) Solar radiative output and its variability: evidence and mechanisms. Astron Astrophys Rev 12:273–320

Gleisner H, Thejll P (2003) Patterns of tropospheric response to solar variability. Geophys Res Lett 30(13):1711. doi:10.1029/2003GL017129

Gray LJ, Haigh JD, Harrison RG (2005) Review of the influences of solar changes on the Earth's climate. Hadley Centre technical note no. 62, Met Office, Exeter, 82 pp

Gray LJ, Rumbold ST, Shine KP (2009) Stratospheric temperature and radiative forcing response to 11-year solar cycle changes in irradiance and ozone. J Atmos Sci 66(8):2402–2417

Haigh J (2003) The effects of solar variability on the Earth's climate. Philos Trans R Soc Ser A 361:95–111

Haigh J, Blackburn M, Day R (2005) The response of tropospheric circulation to perturbations in lower-stratospheric temperature. J Climate 18:3672–3685. doi:10.1175/JCLI3472.1

Hansen J et al (2005) Efficacy of climate forcings. J Geophys Res 110:D18104. doi:10.1029/2005JD005776

Holton JR, Tan H-C (1980) The influence of the equatorial quasi-biennial oscillation on the global circulation at 50 mb. J Atmos Sci 37(10):2200–2208

Hood LL (2004) Effects of solar variability on the stratosphere. In: Pap JM, Fox P (eds) Solar variability and its effects on climate, vol 141, Geophysical monograph series. AGU, Washington, D.C., pp 283–304

Intergovernmental Panel on Climate Change (IPCC) (2007) Climate change 2007: the physical sciences basis, Cambridge University Press, New York. Available at http://ipcc-wg1.ucar.edu/wg1/wg1-report.html

Kalnay E et al (1996) The NCEP/NCAR 40-year reanalysis project. Bull Am Meteorol Soc 77:437–471

Keckhut P, Hauchecorne A, Chanin M (1995) Midlatitude long term variability of the middle atmosphere trends and cyclic and episodic changes. J Geophys Res 100:18887–18897

Keckhut P, Wild J, Gelman M, Miller AJ, Hauchecorne A (2001) Investigations on long-term temperature changes in the upper stratosphere using lidar data and NCEP analyses. J Geophys Res 106:7937–7944

Keckhut P, Cagnazzo C, Chanin M, Claud C, Hauchecorne A (2005) The 11-year solar-cycle effects on the temperature in the upper-stratosphere and mesosphere: part I – assessment of observations. J Atmos Sol Terr Phys 67:940–947. doi:10.1016/j.jastp. 2005.01.008

Kodera K, Shibata K (2006) Solar influence on the tropical stratosphere and troposphere in the northern summer. Geophys Res Lett 33:L19704. doi:10.1029/2006GL026659

Labitzke K et al (2002) The global signal of the 11-year solar cycle in the stratosphere: observations and models. J Atmos Sol Terr Phys 64:203–210

Lean J (2006) Comment on "Estimated solar contribution to the global surface warming using the ACRIM TSI satellite composite" by N. Scafetta and B. J. West. Geophys Res Lett 33:L15701. doi:10.1029/2005GL025342

Matthes K, Kuroda Y, Kodera K, Langematz U (2006) Transfer of the solar signal from the stratosphere to the troposphere: Northern winter. J Geophys Res 111:D06108. doi:10.1029/2005JD006283

Meehl GA, Arblaster JM (2009) A lagged warm event-like response to peaks in solar forcing in the Pacific region. J Climate 22:3647–3660

Meehl GA et al (2009) Amplifying the pacific climate system response to a small 11-Year solar cycle forcing. Sci 325:1114. doi:10.1126/science.1172872

Mo KC, Wang XL, Kistler R, Kanamitsu M, Kalnay E (1995) Impact of satellite data on the CDAS-reanalysis system. Mon Weather Rev 123:124–139

Pawson S, Fiorino M (1999) A comparison of reanalyses in the tropical stratosphere. Part 3: inclusion of the pre-satellite data era. Clim Dyn 15:241–250. doi:10.1007/s003820050279

Powell A, Xu J (2010) An investigation of the relationship between the equatorial quasi-biennial oscillation, the Arctic stratosphere and solar forcing. J Atmos Sol Terrestrial Phys 1354–1363. doi: 10.1016/j.jastp.2010.09.024

Powell A, Xu J (2011) Comparisons of temperature response to solar forcing in the pre- and post periods of satellite data assimilation. Int J Climatol 31:2312–2329. doi:10.1002/joc.2239

Rind D, Lean J, Lerner J, Lonergan P, Leboissitier A (2008) Exploring the stratospheric/tropospheric response to solar forcing. J Geophys Res 113:D24103. doi:10.1029/2008JD010114

Scafetta N, West BJ (2005) Estimated solar contribution to the global surface warming using the ACRIM TSI satellite composite. Geophys Res Lett 32:L18713. doi:10.1029/2005GL023849

Scafetta N, West BJ (2006) Reply to comment by J. L. Lean on Estimated solar contribution to the global surface warming using the ACRIM TSI satellite composite. Geophys Res Lett 33: L15702. doi:10.1029/2006GL025668

Scaife AA, Austin J, Butchart N, Pawson S, Keil M, Nash J, James IN (2000) Seasonal and interannual variability of the stratosphere diagnosed from UKMO TOVS analyses. Q J R Meteorol Soc 126:2585–2604. doi:10.1002 /qj.49712656812

Uppala SM et al (2005) The ERA-40 re-analysis. Q J R Meteorol Soc 131:2691–3012

van Loon H, Labitzke K (2000) The influence of the 11-year solar cycle on the stratosphere below 30 km: a review. Space Sci Rev 94:259–278

van Loon H, Shea DJ (1999) A probable signal of the 11-year solar cycle in the troposphere of the Northern Hemisphere. Geophys Res Lett 26:2893–2896. doi:10.1029/1999GL900596

van Loon H, Shea DJ (2000) The global 11-year solar signal in July August. Geophys Res Lett 27:2965–2968. doi:10.1029/2000GL003764

Willson RC, Mordvinov AV (2003) Secular total solar irradiance trend during solar cycles 21–23. Geophys Res Lett 30(5):3–6

Xu J, Powell A (2010) Ensemble spread and its implication for the evaluation of temperature trends from multiple radiosondes and reanalyses products. Geophys Res Lett 37:L17704. doi:10.1029/2010GL044300

Zou C, Goldberg M, Cheng Z, Grody N, Sullivan J, Cao C, Tarpley D (2006) Recalibration of microwave sounding unit for climate studies using simultaneous nadir overpasses. J Geophys Res 111:D19114. doi:10.1029/2005JD006798

Zou C, Gao M, Goldberg M (2009) Error structure and temperature trends in observations from the microwave sounding unit. J Climate 22:1661–1680

Chapter 5
Development of the Global Multispectral Imager Thermal Emissive FCDRs

Xianjun Hao and John J. Qu

Abstract Generation of high-quality Climate Data Records (CDRs) is critically important for more reliable analysis of global climate change. Since each spaceborne sensor has limited life cycle, integration of remote-sensing measurements from different sensors is necessary. Differences in spectral response and spatial specification of sensors from different missions, as well as variations in calibration and retrieval algorithms, make it complicated to generate long-term consistent CDRs, especially the Fundamental Climate Data Records (FCDRs), i.e., calibrated radiance at top of atmosphere (TOA), which are essential for producing Thematic Climate Data Records (TCDRs) with consistent algorithms. This chapter presents the band mapping approach and results of FCDR generation for the thermal infrared bands of AVHRR and MODIS. Band transfer equations among different versions of AVHRR and MODIS are identified. Error bounds of band mapping are also analyzed statistically using global datasets.

Keywords Climate Data Record • Cross-sensor comparison • Consistency • Calibration • Remote sensing

5.1 Introduction

Global climate change has become an urgent and important issue because of its significant impacts and close relationship with human activities (NRC 2009). More reliable and accurate assessment of global climate change is critical in understanding the complicated changing of the Earth, especially severe weather impacts and human activities. Long-term high-quality consistent Climate Data Records (CDRs)

X. Hao (✉) • J.J. Qu
Department of Geography and GeoInformation Science, Environmental Science and Technology Center, George Mason University, 4400 University Drive, Fairfax, VA 22030, USA
e-mail: xhao1@gmu.edu

J.J. Qu et al. (eds.), *Satellite-based Applications on Climate Change*,
DOI 10.1007/978-94-007-5872-8_5,

are essential for more reliable climate change detection and analysis (NSC 2004; Cao et al. 2008; Hao and Qu 2008). Although satellite remote sensing has become the primary approach for Earth observation, each spaceborne sensor has limited life cycle; integration of remote-sensing measurements from multiple missions is necessary for constructing consistent long-term Climate Data Records. Differences in spectral responses and spatial specifications of sensors from different missions, as well as variations in calibration and retrieval algorithms, make it challenging to generate long-term consistent CDRs, especially the Fundamental Climate Data Records (FCDRs), i.e., calibrated radiance at top of atmosphere (TOA), which are fundamental for producing Thematic Climate Data Records (TCDRs) with consistent algorithms.

As global temperature change has been the focus of climate change study, it is important to integrate long-term remote-sensing measurements of thermal emissive channels and construct thermal emissive Climate Data Records. Major milestone for operational observation of surface temperature is the launch of the satellite TIROS-N in 1978, with the Advanced Very High Resolution Radiometer (AVHRR). From then on, AVHRR has become the primary sensor onboard the NOAA polar-orbiting satellites. AVHRR is a radiometer with four to six channels and daily global coverage at the spatial resolution of 1.1 km (AVHRR/1 had four channels, AVHRR/2 had five channels, and the latest version of AVHRR, i.e., AVHRR/3, has six channels). AVHRR data have been collected and archived continuously and have become of the most important datasets for global change study. From 1999, the National Aeronautics and Space Administration (NASA) launched EOS series of satellites for global observation. The Moderate Resolution Imaging Spectroradiometer (MODIS) is a key instrument aboard the Terra and Aqua satellites of NASA EOS mission. Terra MODIS and Aqua MODIS can cover the entire Earth's surface every 1–2 days, acquiring data in 36 spectral bands ranging in wavelength from 0.4 to 14.4 μm (Salomonson et al. 2006). MODIS provides the capability to improve our understanding of global dynamics and processes occurring on the land, ocean, and atmosphere (Justice et al. 1998; Salomonson et al. 2006). MODIS satellite data products have been widely used for global and regional applications for environment monitoring, natural hazards detection, weather forecasting, and climate change study (Salomonson et al. 2006).

AVHRR and MODIS have been the primary sensors for global surface temperature observation. In near future, the Visible Infrared Imager Radiometer Suite (VIIRS) of the NPP/JPSS mission will be the next-generation operational sensor replacing AVHRR and MODIS. Inter-sensor comparison and analysis has to be conducted to construct Climate Data Records across multiple Earth observation missions. Figure 5.1 illustrates the temporal coverage of AVHRR and MODIS. Figure 5.2 illustrates the spectral response functions of the 11- and 12-μm channels of AVHRR onboard some NOAA satellites and MODIS onboard the Aqua satellite. For each band, although the central wavelengths are similar among different AVHRR versions, differences in spectral response are significant. So, even data products from different versions of AVHRR cannot be simply put together to construct long-term CDRs. The bias and error bound of data products from these sensors has to be identified. MODIS and VIIRS have spectral bands close to

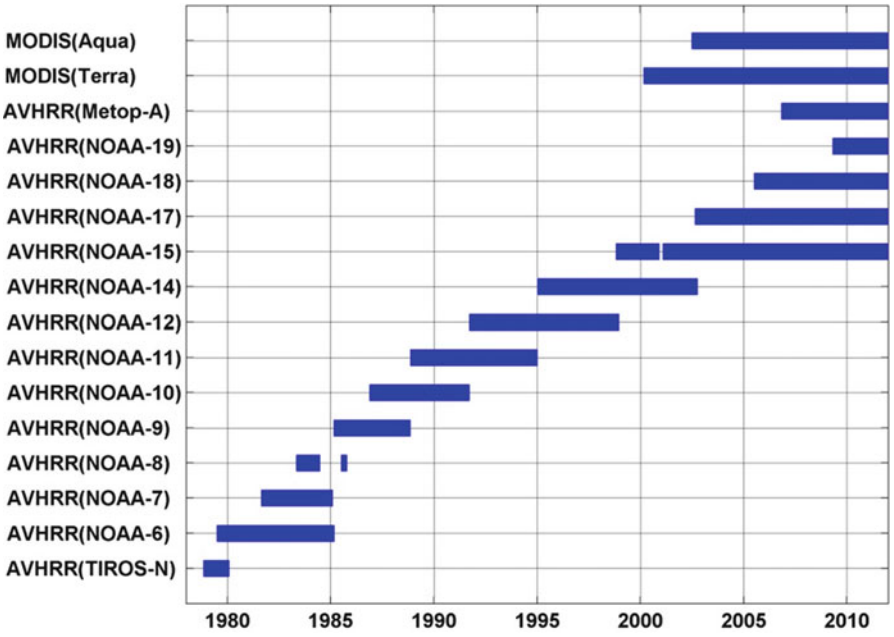

Fig. 5.1 Temporal coverages of AVHRR and MODIS

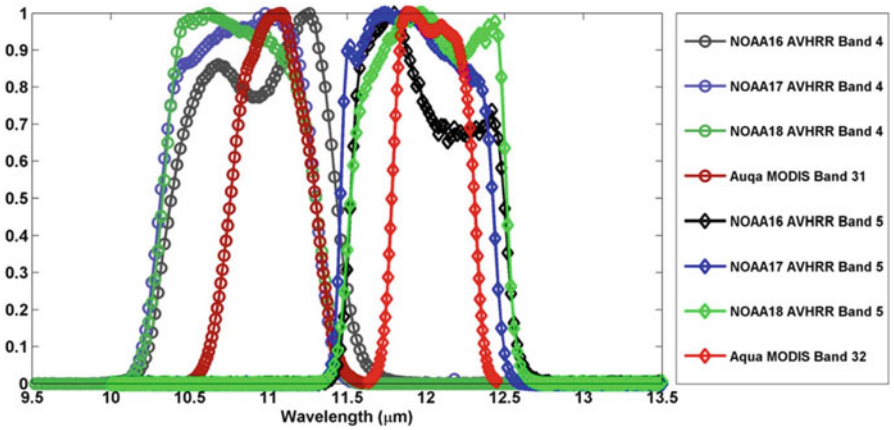

Fig. 5.2 Spectral response functions of AVHRR and MODIS 11- and 12-μm bands

AVHRR bands. Similarly, because of the spectral difference between AVHRR bands and the corresponding MODIS/VIIRS bands, measurements from these sensors cannot be combined together straightforwardly. The impacts of sensor specification difference have to be determined quantitatively. With FCDR, i.e., time series of consistent TOA radiance data, it is feasible to construct other CDRs

more reliably by applying similar algorithms for high-level data products, and it is also possible to obtain error bounds of data among multiple sensors, which are critical in climate change detection and analysis.

Sponsored by Northrop Grumman Space Technology (NGST), EastFIRE Laboratory at George Mason University has been working on cross-sensor comparison/validation/calibration for NPP/NPOESS support since 2003. The hyper-spectral measurements of the Atmospheric Infrared Sounder (AIRS) onboard NASA satellite Aqua were used to simulate thermal emissive bands of MODIS and VIIRS. Band mapping algorithms, as well as software toolkits and testing database, have been developed for MODIS, AIRS comparison, and VIIRS proxy data generation study (Hao et al. 2005a, b, 2007; Qu et al. 2005a, b, 2006a, b; Hao and Qu 2009a). The capability and performance of these approaches have been validated by comparing AIRS-simulated global MODIS SDR and aggregated MODIS SDR at AIRS footprints (Hao et al. 2005a, b). The band mapping approaches can also be used for generating global FCDRs (Hao and Qu 2008, 2009b). In this chapter, we focus on the thermal emissive SDRs at the 11- and 12-μm channels, which are used for surface temperature retrieval. Technical approaches are described in details, and quantitative relationships between thermal emissive measurements of different sensors are investigated and discussed toward the construction of thermal emissive FCDRs.

5.2 Data and Technical Methods

The AIRS (http://airs.jpl.nasa.gov) onboard NASA Aqua satellite is a hyper-spectral sensor in the thermal infrared region. With 2,378 spectral channels, AIRS has high spectral resolution and can provide more accurate information of the atmosphere. AIRS measurements can be used as a bridge to evaluate the spectral differences of various broadband sensors for different missions, such as AVHRR, MODIS, and VIIRS. By convolving the spectral response functions of broadband sensors with AIRS hyper-spectral measurements, proxy data for AVHRR, MODIS, and VIIRS will be generated. Then, a global database can be generated including proxy datasets and AIRS scene characteristics such as satellite zenith angle, satellite azimuth angle, surface type, cloud fraction, etc. Based on analysis of the global testing database, statistical relationship between different sensors, i.e., band transfer equations, can be derived to convert consistent measurements for these sensors. Details of band mapping approach for FCDR generation are illustrated in Fig. 5.3.

The main steps include:

1. Collection of AVHRR/MODIS/VIIRS sensor specification and global AIRS measurements
   - Collect the spectral response functions of AVHRR band 4 and band 5, MODIS band 31 and band 32, and VIIRS band M15 and band M16.
   - Collect global AIRS L1B measurements for selected 8 days during 2002–2008 and in different seasons: 09/06/2002, 01/25/2003, 01/26/2003,

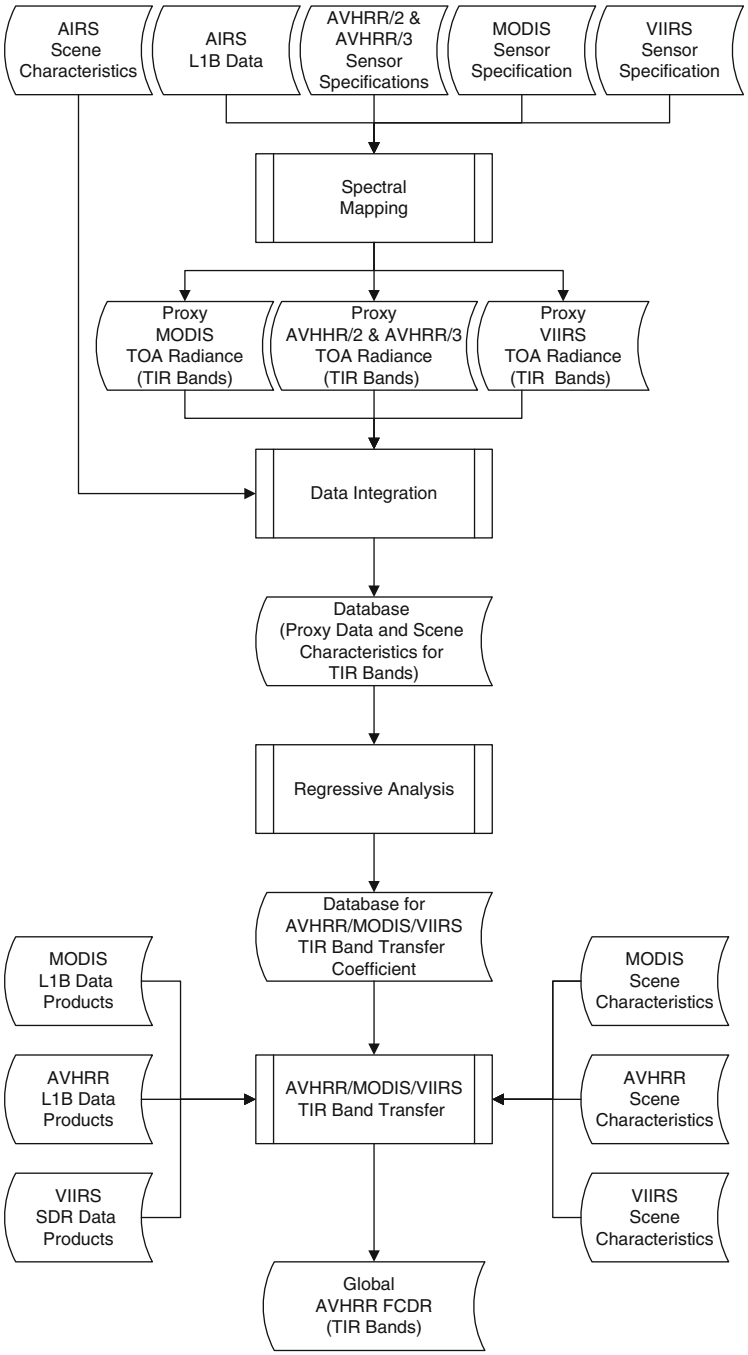

Fig. 5.3 Technical approach for thermal emissive FCDR generation

01/25/2008, 04/09/2008, 06/23/2008, 09/06/2008, and 11/20/2008. In total, 1920 AIRS granules are collected.
- For AIRS FOVs, collect scene characteristics, including surface type, solar angles, view angles, cloud status, etc. These scene characteristics can be determined using AIRS L1B measurements, AIRS level 2 retrieval data products, and MODIS land cover data products.

2. Spectral mapping and proxy data generation
   - Convolve the spectral response functions of AVHRR band 4 and band 5, MODIS band 31 and band 32, and VIIRS band M15 and band M16, with AIRS hyper-spectral thermal infrared measurements to generate global proxy datasets for various versions of AVHRR, MODIS, and VIIRS.
   - MODIS L1B radiance is defined in wavelength domain with unit $Wm^{-2}sr^{-1}/\mu m$, while AIRS radiance data is defined in wavenumber domain with unit $mWm^{-2}sr^{-1}/cm^{-1}$; unit conversion and spectral response function should be taken into account to simulate broadband radiance with AIRS. After unit conversion, proxy measurements can be generated by convolving spectral response functions of various sensors (AVHRR, MODIS, and VIIRS) over AIRS hyper-spectral measurements.
3. Construction of global testing database
   - Combine AIRS-simulated AVHRR/MODIS/VIIRS proxy datasets with AIRS scene characteristics, including surface type, solar angles, view angles, cloud status, etc., to construct a global testing database.
4. Regressive analysis to determine band transfer equations
   - Select one sensor as template for FCDR.
   - Using the testing database, discover the band transfer equations for converting AVHRR/MODIS/VIIRS bands to the selected template sensor through regressive analysis.
   - Construct the database for coefficients in band transfer equations.

   Save the coefficients for band transfer equations for various scene characteristics in database for later use.
5. Producing global AVHRR FCDR data
   - For historical AVHRR measurements, identify scene characteristics and apply the corresponding band transfer equations to convert SDR of old AVHRR versions to the template sensor.
   - For MODIS measurements, identify scene characteristics and apply the band transfer equations to get equivalent MODIS SDRs, which can be combined into AVHRR FCDRs for expansion of temporal coverage.
   - After NPP/JPSS lunch, VIIRS SDRs can also be used to expand the thermal emissive FCDRs.

5.3 Results and Analysis

5.3.1 Validation of Spectral Mapping

Since AIRS and MODIS are on the same satellite, i.e., NASA Aqua, it provides a unique opportunity to evaluate the accuracy of spectral mapping by comparing AIRS-simulated MODIS measurements and spatially aggregated MODIS measurements at AIRS field of views (FOVs). Spatially, the AIRS-simulated AVHRR and MODIS measurements are for AIRS footprints, not for the native AVHRR and MODIS pixels. To evaluate the accuracy of spectral simulation, MODIS L1B measurements at 1-km pixels were aggregated to collocated AIRS footprints through spatial matchup. AIRS has a field of view of $\pm 49.5^{\circ}$ in cross track. Each AIRS scan line contains 90 IR footprints, with a spatial resolution of 13.5 km at nadir and 41 $\times$ 21.4 km at the scan extremes from nominal 705.3-km orbit. MODIS has a field of view of $\pm 55^{\circ}$ in cross track. Each scan MODIS line has 1,354 footprints, with a spatial resolution of 1 km at nadir. AIRS has a 1.1° circular IFOV; thus, as demonstrated in Fig. 5.4a, for a given AIRS pixel, we can find the MODIS pixels within the AIRS footprint by calculating the deviation of scan angle between the AIRS pixel and the MODIS pixel; if the deviation is less than 0.55°, then the MODIS pixel is inside the AIRS pixel. Figure 5.4b illustrated an example of collocated AIRS and MODIS pixels. Average MODIS 1-km data to colocated AIRS pixels will produce "truth" MODIS data at AIRS FOVs and can be used to compare with simulated MODIS.

Based on the global MODIS and AIRS L1 data of the selected 8 days, i.e., 135*90*240*8 = 23,328,000 pixels, the difference between simulated MODIS and aggregated MODIS radiance is quite small. For the 11-μm band, the brightness temperature difference between simulated MODIS and aggregated MODIS is −0.0039 K, with a standard deviation of 0.6031 K, as shown in Fig. 5.5a, b. The brightness temperature difference is less than 1 K for 93.01% of the total 23,328,000 pixels (Table 5.1). And the related difference is less than 1% for 99.15% of all the pixels (Table 5.2). For the 12-μm band, the brightness temperature difference between simulated MODIS and aggregated MODIS is −0.0535 K, with a standard deviation of 0.5461 K, as shown in Fig. 5.5c, d. The brightness temperature difference is less than 1 K for 94.12% of the total 23,328,000 pixels (Table 5.1). And the related difference is less than 1% for 99.36% of all the pixels.

From these statistics of brightness temperature differences over global datasets of the selected 8 days, the simulated MODIS with AIRS hyper-spectral measurements are quite close to the "true" MODIS measurements, i.e., aggregated MODIS measurements at AIRS FOVs. So, it should be fine to use AIRS-simulated proxy data to derive the relationships between different sensors.

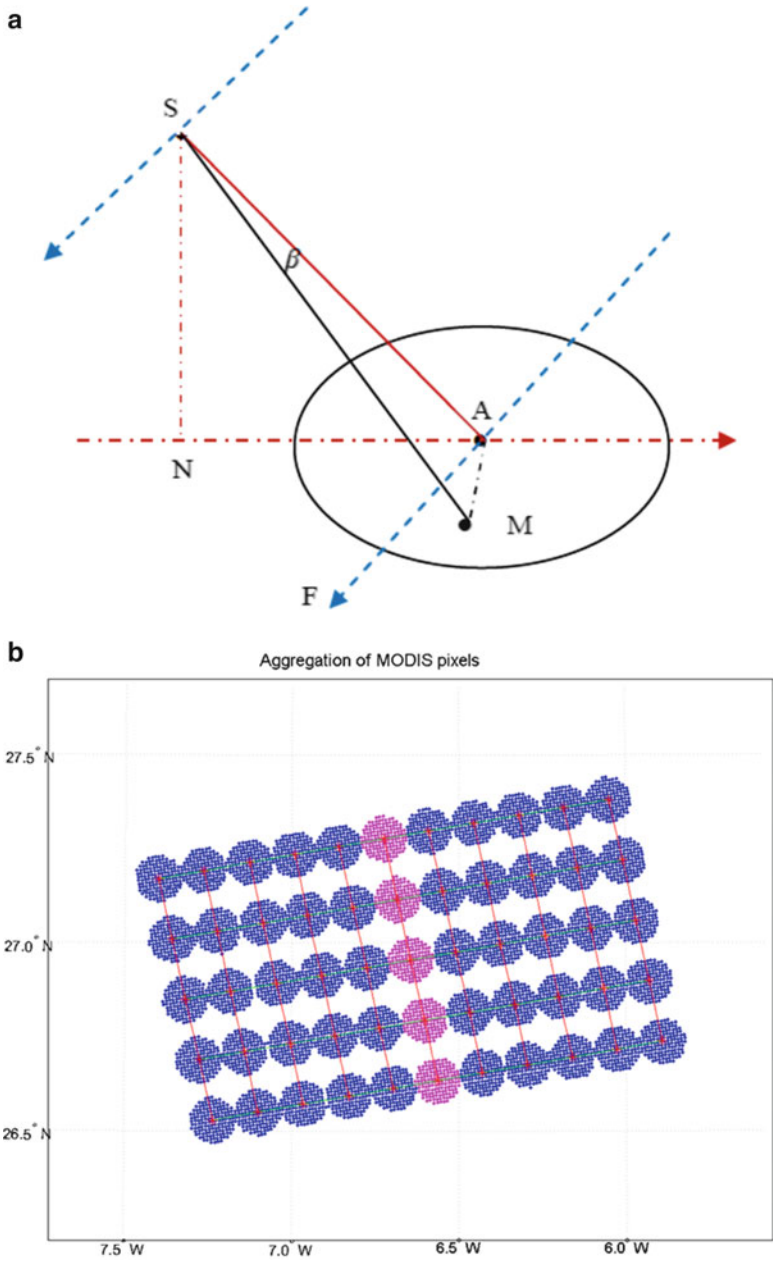

Fig. 5.4 AIRS-MODIS spatial matchup. (**a**) Angular relationship between AIRS pixels and MODIS pixels. (**b**) An example of MODIS pixels aggregated to AIRS footprints

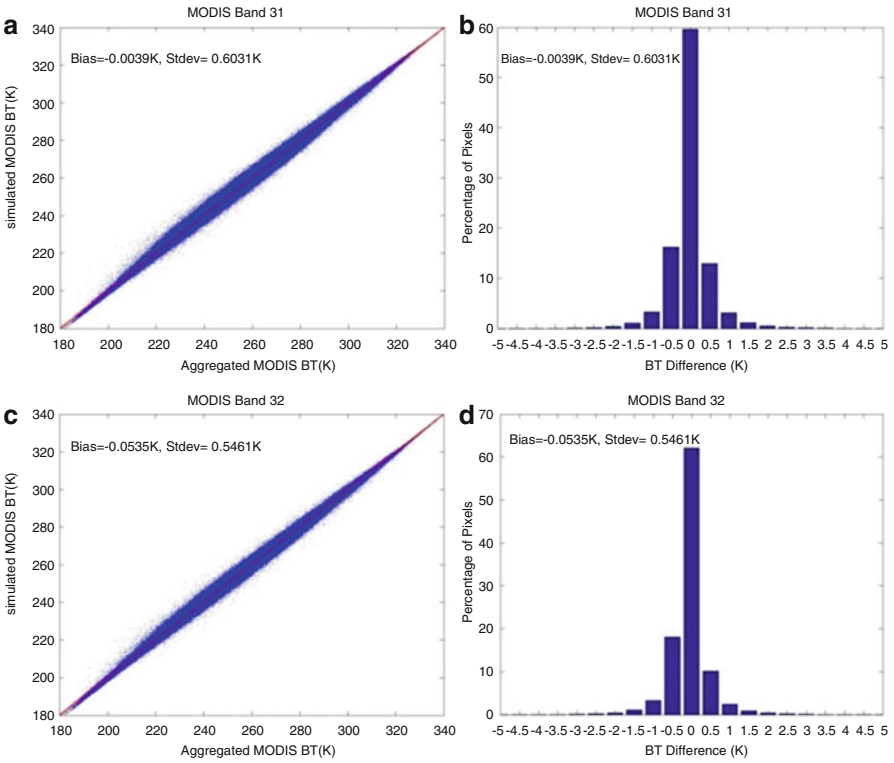

Fig. 5.5 Comparison of AIRS-simulated MODIS and aggregated MODIS at AIRS footprints. (**a**) Brightness temperature of MODIS band 31; (**b**) histogram of band 31 brightness temperature difference between AIRS-simulated MODIS and aggregated MODIS; (**c**) brightness temperature of MODIS band 32; (**d**) histogram of band 32 brightness temperature difference between AIRS-simulated MODIS and aggregated MODIS

Table 5.1 Difference of brightness temperature between simulated MODIS and aggregated MODIS

Band	<1 K (%)	<0.5 K (%)	<0.25 K (%)
Band 31	93.01	80.57	59.66
Band 32	94.12	82.51	62.15

Table 5.2 Relative difference of brightness temperature between simulated MODIS and aggregated MODIS

Band	<1%	<0.5%	<0.2%
Band 31	99.15%	95.70%	81.57%
Band 32	99.36%	96.42%	83.18%

5.3.2 *Band Transfer for FCDR Generation*

Once the global testing database, including simulated proxy data for various version of AVHRR and MODIS sensors, as well as scene characteristics is established, statistical analysis is conducted to derive the relationships between similar bands of different sensors.

Figure 5.6a–c illustrates the linear relationships between Aqua MODIS band 31 and band 4 of NOAA-16 AVHRR, NOAA-17 AVHRR, and NOAA-18 AVHRR, respectively. Band transfer equations among these sensors at 11-μm band and statistics are listed in Table 5.3. For all the selected sensor pairs, linear relationship fits very well, with R^2 higher than 0.999 and very small root-mean-square error (RMSE), which are around MODIS sensor accuracy requirements.

Similarly, Fig. 5.7a–c illustrates the linear relationships between Aqua MODIS band 32 and band 5 of NOAA-16 AVHRR, NOAA-17 AVHRR, and NOAA-18 AVHRR, respectively. Table 5.4 lists the band transfer equations and statistics of the 12-μm band. For all the selected sensor pairs, linear relationship fits even better than the 11-μm band, with R^2 higher than 0.9999 and root-mean-square errors (RMSE) at 0.0412223, 0.0262475, and 0.0373566 K, respectively. These errors meet MODIS sensor accuracy requirements.

For VIIRS, Terra MODIS, and other version of AVHRR sensors, band transfer equations can be determined similarly using the global testing database. More accurate band transfer equations can be obtained if scene characteristics are taken into account (Hao et al. 2005b). So, the band mapping approach is feasible for construction of long-term thermal emissive FCDRs.

5.4 Conclusion and Discussions

In this chapter, technical approaches for thermal emissive FCDR generation with AVHRR, MODIS, and VIIRS measurements are presented, and preliminary results are demonstrated and analyzed based on a global testing database constructed with global AIRS measurements of selected 8 days during year 2002 and 2008. The performance of spectral mapping is investigated by comparing AIRS-simulated MODIS and aggregated MODIS measurements. As the differences between AIRS-simulated MODIS and aggregated MODIS measurements are quite small, it is feasible to use AIRS-simulated proxy datasets for FCDR generation. Band transfer equations are derived, and performances of band transfer models are analyzed statistically. For all the selected sensor pairs, determinant coefficients of linear band transfer equations are almost 1, and the root-mean-square errors are very small, accurate enough for most applications.

Certainly, the presented approach relies on consistent calibration of selected sensors. Calibration consistency and stability are critical for Climate Data Record generation. Inter-sensor calibration based on comparison of measurements from different sensors at collocated sites can help to improve the calibration consistency

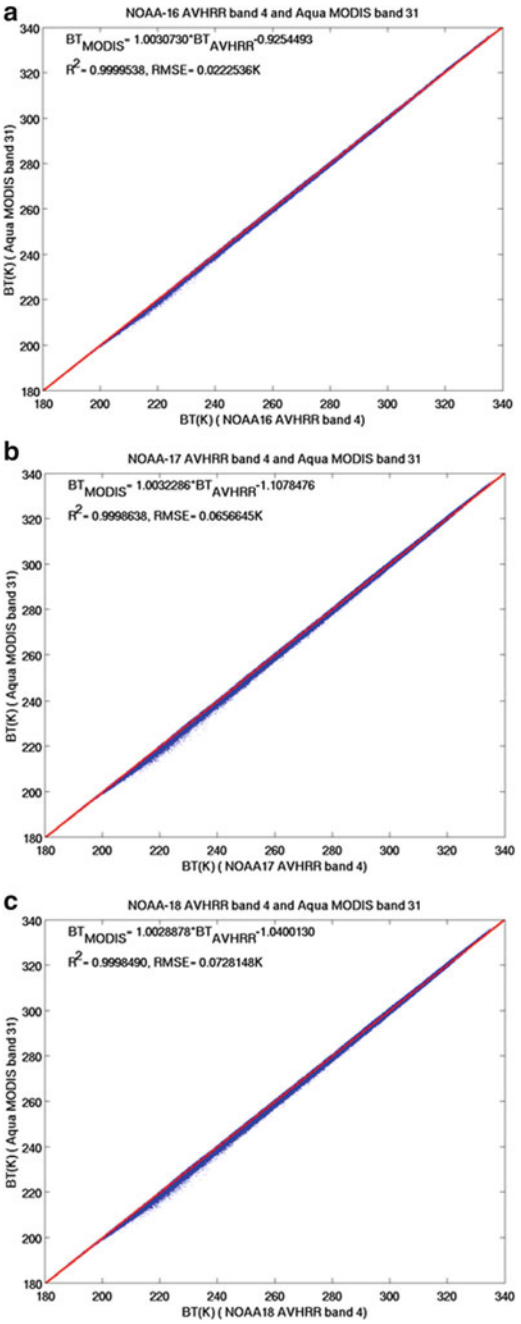

Fig. 5.6 Aqua MODIS band 31 and AVHRR band 4 (**a**) Aqua MODIS band 31 and NOAA-16 AVHRR band 4. (**b**) Aqua MODIS band 31 and NOAA-17 AVHRR band 4. (**c**) Aqua MODIS band 31 and NOAA-18 AVHRR band 4

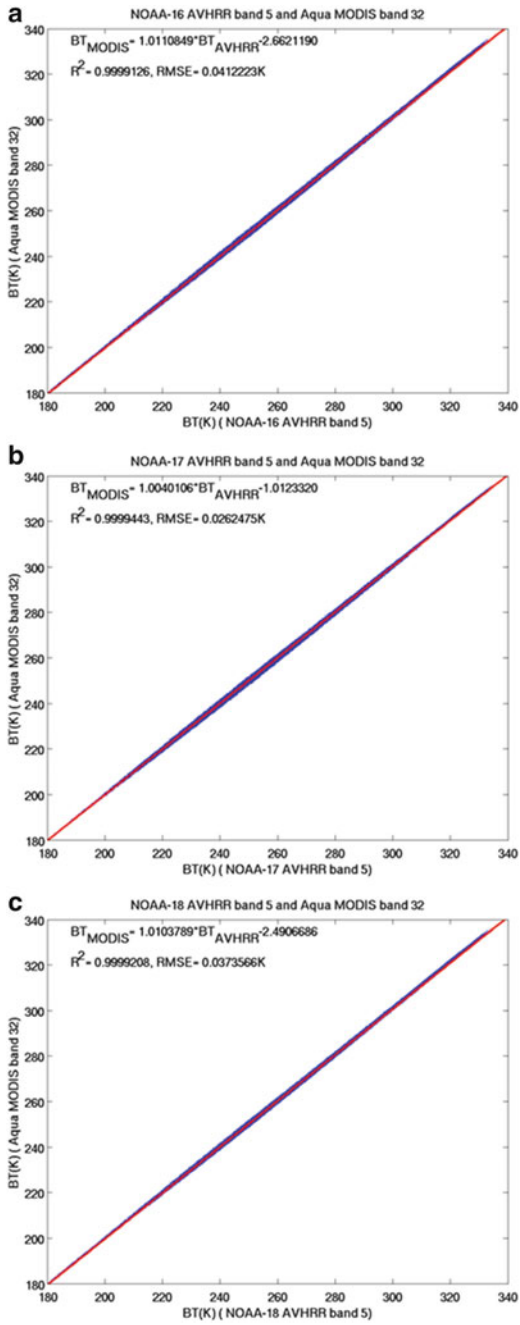

Fig. 5.7 Aqua MODIS band 32 and AVHRR band 5 (**a**) Aqua MODIS band 32 and NOAA-16 AVHRR band 5. (**b**) Aqua MODIS band 32 and NOAA-17 AVHRR band 5. (**c**) Aqua MODIS band 32 and NOAA-18 AVHRR band 5

Table 5.3 Band transfer equations for the 11-μm band

Sensor 1	Sensor 2	Band transfer equation (BT)	R^2	RMSE (K)
MODIS (Aqua)	AVHRR (NOAA-16)	$BT^{(1)} = BT^{(2)} * 1.003073026292936 - 0.925449346110636$	0.9999538	0.0222536
MODIS (Aqua)	AVHRR (NOAA-17)	$BT^{(1)} = BT^{(2)} * 1.003228599446248 - 1.107847591257153$	0.9998638	0.0656645
MODIS (Aqua)	AVHRR (NOAA-18)	$BT^{(1)} = BT^{(2)} * 1.002887837732207 - 1.040012956166496$	0.9998490	0.0728148

Table 5.4 Band transfer equations for the 12-μm band

Sensor 1	Sensor 2	Band transfer equation (BT)	R^2	RMSE (K)
MODIS (Aqua)	AVHRR (NOAA-16)	$BT^{(1)} = BT^{(2)} * 1.011084932447852 - 2.662118959097069$	0.9999126	0.0412223
MODIS (Aqua)	AVHRR (NOAA-17)	$BT^{(1)} = BT^{(2)} * 1.004010642806296 - 1.012331970324046$	0.9999443	0.0262475
MODIS (Aqua)	AVHRR (NOAA-18)	$BT^{(1)} = BT^{(2)} * 1.010378918506728 - 2.490668604967525$	0.9999208	0.0373566

of different sensors (Cao and Heidinger 2002; Heidinger et al. 2002; Cao et al. 2008; Wu et al. 2008, 2009; Xiong et al. 2008a, b; Qu et al. 2008).

Validation of band transfer equations will be conducted in near future by collecting collocated measurements of multiple sensors. The presented approach can also be applied to other sensors. In addition, more hyper-spectral sensors, such as the Infrared Atmospheric Sounding Interferometer (IASI) and Cross-track Infrared Sounder (CrIS), can also be used for proxy data simulation and testing database generation.

References

Cao C, Heidinger A (2002) Inter-comparison of the longwave infrared channels of Terra/MODIS and NOAA-16/AVHRR using simultaneous nadir observations at orbit intersections. In: Barnes W (ed) Earth observing systems VII, Proceedings of SPIE, vol 4814. SPIE, Seattle, pp 306–316

Cao C, Xiong X, Wu A, Wu X (2008) Assessing the consistency of AVHRR and MODIS L1B reflectance for generating fundamental climate data records. J Geophys Res 113:D09114

Hao X, Qu J (2008) Cross-sensor band mapping for developing consistent climate data record of earth observation. Paper presented at SPIE Asia-Pacific remote sensing meeting, Noumea, New Caledonia, 17–21 Nov 2008

Hao X, Qu J (2009a) Fast and highly accurate calculation of band averaged radiance. Int J Remote Sens 30(5):1099–1108

Hao X, Qu J (2009b) Band mapping approach for fundamental climate data records (FCDRs) generation. Paper presented at SPIE optical engineering and applications, San Diego, 2–6 Aug 2009

Hao X, Qu J, Bhoi S, Dasgupta S, Wang W, Xie Y, Wang L, Hauss B, Wang C (2005a) Development and enhancement of calibration/validation toolkit for supporting NPOESS/NPP missions. In: IGARSS 05 proceedings. 2005 I.E. international. Seoul, 25–29 July 2005, vol 1, pp 113–116

Hao X, Qu J, Hauss B, Wang C, Privette JL (2005b) Establishing a proxy database for supporting NPOESS/NPP VIIRS land product pre-launch testing. Paper presented at AGU annual meeting, San Francisco, 5–9 Dec 2005

Hao X, Qu J, Hauss B, Wang C (2007) A high performance approach for brightness temperature inversion. Int J Remote Sens 28(21):4733–4743

Heidinger A, Cao C, Sullivan J (2002) Using MODIS to calibrate AVHRR reflectance channels. J Geophys Res 107(D23):4702

Justice C, Vermote E, Townshend J, Defries R, Roy D, Hall D, Salomonson V, Privette J, Riggs G, Strahler A, Lucht W, Myneni R, Knyazikhin Y, Running S, Nemani R, Wan Z, Huete A, van Leeuwen W, Wolfe R, Giglio L, Muller J, Lewis P, Barnsley M (1998) The moderate resolution imaging spectroradiometer (MODIS): land remote sensing for global change research. IEEE Trans Geosci Remote Sens 36(4):1228–1249

National Research Council (NRC) (2004) Climate data records for environmental satellite. National Academies Press, Washington, D.C

National Research Council (NRC) (2009) Advice to the new administration and congress: actions to make the our nation resilient to severe weather and climate change. Bull Am Meteorol Soc 90(1):102–108

Qu J, Hao X, Hauss B, Wang C, Xiong X, Privette JL (2005a) Toward cross-sensor calibration between two radiometers. Paper presented at NPP science team meeting, Annapolis, Jan 2005

Qu J, Hao X, Hauss B, Wang C, Privette JL (2005b) A new approach for radiometric cross calibration of satellite-borne radiometers. In: IGARSS 05 proceedings, 2005 I.E. international. Seoul, 25–29 July 2005, vol 6, pp 4142–4145

Qu J, Hao X, Xiong X, Hauss B, Wang C (2006a) Supporting NPOESS/NPP pre-launch calibration and verification with a cross-sensor mapping system. Paper presented at SPIE annual conference, San Diego, 13–17 Aug 2006

Qu J, Hao X, Xiong X, Privette JL (2006b) Cross-instrument calibration between MODIS and AIRS. Paper presented at MODIS science team meeting, Baltimore, 4–6 Jan 2006

Qu J, Hao X, Xiong X, Mango S (2008) Integrating the cross-instrument calibration and validation system for GEOSS support. Paper presented at SPIE Asia-Pacific remote sensing meeting, Noumea, New Caledonia, 17–21 Nov 2008

Salomonson V, Barnes W, Masuoka EJ (2006) Introduction to MODIS and an overview of associated activities. In: Qu J et al (eds) Earth science satellite remote sensing, vol I. Springer, Berlin, pp 12–31

Wu A, Xiong X, Cao C (2008) Terra and Aqua MODIS inter-comparison of three reflective solar bands using AVHRR onboard the NOAA-KLM satellites. Int J Remote Sens 29(7):1997–2010

Wu A, Xiong X, Cao C (2009) Tracking the calibration stability and consistency of the 3.7, 11.0 and 12.0 μm channels of the NOAA-KLM AVHRR with MODIS. Int J Remote Sens 30 (22):5901–5917

Xiong X, Chiang K, Wu A, Barnes W, Guenther B, Salomonson V (2008a) Multiyear on-orbit calibration and performance of Terra MODIS thermal emissive bands. IEEE Trans Geosci Remote Sens 46(6):1790–1803

Xiong X, Wu A, Cao C (2008b) On-orbit calibration and inter-comparison of Terra and Aqua MODIS surface temperature spectral bands. Int J Remote Sens 29(17):5347–5359

Chapter 6
Global Precipitation Monitoring

Ralph Ferraro and Thomas Smith

Abstract Satellite observations play a vital role in the global monitoring of precipitation because they fill in large data voids where conventional measurements such as surface rain gauges and weather radars are primarily restricted to populated land regions. Geostationary satellites, containing visible and infrared sensors, provide the most continuous observations from space; they can infer surface precipitation through relationships between cloud properties and precipitation rate. Passive microwave sensors, which operate primarily on low Earth-orbiting satellites, provide a more direct measurement of rainfall and global coverage; however, they observe the Earth less frequently than the geostationary satellites. This chapter summarizes the strengths and weaknesses of the various satellite retrieval algorithms, then describes emerging blended precipitation products that merge different satellite measurements to achieve the best possible rainfall product. Examples of the utility of such data are also provided.

Keywords Satellite • Precipitation • Passive Microwave • Infrared

6.1 Introduction

The remote sensing of precipitation is a vital component to the integrated observing of precipitation on the Earth. While weather radars and rain gauges are the primary source of precipitation information, they are typically restricted to populated areas

R. Ferraro (✉) • T. Smith
Cooperative Research Programs, NOAA/NESDIS/Center for Satellite Applications and Research (STAR), 5830 University Research Court, College Park, MD 20740, USA
e-mail: Ralph.R.Ferraro@noaa.gov; Tom.Smith@noaa.gov

J.J. Qu et al. (eds.), *Satellite-based Applications on Climate Change*,
DOI 10.1007/978-94-007-5872-8_6,

over land and can only extend out a short distance over oceans. Satellites, therefore, provide crucial information to fill in these huge data voids, especially over unpopulated regions and oceans. By integrating all available satellite information with surface measurements in a "seamless" manner, the best possible global precipitation climatology can be assembled. This chapter will begin by briefly describing the various satellite precipitation retrieval methods, present the current state of combined satellite and surface rainfall techniques, show some examples of such datasets to depict global precipitation patterns, and conclude by describing the anticipated advances over the upcoming decade.

6.2 Satellite Precipitation Retrieval Methods

A number of different methods are used to retrieve rainfall from satellites and are summarized in Table 6.1. In general, the methods can be categorized into low Earth orbiting (LEO) and geostationary Earth orbiting (GEO), as well as by their observing spectral ranges (visible, infrared, passive microwave, active microwave) or "multispectral" (i.e., use of one or more of these individual spectrums). Some brief background on the various retrieval techniques is described.

6.2.1 Visible and Infrared Methods

Visible (VIS) and infrared (IR) techniques were the first satellite methods to be developed and are rather simple to apply (Lovejoy and Austin 1979). However, these techniques typically show a relatively low degree of accuracy. On the other hand, GEO weather satellite VIS and IR imagers uniquely provide the rapid temporal update cycle (e.g., 30 min or less) needed to capture the growth and decay of precipitating clouds.

A complete overview of the early work and physical premises of VIS and thermal IR (10.5–12.5 μm) techniques is provided by Barrett and Martin (1981), while Kidder and Vonder Haar (1995) present some of the more recent results. The rainfall retrieval in these wavelengths is based on the fact that bright (optically thick) clouds are positively correlated with regions of convective rainfall (Woodley and Sancho 1971). On the other hand, clouds with cold tops in the IR imagery produce more rainfall than those with warmer tops (Scofield 1987). However, the correspondence between cold tops and visible bright spots is far from perfect and is not always well correlated with surface rainfall (especially in stratiform rainfall regimes).

Various approaches have been developed to stress particular aspects of the sensing of cloud physics properties to settle differences between VIS and IR retrievals and measured rainfall. The methods are sometimes classified as cloud indexing (e.g., Arkin and Meisner 1987), bi-spectral schemes (e.g., Lovejoy and Austin 1979), life history (e.g., Griffith et al. 1978), and cloud model-based (e.g., Adler and Negri 1988). More recently, multispectral (i.e., VIS and IR combined)

Table 6.1 Summary of satellite methods for the retrieval of precipitation

Observation spectrum	Satellite type	Sensor examples	Strength	Weakness
Visible (VIS)	GEO	GOES Imager	Cloud type	Cloud tops
	LEO	AVHRR	Cloud evolution	Indirect rain rate
Infrared (IR)	GEO	GOES Imager	Cloud temperature	Cirrus contamination
	LEO	AVHRR	Cloud evolution	Indirect rain rate
Passive microwave (PMW)	LEO	SSM/I	Direct measure of rain, especially over ocean	Poor temporal sampling
		AMSR-E		Coarse spatial resolution
		TMI		Indirect rain rate (land)
Active microwave (AMW)	LEO	TRMM PR	Direct measure of vertical structure of rain	Narrow swath width
		CloudSat CPR		Poor temporal sampling
				Rain rate sensitivity/ saturation

has emerged which attempts to utilize the strengths of both wavelengths (e.g., Ba and Gruber 2001).

To illustrate the spatial coverage and information content available from IR satellite measurements, Fig. 6.1 gives a multi-satellite (i.e., numerous GEO and LEO satellites) composite of IR imagery from 1500 UTC, 2 June 2010. This data is freely available from the Naval Research Laboratory (NRL) in Monterey, CA, at http://www.nrlmry.navy.mil/sat_products.html. If one looks closely at this IR composite, the cloud patterns associated with midlatitude cyclones are quite evident by the large, bright features that correspond to high-level clouds. On the other hand, the tropical regions are dominated by cloud clusters corresponding to tropical convective features that are associated with the Intertropical Convergence Zone (ITCZ). The darker clouds are lower level clouds, typically associated with stratus clouds which may or may not be associated with rainfall. A comparable VIS image (not shown) would show other information but would be restricted to approximately a 180° longitudinal zone where sunlight is reflecting off the cloud tops.

6.2.2 Passive Microwave Methods

Unlike VIS and IR signals, microwave (MW) energy can penetrate clouds, in particular, cirrus clouds, and its signal has a strong interaction with precipitation-size drops and ice particles. This direct impact on microwave measurements by hydrometeors allows for the quantitative detection of precipitation properties in the atmosphere as well as on the surface. It should be pointed out that passive MW (PMW) means naturally emitted radiation from the Earth's surface and atmosphere

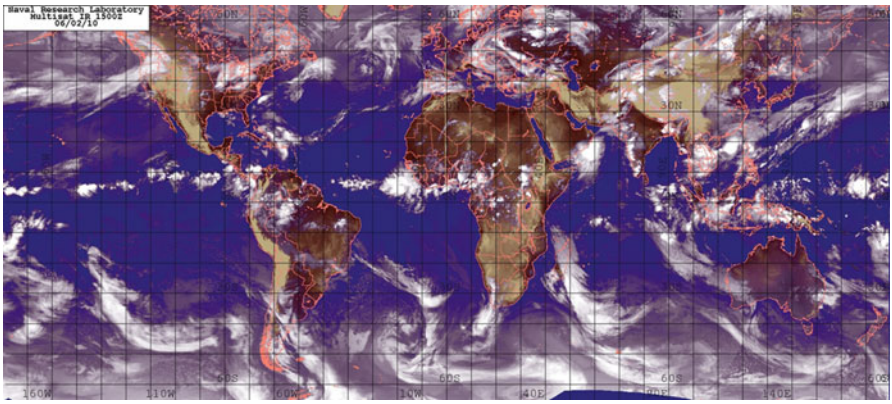

Fig. 6.1 Multi-satellite (i.e., numerous GEO and LEO satellites) composite of IR imagery from 1500 UTC, 2 June 2010 (Courtesy of the Naval Research Laboratory (NRL) in Monterey, CA (http://www.nrlmry.navy.mil/sat_products.html))

that interacts with clouds and precipitation and is measured by a radiometer on board a satellite.

Most passive microwave radiometers launched to date operate in frequencies ranging from 6 to 190 GHz. At different frequencies, microwave radiometers observe different parts of the rain profile. Below 20 GHz, emission by precipitation-size drops dominates, and ice particles above the rain layer are nearly transparent. Above 60 GHz, ice scattering dominates, and the radiometers cannot sense the raindrops below the freezing layer. Both emission and scattering effects are important for frequencies between 20 and 60 GHz. In general, emission by liquid drops raises brightness temperature, while scattering by ice particles has the opposite effect. Window channels (i.e., wavelengths which have very little contamination due to atmospheric constituents like water vapor and oxygen) can measure down to the Earth's surface and are strongly influenced by surface properties (i.e., vegetation and soil moisture). Other frequencies are sensitive to oxygen or water vapor/cloud droplet absorption. These microwave properties set the foundation for the development of rainfall estimation schemes.

There are two major categories in rainfall estimation using passive microwave radiometry: emission-based method and scattering-based method. Emission-based rainfall algorithms are mostly applicable over ocean because water surfaces are relatively homogeneous and provide a cold background due to low emissivity. The presence of raindrops allows for absorption and emission over the water surfaces and results in a dramatic warming of the satellite measurements. Some of the earliest emission techniques were developed with the Nimbus-5 and Nimbus-6 Electrically Scanning Microwave Radiometer (ESMR) (Wilheit et al. 1977). Significant advances were made through the Special Sensor Microwave/Imager (SSM/I) series, first launched in 1987 and followed by five more instruments which operated effectively through much of 2009 (e.g., Olson 1989; Ferraro and Marks 1995; Smith et al. 1994).

The SSM/I has been replaced with the Special Sensor Microwave Imager Sounder (SSMIS) which is in operation at the time of this writing. Today, the Goddard profiling algorithm (GPROF), a sophisticated inversion algorithm based on cloud resolving models and radiative transfer calculations (Kummerow et al. 1996, 2001), is widely used on a variety of sensors such as the SSM/I, Tropical Rainfall Measuring Mission (TRMM) Microwave Imager (TMI), and the Advanced Microwave Sounding Radiometer-Earth Observing System (EOS) (AMSR-E) (Wilheit et al. 2003).

Due to the high and more varying emissivity of the land surface, the only reliable means of detecting rainfall over land is by isolating depressed brightness temperatures as a result of scattering by millimeter-sized ice particles that exist in most rain clouds. Since the signal being captured is a result of ice particles instead of raindrops, the scattering-based rainfall estimation is an indirect measure of rainfall, as it relates the magnitude of the scattering near the freezing layer to surface rainfall. The launch of the SSM/I in 1987 provided the first opportunity to retrieve rain rate through scattering at higher frequency (85 GHz). Noteworthy studies in this regard include Spencer et al. (1989), Grody (1991), and Ferraro and Marks (1995). GPROF adopted this method over land as well (McCollum and Ferraro 2003; Wang et al. 2009; Gopolan et al. 2010) and has been used for TMI and AMSR-E.

Zhao and Weng (2002) took advantage of the highly scattering nature of 89 GHz and in particular 150 GHz radiances from the Advanced Microwave Sounding Unit-B (AMSU-B) and retrieved ice water path (IWP) using scattering parameters measured at these two channels. The derived IWP is then converted into the surface rainfall rate (RR) through an IWP and rainfall rate relationship developed from cloud model results (Weng et al. 2003). This rain rate product is being operationally generated at National Environmental Satellite, Data, and Information Service (NESDIS) of National Oceanic and Atmospheric Administration (NOAA). This algorithm has also been applied to Microwave Humidity Sounder (MHS) with some modification since AMSU-B and MHS have very similar channels. Vila et al. (2007) added an emission-based component to this rainfall algorithm to account for oceanic rain systems that have little or no ice in them.

Figure 6.2 illustrates the use of passive MW measurements to retrieve rainfall. Shown is the Naval Research Laboratory (NRL) passive MW composite, overlaid on the global IR composite that was presented in Fig. 6.1. The various color shades indicate the intensity of rainfall derived from the array of MW sensors used in this composite (e.g., SSM/I, AMSU, TMI, and AMSR-E).

6.2.3 Active Microwave Methods

In contrast to passive microwave radiometers, active microwave sensors provide their own source of microwave radiation and are able to determine fine-scale and vertical distribution of rainfall. In orbit since 1997, the precipitation radar (PR) on

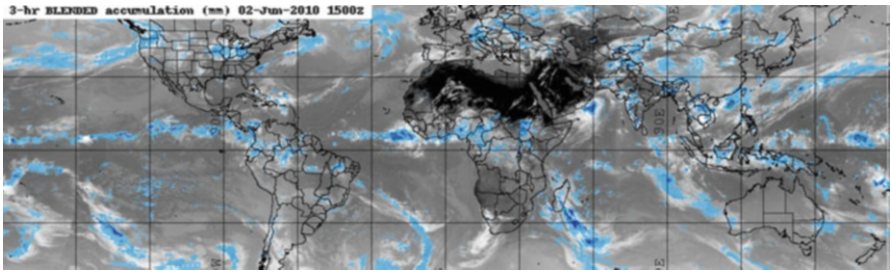

Fig. 6.2 NRL passive MW composite, overlaid on the global IR composite that was presented in Fig. 6.1. The various *blue color shades* indicate the intensity of rainfall derived from the array of MW sensors used in this composite (e.g., SSM/I, AMSU, TMI, and AMSR-E)

the TRMM satellite is the first instrument designed to measure rain from space (Kummerow et al. 1998; Iguchi et al. 2000). Although an excellent source of rainfall information directly, its primary purpose is to be used in conjunction with the more widely available satellites that contain only PMW sensors. With coincident TMI and PR data, significant advances have been made over the TRMM mission life to improve the current state of passive MW retrievals through the better understanding of precipitation and cloud microphysics (Hirose et al. 2009; Gopolan et al. 2010; Wang et al. 2009).

Launched in April 2006, CloudSat is the first millimeter wavelength cloud radar in space (Stephens et al. 2002). The Cloud Profiling Radar (CPR) aboard CloudSat operates at 94 GHz as opposed to 13.8 GHz on PR; thus, it is sensitive to clouds and light precipitation rates, including snowfall (e.g., Matrosov 2007; L'Ecuyer and Stephens 2002; Liu 2008). CloudSat has recently been instrumental in advancing the understanding of cold season precipitation and our ability to retrieve it from PMW sensors.

6.3 Multisensor Global Rainfall Products

The sensors discussed so far each has their limitations which make them unsuitable for use in certain situations. For example, PMW estimates over the ocean might be more accurate than GEO-IR estimates, but the latter are better suited for studies of the diurnal cycle due to the superior sampling obtained from a GEO satellite. On the other hand, most GEO-IR sensors only cover a limited geographic domain, whereas the LEO essentially covers the entire globe. By optimizing the strengths and weaknesses of each data source and combining them with surface measurements where they are deemed to be the most reliable, combined datasets can be superior to estimates from individual sensors. This section will describe some of these "merged" rainfall datasets and present some examples of their utility for global climate monitoring.

For a little historical perspective on this topic, several efforts to intercompare and evaluate various types of precipitation algorithms using remotely sensed information were carried out during the 1990s. The WetNet (Dodge and Goodman 1994) Precipitation Intercomparison Projects (PIP) evaluated multiple global and near-global precipitation algorithms including merged satellite datasets (Barrett et al. 1994; Kniveton et al. 1994; Smith et al. 1998; Adler et al. 2001). The Global Precipitation Climatology Project (GPCP) similarly sponsored three Algorithm Intercomparison Projects (AIP; Ebert et al. 1996) that compared precipitation estimated from satellite observations against high-resolution observations from rain gauges and radars over limited domains (Arkin and Xie 1994; Ebert and Manton 1998). For the most part, these studies showed that PMW estimates were more accurate than IR estimates on an instantaneous basis, but algorithms which combine PMW and IR estimates were superior. However, these intercomparisons did not show significant differences between individual algorithms of a common type. It remains the case that several merged satellite products exist without a clear consensus on which is superior, and it is common to see a range of similar datasets used in the literature.

Perhaps the best known and widely used global precipitation climatology comes from the Global Precipitation Climatology Project (GPCP; Huffman et al. 1997; Adler et al. 2003). The GPCP was developed in the 1990s and during the pre-TRMM era. It combines satellite precipitation from SSM/I with IR estimates (from both geosynchronous and low orbit) and then anchors the estimates with a robust surface rain gauge dataset which takes precedence over land. A similar product, the Climate Prediction Center Merged Analysis of Precipitation (CMAP; Xie and Arkin 1997), also emerged in the same time frame as GPCP and yields similar results when looking at global-scale precipitation patterns on seasonal to interannual time scales. The current version of the GPCP 2.5° monthly mean dataset is the version two dataset (Adler et al. 2003) which improved on the first version with a longer record and the addition of TOVS data for improved estimates at mid- and higher latitudes. Both CMAP and GPCP have problems with high-latitude precipitation due to the lack of reliable data: there are few gauges in these sparsely populated regions, and available satellite-derived precipitation estimates are of limited use over ice- or snow-covered surfaces.

Figure 6.3 shows the GPCP V2 global precipitation product for a 30-year period, 1979–2008. The figure shows the seasonal precipitation for December–January (DJF) and June–August (JJA). The heaviest precipitation over land occurs during the summer season, as evident by the shifts between hemispheres during winter to summer. The tropical zones, namely, the ITCZ, exhibits the wettest precipitation on the Earth, over both the land and ocean zones. Other seasonal features are evident such as monsoonal regions (e.g., India and North America), midlatitude cyclone storm tracks, and the shift of the ITCZ.

The GPCP dataset is also extremely useful for monitoring seasonal to interannual changes in precipitation patterns. A good example of this is provided in Fig. 6.4, which shows the tropical rainfall anomalies over the central Pacific Ocean for the 30-year period (1979–2008). This region is typically where the

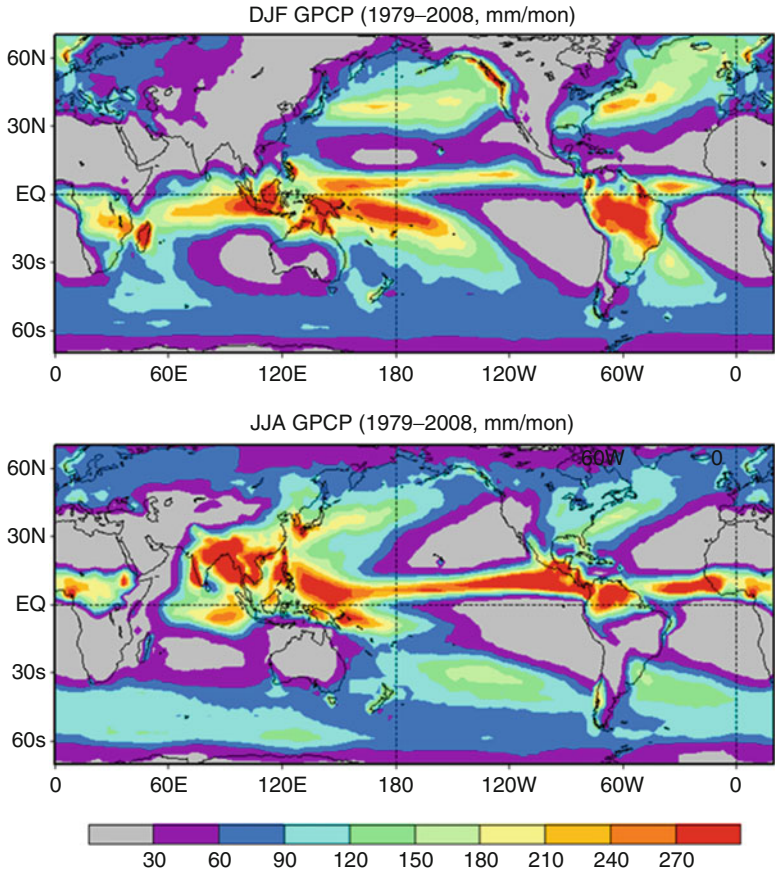

Fig. 6.3 GPCP December, January, and February (*top*) and June, July, and August (*bottom*) 30-year rainfall climatology (mm per month)

largest changes in sea surface temperature (SST; not shown) occur during El Niño/La Niña events. Most obvious in this figure are the large periods and areal coverage of above/below normal rainfall associated with the SST changes with the El Niño/La Niña phenomenon.

Although the monthly 2.5° products are most commonly used, higher-resolution products also exist as part of the GPCP suite. A pentad (5-day mean) version of GPCP combines similar satellite inputs as the monthly product with a different gauge dataset (Xie et al. 2003). This experimental dataset is also produced on a 2.5° resolution grid and starts in 1979. A 1-degree, daily version of the GPCP dataset is also available which starts in 1996 and combines IR from geosynchronous and low orbits with the GPCP version 2 monthly product and AIRS and TOVS estimates (Huffman et al. 2001). GPCP also plans on adding a 3-hourly global product to its version 3 set of products, expected sometime in 2011.

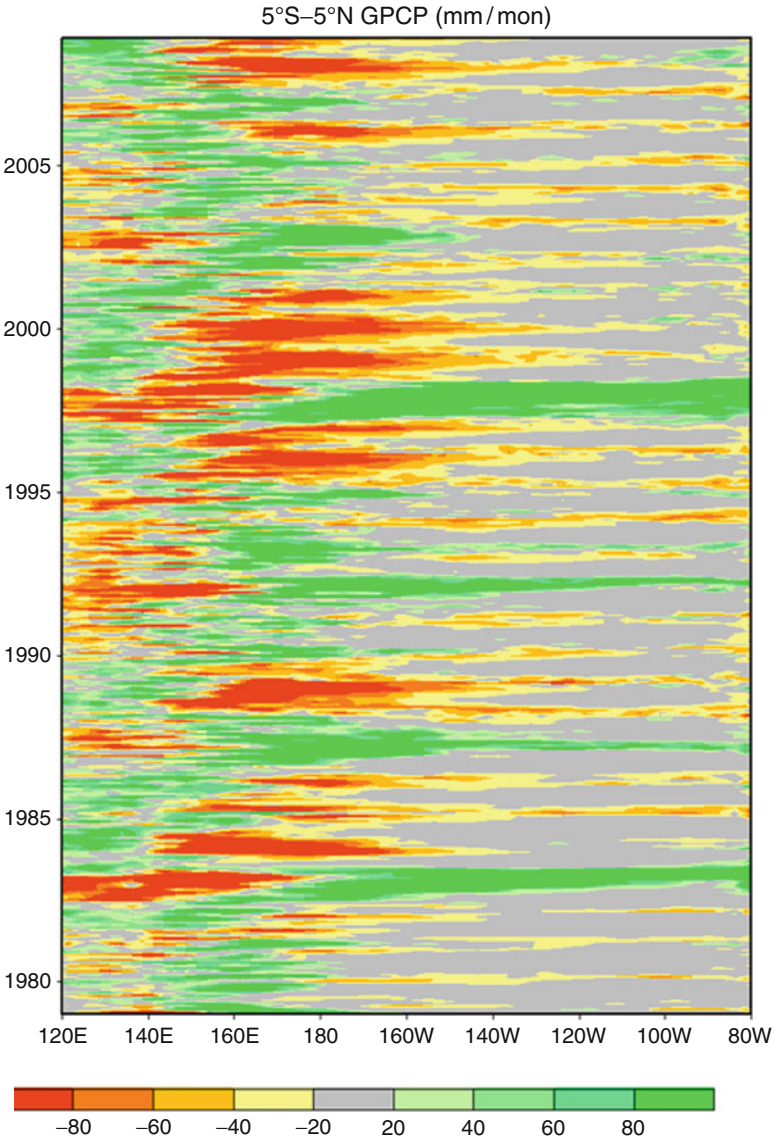

Fig. 6.4 GPCP interannual rainfall anomalies (from the 1979 to 2008 base period) (mm per month) for latitudinal band 5 S to 5 N over the tropical Pacific Ocean. The largest anomalies (*brightest green* and *red areas*) are associated with El Niño (above normal rainfall) and La Niña (below normal rainfall)

Over the past decade, recent increases in the availability of PMW data (SSM/I, TMI, AMSU, AMSR) have led to the emergence of several near-global, high-resolution products which have been showing utility for near-real time use.

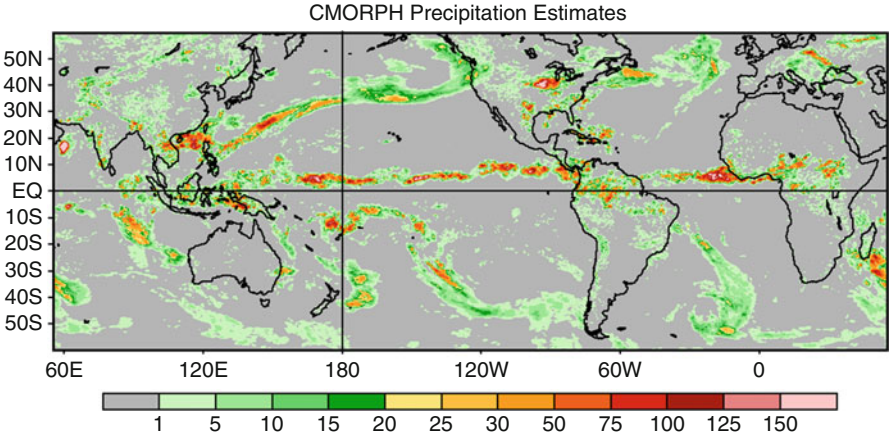

Fig. 6.5 CMORPH rainfall estimate (mm per day) for 2 June 2010

Although not truly global, these products have found a wealth of users in the weather forecasting, climate monitoring, and hydrological communities. Typically, they cover the geographic domain of 60ºS to 60ºN, have 3-h temporal sampling, and are at 0.25° spatial resolution. Commonly referred to as high-resolution precipitation products (HRPPs), they use the high spatial and temporal resolution of IR data to resolve deficiencies in resolution of the higher quality PMW data, although there are substantial differences between the exact methodologies employed. The HRPPs can be categorized into two broad types: adjustment-based techniques where IR data is calibrated using PMW estimates (where the two are often then combined) and motion-based techniques, where the IR data is used to interpolate between successive PMW overpasses.

The Pilot Evaluation of High-Resolution Precipitation Products (PEHRPP; Sapiano and Arkin 2009) was established to intercompare and validate these datasets. PEHRPP included a number of high-resolution datasets: the TRMM Multi-satellite Precipitation Analysis (TMPA; Huffman et al. 2007), the CPC Morphing technique (CMORPH; Joyce et al. 2004), the Hydro-Estimator (Scofield and Kuligowski 2003), the NRL-Blended technique (NRL-Blended; Turk and Miller 2005), Precipitation Estimation from Remotely Sensed Information using Artificial Neural Networks (PERSIANN; Hsu et al. 1997; Sorooshian et al. 2000), and the Global Satellite Mapping of Precipitation (GSMaP) project (Aonashi et al. 2009). CMORPH is the only motion-based technique out of these six. Figure 6.5 presents an example of the CMORPH product.

6.4 Summary and Future

There are various techniques to retrieve rainfall from satellites, each with their own set of attributes that are dictated by the particular needs for the information. For short-term, high spatial resolution applications like flash flood forecasting, the IR

methods are generally preferred. For global climate scales, the PMW measurements are usually preferred. When IR and PMW are combined with surface rain gauges, the best possible product can be generated and used for global-scale applications, such as the GPCP and CMAP products. These products have proven to be of tremendous value in gaining a better understanding of the global precipitation patterns on seasonal to interannual time scales.

Many of the early methods were developed using sensors that were not necessarily flown for rainfall retrieval but more for tracking cloud features and monitoring atmospheric temperature and moisture. Current and near-term missions are now being designed specifically for precipitation monitoring and improving our understanding of precipitating systems and utilize space-based radars, such as TRMM and CloudSat.

On the horizon is the GPM (Global Precipitation Measurement) mission, which is a joint US-Japan mission designed to extend TRMM's observations of precipitation to higher latitudes, with more frequent sampling (Smith et al. 2007). The GPM Core satellite will carry a dual-frequency precipitation radar that will measure a broader spectrum of precipitation types than its predecessor on TRMM (Iguchi et al. 2002). GPM will also feature a "constellation" of PMW sensors that will utilize the GPM Core to advance science improvements and that will achieve 3-hourly or less global precipitation retrievals. Several prototype GPM-era products are already in existence such at the CMORPH and TMPA products previously described.

Acknowledgements The authors would like to thank our colleagues, H. Meng, M. Sapiano, D. Vila, and N. Wang for their contributions to this chapter. Additionally, we would like to recognize the Naval Research Laboratory in Monterey, CA, and the Climate Prediction Center in Camp Springs, M.D., for use of their imagery obtained from their web sites.

References

Adler RF, Negri AJ (1988) A satellite infrared technique to estimate tropical convective and stratiform rainfall. J Appl Meteorol 27:30–51

Adler RF, Kidd C, Petty G, Morrissey M, Goodman HM (2001) Intercomparison of global precipitation products: the third precipitation intercomparison project (PIP-3). Bull Am Meteorol Soc 82:1377–1396

Adler RF, Huffman GJ, Chang A, Ferraro R, Xie P, Janowiak J, Rudolf B, Schneider U, Curtis S, Bolvin D, Gruber A, Susskind J, Arkin P, Nelkin E (2003) The version-2 global precipitation climatology project (GPCP) monthly precipitation analysis (1979-present). J Hydrometeorol 4:1147–1167

Aonashi K, Awaka J, Hirose M, Kozu T, Kubota T, Liu G, Shige S, Kida S, Seto S, Takahashi N, Takayabu Y (2009) GSMaP passive microwave precipitation retrieval algorithm: algorithm description and validation. J Meteorol Soc Jpn 87:119–136

Arkin PA, Meisner BN (1987) The relationship between large-scale convective rainfall and cold cloud over the Western Hemisphere during 1982-84. Mon Weather Rev 115:51–74

Arkin PA, Xie PP (1994) The global precipitation climatology project: first algorithm intercomparison project. Bull Am Meteorol Soc 75:401–419

Ba MB, Gruber A (2001) GOES multispectral rainfall algorithm (GMSRA). J Appl Meteorol 40:1500–1514
Barrett EC, Martin DW (1981) The use of satellite data in rainfall monitoring. Academic, London
Barrett EC, Dodge J, Goodman HM, Janowiak J, Kidd C, Smith EA (1994) The first WetNet precipitation intercomparison project. Remote Sens Rev 11:49–60
Dodge J, Goodman HM (1994) The WetNet project. Remote Sens Rev 11:5–21
Ebert EE, Manton MJ, Arkin PA, Allam RJ, Holpin CE, Gruber A (1996) Results from the GPCP algorithm intercomparison programme. Bull Am Meteorol Soc 77:2875–2887
Ebert EE, Manton MJ (1998) Performance of satellite rainfall estimation algorithms during TOGA COARE. J Atmos Sci 55:1537–1557
Ferraro RR, Marks GF (1995) The development of SSM/I rain-rate retrieval algorithms using ground-based radar measurements. J Atmos Ocean Technol 12:755–770
Gopolan K, Wang NY, Liu C, Ferraro R (2010) Version 7 of the TRMM 2A12 land precipitation algorithm. J Atmos Ocean Technol 27:1343–1354
Griffith CG, Woodley WL, Grube P, Martin DW, Stout J, Sikdar DN (1978) Rain estimation from geosynchronous satellite imagery – visible and infrared studies. Mon Weather Rev 106:1153–1171
Grody NC (1991) Classification of snow cover and precipitation using the special sensor microwave/imager (SSM/I). J Geophys Res 96:7423–7435
Hirose M, Oki R, Short D, Nakamura K (2009) Regional characteristics of scale-based precipitation systems from ten years of TRMM PR data. J Meteorol Soc Jpn 87:353–368
Hsu K, Gao X, Sorooshian S, Gupta HV (1997) Precipitation estimation from remotely sensed information using artificial neural networks. J Appl Meteorol 36:1176–1190
Huffman GJ, Adler RF, Arkin PA, Chang A, Ferraro R, Gruber A, Janowiak J, McNab A, Rudolf B, Schneider U (1997) The global precipitation climatology project (GPCP) combined precipitation dataset. Bull Am Meteorol Soc 78:5–20
Huffman GJ, Adler RF, Morrissey MM, Bolvin DT, Curtis S, Joyce R, McGavock B, Susskind J (2001) Global precipitation at one-degree daily resolution from multisatellite observations. J Hydrometeorol 2:36–50
Huffman GJ, Adler RF, Bolvin DT, Gu G, Nelkin EJ, Bowman KP, Hong Y, Stocker E, Wolff D (2007) The TRMM multisatellite precipitation analysis (TMPA): quasi-global, multiyear, combined-sensor precipitation estimates at fine scales. J Hydrometeorol 8:38–55
Iguchi T, Kozu T, Meneghini R, Awaka J, Okamoto K (2000) Rain-profiling algorithm for the TRMM precipitation radar. J Appl Meteorol 39:2038–2052
Iguchi T, Oki R, Smith EA, Furuhama Y (2002) Global precipitation measurement program and the development of dual-frequency precipitation radar. J Comm Res Lab 49:37–45
Joyce RJ, Janowiak JE, Arkin PA, Xie P (2004) CMORPH: a method that produces global precipitation estimates from passive microwave and infrared data at high spatial and temporal resolution. J Hydrometeorol 5:487–503
Kidder SQ, Vonder Haar TH (1995) Satellite meteorology: an introduction. Academic, New York
Kniveton DR, Motta BC, Goodman HM, Smith M, LaFontaine FJ (1994) The first WetNet precipitation intercomparison project: generation of results. Remote Sens Rev 11:243–302
Kummerow C, Olson WS, Giglio L (1996) A simplified scheme for obtaining precipitation and vertical hydrometeor profile from passive microwave. IEEE Trans Geosci Remote Sens 34:1213–1232
Kummerow C, Barnes W, Kozu T, Shiue J, Simpson J (1998) The tropical rainfall measuring mission (TRMM) sensor package. J Atmos Ocean Technol 15:809–817
Kummerow C, Hong Y, Olson WS, Yang S, Adler RF, McCollum J, Ferraro R, Petty G, Shin D, Wilheit TT (2001) The evolution of the Goddard profiling algorithm (GPROF) for rainfall estimation from passive microwave sensors. J Appl Meteorol 40:1801–1819
L'Ecuyer TS, Stephens GL (2002) An estimation-based precipitation retrieval algorithm for attenuating radars. J Appl Meteorol 41:272–285
Liu G (2008) Deriving snow cloud characteristics from CloudSat observations. J Geophys Res 113. doi:10.1029/2007JD0009766

Lovejoy S, Austin GL (1979) The delineation of rain areas from visible and IR satellite data from GATE and mid-latitudes. Atmos-Ocean 17:77–92
Matrosov S (2007) Potential for attenuation-based estimates of rainfall rate from CloudSat. Geophys Res Lett 34:L05817. doi:10.1029/2006GL029161
McCollum JR, Ferraro RR (2003) The next generation of NOAA/NESDIS SSM/I, TMI and AMSR-E microwave land rainfall algorithms. J Geophys Res 108:8382–8404
Olson WS (1989) Physical retrieval of rainfall rates over the ocean by multispectral microwave radiometry: application to tropical cyclones. J Geophys Res 94:2267–2280
Sapiano MRP, Arkin PA (2009) An inter-comparison and validation of high resolution satellite precipitation estimates with three-hourly gauge data. J Hydrometeorol 10:149–166
Scofield RA (1987) The NESDIS operational convective precipitation technique. Mon Weather Rev 115:1773–1792
Scofield RA, Kuligowski RJ (2003) Status and outlook of operational satellite precipitation algorithms for extreme-precipitation events. Weather Forecast 18:1037–1051
Smith EA, Xiang X, Mugnai A, Tripoli GJ (1994) Design of an inversion-based precipitation profile retrieval algorithm using an explicit cloud model for initial guess microphysics. Meteorol Atmos Phys 54:53–78
Smith EA et al (1998) Results of WetNet PIP-2 project. J Atmos Sci 55:148–1536
Smith EA et al (2007) International global precipitation measurement (GPM) program and mission: an overview. In: Levizzani V, Bauer P, Turk J (eds) Measuring precipitation from space, EURAINSAT and the future, vol 28, Advances in global change research. Springer, Dordrecht, pp 611–653
Sorooshian S, Hsu K, Gao X, Gupta HV, Imam B, Braithwaite D (2000) Evaluation of PERSIANN system satellite-based estimates of tropical rainfall. Bull Am Meteorol Soc 81:2035–2046
Spencer RW, Goodman HM, Hood RE (1989) Precipitation retrieval over land and ocean with the SSM/I: identification and characteristics of the scattering signal. J Atmos Ocean Technol 6:254–273
Stephens G et al (2002) The CloudSat mission and the ATrain. Bull Am Meteorol Soc 83:1771–1790
Turk FJ, Miller SD (2005) Toward improved characterization of remotely sensed precipitation regimes with MODIS/AMSR-E blended data techniques. IEEE Trans Geosci Remote Sens 43:1059–1069
Vila D, Ferraro RR, Joyce R (2007) Evaluation and improvement of AMSU precipitation retrievals. J Geophys Res 112:D20119. doi:10.1029/2007JD008617
Wang N, Liu C, Ferraro R, Wolff D, Zipser E, Kummerow C (2009) The TRMM 2A12 land precipitation product – status and future plans. J Meteorol Soc Jpn 87:237–253
Weng F, Zhao L, Poe G, Ferraro R, Li X, Grody N (2003) AMSU cloud and precipitation algorithms. Radio Sci 338:8068–8079
Wilheit TT, Chang A, Rao M, Rodgers E, Theon J (1977) A satellite technique for quantitatively mapping rainfall rates over the oceans. J Appl Meteorol 16:551–560
Wilheit TT, Kummerow C, Ferraro R (2003) Rainfall algorithms for AMSR-E. IEEE Trans Geosci Remote Sens 41:204–214
Woodley WL, Sancho R (1971) A first step towards rainfall estimation from satellite cloud photographs. Weather 26:279–289
Xie P, Arkin PA (1997) Global pentad precipitation analysis based on gauge observations, satellite estimates and model outputs. In: Extended abstracts, American Geophysical Union 1997 fall meeting, AGU, San Francisco, 1997
Xie P, Janowiak JE, Arkin PA, Adler R, Gruber A, Ferraro R, Huffman G, Curtis S (2003) GPCP pentad precipitation analyses: an experimental dataset based on gauge observations and satellite estimates. J Climate 16:2197–2214
Zhao L, Weng F (2002) Retrieval of ice cloud parameters using the AMSU. J Appl Meteorol 41:384–395

Chapter 7
Developing a Historical Precipitation Record

Thomas M. Smith

Abstract Knowing historical precipitation is important for climate monitoring and for evaluating coupled climate models designed to simulate changes in precipitation associated with climate change. Over land gauge-based analyses are sufficient to determine large-scale variations over the twentieth century. Over oceans satellite-based analyses can be used beginning 1979. However, there are few direct or remote sensing observations of oceanic precipitation variations before 1979. For the pre-satellite time, it is possible to use reconstructions based on the available data to analyze some oceanic precipitation variations. Evaluations of the available data and methods have shown that large-scale variations in twentieth-century oceanic precipitation may be reconstructed. Reconstructions based on spatial covariance and historical gauge data represent seasonal to interannual variations. Reconstructions based on correlations with sea-surface temperature (SST) and sea-level pressure (SLP) represent multi-decadal variations. Combining these two types of reconstructions yields a merged reconstruction with the best features of both.

This review describes how the reconstructions are developed and discusses their major features. The merged reconstruction indicates increasing precipitation with increasing global temperature, consistent with theoretical estimates. However, the reconstruction indicates that the change is not steady and has a shift associated with the climate shift noted in Pacific SSTs in the 1970s.

Keywords Climate • Precipitation • Reconstruction

T.M. Smith (✉)
Cooperative Institute of Climate Studies, ESSIC, University of Maryland, College Park, MD 20742, USA
e-mail: tom.smith@noaa.gov

J.J. Qu et al. (eds.), *Satellite-based Applications on Climate Change*,
DOI 10.1007/978-94-007-5872-8_7,

7.1 Introduction

Global precipitation can be monitored using a number of satellite-based estimates combined with gauge estimates over land. As discussed in Ferraro et al.'s paper on global precipitation in this book, satellite-based precipitation estimates began in 1979 using infrared instruments. Over time more satellite estimates from both infrared and microwave instruments were developed. The Global Precipitation Climatology Project (GPCP, Adler et al. 2003) adjusted these different estimates to minimize satellite-to-satellite bias and merged them with gauge data to produce a monthly product for climate analyses beginning 1979.

Climate variations have been documented over multi-decadal time scales (e.g., see Trenberth et al. 2007). The available gauge-based analyses can describe large-scale precipitation variations over most land regions beginning about 1900. However, most of the Earth's surface is covered by oceans, and evaluation of that component of the global hydrologic cycle has required satellite sampling. For most of the twentieth century, there is a large gap in the record for ocean regions. Filling the gap would allow the historical response to climate change to be better understood and would provide historical perspective to precipitation monitoring products. In addition, climate models used to forecast precipitation changes with changing global temperatures could be better validated and improved using oceanic precipitation over the twentieth century. Therefore, attempts have been made to reconstruct historical oceanic precipitation. This chapter briefly reviews those precipitation reconstructions and discusses how well historical oceanic variations can be evaluated.

7.2 Historical Reconstructions

A reconstruction uses the available historical data and globally complete statistics describing those data to perform an analysis. For most global climate fields, satellite-based data are critical for developing the reconstruction statistics. Since the mean-annual cycle is defined by these modern base data, reconstructions are performed on anomalies from the annual cycle. The annual cycle can be added back onto the reconstruction anomaly later if desired. An example is the historical sea-surface temperature (SST) anomaly reconstruction (Smith et al. 1996), based on covariance maps produced using a satellite and in situ SST analysis. The covariance maps were produced using empirical orthogonal function (EOF) analysis (e.g., see Davis 1976 for a detailed definition of EOF analysis). An EOF analysis (also called principal component analysis) decomposes a time series of maps into a set of spatial fields or modes, $E_i(x)$, and associated time series, $a_i(t)$, for a set of modes $i = 1, 2, \ldots, N$. The modes are only a function of space, x, while the time-series weights for the modes are a function of only time, t. Each mode represents an orthogonal component of the full field's variance, and an approximation of the true field, $F(x,t)$, can be reconstructed from the weighted sum of the modes,

$$F(x,t) \approx \sum_{i=1}^{N} E_i(x) a_i(t) \tag{7.1}$$

As more modes are used in the approximation, it approaches the true field. The modes are ordered such that the first mode explains the most variance, the second explains the second most variance, etc. For an EOF-based reconstruction, the spatial modes, $E_i(x)$, may be computed from a satellite-based analysis of modern data. The historical time-series weights are estimated from the available historical data. Since historical data are typically sparse, statistical testing is done to ensure that there is enough sampling to reliably sample the set of modes used, with poorly sampled modes omitted from the analysis. The historical time-series weights are computed to minimize the error of the reconstruction fit at locations where historical data are available. For each time, the best-fit weights are obtained by solving

$$\sum_{i=1}^{N} \left[a_i \sum_{x=1}^{K} E_i(x) E_j(x) \delta(x) A(x) \right] = \sum_{x=1}^{K} \left[D(x) E_j(x) \delta(x) A(x) \right], \quad j = 1, 2, \ldots, N \tag{7.2}$$

where K is the number of spatial regions, the delta function $\delta(x) = 1$ if data are defined for region x and $\delta(x) = 0$ otherwise, and $A(x)$ is the relative area of region x. The partly sampled data used for the reconstruction are represented by $D(x)$.

The EOF method can reconstruct variations described by modes with large enough scales to be sampled by the available historical data. Small-scale variations are filtered out of the analysis. Variations not represented in the set of reconstruction modes will also be filtered out of the analysis. This filtering gives the analysis spatially smooth features. The goal of a reconstruction is to represent large-scale historical variations associated with climate. These reconstructions cannot represent fine-scale features, which require much more data to resolve.

The EOF method was used to reconstruct precipitation (Xie et al. 2001; Efthymiadis et al. 2005). They used satellite-based data to define modes and gauge data to compute weights. Both studies found that oceanic precipitation variations associated with El Niño/Southern Oscillation (ENSO) variations are best reconstructed. That is because ENSO variations have very large scales over both land and sea, and they are usually described by the first few modes. Such large-scale variations are easily sampled by the available gauge sampling. Outside of the tropics, both analyses had less skill, with lowest extratropical skill in mid-oceanic regions far from gauge sampling.

7.3 An Improved EOF-Based Reconstruction

In an attempt to improve on the ocean-area reconstructions noted above, data and methods for precipitation reconstructions were reviewed and reevaluated (Smith et al. 2008b). As part of this effort, several satellite-based analyses were evaluated

for possible use as base data, including GPCP and CMAP (CPC Merged Analysis of Precipitation, Xie and Arkin 1997). We found that both gave consistent representations of interannual variations. However, the CMAP had a decreasing multi-decadal tendency, opposite the tendency of GPCP and other satellite estimates such as Wentz et al. (2007). That opposite CMAP tendency appears to be caused by how satellite data are adjusted to reduce their satellite-to-satellite biases. In CMAP large-scale tropical adjustments are performed against a few island stations. Those few stations reasonably represent the interannual variations that CMAP was developed to evaluate, but they may not be representative of multi-decadal variations. By comparison, GPCP was developed for climate studies on a range of time scales, including decadal. Therefore, the GPCP satellite-to-satellite bias adjustments are made relative to a satellite standard and do not depend on limited sampling.

Several gauge-based analyses were also evaluated for reconstructions. Gauge analyses were available on different spatial grids, most either 2.5° or 5° spatially. For these analyses, the 5° grid was chosen as the reconstruction grid so that all of the gauge analyses may be used. Grid analyses also cover different periods, but the longest analyses began in 1900. Historical gauge analyses evaluated include the analyses from the Global Historical Climatology Network (GHCN, Vose et al. 1998) 1900–2008, the Global Precipitation Climatology Centre (GPCC, Rudolf 2005; Schneider et al. 2008) 1901–2007, and the Climate Research Unit (CRU, Hulme et al. 1998) 1900–1998.

In an earlier study (Smith et al. 2010), GPCP base data were used to compute EOF modes, which were then used with each of these gauge analyses to perform a reconstruction. Over land those reconstructions are similar for most of the overlap analysis period. Before about 1930 the EOF-based reconstruction using GHCN had weaker variations. That is because the GHCN does not fill regions with missing data, while the others each use some limited interpolation to fill missing stations. To ensure that noise is filtered out of our EOF-based reconstruction, the relative sampling of each mode is checked using the data in each historical month. Modes that are not adequately sampled are not used in the reconstruction. Omitting modes damps the reconstructed signal. Since the GHCN analysis tends to be sparser than the others before about 1930, its signal is damped for that period.

These EOF-based reconstructions were found to consistently represent interannual oceanic variations such as those associated with ENSO and the North Atlantic Oscillation (NAO). In addition, the improved reconstructions retain more Northern Hemisphere oceanic variance than earlier reconstructions. However, the oceanic multi-decadal components of the EOF-based reconstructions are less consistent. This suggests that the weaker multi-decadal signal requires more sampling, while the stronger interannual climate modes can be resolved by available gauges. To better resolve the multi-decadal signal, we developed an indirect method of reconstructing precipitation, which is described below.

The EOF-filtered GPCP, called REOF(GPCP), has variations similar to the gauge-based reconstructions in the overlap times (see Fig. 7.3). Without filtering, the GPCP variance increases in time, because the newer satellites resolve more

variations. This suggests that the modern gauge sampling is adequate to resolve most variations spanned by the set of EOF modes used. Therefore, a blended EOF-based reconstruction can be formed using REOF(GPCP) to update the historical analysis. For the historical analysis, the EOF-based reconstruction from CRU gauge data was used, gradually shifting from the historical analysis to REOF(GPCP) data over 1979 to 1988. We call this reconstruction the REOF(blend).

7.4 An Improved CCA-Based Reconstruction

An indirect reconstruction method based on canonical correlation analysis (CCA) was developed using analyses of SST and sea-level pressure (SLP). The CCA (Barnett and Preisendorfer 1987) was adapted for reconstructing precipitation (Smith et al. 2009a). The method, referred to as RCCA, is summarized here. The RCCA specifies precipitation anomalies from SST and SLP anomalies, which are both much better sampled over the oceans. Annual averages are specified using annual predictors. For annual average anomalies, both SST and SLP are related to large-scale precipitation variations. Our goal is to use the superior oceanic sampling of the predictors to more reliably determine oceanic precipitation multi-decadal variations. The RCCA of annual-average precipitation anomalies is computed 75°S–75°N over both land and ocean regions, although we are most concerned with improving the oceanic multi-decadal signal. In polar latitudes, both predictor data and satellite precipitation training data are not reliable enough for meaningful reconstructions.

As with the EOF-based reconstruction, GPCP anomalies are used to form base statistics. The predictors include a SST analysis (Smith et al. 2008a) and a SLP analysis (Allan and Ansell 2006). These predictor analyses allow the reconstruction to extend back to 1900. The SLP analysis is through 2004, with updates afterwards. Because the SLP updates are computed differently from their historical analysis, the update variance is larger than in the historical period. Therefore, the RCCA base period used is 1979–2004 to keep that artificial variance change out of its statistics. The predictor and GPCP anomalies are averaged annually before computing the reconstruction statistics. The annual predictor fields are then used to reconstruct the annual anomalies beginning 1900.

This indirect RCCA can resolve large-scale precipitation variations, including multi-decadal variations. Reliability is shown by comparison over land regions where there are independent data for validation. Gauge data are included in the GPCP base data, so for 1979–2004 the validation is not independent. Outside that period, no gauge data are used in the RCCA, so the gauges can be used for independent validation before 1979. To avoid sampling differences, averages of the annual RCCA and GHCN gauge analysis are computed over only regions with gauge data (Fig. 7.1). The GPCP base data averaged over gauge regions are also included for comparison. The strong correlation between the RCCA and the GHCN in the independent period shows the ability of this method to resolve both

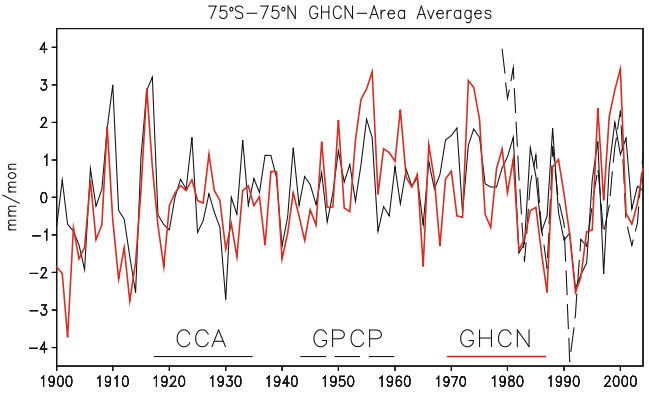

Fig. 7.1 Annual and 75°S–75°N average precipitation anomalies from the RCCA, GHCN, and GPCP. Averages omit data where GHCN is not available

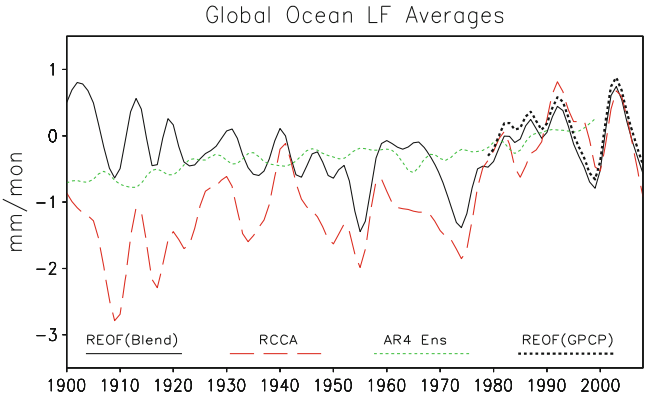

Fig. 7.2 Ocean-area averaged precipitation anomalies from the blended EOF-based reconstruction, REOF(blend), the RCCA, the AR4 ensemble coupled models, and the EOF-filtered GPCP, REOF(GPCP). All are low-pass filtered to emphasize multi-decadal variations

interannual and multi-decadal averages. Testing showed that most of the RCCA variance is derived from the SST predictor, including most of the land-area variations. However, adding the SLP improves the skill and it is retained in the analysis.

The RCCA was motivated by the need for better resolution multi-decadal oceanic variations compared to the REOF(blend). Comparisons of these analyses averaged over ocean areas show the differences (Fig. 7.2). Here the annual-spatial averages are filtered using a weighted 7-year filter (see Smith et al. 2010). In addition, the ensemble average of fourth Assessment Report (AR4) coupled models is also shown through 1999, along with REOF(GPCP) since 1979. The AR4 coupled ocean–atmosphere models to help evaluate climate change from changes caused by greenhouse gases and aerosols (Randall et al. 2007). Note that for the

satellite period, all of the reconstructions give similar multi-decadal variations and indicate an increase in oceanic precipitation with time. The AR4 ensemble indicates an increase with time over the twentieth century, which reflects the theoretical response of precipitation to increased greenhouse gas and aerosol forcing. With a warming troposphere, theory states that there will be more evaporation and higher rainfall (e.g., Allan and Soden 2008). For the first half of the twentieth century, the REOF(blend) shows an opposite tendency, suggesting that the gauge network may not be adequate to specify the oceanic multi-decadal signal for much of the twentieth century.

The RCCA indicates a general warming tendency throughout the period, but it is not as steady as the AR4 ensemble model tendency. One major difference is the influence of interannual variations in the RCCA. Interannual variations occur in the individual AR4 models, but they are not phase locked and so are averaged out of the ensemble. Another difference is the positive shift in the RCCA in the mid 1970s. That shift is associated with a climate shift reflected in the Pacific SSTs (Trenberth 1990; Zhang et al. 1997). Evaluation of individual RCCA modes indicates that the 1970s shift is mostly due to an ENSO-like mode which responds to the ENSO-like shift in SSTs (Smith et al. 2009b). The AR4 models do not consistently resolve the 1970s climate shift, although models are capable of demonstrating such shifts. For example, a model was used to show that the 1970s shift is likely caused by a combination of external forcing and internal Pacific multi-decadal variability, which influenced the timing of the shift (Meehl et al. 2009).

7.5 Merged Reconstruction

Our analyses showed that the REOF(blend) is capable of describing seasonal to interannual variations, but its representation of oceanic multi-decadal signals appears to be less reliable. The RCCA yields accurate multi-decadal signals where it can be validated with independent data, but since it is an analysis of annual averages, its representation of interannual and shorter-period variations is damped. The REOF(blend) and RCCA standard deviations have consistent differences over the analysis period, with the REOF(blend) systematically higher (Fig. 7.3). There is a slight negative trend in both standard deviations, but that is much less than the interannual changes over the period. In addition, although the RCCA multi-decadal representation of land variations is strong, the availability of local gauges makes the REOF(blend) representation of land variations superior. In order to take advantage of the best qualities of each analysis, we merged the REOF(blend) and the RCCA. Details of the merging are given elsewhere (Smith et al. 2010) and outlined here.

To merge the analyses, both are first filtered using the same weighted 7-year filter to separate a low- from a high-frequency component of each. In ocean areas, the low-frequency component of the REOF(blend) was replaced with the low-frequency component of the RCCA. In 5° areas that are partly ocean, the adjustment is proportional to the fraction of ocean area. In areas that are all land, no adjustment

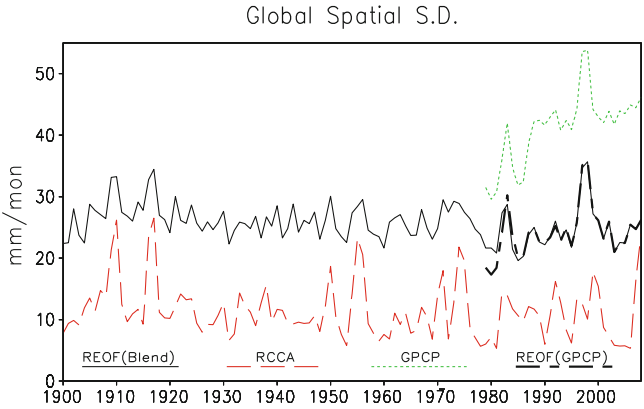

Fig. 7.3 Global spatial standard deviation of the indicated analyses

is done. The adjustment is done monthly, with the annual adjustment linearly interpolated to the month.

An indication of interannual variations associated with climate modes is given by correlations against the Southern Oscillation Index (SOI, Trenberth 1984) and the NAO index (Hurrell 1995). For the SOI, annual-average values are used, while for the NAO December to March averages are used (Fig. 7.4). As expected, the SOI correlation is strongest in the tropics, with extensions into the extra tropics into areas influenced by the SOI. The NAO correlations are strongest in the Northern Hemisphere, and its known influence on Europe and North America is reflected (Hurrell et al. 2003). For both the oceanic analysis shows extensions of the influence from land to adjacent oceanic regions. Thus, a more complete description of the influence of the climate modes over the twentieth century is available using the reconstruction.

Trends in the merged reconstruction (Fig. 7.5) indicate that the tropical oceans account for most of the global trend. Land trends are much weaker than the oceanic trends, and they also tend to be out of phase. The out-of-phase relationship may reflect shifts of precipitation from land to ocean areas over the twentieth century. A similar out-of-phase land-sea relationship was noted for ENSO events (Adler et al. 2008). These results suggest that the multi-decadal relationships may share features with the ENSO relationships.

7.6 Conclusions

This chapter shows that it is possible to reconstruct large-scale features of oceanic precipitation variations beginning 1900. Reconstructions require accurate base data such as analyses using satellite-based observations. The base data are needed to form statistics that can be used with the limited historical data to reconstruct

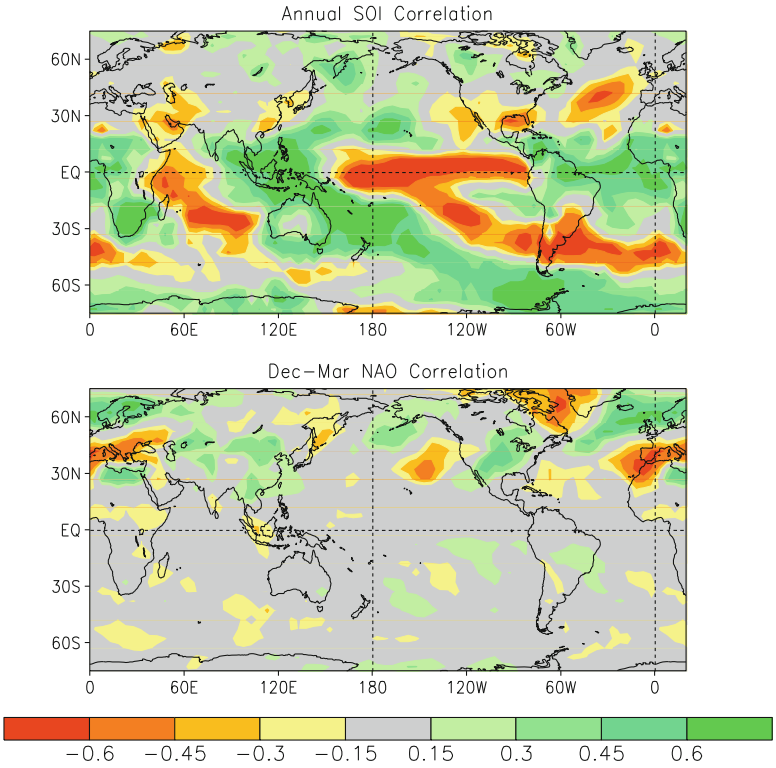

Fig. 7.4 Correlation of the merged reconstruction with the SOI and the NAO indices, 1900–2000. Annual averages are used for the SOI correlation, and Dec–Mar averages are used for the NAO

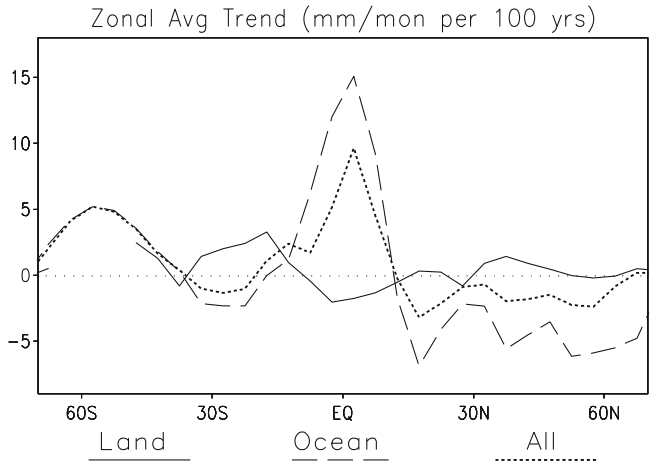

Fig. 7.5 Trends of the merged reconstruction (1900–2008) averaged zonally over land, oceans, and all areas

climate-scale variations. These reconstructed fields are important for monitoring climate and its changes over long periods and for helping to validate climate models that simulate twentieth-century variations.

Improvements in reconstructions may be possible if satellite analyses can be improved. In addition, as longer records with more satellite-based observations become available, the base data may be able to support improved reconstruction statistics. Additional improvements can be obtained by including new data sources that may provide independent information. For example, an extended dynamic atmospheric reanalysis was produced by assimilating measured surface fields (Compo et al. 2006). In the future, we intend to examine precipitation from that reanalysis as well as from other sources as the data become available. The merged reconstruction discussed here is available to the public online at http://cics.umd.edu/~tsmith/recpr/.

Acknowledgements Precipitation reconstructions produced by the author are a result of joint work involving P. A. Arkin, M. R. P. Sapiano, and C.-Y. Chang. This work also benefited from discussions with R. Adler, J. Janowiak, A. Mariotti, R. Reynolds, R. Vose, P. Xie, and anonymous reviewers. Data used for reconstruction include the GHCN and SST data from the National Climatic Data Center, the GPCP from NASA, the GPCC from Deutscher Wetterdienst, the CRU analysis from Univ. of East Anglia, and the SLP data from the UK Met. Office Hadley Centre, www.metoffice.gov.uk/hadobs. Some of this research was supported by the Climate Change Data and Diagnostic Program Element of the NOAA Climate Program Office and the Cooperative Institute for Climate and Satellites, NOAA Grant NA17EC1483. The contents of this chapter are solely the opinions of the author and do not constitute a statement of policy, decision, or position on behalf of NOAA or the US government.

References

Adler RF, Huffman GJ, Chang A, Ferraro R, Xie PP, Janowiak J, Rudolf B, Schneider U, Curtis S, Bolvin D, Gruber A, Susskind J, Arkin P, Nelkin E (2003) The version-2 global precipitation climatology project (GPCP) monthly precipitation analysis (1979-present). J Hydrometeor 4:1147–1167

Adler RF, Gu G, Wang J-J, Huffman GJ, Curtis S, Bolvin D (2008) Relationships between global precipitation and surface temperature on inter-annual and longer time scales (1979–2006). J Geophys Res 113:D22104. doi:10.1029/2008JD010536

Allan RJ, Ansell TJ (2006) A new globally complete monthly historical mean sea level pressure data set (HadSLP2): 1850–2004. J Climate 19:5816–5842

Allan RP, Soden BJ (2008) Atmospheric warming and the amplification of precipitation extremes. Science 321:1481–1484

Barnett TP, Preisendorfer R (1987) Origins and levels of monthly and seasonal forecast skill for United States surface air temperatures determined by canonical correlation analysis. Mon Weather Rev 115:1825–1850

Compo GP, Whitaker JS, Sardeshmukh PD (2006) Feasibility of a 100-year reanalysis using only surface pressure data. Bull Am Meteorol Soc 87:175–190

Davis RE (1976) Predictability of sea surface temperature and sea level pressure anomalies over the North Pacific Ocean. J Phys Oceanogr 6:249–266

Efthymiadis D, New M, Washington R (2005) On the reconstruction of seasonal oceanic precipitation in the presatellite era. J Geophys Res 110:D06103. doi:10.1029/2004JD005339

Hulme M, Osborn TJ, Johns TC (1998) Precipitation sensitivity to global warming: comparison of observations with HadCM2 simulations. Geophys Res Lett 25:3379–3382

Hurrell JW (1995) Decadal trends in the North Atlantic Oscillation: regional temperatures and precipitation. Science 269:676–679

Hurrell JW, Kushnir Y, Ottersen G, Visbeck M (2003) An overview of the North Atlantic Oscillation. In: Hurrell JW, Kushnir Y, Ottersen G, Visbeck M (eds) The North Atlantic Oscillation: climate significance and environmental impact, vol 134, Geophysical monograph series. American Geophysical Union, Washington, D.C., pp 1–35

Meehl GA, Hu A, Santer BD (2009) The mid-1970s climate shift in the Pacific and the relative roles of forced versus inherent decadal variability. J Climate 22:780–792

Randall DA, Wood RA, Bony S, Colman R, Fichefet T, Fyfe J, Kattsov V, Pitman A, Shukla J, Srinivasan J, Stouffer RJ, Sumi A, Taylor KE (2007) Climate models and their evaluation. In: Solomon S, Qin D, Manning M, Chen Z, Marquis M, Averyt KB, Tignor M, Miller HL (eds) Climate change 2007: the physical science basis. Contribution of Working Group I to the Fourth Assessment Report of the Intergovernmental Panel on Climate Change. Cambridge University Press, Cambridge/New York

Rudolf B (2005) Global precipitation analysis products of the GPCC. DWD, Klimastatusbericht 2004, 163–170. ISSN 1437-7691, ISSN 1616-5063 (Internet www.ksb.dwd.de). ISBN 3-88148-402-7

Schneider UT, Fuchs A, Meyer-Christoffer A, Rudolf B (2008) Global precipitation analysis products of the GPCC. Global Precipitation Climatology Centre (GPCC), DWD, Internet Publikation, 1–12 (pdf 1414 KB)

Smith TM, Reynolds RW, Livezey RE, Stokes DC (1996) Reconstruction of historical sea surface temperatures using empirical orthogonal functions. J Climate 9:1403–1420

Smith TM, Reynolds RW, Peterson TC, Lawrimore J (2008a) Improvements to NOAA's historical merged land-ocean surface temperature analysis (1880–2006). J Climate 21:2283–2296

Smith TM, Sapiano MRP, Arkin PA (2008b) Historical reconstruction of monthly oceanic precipitation (1900–2006). J Geophys Res 113:D17115. doi:10.1029/2008JD009851

Smith TM, Arkin PA, Sapiano MRP (2009a) Reconstruction of near-global annual precipitation using correlations with sea surface temperature and sea level pressure. J Geophys Res 114: D12107. doi:10.1029/2008JD011580

Smith TM, Sapiano MRP, Arkin PA (2009b) Modes of multi-decadal oceanic precipitation variations from a reconstruction and AR4 model output for the 20th century. Geophys Res Lett 36:L14708. doi:10.1029/2009GL039234

Smith TM, Arkin PA, Sapiano MRP, Chang C-Y (2010) Merged statistical analyses of historical monthly precipitation anomalies beginning 1900. J Climate 23:5755–5770

Trenberth KE (1984) Signal versus noise in the Southern Oscillation. Mon Weather Rev 112:326–332

Trenberth KE (1990) Recent observed interdecadal climate changes in the Northern hemisphere. Bull Am Meteorol Soc 71:988–993

Trenberth KE, Jones PD, Ambenje P, Bojariu R, Easterling D, Klein Tank A, Parker D, Rahimzadeh F, Renwick JA, Rusticucci M, Soden B, Zhi P (2007) Observations: surface and atmospheric climate change. In: Solomon S, Qin D, Manning M, Chen Z, Marquis M, Averyt KB, Tignor M, Miller HL (eds) Climate change 2007: the physical science basis. Contribution of Working Group I to the Fourth Assessment Report of the Intergovernmental Panel on Climate Change. Cambridge University Press, Cambridge/New York

Vose RS, Peterson TC, Hulme M (1998) The global historical climatology network precipitation database: version 2.0. In: Proceedings of the 9th symposium on global change studies, American Meteorological Society, Boston, 1998

Wentz FJ, Ricciarudlli L, Hilburn K, Mears C (2007) How much more rain will global warming bring? Science 317:233–235

Xie P, Arkin PA (1997) Global precipitation: a 17-year monthly analysis based on gauge observations, satellite estimates, and numerical model outputs. Bull Am Meteorol Soc 78:2539–2558

Xie P, Chen M, Janowiak JE, Arkin PA, Smith TM (2001) Reconstruction of the oceanic precipitation: preliminary results. In: Proceedings of the 26th annual climate diagnostics and prediction workshop, La Jolla, 2001. Copies available at: http://www.cpc.ncep.noaa.gov/products/outreach/publications.shtml

Zhang Y, Wallace JM, Battisti DS (1997) ENSO-like interdecadal variability: 1900–93. J Climate 10:1004–1020

Chapter 8
Atmospheric Temperature Climate Data Records from Satellite Microwave Sounders

Cheng-Zhi Zou

Abstract This chapter reviews the simultaneous nadir overpass (SNO) method to remove time-varying inter-satellite biases at the swath level for developing a well-inter-calibrated Level-1c radiance fundamental climate data record (FCDR) from the microwave sounding unit (MSU) and advanced MSU observations onboard historical NOAA polar-orbiting satellite series. The SNO method has effectively minimized scene temperature-dependent radiance biases and solar heating-related instrument temperature variability in the radiances, resulting in global mean inter-satellite biases of only 0.05–0.1 K. Twenty years of the SNO-calibrated Level-1c radiances had been assimilated into the NCEP Climate Forecast System Reanalysis (CFSR) and NASA Modern Era Retrospective analysis for Research and Applications (MERRA) reanalysis, yielding much consistent bias correction patterns across different satellites compared to those using prelaunch-calibrated radiances.

The SNO-calibrated radiances were further used to generate the NOAA Center for Satellite Applications and Research (STAR) version of deep-layer atmospheric temperature climate data record. The chapter reviews various residual bias correction algorithms for developing the STAR layer temperature time series, including antenna pattern correction, limb adjustment, diurnal drift correction, geo-location-dependent bias removal, and channel frequency difference between MSU and AMSU. With these adjustments, well-merged atmospheric temperature time series were generated for climate change monitoring and research.

Keywords Simultaneous nadir overpass • Inter-satellite calibration • Microwave sounding unit • Residual bias correction • Atmospheric temperature climate data record • Long-term atmospheric temperature trends

C.-Z. Zou (✉)
NOAA/NESDIS/Center for Satellite Applications and Research,
5830 University Research Court, College Park, MD 20740, USA
e-mail: cheng-zhi.zou@noaa.gov

J.J. Qu et al. (eds.), *Satellite-based Applications on Climate Change*,
DOI 10.1007/978-94-007-5872-8_8,

8.1 Introduction

Accurate determination of the atmospheric temperature variability and trends is an important component in global change monitoring and research. The global atmospheric temperature trend is an important indicator of whether the Earth is warming or cooling. Additionally, knowledge of the atmospheric temperature trends at both global and regional scales is crucial for validating consistencies of the simulated atmospheric and surface changes in climate model simulations. For instance, moist adiabatic theory predicts that the tropical troposphere warms faster than the surface, which has been seen in most climate model simulations (Santer et al. 2005). However, such a relationship needs to be verified by observations. Observational verifications of climate model simulations affect scientific views on the reliability of climate model projections of future climate changes, which in turn are foundations for making policy decisions on prevention, mitigation, and adaptation strategies for global change.

Development of climate data record (CDR) is desirable for reliably detecting atmospheric temperature trends. A CDR is defined as "a time series of measurements of sufficient length, consistency, and continuity to determine climate variability and change" (NRC 2004). In this regard, the long-term observations from the microwave sounders including microwave sounding unit (MSU) and advanced microwave sounding unit-A (AMSU-A) onboard NOAA, NASA, and MetOp-A polar-orbiting satellites provide unique opportunities for an atmospheric temperature CDR development. The MSU and AMSU-A are cross-scanning instruments which make respectively 11 and 30 Earth observations during each scan. The MSU observations covered the period from 1979 to 2006, with four channels to measure the temperature profiles from the surface to the lower stratosphere. As its successor, the AMSU-A is a 15-channel instrument making temperature profile observations from the surface to the upper stratosphere. The AMSU-A observations cover the period from 1998 to the present and onward into the future. The MSU/AMSU instruments were designed primarily for weather monitoring; however, because of their long-term continuity, global coverage, insensitivity to cloud effects, and frequency stability, their observations have been widely used for atmospheric temperature variability and trend investigations (Spencer and Christy 1992a, b; Spencer et al. 2006; Trenberth and Hurrell 1997; Hurrell and Trenberth 1997, 1998; Hurrell et al. 2000; Christy et al. 1998, 2000, 2003; Prabhakara and Iacovazzi 1999; Prabhakara et al. 2000; Wentz and Schabel 1998; Mears et al. 2003; Mears and Wentz 2005, 2009a, b; Vinnikov and Grody 2003; Grody et al. 2004; Vinnikov et al. 2006; Fu et al. 2004; Fu and Johanson 2004, 2005; Johanson and Fu 2006; Zou et al. 2006, 2009; Zou and Wang 2010, 2011). The importance of the MSU/AMSU observations for climate change detection and its related studies has been well reviewed in the US Climate Change Science Program Synthesis and Assessment report (Karl et al. 2006) and the fourth Intergovernmental Panel on Climate Change report (Solomon et al. 2007).

Satellite-based CDRs are further segmented into fundamental CDRs (FCDRs), which are calibrated and quality controlled sensor data that have been improved over time, and thematic CDRs (TCDRs), which are geophysical variables derived from the FCDRs (NRC 2004). For MSU/AMSU, the FCDR is the swath Level-1c radiance data that are produced immediately after the instrument calibration. Since FCDR is used for subsequent satellite retrievals and data assimilations in numerical weather predictions and modeling reanalyses, its quality has a significant impact on the accuracies of these subsequent applications. Consistent, high-quality FCDR should have instrument calibration errors removed as much as possible.

Although fundamentally important, however, the FCDR is usually not directly used for climate change analysis due to data irregularity in location and time and also because of different interpretations of the radiance data from the retrieved geophysical variables that are used to describe the climate change. As a result, a TCDR is developed on top of the FCDR for the purpose of direct climate analysis and trend calculations. A TCDR (thematic climate data record) is generally a gridded dataset with fixed time interval that is easy to use. However, developing TCDR requires more bias corrections and adjustments of different error sources than applied for FCDR development. These include satellite sampling errors such as those related to satellite drift. Retrieval algorithms are also needed for many geophysical variables when there is a nonlinear relationship between the radiances and the physical variables to be retrieved. These bias correction and retrieval processes cause the TCDRs to have more error sources than the FCDRs.

Recently, significant progress has been made at NOAA/NESDIS in the development of both the FCDR and atmospheric temperature TCDR from the MSU/AMSU observations using the simultaneous nadir overpass (SNO) intercalibration methodology (Zou et al. 2006, 2009; Zou and Wang 2010, 2011). The method largely removed instrument calibration errors related to inaccurate calibration nonlinearity and solar heating variability on the instrument and thus resulted in a consistent, high-quality radiance FCDR. Such a feature in the FCDR has the advantage that it prevents instrument calibration errors from transferring to the gridded analysis level where they, if not corrected, could become mixed up with the diurnal drift errors. This error coupling may cause difficulties in bias correction in the TCDR development and ultimately cause uncertainties in the trend determination. In addition, with biases removed, identical multi-satellite FCDRs can be an ideal candidate as an anchor or reference dataset for bias corrections of other observations in reanalysis data assimilation, which may help the climate reanalysis to be consistent with the satellite observations as much as possible.

In this chapter, the SNO methodology for MSU/AMSU inter-satellite calibration is reviewed, and the resulting FCDR performance in terms of inter-satellite bias reduction is described. Impact of the inter-calibrated FCDR on the reanalysis bias correction improvement is demonstrated. Bias correction approaches of various error sources for MSU/AMSU atmospheric temperature TCDR are described. Finally, updated 34-year atmospheric temperature trends derived from the SNO-calibrated TCDR are provided.

8.2 Methodology for Consistent MSU/AMSU FCDR Development

The development of MSU/AMSU Level-1c radiance FCDR mainly involves accurate calibration of the satellite raw count data to remove instrument specific errors. This requires an understanding of two fundamental processes: the calibration principles and the origin of the calibration errors. The following subsections describe these two processes, followed by an introduction of the SNO approaches for the removal of calibration errors. The last subsection evaluates the performance of the SNO-calibrated FCDR in modeling reanalysis applications.

8.2.1 MSU/AMSU Level-1c Calibration

The MSU and AMSU instruments use an onboard calibration method that includes two calibration targets as its end point references: the cosmic space cold target and an onboard blackbody warm target. Cold space has a temperature of 2.73 K, and the warm target temperature is measured by the platinum resistance thermometers (PRT) embedded in the blackbody target. In each scan cycle, the MSU/AMSU looked at these targets as well as the Earth, and the signals in the form of electric voltage were converted to digital counts through an analog-to-digital converter. These digital counts were output as raw observations. The Level-1c calibration equation, also known as the radiometer transfer function, for converting the raw count observations to the radiances using the two calibration targets is written as (Zou et al. 2006, 2009)

$$R = R_{\mathrm{L}} - \delta R + \mu Z, \tag{8.1}$$

where R is the Earth scene radiance, $R_{\mathrm{L}} = R_{\mathrm{c}} + S(C_{\mathrm{e}} - C_{\mathrm{c}})$, representing the dominant linear response and $Z = S^2(C_{\mathrm{e}} - C_{\mathrm{c}})(C_{\mathrm{e}} - C_{\mathrm{w}})$ is a nonlinear response. C represents the raw count data of the satellite observations, and $S = R_{\mathrm{w}} - R_{\mathrm{c}}/C_{\mathrm{w}} - C_{\mathrm{c}}$ is the slope determined by the two calibration targets. The subscripts e, w, and c refer to the Earth view, onboard blackbody warm target view, and cold space view, respectively; δR represents a radiance offset; and μ is a nonlinear coefficient. A schematic viewing of this calibration process is illustrated in Fig. 8.1.

Equation (8.1) is a modified version of the calibration algorithm originally suggested by Mo (1995a), where δR was assumed to be zero and the nonlinear coefficient μ was obtained from prelaunch chamber test datasets (Mo 1995b; Mo et al. 2001). The prelaunch calibration was used to generate NOAA operational Level-1c radiance products and is thus also referred to as the NOAA operational calibration. The prelaunch calibration was conducted for each MSU/AMSU instruments independently and thus left residual biases between satellites. In the postlaunch calibration as described in this chapter, the offset δR was included in

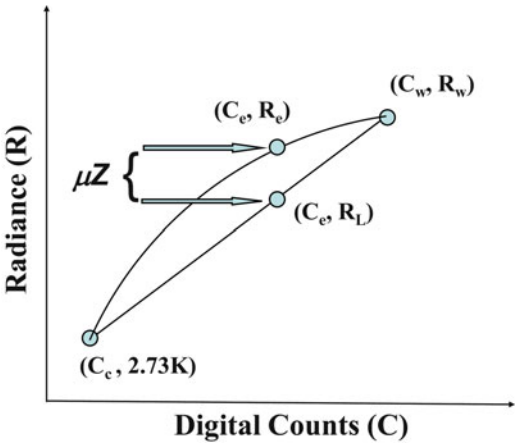

Fig. 8.1 Schematic viewing the calibration principle of the MSU/AMSU instruments. Symbols used in the plot are defined in the main text

Eq. (8.1) to allow for inter-satellite calibration, and the calibration coefficients, δR and μ, were obtained using SNO matchups (Zou et al. 2006, 2009). There are other detailed differences between the prelaunch and postlaunch calibration processes. For example, the raw count values of the calibration targets in Eq. (8.1) were averages over adjacent scan lines in prelaunch calibration (Mo 1995b; Mo et al. 2001). In postlaunch calibration, however, target count values of a single scan line were used for radiance calculations of each footprint observation in that scan line. The processing details described in this chapter are specifically applied to the SNO postlaunch calibration.

In Eq. (8.1), the cold space radiance R_c is specified to be 9.6×10^{-5} mW (sr m^2 cm^{-1})$^{-1}$ for all scan lines of both the MSU and AMSU observations. This corresponds to a brightness temperature of 4.78 K that includes the cold space temperature of 2.73 K plus an increase of about 2 K owing to the antenna side-lobe radiation. The algorithms described in Kidwell (1998) for MSU and in Goodrum (2000) for AMSU-A are used to compute R_w. Once the offsets and the nonlinear coefficient are known, radiance is computed through Eq. (8.1), and the brightness temperature, T_b, is then computed using the Planck function.

The system parameters for MSU and AMSU are different; thus, the processing details are slightly different for the two instruments. For instance, the MSU has 11 Earth views, one space view, and one warm target view in each scan line. There are 2 PRTs embedded on the blackbody target. In contrast, each scan line in the AMSU observations contains 30 Earth views, two space views, and two warm target views. The PRTs on each target ranges from 5 to 7, depending on instrument subunits. For the MSU, the one space and blackbody views are used to calibrate the 11 Earth views in each scan line. However, the averages of the two space views or blackbody views are used to calibrate the 30 Earth views for the AMSU-A instrument. The warm target temperature is the average of the available good PRT measurements for each instrument. Generally, there is a blackbody target for each antenna system, but there are more than one antenna system for each instrument unit. These differences between the MSU and AMSU-A units and antenna systems are listed in Table 8.1.

Table 8.1 Channel and scanning view numbers for each MSU and AMSU-A antenna systems

Instrument antenna systems	MSU-1	MSU-2	AMSU-A A1-1	AMSU-A A1-2	AMSU-A A2
Channels	1–2	3–4	6–7, 9–15	3–5, 8	1–2
Earth views per scan line	11	11	30	30	30
Blackbody and space views per scan line	1	1	2	2	2
PRTs in each warm target	2	2	5	5	7

Note that the MSU has two antenna systems: 1 and 2. AMSU-A has two units, A1 and A2, where A1 has two antenna systems, A1-1 and A1-2, and A2 has its own antenna system

8.2.2 Solar Heating-Related Instrument Temperature Variability

A major calibration error that needs to be removed from the radiance FCDR is the instrument temperature variability induced by solar heating differences on the instrument, which originates from seasonal solar angle changes relative to the satellite orbit normal over a year and its yearly differences due to satellite orbital drifts. As an example, Fig. 8.2 shows the warm target temperature time series for NOAA-10 through NOAA-15, which contains representative examples for both the MSU (NOAA-10 through NOAA-14) and AMSU-A (NOAA-15) instruments. It is seen that these warm target temperatures, which are at the ambient instrument temperature, all incurred large seasonal and interannual variability due to solar heating variations of the instruments.

The instrument temperature variability as shown in Fig. 8.2 causes variations of the spacecraft thermal emission, which are received as part of the signals in the antenna side-lobe views of the Earth and the calibration targets. For instruments having a perfectly linear radiometer transfer function, the instrument thermal emission signals can be mostly removed by the linear calibration equation. In reality, however, most instruments are slightly nonlinear. Inaccurate expressions of the nonlinearities cause residual instrument temperature variability to manifest in the radiance time series. Figure 8.3 shows the global ocean-mean inter-satellite brightness temperature difference time series for MSU channel 2 onboard TIROS-N through NOAA-14 based on the NOAA operational calibrated radiances. The time series was generated by averaging seven near-nadir, limb-corrected radiances in each scan line over the global ocean for each satellite. In the global difference time series, dominate climate signals are canceled out by nearly identical observations from two overlapping satellites so that only instrument calibration errors and observation sampling errors such as those related to diurnal drift remain. Fortunately, diurnal drift errors can be ignored in global ocean means for MSU channel 2 observations (Mears et al. 2003; Zou et al. 2009); thus, any errors in the inter-satellite difference time series can be traced to the instrument calibration errors. As shown in Fig. 8.3, NOAA operational calibration results in inter-satellite biases that are a few tenths of a degree (Kelvin), and these biases change with time with their variability highly correlated to the instrument warm target temperature variations

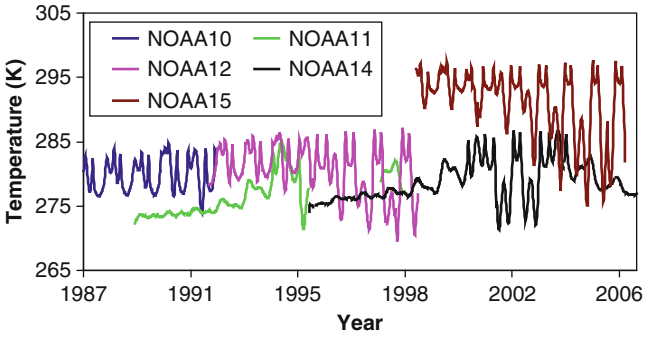

Fig. 8.2 Warm target temperature time series for the MSU instrument from NOAA-10 through NOAA-14 and for AMSU-A instrument on NOAA-15. The temperature variability reflects solar heating variations on the instrument

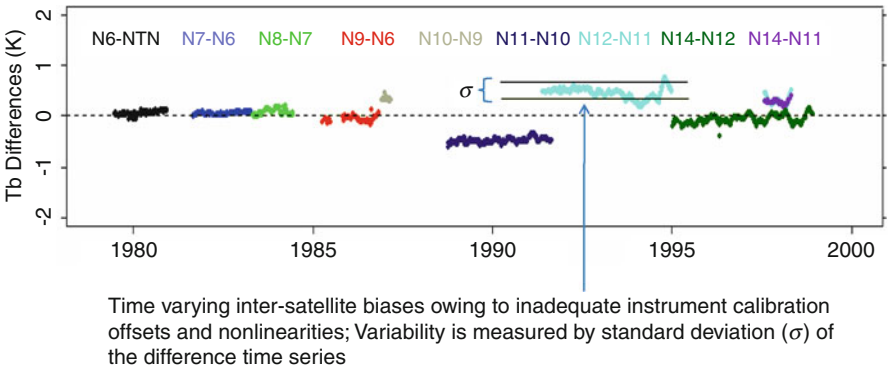

Fig. 8.3 Global ocean-mean inter-satellite brightness temperature difference time series for MSU channel 2 (53.74 GHz single sideband) onboard TIROS-N through NOAA-14 derived from the NOAA operational calibrated radiances. The global ocean means are an average of seven near-nadir, limb-corrected radiances in each scan line over the global ocean for each satellite

(e.g., Christy et al 2000; Zou et al. 2006). This indicates inaccurate nonlinearities in the prelaunch calibration. Essentially, more accurate calibration offsets and nonlinearities are required to reduce the time-varying inter-satellite biases for development of more accurate MSU/AMSU FCDRs.

8.2.3 A SNO Technique for Inter-satellite Calibration and FCDR Development

A SNO approach was developed at NOAA/NESDIS (Zou et al. 2006, 2009) to remove the solar heating-induced instrument temperature variability and inter-satellite

biases in Level-1c radiances. The SNO matchups, accumulated using Cao et al. (2004) algorithm, contain simultaneous observations over the polar regions that are less than 2 min apart and within 111 km ground distance apart for the nadir pixels from any NOAA satellite pairs. The SNO method leverages the SNO matchups to ensure they do not contain sampling errors such as the diurnal drift errors. Therefore, the statistical differences in the SNO matchups represent instrument calibration errors in the satellite pairs.

Applying the calibration equation (8.1) to the SNO matchups between two satellites, represented by k and j, a radiance error between them is derived as (Zou et al. 2006)

$$\Delta R = \Delta R_{\mathrm{L}} - \Delta\delta R + \mu_k Z_k - \mu_j Z_j + E, \tag{8.2}$$

where $\Delta R_{\mathrm{L}} = R_{\mathrm{L},k} - R_{\mathrm{L},j}$ and $\Delta\delta R = \delta R_k - \delta R_j$. E is a residual term related to the spatial and time differences between the satellites k and j and is ignored. In (8.2), ΔR_{L}, Z_k, and Z_j are a function of the measurements, while $\Delta\delta R$, μ_k, and μ_j are unknown coefficients. Regression methods were used to solve for these coefficients from the SNOs in which the summation of $(\Delta R)^2$ is minimized. However, because there is a high degree of colinearity between Z_k and Z_j for the SNOs, only $\Delta\delta R$ and the difference between μ_k and μ_j, $(\mu_k - \mu_j)$, can be determined from regressions (Zou et al. 2006). By definition, the regression procedure resulted in zero mean inter-satellite biases in the SNO matchups. In addition, scene temperature dependency in biases between the two satellites was also significantly reduced with appropriate regression solutions of $(\mu_k - \mu_j)$. Figure 8.4 shows an example of the brightness temperature differences in the SNO matchups between NOAA-10 and NOAA-11 before and after the application of the SNO regression coefficients in the calibration equation (8.1). It is clearly seen that the SNO regressions removed mean inter-satellite biases in the satellite pairs and the scene temperature dependency in the biases.

Based on these SNO regression characteristics, a sequential procedure was developed to solve for coefficients for all NOAA satellites (Zou et al. 2006, 2009). In the sequential procedure, the calibration coefficient, $\Delta\delta R$ and μ, of an arbitrarily selected reference satellite was assumed to be known first, and then coefficients of all other satellites were determined sequentially (one by one) from regressions of the SNO matchups between satellite pairs, starting from the satellite closest to the reference satellite. NOAA-10 was arbitrarily selected as the reference satellite for MSU instrument, and its offset was assumed to be zero. The sequential procedure reduced the problem to the determination of the nonlinear coefficient, μ_{N10}, of the reference satellite; since once μ_{N10} is known, calibration coefficients of all other satellites are solved from the SNOs. This reference satellite problem was tied to the removal of the solar heating-related instrument temperature variability in the Level-1c radiance data.

An end-to-end approach was developed to determine the root-level calibration coefficient by minimizing instrument temperature signals in the end-level inter-satellite

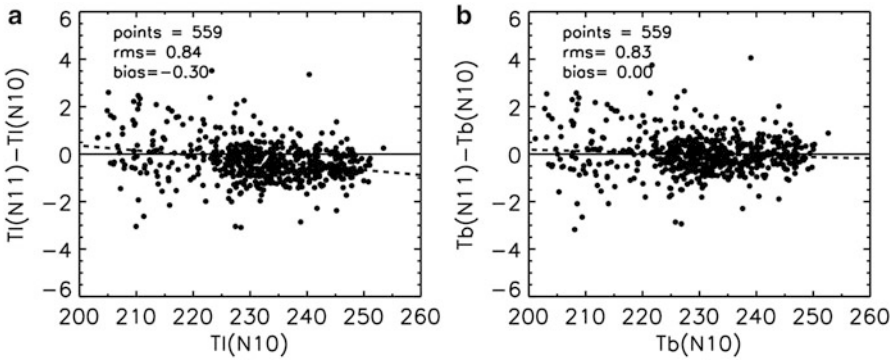

Fig. 8.4 Scatter plots showing effects of the SNO calibration on the error statistics and distribution of the MSU channel 2 brightness temperature difference between NOAA-10 and NOAA-11. (**a**) SNO data between T_L(N10) and $\delta T_L = T_L$(N11) − T_L(N10); (**b**) SNO data between T_b(N10) and $\delta T_b = T_b$(N11) − T_b(N10), where T_L represents linear calibrated brightness temperature and T_b the SNO-calibrated brightness temperature (Plots from Zou et al. 2006)

difference time series of the gridded temperature. In this approach, a series of sensitivity experiments were conducted in which μ_{N10} changed in a reasonable range [e.g., 0–12.5 (sr m^2 cm^{-1}) (mW)$^{-1}$ for all MSU channels]. For each given μ_{N10}, a set of calibration coefficients for all other satellites were obtained sequentially from regressions of their SNO matchups. These calibration coefficients were then applied globally to every observation footprint to obtain a Level-1c radiance dataset for each satellite from Eq. (8.1). Next, a limb correction was applied to adjust different incident angles of the off-nadir footprints to the nadir direction, and global ocean-mean brightness temperatures were further obtained by averaging seven near-nadir, limb-corrected radiances for each sensitivity experiment. Similar to Fig. 8.3, the ocean-mean data are used here for evaluating inter-satellite radiance biases that are related to instrument temperature variability.

The global ocean-mean inter-satellite bias variability, as measured by the mean standard deviation (σ_m) of the inter-satellite difference time series for all satellite pairs, is evaluated for all the sensitivity experiments. Figure 8.5 shows σ_m versus μ_{N10} for all the sensitivity experiments. The quantity σ is a measurement of instrument calibration errors related to the instrument temperature signals in the radiance datasets. Figure 8.3 showed an example of this quantity for a particular satellite pair. The final calibration point for μ_{N10} is selected when the mean instrument calibration error is minimized.

The new calibration coefficients resulted in a FCDR with much smaller solar heating-related calibration errors compared to the prelaunch calibration. Figure 8.6 shows a similar global ocean-mean inter-satellite brightness temperature difference time series as in Fig. 8.3 except for the SNO-calibrated radiances. As seen, the instrument temperature-related variability as observed in Fig. 8.3 for NOAA-10 through NOAA-14 is mostly removed, and their inter-satellite biases are significantly reduced. Quantitatively, the inter-satellite biases and σ_m for the SNO

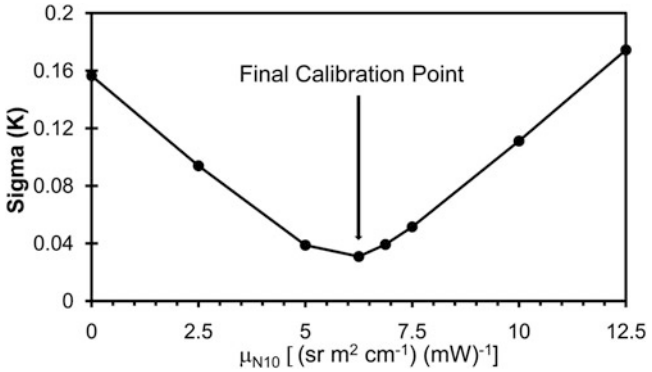

Fig. 8.5 Mean standard deviation (σ_m) of the inter-satellite different time series for all satellite pairs versus μ_{N10} in the sensitivity experiments for MSU channel 2. See Fig. 8.3 for a schematic viewing of σ for a particular satellite pair. The μ_{N10} value corresponding to the minimum of σ_m is selected as the final calibration point

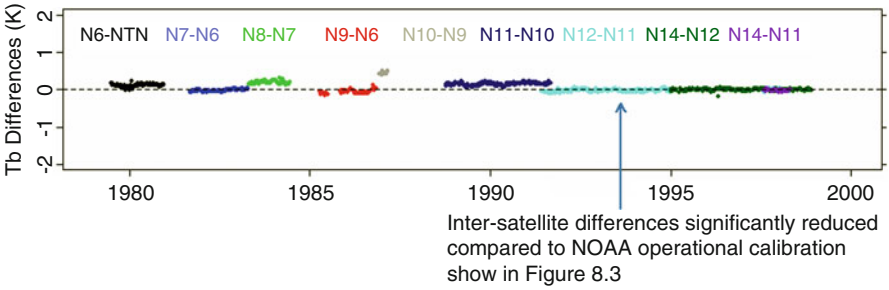

Fig. 8.6 Similar to Fig. 8.3 but for SNO-calibrated MSU Level-1c data, where calibration coefficients were obtained sequentially from SNO matchups with the requirement of minimizing global ocean-mean inter-satellite T_b differences (σ_m) for all satellite pairs

calibration are about 0.05 and 0.03 K, respectively, compared to 0.5 and 0.1 K in the NOAA operational calibration in Fig. 8.3.

8.2.4 Data Assimilation of Radiance FCDR in Climate Reanalysis

The SNO-calibrated FCDR is expected to have good impact on the climate reanalysis development since the instrument calibration errors have been minimized. As an effort to test the performance of the inter-satellite calibration for climate reanalysis improvement, 20 years (1987–2006) of SNO-calibrated MSU Level-1c radiances for channels 2, 3, and 4 onboard NOAA-10 through NOAA-14 were assimilated into the new generation of NCEP Climate Forecast System Reanalysis

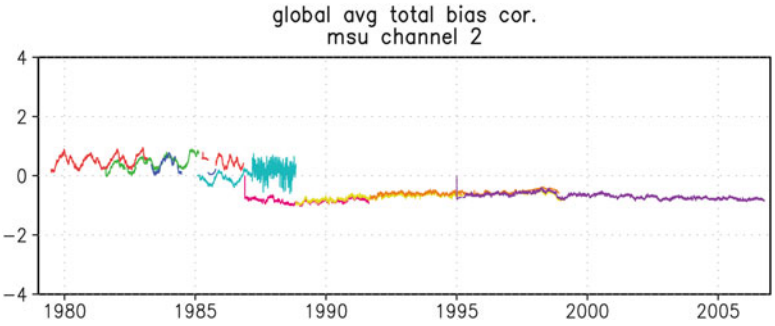

Fig. 8.7 Daily averaged global mean total bias correction (Kelvin) for MSU channel 2 onboard satellites NOAA-6 to NOAA-14. The time series from 1979 to 1988 in four different colors (with larger seasonal variability) are for NOAA-6 through NOAA-9, and the smoother time series from 1987 to 2007 in other four different colors are for NOAA-10 through NOAA-14 (Plot from Saha et al. 2010)

(CFSR) and NASA Modern Era Retrospective analysis for Research and Applications (MERRA) reanalysis (Saha et al. 2010; Rienecker et al. 2011). Since the CFSR and MERRA reanalysis cover the entire period of MSU observations from 1978 to 2006, they actually assimilated two different MSU Level-1c data: the NOAA operational calibrated for TIROS-N through NOAA-9 and the postlaunch SNO calibrated for NOAA-10 through NOAA-14. The fact that radiances from these different calibration procedures were assimilated into the same system serves as an ideal experiment for evaluating the impact and performance of the SNO inter-satellite calibration effort. Figure 8.7 shows the total bias correction patterns of MSU channel 2 in the CFSR for the eight satellites from NOAA-6 through NOAA-14. The total bias correction is a global mean difference between the satellite observations and a background short-term forecast field. This quantity is an indicator of how well the observations agree with the model. These biases can also be used to determine the comparability of two different satellites, since differencing of the bias corrections of two satellites gives inter-satellite difference information similar to the inter-satellite bias analysis shown in Figs. 8.3 and 8.6.

As seen in Fig. 8.7, the bias corrections for NOAA-6 through NOAA-9 exhibit obvious seasonal and interannual variability. As discussed earlier, this variability is related to the solar heating-induced instrument temperature variations. In addition, the bias correction values for NOAA-6 through NOAA-9 are different for different satellites, indicating larger relative offsets between these satellites. This occurs because each individual satellite was calibrated independently in prelaunch calibrations. Similar bias correction patterns were also found for NOAA-10 through NOAA-14 when operational calibrated radiances for these satellites were assimilated into the ERA-Interim reanalysis (Dee and Uppala 2009). In contrast, no instrument temperature variability is observed in bias corrections of the SNO-calibrated MSU observations for NOAA-10 through NOAA-14. Moreover, the bias correction values for NOAA-10 through NOAA-14 are nearly the same, resulting in more consistent

bias correction patterns for these satellites. Differencing of the bias corrections of two satellites gives inter-satellite difference information. With a differencing of the bias corrections for two SNO-calibrated satellites, one can see that the bias corrections are consistent with Fig. 8.6 where inter-satellite biases are on the magnitude of 0.05–0.1 K for NOAA-10 through NOAA-14 (Zou et al. 2006). In summary, bias correction pattern analyses indicate that the inter-calibrated MSU data have reached their performance expectation in the reanalysis data assimilation.

One remaining problem in the inter-satellite calibration is that the absolute value of the inter-calibrated MSU/AMSU brightness temperature has not been adjusted to an absolute truth, although inter-satellite biases have been removed. This is part of the reason for the relative biases between the climate reanalysis and inter-calibrated MSU observations as shown in Fig. 8.7 after 1987. As described earlier, the calibration offset of the reference satellite, δR_{N10}, was arbitrarily assumed to be zero. This assumption does not affect the variability and trend analysis of the TCDR products developed from the FCDR. However, it influences the relative biases between the reanalysis and FCDR. This offset needs to be determined in FCDR validation processes against certain reference observations. Plans for such a validation are being developed at NOAA/NESDIS as part of the effort of FCDR and TCDR development. Once this is done, the bias removed, identical multi-satellite MSU/AMSU FCDRs may be used as an anchor or reference dataset for bias corrections of other observations in the reanalysis data assimilation. This is expected to help the climate reanalysis to be more consistent with the satellite observations.

8.3 Atmospheric Temperature TCDR from Merged MSU/AMSU-A Data

Development of atmospheric temperature TCDR involves proper treatment of errors from several different sources. These include, but are not limited to, antenna pattern effect, incident angle effect, diurnal drift errors, short overlaps between certain satellite pairs, Earth-location dependency in biases, residual biases left from non-perfect instrument calibration, orbital decay, and frequency differences between MSU and AMSU-A channels. Correction algorithms for these effects have been developed by different investigators for TCDR development. In the following, the algorithms implemented in the NOAA MSU/AMSU atmospheric temperature TCDR are briefly described.

8.3.1 Antenna Pattern Correction

When the satellite antenna main beam looks at the Earth to make an observation, the antenna side lobes receive a small amount of radiation from cold space, the

spacecraft, and the Earth. The correction for this effect, the so-called antenna pattern correction, results in brightness temperature differences of about 0.5–2 K. Mo (1999) has developed a set of antenna pattern correction coefficients for the AMSU-A instrument. For a specific channel, this correction adds a same constant for a satellite. Thus, it does not affect the inter-satellite calibration results. However, similar to the calibration offset, it influences the absolute values of the brightness temperature and bias corrections in the reanalysis data assimilation. This correction is currently set to be optional for implementation in the NOAA MSU/AMSU FCDR and TCDR products, depending on needs for brightness temperature validations against other observations.

8.3.2 Limb Adjustment

A limb correction adjusts different incident angles of the off-nadir footprints to the nadir direction. This correction is necessary for use of the off-nadir footprints in the time series to increase observation samples and reduce noise- and sampling-related biases. Limb-correction algorithms and coefficients have been developed by Goldberg et al. (2001) for both the MSU and AMSU satellites using statistical methods. Zou et al. (2009) examined the impact of the limb correction on the MSU time series and found robust trend results when different limb-corrected footprints were included in the time series. Currently, the Goldberg et al. (2001) limb-correction coefficients are used as part of the NOAA MSU/AMSU TCDR processing system.

8.3.3 Diurnal Drift Correction

The diurnal drift errors are caused by satellite orbital drifts, which are measured by the slow evolution in the local equator crossing time (LECT) as a sun-synchronous satellite ages. The satellite orbital drifts result in a change of local observation time that, if not corrected, may introduce a false climate trend by bringing the diurnal trend into it. Its effect is particularly large for the land areas of the lower- and mid-tropospheric temperature channels (e.g., MSU channel 2 and AMSU-A channel 5) where diurnal amplitude is large. It is also important for stratospheric temperature channels.

Two correction methods were developed by previous investigators: Christy et al. (2000) corrected the diurnal drift effect using diurnal anomalies estimated by accumulating the local MSU or AMSU-A observations from different scan positions at different local times, and Mears et al. (2003) used diurnal anomaly climatology generated from NCAR Community Climate Model (CCM) for the correction. The two methods have caused larger trend differences in the MSU observations (Mears and Wentz 2005). Currently, the diurnal anomalies developed

by Mears et al. (2003) are used for the diurnal drift corrections in version 2.0 and earlier versions of the NOAA MSU/AMSU temperature of mid-atmosphere (TMT) product. This is a merged product from MSU channel 2 and AMSU-A channel 5 observations. To reduce uncertainties in the diurnal anomaly dataset, a scaling factor to multiply the anomaly amplitude is introduced. An optimum scaling factor is obtained by minimizing inter-satellite differences over land. Impact studies showed that this correction generated a consistent TMT trend between the land and oceans (Zou and Wang 2010), suggesting that the diurnal anomaly is reasonable.

Other products such as temperatures of the upper troposphere (TUT) and lower stratosphere (TLS) do not include a diurnal drift correction since its effect can be ignored for these channels (Zou et al. 2009).

8.3.4 Residual Inter-satellite Bias Correction

Although inter-satellite biases and the solar heating-induced temperature variability signals in the radiances were mostly removed from the SNO Level-1c calibration, small residual errors still exist in the gridded inter-satellite difference time series (Fig. 8.6). These small residual biases need to be completely removed before merging the satellite data for TCDR generation. Empirical correction algorithms have been developed by different investigators to remove these biases (Christy et al. 2000). It was shown that using the Christy et al. (2000) approach on top the SNO calibration yielded stable MSU trends (Zou and Wang 2010). In the Christy et al. (2000) approach, a best fit empirical relationship between the brightness temperature correction term and the warm target temperature is obtained for the difference time series as shown in Fig. 8.3 by solving multi-regression equations, and then the best fit is removed from the unadjusted time series. The correction result on MSU channel 2 for this method is shown in Fig. 8.8. As seen, after the residual bias correction, global ocean-mean inter-satellite differences are nearly zero for all overlaps with no obvious bias drift.

Currently, global ocean-mean residual biases are corrected using the Christy et al. (2000) approach in the NOAA MSU/AMSU TCDR products.

8.3.5 Correction of the Earth-Location-Dependent Biases

Although SNO calibration minimized global mean inter-satellite biases and instrument temperature signals in the Level-1c data, Earth-location-dependent inter-satellite biases still exist for certain channels on certain satellites in the gridded time series (Zou et al. 2009). This occurred because the nonlinearity of the radiometer transfer function was assumed to be a quadratic type. It is possible that higher-order nonlinearities exist for certain channels and these unresolved nonlinearities in the calibration equation may cause inter-satellite biases to depend

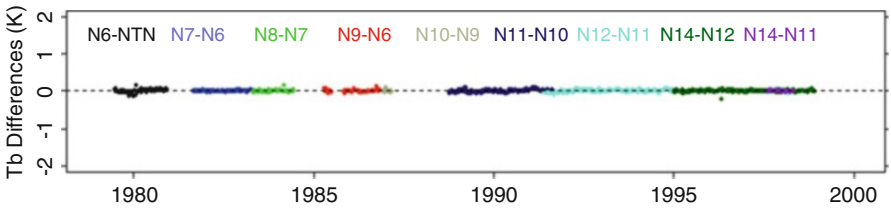

Fig. 8.8 Same as Fig. 8.6 but after residual bias correction was applied

on the Earth location (Zou et al. 2009). In addition, unevenly sampled satellite observations in different grid cells will cause sampling-related Earth-location-dependent biases. To remove these biases, a grid-cell-dependent constant bias correction was always applied as a final step before merging the satellite data. This correction ensures that inter-satellite biases at all grid cells tend to zero so that more reliable regional trends can be obtained from the merged time series.

8.3.6 Frequency Differences Between MSU and AMSU Channels

The MSU is a 4-channel instrument, while AMSU-A has 15 channels. The AMSU channels 5, 7, and 9 are the equivalent channels for the MSU channel 2, 3, and 4, but with slightly different channel frequencies. These frequency differences cause a temperature difference on the order of 2–5 K between MSU and AMSU-A observations since they observe different layers of the atmosphere. Depending on atmospheric lapse rate climatology, these temperature differences also vary with seasons, geographic locations, and channels (Iacovazzi et al. 2009; Zou and Wang 2011). To reduce these type of biases, yearly mean monthly bias statistics between MSU and AMSU-A are derived for each of their equivalent channels and grid cells. These biases are then subtracted from the monthly AMSU-A data, so that they become MSU equivalent channel observations.

8.3.7 Well-Merged NOAA Version 2.0 MSU/AMSU Atmospheric Temperature TCDR

With instrument calibration and bias correction approaches as described above, version 2.0 of a climate-quality, 34-year (1979–present) MSU/AMSU atmospheric temperature TCDR has been generated at NOAA/NESDIS. This is a global gridded dataset with 2.5° latitude by 2.5° longitude grid resolution. Both monthly and pentad data are available. The TCDR includes temperature mid-troposphere (TMT, MSU channel 2 merged with AMSU-A channel 5), temperature tropopause and stratosphere (TTS, MSU channel 3 merged with AMSU-A channel 7; also

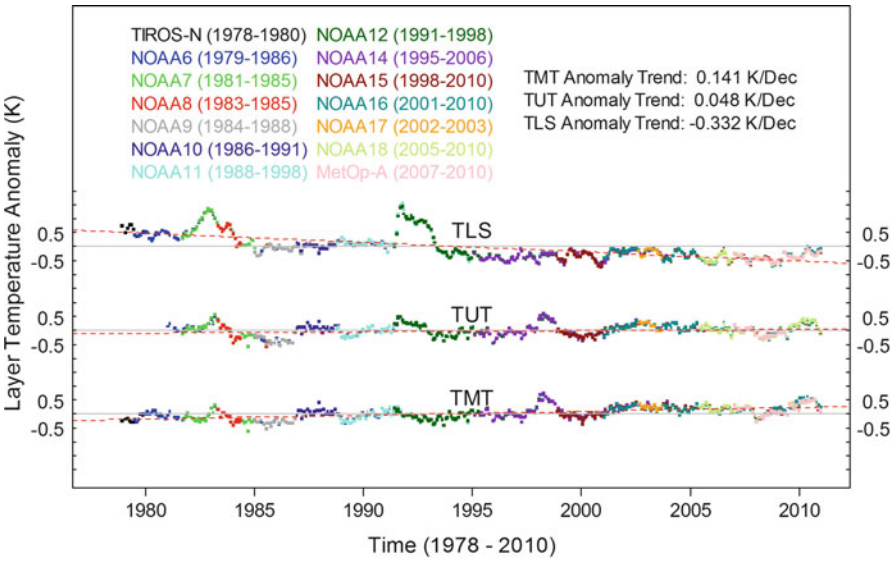

Fig. 8.9 Monthly global mean anomaly time series for temperature mid-troposphere (*TMT*), temperature tropopause and stratosphere (*TTS*), and temperature lower stratosphere (*TLS*) for different satellites after all calibrations and bias corrections are done. Merged time series are obtained by averaging available satellite observations at any data point

known as TUT abbreviated for temperature upper troposphere), and temperature lower stratosphere (TLS, MSU channel 4 merged with AMSU-A channel 9). Figure 8.9 shows global mean pentad anomaly time series for these variables for all satellites used in the dataset (TIROS-N through NOAA-18 and MetOp-A). In the plot, different colors represent different satellites. As seen, different satellites agree with each other on a point-by-point basis during overlapping observations, indicating high quality of intercalibration and merging in the time series.

From these time series, an updated temperature trend for different atmospheric layers is obtained. The global mean 32-year trend from 1979 to 2010 for the TMT and TLS is respectively 0.141 K/decade and −0.332 K/decade, and the 30-year (1981–2010) trend for TTS is 0.048 K/decade.

8.4 Conclusion and Data Availability

A climate-quality MSU/AMSU radiance FCDR and atmospheric temperature TCDR have been developed at NOAA/NESDIS using SNO calibration methodology. The FCDR consists of SNO-calibrated Level-1c radiances for different MSU and AMSU channels. Instrument calibration errors related to inaccurate calibration nonlinearity and solar heating-induced instrument temperature variability have been minimized in the FCDR. The TCDR includes TMT, TTS, and TLS from

merged MSU and AMSU observations. Many instrument calibration and sampling errors have been removed or minimized in the TCDR. These FCDR and TCDR are expected to benefit many climate change monitoring and research areas including data assimilation of the FCDR in modeling reanalysis development, consistent satellite retrievals from FCDR, use of TCDR in climate trend detection, and validations of climate model simulations. Good impacts of the recalibrated MSU FCDR on reanalysis bias corrections have already been achieved in the NCEP CFSR and NASA MERRA reanalysis systems. It is expected that future reanalyses will benefit more from assimilating the SNO-recalibrated AMSU-A data.

The FCDRs and TCDRs are publicly available from the NESDIS/STAR website with the URL address: http://www.star.nesdis.noaa.gov/smcd/emb/mscat/mscatmain.htm. At the time of this writing, the SNO-recalibrated radiance FCDRs for MSU channels 2, 3, and 4 onboard TIROS-N through NOAA-14 and AMSU-A channels 4–14 onboard NOAA-15 through NOAA-18 and MetOp-A are available for downloading through the website. In addition, global MSU-only TCDRs for TMT, TTS, and TLS from 1979 to 2006 and merged MSU/AMSU TCDRs from 1979 to the present for these same variables are both available through the website. These are gridded datasets with 2.5° latitude by 2.5° longitude resolution. Both monthly and pentad data are provided for seamless climate change monitoring.

References

Cao C, Weinreb M, Xu H (2004) Predicting simultaneous nadir overpasses among polar-orbiting meteorological satellites for the intersatellite calibration of radiometers. J Atmos Ocean Technol 21:537–542

Christy JR, Spencer RW, Lobel ES (1998) Analysis of the merging procedure for the MSU daily temperature time series. J Climate 11:2016–2041

Christy JR, Spencer RW, Braswell WD (2000) MSU tropospheric temperatures: data set construction and radiosonde comparisons. J Atmos Ocean Technol 17:1153–1170

Christy JR, Spencer RW, Norris WB, Braswell WD (2003) Error estimates of version 5.0 of MSU-AMSU bulk atmospheric temperature. J Atmos Ocean Technol 20:613–629

Dee D, Uppala S (2009) Variational bias correction of satellite radiance data in the ERA-interim reanalysis. Q J R Meteorol Soc 135:1830–1841. doi:10.1002/qj.493

Fu Q, Johanson CM (2004) Stratospheric influence on MSU-derived tropospheric temperature trends: a direct error analysis. J Climate 17:4636–4640

Fu Q, Johanson CM (2005) Satellite-derived vertical dependence of tropical tropospheric temperature trends. Geophys Res Lett 32:L10703. doi:10.1029/2004GL022266

Fu Q, Johanson CM, Warren SG, Seidel DJ (2004) Contribution of stratospheric cooling to satellite-inferred tropospheric trends. Nature 429:55–58

Goldberg MD, Crosby DS, Zhou L (2001) The limb adjustment of AMSU-A observations: methodology and validation. J Appl Meteor 40:70–83

Goodrum G (ed) (2000) NOAA KLM user's guide. http://www2.ncdc.noaa.gov/docs/klm/cover.htm. Amended 5 Apr 2004

Grody NC, Vinnikov KY, Goldberg MD, Sullivan J, Tarpley JD (2004) Calibration of multisatellite observations for climate studies: microwave sounding unit (MSU). J Geophys Res 109. doi:10.1029/2004JD005079

Hurrell JW, Trenberth KE (1997) Spurious trends in satellite MSU temperatures from merging different satellite records. Nature 386:164–167
Hurrell JW, Trenberth KE (1998) Difficulties in obtaining reliable temperature trends: reconciling the surface and satellite microwave sounding unit records. J Climate 11:945–967
Hurrell JW, Brown SJ, Trenberth KE, Christy JR (2000) Comparison of tropospheric temperatures from radiosondes and satellites: 1979–1998. Bull Am Meteor Soc 81:2165–2177
Iacovazzi RA Jr, Cao C, Boukabara S (2009) Analysis of polar-orbiting operational environmental satellite NOAA-14 MSU and NOAA-15 AMSU-A relative measurement biases for climate change detection. J Geophys Res 114:D09107. doi:10.1029/2008JD011588
Johanson CM, Fu Q (2006) Robustness of tropospheric temperature trends from MSU channels 2 and 4. J Climate 19:4234–4242
Karl TR et al (eds) (2006) Temperature trends in the lower atmosphere: steps understanding and reconciling differences. Climate change science program and subcommittee on global change research. Washington, D.C. http://www.climatescience.gov/Library/sap/sap1-1/finalreport/sap1-1-final-all.pdf
Kidwell KB (ed) (1998) NOAA polar orbiter data user's guide. http://www2.ncdc.noaa.gov/docs/podug/index.htm, September 2000 revision
Mears CA, Wentz FJ (2005) The effect of diurnal correction on the satellite-derived lower tropospheric temperature. Science 309:1548–1551
Mears CA, Wentz FJ (2009a) Construction of the remote sensing systems V3.2 atmospheric temperature records from the MSU and AMSU microwave sounders. J Atmos Ocean Technol 26:1040–1056
Mears CA, Wentz FJ (2009b) Construction of the RSS V3.2 lower-tropospheric temperature dataset from the MSU and AMSU microwave sounders. J Atmos Ocean Technol 26:1493–1509
Mears CA, Schabel MC, Wentz FJ (2003) A reanalysis of the MSU channel 2 tropospheric temperature record. J Climate 16:3650–3664
Mo T (1995a) A study of the microwave sounding unit on the NOAA-12 satellite. IEEE Trans Geosci Remote Sens 33:1141–1152
Mo T (1995b) Calibration of the advanced microwave sounding unit-A for NOAA-K. NOAA technical report NESDIS 85, US Department of Commerce, Washington DC
Mo T (1999) AMSU-A antenna pattern corrections. IEEE Trans Geosci Remote Sens 37:103–112
Mo T, Goldberg MD, Crosby DS, Cheng Z (2001) Recalibration of the NOAA microwave sounding unit. J Geophys Res 106:10145–10150
National Research Council (2004) Climate data records from Environmental Satellites. Washington, D.C.
Prabhakara C, Iacovazzi RA Jr (1999) Comments on "analysis of the merging procedure for the MSU daily temperature time series". J Climate 12:3331–3334
Prabhakara C, Iaccovazzi RA Jr, Yoo J-M, Dalu G (2000) Global warming: evidence from satellite observations. Geophys Res Lett 27:3517–3520
Rienecker MM et al (2011) MERRA: NASA's modern-era retrospective analysis for research and applications. J Climate 24:3624–3648. doi:10.1175/JCLI-D-11-00015.1
Saha S et al (2010) The NCEP climate forecast system reanalysis. Bull Am Meteorol Soc 91:1015–1057. doi: http://dx.doi.org/10.1175/2010BAMS3001.1
Santer BD et al (2005) Amplification of surface temperature trends and variability in the tropical atmosphere. Science 309:1551–1556
Solomon S, Qin D, Manning M, Marquis M, Averyt K, Tignor MMB, Miller HL HL Jr, Chen Z (eds) (2007) Climate change 2007: the physical science basis. Cambridge University Press, Cambridge
Spencer RW, Christy JR (1992a) Precision and radiosonde validation of satellite gridpoint temperature anomalies. Part I: MSU channel 2. J Climate 5:847–857
Spencer RW, Christy JR (1992b) Precision and radiosonde validation of satellite gridpoint temperature anomalies. Part II: tropospheric retrieval and trends during 1979–90. J Climate 5:858–866

Spencer RW, Christy JR, Braswell WD, Norris WB (2006) Estimation of tropospheric temperature trends from MSU channels 2 and 4. J Atmos Ocean Technol 23:417–423

Trenberth KE, Hurrell JW (1997) How accurate are satellite "thermometers". Nature 389:342–343

Vinnikov KY, Grody NC (2003) Global warming trend of mean tropospheric temperature observed by satellites. Science 302:269–272

Vinnikov KY, Grody NC, Robock A, Stouffer RJ, Jones PD, Goldberg MD (2006) Temperature trends at the surface and in the troposphere. J Geophys Res 111:1–14. D03106, doi:10.1029/2005JD006392

Wentz FJ, Schabel M (1998) Effects of satellite orbital decay on MSU lower tropospheric temperature trends. Nature 394:661–664

Zou C-Z, Wang W (2010) Stability of the MSU-derived atmospheric temperature trend. J Atmos Ocean Technol 27:1960–1971

Zou C-Z, Wang W (2011) Inter-satellite calibration of AMSU-A observations for weather and climate applications. J Geophys Res 116:D23113. doi:10.1029/2011JD016205

Zou C-Z, Goldberg MD, Cheng Z, Grody N, Sullivan J, Cao C, Tarpley D (2006) Recalibration of microwave sounding unit for climate studies using simultaneous nadir overpasses. J Geophys Res 111:D19114. doi:10.1029/2005JD006798

Zou C-Z, Gao M, Goldberg MD (2009) Error structure and atmospheric temperature trends in observations from the microwave sounding unit. J Climate 22:1661–1681. doi:10.1175/2008JCLI2233.1

Chapter 9
Monitoring Change in the Arctic

Jeffrey R. Key, Xuanji Wang, and Yinghui Liu

Abstract Modeling studies have shown that the Arctic is one of the most sensitive regions on Earth to global climate change due primarily to the positive feedback between surface temperature, surface albedo, and ice extent. Because in situ measurements in this harsh environment are costly, satellites are a critical source of information for monitoring and evaluating changes in the Arctic climate system. Satellite data can be used to measure polar winds, clouds, sea ice, snow cover, and glaciers. Applications of space-based imager and sounder data have shown that over the last three decades, the Arctic has warmed and become cloudier in spring and summer, but cooled and become less cloudy in winter. Arctic sea ice has declined substantially and at a greater rate than that predicted by most climate models. Snow cover has decreased in many areas, and vegetation growth has increased at high latitudes. Satellite products have also been used to demonstrate the complex feedbacks between clouds and sea ice, providing insight into the possible future state of Arctic climate.

9.1 Introduction

The Arctic has become an area of considerable interest for studying the Earth's changing climate (e.g., ACIA 2005; Overland 2009). Satellite observations have shown that Northern Hemisphere sea ice extent and thickness have been decreasing beyond the expectation of natural climate variability (Rothrock et al. 1999; Vinnikov et al. 1999; Parkinson et al. 1999; Cavalieri et al. 1999; Maslanik et al. 2007; Kwok and

J.R. Key (✉)
Center for Satellite Applications and Research, NESDIS, NOAA, Madison, WI, USA
e-mail: Jeff.Key@noaa.gov

X. Wang • Y. Liu
Cooperative Institute for Meteorological Satellite Studies,
University of Wisconsin, Madison, WI, USA

J.J. Qu et al. (eds.), *Satellite-based Applications on Climate Change*,
DOI 10.1007/978-94-007-5872-8_9,

Untersteiner 2011; Comiso 2012) and that changes are also evident in other climate parameters such as surface air temperature, atmospheric circulation, precipitation, snowfall, biogeochemical cycling, and vegetation (Curry et al. 1996; Wallace et al. 1996; Rigor et al. 2000; Groves and Francis 2002; Chapman and Walsh 1993; Myneni et al. 1997; Wang and Key 2003; Wang et al. 2012). A comprehensive review of recent changes in the Arctic cryosphere (snow and ice) is available in AMAP (2011).

Numerous modeling studies have shown that the Arctic is one of the most sensitive regions on Earth to global climate change due primarily to the positive feedback between surface temperature, surface albedo, and ice extent, known as the ice-albedo feedback (Manabe et al. 1992; Manabe and Stouffer 1994; Miller and Russell 2000; Meehl and Washington 1990; Curry et al. 1996). This theory of "polar amplification" has been confirmed by observational evidence, though records of Arctic climate change are brief and geographically sparse. There are a number of potential causes for Arctic climate change: changes in the large-scale atmospheric circulation (e.g., Graversen et al. 2008; Overland 2009), the ice-albedo feedback (Perovich et al. 2008), changes in greenhouse gas amounts and the associated radiative forcing (Serreze et al. 2007; Graversen and Wang 2009) and clouds (Liu et al. 2008; Kay and Gettelman 2009), and changes in ocean circulation and the inflow of warm ocean water (Shimada 2006).

The Arctic, roughly defined here as the area poleward of 60° north latitude (Fig. 9.1), has a complex climate system that is strongly influenced by both internal processes and external forcings. Being one of the Earth's "heat sinks" (the other is the Antarctic), atmospheric and oceanic heat and moisture fluxes dominate large-scale Arctic climate patterns. Interactions between the ocean, atmosphere, and cryosphere not only control local processes such as the surface energy budget but also feed back to the global climate system. Changes in Arctic climate can have a profound impact on midlatitude weather.

Monitoring the Arctic climate system requires accurate measurements of the atmosphere, cryosphere, and ocean. This includes, but is not limited to, snow cover; sea, lake, and land ice; cloud; atmospheric temperature and humidity structure; winds; and sea surface temperature. Measurements of the following quantities are needed:

- Clouds: cover, thermodynamic phase, height, optical thickness, particle size
- Atmospheric temperature and humidity profiles
- Wind speed, direction, height
- Snow: extent (cover), snow water equivalent (SWE), depth
- Sea and lake ice: extent (cover), concentration, thickness, motion
- Surface temperature and albedo

These are not the only climate variables of interest, but they are the variables that have significant impacts on climate, change on hourly to annual time scales, and can be measured with sufficient accuracy from space. Other quantities for which space-based remote sensing methods continue to be developed include solid precipitation, permafrost characteristics, glaciers, ice sheets, and freshwater ice. Table 9.1 lists the satellite sensors that can be used to estimate many of the essential climate variables (ECVs) in the polar regions.

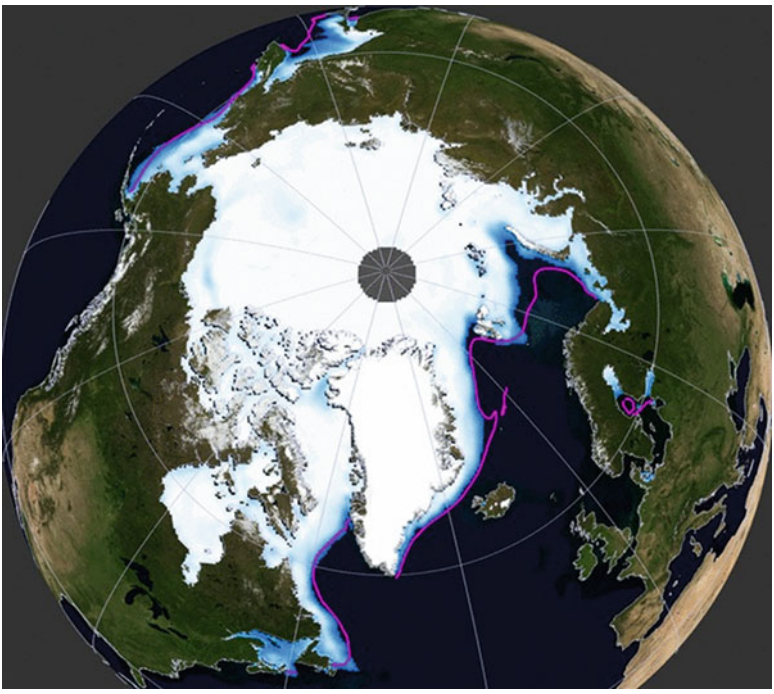

Fig. 9.1 The Arctic, with the March 2009 sea extent (Image by Matt Savoie, National Snow and Ice Data Center, University of Colorado, Boulder, using SSM/I data overlaid onto the NASA Blue Marble). The 60°N latitude circle is shown

The purpose of this chapter is to summarize satellite remote sensing methods and applications for monitoring Arctic climate characteristics, including recent trends. The emphasis will be on the physical climate system, though not all aspects of the physical system can be examined here. Instead, methods and applications for satellite remote sensing of the high latitudes will focus on winds, clouds, surface temperature and albedo, and sea ice. Applications of satellite data sets to climate change detection will also be described.

9.2 Winds

Satellite-derived wind fields are most valuable where few observations exist and model analyses are less accurate as a result. Like the oceans at lower latitudes, the polar regions suffer from a lack of observational data. World Meteorological Organization (WMO) stations, which provide regular wind observations from rawinsondes, are scattered across the coastal areas and the interior of Canada, Alaska, Russia, and northern Europe. However, there is little or no coverage of the Arctic Ocean, the interior of Greenland, the interior of Antarctica, and the oceans surrounding Antarctica. With a gap in the observing systems over the polar

Table 9.1 Current and future satellites and sensors for key Arctic climate variables

Sensor types	Laser and radar altimeters	Synthetic aperture radar (SAR)	Scatterometers	Visible/infrared imagers	Atmospheric sounders	Passive microwave	Gravity
Satellites and sensors	ICESat, ERS-2, Envisat, CryoSat-2, Sentinel-3	ERS-2 SAR, Envisat ASAR, Radarsat1-2, ALOS-PALSAR, TERRASAR-X, COSMO-SKYMED, RISAT, Sentinel-1	ERS2-Wind Scat, QuikScat, MetOp-ASCAT, OCEANSAT-2, HY-2A Scat	SPOT 1–5, Landsat, ASTER, Sentinel-2, AVHRR, MODIS, VIIRS, HY-1	HIRS, AMSU, IASI, SSMIS, MIS	SSMI, AMSR-E, WindSat, SMOS, HY-2A	GRACE, GOCE
Atmosphere				Winds, cloud properties (amount, height, phase, thickness)	Temperature and humidity profiles	Surface winds (ice-free)	
Ice sheets	Elevation/ thickness change	Motion, extent	Extent, snow/ice facies	Extent		Melt/freeze onset	Mass change
Glaciers and ice caps	Surface topography and change	Velocity, topography, facies, lakes	Facies	Extent, velocity, snow line			Mass change
Sea ice	Freeboard/ thickness	Motion, extent, floe size distribution	Extent, melt/freeze onset, motion	Extent, floe size distribution, melt ponds		Extent, concentration, snow thickness	Geoid
Snow	Accumulation	Accumulation	Accumulation	Extent		Extent, thickness	Mass loading

Solid precipitation and SWE						Mass loading
Temperature				Temperature	Temperature	
Albedo				Albedo		
Lake and river ice	Thickness	Motion, extent	Extent, melt/freeze onset	Extent, floe size distribution, melt ponds	Extent, snow thickness	
Permafrost and frozen ground		Motion, slope failures, surface deformation, thermokarst subsidence	Freeze-thaw status of the active layer	Coastal erosion, thermokarst, permafrost surface indicators, land cover, surface temperature	Freeze-thaw status of the active layer	Mass change due to ground ice melting

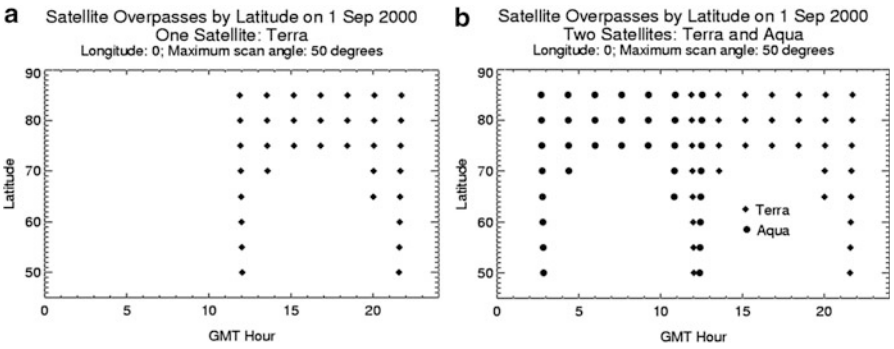

Fig. 9.2 Time differences between successive overpasses of the Terra satellite (**a**) as a function of latitude over the course of a 24-h period at the prime meridian and for both Terra and Aqua (**b**). Only overpasses with sensor view angles less than 50° are considered

regions that cannot be filled by geostationary satellites because of poor viewing geometry, polar-orbiting satellites are needed.

To estimate winds, clouds and water vapor features are tracked in sequential images under the assumption that their movement represents the local airflow. It is therefore necessary to track features over time in a sequence of images. Statistical analyses of visible, infrared, and water vapor wind data sets from geostationary satellites versus rawinsonde data have shown that the optimal processing intervals are 5 min for visible imagery of 1 km resolution and 30 min for water vapor imagery of 8 km resolution (Velden et al. 2000). How often can we obtain successive images for wind vectors from a polar-orbiting satellite? The answer depends on the latitude and the number of satellites. Figure 9.2a shows the frequency of time differences between successive overpasses at a given latitude-longitude point during one 24-h period with a single satellite (Terra). The points show only those overpasses where the sensor, the Moderate Resolution Imaging Spectroradiometer (MODIS), would view the Earth location at an angle of 50° or less. At larger scan angles, the sensor would view the area near the pole on every overpass. At 60° latitude, there are two overpasses separated by about 10 and 13 h. No useful wind information can be obtained at this latitude with only one satellite. At 80° there are many views separated by the orbital period of 100 min, but there is still a 13-h gap each day. Although the 100-min temporal sampling is significantly longer than the optimal processing intervals for geostationary satellites, in theory wind vectors can be obtained during part of every day for the area poleward of approximately 70° latitude. Figure 9.2b shows the coverage with two satellites: Terra and Aqua. Temporal gaps of a few hours still exist at the lower latitudes of the polar regions, but at the higher latitudes, the temporal coverage is very good. With additional satellites, e.g., the NOAA operational weather satellites with the Advanced Very High Resolution Radiometer (AVHRR), it would be possible to obtain successive views of a given location within minutes of each other.

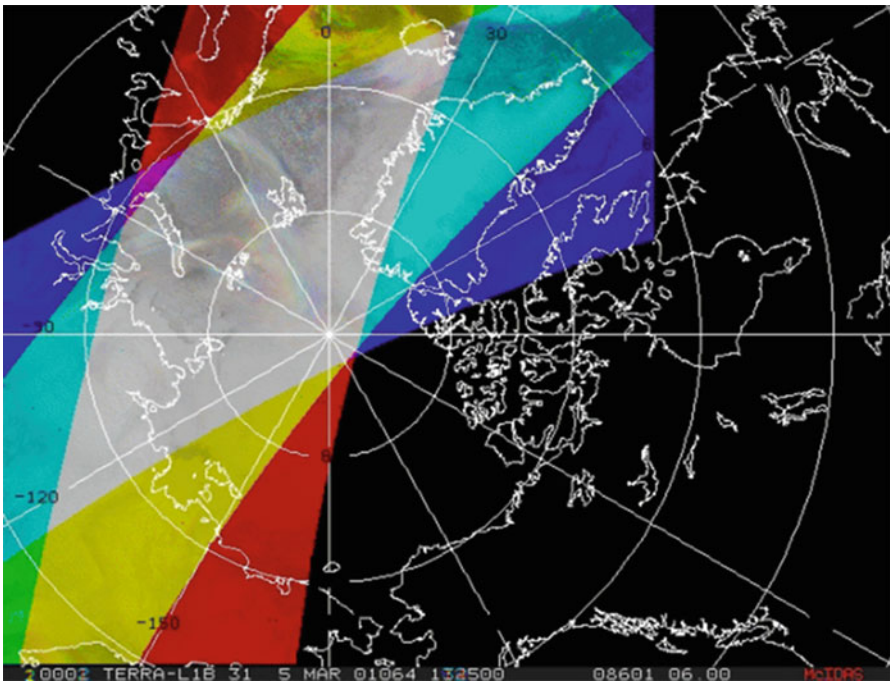

Fig. 9.3 Three successive MODIS orbits over the Arctic (*red*, *green*, *blue*). The overlap of the orbits (*whitish-gray shade*) is the area for which wind vectors can be estimated with each triplet of orbits

Cloud and water vapor tracking with MODIS data is based on the established procedure used for the GOES, which is essentially that described in Merrill (1989), Nieman et al. (1997), and Velden et al. (1997, 1998). Cloud features are tracked in the infrared (IR) window band at 11 μm on MODIS and the Advanced Very High Resolution Radiometer (AVHRR), and water vapor (WV) features are tracked in the 6.7 μm band on MODIS. Even though AVHRR and MODIS have a visible channel, it is not generally useful for winds in polar regions because of the long winter darkness and low sun angles during the summer that make feature tracking difficult. With monthly average cloud amounts over the Arctic and Antarctic ranging from 50 to 90% and annual mean cloud coverage of about 70% over the Arctic, potential cloud targets are numerous (Key et al. 2003).

The methodology employed for wind vector estimation requires three successive images for wind retrievals. With geostationary satellites, the spatial coverage is constant, but with a polar-orbiting satellite, the coverage from each successive orbit changes, so wind retrievals can only be done for the area of overlap between successive orbit triplets. This is illustrated for MODIS in Fig. 9.3. For each 200-min time period (three successive orbits each separated by 100 min), wind vectors can be obtained for the area of overlap.

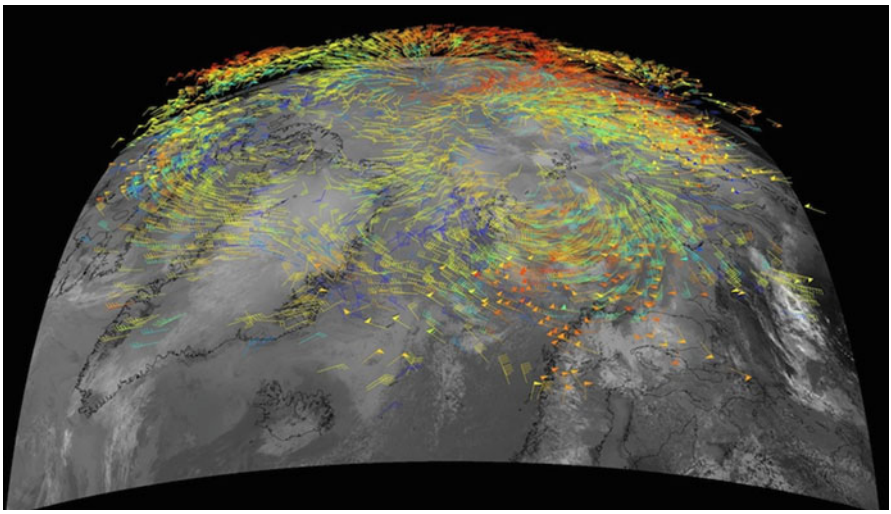

Fig. 9.4 Wind vectors over the Arctic on 7 June 2009, derived from Moderate Resolution Imaging Spectroradiometer (MODIS) data. Colors indicate wind heights, from *blue* (low, near surface) to *red* (high, 10 km)

Wind vector heights are assigned by any one of three methods. The infrared window method assumes that the mean of the lowest (coldest) brightness temperature values in the target sample is the temperature at the cloud top. This temperature is compared to a numerical forecast of the vertical temperature profile to determine the cloud height. The method is reasonably accurate for opaque clouds but inaccurate for semitransparent clouds. The CO_2 slicing method works well for both opaque and semitransparent clouds. Cloudy and clear radiance differences in one or more carbon dioxide bands (e.g., 13.3, 13.6, 13.9, or 14.2 μm on MODIS) and infrared window bands are ratioed and compared to the theoretical ratio of the same quantities, calculated for a range of cloud pressures. The cloud pressure that gives the best match between the observed and theoretical ratios is chosen (Menzel et al. 1983; Frey et al. 1999). The H_2O-intercept method of height determination can be used as an additional metric or in the absence of a CO_2 band. This method examines the linear relationship between clusters of clear and cloudy pixel values in water vapor-infrared window brightness temperature space, predicated on the fact that radiances from a single cloud deck for two spectral bands vary linearly with cloud fraction within a pixel (Schmetz et al. 1993). The height of clear-sky water vapor wind vectors is determined by comparing the water vapor brightness temperature to a collocated model temperature profile, analogous to the IR window method for cloud features. However, the brightness temperature of the feature being tracked corresponds more to a layer than a level, as will the retrieved wind vector height (Rao et al. 2002).

An example of polar winds derived from MODIS over the course of a day is shown in Fig. 9.4. Wind vectors are color-coded to represent their relative heights.

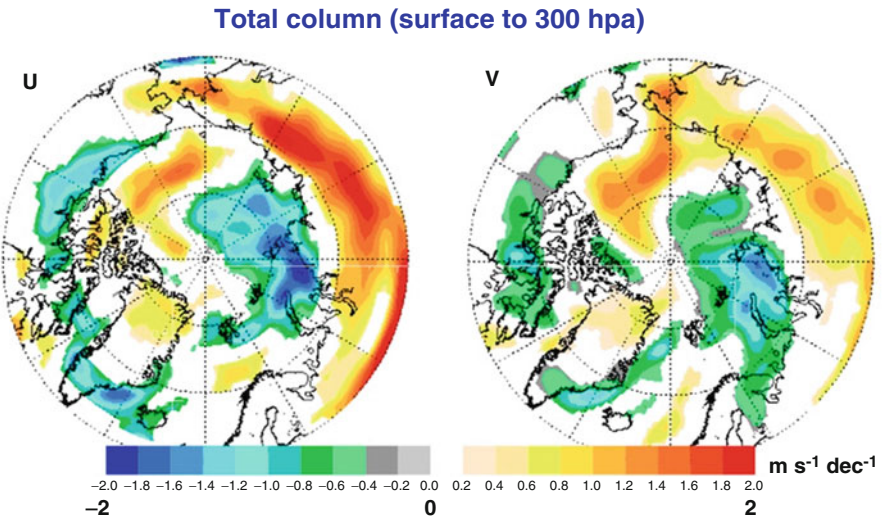

Fig. 9.5 23-year trends (1979–2001) in zonal (*left*) and meridional (*right*) wind derived from TOVS temperature profiles over the entire year for the entire column, surface to 300 hPa (Courtesy of J. Francis)

An attempt to improve the three-dimensional wind fields for climate reanalyses was undertaken by Francis et al. (2005) using satellite-derived temperature profiles from the TIROS Operational Vertical Sounder (TOVS). The TOVS Polar Pathfinder (TOVS Path-P) product (Francis and Schweiger 1999), specifically designed for polar applications, was used to compute the thermal wind with a mass conservation technique (Zou and Van Woert 2002; Francis et al. 2005). One drawback of this approach is that the resultant wind field would be nearly geostrophic and would not take into account any significant ageostrophic motions in the flow (Zou and Van Woert 2001). The thermal wind product would therefore be less accurate in regions of significant ageostrophic flow, such as in the entrance and exit regions of jet streaks, and in strongly curved flows, as the geostrophic balance only occurs when there is no curvature in the flow.

Nevertheless, an examination of the TOVS-derived thermal winds has proven useful for Arctic climate studies. Trends and anomalies for the period 1979–2001 were calculated for both meridional and zonal winds at eight levels between the surface and 300 hPa (Francis et al. 2005). It was found that zonal winds are more westerly over Eurasia and the western Arctic Ocean, while westerlies have weakened over northern Canada (Fig. 9.5). Combined with the corresponding pattern in meridional winds, these results suggest that the polar vortex has, on average, shifted toward Siberia. Changes in meridional winds are consistent with observed trends in melt onset date and sea ice concentration in the marginal seas.

Because winds derived from polar-orbiting satellite imagers better capture the ageostrophic component of the wind and because they have been shown to improve weather forecasts (Key et al. 2003; Velden et al. 2005), they could also be used to

improve reanalysis wind fields. A 30-year data set of AVHRR polar winds was created for climate studies and used in reanalyses (Dworak and Key 2009). An analysis of this historical AVHRR wind product has shown that the AVHRR winds were, on average, slower in regions of positive vorticity (troughs and cyclones) and faster in regions of negative vorticity (ridges and anticyclones) than the European Center for Medium-Range Weather Forecasts (ECMWF) reanalysis (ERA-40). Furthermore, AVHRR is noticeably faster than ERA-40 in jet streaks, an indication that AVHRR has stronger winds in jet streams overall. Therefore, the use of the historical AVHRR wind product in future reanalyses should result in more accurate wind fields (Fig. 9.5).

9.3 Clouds

Clouds affect Arctic climate primarily though the absorption, emission, and scattering of radiation (Wang and Key 2003; Wang and Key 2005a, b). Cloud detection and characterization play a crucial role in satellite retrievals of other climate variables. However, the detection of clouds in the polar regions is arguably more difficult than any place else on Earth. Clouds are often warmer than the surface due to ubiquitous low-level temperature inversions. In addition to a low thermal contrast between clouds and the surface, clouds, snow, and ice have similar reflectances in the visible portion of the spectrum (Key and Barry 1989). Nevertheless, reasonably accurate cloud detection can be done with a variety of spectral and temporal tests optimized for high-latitude conditions (Frey et al. 2008). Cloud particle phase uses near-infrared reflectances (daytime) and infrared brightness temperature differences to separate ice and liquid ("water") clouds (Key and Intrieri 2000). Cloud optical depth and particle effective radius retrievals use absorbing and nonabsorbing wavelengths, where the absorbing wavelength is more sensitive to particle size and the nonabsorbing wavelength is more sensitive to optical depth. Cloud temperature is calculated from the infrared window brightness temperature, adjusted for surface emission if the cloud transmittance is greater than 1%. For more algorithm details, see Key (2002).

There are two major satellite-derived, multi-decadal, polar-specific data sets that can be used to monitor and study atmospheric characteristics in the polar regions: the AVHRR Polar Pathfinder (APP) (Fowler et al. 2000; Meier et al. 1997) and the TOVS Path-P products. Other global data sets such as the International Satellite Cloud Climatology Project (ISCCP) cloud data set (Rossow et al. 1996) and PATMOS-x can also be employed, but they are not optimized for polar studies, and the uncertainties are generally higher than in the APP and TOVS Path-P products. The APP data set was extended (hereinafter "APP-x") to include the retrievals of cloud fraction, cloud optical depth, cloud particle phase and size, cloud top temperature and pressure, surface skin temperature, surface broadband albedo, and radiative fluxes as well as cloud radiative effects ("cloud forcing") (Wang and

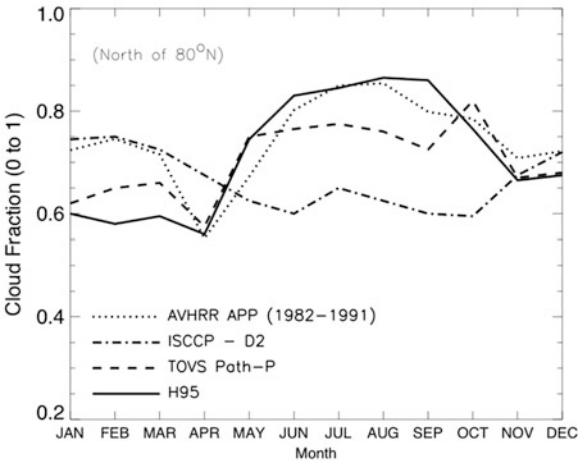

Fig. 9.6 Annual cycle of cloud fraction from surface-based observations (H95) and satellite retrievals (ISCCP-D2, TOVS Path-P, and APP-x) for the Arctic region north of 80°N over the period 1982–1991 (Wang and Key 2005a)

Key 2003). The consistency of the APP-x products from different satellites over the period of 1982–1999 was investigated and found no observable bias by Wang and Key (2003).

Figure 9.6 shows an annual cycle of the total cloud fraction (cloud amount) based on the surface observations (Hahn 1995), the International Satellite Cloud Climatology Project (ISCCP) D2 data set, the TOVS Path-P data set (Schweiger et al. 1999), and the extended AVHRR Polar Pathfinder (APP-x) data set. The surface-based climatology does not include clear-sky ice crystal precipitation. These low-level ice crystal clouds occur in winter about 20–50% of the time and are often thick enough to have a significant radiative effect (Curry and Ebert 1992; Curry et al. 1996), which should be considered in satellite retrievals of other Arctic climate parameters. The APP-x data show that, as expected, the Arctic is one of the cloudiest regions on the Earth with annual mean cloud coverage of about 70%.

About 70% of the clouds are in solid phase (ice) in winter, and about the same proportion of the clouds is in liquid phase in summer. Mixed-phase and multilayer clouds are not identified as such in APP-x. In winter more ice clouds occur over the Arctic landmasses than the Arctic Ocean, with the particle sizes as large as 30 μm. Summertime clouds are predominantly liquid and equally distributed over the landmass and ocean regions with the average particle size of 10 μm. In general, visible cloud optical depth is about 5–6 for the Arctic overall. Optically thick clouds occur in transition seasons for every region in the Arctic except the GIN seas where thick clouds are in summer. The Arctic cloud top temperature basically follows the surface temperature variation in space and time. Overall the cloud temperature is lower than the surface temperature.

Cloud fraction has not changed significantly over the Arctic on an annual time scale. However, APP-x shows that cloud cover has increased in spring and summer, but decreased over the central Arctic Ocean in winter. Figure 9.7 shows the trends in cloud particle phase, effective radius, and optical depth for four seasons and the

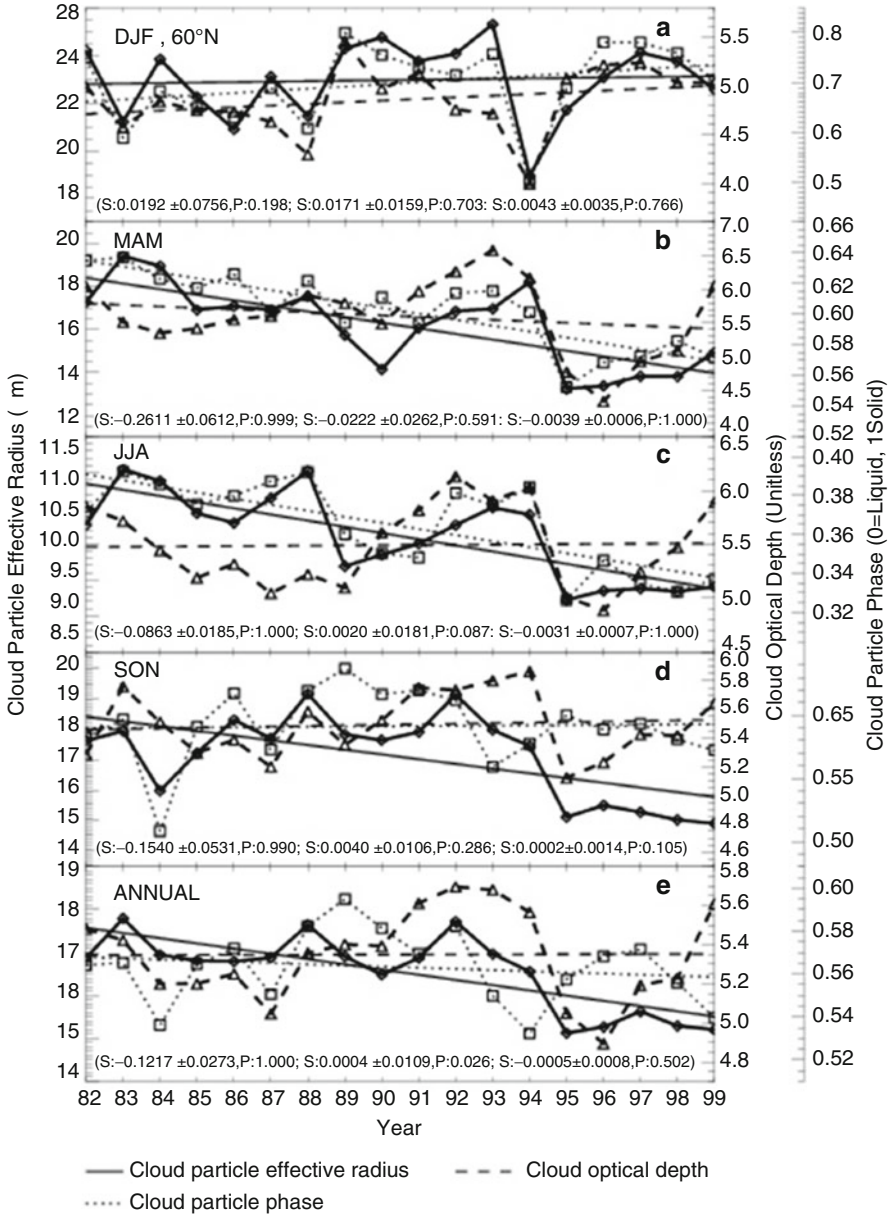

Fig. 9.7 Time series and trends of cloud particle phase, effective radius, and optical depth in winter (*DJF*), spring (*MAM*), summer (*JJA*), and autumn (*SON*) over the period of 1982–1999 for the Arctic region north of 60°N from APP-x. Numbers in parentheses are the trend slope per year ("*S*") with its standard deviation and the *F* test confidence level ("*P*"). The first pair of *S* and *P* denotes the cloud particle effective radius trend (*solid line*), the second pair is for the cloud optical depth trend (*dashed line*), and the third pair represents the cloud particle phase trend (*dotted line*)

annual mean for the Arctic Ocean and surrounding landmasses north of 60°N. Cloud particle phase is indicated by two numbers: 0 for liquid phase, 1 for solid phase (ice), and a number between 0 and 1 for averages over time and/or space. A number less than 0.5 indicates that liquid-phase clouds dominate; a value greater than 0.5 indicates that ice clouds dominate. The cloud particle effective radius for liquid droplets is the ratio of the third to second moments of the drop size distribution. In spring and summer clouds are increasingly in liquid phase. The effective radius has decreased over the Arctic seas except North Pole and the GIN Seas in spring. No significant trend in cloud optical depth was found in spring or summer. On an annual time scale, cloud particle effective radius has been decreasing mainly over the western part of the Arctic and Chukchi Sea. This agrees with tropospheric warming trends.

The influence of changes in cloud cover on sea-ice extent and vice versa is an important part of the Arctic climate feedback process, but has not been studied extensively until recently. On the time scale of a single season, changes in cloud amount may have a minimal influence on summer sea-ice melt, although there are clearly interdependencies between trends in cloud cover, surface temperature, and sea ice extent. Over the past few decades, more than 80% of the observed surface warming in the western Arctic Ocean during autumn is attributable to decreasing sea ice, and over 80% of the winter surface cooling in the central Arctic is a result of changes in cloud cover. In spring, only about half of the surface warming is a result of changes in cloud cover (Liu et al. 2009). Using satellite data, Liu et al. (2012) found that a 1% decrease in sea ice concentration leads to a 0.36–0.47% increase in cloud cover, and that 22–34% of the variance in cloud cover can be explained by changes in sea ice.

9.4 Surface Temperature and Albedo

Surface air temperature has been recorded at land-based and drifting ice meteorological stations for decades, and a long time series over the Arctic Ocean is available from Russian "North Pole" (NP) drifting stations, drifting ice buoys, and coastal station observations (Martin et al. 1997; Martin and Munoz 1997). While a valuable source of information, the in situ data do not provide spatial details that can be obtained from satellite data.

With satellite data, surface temperature is calculated with a split-window infrared algorithm using 11 and 12 μm brightness temperatures, similar in form to the traditional method used for sea surface temperatures (Key et al. 1997b). Over the annual cycle, the Arctic surface temperature varies most for the landmasses and least for the Arctic Ocean. Figure 9.8 shows the spatial distribution of the annual mean surface temperature. Central Greenland has the lowest surface temperature, as low as −30°C, and the Arctic Ocean and coastal areas are colder than the landmasses.

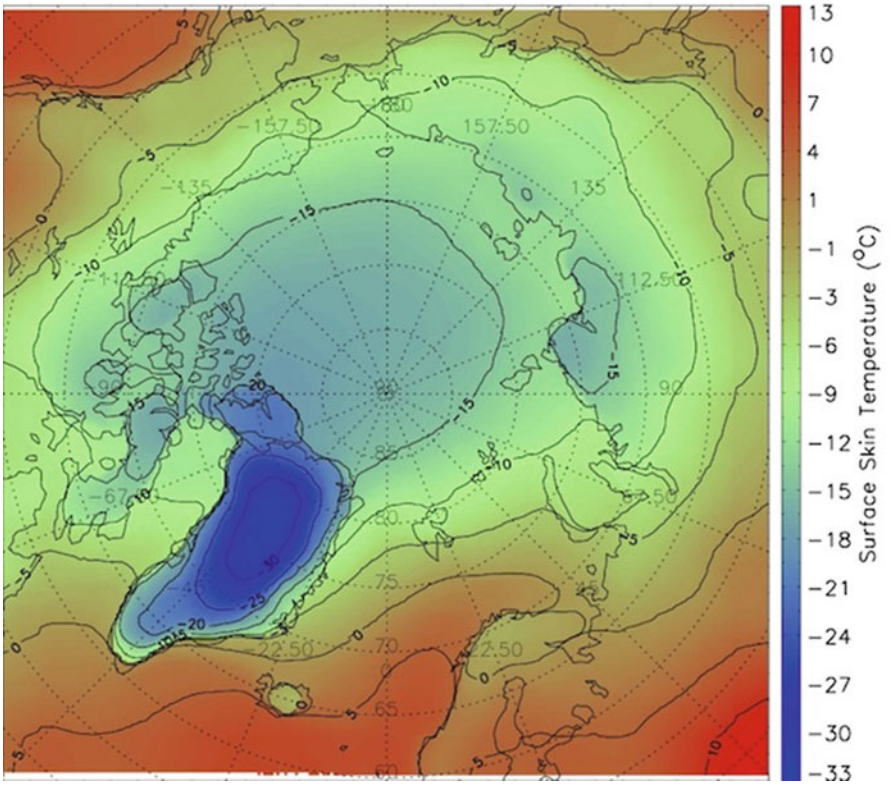

Fig. 9.8 Spatial distribution of annual mean surface skin temperature (°C) averaged over the period 1982–1999 on a local solar time of 14:00 (From Wang and Key 2005a)

In situ measurements of surface broadband albedo are sparse, particularly over the Arctic Ocean. Most studies report results for individual stations or as regional results (cf. Serreze et al. 1998). Satellite data therefore plays an important role in assessing the climatology of this parameter. Surface albedo retrieval uses visible and near-infrared reflectances and employs corrections for anisotropic reflectance and atmospheric effects. An anisotropic correction is performed for the top-of-atmosphere (TOA) reflectance (clear sky only), which is then converted from narrow band to broadband albedo. An atmospheric correction is then done to obtain the surface albedo, and an adjustment is done to account for cloud radiative effects in cloudy pixels (Key et al. 2001). Surface reflectance can be specified as "inherent" albedo or "apparent" albedo. The inherent albedo is the "true," no-atmosphere, or "black-sky" albedo of the surface, which is independent of the changes in the atmospheric conditions. The apparent albedo is what would be measured by up- and down-looking radiometers and varies with the atmospheric conditions.

There are two peaks in the annual cycle of the surface albedo for the Arctic region north of 60°N: one in the early spring (about 60%) and the other in autumn (about 35%). The relatively low wintertime albedo corresponds to the low-latitude regions with less snow/ice coverage, because the dark, high-latitude areas are excluded from the statistics. The autumn peak is due to freeze-up, but more open water areas in autumn result in a lower albedo than in spring. Over the Arctic Ocean, the spring maximum surface albedo is about 60%, but the autumn second maximum albedo is only about 23%. The Arctic annual mean surface albedo has a spatial distribution similar to surface temperature.

9.5 Radiative Fluxes and Cloud Forcing

Very few studies have been performed on the spatial and temporal distribution of surface radiation in the Arctic. Serreze et al. (1998) studied a monthly climatology of the global radiation (downwelling solar radiation) for the Arctic with measurements from the drifting ice stations, but these in situ measurements do not provide much information on spatial patterns. Can satellite data be used to estimate surface radiation fields? The approach is to use satellite-derived cloud and surface properties, with a radiative transfer model to calculate upwelling and downwelling shortwave and longwave radiative fluxes. Radiative transfer models tend to be too slow for use with satellite data on a pixel-by-pixel basis, so alternative methods are sought. One method that has been very successful is a neural-network implementation of a two-stream radiative transfer model (Key and Schweiger 1998), which is accurate and computationally efficient.

How well we can estimate the radiation budget from space depends on how well we can estimate the quantities that directly affect it. Key et al. (1997a) investigated uncertainties of satellite-derived surface and cloud properties and surface radiation budget at the high latitudes and how they combine into an overall uncertainty in radiative fluxes. They concluded that the accuracy in estimating radiation budgets from satellite is appropriate for a wide range of process studies at monthly time scales. They found that although improvements in retrievals are desirable, currently available methods can provide surface net radiation estimate with uncertainties similar to those of surface-based climatologies.

Clouds affect the climate system primarily through their impact on the surface and TOA radiation budgets. Clouds attenuate sunlight causing a decrease in the downwelling shortwave radiation at the surface during the daytime. Clouds also emit infrared radiation to the surface, resulting in a greater downwelling longwave flux than in clear conditions. Therefore, clouds have a cooling effect on the surface in the shortwave, but a warming effect in terms of infrared radiation. Overall the effect of clouds on the radiation budget depends on the balance between shortwave and longwave budgets. The cloud radiative effect is also commonly called “cloud

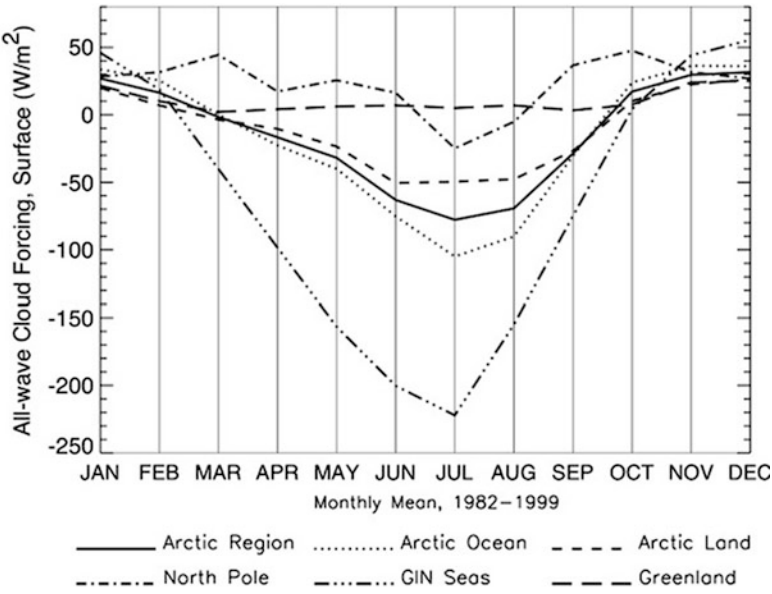

Fig. 9.9 Annual cycle of net all-wave cloud forcing for six Arctic regions averaged over the period 1982–1999 on a local solar time of 14:00

forcing." Cloud forcing is calculated from net shortwave and longwave radiative fluxes at the surface or TOA. It is defined as

$$\mathrm{CF}_{\lambda,z} = \int_0^{A_\mathrm{c}} \frac{\partial F_{\lambda,z}}{\partial a} \mathrm{d}a = F_{\lambda,z}(A_\mathrm{c}) - F_{\lambda,z}(0) \tag{9.1}$$

where $F_{\lambda,z}$ is the net flux (W/m^2) in shortwave or longwave radiation at the surface or TOA, λ is the wavelength, z is the altitude above the surface, and A_c is the cloud fraction in the scene. The net flux is equal to the downwelling minus upwelling fluxes. The all-wave cloud forcing can be calculated by

$$\mathrm{CF}_z = \mathrm{CF}_{\mathrm{shortwave}} + \mathrm{CF}_{\mathrm{longwave}} \tag{9.2}$$

Figure 9.9 shows the annual cycle of the shortwave, longwave, and all-wave cloud forcing at the surface. As discussed above, the shortwave cloud forcing is always negative, while the longwave cloud forcing is always positive and follows the annual cycle of cloud fraction. In the cold season (October–March), the all-wave cloud forcing is positive, implying a warming effect of the clouds on the surface. In the warm season (April–September), the all-wave cloud forcing is negative, indicating a cooling effect of the clouds on the surface. On annual average

clouds have a warming effect over Greenland and the North Pole area (north of 80°N). In winter, clouds have a warming effect on the surface almost everywhere over the Arctic region north of 60°N, but in summer the cloud warming effect only holds for Greenland and the western part of the central Arctic region as a result of the high surface albedo.

9.6 Sea Ice

The Arctic Ocean and surrounding seas occupy an area of about 14 million km^2, most of which are ice covered in late winter. The pack ice in the Arctic is a mixture of young and old floes that are highly variable in thickness and extent. Sea ice is a key component of the climate system for several reasons. It limits exchanges of heat and moisture between the ocean and the atmosphere. The large difference in reflectivity of ice and ocean results in more heat being absorbed by the ocean instead of being reflected back into the atmosphere. When ice extent declines, this ice-albedo feedback will amplify the effect of warming in high latitudes. The interannual fluctuations and long-term trends in ice thickness and extent have important effects not only on Arctic climate but also on global climate change through complex feedbacks.

Visible/IR satellite sensors can provide information on ice extent, concentration, motion, and melt, but coverage is limited due to frequent cloud cover. While AVHRR provides a long time series for recent climate studies, MODIS, operating since 1999, has more robust spectral information and higher spatial resolution. Dual-polarized, multifrequency passive microwave radiometers are more commonly used for ice studies than visible/IR imagers (Cavalieri et al. 1999; Drobot and Anderson 2001). They provide near-complete daily coverage of the polar regions under all sky conditions for characteristics such as concentration, extent, motion, and melt. These time series extend back to late 1978 from the Nimbus-7 Scanning Multichannel Microwave Radiometer (SMMR) through a series of Defense Meteorological Satellite Program (DMSP) Special Sensor Microwave/Imager (SSM/I) sensors, providing more than a quarter century record that can track interannual trends and variability.

For climate studies, however, caution must be exercised because the time series combine data from several different satellites and sensors. Slight variations in instrumentation and orbits necessitate inter-sensor calibration for a consistency. The derived ice characteristics are generally accurate in areas where the emissivity of sea ice is predictable and well defined (as in dry and relatively thick seasonal and perennial ice), but the errors can be considerable in newly formed ice and in areas of melt. Additionally, the spatial resolution of these products (10–25 km) is such that detailed information on the ice cover, such as deformation, melt-pond and lead formation, and ridging, cannot be obtained. Figure 9.10 shows the seasonal cycle of Arctic sea ice extent from passive microwave sensors for recent years with low ice extents.

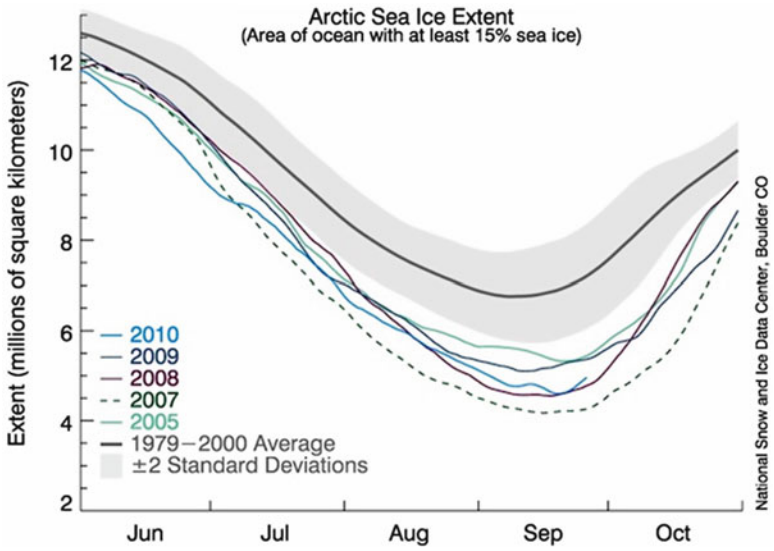

Fig. 9.10 Daily Arctic sea ice extent as of 26 September 2010, along with daily ice extents for years with the previous four lowest minimum extents. The *solid light blue line* indicates 2010, *solid dark blue* shows 2009, *pink* shows 2008, *dashed green* shows 2007, *light green* shows 2005, and *solid gray* indicates average extent from 1979 to 2000. The *gray area* around the average line shows the two standard deviation range of the data (Courtesy of the National Snow and Ice Data Center)

Newer passive microwave sensors, such as the Japanese Advanced Microwave Scanning Radiometer (AMSR), provide higher spatial resolution data and additional channels. The newest passive microwave technology is the polarimetric sensor, like the WindSat/Coriolis instrument. Synthetic aperture radar (SAR), an active microwave technology, provides detailed images of the ice cover at spatial resolutions as high as 30 m. The advent of SAR revolutionized the capabilities of the operational centers, allowing much higher quality analysis including information on lead location/orientation, ice type, and new ice formation. SAR instruments on ERS-1/2, Radarsat, Envisat, and Advanced Land Observing Satellite (ALOS) provide useful high-resolution information on deformation, leads, ridging, and new ice production (Fig. 9.11).

Scatterometry provides information on a spatial scale similar to that of passive microwave imagers but can provide better information on perennial ice cover as well complementary information on other properties due to different sensitivities to certain characteristics of the ice surface such as snow cover and melt. The ERS-1/2 and NASA (NSCAT) scatterometers launched in the early and mid-1990s, respectively, began the scientific application of routine scatterometer data to operational applications including sea ice. The SeaWinds instrument on the NASA QuikScat and the Japanese Advanced Earth Observing Satellite (ADEOS) have

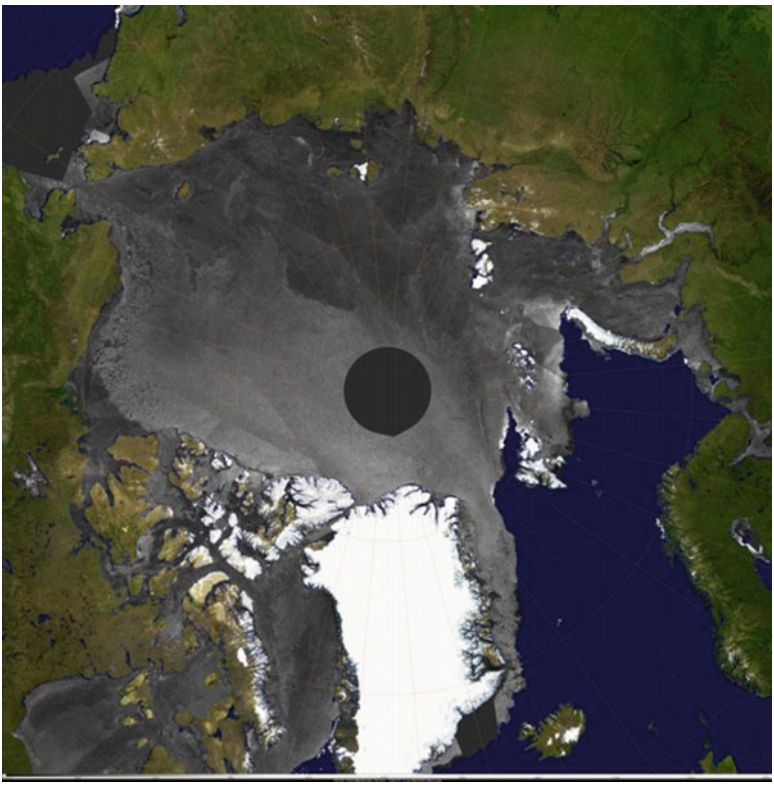

Fig. 9.11 Envisat ASAR and visible (MERIS) composite mosaic from 14 January 2006 (Courtesy of Microsoft Vexcel UK, ESA PolarView Consortium)

since provided routine polar Ku-band observations since 1999. MetOp-A, the first in a series of three satellites, ensures continuity in the C-band time series of advanced scatterometer (ASCAT) measurements for the next 15 years.

While ice extent is the most commonly examined sea ice variable, the most important is ice thickness. In situ, ship, submarine, and EM observations of thickness are limited spatially and temporally. Unfortunately, thickness is the most difficult ice property to estimate from space. The NASA ICESat satellite has a laser altimeter, though it recently failed, that can provide estimates of sea ice surface elevation. Laser altimeters are subject to cloud contamination, limiting the geographic coverage of useful surface data. Altimeters do not measure ice thickness directly, but rather they measure the elevation at the top of the surface, including the overlying snow cover. Accurate estimates of sea ice thickness therefore require some assumptions about snow depth and the relationship between ice draft (the part of the ice below the water level) to ice thickness. ICESat was designed primarily for ice sheet and glacier detection, not sea ice, and was originally to have flown in parallel with CryoSat, whose radar altimeter was optimized for sea ice. Unfortunately, CryoSat never

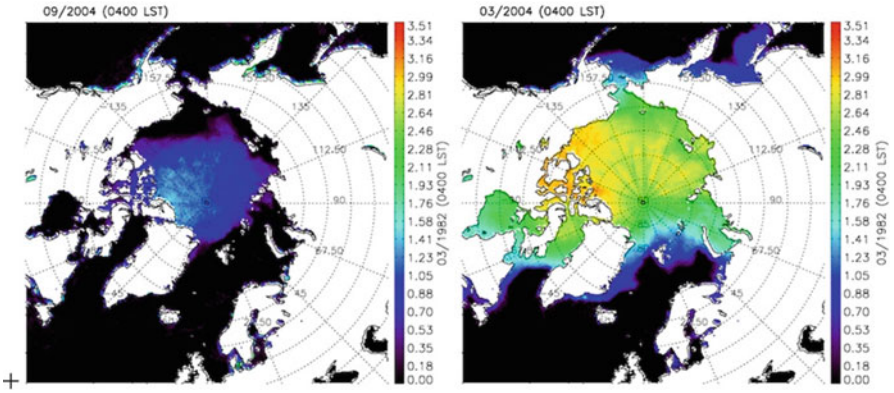

Fig. 9.12 September (*left*) and March (*right*) 2004 sea ice thickness (04:00 local solar time) estimated with the energy budget approach of Wang et al. (2010) using AVHRR data

reached orbit. Although ICESat may not be sensitive enough to obtain precise ice thickness estimates, it has made a significant step toward routine observation of ice thickness from space, with reasonable basin-wide thickness distribution fields having been produced during intervals of laser operation. CryoSat-2 is now operating well and provides valuable information on sea ice thickness. The combination of laser and radar altimeters can provide an estimate of snow depth on ice, because the radar signal generally comes from the snow-ice interface and the laser signal comes from the top of the snow cover.

Another approach to estimating ice thickness is to use satellite-derived cloud and surface properties with a surface energy budget model to solve for ice thickness. Wang et al. (2010) developed such a method (Fig. 9.12). It is currently being applied to the relatively long time series of AVHRR data for studies of recent trends.

Acknowledgements This work was supported by the National Oceanic and Atmospheric Administration (NOAA) Arctic Research Office, NASA, and the National Science Foundation. David Santek and Richard Dworak contributed to the research on polar winds. Walt Meier and Don Cline provided input on sea ice and snow cover, respectively. The views, opinions, and findings contained in this report are those of the author(s) and should not be construed as an official National Oceanic and Atmospheric Administration or US government position, policy, or decision.

References

ACIA (2005) Arctic climate impact assessment: impacts of a warming arctic. Cambridge University Press, Cambridge

AMAP (2011) Snow, water, ice, and permafrost in the Arctic (SWIPA): climate change and the cryosphere. Arctic Monitoring and Assessment Programme, Oslo, p 538

Cavalieri DJ, Parkinson CL, Gloersen P, Comiso JC, Zwally HJ (1999) Deriving long-term time series of sea ice cover from satellite passive-microwave multisensor data sets. J Geophys Res 104(7):15803–15814
Chapman WL, Walsh JE (1993) Recent variations of sea ice and air temperature in high latitudes. Bull Amer Meteor Soc 74(1):33–47
Curry JA, Ebert EE (1992) Annual cycle of radiative fluxes over the Arctic Ocean: sensitivity to cloud optical properties. J Climate 5:1267–1280
Curry JA, Rossow WB, Randall D, Schramm JL (1996) Overview of Arctic cloud and radiation characteristics. J Climate 9(8):1731–1764
Drobot S, Anderson M (2001) Snow melt onset over Arctic sea ice from SMMR and SSM/I Tbs. National Snow and Ice Data Center, Boulder, Digital Media
Dworak R, Key J (2009) 20 years of polar winds from AVHRR: validation and comparison to the ERA-40. J Appl Meteorol Clim 48(1):24–40
Fowler C, Maslanik J, Haran T, Scambos T, Key J, Emery W (2000) AVHRR polar pathfinder twice-daily 5 km EASE-grid composites. National Snow and Ice Data Center, Boulder, Digital media
Francis JA (2002) Validation of reanalysis upper-level winds in the Arctic with independent rawinsonde data. Geophys Res Lett 29:1315
Francis JA, Schweiger AJ (1999) The NASA TOVS Polar Pathfinder. 18 years of Arctic data. In: Proceedings of the fifth conference on polar meteorology and oceanography, American Meteorological Society, Dallas, 10–15 Jan 1999
Francis JA, Hunter E, Zou CZ (2005) Arctic tropospheric winds derived from TOVS satellite retrievals. J Climate 18:2270–2285
Frey R, Baum BA, Menzel WP, Ackerman SA, Moeller CC, Spinhirne JD (1999) A comparison of cloud top heights computed from airborne LIDAR and MAS radiance data using CO2-slicing. J Geophys Res 104(D20):24547–24555
Frey R, Ackerman S, Liu Y, Strabala K, Zhang H, Key J, Wang X (2008) Cloud detection with MODIS, part I: improvements in the MODIS cloud mask for collection 5. J Atmos Ocean Tech 25:1057–1072. doi:10.1175/2008JTECHA1052.1
Graversen RG, Wang M (2009) Polar amplification in a coupled climate model with locked albedo. Clim Dynam 33:629–643
Graversen RG, Mauritsen T, Tjernström M, Källen E, Svensson G (2008) Vertical structure of recent Arctic warming. Nature 451:53–57
Groves DG, Francis JA (2002) Variability of the Arctic atmosphere moisture budget from TOVS satellite data. J Geophys Res 107. doi:10.1029/2002/D002285
Hahn C (1995) The effect of moonlight on observation of cloud cover at night, and application to cloud climatology. J Climate 8:1429–1446
Kay JE, Gettelman A (2009) Cloud influence on and response to seasonal Arctic sea ice loss. J Geophys Res 114:D18204. doi:10.1029/2009JD011773
Key JR (2002) The cloud and surface parameter retrieval (CASPR) system for polar AVHRR. Cooperative Institute for Meteorological Satellite Studies, University of Wisconsin, Madison, p 59
Key J, Barry RG (1989) Cloud cover analysis with Arctic AVHRR, part 1: cloud detection. J Geophys Res 94(D15):18521–18535
Key J, Intrieri J (2000) Cloud particle phase determination with the AVHRR. J Appl Meteorol 36 (10):1797–1805
Key JR, Schweiger AJ (1998) Tools for atmospheric radiative transfer: streamer and FluxNet. Comput Geosci 24(5):443–451
Key J, Schweiger AJ, Stone RS (1997a) Expected uncertainty in satellite-derived estimates of the high-latitude surface radiation budget. J Geophys Res 102(C7):15837–15847
Key J, Collins J, Fowler C, Stone R (1997b) High-latitude surface temperature estimates from thermal satellite data. Remote Sens Environ 61:302–309
Key JR, Wang X, Stroeve JC, Fowler C (2001) Estimating the cloudy sky albedo of sea ice and snow from space. J Geophys Res 106(D12):12489–12497

Key J, Santek D, Velden CS, Bormann N, Thepaut J-N, Riishojgaard LP, Zhu Y, Menzel WP (2003) Cloud-drift and water vapor winds in the polar regions from MODIS. IEEE Trans Geosci Remote Sens 41(2):482–492

Liu Y, Key J, Wang X (2008) The influence of changes in cloud cover on recent surface temperature trends in the Arctic. J Climate 21:705–715. doi:10.1175/2007JCLI1681.1

Liu Y, Key J, Wang X (2009) Influence of changes in sea ice concentration and cloud cover on recent Arctic surface temperature trends. Geophys Research Lett 36:L20710. doi:10.1029/2009GL040708

Liu Y, Key JR, Liu Z, Wang X, Vavrus SJ (2012) A cloudier Arctic expected with diminishing sea ice. Geophys Res Lett 39:L05705, doi:10.1029/2012GL051251

Manabe S, Stouffer RJ (1994) Multiple-century response of a coupled ocean-atmosphere model to an increase of atmospheric carbon dioxide. J Climate 7(1):5–23

Manabe S, Spelman MJ, Stouffer RJ (1992) Transient response of a coupled ocean-atmosphere model to gradual changes of atmospheric CO2. Part II: seasonal response. J Climate 5 (2):105–126

Martin SE, Munoz E (1997) Properties of the Arctic 2-m air temperature for 1979-present derived from a new gridded data set. J Climate 10:1428–1440

Martin SE, Munoz E, Dreucker R (1997) Recent observations of a Spring-Summer warming over the Arctic Ocean. Geophys Res Lett 26:1259–1262

Meehl GA, Washington WM (1990) CO2 climate sensitivity and snow-sea-ice parameterization in an atmospheric GCM coupled to a mixed-layer ocean model. Climate Change 16:283–306

Meier W, Maslanik JA, Key JR, Fowler CW (1997) Multiparameter AVHRR derived products for Arctic climate studies. Earth Interactions, 1, paper no. 5 (electronic journal only)

Menzel WP, Smith WL, Stewart TR (1983) Improved cloud motion vector and altitude assignment using VAS. J Climate Appl Meteorol 22:377–384

Merrill R (1989) Advances in the automated production of wind estimates from geostationary satellite imaging. In: Proceedings fourth conference satellite meteorology, Amer. Meteorol. Soc., San Diego, 1989, pp 246–249

Miller JR, Russell GL (2000) Projected impact of climatic change on the freshwater and salt budgets of the Arctic Ocean by a GCM. Geophys Res Lett 27:1183–1186

Myneni RB, Keeling CD, Tucker CJ, Asrar G, Nemani RR (1997) Increased plant growth in the northern high latitudes from 1981 to 1991. Nature 386:698–702

Nieman SJ, Menzel WP, Hayden CM, Gray D, Wanzong ST, Velden CS, Daniels J (1997) Fully automated cloud-drift winds in NESDIS operations. Bull Am Meteorol Soc 78(6):1121–1133

Overland JE (2009) The case for global warming in the Arctic. In: Influence of climate change on the changing Arctic and Sub-Arctic conditions. Springer, Dordrecht, pp 13–23

Parkinson CL, Cavalieri DJ, Gloersen P, Zwally HJ, Comiso JC (1999) Arctic sea ice extents, areas, and trends, 1978-1996. J Geophys Res 104(C9):20837–20856

Perovich DK, Richter-Menge JA, Jones KF, Light B (2008) Sunlight, water, and ice: extreme Arctic sea ice melt during the summer of 2007. Geophys Res Lett 35:L11501. doi:10.1029/2008GL034007

Rao PA, Velden CS, Braun SA (2002) The vertical error characteristics of GOES-derived winds: description and experiments with numerical weather prediction. J Appl Meteorol 41(3):253–271

Rigor I, Colony RL, Martin S (2000) Variations in surface air temperature observations in the Arctic, 1979–97. J Climate 13:896–914

Rossow WB, Walker A, Beuschel D, Roiter M (1996) International satellite cloud climatology project (ISCCP) documentation of cloud data. World Climate Research Programme, NASA, Goddard Institute of Space Studies, p 115

Rothrock DA, Yu Y, Maykut GA (1999) Thinning of the Arctic sea-ice cover. Geophys Res Lett 26(23):3469–3472

Schmetz J, Holmlund K, Hoffman J, Strauss B, Mason B, Gaertner V, Koch A, van de Berg L (1993) Operational cloud motion winds from METEOSAT infrared images. J Appl Meteorol 32:1206–1225

Schweiger AJ, Lindsay RW, Key JR, Francis JA (1999) Arctic cloud in multiyear satellite data set. Geophys Res Lett 26(13):1845–1848

Serreze M et al (1998) A new monthly climatology of global radiation for the Arctic and comparisons with NCEP-NCAR reanalysis and ISCCP-C2 fields. J Climate 11:121–136

Serreze MC, Holland MM, Stroeve J (2007) Perspectives on the Arctic's shrinking sea-ice cover. Science 315:1533–1536. doi:10.1126/science.1139426

Shimada K (2006) Pacific ocean inflow: influence on catastrophic reduction of sea ice cover in the Arctic Ocean. Geophys ResLett 33:L08605. doi:10.1029/2005GL025624

Velden CS, Hayden CM, Nieman SJ, Menzel WP, Wanzong S, Goerss JS (1997) Upper-tropospheric winds derived from geostationary satellite water vapor observations. Bull Am Meteorol Soc 78(2):173–196

Velden CS, Olander TL, Wanzong S (1998) The impact of multispectral GOES-8 wind information on Atlantic tropical cyclone track forecasts in 1995. Part 1: dataset methodology, description and case analysis. Mon Weather Rev 126:1202–1218

Velden CS, Stettner D, Daniels J (2000) Wind vector fields derived from GOES rapid-scan imagery. In: Proceedings of the 10th conference on satellite meteorology, Long Beach, 9–14 Jan 2000, pp 20–23

Velden C, Daniels J, Settner D, Santek D, Key J, Dunion J, Holmlund K, Dengel G, Bresky W, Menzel P (2005) Recent innovations in deriving tropospheric winds from meteorological satellites. Bull Am Meteorol Soc 86:205–223

Vinnikov KY, Robock A, Stouffer RJ, Walsh JE, Parkinson CL, Cavalieri DJ, Mitchell JFB, Garrett D, Zakharov VF (1999) Global warming and northern hemisphere sea ice extent. Science 286:1934–1937

Wallace JM, Zhang Y, Bajuk L (1996) Interpretation of interdecadal trends in Northern Hemisphere surface air temperature. J Climate 9:249–259

Wang X, Key JR (2003) Recent trends in Arctic surface, cloud, and radiation properties from space. Science 299:1725–1728

Wang X, Key J (2005a) Arctic surface, cloud, and radiation properties based on the AVHRR Polar Pathfinder data set. Part I: spatial and temporal characteristics. J Climate 18(14):2558–2574

Wang X, Key J (2005b) Arctic surface, cloud, and radiation properties based on the AVHRR Polar Pathfinder data set. Part II: recent trends. J Climate 18(14):2575–2593

Wang X, Key J, Liu Y (2010) A thermodynamic model for estimating sea and lake ice thickness with optical satellite data. J Geophys Res Oceans 115:14

Zou CZ, Van Woert ML (2001) The role of conservation of mass in the satellite-derived poleward moisture transport over the Southern Ocean. J Climate 14:997–1015

Zou CZ, Van Woert ML (2002) Atmospheric wind retrievals from satellite soundings over the middle- and high-latitude oceans. Mon Weather Rev 130:1771–1791

Chapter 10
Assessing Hurricane Intensity Using Satellites

Mark DeMaria, John A. Knaff, and Raymond Zehr

Abstract Tropical cyclones spend most of their life cycle over the tropical and subtropical oceans. Because of the lack of in situ data in these regions, satellite observations are fundamental for tracking and estimating the intensity of these storms for real-time forecasting and monitoring climate trends. This chapter reviews methods for estimating tropical cyclone intensity from satellites, including those based on visible, infrared, and microwave instruments. Satellite intensity estimates are transitioning from subjective to objective methods, and new instruments on the next generation of NOAA low-earth orbiting and geostationary satellites hold promise for continued improvement in satellite analysis of tropical cyclones.

10.1 Introduction

The large loss of life and unprecedented damage caused by US landfalling hurricanes in the 2000s (Lili 2002; Isabel 2003, Charley, Frances, Ivan, Jeanne 2004; Dennis, Katrina, Wilma 2005; Ike 2008) raises the question of whether the Atlantic hurricane climate is changing. This question has considerable societal and economic implications for residents along the US gulf and east coasts and in other coastal regions around the globe. Emanuel (2007) showed a high correlation between decadal increases in Atlantic sea surface temperatures (SST) and an integrated measure of Atlantic basin tropical cyclone activity called the power dissipation index (PDI). This correlation suggests that the recent changes in hurricane activity may have a connection with global warming.

M. DeMaria (✉) • J.A. Knaff
RAMMB Branch, NOAA/NESDIS/Center for Satellite Applications and Research,
Fort Collins, CO, USA
e-mail: Mark.DeMaria@noaa.gov

R. Zehr
Colorado State University, Cooperative Institute for Research in the Atmosphere,
Fort Collins, CO 80523, USA

J.J. Qu et al. (eds.), *Satellite-based Applications on Climate Change*,
DOI 10.1007/978-94-007-5872-8_10,

The question of whether the hurricane climate is changing is complicated by two main factors, and recent observational and modeling studies have sometimes produced conflicting results (Knutson et al. 2010). First, tropical cyclone (TC) activity in the Atlantic (and other regions as well) undergoes significant natural variability on annual and multi-decadal time scales (Kossin et al. 2010). Second, the observing systems for measuring TC activity have varied extensively in the last century (Landsea et al. 2010). Before the mid-1940s, the primary source for TC information was ship reports. Aircraft reconnaissance became available in the mid-1940s, low-earth orbiting (LEO) satellites in the mid 1960s, and operational geostationary satellites in the 1970s. In addition, the instrumentation from aircraft reconnaissance has varied considerably, and this data was routinely available only for the Atlantic and western North Pacific through 1987. After 1987, west Pacific TC reconnaissance was discontinued. Thus, it is not always obvious whether long-term TC increases are physical or are due to improvements in the ability to monitor them.

Because TCs spend most of their lifetime over the tropical and subtropical oceans and the limited availability of in situ and aircraft observations, satellite data is fundamentally important for the analysis and forecasting of TCs. In fact, just a few years after the launch of the first meteorological satellite (TIROS-1) in 1960, methods began to be developed to estimate TC intensity from satellite imagery (Hubert and Timchalk 1969). These early attempts were not completely satisfactory, but about a decade later the very successful Dvorak method was developed (Dvorak 1975). In this chapter, the use of satellite data for estimating TC intensity is described. Satellite data also have many other TC applications, including position and structure analysis and atmosphere and ocean numerical forecast model initialization, but these topics are beyond the scope of this chapter. Accurate TC intensity estimation is important for both short-term forecasting and for monitoring changes in global TC activity.

This chapter begins with a description of the Dvorak intensity estimation technique, which is still a cornerstone of operational TC analysis around the globe. The intensity of a TC is quantified as the maximum sustained surface wind speed associated with the storm. Another indicator of TC intensity is the minimum sea-level pressure near its center. Newer methods that make use of passive microwave sensors are also presented. General methods for satellite wind estimation and their application to TCs are also briefly described. This chapter concludes with a summary of how forecasters combine TC information from many sources and a look toward future satellite capabilities.

10.2 The Dvorak Tropical Cyclone Intensity Estimation Method

The Dvorak technique estimates tropical cyclone intensity using satellite imagery. It was one of the first innovative applications of meteorological satellite imagery, and it is still widely used today at tropical cyclone forecast centers throughout the world (Velden et al. 2006). The Dvorak technique was developed in the early 1970s by Vernon Dvorak and his colleagues at NOAA NESDIS.

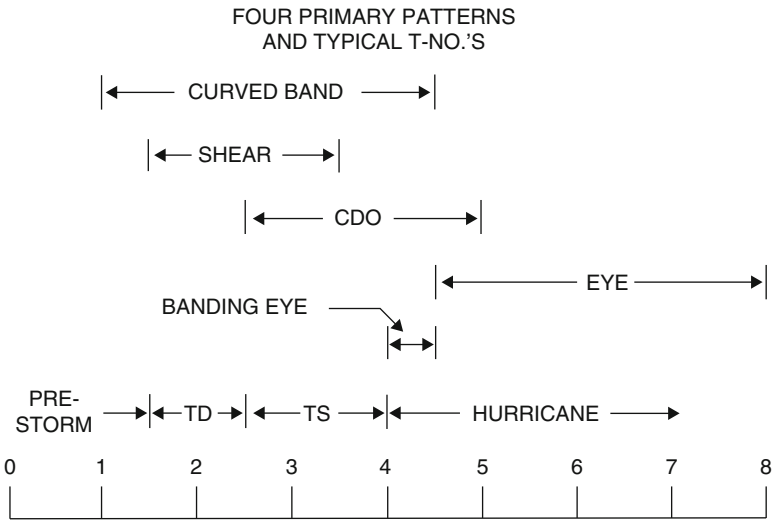

Fig. 10.1 The primary Dvorak cloud patterns in relation to T-number and tropical cyclone intensity ranges

10.2.1 Operational Dvorak Technique

The Dvorak technique (Dvorak 1984) primarily uses satellite observed cloud patterns and infrared (IR) cloud top temperatures to estimate intensity, with independent methods for visible and IR satellite imagery. It uses an intensity unit called a T-number in increments of ½ ranging from T1 to T8. The Dvorak T-number intensity scale is normalized according to typical observed daily changes in intensity (one T-number per day). T2.5 is the minimal tropical storm intensity (18.0 m/s), T4.0 is minimal hurricane intensity (33.4 m/s), T6.0 has a wind maximum of 59.1 m/s, and T8.0 approximates a record maximum intensity (87.4 m/s).

The cloud patterns in the Dvorak technique are divided into the four basic patterns in Fig. 10.1 (curved band, shear, central dense overcast, and eye), with a fifth sub-pattern called a banded eye. With weaker intensities, the analysis is usually based on either the curved band pattern or the shear pattern. Using the curved band analysis, the extent to which a spiral shaped band of deep convective clouds surrounds the tropical cyclone center determines the intensity. The shear pattern refers to the cloud pattern observed when broadscale vertical wind shear induces a distinctly asymmetric cloud pattern with respect to the tropical cyclone low-level circulation center. The degree of deep convective cloud displacement due to the vertical shear decreases with intensification.

As a TC intensifies, the cloud pattern typically evolves into what is called a central dense overcast (CDO), which describes the deep convective clouds that surround the center. As intensification continues, an eye is observed within this central dense overcast. The eye is the familiar cloud-free or cloud minimum area

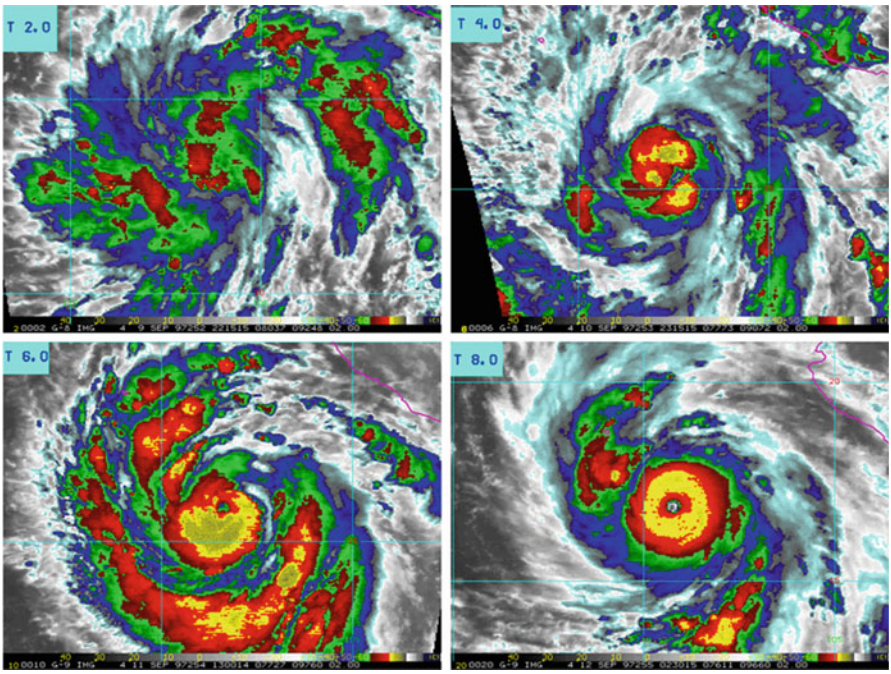

Fig. 10.2 Enhanced IR images of Hurricane Linda with Dvorak intensities T2, T4, T6, and T8. Hurricane Linda was located in the eastern North Pacific, southwest of Mexico, during 9–17 September 1997

associated with the lowest pressure at the tropical cyclone center. The eye is surrounded by a circular area which has the strongest winds within very deep clouds and heavy rain, known as the eyewall. The Dvorak technique analyzes visible features and IR temperatures of the eye and the surrounding deep clouds to assign the intensity. In general, the Dvorak tropical cyclone intensity increases as the eye gets warmer and better defined, and the surrounding clouds get colder and more symmetric. A continuous very cold circular ring of cloud tops generated by the eyewall along with a warm eye temperature indicates an intense tropical cyclone. Enhanced IR images of Dvorak intensities T2, T4, T6, and T8 are shown in Fig. 10.2 with Hurricane Linda that was located in the eastern North Pacific in September 1997.

An analysis of errors associated with Dvorak intensity estimates in comparison with the "best track" values is shown in Fig. 10.3. The best track is determined by the post-storm analysis of all available information, including aircraft intensity estimates, and is considered ground truth. Figure 10.3 shows that the Dvorak maximum wind estimates are normally accurate to within 5–10 kt but can sometimes be much larger. Knaff et al. (2010) performed a systematic analysis of the errors and biases of the Dvorak intensities. The results show that some of these biases are systematic and can be corrected, which would lead to further improvement of the operational Dvorak method.

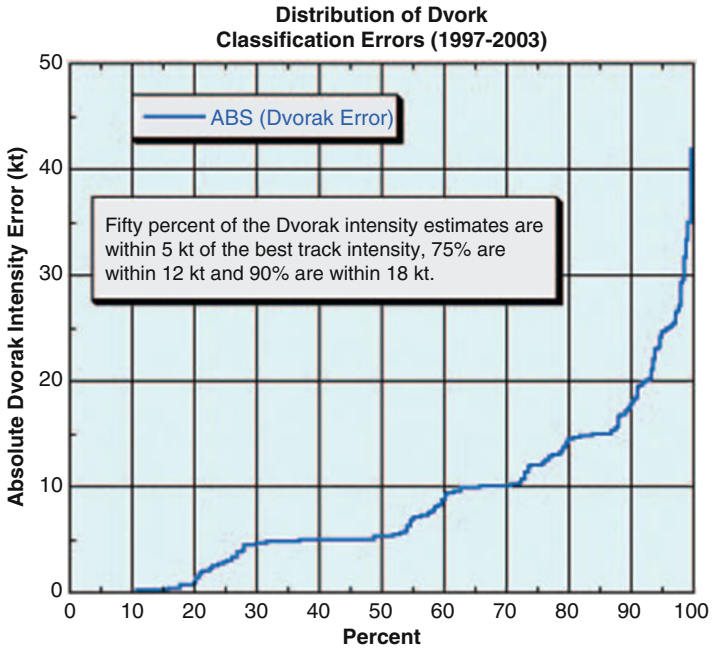

Fig. 10.3 Errors of the Dvorak tropical cyclone intensity estimation technique (From Velden et al. 2006)

10.2.2 Improved Objective Dvorak Approaches

Following Dvorak's original work, research and development efforts have been focused on replicating and refining the Dvorak approach with objective and automated routines using the IR temperatures (Velden et al. 2006). Automated Dvorak techniques give reliable results that are quickly updated as the latest IR satellite image becomes available, and the tropical cyclone intensity data supplement the general use of satellite data for analysis and forecasting.

Initial automated techniques were analogous to the operational Dvorak technique's enhanced IR (EIR) method (Dvorak 1984; Zehr 1989; Velden et al. 1998). The original goal of using computer-based objective methodology to achieve the accuracy of the operational Dvorak technique was accomplished, however, with important limitations. The automated routines could only be applied to storms at greater than minimal hurricane intensity. Also, a user-located storm center was needed. With continued research and development, the advanced objective Dvorak technique (AODT) emerged (Olander et al. 2004). The most recent version of the objective algorithm progression is the advanced Dvorak technique (ADT). Unlike the earlier techniques that attempt to mimic the operational technique, ADT is focused on revising and extending the method beyond the original application and constraints. The ADT is fully automated for real-time analysis and

continues to be improved (Olander and Velden 2007). Automated center finding algorithms are also under development (Wimmers and Velden 2010).

10.3 Satellite Microwave Intensity Estimation Techniques

In parallel with applications of visible and IR imagery such as the Dvorak technique, microwave observations from LEO satellites provided important observations of tropical cyclones in the 1970s and 1980s (Kidder et al. 2000). Microwave data have two main advantages over visible and IR images: (1) microwave radiation penetrates clouds; (2) Microwave radiation is sensitive to a wide variety of geophysical parameters, such as temperature, water vapor, cloud liquid water, cloud ice water, rain, and surface wind speed.

Microwave sensors can be divided into the two basic categories of imagers and sounders. Similar to IR and visible imagery, microwave imagery provides information about atmospheric and cloud properties due to the interaction with the upwelling radiation. Sounders measure microwave radiation in a range of frequencies centered about an atmospheric absorption band to provide vertical profiles of atmospheric moisture. TC intensity estimation techniques from microwave sounders have generally been more successful than those from microwave imagery. These are described first, followed by attempts to utilize microwave imagery.

10.3.1 Microwave Sounder Applications

The first operational microwave soundings were obtained from the microwave sounding unit (MSU) on TIROS-N, beginning in 1978, after successful demonstration on NIMBUS-5 earlier that decade. Shortly after this data became available, techniques to estimate TC intensity began to emerge (e.g., Kidder et al. 1978). An advantage of sounding methods compared to the Dvorak technique is that they have a firmer physical foundation. The minimum surface pressure near the center of a tropical cyclone is directly related to the vertical atmospheric temperature profile above that point through the hydrostatic equation. The minimum sea-level pressure has a strong relationship with the maximum surface wind through the horizontal momentum equations. To a reasonable level of approximation, these equations are diagnostic. For example, in the case of steady circular flow that occurs in strong tropical cyclones above the boundary layer, the wind and pressure field are related through the gradient wind equation.

A rather severe limitation of the early TC estimation techniques from the MSU was the 150-km footprint size of the measurements. This is much larger than the scale of the tropical cyclone eye, so the very warm temperatures in the eye cannot be resolved. This situation improved considerably beginning in 1998, when the advanced microwave sounding unit (AMSU) with its improved resolution began

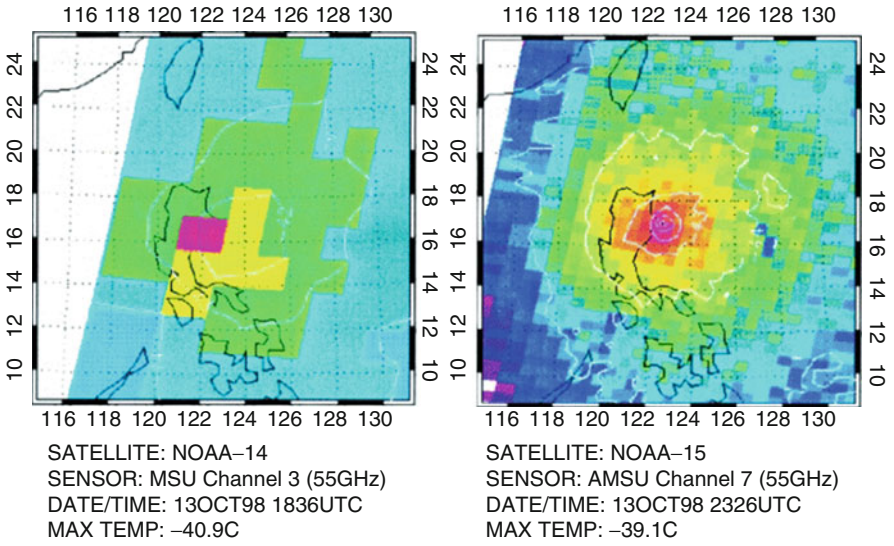

Fig. 10.4 An illustration of the improvement in spatial resolution of the AMSU over the MSU for Typhoon Zeb from the western North Pacific (From Kidder et al. 2000)

observing tropical cyclones. A comparison of the resolution of the MSU and AMSU is shown in Fig. 10.4 for Typhoon Zeb in the western North Pacific. The horizontal footprint of AMSU-A is about 50 km near nadir.

Observations and high-resolution modeling studies of tropical cyclones show that the warm core is a maximum near the storm center and the scale of the warm core increases with height due to the tendency for outward sloping eyewalls. Also, the strongest warm anomaly relative to that outside of the storm is a maximum in the middle and upper troposphere (e.g., Hawkins and Imbembo 1976; Stern and Nolan 2012). Based on this observed structure, two approaches have been taken to estimate TC intensity from AMSU. In the first approach, brightness temperatures from AMSU channels that sense the upper troposphere are used directly to estimate the warm core (Spencer and Braswell 2001; Brueske and Velden 2003). The characteristics of the warm core are then related to the TC intensity. In the second approach, temperature retrieval algorithms are applied using all of the AMSU-A channels to provide a three-dimensional temperature structure. Using an upper boundary condition from a large-scale analysis, the hydrostatic equation is integrated downward to provide the pressure field at each vertical level. The pressure gradient can then be calculated, and the wind field is determined from an appropriate approximation of the horizontal momentum equations. This method was applied by Demuth et al. (2004), assuming radially symmetric temperature and wind fields relative to the storm center, so that the gradient wind equation could be used. Figure 10.5 shows an example of the temperature anomaly and wind speed estimated by this technique. This figure shows that this retrieval method can also be used to provide information about the horizontal and vertical structure of a storm.

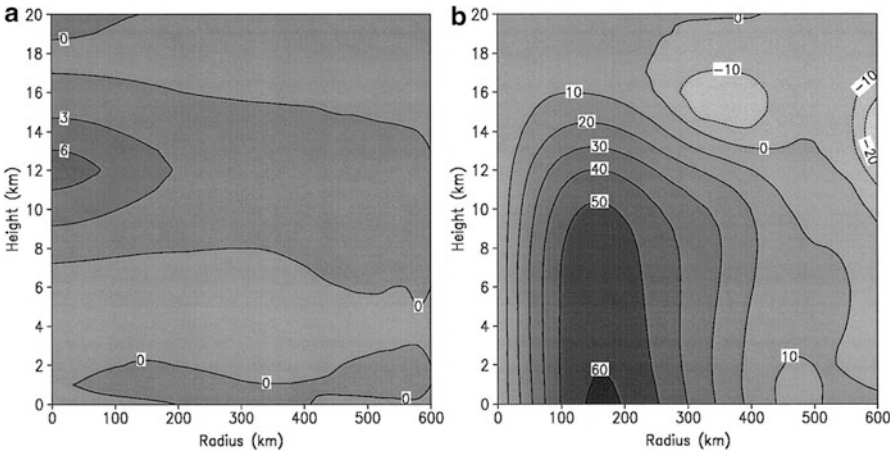

Fig. 10.5 Radial-height cross sections for Hurricane Gert on 16 Sept. 1999 of AMSU-retrieved (**a**) temperature anomalies (8 °C), showing the warm core at a height of approximately 12 km, and (**b**) gradient winds (kt), showing that the MSW occurs at approximately 175 km from the storm center (From Demuth et al. 2004)

Although the retrieved wind structure in Fig. 10.5 is qualitatively similar to a tropical cyclone with cyclonic tangential winds decreasing with height and a larger scale anticyclone at upper levels, the inner core is still not represented well. The low-level radius of maximum wind is about 175 km, which is much too large, and the retrieved maximum wind of about 60 kts is much lower than what was observed for Hurricane Gert at this time. To help correct for the lack of resolution, a statistical bias correction is applied to several parameters from the retrieved fields (Demuth et al. 2006) to improve the accuracy of the method. A scale correction is also applied to the AMSU retrieval method described by Brueske and Velden (2003). That algorithm also makes use of the AMSU-B moisture channels, which have a footprint size about 1/3 that of AMSU-A, to provide an eye-size estimate. The eye-size information is used to help correct for the low resolution of the AMSU-A channels. Both of the TC intensity estimation techniques described above have been used operationally by the National Hurricane Center and the Joint Typhoon Warning Center for the past several years. The average accuracy of the AMSU methods is not quite as good as the Dvorak method, especially for very small cyclones, but it provides an independent estimate of intensity.

10.3.2 Microwave Imagery Applications

Microwave imagery has been available from LEO satellite systems for the past few decades, including Special Sensor Microwave/Imager (SSMI), Special Sensor Microwave Imager Sounder (SSMIS), Tropical Rainfall Measuring Mission (TRMM)

Microwave Imager (TMI), and Advanced Microwave Scanning Radiometer-EOS (AMSR-E). As described above, channels from the AMSU-B sounder can also be used for imagery applications. The microwave imager instruments have much higher spatial resolution than the sounder data and provide detailed information about cloud and rain structure below the cloud top. Figure 10.6 shows an 85-GHz microwave image from SSMI for Hurricane Celia in the eastern North Pacific and the corresponding color-enhanced GOES IR (channel 4) image. The microwave imagery shows more clearly the cloud organization below the cirrus canopy in the IR image.

Despite the usefulness of microwave imagery for qualitative interpretation of tropical cyclone structure, a quantitative algorithm for intensity estimation with sufficient accuracy has yet to be developed. Bankert and Tag (2002) described a microwave imagery technique based on a nearest neighbor approach that could be fully automated. However, the average errors were about twice as large as those from the Dvorak technique. The use of microwave imagery for TC intensity estimation remains an area of active research.

10.4 Other Wind Estimation Techniques

Wind estimates from satellites have application to many phenomena in addition to tropical cyclones. Wind vectors can be estimated in the atmosphere by tracking features in subsequent images from geostationary satellites. This technique can also be applied at high latitudes with polar-orbiting imagery, since the temporal coverage from those satellites is much higher there (Dworak and Key 2009). Development of feature track wind algorithms began shortly after the availability of the first satellite observations, and improvements continue to be made (e.g., Velden and Bekda 2009).

Surface winds over the ocean can also be estimated from scatterometers on LEO satellites. These techniques are described in more detail in Chap. 8. The scatterometer winds have proved to be very useful for tropical cyclone intensity and structure analysis.

The AMSU retrieval technique described in Sect. 10.3 can be generalized to provide three-dimensional estimates of the horizontal wind. For that application, the gradient wind balance assumption is replaced by the more general nonlinear balance equation (Bessho et al. 2006). The three-dimensional AMSU winds are useful for TC structure analysis and are also being applied to other phenomena, including the atmospheric response to the Gulf Stream (O'Neill et al. 2010).

The three wind estimate techniques (feature track winds, scatterometer winds, and generalized AMSU retrievals) can all be used for tropical cyclone intensity estimation. However, low-level feature track winds are usually not available near the center of tropical cyclones due to the cirrus canopy. The scatterometer signal can attenuate at very high wind speeds, and there are some complications due to rain contamination and the footprint size. The generalized AMSU winds also have a limitation due to the instrument resolution. Thus, these techniques have application to TC intensity estimation, but generally can provide a lower bound estimate, and are used in combination with other information.

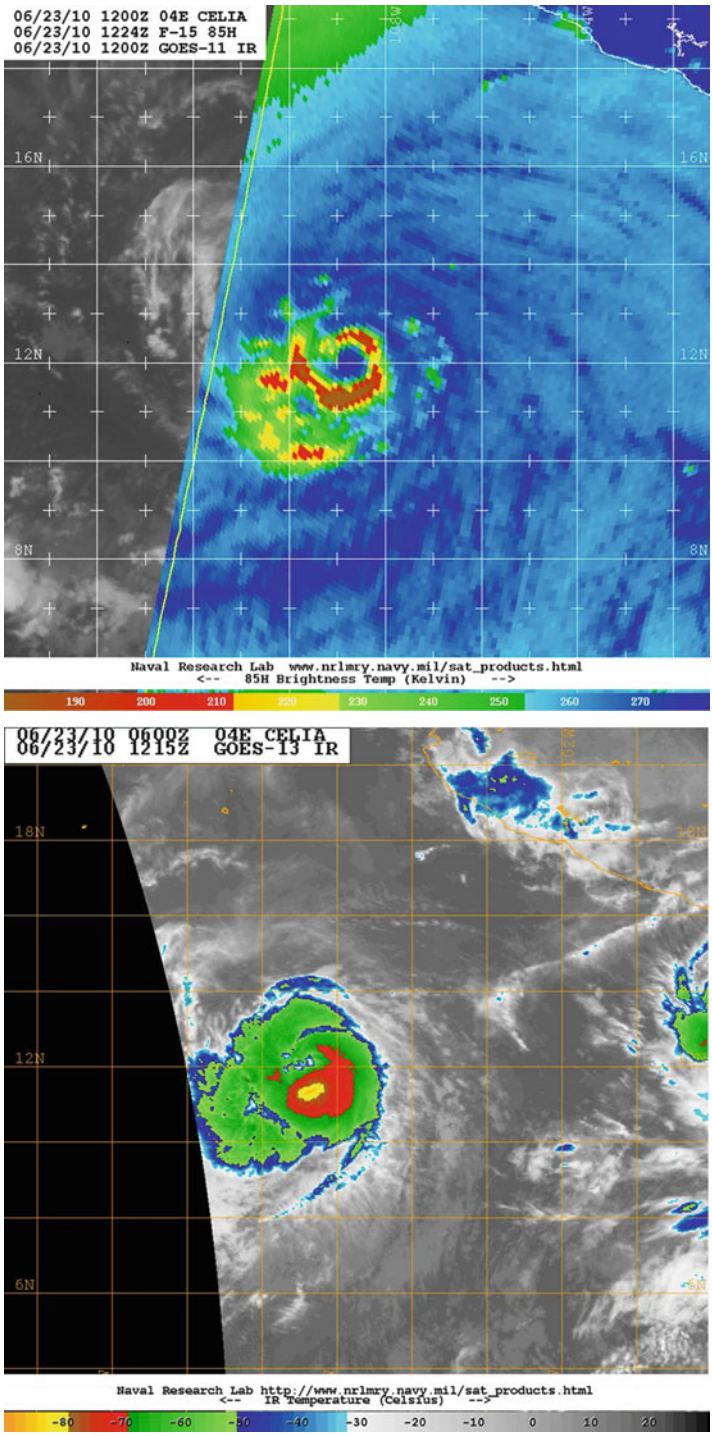

Fig. 10.6 85 GHz (*top*) and GOES channel 4 IR (*bottom*) image of Hurricane Celia at 12 UTC on 23 June 2010

10.5 Forecaster Applications

Hurricane forecasters and analysts assign intensity to tropical cyclones by using all available information. In addition to the satellite data, aircraft observations provide important intensity information, with more direct measurements of central pressure and maximum wind. At times, surface and ship observations also provide critical intensity data. Since the critical aircraft and surface data are not always available, but more directly measure the intensity, they are also needed for validation and refinement of the satellite intensity estimates.

Because each of the satellite TC intensity estimate techniques has their limitations, they are usually used in combination. The methods that use geostationary data have better temporal resolution and can be used to detect short-term trends. The methods that use LEO data are compared to the geostationary-based estimates when they are available, and forecasters make a subjective estimate of the TC intensity. Methods are also being developed to objectively combine satellite-based intensity estimates, using a satellite consensus (SATCON). These methods take advantage of the strengths and weaknesses of each method to provide an optimal TC intensity estimate (Herndon et al. 2010).

10.6 Future Outlook

The next decade should provide new opportunities for improving satellite-based intensity estimates. The next-generation GOES satellite beginning with GOES-R (expected launch date of late in 2015) will include an Advanced Baseline Imagery (ABI). The ABI will include 16 channels, with improved spatial, temporal, and radiometric resolution. The ABI has the potential to improve the existing Dvorak technique and lead to new methods that make better use of the multispectral imagery.

The next-generation NOAA polar-orbiting satellite will include an Advanced Technology Microwave Sounder (ATMS), which will have improved resolution when compared to the AMSU. As described in Sect. 11.3, the horizontal resolution of the AMSU is still coarse relative to the scale of the TC eye. The satellites will also include a hyperspectral IR sounder, which can be used in combination with the ATMS to provide more accurate temperature soundings. Although the IR sounding capabilities are primarily limited to clear regions, it may be possible to get accurate soundings in the eyes of storms with well-defined eyes. The ATMS and high spectral resolution Cross-track Infrared Sounder (CrIS) are now available on the recently launched Suomi National Polar-orbiting Partnerships (S-NPP), and preliminary results show great potential for utilizing this new data to improve the satellite estimates of tropical cyclone position, intensity, and structure.

References

Bankert RL, Tag PM (2002) An automated method to estimate tropical cyclone intensity using SSM/I imagery. J Appl Meteorol 41:461–472

Bessho K, DeMaria M, Knaff JA (2006) Tropical cyclone wind retrievals from the advanced microwave sounder unit (AMSU): Application to surface wind analysis. J Appl Meteorol 45:399–415

Brueske KF, Velden CS (2003) Satellite-based tropical cyclone intensity estimation using the NOAA–KLM series advanced microwave sounding unit (AMSU). Mon Weather Rev 131:687–697

Demuth JL, DeMaria M, Knaff JA, Vonder Haar TH (2004) Validation of an advanced microwave sounding unit tropical cyclone intensity and size estimation algorithm. J Appl Meteorol 43:282–296

Demuth JL, DeMaria M, Knaff JA (2006) Improvement of advanced microwave sounding unit tropical cyclone intensity and size estimation algorithms. J Appl Meteorol Climatol 45:1573–1581

Dvorak VF (1975) Tropical cyclone intensity analysis and forecasting from satellite imagery. Mon Weather Rev 103:420–430

Dvorak VF (1984) Tropical cyclone intensity analysis using satellite data. NOAA Tech. Rep. NESDIS11, p 47 [Available from NOAA/NESDIS, 5200 Auth Rd., Washington, DC 20233.]

Dworak R, Key JR (2009) Twenty years of polar winds from AVHRR: validation and comparison with ERA-40. J Appl Meteorol Climatol 48:24–40

Emanuel K (2007) Environmental factors affecting tropical cyclone power dissipation. J Climate 20:5497–5509

Hawkins HF, Imbembo SM (1976) The structure of a small, intense Hurricane—Inez 1966. Mon Weather Rev 104:418–442

Herndon DC, et al (2010) The CIMSS satellite consensus (SATCON) tropical cyclone intensity algorithm. 29th conf. on Hurricanes and Tropical Meteorology, Tuscon, Amer. Meteor. Soc., 4d.4. [Available online at http://ams.confex.com/ams/29Hurricanes/techprogram/paper_167959.htm.]

Hubert LF, Timchalk A (1969) Estimating hurricane wind speeds from satellite pictures. Mon Weather Rev 97:382–383

Kidder SQ, Gray WM, Vonder Haar TH (1978) Tropical cyclone outer surface winds derived from satellite microwave sounder data. Mon Weather Rev 108:144–152

Kidder SQ et al (2000) Satellite analysis of tropical cyclones using the advanced microwave sounding unit (AMSU). Bull Am Meteorol Soc 83:1241–1259

Knaff JA, Brown DP, Courtney J, Gallina GM, Beven JL II (2010) An evaluation of Dvorak technique–based tropical cyclone intensity estimates. Weather Forecast 25:1362–1379

Knutson TR, McBride J, Chan J, Emanuel KA, Holland G, Landsea C, Held IM, Kossin J, Srivastava AK, Sugi M (2010) Tropical cyclones and climate change. Nat Geosci 3(3):157–163

Kossin JP, Camargo SJ, Sitkowski M (2010) Climate modulation of North Atlantic hurricane tracks. Am Meteorol Soc J Clim 23:3057–3076

Landsea CW, Vecchi GA, Bengtsson L, Knutson TR (2010) Impact of duration thresholds on Atlantic tropical cyclone counts. J Climate 23:2508–2519

O'Neill LW, Chelton DB, Esbensen SK (2010) The effects of SST-induced surface wind speed and direction on gradients on mid-latitude surface vorticity and divergence. J Climate 23:255–281

Olander T, Velden CS (2007) The advanced Dvorak technique (ADT) – continued development of an objective scheme to estimate tropical cyclone intensity using geostationary infrared satellite imagery. Weather Forecast 22:287–298

Olander T, Velden CS, Kossin J (2004) The advanced objective Dvorak technique (AODT): latest upgrades and future directions. In: Proceedings 26th AMS hurricane and tropical meteorology conference, Miami, FL, Amer Meteor Soc P1.19

Spencer RW, Braswell WD (2001) Atlantic tropical cyclone monitoring with AMSU-a: estimation of maximum sustained wind speeds. Mon Weather Rev 129:1518–1532

Stern DP, Nolan DS (2012) On the height of the warm core in tropical cyclones. J Atmos Sci 69:1657–1680

Velden CS, Bekda KM (2009) Identifying the uncertainty in determining satellite-derived atmospheric motion vector height attribution. J Appl Meteorol Climatol 48:450–463

Velden CS, Olander TL, Zehr RM (1998) Development of an objective scheme to estimate tropical cyclone intensity from digital geostationary satellite infrared imagery. Weather Forecast 13:172–186

Velden CS et al (2006) The Dvorak tropical cyclone intensity estimation technique: a satellite-based method that has endured for over 30 years. Bull Am Meteorol Soc 87:1195–1210

Wimmers AJ, Velden CS (2010) Objectively determining the rotational center of tropical cyclones in passive microwave satellite imagery. J Appl Meteorol Climatol 49:2013–2034

Zehr R (1989) Improving objective satellite estimates of tropical cyclone intensity. Preprints, 18th conf. on Hurricanes and Tropical Meteorology, San Diego, Amer. Meteor. Soc., J25–J28

Chapter 11
Satellite-Based Ocean Surface Turbulent Fluxes

Long S. Chiu, Si Gao, and Chung-Lin Shie

Abstract Ocean surface turbulent fluxes of momentum, heat, and water vapor respond to and determine the coupling between the atmosphere and the ocean and are excellent indicators of air–sea interactions at most temporal and spatial scales. These fluxes can be determined from bulk properties at the sea surface. By combining satellite observations of bulk properties such as sea surface temperature, wind, and humidity, estimates of these fluxes are available globally. The bulk aerodynamic formulations of these fluxes are first reviewed. Satellite retrieval techniques of these bulk properties and operational or semi-operational ocean surface flux products such as the Hamburg Ocean Atmosphere Parameters and Fluxes from Satellite Observations (HOAPS), the Japanese Oceanic Fluxes with the Use of Remote Observations (J-OFURO), and the US NASA Goddard Space Flight Center Satellite-Based Sea Surface Turbulent Fluxes (GSSTF), as well as merged approach of the Objectively Analyzed Air–Sea Fluxes for the global ocean (OAFlux) are described, and their error and uncertainties are briefly discussed.

Keywords Bulk formulae • Momentum • Heat and latent heat flues • Air–sea interactions • HOAPS • J-OFURO • GSSTF • OAFlux

L.S. Chiu (✉) • S. Gao
Department of Atmospheric, Oceanic and Atmospheric Sciences,
College of Science, George Mason University, Fairfax, VA 22030, USA
e-mail: lchiu@gmu.edu; sgao2@gmu.edu

C.-L. Shie
Joint Center for Earth Systems Technology, University of Maryland,
Baltimore County, Baltimore, MD 21228, USA

Code 612.0, Mesoscale Atmospheric Processes Laboratory,
NASA/Goddard Space Flight Center, Greenbelt, MD 20771, USA
e-mail: chung-lin.shie-1@nasa.gov

J.J. Qu et al. (eds.), *Satellite-based Applications on Climate Change*,
DOI 10.1007/978-94-007-5872-8_11,

11.1 Introduction

The Earth's climate is shaped by a myriad of interacting processes between components of the Earth system – the atmosphere, hydrosphere, lithosphere, biosphere, and anthrosphere. Among the interacting processes are the energy cycle, water cycle, and other biogeochemical cycles. Covering 70% of the Earth's surface and containing 96% of the global freshwater, the ocean is the major storage of water substances. The radiant energy falling on the sea surface is mostly offset by the flux of longwave radiation emanating from the sea surface and the fluxes of sensible heat and latent heat. Oceanic evaporation is the dominant mass flux in the global water cycle. The condensational heat release during the process of cloud formation is a major driving force for atmospheric motions. With its huge storage and heat capacity, the ocean has a significant role in shaping the climate of the Earth system and its variability.

Estimates of these air–sea fluxes have been based on marine surface observations (Bunker 1976; Hastenrath 1980; Weare et al. 1981; Esbensen and Reynolds 1981; Isemer and Hasse 1985, 1987; Hsiung 1985; Oberhuber 1988; Cayan 1992; da Silva et al. 1994; Josey et al. 1998). A major limitation of these estimates is the inadequate sampling. Historically, measurements are collected by Ships of Opportunity. The advent of satellite observations provided global ocean coverage, reducing the uncertainty in these air–sea flux measurements.

In Sect. 11.2, we discuss the transfer mechanisms occurring at the air–sea interface and present the bulk formulae for estimating the flux transfers. Bulk parameters from satellite observations are introduced in Sect. 11.3. Section 11.4 describes various research or operational products that integrate the bulk parameters to produce surface flux products. An assessment of these products is presented in Sect. 11.5. Finally, Sect. 11.6 contains a summary and outlook for the use of these products in climate research and operational applications.

11.2 Transfer at the Air–Sea Interface

The sea surface is the interface between the atmosphere and the ocean through which the exchange of radiant energy, momentum, heat, and moisture occurs. Atmospheric motion keeps the sea surface in motion, making the flux exchange through a nonsteady material surface. The fluxes are defined relative to a predefined fixed level above the average sea surface. The atmospheric boundary layer is typically 1 km to a few km in height. The atmospheric boundary layer can be divided into a constant flux sub-layer and a transition layer to the free atmosphere. The constant flux sub-layer is typically 10–100 m thick or 10–20% of the boundary layer height, in which the flux values do not deviate more than ~10% from their mean. Right at the surface is the viscous sub-layer, typically <1 cm thick, in which molecular processes dominate. Through the boundary layer, the surface communicates with the free atmosphere by the transfer of buoyancy and momentum through the constant flux sub-layer and by entrainment from above the

transition layer (Lykossov 2001). A detail discussion of the atmospheric and oceanic boundary layer is in Kraus and Businger (1994).

In bulk aerodynamic formulation, the turbulent transfer of momentum (or surface stress, τ), sensible heat flux (SHF), and latent heat flux (LHF) at the air–sea interface can be written as

$$\tau = \rho C_{\mathrm{D}} |(U - U_{\mathrm{s}})| (U - U_{\mathrm{s}}) \tag{11.1a}$$

$$\mathrm{SHF} = \rho C_{\mathrm{p}} C_{\mathrm{H}} (U - U_{\mathrm{s}})(T_{\mathrm{s}} - T_{\mathrm{a}}) \tag{11.1b}$$

$$\mathrm{LHF} = \rho L_{\mathrm{v}} C_{\mathrm{E}} (U - U_{\mathrm{s}})(Q_{\mathrm{s}} - Q_{\mathrm{a}}) \tag{11.1c}$$

where ρ is air density; C_{p} the specific heat at constant pressure; L_v the latent heat of vaporization; C_{D}, C_{H}, and C_{E} are, respectively, the bulk transfer coefficients for momentum, sensible heat, and latent heat; U is the air velocity; and U_{s} is ocean surface current. Surface stress is a vector and has a magnitude of the square of the wind difference $|(U - U_{\mathrm{s}})|^2$ in the direction of $(U - U_{\mathrm{s}})$. $|(U - U_{\mathrm{s}})|$ is the absolute value of the difference of surface wind and ocean surface current.

The surface wind U is typically a few to tens of m s^{-1} and $U_{\mathrm{s}} \sim$ cm s^{-1}; hence, in most cases the assumption $(U - U_{\mathrm{s}}) \approx U$ is made.

With input parameters such as wind speed (U), the sea surface temperature (T_{s}), the air potential temperature (T_{a}), the air specific humidity (Q_{a}) at the reference height, and the saturation specific humidity (Q_{s}) which is determined by T_{s} through the Clausius–Clapeyron relation, the fluxes can be calculated with the appropriate transfer coefficients.

Based on similarity theory, the surface fluxes in Eqs. (11.1a, 11.1b, 11.1c) can also be derived from scale analysis with scaling parameters for wind or friction velocity (u^*), temperature (θ^*), and humidity (q^*) defined as

$$\tau = \rho u^{*2} \tag{11.2a}$$

$$\mathrm{SHF} = -\rho C_{\mathrm{p}} u^* \theta^* \tag{11.2b}$$

$$\mathrm{LHF} = -\rho L_{\mathrm{v}} u^* q^* \tag{11.2c}$$

For a given surface skin temperature θ_{s} (or SKT) and wind, temperature, and humidity at a measurement or reference heights within the atmospheric surface layer, the scaling parameters are solved through the roughness lengths z_0 and dimensionless gradients of wind, temperature, and humidity. The dimensionless gradients of wind, potential temperature, and humidity are functions of the stability parameter z/L, where z is the measurement height and L is the Monin–Obukhov length, $L = -u^{*3}/\kappa\, B_0$, where κ is the von Karman constant $\kappa \sim 0.4$ and B_0 is the buoyancy, $B_0 = g\, w'\rho'$, where g is the gravitational acceleration and w' and ρ' are the fluctuations of vertical velocity and density, and is defined as positive for stable and negative for unstable boundary layers (see Garratt 1992; Chou et al. 2003). The transfer coefficients of momentum, heat, and moisture flux are therefore

functions of the vertical gradient of wind speed, temperature, and moisture near the surface and are affected by the stability of the surface air. The atmosphere is mostly under near neutral or stable conditions, and most of the retrieval techniques use drag coefficients under neutral conditions, in lack of atmospheric stability information. The expressions of the coefficients for stable and unstable boundary layer can be found elsewhere (Garratt 1992).

Similarity theory predicted that under low wind conditions the transfer coefficients of sensible and moisture increase with increasing wind speed, because the increased roughness facilitates the transfer of heat and vapor (Liu et al. 1979). Field and laboratory measurements suggested that the drag coefficient (C_D) flattens or decreases with high wind speed near 22–23 m s^{-1} (Black et al. 2007) or at 33 m s^{-1} (Powell et al. 2003; Donelan et al. 2004). Observations also suggest that the transfer coefficient for water vapor, or the Dalton number, C_E is constant with wind speed up to hurricane-force winds of 33 m s^{-1} (Black et al. 2007).

11.3 Satellite Estimation of Input Parameters

11.3.1 Wind Stress

Winds are measured using active and passive microwave sensors. A scatterometer is an active microwave sensor. It operates by sending a pulse of electromagnetic energy and measures the backscatter signal from the sea surface at different azimuth angles. The return signal is a function of the sea surface roughness, the azimuth angle relative to the surface wind, and the earth's incidence angle. Surface roughness is a response of the ocean surface to wind forcing resulting in capillary wave generation. Weather prediction model provides ancillary information about the wind direction to give both the direction and the magnitude of the stress (Atlas et al. 2011). Scatterometers can provide global near-surface (at 10-m height) wind speed and direction retrievals. It should be emphasized that scatterometers measure surface roughness and hence are measuring the stress ($U - U_s$) and not the actual atmospheric wind. In the absence of information about the atmospheric stability, the derived geophysical product is the wind under neutral conditions (Liu et al. 2010).

Seasat is the first satellite mission for ocean monitoring. It carries the first spaceborne scatterometer – the Seasat-A Scatterometer System (SASS) (Born et al. 1981). Although the mission lasted for only 3 months, it collected a unique set of synoptic data on ocean winds, waves, temperature, and topography and served as a proof of concept to follow-on missions that include the Advanced Microwave Instrument (AMI) on Earth Resource Satellite 1 and 2 (ERS-1 and ERS-2), NASA Scatterometer (NSCAT) on Advanced Earth Observing Satellite (ADEOS), SeaWinds on Quick Scatterometer (QuikSCAT), SeaWinds on Advanced Earth Observing Satellite 2 (ADEOS-2), and Advanced Scatterometer (ASCAT). These instruments provide almost all-weather wind speed and direction information except in heavily raining conditions (Freilich and Dunbar 1999; Draper

and Long 2004; Weissman et al. 2002) or proximity to coastal areas (~15 km for QuikSCAT and 30 km for ASCAT). The data typically have in-swath spatial resolution of 25 km, and some product for hurricane studies has ultrahigh resolution of 2.5 km (Williams and Long 2008). Because of the narrow satellite swath and orbit, temporal sampling is rather limited. Synthetic Aperture Radars (SARs) are able to provide wave spectrum from kilometer to capillary wave scales, hence wind field monitoring capability (Beal et al. 2005). Use of multiple scatterometers can greatly improve the temporal sampling and directional measurements and help fill in the data gaps in rainy conditions.

Passive microwave radiometers measure electromagnetic radiation from the ocean surface at several frequencies and routinely provide global near-surface wind speed estimates over rain-free ocean at a spatial resolution of roughly 25 km. Wind measuring microwave sensors include the Scanning Multichannel Microwave Radiometer (SMMR) onboard the NIMBUS-7 satellite, the Special Sensor Microwave Imager (SSM/I) and the Special Sensor Microwave Imager/Sounder (SSMIS) onboard the Defense Meteorological Satellite Program (DMSP), the Tropical Rainfall Measuring Mission (TRMM) Microwave Imager (TMI), and the Advanced Microwave Scanning Radiometer – Earth Observing System (AMSR-E). Retrieval algorithms of wind speed include the traditional D-matrix (Lo 1983), regression (Goodberlet et al. 1989; Goodberlet and Swift 1992), neural network (Krasnopolsky et al. 1995), and physical approaches (Wentz et al. 1986). Resolution of the ambiguity in wind direction (Wentz 1992) requires polarization measurements at $\pm 45^{\circ}$ in addition to the horizontal and vertical polarizations (Dzura et al. 1992; Gasiewski and Kunkee 1993), or the use of variational analysis methods (Atlas et al. 1991). These wind retrievals are quite accurate under typical ocean conditions (Mears et al. 2001; Meissner et al. 2001), and there are good agreements between passive radiometer winds and scatterometer winds (Wentz et al. 2007).

11.3.2 Sea Surface Temperature

Skin sea surface temperature (SST), which is the temperature at the interface between the ocean and the atmosphere, should be used to compute LHF and SHF (Curry et al. 2004). Skin (~10–20 μm) or subskin (~1–2 mm) SSTs determined from satellites include estimates from infrared and passive microwave radiometry. Both types of observations have their own strengths and weaknesses. Infrared SST measurements have good spatial resolution (1–10 km), radiometric accuracy (0.2–0.8 K) (Donlon et al. 2007), and long heritage (~30 years). However, they require atmospheric correction and fail over cloudy situations, under which a lot of interesting meteorological phenomena occur, such as over a hurricane. Infrared instruments for deriving SST include the Advanced Very High-Resolution Radiometer (AVHRR), the Advanced Along-Track Scanning Radiometer (AATSR), the Geostationary Operational Environmental Satellite (GOES) Imager, and the Moderate Resolution Imaging Spectroradiometer (MODIS) (see Sun 2011). Passive microwave sensors can measure SST through clouds with lower accuracy (0.5–1 K) and resolution

(25–50 km). Passive microwave instruments for SST retrievals include SMMR, TMI, and AMSR-E. SST observations have been greatly improved by combination of multiple infrared and microwave sensors (Donlon et al. 2007).

11.3.3 Surface-Air Temperature and Humidity

Determining T_a and Q_a from satellites is difficult and remains challenging. Satellite sounders such as the Atmospheric Infrared Sounder (AIRS) and the Advanced Microwave Sounding Unit (AMSU) provide profiles of air temperature and humidity, but do not adequately resolve the boundary layer. Microwave sensor channels are mostly sensitive to the total precipitable water (W) or water vapor within a thin layer, typically 500 m, close to the sea surface (WB) (e.g., Liu 1986; Schulz et al. 1993).

Climatologically, there is a strong relationship between the total columnar precipitable water and the surface-air humidity (Liu 1986). This relationship is based on the strong coupling and feedbacks between the surface and the atmosphere above the boundary layer. However, for mesoscale systems, such as fronts and cold air outbreaks, this relation is inadequate for describing the surface property using columnar measurements. Application of the climatological relationship to SSM/I data produced large spatial bias in LHF estimates (Esbensen et al. 1993; Schlussel et al. 1995; Schulz et al. 1997). Schulz et al. (1993), Schlussel et al. (1995), and Bentamy et al. (2003) improved Q_a retrieval by establishing a relationship between Q_a and WB which is estimated from SSM/I. Chou et al. (1995) classified sounding data observed during the First Global Atmospheric Research Program (GARP) Global Experiment (FGGE) and found that the first two Empirical Orthogonal Functions (EOFs) of the vertical moisture profile can explain most of the variance. By solving two simultaneous equations involving the W and WB, Q_a is estimated. This technique incorporates additional information about the vertical structure of the atmosphere that has not been considered in previous retrievals.

Early methods (e.g., Liu 1988; Kubota and Shikauchi 1995) determined T_a from satellite observations by using a specified value of relative humidity (usually 80%) with a known Q_a via the Clausius–Clapeyron relationship. The spatial and temporal variations of relative humidity are as yet relatively unexplored. Subsequent studies by Jourdan and Gautier (1995) and Konda et al. (1996) used additional variables such as W, SST, and wind speed to estimate T_a. More recent improvement of Q_a and T_a estimates involves the use of robust techniques such as artificial neural networks (Jones et al. 1999; Roberts et al. 2010) and genetic algorithms (Singh et al. 2005, 2006), or from a combination of multisensor observations (Jackson et al. 2006, 2009; Jackson and Wick 2010).

11.4 Satellite-Based Flux Data Sets

By employing the suite of input parameters, satellite-based turbulent fluxes can be calculated using bulk parameters derived from satellite observations. Widely used products include the Hamburg Ocean Atmosphere Parameters and Fluxes from Satellite Data (HOAPS), the Japanese Ocean Flux Data Sets with Use of Remote Sensing Observations (J-OFURO), and the Goddard Satellite-Based Surface Turbulent Fluxes (GSSTF). These products are discussed below.

11.4.1 HOAPS

HOAPS is produced by University of Hamburg and Max Planck Institute for Meteorology in Germany. The most recent version is version 3 (HOAPS-3, Andersson et al. 2010). All variables are derived from SSM/I data except for AVHRR Oceans Pathfinder SST product. A neural network algorithm is used to derive U. Q_a is obtained using the linear relationship of Bentamy et al. (2003). Q_s is computed from the AVHRR SST using the Magnus formula (Murray 1967) with a constant salinity correction factor of 0.98. T_a is estimated from the SST with the assumptions of 80% constant relative humidity and a constant surface-air temperature difference of 1 K. Latent and sensible heat fluxes are calculated using the Coupled Ocean–Atmosphere Response Experiment (COARE) 2.6a bulk algorithm (Fairall et al. 1996, 2003).

The HOAPS-3 data sets cover the time period from July 1987 to December 2005. HOAPS-G pentad and monthly data sets with 0.5° resolution and HOAPS-C twice daily data set with 1° resolution are available at the website (http://www.hoaps.zmaw.de).

11.4.2 J-OFURO

J-OFURO is produced by the School of Marine Science and Technology at Tokai University in Japan. The most recent version 2 of J-OFURO (J-OFURO2, Tomita et al. 2010) determines U, Q_a, and SST (Q_s) from multisatellite and sensor observations. U is obtained from a combination of microwave radiometers (SSM/I, AMSR-E, and TMI) and scatterometers (ERS-1, ERS-2, and QuikSCAT). Q_a is derived from SSM/I measurements. SST is taken from the Merged satellite and in situ data Global Daily SST (MGDSST) analysis provided by Japanese Meteorological Agency (JMA). T_a is obtained from NCEP/DOE reanalysis. COARE 3.0 bulk algorithm (Fairall et al. 2003) is used for the transfer coefficients to estimate LHF and SHF.

The J-OFURO2 turbulent heat fluxes cover the time period from January 1988 to December 2006. Daily and monthly means with 1° resolution are available at the website (http://dtsv.scc.u-tokai.ac.jp/j-ofuro).

11.4.3 GSSTF

GSSTF is produced by NASA's Goddard Space Flight Center. The latest version 2c or (GSSTF2c) was released in November 2011. In the prior version 2b (GSSTF2b), Q_a is derived from SSM/I V6 total columnar precipitable water and bottom-layer precipitable water as described in Chou et al. (1995, 1997). U is obtained from SSM/I V6 retrievals. T_a and SST are taken from NCEP/DOE reanalysis. Chou et al. (2003) bulk algorithm is used to calculate turbulent flux. The GSSFT2b turbulent fluxes cover the time period from July 1987 to December 2008. Daily and monthly data sets with 1° resolution are available via the anonymous FTP (ftp://measures.gsfc.nasa.gov/data/s4pa/GSSTF/) through the Goddard Earth Sciences Data and Information Services Center (GES DISC). There are two sets of GSSTF2b data: sets 1 and 2 (Shie et al. 2010; Shie 2010). Set 1 was found to show a spurious increasing global LHF, especially after 2000. Noting the large trends in set 1, set 2 is produced by removing satellite products that have a relatively larger trend in LHF. The satellites not included in set 2 are the DMSP F13 and F15 SSM/Is. Analyses of LHF showed linear trends of 23.1 and 15% over the period 1987–2008, with the surface sea–air humidity difference ($Q_s - Q_a$) accounting for 20 and 12.3%, for set 1 and set 2, respectively, and wind change contributing to 3.1% for both sets (Chiu et al. 2012). Hilburn and Shie (2011) noted a drift in the Earth incidence angle (EIA), and a correction algorithm which incorporates the satellites' attitude has been developed to account for the drift in EIA. The EIA is the angle between the line of sight of the satellite sensor and the zenith at the Earth's surface. This correction has been applied to the SSM/I brightness temperature (T_b), and the latest version, GSSTF2c (Shie et al. 2011; Shie 2011), is now available from the same GES DISC anonymous FTP. The EIA corrected T_b's in GSSTF2c has reduced the trends, especially in the latent heat flux (Shie and Hilburn 2011; Shie 2011).

11.4.4 Combined Approach

Surface turbulent fluxes can also be derived from global model results that are constrained by surface and rawinsonde observations and satellite measurements. Such products are called reanalyses, which include NCEP's older reanalysis (NCEP/NCAR and NCEP/DOE) and the latest Climate Forecast System Reanalysis (CFSR), ECMWF's 40-year reanalysis (ERA-40) and interim reanalysis (ERA–Interim), JMA's Japanese 25-year ReAnalysis (JRA-25), and the most recent NASA GMAO's Modern Era Retrospective Analysis for Research and Applications (MERRA).

The Woods Hole Oceanographic Institution produced the Objectively Analyzed Air–Sea Fluxes (OAFlux) by combining bulk variables derived from satellites and those from reanalysis (Yu et al. 2008). Satellite inputs include U from SSM/I, AMSR-E, and QuikSCAT; SST from NOAA OI analysis by Reynolds et al. (2007);

and 10-m Q_a derived from SSM/I using Chou et al. (1995, 1997) technique which is adjusted to the height of 2 m based on COARE 3.0 algorithm. All bulk variables are also from NCEP/NCAR, NCEP/DOE, and ERA-40. The optimal fields of such variables obtained by an advanced objective analysis approach (Yu and Weller 2007) are then employed to compute LHF and SHF using COARE 3.0 algorithm. One-degree daily mean (1985 onward) and monthly mean (1958 onward) data are available at their website (http://oaflux.whoi.edu/).

11.5 Error Estimates and Uncertainties

Figures 11.1, 11.2, and 11.3 show examples of the seasonal variations of the stress, sensible heat, and latent heat flux estimates. These seasonal climatologies are computed from GSSTF2b set 1. Comparisons of the climatology, nonseasonal variations, and trends of HOAPS, J-OFURO, and GSSTF2 are described elsewhere (Chiu et al. 2008, 2012).

Certainly there are biases and uncertainties in surface turbulent flux products. The flux biases can be classified into sampling errors, errors in the input bulk variables, and

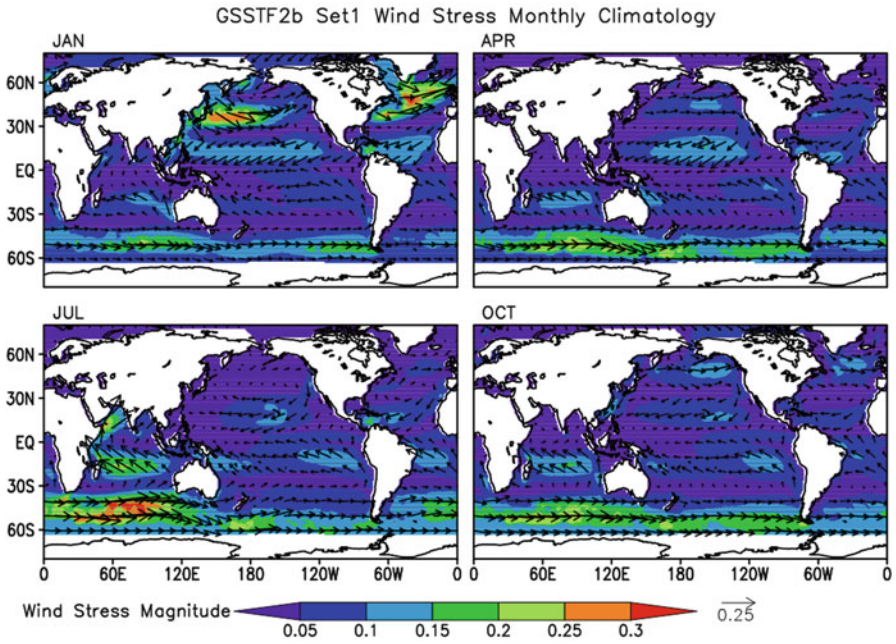

Fig. 11.1 Wind stress climatology for January, April, July, and October from GSSTF2b set 1 (1998–2008). Unit: N m^{-2}

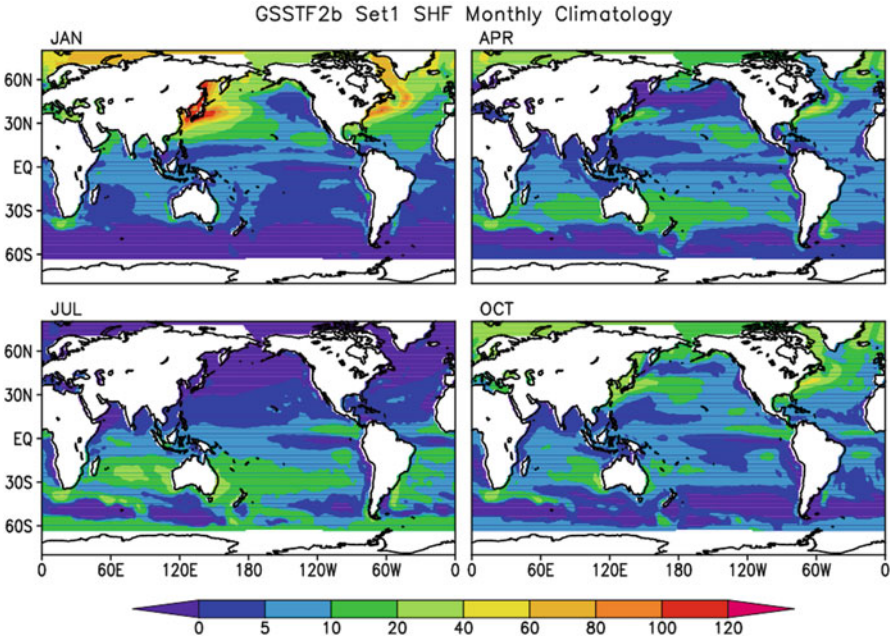

Fig. 11.2 Same as Fig. 11.1 except for surface sensible heat flux. Units: W m^{-2}

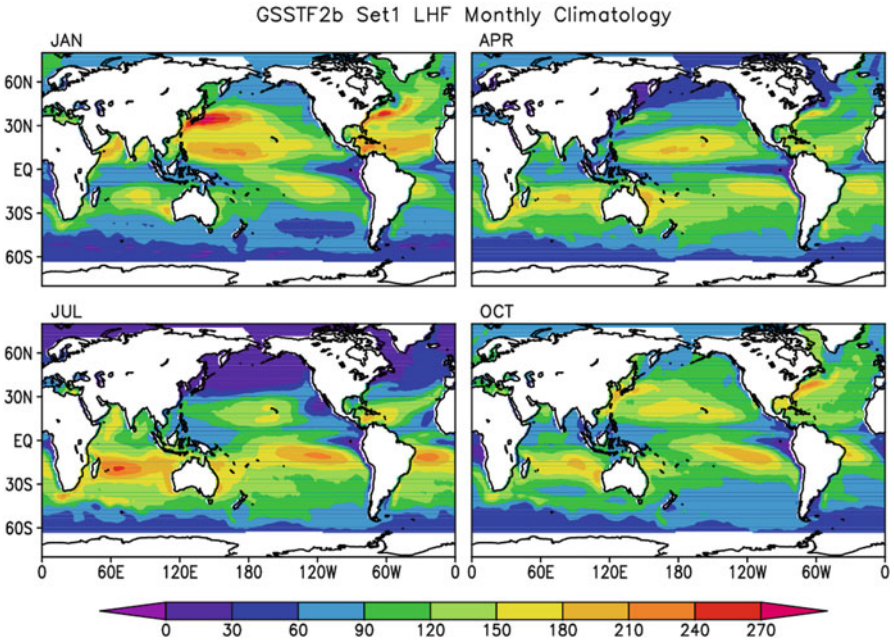

Fig. 11.3 Same as Fig. 11.1 except for surface latent heat flux. Units: W m^{-2}

the algorithm error (Zeng et al. 1998; Brunke et al. 2002, 2003). Brunke et al. (2011) evaluate six reanalysis (MERRA, ERA-40, ERA–Interim, NCEP/NCAR, NCEP/DOE, and CFSR), four satellite-based flux products (GSSTF2, GSSTF2b, J-OFURO2, and HOAPS), and the merged product (OAFlux) by comparison with direct covariance LHF and SHF and inertial-dissipation wind stress measurements from cruises over the tropics and mid- and high latitudes. The biases range from -3.0 to 20.2 W m^{-2} for LHF, -1.4 to 6.0 W m^{-2} for SHF, and -7.6 to 7.9 $\times$ 10^{-3} N m^{-2} for wind stress. The ranges of the biases are small for moderate wind speeds but diverge for strong wind speeds (10–20 m s^{-1}). The bulk variable-caused uncertainty dominates SHF and wind stress biases of many products. MERRA is found to be the "best performing" among all three reanalysis-based fluxes. Of the satellite-based products, GSSTF2b is among "best performing" for LHF and SHF.

11.6 Summary and Outlook

Satellite-based ocean surface turbulent flux products have been improved in recent years with better understanding of the mechanisms of air–sea exchange leading to improved bulk flux algorithms. The improved algorithms are complemented by more accurate satellite retrievals of input meteorological and oceanic variables. Discrepancies among these products are mostly due to different input variables. "Trends" in these products have been noted (Chiu et al. 2008) and can mostly be attributed to satellite attitude and inter-satellite calibrations. More accurate satellite attitude calculations (Hilburn and Shie 2011) and efforts to recalibrate all SSM/I satellites, such as the development of the "fundamental climate data record" by NOAA (Kummerow 2009), will lead to more homogeneous microwave data sets that will be applicable for climate studies.

Accurate turbulent air–sea flux estimates are crucial for advancing our understanding of the dynamics of air–sea interactions at the mesoscale to global scale. Assessment of the trends and variabilities will help quantify the relative role of the atmosphere and ocean in global change. At the basin and regional scales, LHF has shown to impact monsoons and hurricanes (Gautam et al. 2005; Gao and Chiu 2010), and the inclusion of LHF derived from the OAFlux merged products has a significant impact on the prediction of typhoon intensity (Gao and Chiu 2012). The major limitations of satellite-based flux products for tropical cyclone studies are their relatively coarse spatial and temporal resolution or limited coverage. High-resolution (0.25°) ocean surface turbulent flux data sets aimed at the regional to hurricane scales have been or are being produced (Shie et al. 2009; Liu et al. 2011). From these new data sets, improved understanding of the dynamics of air–sea interactions at global to regional scales will emerge, and their impact on operational applications and climate studies will soon be realized.

Abbreviations

AATSR	Advanced Along-Track Scanning Radiometer
ADEOS	Advanced Earth Observing Satellite
ADEOS-2	Advanced Earth Observing Satellite 2
AIRS	Atmospheric Infrared Sounder
AMSR-E	Advanced Microwave Scanning Radiometer-Earth Observing System
AMSU	Advanced Microwave Sounding Unit
ASCAT	Advanced Scatterometer
AVHRR	Advanced Very High Resolution Radiometer
CFSR	Climate Forecast System Reanalysis
COARE	Coupled Ocean–Atmosphere Response Experiment
DMSP	Defense Meteorological Satellite Program
DOE	Department of Energy
ECMWF	European Centre for Medium-Range Weather Forecasts
EIA	Earth incidence angle
ERA-40	European Centre for Medium-Range Weather Forecasts' 40-year reanalysis
ERS-1	Earth Resource Satellite 1
ERS-2	Earth Resource Satellite 2
FGGE	First Global Atmospheric Research Program Global Experiment
GARP	Global Atmospheric Research Experiment
GES	DISC Goddard Earth Sciences Data and Information Services Center
GOES	Geostationary Operational Environmental Satellite
GSSTF	Goddard Space Flight Center Satellite-based Sea surface Turbulent Fluxes
HOAPS	Hamburg Ocean Atmosphere Parameters and fluxes from Satellite observations
JMA	Japanese Meteorological Agency
J-OFURO	Japanese Oceanic Fluxes with the Use of Remote Observations
JRA-25	Japanese 25-year ReAnalysis
LHF	Latent heat flux
MERRA	Modern Era Retrospective Analysis for Research and Applications
MGDSST	Merged satellite and in-situ data Global Daily SST
MODIS	Moderate Resolution Imaging Spectroradiometer
NASA	National Aeronautics and Space Administration
NCAR	National Center for Atmospheric Research
NCEP	National Centers for Environmental Prediction
NSCAT	NASA Scatterometer
OAFlux	Objectively Analyzed Air-sea Fluxes
QuikSCAT	Quick Scatterometer
SAR	Synthetic Aperture Radars
SASS	Seasat-A Scatterometer System
SHF	Sensible heat flux

SMMR	Scanning Multichannel Microwave Radiometer
SSM/I	Special Sensor Microwave Imager
SSMIS	Special Sensor Microwave Imager/Sounder
SST	Sea surface temperature
TMI	Tropical Rainfall Measuring Mission Microwave Imager
TRMM	Tropical Rainfall Measuring Mission

Acknowledgments
This study is supported by the MEaSUREs Program of NASA Science Mission Directorate – Earth Science Division.

References

Andersson A, Fennig K, Klepp C, Bakan S, Graßl H, Schulz J (2010) The Hamburg ocean atmosphere parameters and fluxes from satellite data – HOAPS-3. Earth Syst Sci Data 2:215–234

Atlas R, Bloom SC, Hoffman RN, Ardizzone JV, Brin G (1991) Space-based surface wind vectors to aid understanding of air-sea interactions. EOS, Trans Am Geophys Union 72:201–208

Atlas RM, Hoffman RN, Ardizzone J et al (2011) A cross-calibrated, multi-platform ocean surface wind velocity product for meteorological and oceanographic applications. Bull Am Meteorol Soc 92:157–174

Beal RC, Young G, Monaldo F, Thompson DR, Winstead N.S, Scott CA (2005) High resolution wind monitoring with wide swath SAR: a user's guide, Department of Commerce, NOAA, NESDIS and Office of Research and Applications, Washington D.C.

Bentamy A, Katsaros KB, Mestas-Nuñez AM, Drennan WM, Forder EB, Roquet H (2003) Satellite estimates of wind speed and latent heat flux over the global oceans. J Climate 16:637–656

Black PG, D'Asaro EA, Drennan WM, French JR, Niiler PP, Sanford TB, Terrill EJ, Walsh EJ, Zhang JA (2007) Air-sea exchanges in hurricanes. Bull Am Meteorol Soc 88:357–374

Born GH, Lame DB, Rygh PJ (1981) A survey of the goals and accomplishments of the seasat mission. In: Gower JFR (ed) Oceanography from space. Plenum Press, New York

Brunke MA, Zeng X, Anderson S (2002) Uncertainties in sea surface turbulent flux algorithms and data sets. J Geophys Res 107:3141. doi:10.1029/2001JC00092

Brunke MA, Fairall CW, Zeng X, Eymard L, Curry JA (2003) Which bulk aerodynamic algorithms are least problematic in computing ocean surface turbulent fluxes? J Climate 16:619–635

Brunke MA, Wang Z, Zeng X, Bosilovich M, Shie C-L (2011) An assessment of the uncertainties in ocean surface turbulent fluxes in 11 reanalysis, satellite-derived, and combined global data sets. J Climate 24:469–5493

Bunker AF (1976) Computation of surface energy flux and annual air-sea interaction cycle of the North Atlantic Ocean. Mon Weather Rev 104:1122–1140

Cayan DR (1992) Latent and sensible heat flux anomalies over the northern oceans: the connection to monthly atmospheric circulation. J Climate 5:354–369

Chiu LS, Chokngamwong R, Xing Y, Yang R, Shie C-L (2008) Trends and variations of global oceanic evaporation datasets from remote sensing. Acta Oceanol Sin 27:124–135

Chiu LS, Gao S, Shie C-L (2012) Oceanic evaporation: variability and trends. In: Escalante-Ramirez B (ed) Remote sensing – applications. InTech, Rijeka

Chou S-H, Atlas RM, Shie C-L, Ardizzone J (1995) Estimates of surface humidity and latent heat fluxes over oceans from SSM/I data. Mon Weather Rev 123:2405–2425
Chou S-H, Shie C-L, Atlas RM, Ardizzone J (1997) Air–sea fluxes retrieved from special sensor microwave imager data. J Geophys Res 102:12705–12726
Chou S-H, Nelkin E, Ardizzone J, Atlas RM, Shie C-L (2003) Surface turbulent heat and momentum fluxes over global oceans based on the Goddard satellite retrievals, version 2 (GSSTF2). J Climate 16:3256–3273
Curry JA et al (2004) SEAFLUX. Bull Am Meteorol Soc 85:409–424
da Silva AM, Young CC, Levitus S (1994) Atlas of surface marine data, vol 3, Anomalies of heat and momentum fluxes. NOAA/NESDIS, Washington, D.C
Donelan MA, Haus BK, Reul N, Plant WJ, Stiassnie M, Graber HC, Brown OB, Saltzman ES (2004) On the limiting aerodynamic roughness of the ocean in very strong winds. Geophys Res Lett 31:L18306. doi:10.1029/2004GL019460
Donlon C et al (2007) The global ocean data assimilation project experiment high resolution sea surface temperature pilot project. Bull Am Meteorol Soc 88:1197–1213
Draper DW, Long DG (2004) Evaluating the effect of rain on SeaWinds scatterometer measurements. J Geophys Res 109:C02005. doi:10.1029/2002JC001741
Dzura MS, Etkin VS, Khrupin AS, Paspelov MN, Raev MD (1992) Radiometers-polarimeters: principles of design and applications for sea surface microwave emission polarimetry. In; Proceedings of the IGARSS 92 conference, Houston, 1992, IEEE Press, Piscataway
Esbensen SK, Reynolds RW (1981) Estimating monthly averaged air-sea transfer of heat and momentum using the bulk aerodynamic method. J Phys Oceanogr 11:457–465
Esbensen SK, Chelton DB, Vockers D, Sun J (1993) An analysis of errors in spatial sensor microwave imager evaporation estimates over the global oceans. J Geophys Res 98:7081–7101
Fairall CW, Bradley EF, Rogers DP, Edson JB, Young GS (1996) Bulk parameterization of air-sea fluxes for tropical ocean-global atmosphere coupled-ocean atmosphere response experiment. J Geophys Res 101:3747–3764
Fairall CW, Bradley EF, Hare JE, Grachev AA, Edson JB (2003) Bulk parameterization of air-sea fluxes: updates and verification for the COARE algorithm. J Climate 16:571–591
Freilich MH, Dunbar RS (1999) The accuracy of the NSCAT-1 vector winds: comparisons with NDBC buoys. J Geophys Res 104:11231–11246
Gao S, Chiu LS (2010) Surface latent heat flux associated with rapidly intensifying tropical cyclone. Int J Remote Sens 31:4699–4710
Gao S, Chiu LS (2012) Development of statistical typhoon intensity prediction: application to satellite observed rain rate and surface evaporation (STIPER). Weather Forecast 27:240–250
Garratt JR (1992) The atmospheric boundary layer. Cambridge University Press, Cambridge
Gasiewski AJ, Kunkee DB (1993) Calibration and application of polarization-correlating radiometers. IEEE Trans Microw Theory Tech 41(5):767–772
Gautam R, Cervone G, Singh RP, Kafatos M (2005) Characteristics of meteorological parameters associated with hurricane Isabel. Geophys Res Lett 32:L04801. doi:10.1029/2004GL021559
Goodberlet MA, Swift CT (1992) Improved retrievals from the DMSP wind speed algorithm under adverse weather conditions. IEEE Trans Geosci Remote Sens 30:1076–1077
Goodberlet MA, Swift CT, Wilkerson JC (1989) Remotes sensing of ocean surface wind with the special sensor microwave imager. J Geophys Res 94:14547–14555
Hastenrath S (1980) Heat budget of tropical ocean and atmosphere. J Phys Oceanogr 10:159–170
Hilburn KA, Shie C-L (2011) Decadal trends and variability in Special Sensor Microwave Imager (SSM/I) brightness temperatures and Earth incidence angle. Report no. 092811, Remote sensing systems, Santa Rosa
Hsiung J (1985) Estimates of global oceanic meridional heat transport. J Phys Oceanogr 15:1405–1413
Isemer H-J, Hasse L (1985) The bunker climate atlas of the north Atlantic ocean, vol 1, Observations. Springer, Heidelberg/New York/Tokyo

Isemer H-J, Hasse L (1987) The bunker climate atlas of the north Atlantic ocean, vol 2, Air-sea interactions. Springer, Heidelberg/New York/Tokyo

Jackson DL, Wick GA (2010) Near-surface air temperature retrieval derived from AMSU-A and sea surface temperature observations. J Atmos Oceanic Tech 27:1769–1776

Jackson DL, Wick GA, Bates JJ (2006) Near-surface retrieval of air temperature and specific humidity using multi-sensor microwave satellite observations. J Geophys Res 111:D10306. doi:10.1029/2005JD006431

Jackson DL, Wick GA, Robertson FR (2009) Improved multi-sensor approach to satellite retrieved near-surface specific humidity observations. J Geophys Res 114:D16303. doi:10.1029/2008JD011341

Jones C, Peterson P, Gautier C (1999) A new method for deriving ocean surface specific humidity and air temperature: an artificial neural network. J Appl Meteorol 38:1229–1245

Josey SA, Kent EC, Taylor PK (1998) The Southampton Oceanography Centre (SOC) ocean–atmosphere heat, momentum and freshwater flux atlas. Southampton Oceanography Centre, Report no. 6, Southampton

Jourdan D, Gautier C (1995) Comparison between global latent heat flux computed from multisensor (SSM/I and AVHRR) and from in situ data. J Atmos Oceanic Tech 12:46–72

Konda M, Imasato N, Shibata A (1996) A new method to determine near-sea surface air temperature by using satellite data. J Geophys Res 101:14349–14360

Krasnopolsky V, Breaker LC, Gemmeill WH (1995) A neural network as a non-linear transfer function model for retrieving surface wind speeds from the special sensor microwave/imager. J Geophy Res 100:11033–11045

Kraus EB, Businger JA (1994) Atmosphere–ocean interaction. Oxford University Press, New York

Kubota M, Shikauchi A (1995) Air temperature at ocean surface derived from surface-level humidity. J Oceanogr 51:619–634

Kummerow C (2009) Development of A fundamental climate data record for SSM/I, SSMIS and future microwave sensors, NOAA CDR selections. Available online at http://www1.ncdc.noaa.gov/pub/data/sds/cdr/abstracts/2009/kummerow.pdf. Accessed on 10 Dec 2011

Liu WT (1986) Statistical relation between monthly mean precipitable water and surface-level humidity over global oceans. Mon Weather Rev 114:1591–1602

Liu WT (1988) Moisture and latent heat flux variabilities in the Tropical Pacific derived from satellite data. J Geophys Res 93:6749–6760

Liu WT, Katsaros KB, Businger JA (1979) Bulk parameterization of the air-sea exchange of heat and water vapor including the molecular constraints at the interface. J Atmos Sci 36:1722–1735

Liu WT, Xie X, Tang W (2010) Scatterometer's unique capability in measuring ocean surface stress. In: Barale V, Gower JFR, Alberotanza L (eds) Oceanography from space. Springer, Heidelberg

Liu J, Curry JA, Clayson CA, Bourassa MA (2011) High-resolution satellite surface latent heat fluxes in North Atlantic hurricanes. Mon Weather Rev 139:2735–2747

Lo RC (1983) A comprehensive description of the Special Sensor Microwave Imager (SSM/I) environmental parameter extraction algorithm. Naval Research Laboratory Memo report 5199, Washington D.C.

Lykossov VN (2001) Atmospheric and oceanic boundary layer physics. In: Jones I, Toba Y (eds) Wind stress over the oceans. Cambridge University Press, Cambridge

Mears CA, Smith DK, Wentz FJ (2001) Comparison of special sensor microwave imager and buoy-measured wind speeds from 1987 to 1997. J Geophys Res 106:11719–11729

Meissner T, Smith DK, Wentz FJ (2001) A 10-year intercomparison between collocated special sensor microwave imager oceanic surface wind speed retrievals and global analyses. J Geophys Res 106:11731–11742

Murray FW (1967) On the computation of saturation vapor pressure. J Appl Meteorol 6:203–204

Oberhuber JM (1988) An atlas based on the 'COADS' data set: the budgets of heat, buoyancy and turbulent kinetic energy at the surface of the global ocean, Max Planck Institute for Meteorology, Report no. 15, Hamburg

Powell MD, Vickery PJ, Reinhold TA (2003) Reduced drag coefficient for high wind speeds in tropical cyclones. Nature 422:279–283

Reynolds RW, Smith TM, Liu C, Chelton DB, Casey KS, Schlax MG (2007) Daily high-resolution-blended analyses for sea surface temperature. J Climate 20:5473–5496

Roberts B, Clayson CA, Robertson FR, Jackson DL (2010) Predicting near-surface characteristics from SSM/I using neural networks with a first guess approach. J Geophys Res 115:D19113. doi:10.1029/2009JD013099

Schlussel P, Schanz L, English G (1995) Retrieval of latent heat flux and longwave irradiance at sea surface differences at the sea surface from SSM/I and AVHRR measurements. Adv Space Res 16:107–116

Schulz J, Schlussel P, Grassl H (1993) Water vapour in atmospheric boundary layer over oceans from SSM/I measurements. Int J Remote Sens 14:2773–2789

Schulz J, Jeans M, Stefan E, Schlussel P (1997) Evaluation of satellite-derived latent heat fluxes. J Climate 10:2782–2795

Shie C-L (2010) Science background for the reprocessing and Goddard Satellite-based Surface Turbulent Fluxes (GSSTF2b) data set for global water and energy cycle research. Science document for the distributed GSSTF2b via Goddard Earth Sciences (GES) Data and Information Services Center (DISC), 18 pp. Available online at http://disc.sci.gsfc.nasa.gov/measures/documentation/Science-of-the-data.pdf. Accessed on 10 Dec 2011

Shie C-L (2011) Science background for the reprocessing and Goddard Satellite-based Surface Turbulent Fluxes (GSSTF2c) data set for global water and energy cycle research. Science document for the distributed GSSTF2c via Goddard Earth Sciences (GES) Data and Information Services Center (DISC), 19 pp. Available online at http://disc.sci.gsfc.nasa.gov/measures/documentation/Science-of-the-data.GSSTF2c.pdf. Accessed on 10 Dec 2011

Shie C-L, Hilburn K (2011) A satellite-based global ocean surface turbulent fluxes dataset and the impact of the associated SSM/I brightness temperature. In: Proceeding of the 2011 EUMESAT meteorological satellite conference, Oslo, 5–9 Sept 2011

Shie C-L et al (2009) A note on reviving the Goddard Satellite-Based Surface Turbulent Fluxes (GSSTF) dataset. Adv Atmos Sci 26:1071–1080

Shie C-L, Chiu LS, Adler R, Lin I-I, Nelkin E, Ardizzone J (2010) The Goddard Satellite-Based Surface Turbulent Fluxes Dataset – Version 2b (GSSTF 2b) distributed via Goddard Earth Sciences (GES) Data and Information Services Center (DISC) in October 2010. Available online at http://disc.sci.gsfc.nasa.gov/daac-bin/DataHoldingsMEASURES.pl?PROGRAM_List=ChungLinShie_OldVer. Accessed on 10 Dec 2011

Shie C-L, Hilburn K, Chiu LS, Adler R, Lin I-I, Nelkin E, Ardizzone J (2011) The Goddard Satellite-Based Surface Turbulent Fluxes Dataset – Version 2c (GSSTF 2c) distributed via Goddard Earth Sciences (GES) Data and Information Services Center (DISC) in October 2011. Available online at http://disc.sci.gsfc.nasa.gov/daac-bin/DataHoldingsMEASURES.pl?PROGRAM_List=ChungLinShie. Accessed on 10 Dec 2011

Singh R, Joshi PC, Kishtawal CM (2005) A new technique for estimation of surface latent heat fluxes using satellite-based observations. Mon Weather Rev 133:2692–2710

Singh R, Joshi PC, Kishtawal CM, Pal PK (2006) A new method for estimation of near surface specific humidity over global oceans. Meteorol Atmos Phys 94:1–10

Sun D (2011) Ocean remote sensing. In: Yang C, Wong D, Maio Q, Yang R (eds) Advanced geoinformation science. CRC Press, Boca Raton

Tomita H, Kubota M, Cronin MF, Iwasaki S, Konda M, Ichikawa H (2010) An assessment of surface heat fluxes from J-OFURO2 at the KEO and JKEO sites. J Geophys Res 115:C03018. doi:10.1029/2009JC005545

Weare BC, Strub PT, Samuel MD (1981) Annual mean surface heat fluxes in the tropical Pacific Ocean. J Phys Oceanogr 11:705–717

Weissman DE, Bourassa MA, Tongue J (2002) Effects of rain rate and wind magnitude on SeaWinds scatterometer wind speed errors. J Atmos Oceanic Technol 19:738–746

Wentz FJ (1992) Measurement of oceanic wind vector using satellite microwave radiometers. IEEE Trans Geosci Remote Sens 30:960–972

Wentz FJ, Ricciardulli L, Hilburn KA, Mears CA (2007) How much more rain will global warming bring? Science 317:233–235

Wentz FJ, Mattox LA, Peteherych S (1986) New algorithms for microwave measurements of ocean winds: applications to SeaSat and the special sensor microwave imager. J Geophys Res 91:2289–2307

Williams BA, Long DG (2008) Estimation of hurricane winds from SeaWinds at ultra high resolution. IEEE Trans Geosci Remote Sens 46:2924–2935

Yu L, Weller RA (2007) Objectively analyzed Air-Sea heat fluxes for the global ice free oceans (1981–2005). Bull Am Meteorol Soc 88:527–539

Yu L, Jin X, Weller RA (2008) Multidecade global flux datasets from the Objectively Analyze Air-sea Fluxes (OAFlux) project: latent and sensible heat fluxes, ocean evaporation, and related surface meteorological variables. Woods Hole Oceanographic Institution OAFlux Project technical report OA-2008-01, Woods Hole

Zeng X, Zhao M, Dickinson RE (1998) Intercomparison of bulk aerodynamic algorithms for the computation of sea surface fluxes using TOGA COARE and TAO data. J Climate 11:2628–2644

Chapter 12
Satellite-Monitored Snow Cover in the Climate System

Li Xu

Abstract Snow cover plays an important role at climate system. Before the era of "satellite meteorology," traditional sources of snow observations were usually obtained from ground-based meteorological networks, in which only the presence or absence of snow along with snow depth is measured on a daily basis. Given the scarcity of ground-based, in situ stations, it is difficult to adequately capture the spatial variability of snow cover, particularly in remote, and difficult to access regions such as polar region and Tibetan Plateau. The remote sensing from the satellite provides an excellent method to monitor and observed global snow-cover distribution and evolution. In this chapter, we reviewed the role of snow in climate system, satellite snow observation and monitoring, snow–climate interaction, and snow–atmosphere coupling strength.

12.1 The Role of Snow Cover in the Climate System

As a key component of the cryosphere, snow cover modifies the thermal characteristics of land surfaces to modulate energy and moisture exchange with the atmosphere above it (Cohen and Rind 1991). Because of their strong thermal forcing to the lower atmosphere, snow-cover anomalies potentially play an important role in climate fluctuations and predictability. For instance, observational studies have even found a significant connection between snow anomalies over the Eurasia and the remote Asian monsoon (Bamzai and Shukla 1999; Xu and Li 2010; Xu et al. 2009). Various GCM modeling studies (Bamzai and Marx 2000;

L. Xu (✉)
Department of Atmospheric, Oceanic and earth Sciences, George Mason University, 4400 University Dr., Fairfax, VA 22030, USA

Center for Ocean-Land-Atmosphere Studies, Calverton, MD 20705, USA
e-mail: Lixu@cola.iges.org

J.J. Qu et al. (eds.), *Satellite-based Applications on Climate Change*,

DOI 10.1007/978-94-007-5872-8_12,

Barnett et al. 1988; Dash et al. 2005; Dong and Valdes 1998; Vernekar et al. 1995) have been conducted to support this snow–monsoon inverse relationship.

The direct impact of snow cover, known as the snow albedo effect, will dramatically change the land surface energy budget and then influences air temperature, density, pressure, etc. Walsh et al. (1982) demonstrated that the presence of snow cover is associated with near-surface cooling of 5–10 K in the lower troposphere. The indirect impact, also known as the snow hydrological effect, is a result of anomalous soil moisture from snowmelt that will later impact the atmosphere through land–climate interactions. However, very few studies have investigated this issue, partially due to the complicated snowmelt and runoff processes and the unavailability of accurate snow water content datasets.

Besides the direct and indirect snow effects, positive and negative snow–atmosphere feedbacks will further amplify or ameliorate anomalies. The most important positive feedback is the snow albedo feedback. Snow has the highest albedo in nature. This causes the land surface to reflect more of the incoming solar radiation. With warmer temperatures, the area of snow-cover decreases and land surfaces absorb an increasing fraction of solar radiation. This increase of total absorbed solar radiation contributes to continued and accelerated melting and warming. On the other hand, a colder climate will keep more snow cover and sustain lower air temperatures (Wiscombe and Warren 1980). Another important but less known negative (self-regulating) feedback is the snowfall-stability feedback, first suggested by Walland and Simmonds (1996). With the sudden increase in snow cover after a snow storm, the air temperature in the lower troposphere decreases and static stability of the atmosphere increases; this reduces the probability of subsequent snowfall; reducing snowfall further results in decreasing snow cover by snow sublimation and blowing snow event; decreasing snow cover at the land surface increases the sensible heating to the atmosphere and decreases the static stability, increasing the probability of snowstorms. This negative feedback keeps the snow cover relatively stable over high latitudes in the winter.

12.2 Satellite Snow Monitoring

Accurate observations or monitoring of the snow cover across the globe has great potential applications to weather, climate, and hydrology. Systematic measurements of snow depth at meteorological observation stations have been collected for over a century. At these stations, only the presence or absence of snow along with snow depth is measured on a daily basis by a snow stick or stake. Due to the sparseness of measuring stations, it is difficult to adequately capture the spatial variability of snow cover on a global scale. Furthermore, most of these observations are limited to snow depth, which is not suitable for snow modeling due to rapid gravity compaction. In other words, density can vary greatly, making it difficult to estimate the mass of water in the snow pack. Until the development of automatic stations like SNOTEL (snow telemetry) in recent decades, accurate real-time measurement of snow water equivalent (SWE) was not available. However, the point measurement at stations can

only give a potentially representative status in the given locality. Also, the snow extent or snow-cover fraction (SCF) cannot be measured easily in situ.

With developments in remote sensing, satellite-derived snow information has become an important alternative data source. Weekly snow mapping of the Northern Hemisphere using National Oceanographic and Atmospheric Administration (NOAA) and National Environmental Satellite, Data, and Information Service (NESDIS) data began in 1966 (Robinson et al. 1993). However, the coarse spatial resolution (1° over Northern Hemisphere) in the NESDIS data cannot well represent the patchy and shallow snow cover at middle latitudes. In recent decades, the NOAA Interactive Multisensor Snow and Ice Mapping System (IMS) increased spatial resolution of snow maps to 24 km (Ramsay 1998). Besides visible images, passive microwave SSMR-SMM/I (Chang et al. 1987), and AMSR-E (Chang and Rango 2000) also provide snow water estimation over the globe at low resolution, although the accuracy still cannot reach the requirements for many modeling applications.

With improvements in polar-orbiting satellites, the National Aeronautics and Space Administration (NASA) Earth Observing System (EOS) Terra satellite was launched on December 18, 1999, with a complement of five instruments, one of which is Moderate-Resolution Imaging Spectroradiometer (MODIS). Besides the comprehensive observations of cloud, ocean, and earth surface characteristics available from the Terra MODIS, a snow-cover product has been available since February 2000. With substantially improved spatial resolution (500 m globally), high temporal frequency (daily), enhanced capability to separate snow and clouds (Hall et al. 2001, 2002) due to more spectral bands (particularly in the shortwave infrared), as well as a consistently applied, automated snow-mapping algorithm (Riggs and Hall 2002), MODIS provides quantitative monitoring of global snow extent, even in inaccessible regions such as the Tibetan Plateau (TP) and the Himalayas. In particular, the single satellite platform provides excellent consistency with MODIS snow data that are hard to obtain in previous satellite datasets.

The quality of MODIS snow data has been evaluated in several previous studies (e.g., Hall et al. 2001; Klein and Barnett 2003). As determined by prototype MODIS data, annually averaged, estimated error for Northern Hemisphere snow-cover maps is approximately 8% in the absence of clouds (Hall et al. 2002). The cloud mask, however, must be applied carefully, since there is a tendency to overestimate cloud cover (Ackerman et al. 1998). In addition, confusion in identifying cloud over snow has been observed in high-elevation regions, e.g., the Sierra Nevada in California and Southern Alps of New Zealand (Hall et al. 2001). This problem has been partially improved in the most recent MODIS data products (Riggs and Hall 2002). Pu et al. (2007) evaluate the MODIS snow data over the Tibetan Plateau, the third "polar" in the world, shown a practical good detection of scatter patchy snow over these regions.

Figure 12.1 shows the MODIS-monitored Northern Hemisphere snow-cover fraction (SCF, %) from January to December. Note that during winter there are some blank areas in high-latitude region due to the polar night. From September to February, snows accumulate in high-latitude polar regions and then gradually extend to the south. The Tibetan Plateau, although located in the middle latitudes

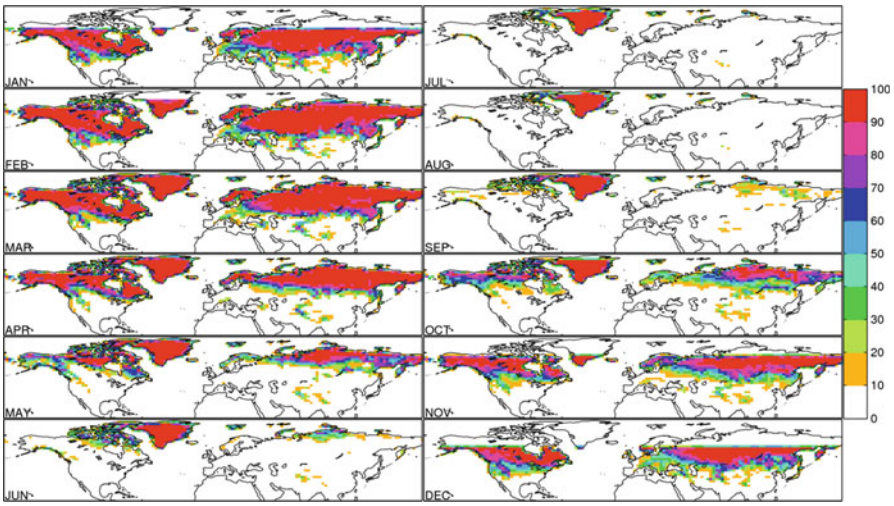

Fig. 12.1 Shows The MODIS-monitored Northern Hemisphere snow-cover fraction (SCF, %) from January to December. Note that during winter, there are some blank areas in high-latitude region due to the polar night

(roughly 25–45°N), begins to build up shallow snow cover in October due to its high elevation. During the snow maximum (the end of February), more than half of the North American continent and a large portion of Eurasia are covered by snow (SCF larger than 90%). The transition zone of the snow line (edge) reaches approximately 50°N. Tibet and the Rocky Mountains are two noteworthy snow regions in the middle latitudes. From March to August, the snow cover gradually depletes toward the North Pole due to the increase in solar energy. The moving of the snow line is generally parallel with the latitude lines, except in mountainous regions where there exists some patchy scattered snow at high elevations.

It is still difficult to obtain a complete, accurate global SWE dataset only based on in situ observations, due to limited observational stations with SWE measurements, as described earlier. Passive microwave remote sensing, such as SSMR-SMM/I (Chang et al. 1987) and AMSR-E (Chang and Rango 2000), could provide snow water estimation with relative larger errors. In the future, data assimilation incorporated with land surface models has proved to provide the best estimation of SWE by optimally merging observation and model information to minimize potential errors (Pan et al. 2003; Rodell et al. 2004).

12.3 Snow–Climate Interaction

Observational studies have demonstrated that regional-scale snow-cover anomalies are strongly linked with many large-scale general circulation anomalies, such as summer monsoon onset and intensity (Bamzai and Shukla 1999), lagged changes in

the northern annual mode (Thompson et al. 2000), typhoons over the western Pacific (Xie et al. 2005), and the outbreak of cold waves at middle latitudes (Vavrus 2007).

Over 100 years ago, Blanford (1884) first suggested that the variability of continental snow cover might exert a thermal forcing on the land surface and consequently influence the Asian summer monsoon and its rainfall. Based on Blanford's hypothesis, Walker (1910) found a negative correlation between Himalayan snow depth at the end of May and the amount of summer rainfall over India. Hahn and Shukla (1976) first used modern observations to confirm an apparent relationship between the Eurasian snow cover and the Indian monsoon rainfall based on NOAA/NESDIS snow mappings derived from satellite visible imagery. There have been many empirical studies focused on this relationship between winter/spring snow cover and the Indian summer monsoon rainfall (Bamzai and Shukla 1999; Dey and Kumar 1983; Dickson 1984; Hahn and Shukla 1976; Kripalani and Kulkarni 1999; Parthasarathy and Yang 1995; Sankar-Rao et al. 1996; Yang 1996).

In particular, the snow cover over the Tibetan Plateau (TP) is believed to exert a significant influence on the summer rainfall over East Asia (EA). As EA is located in the downstream region of the TP, the snow-cover anomalies over the TP could exert a stronger thermal forcing on the East Asian Summer Monsoon (EASM). Chen and Yan (1979, 1981) first found that positive snow depth anomalies over the Tibetan Plateau in boreal winter–spring are accompanied by above normal May–June rainfall in southern China. Other observational studies (Chen et al. 2000; Wu and Qian 2003), however, suggested a negative correlation between Tibetan winter snow depth and subsequent summer precipitation over southern China, but indicated a positive correlation over the Yangtze River Basin (YRB). Chen and Wu (2000) obtained positive correlations over the Yangtze River region but negative correlations in South China for JJA. It has also been found that the correlation of rainfall with the Tibetan Plateau winter snow depth has a pronounced change from July to August and the correlation for JJA rainfall differs from that for May–June (Chen and Wu 2000). Although the snow-cover connection with EASM is not very robust, snow cover is applied as one of four key predictors besides ENSO, subtropical high, and blocking for short-range climate prediction at National Climate Center of China (Xu and Li 2010; Zhao 1999).

Aside from the monsoon, other linkages between snow cover and atmospheric circulation have been discovered by numerous observation studies. Studies show that excessive summer–autumn snow coverage over Eurasia favors unusually cold winters over Europe and the USA, due to forcing of the negative phase of Arctic oscillation (Cohen and Entekhabi 1999). Subsequent studies confirmed the physical mechanism of this relationship (Cohen and Saito 2003; Gong et al. 2002, 2004a; Saito et al. 2001): early-season snow-cover anomalies trigger vertically propagating planetary waves that quickly alter the stratospheric polar vortex. These observational linkages between snow cover and atmospheric circulation have motivated efforts for seasonal climate forecasts based on snow anomalies.

In addition to being a climate predictor, snow cover also has profound ecological and societal impact on the hydrosphere since snowpack strongly affects the

underlying soil temperature and local river runoff. Groisman et al. (1994) found a retreat of North American springtime snow associated with strong warming. The extent of boreal snow during spring was significant lower during the 1990s than at any time in the previous century (IPCC 2007). Barnett et al. (2005) concluded future water supplies may be hindered in a warmer climate with less snowfall and earlier melting. In the background of global warming, how the snow cover will change is a challenging scientific question.

12.4 Numerical Simulations

Atmospheric general circulation models (AGCMs) coupled with various Land Surface Models LSMs are popular tools for examining the snow–atmosphere interaction studies, largely because the numerical model can be easy manipulated via deliberate changes to physics processes or parameterizations in controlled experiments. Numerical simulations also provide a method to explore the climate system with some extreme snow situations that could not happen in nature.

Various AGCM modeling studies (Bamzai and Marx 2000; Barnett et al. 1988; Dash et al. 2005; Dong and Valdes 1998; Vernekar et al. 1995) have been conducted to support the snow–monsoon inverse relationship first suggested by Blanford (1884). These studies indicate the AGCMs are able to reproduce an inverse snow–monsoon relationship and snow-cover and snow-mass impact on climate on a seasonal time scale. Ferranti and Molteni (1999) investigated the effect of springtime snow conditions over Eurasia on the monsoon circulation by using ensemble simulations. The results suggested Eurasian snow depth is probabilistically predictable and that it does influence the seasonal-mean monsoon independently of the ENSO phase. As a result, proper observations and simulations of the Eurasian snowfield can provide an additional and independent contribution to monsoon prediction.

Several prior studies have attempted to quantify the snow role in the cold region climate (Gong et al. 2004b; Vavrus 2007; Walsh et al. 1985; Watanabe and Nitta 1998). However, those earlier works have been limited in spatial and temporal extent. Prescribed excessive or deficient snow over a specific region, such as Eurasia and Siberia, has been investigated based on the observed fluctuation over monthly to seasonal time scales.

Due to the limitation and imperfections of snow schemes in land surface models, some simulation studies get conflicting results, even with the same model. For example, Zhang and Tao (2001) created a conceptual model to explain the possible mechanism on the impact of the inphase change of snow cover over the TP with the EASM and summer rainfall over Yangtze River Basin. They further verified their conclusion by model simulations with excessive/deficient snow depth in the winter. However, with the same IAP-9L AGCM model and the updated snow data, Li and Chen (2006) obtained an opposite result.

12.5 Snow–Atmosphere Coupling Experiment

Xu (2011) designed a series numerical experiment to investigate the role of snow cover as a source of predictability at seasonal time scales over the Northern Hemisphere. A global climate model is used, consisting of the fully coupled land and atmosphere components of the Community Climate System Model. Ensembles of boreal spring–summer climate simulations are made with specified climatological sea surface temperatures. Following the methodology of the Global Land–Atmosphere Coupling Experiment (GLACE), a control ensemble is created with perturbed initial atmospheric states and realistic land surface initialization. In the test cases, snow-cover fraction and snow water equivalent are specified in all ensemble members based on model-simulated snow information or realistic snow data from remote sensing and an operational land surface analysis. The snow–atmosphere coupling strength is quantified as in GLACE as the degree to which identically constrained snow boundary conditions reduce the ensemble spread of key meteorological variables like precipitation and near-surface air temperature. The snow albedo effect, snow hydrological effect, or mixed effects are estimated by different experiments and snow stages. Metrics of potential predictability and feedback are also investigated.

From spring to early summer, the snow-covered regions demonstrate significant coupling to the atmosphere over large portions of the Northern Hemisphere (Fig. 12.2). The local coupling between snow state and atmosphere is found to have three distinct stages: the stable-snow period before snowmelt when interactions are through radiative processes controlled by albedo, the period after snowmelt when interactions are through the delayed hydrologic effect of soil moisture anomalies resulting from snow anomalies, and the intervening period during snowmelt when both radiative and hydrologic effects are important. The coupling strength is strongest during the snowmelt period along the transient zone between snow-covered and snow-free areas and migrates northward with the retreating snow line. The coupling strength due to the hydrological effect (soil moisture impact) after snowmelt is generally stronger than the coupling strength due to the albedo effect (radiative impact) before snowmelt. The Tibetan Plateau is a special snow–atmosphere coupling region due to its high incident solar radiation caused by its high altitude and relatively low latitude.

Figure 12.3 shows the zonal mean over land of coupling strengths shown in Fig. 12.2. At all latitudes, the coupling strength is strongest during snowmelt and weakest before the snowmelt. The coupling strength generally increases with latitude to a peak at roughly 50–65° but then decrease sharply north of 70°. There is a local maximum of coupling strength at roughly 34° caused by the Tibetan Plateau. Before snowmelt, the coupling strength is mainly due to the snow albedo effect as shortwave radiation increases during spring. During the snowmelt period, the SWE and SCF have peak variability. Both albedo and hydrological effects contribute to the coupling strength during snowmelt. The hydrological effect after snowmelt has a stronger than the snow albedo effect before melting. The potential predictably from accurate

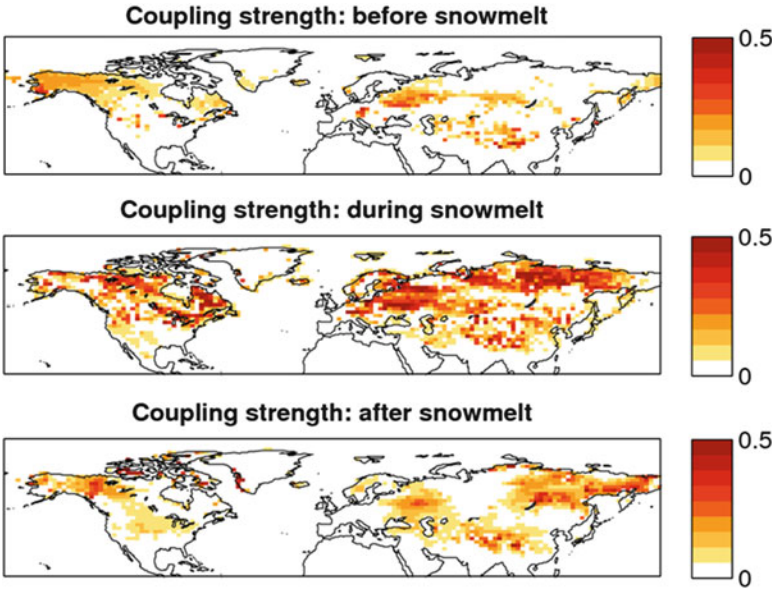

Fig. 12.2 The air temperature–snow coupling strength before, during, and after the snowmelt stage as defined in the text (From Xu and Dirmeyer (2011))

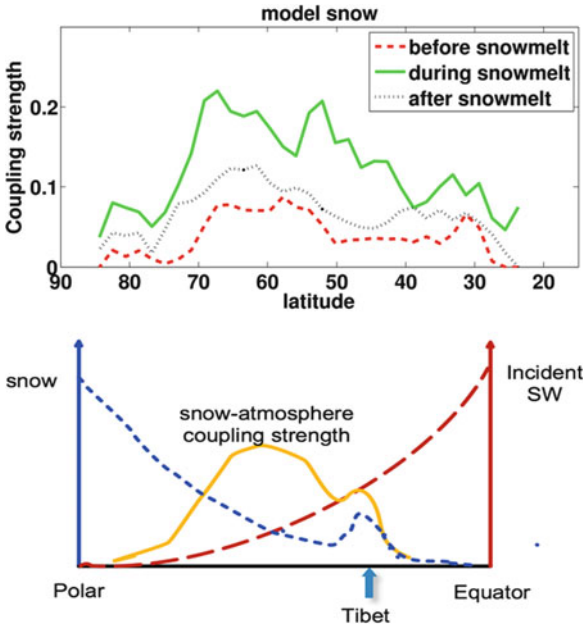

Fig. 12.3 The *top panel* shows the zonal mean (land points only) of air temperature coupling strength at different snow stages defined in the text. The *bottom panel* demonstrates a conceptual model of coupling strength (*solid line*) as a function of latitude. The *right axis* is the incident solar radiation (SW; *long dashed line*), and the *left axis* indicates the snow depth and snow-cover fraction (*short dashed line*) (Reproduced from Xu and Dirmeyer (2011))

knowledge of snow distribution is highly correlated with the snow–atmosphere coupling strength. Conceptual models are proposed to explain the mechanisms behind the timing and spatial distribution of snow–atmosphere coupling.

12.6 Summary

In summary, snow cover is an integral component of the earth climate system. Observational studies have demonstrated strong snow impacts and interaction with local weather and climate through both radiative and hydrological effects. The satellite remote sensing provides an excellent method to observe the snow cover, both in visible and passive microwave. The numerical simulations provide a "virtual lab" to study snow–climate interaction. Numerical experiments illustrated some key aspects of snow–atmosphere coupling behavior even though these couplings and interactions are difficult to investigate by only observation-based studies. Inspired by GLACE, Xu (2011) expand the GLACE-type experimental framework to reveal snow–atmosphere coupling strength and its potential application to short-range climate prediction.

References

Ackerman SA, Strabala KI, Menzel WP, Frey RA, Moeller CC, Gumley LE (1998) Discriminating clear sky from clouds with MODIS. J Geophys Res 103:32141–132157

Bamzai AS, Marx L (2000) COLA AGCM simulation of the effect of anomalous spring snow over Eurasia on the Indian summer monsoon. Q J R Meteorol Soc 126:2575–2584

Bamzai AS, Shukla J (1999) Relation between Eurasian snow cover, snow depth, and the Indian summer monsoon: an observational study. J Climate 12:3117–3132

Barnett TP, Dumenil L, Schlese U, Roeckner E (1988) The effect of Eurasian snow cover on global climate. Science 239:504–507

Barnett TP, Adam JC, Lettenmaier DP (2005) Potential impacts of a warming climate on water availability in snow-dominated regions. Nature 438:303–309

Blanford HF (1884) On the connection of Himalayan snowfall and seasons of drought in India. Proc R Soc Lond 37:3–22

Chang ATC, Rango A (2000) Algorithm Theoretical Basis Document (ATBD) for the AMSR-E snow water equivalent algorithm. NASA/GSFC, Greenbelt

Chang ATC, Foster JL, Hall DK (1987) Nimbus-7 SMMR derived global snow cover parameters. Ann Glaciol 9:39–44

Chen L-T, Wu R (2000) Interannual and decadal variations of snow cover Qinghai-Xizang plateau and their relationship to summer monsoon rainfall in China. Adv Atmos Sci 17:18–30

Chen LT, Yan ZX (1979) Impact of the snow cover over the Tibetan plateau in winter and spring on the atmospheric circulation and the precipitation in South China during the rainy season. I. Water Resources and Electric Power Press, Beijing, pp 185–195

Chen LT, Yan ZX (1981) Statistics of the impacts on early summer monsoon of the anomalous snow cover in winter and spring over the Tibetan Plateau. In: Proceedings of the symposium of the Tibetan plateau meteorology, Geneva, 1981, pp 151–161

Chen Q-J, Gao B, Li W-J (2000) Studies on relationships among winter snow cover over the Tibetan plateau and droughts/floods during Meiyu season in the middle and lower reaches of the Changjiang river as well as in the atmosphere/ocean system. Acta Meteorol Sina 58:582–595

Cohen J, Entekhabi D (1999) Eurasian snow cover variability and northern hemisphere climate predictability. Geophys Res Lett 26:345–348

Cohen J, Rind D (1991) The effect of snow cover on the climate. J Climate 4:689–706

Cohen JL, Saito K (2003) Eurasian snow cover, more skillful in predicting U.S. Winter climate than the NAO/AO? Geophys Res Lett 30:CLM 3–1–CLM 3–4

Dash SK, Singh GP, Shekhar MS, Vernekar AD (2005) Response of the Indian summer monsoon circulation and rainfall to seasonal snow depth anomaly over Eurasia. Clim Dyn 24:1–10

Dey B, Kumar B (1983) Himalayan winter snow cover area and summer monsoon rainfall over India. J Geophys Res 88:5471–5474

Dickson RR (1984) Eurasian snow cover versus Indian monsoon rainfall: an extension of the hahn-shukla results. J Appl Meteorol 23:171–173

Dong B, Valdes PJ (1998) Modelling the Asian summer monsoon rainfall and Eurasian winter/spring snow mass. Q JR Meteorol Soc 124:2567–2596

Ferranti L, Molteni F (1999) Ensemble simulations of Eurasian snow-depth anomalies and their influence on the summer Asian monsoon. Q J R Meteorol Soc 125:2597–2610

Gong G, Entekhabi D, Cohen J (2002) A large-ensemble model study of the wintertime AO–NAO and the role of interannual snow perturbations. J Climate 15:3488–3499

Gong G, Entekhabi D, Cohen J (2004a) Orographic constraints on a modeled Siberian snow–Tropospheric–Stratospheric teleconnection pathway. J Climate 17:1176–1189

Gong G, Entekhabi D, Cohen J, Robinson D (2004b) Sensitivity of atmospheric response to modeled snow anomaly characteristics. J Geophys Res Atmos 109:13

Groisman PY, Karl TR, Knight RW, Stenchikov GL (1994) Changes of snow cover, temperature, and radiative heat balance over the northern hemisphere. J Climate 7:1633–1656

Hahn DG, Shukla J (1976) An apparent relationship between Eurasian snow cover and Indian monsoon rainfall. J Atmos Sci 33:2461–2462

Hall DK, Riggs GA, Salomonson VV (2001) Algorithm Theoretical Basis Document (ATBD) for the MODIS snow and sea ice-mapping algorithms. NASA GSFC, Greenbelt

Hall DK, Riggs GA, Salomonson VV, DiGirolamo NE, Bayr KJ (2002) MODIS snow-cover products. Remote Sens Environ 83:181–194

IPCC (2007) Climate change 2007: the scientific basis. Cambridge University Press, Cambridge, p 944

Kripalani RH, Kulkarni A (1999) Climatology and variability of historical Soviet snow depth data: some new perspectives in snow-Indian monsoon teleconnections. Clim Dyn 15:475–489

Klein AG, Barnett AC (2003) Validation of daily MODIS snow cover maps of the Upper Rio Grande River Basin for the 2000–2001 snow year. Remote Sens Environ 86:162–176

Li Q, Chen Y (2006) Impact of anomalous snow cover over Tibetan plateau on east Asian summer monsoon climate. J PLA Univ Sci Technol 7:605–612

Pan M et al (2003) Snow process modeling in the North American Land Data Assimilation System (NLDAS): 2. Evaluation of model simulated snow water equivalent. J Geophys ResAtmos 108:14

Parthasarathy B, Yang S (1995) Relationships between regional Indian summer monsoon rainfall and Eurasian snow cover. Adv Atmos Sci 12:143–150

Pu Z, Xu L, Salomonson VV (2007) MODIS/Terra observed seasonal variations of snow cover over the Tibetan Plateau. Geophys Res Lett 34:1–6

Ramsay BH (1998) The interactive multisensor snow and ice mapping system. Hydrol Processes 12:1537–1546

Riggs GA, Hall DK (2002) Reduction of cloud obscuration in the MODIS snow data product. In: Proceedings of the 59th eastern snow conference, Stowe, pp 4–6

Robinson DA, Dewey KF, Heim RR Jr (1993) Global snow cover monitoring: an update. Bull Am Meteorol Soc 74:1689–1696
Rodell M et al (2004) The global land data assimilation system. Bull Am Meteorol Soc 85:381–394
Saito K, Cohen J, Entekhabi D (2001) Evolution of atmospheric response to early-season Eurasian snow cover anomalies. Mon Weather Rev 129:2746–2760
Sankar-Rao M, Lau KM, Yang S (1996) On the relationship between Eurasian snow cover and the Asian summer monsoon. Int J Climatol 16:605–616
Thompson DWJ, Wallace JM, Hegerl GC (2000) Annular modes in the extratropical circulation. Part II: trends. J Climate 13:1018–1036
Vavrus S (2007) The role of terrestrial snow cover in the climate system. Clim Dyn 29:73–88
Vernekar AD, Zhou J, Shukla J (1995) The effect of Eurasian snow cover on the Indian monsoon. J Climate 8:248–266
Walker GT (1910) Correlations in seasonal variations of weather. Mem India Meteorol Dept 21:22–45
Walland DJ, Simmonds I (1996) Modelled atmospheric response to changes in northern hemisphere snow cover. Clim Dyn 13:25–34
Walsh JE, Tucek DR, Peterson MR (1982) Seasonal snow cover and short-term climatic fluctuations over the United-States. Mon Weather Rev 110:1474–1485
Walsh JE, Jasperson WH, Ross B (1985) Influences of snow cover and soil moisture on monthly air temperature. Mon Weather Rev 113:756–768
Watanabe M, Nitta T (1998) Relative impacts of snow and sea surface temperature anomalies on an extreme phase in the winter atmospheric circulation. J Climate 11:2837–2857
Wiscombe WJ, Warren SG (1980) A model for the spectral albedo of snow. I: pure snow. J Atmos Sci 37:2712–2733
Wu T-W, Qian Z-A (2003) The relation between the Tibetan winter snow and the Asian summer monsoon and rainfall: an observational investigation. J Climate 16:2038–2051
Xie L, Yan T, Pietrafesa LJ, Karl T, Xu X (2005) Relationship between western North Pacific typhoon activity and Tibetan plateau winter and spring snow cover. Geophys Res Lett 32:1–4
Xu L (2011) Snow cover as a source of climate predictability: mechanisms of snow-atmosphere coupling. Dissertation, Atmospheric,Oceanic and Earth Sciences, George Mason University, p 241
Xu L, Dirmeyer P (2011) Snow-atmosphere coupling strength in a global atmospheric model. Geophys Res Lett 38:L13401
Xu L, Li Y (2010) Reexamining the impact of Tibetan snow anomalies to the East Asian summer monsoon using MODIS snow retrieval. Clim Dyn 35:1039–1053
Xu L, Gao H, Li Y-Q (2009) Sensible heating over the Tibetan plateau linked to the onset of Asian monsoon. Atmos Ocean Sci Lett 2:350–356
Yang S (1996) ENSO-snow-monsoon associations and seasonal-interannual predictions. Int J Clim 16:125–134
Zhang S, Tao S (2001) Influence of snow cover over the Tibetan plateau on Asian summer monsoon. Chin J Atmos Sci 25:372–390
Zhao Z (1999) The summer rainfall in China and its environment field. China Meteorological Press, Beijing

Chapter 13
Evapotranspiration Estimates from Remote Sensing for Irrigation Water Management

Timothy C. Martin, Richard G. Allen, Larry E. Brazil, J. Philip Burkhalter, and Jason S. Polly

Abstract Climate change impacts and increasing demands on Morocco's water resources present serious challenges to irrigation districts and water managers. Modernization of irrigation practices and delivery systems can help conserve water by improving efficiencies and water productivity. Satellite imagery from Landsat and MODIS and the METRIC surface energy balance method were used to derive objective estimates of crop evapotranspiration (ET) in three Moroccan irrigation sectors. The METRIC analysis requires satellite imagery with thermal (surface temperature) information, as well as high-quality weather data. The spatially distributed ET estimate maps were combined with surface water supply records and weather data and used as inputs to a water balance analysis to estimate the quantity of supplemental groundwater used for irrigation. The results are useful as a pre-project, baseline condition for investments in irrigation methods and system improvements. The remote sensing data analysis provides useful results for large irrigated areas that have little information on crop consumptive use and irrigation efficiency and almost no information on groundwater abstraction. A similar approach can be used to monitor and assess the system during and after the irrigation improvement project is completed.

Keywords Evapotranspiration • ET • Remote sensing • Energy balance • Morocco • Irrigation • Consumptive use • METRIC

T.C. Martin (✉) • L.E. Brazil • J.P. Burkhalter • J.S. Polly
Riverside Technology inc., 2950 East Harmony Road, Fort Collins, CO, USA
e-mail: tim.martin@riverside.com; larry.brazil@riverside.com; phil.burkhalter@riverside.com; jason.polly@riverside.com

R.G. Allen
Department of Agricultural and Biological Engineering, Kimberly Research and Extension Center, University of Idaho, Kimberly, ID, USA
e-mail: rallen@kimberly.uidaho.edu

J.J. Qu et al. (eds.), *Satellite-based Applications on Climate Change*,
DOI 10.1007/978-94-007-5872-8_13,

13.1 Introduction

Global warming is expected to change not only atmospheric temperature but also climatic variables such as humidity, precipitation, and net terrestrial solar radiation (IPCC 2007). Also predicted are an intensified hydrological cycle and altered evapotranspiration, with implications for irrigated crops, ecosystems services, and feedback to the regional and global climate (Jung et al. 2010).

With increasing demands on limited water supplies, exacerbated by a changing climate, understanding when, where, and how much water is consumptively used is increasingly important. In many arid regions of the world, irrigated agriculture is the dominant water user, and monitoring irrigation system performance and improving efficiency of water use are integral to sustainable water management.

Physically based actual crop evapotranspiration (ET) from remote sensing can be used to measure water use from all sources, including precipitation and irrigation from both surface and groundwater. The actual ET is measured for each pixel of each satellite image acquired during an irrigation season, yielding spatially and temporally distributed maps of ET. These products can then be used in GIS processing with spatial analyses to produce a range of statistics, reports, visualizations, and other results for use by water resources planners, managers, and irrigators. In Morocco, for example, groundwater policy and regulation are not well established, and reliable data on the location and quantity of groundwater use are not available. Satellite-derived ET maps, combined with surface water supply data, can be used to analyze the efficiency of irrigation water supply from all sources and to estimate the contribution of groundwater.

The spatial distribution and availability of water are critical for sustainable development of modern societies and for maintaining and protecting natural ecosystems. Sufficient water supplies are required for agricultural, municipal, industrial, recreational, and other uses. Economic progress often depends on development of water supply infrastructures that store and distribute surface waters and exploit underground aquifers.

13.2 Objective and Approach

Morocco has invested heavily in water supply infrastructure and large-scale irrigation systems to secure water for urban and agricultural demands; however, these supply oriented measures were not coupled with policies and development aimed at sustainable water management and conservation. Recently, the World Bank and government of Morocco formulated the $115 M Oum Er Rbia Irrigated Agriculture Modernization Project (MA Project) to help participating farmers increase productivity and, simultaneously, promote more sustainable use of irrigation water to overcome current and future water deficits. This irrigation modernization program seeks to conserve water by converting to more efficient irrigation technology and to relieve unsustainable groundwater abstraction rates. The surface water resources of the irrigation schemes are monitored and regulated by the government of Morocco;

however, groundwater use is largely unregulated and abstraction rates generally are not known. The World Bank program conserves water in part by converting fixed rotation delivery to water on-demand systems and by helping farmers shift to higher value crops. Two of the program's success indicators are (1) improved "water productivity," defined as benefit or value per unit of water consumed by the beneficiary farmers, and (2) reduced groundwater consumption for irrigation.

Riverside Technology, inc. (Riverside) was contracted by the World Bank to process and analyze satellite imagery to estimate crop water use in selected sectors of three large and economically important irrigation districts in the Oum Er Rbia and Tensift river basins of Morocco. The Riverside team used surface energy balance methodology to estimate and map actual evapotranspiration (ET) from remote sensing data. The ET maps were the core foundation for additional analyses, which estimated the water balance and groundwater use in pilot sector areas selected for water efficiency improvements and for distributing a predictable (and sustainable) allocation of surface water to farmers while limiting or reducing their need for groundwater consumption. The results will also provide a baseline of water use and water productivity for comparison with post-project conditions to assess the impacts of the project intervention.

13.3 Climate and Water Availability in Morocco

Morocco's water resources are unevenly distributed and unreliable, and under a changing climate, the country's water resources are predicted to become even more scarce. The natural reductions of water supply are exacerbated by increasing demands from Moroccan economic development and from an increasingly urban population. Agricultural production and processing makes up 85% of Morocco's water use and employs 40% of the workforce. The national agriculture strategic plan recognizes the importance of agriculture and the direct correlation between the amount and seasonality of rainfall and the national GDP (Ministry of Agriculture Morocco 2008).

During drought years, rainfall in Morocco can be as little as one-third of the "normal" amount. A pressing concern is how future demand for water will be met. Groundwater pumping, already at 30% of total water use, is used for irrigation expansion and to supplement surface irrigation water shortages (AquaStat Database; FAO 2004), yet groundwater levels are falling rapidly in many regions. Concerns about the future of Morocco's water resources have been widely recognized. Arnell (1999) predicted that Morocco would shift from a medium to highly water-stressed country[1] by 2025, with a 25–50% decrease in both maximum monthly runoff and minimum annual runoff by 2050.

Water resources supply and management is one of Morocco's most important national issues and is the subject of recent policy and national action plans. The issue

[1] Water stress is defined by the ratio of withdrawals to renewable water resources with "medium" stress in the range of 20–40% and "high" water stress when the ratio is over 40% (Arnell 1999).

was recognized in Morocco's Plan Maroc Vert (PMV), or Green Plan, the country's strategy to transform its agriculture sector.

As a whole, the Mediterranean is expected to be one of the world's regions most affected by future climate change, with increasing temperature and decreasing availability of water resources (Hulme et al. 2000; Ragab and Prudhomme 2002; Agoumi 2003; El Ghissassi 2005). Morocco has experienced frequent and lasting drought over the past several decades, demonstrating its vulnerability to irrigation water scarcity and threatening livelihoods of farmers and nomad families (e.g., Chaouki et al. 1995). Rainfall predictions in climate assessments and studies of the highly diverse river basins in Morocco and the surrounding region are inconsistent, but these studies consistently predict higher temperatures in the region. Born et al. (2008a, b) studied present and future climate variability of northwestern Africa using IPCC AR4 data and concluded that the region will continue to experience drying and warming trends in the future. Driouech et al. (2010) compared more than ten RCM outputs over Morocco, all of which showed a decrease in precipitation and a change in occurrence and distribution of extreme events for the future (2021–2050). Using the Weather Research and Forecast (WRF) model with IPCC AR4 GCM output as forcing fields, Patricola and Cook (2010) simulated Morocco and North Africa present (1981–2000) and future (2081–2100) climate variation. Based on their results, they predicted little change in future precipitation and an increase of 5°C in future temperature.

Recent decreases in precipitation have reduced water available for irrigation across the country, particularly in the Oum Er Rbia basin. Half of Morocco's large-scale irrigation systems are in this basin, which produces much of the nation's crops. However, agricultural production is constrained by water rationing, as irrigation agencies have distributed, on average, only 60% of the necessary water over the last decade. Farmers have made up for this reduction in surface water by using groundwater (Bennani et al. 2001), and as a result, water-table levels are declining at an alarming rate in the Oum Er Rbia basin. Quantitative estimates of the potential impacts of climate change on Morocco's water resources suggest a decline of 10–15% of the renewable surface water and groundwater by the year 2020 (Bennani et al. 2001).

13.4 Methodology for Estimating Evapotranspiration

13.4.1 Introduction to METRIC

Satellite data are ideally suited for deriving spatially continuous fields of ET using energy balance techniques. Mapping EvapoTranspiration at high Resolution with Internalized Calibration (METRIC™) is a satellite-based image-processing tool for calculating ET as a residual of the energy balance at the earth's surface. METRIC can function as an operational model for producing maps of ET for regions smaller than a few hundred kilometers in scale and at high resolution and typically uses Landsat imagery having 30-m resolution in the short wave and 60–120-m resolution

in the thermal band. It also is applied with MODIS satellite data, which have a 1,000-m resolution in the thermal band for larger areas where the courser resolution is sufficient. METRIC is particularly relevant for the Morocco study area because of the World Bank MA project's need for monthly ET estimates of irrigation schemes targeted for improvement and rehabilitation, the existence of a long-term meteorological record at key sites, and an archive of quality Landsat data including the essential thermal bands. The surface energy balance in METRIC has advantages over conventional ET estimations based on crop coefficient curves or vegetation indices, in that specific crop or vegetation types are not required, and the energy balance can detect reduced ET under water shortages, saline soils, or other constraints.

METRIC employs calibration principles and techniques used by the pioneering model SEBAL (Surface Energy Balance Algorithms for Land), an important energy balance model developed by Bastiaanssen et al. (1998). In particular, METRIC uses a calibrated inverse-modeling approach at extreme conditions (Allen et al. 2007a), which was pioneered in SEBAL for estimating the near-surface temperature gradient (dT) as an indexed function of radiometric surface temperature, thereby eliminating the need for absolutely accurate aerodynamic surface temperature or the need for air temperature measurements for estimating sensible heat flux at the surface. METRIC employs internal calibration of the satellite-based energy balance at two extreme conditions (dry and wet), using locally available weather data.

Professionals familiar with energy balance, aerodynamics, and basic radiation physics design METRIC algorithms for applications. The primary inputs for the model are shortwave and longwave (thermal) satellite images (e.g., Landsat and MODIS), a digital elevation model, and ground-based weather data measured within or near the area of interest. ET images developed from Landsat provide means to quantify ET on a field basis in terms of both rate and spatial distribution. The auto-calibration in METRIC for each image uses an alfalfa-based reference ET (ET_r) that is derived from hourly weather data. The internal calibration and the use of the indexed temperature gradient reduce or eliminate the need for atmospheric correction of T_s and reflectance (albedo) measurements using radiative transfer models. The internal calibration also reduces impacts of biases in estimation of aerodynamic stability correction and surface roughness (Allen et al. 2007a).

METRIC uses weather-based reference ET so that both calibration and extrapolation of instantaneous ET to 24-h and longer periods compensate for regional advection effects where ET can exceed daily net radiation.

13.4.2 METRIC Development History

The innovative component of SEBAL and METRIC is that the energy balance modeling uses a dT that is indexed to radiometric surface temperature, which has eliminated the need for absolute surface temperature calibration—a major impediment to operational satellite ET. The theoretical and computational basis of SEBAL

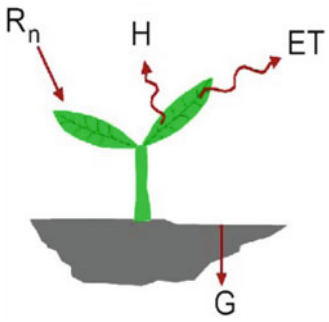

Fig. 13.1 Energy balance relationships that yield ET (Morse et al. 2005). R_n is net radiation (sum of all incoming and outgoing shortwave and longwave radiation at the surface), G is sensible heat flux conducted into the ground, and H is sensible heat flux convected into the air. R_n is computed from satellite-measured narrowband reflectances and surface temperature; G is estimated from R_n, surface temperature, and a vegetation index; and H is estimated from surface temperature ranges, surface roughness, and wind speed using buoyancy corrections

is described in Bastiaanssen et al. (1998, 2005) and Bastiaanssen (2000). The basis and principles for METRIC are described in Allen et al. (2005, 2007a). ET is determined by applying an energy balance at the surface (Fig. 13.1), where energy consumed by the ET process is calculated as a residual of the surface energy equation:

$$LE = R_n - G - H \tag{13.1}$$

where LE is the latent energy consumed by ET, R_n is net radiation (sum of all incoming and outgoing shortwave and longwave radiation at the surface), G is sensible heat flux conducted into the ground, and H is sensible heat flux convected to the air. Energy absorbed into the canopy and by photosynthesis is generally less than a few percent and is ignored in Eq. 13.1. One advantage of energy balance over vegetation-based methods is that actual ET rather than potential ET (based on amount of vegetation) is computed to capture reductions in ET caused by stresses due to disease, salinity, or shortage of soil moisture. A disadvantage of the energy balance approach is that the computation of LE is only as accurate as the combined estimates for R_n, G, and H following correction for biases. METRIC attempts to overcome this disadvantage by focusing internal calibration not on LE, but on H to absorb intermediate estimation errors and biases.

In both METRIC and SEBAL, the sensible heat flux H (W m^{-2}) is estimated from an aerodynamic function where:

$$H = \rho_{air} C_p \frac{dT}{r_{ah,1,2}} \tag{13.2}$$

where ρ_{air} is air density (kg m^{-3}), C_p is specific heat of air at constant pressure (J kg^{-1} K^{-1}), and $r_{ah,1,2}$ is aerodynamic resistance (s m^{-1}) between two near-surface heights z_1 and z_2 (generally 0.1 and 2 m above the zero-plane displacement height) computed as a function of estimated aerodynamic roughness of the particular pixel. In METRIC, the $r_{ah,1,2}$ calculation uses wind speed extrapolated from some blending height above the ground surface (typically 100–200 m) and an iterative stability correction scheme based on the Monin-Obhukov functions (Allen et al. 1996). The dT parameter (K) represents the near-surface temperature difference between z_1 and z_2. dT is used in Eq. 13.2 because of the difficulty in estimating surface temperature (T_s) accurately from satellites due to uncertainty in atmospheric attenuation or contamination, radiometric calibration of the sensor, and unknown values for air temperature, T_a, above any particular surface in an image, where T_a can vary by more than 5°C between cold and dry conditions. Equation 13.2 is relatively unique to SEBAL and METRIC and contrasts with classical approaches where H is estimated using T_s and T_a—factors with a great deal of uncertainty that can cause large error in the estimate for H. Elevating dT above the surface eliminates the need to estimate roughness length for sensible heat transfer, z_{oh}, the partitioning of LE between E and T, and the degree of vegetation clumping. It is the blended dT that Bastiaanssen et al. (1998) found to be linearly related to radiometric surface temperature, T_s.

dT is approximated as a relatively simple linear function of T_s as pioneered by Bastiaanssen (1995):

$$dT = a + b\,T_{s\ datum} \tag{13.3}$$

where a and b are empirically determined constants for a given satellite image and $T_{s\ datum}$ is surface temperature adjusted to a common elevation datum for each image pixel using a digital elevation model and customized lapse rate. The near-surface temperature gradient over the two calibration pixels (cold pixel and hot pixel) is computed using the inverse of Eq. 13.2:

$$dT = \frac{H\,r_{ah}}{\rho_{air}\,C_p} \tag{13.4}$$

where r_{ah} is computed for the roughness and stability conditions of the cold and hot pixels.

13.4.3 Calibration via Reference Evapotranspiration

METRIC uses the standardized ASCE Penman-Monteith equation for the alfalfa reference ET_r (ASCE – EWRI 2005) to calibrate the energy balance functions. ET_r is typically 20–30% greater than grass reference ET (ET_o). ET_r is used to

approximate the ET of the cold-pixel calibration condition because METRIC does not require the specific crop type for computation by pixel, thus eliminating the need for relatively costly crop classification exercises.

The calibration of the sensible heat process equations to ET_r corrects the surface energy balance for lingering systematic computational biases associated with empirical functions used to estimate some components and uncertainties in other estimates, as summarized by Allen et al. (2005). Included are atmospheric correction, albedo calculation, net radiation calculation, surface temperature from the satellite thermal band, air temperature gradient function used in sensible heat flux calculation, aerodynamic resistance including stability functions, soil heat flux function, and wind speed field. This list of biases plagues essentially all surface energy balance computations that use satellite imagery as the primary spatial information resource. Most polar orbiting satellites orbit about 700 km above the earth's surface, yet the transport of vapor and sensible heat from land surfaces is strongly impacted by aerodynamic processes including wind speed, turbulence, and buoyancy, all of which are essentially invisible to satellites. In addition, precise quantification of albedo, net radiation, and soil heat flux is uncertain and potentially biased. Therefore, even though best efforts are made to estimate each of these parameters as accurately and as unbiased as possible, some biases do occur, and calibration to ET_r helps to compensate for this by introducing a bias correction into the calculation of H. The result is that biases inherent to R_n, G, and subcomponents of H are largely canceled by the subtraction of a bias-canceling estimate for H. The result is an ET map with values ranging between near zero and near ET_r, for images having a range of bare or nearly bare soil and full vegetation cover.

13.4.4 Calculation of Evapotranspiration

ET at the instant of the satellite image is calculated for each pixel by dividing LE from Eq. 13.1 by latent heat of vaporization:

$$ET_{inst} = 3,600 \frac{LE}{\lambda \rho_w} \tag{13.5}$$

where ET_{inst} is instantaneous ET (mm h^{-1}), 3,600 converts from seconds to hours, ρ_w is the density of water [~1,000 kg m^{-3}], and λ is the latent heat of vaporization (J kg^{-1}) representing the heat absorbed when a kilogram of water evaporates. The reference ET fraction (ET_rF) is calculated as the ratio of the computed instantaneous ET (ET_{inst}) from each pixel to the reference ET (ET_r) computed from weather data:

$$ET_rF = \frac{ET_{inst}}{ET_r} \tag{13.6}$$

where ET_r is the estimated instantaneous rate (interpolated from hourly data) (mm h^{-1}) for the standardized 0.5 m tall alfalfa reference at the time of the image. Generally, only one or two weather stations are required to estimate ET_r for a Landsat image that measures 180 × 180 km, as discussed below. ET_rF is the same as the well-known crop coefficient K_c when used with an alfalfa reference basis and is used to extrapolate ET from the image time to 24-h or longer periods.

One should generally expect ET_rF values to range from 0 to about 1.0 (Wright 1982; Jensen et al. 1990). At a completely dry pixel, $ET = 0$ and therefore $ET_rF = 0$. A pixel in a well-established field of alfalfa or corn can occasionally have an ET slightly greater than ET_r and, therefore an $ET_rF > 1$, perhaps up to 1.1 if it has been recently wetted by irrigation or precipitation. However, ET_r generally represents an upper bound on ET for large expanses of well-watered vegetation. In calculation of ET_rF, each pixel retains a unique value for ET_{inst} that is derived from a common value for $ET_{r,}$ which is derived from the representative weather station data.

Daily values of *24-h evapotranspiration* (ET_{24}) are generally much more useful than the instantaneous ET that is derived from the satellite image. In the METRIC process, ET_{24} is estimated by assuming that the instantaneous ET_rF computed at image time is the same as the average ET_rF over the 24-h average. The consistency of ET_rF over a day has been demonstrated by various studies, including Romero (2004), Colaizzi et al. (2006) and Allen et al. (2007a).

The assumption of constant ET_rF during a day has been shown to be valid for agricultural crops that have been developed to maximize photosynthesis and thus stomatal conductance. The advantage of using ET_rF is that it accounts for the increase in ET_{24} that can occur under advective conditions, impacts of which are represented well by the Penman-Monteith equation.

The ET_{24} (mm/day) is computed for each image pixel as

$$ET_{24} = (EF)(R_{n24}) \tag{13.7}$$

or

$$ET_{24} = C_{rad}(ET_rF)(ET_{r24}) \tag{13.8}$$

where ET_rF (or EF) is assumed equal to the ET_rF (or EF) determined at the satellite overpass time, ET_{r24} is the cumulative 24-h ET_r for the day of the image, and C_{rad} is a correction term used in sloping terrain to correct for variation in 24-h vs. instantaneous energy availability.

After ET and ET_rF have been determined using the energy balance and the application of the single dT function, then, when interpolating between satellite images, a full grid for ET_r is used for the extrapolation over time to account for both spatial and temporal variation in ET_r. The ET_r grid is generally made on a 3- or 5-km base using as many quality-controlled weather stations located within and in the vicinity of the study area as are available. Depending on data availability and the density of the weather stations, various gridding methods can be used, including kriging, inverse distance, and splining.

Monthly and seasonal evapotranspiration "maps" are derived from a series of ET_rF images by interpolating ET_rF on a pixel-by-pixel basis between processed images and multiplying, on a daily basis, by the ET_r for each day. The interpolation of ET_rF between image dates is not unlike the construction of a seasonal K_c curve (Allen et al. 1998), where interpolation is done between discrete values for K_c.

The METRIC approach assumes that the ET for the entire area of interest changes in proportion to change in ET_r at the weather station. This is a generally valid assumption and is similar to the assumptions used in the conventional application of $K_c \times ET_r$. This approach is effective in estimating ET for both clear and cloudy days between the clear-sky satellite image dates. Tasumi et al. (2005) showed that the ET_rF was consistent between clear and cloudy days using lysimeter measurements at Kimberly, Idaho. ET_r is computed at a specific weather station location and therefore may not represent the actual condition at each pixel. However, because ET_r is used only as an index of the relative change in weather, specific information at each pixel is retained through the ET_rF.

Cumulative ET for any period, for example, month, season, or year is calculated as:

$$ET_{\text{period}} = \sum_{i=m}^{n} \left[\left(ET_rF_i \right) \left(ET_{r24\,i} \right) \right] \tag{13.9}$$

where ET_{period} is the cumulative ET for a period beginning on day m and ending on day n, ET_rF_i is the interpolated ET_rF for day i, and ET_{r24i} is the 24-h ET_r for day i. Units for ET_{period} will be in mm when ET_{r24} is in mm d^{-1}. The interpolation between values for ET_rF is best made using a curvilinear interpolation function (e.g., a spline function) to better fit the typical curvilinearity of crop coefficients during a growing season (Wright 1982). Generally, one satellite image per month is sufficient to construct an accurate ET_rF curve to estimate seasonal ET (Allen et al. 2007a). During periods of rapid vegetation change, a more frequent image interval may be desirable. Examples of splining ET_rF to estimate daily and monthly ET are given in Allen et al. (2007a) and Singh et al. (2008).

Moderately high-resolution satellites, such as Landsat, provide the opportunity to view evapotranspiration on a field-by-field basis, which can be valuable for water rights management, irrigation scheduling, and discrimination of ET among crop types (Allen et al. 2007b). The disadvantage of high-resolution imagery is less frequent image acquisition. In the case of Landsat, the return interval is 16 days. As a result, monthly ET estimates are based on one or two satellite images per month; however, for areas influenced by clouds, there may be 32 or more days between high-quality images. This can be rectified by combining multiple Landsats (5 with 7) or by using data fusion techniques, where a more frequent but more coarse system like MODIS is used as a carrier of information during periods without quality Landsat images (Gao et al. 2006; Anderson et al. 2010).

13.5 METRIC Applications for Morocco Water Management

13.5.1 Study Area

The World Bank and government of Morocco's Oum Er Rbia Irrigated Agriculture Modernization Project (MA Project) selected 12 irrigation pilot sectors in 3 ORMVA (Office Régional de Mise en Valeur Agricole) water management districts in the Oum Er Rbia basin and in the adjacent Tensift river basin. Some of the pilot sectors were selected for early project irrigation improvements or modernization; others were selected as comparison sectors to assess project impacts (Driss). Figure 13.2 shows the pilot sectors and ORMVA boundaries; Haouz and Tadla are located near the base of the Atlas Mountains, while Doukkala is near the Atlantic coast. These three ORMVAs contain 356,220 Ha of developed irrigated agriculture (El Faiz et al. 2001).

13.5.2 Method

The Tadla, Doukkala, and Haouz water districts required a standard METRIC application, described in Sect. 4, although surface temperature was calculated

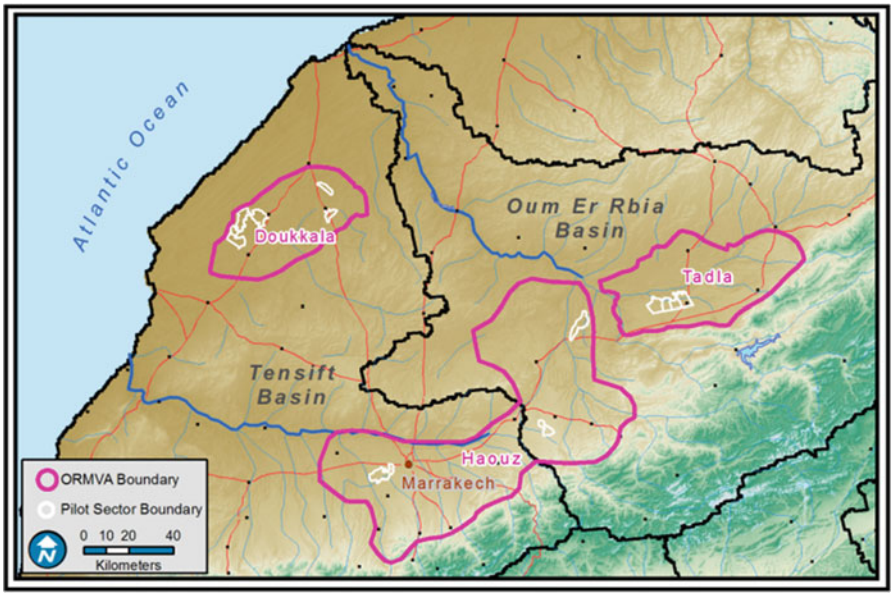

Fig. 13.2 Overview of study area showing Morocco water districts (ORMVAs) Tadla, Doukkala, and Haouz and pilot irrigation sectors

Table 13.1 Weather stations providing meteorological data for the three water districts (ORMVAs)

ORMVA	Weather station	Elevation (m)	Latitude (N)	Longitude (W)	Data quality
Tadla	Oulad Gnaou	450	32.290	6.522	Good
Doukkala	Khemis Zemamra	165	32.622	8.699	Good
Haouz	Ounasda	430	32.117	7.350	Good

using the traditional SEBAL approach (Bastiaanssen et al. 1998; Hong 2008) because METRIC required calibration coefficients that are not available for Morocco. These and other details of the study are fully described in the project final report (Riverside Technology, Inc. 2010).

Morocco has a network of weather stations that provided meteorological data for agriculture, water management, and other applications. Bi-hourly data from three of these stations (Table 13.1) were acquired for this study and included the following parameters: actual vapor pressure, solar radiation, wind speed and direction, relative humidity, air temperature and dew point, and computed reference ET (alfalfa). The meteorological data required quality control, including some filling and error correction, but overall were of good quality and adequate for this study.

A complete inventory of available Landsat 5 images and key meteorological inputs was conducted for each of the three Morocco water districts. A total of 18 Landsat images were acquired and processed for the 2006–2007 study period; an example Landsat image of the Doukkala district is shown in Fig. 13.3. Landsat 5 images are acquired every 16 days, whereas the lower resolution MODIS images are acquired much more frequently. For most places on the earth, two MODIS measurements per day are collected, one in the morning (Terra) and another in the afternoon (Aqua). However, the view angle on some days can be as much as 57° off nadir, reducing the clarity of image detail and mixing information among adjacent pixels. Typically an image is collected every 4 days with each MODIS satellite when the view angle is within ± 20° of nadir, yielding high detail (up to 250 m in the red and near infrared bands). For parts of the study region, the time periods between cloud-free Landsat images were 32 or more days, requiring interpolation of ET_rF. Because of these excessive time gaps between useful Landsat images, Allen and Trezza (2009) developed a data fusion method for extending the METRIC-based ET record using MODIS as a transfer mechanism between Landsat images. For this technique, ratios of ET_rF were developed from the cloud-free Landsat images (30-m ground resolution) to the underlying NDVI from MODIS images (250-m resolution) acquired on, or about, the same day. The ratios were then interpolated between Landsat images, and for every available MODIS date, ET_rF was estimated by multiplying MODIS NDVI by the interpolated ratios. The result was a time-integrated ET_rF that followed the evolution of NDVI as monitored by MODIS, but retained much of the 30-m resolution of Landsat. This technique does not account directly for evaporation from precipitation or irrigation occurring between Landsat image dates; rather, it estimates evaporation for the image gap period based on the wetting frequencies prior to and beyond the endpoint Landsat image dates.

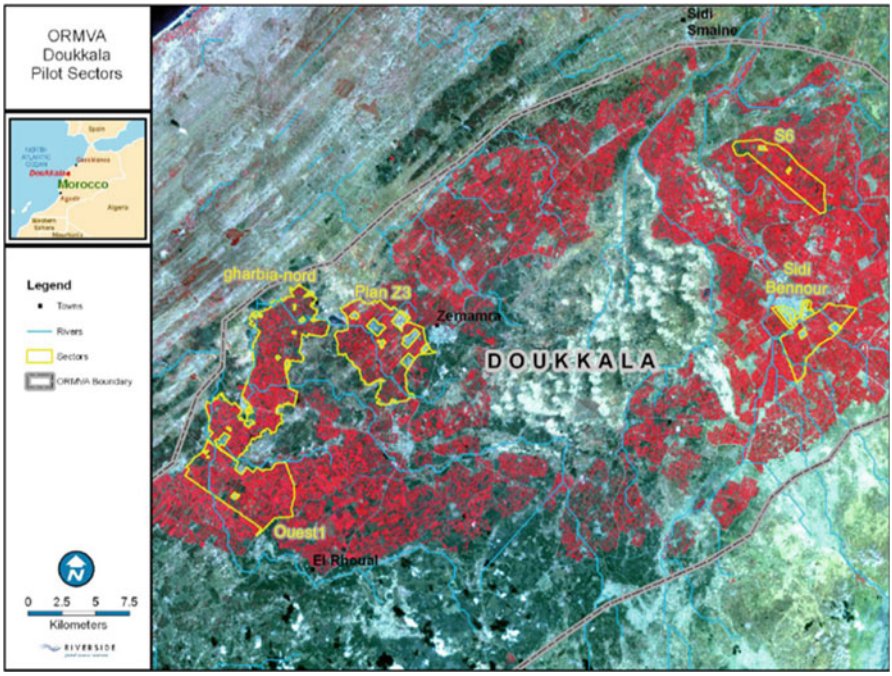

Fig. 13.3 Landsat image of ORMVA Doukkala Pilot sectors

As a result of applying the METRIC methodology, daily images of spatially distributed fractions of the calculated reference ET value (ET_rF) became available. These maps (referred to as ET_rF maps) were derived from the METRIC-processed Landsat images interpolated daily via correlation with reference meteorological data and cubic splining. Monthly and seasonal estimates of actual ET were computed with GIS analysis by summation of the daily ET images.

13.5.3 ET Estimates

By applying the METRIC method and interpolation techniques and combining MODIS and Landsat data, ET results for individual parcels were discerned nearer to the original 30-m resolution of Landsat images than to the 250-m resolution of the MODIS-based NDVI. This was accomplished by ratio of 30-m pixels for ET_rF/NDVI, allowing ET_rF_L/$NDVI_M$ ratios along field edges to retain much of their boundary definition. As shown in Fig. 13.4, the edges of irrigation center pivot parcels remain relatively clear and well defined. The derived ET_rF for some interior pixels takes on the blocky form of the 250-m MODIS NDVI pixels.

Monthly ET images were generated by multiplying daily ET_rF by the corresponding daily alfalfa-based reference evapotranspiration (ET_r) within a monthly cubic splining

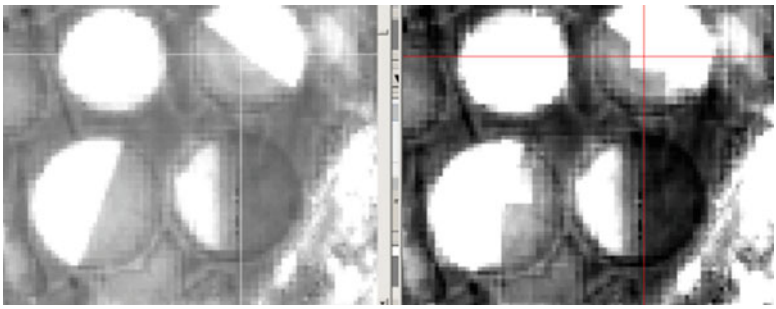

Fig. 13.4 ETrF derived from Landsat (*left*) and ETrF for the same area derived from a MODIS image (*right*) using the ETrFL/NDVIM ratio technique

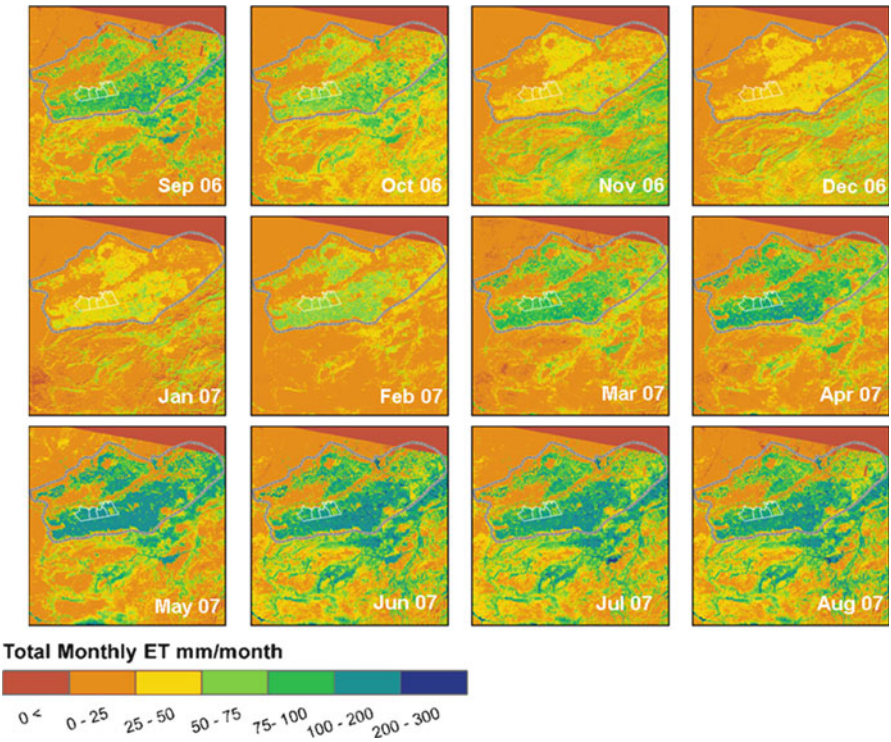

Fig. 13.5 METRIC model results of monthly ET images for the ORMVA Tadla

interpolation procedure. ET_r values represent the ET rate expected from a well-defined surface of full-cover alfalfa and are computed using the point weather data from the weather stations listed in Table 13.1. The resulting monthly ET maps provided the basis for review and further analyses. For the ORMVA Tadla (Fig. 13.5), ET is shown in mm/month for each 30-m pixel for the entire irrigated area and for the pilot irrigation schemes targeted by the World Bank-funded irrigation improvement project.

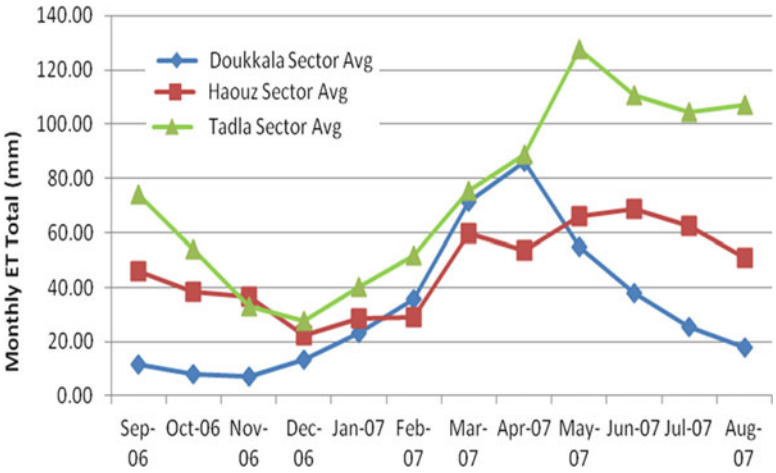

Fig. 13.6 Distribution of monthly ET for each ORMVA

Using this monthly time series of spatially distributed ET, simple GIS analysis produced statistics and charts for each of the three study areas. For example, monthly mean ET by ORMVA (Fig. 13.6) shows Tadla with consistently higher ET throughout the year, indicating higher quantity and more effective irrigation as compared with Doukkala and Haouz. Also, the temporal distribution of ET_{act} for Tadla shows a later and more extended peak, sustained much later into the summer than the other areas, which are known to have a more limited irrigation water supply. For Doukkala, the primary growing season (indicated by peak ET_{act}) is relatively short, with 65–70% of the total annual ET_{act} occurring during February through May.

Annual ET maps for the period of study, Sept 2006–Aug 2007, are shown in Fig. 13.7 for each of the three ORMVA study areas. An enlargement of the association annour in the Tadla area is shown to illustrate the detail achieved for the ET maps. Annual ET values greater than approximately 400 mm are shown in the predominantly irrigated areas. In the relatively well-watered Tadla ORMVA, the irrigated areas are particularly pronounced with annual ET typically exceeding 800 mm.

13.6 Water Balance Analysis

13.6.1 Method

A simplified water balance analysis was conducted at the irrigation sector level for each ORMVA on a monthly time step with surface and subsurface storage assumed

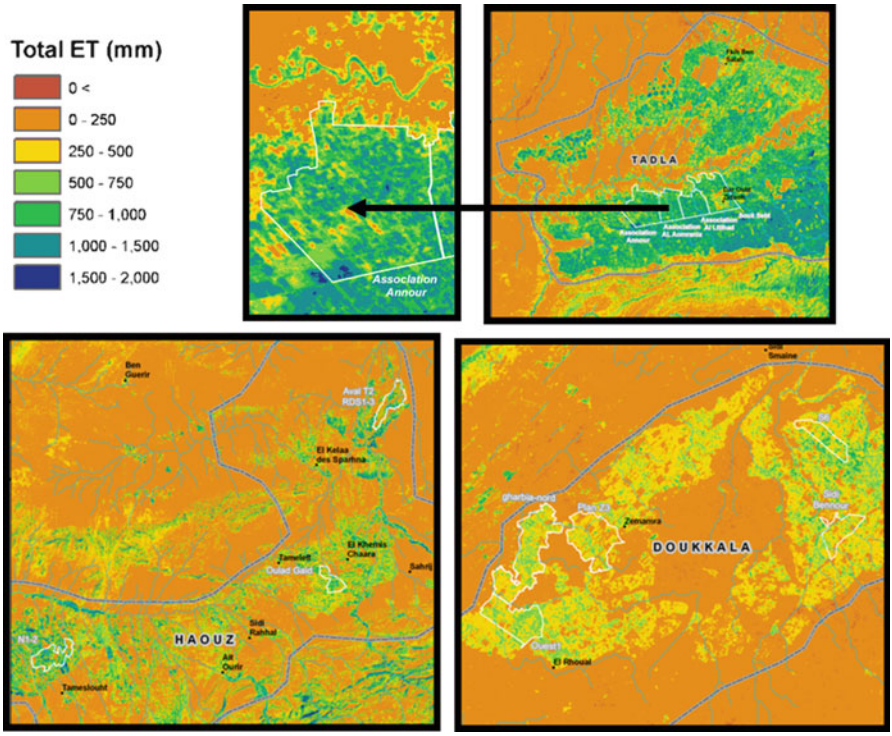

Fig. 13.7 Annual ET (Sept. 2006–Aug. 2007) for all three ORMVAs with an enlargement of a pilot irrigation sector in Tadla showing detail of Landsat and METRIC model results

to be zero. The water balance was formulated as an estimate of the irrigation supplied by groundwater resources:

$$GW_{\text{abstract}} = ET_{\text{act}} - P_{\text{effect}} - SW_{\text{irrig}} \tag{13.10}$$

where GW_{abstract} is the groundwater resources abstracted for irrigation and consumed by crops; ET_{act} is the actual evapotranspiration—the total crop consumption—taken from the METRIC-derived actual ET maps; P_{effect} is the effective precipitation that contributes to satisfying crop demands and computed from gridded precipitation estimates based on weather station data analysis described in Sect. 4 and validated with satellite-based grid data; and SW_{irrig} is the surface water irrigation deliveries per ORMVA records for each irrigated perimeter (average size approximately 100 ha), with volumes converted to irrigation depth based on adjusted irrigated sector areas calculated using GIS tools. In addition, a groundwater indicator was derived for monitoring and assessing irrigation performance:

$$\text{GW Indicator } (\%) = (GW_{\text{abstract}}/ET_{\text{act}}) \times 100 \tag{13.11}$$

A secondary performance indicator known as depleted fraction (DF), taken from Kselik et al. (2008) was computed as

$$DF = ET_{\text{act}}/(P_{\text{effect}} + SW_{\text{irrig}}) \tag{13.12}$$

A DF value less than 1.0 would indicate that groundwater resources are not required to supplement the precipitation and surface water supplies to meet crop demands.

In addition to assessing irrigation water management for the study period, these water balance and performance indicators should provide water managers and decision-makers with data for long-term monitoring as water management improvement measures are implemented.

13.6.2 Water Balance Analysis Results

All input data required for the monthly water balance analysis were prepared as GIS-compatible files. A water balance analysis tool was developed to aid in computing and visualizing results in both tabular and graphical form. Table 13.2 shows ET summaries by pilot sectors for each corresponding ORMVA. Figure 13.8 displays the annual data in graphical form.

Water balance results (Table 13.2 and Fig. 13.8) display annual ET_{act}, effective precipitation, surface water irrigation, and groundwater abstraction. The average annual ET_{act} estimates for the Tadla sectors are more than 50% higher than for the Haouz sectors and more than double those in the Doukkala sectors, based on a weighted average over the total area of the investigated sectors within the ORMVAs.

On an annual basis, the average unit volume of surface water available for the investigated sectors in Tadla is 99% greater than the amount available for Haouz and 78% greater than the amount available for Doukkala. This is consistent with, and likely a contributor to, the lower ET_{act} reported above for these two sectors. In addition, based on the water balance analysis results, the contribution of groundwater resources (as evident in the values of GW_{abstract} and GW Indicator) is higher for Tadla and Haouz than for the Doukkala sectors.

The weighted average annual GW Indicator is 30.5% for the sectors in Tadla, 36.7% for the sectors in Haouz, and −19.3% for the sectors in Doukkala. In terms of DF, the weighted average annual value is 1.44 for the investigated sectors in Tadla, 1.63 for the sectors in Haouz, and 0.91 for the sectors in Doukkala. In Table 13.2, performance indicators are shown for each of the pilot sectors. DF value less than 1.0 for sectors would indicate that groundwater resources are not required to supplement the precipitation and surface supplies to meet crop demands.

Extensive analysis was conducted for each of the irrigation sectors, including water balance analysis providing groundwater recharge estimates where consumptive

Table 13.2 Water balance analysis results (Sept. 2006–Aug. 2007)

ORMVA	Sector	Irrig. area (Ha)	ET_{act} (mm)	P_{effect} (mm)	SW_{irrig} (mm)	$GW_{abstract}$ (mm)	GW indicator (% of ET_{act})	Depleted fraction
Tadla	AUEA Arraja	2,691	827	142	450	235	28.4	1.40
Tadla	AUEA Alittihad	1,745	990	142	515	333	33.6	1.51
Tadla	AUEA Alomrania	1,858	903	142	529	231	25.6	1.34
Tadla	AUEA Annour	3,178	859	142	429	288	33.5	1.50
Haouz	RD N1-2	4,350	642	111	219	313	48.7	1.95
Haouz	Oulad Gaid	2,146	592	111	258	223	37.7	1.61
Haouz	RD S1.3	3,716	453	111	243	99	21.9	1.28
Doukkala	Nord-Gharbia	4,380	377	181	223	−27	−7.2	0.93
Doukkala	Ouest 1-Gharbia	2,698	447	181	242	23	5.2	1.05
Doukkala	S6-Sidi Smail	1,303	449	181	176	92	20.4	1.26
Doukkala	sidi Bennour small sectors	1,241	374	181	202	−10	−2.6	0.98
Doukkala	Z3-Zem amra	2,858	320	181	415	−276	−86.4	0.54

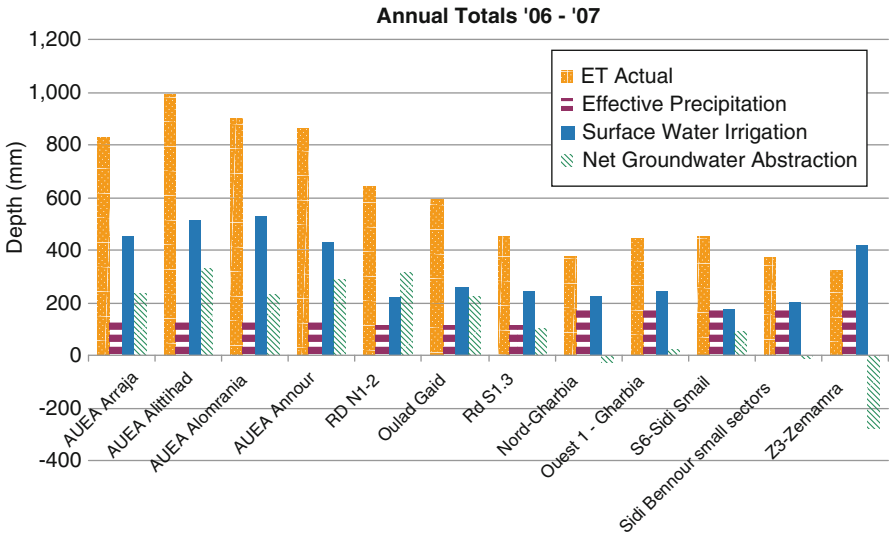

Fig. 13.8 Water balance analysis results (Sept. 2006–Aug. 2007) for the four Tadla sectors (*left*), three Haouz sectors (*middle*), and five Doukkala sectors (*right*)

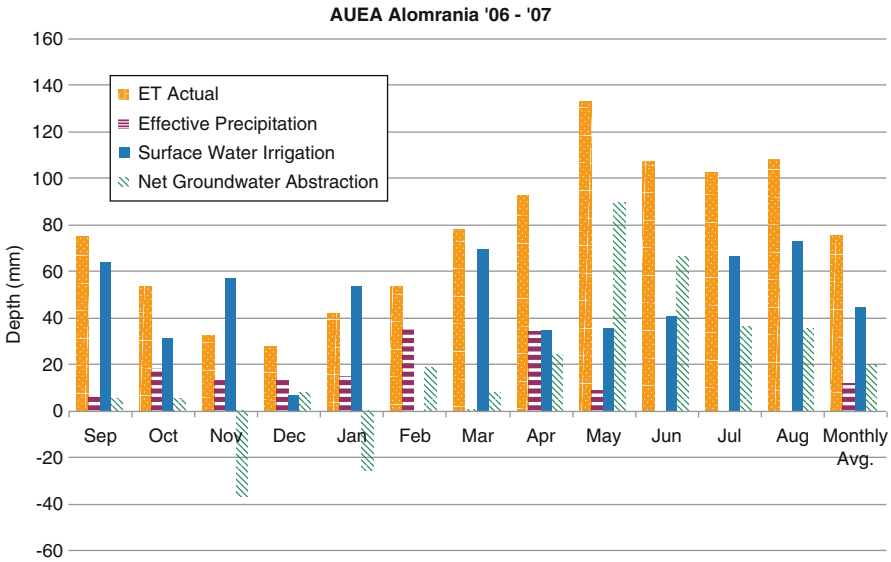

Fig. 13.9 Monthly water balance in sector AUEA Alomrania (Tadla) showing high rates of groundwater use during May and June and very low use or recharge during September–March

use is lower than observed system inputs. Monthly results for a pilot sector, AUEA Alomrania, are shown in Fig. 13.9 as a representative example of the detailed analysis conducted for each of the sectors in the three ORMVAs. In this sector, there is a net recharge for the months of November and January.

13.7 Summary and Conclusion

Global studies suggest that North Africa and the Mediterranean will be significantly affected by future climate change with increases in temperature and likely decreases in the availability of water resources. The remote sensing, GIS, and modeling tools developed under this study provided objective estimates of actual ET for important irrigated agriculture in Morocco. Combined with conventional data on surface water deliveries, analysis of the ET results provide managers with water balance and estimates of groundwater pumping, which are especially useful for monitoring in regions with limited, reliable ground information. The monthly, high-resolution ET maps provide spatial and temporal data for analysis and visualization of irrigation water use. The results are being used by the government of Morocco and the World Bank as a baseline condition prior to implementation of the irrigation system improvement project. A similar analysis is planned for mid- and post-project conditions to assess the impacts of the project improvements and interventions on irrigation water efficiency and conservation. Combined with socioeconomic information, the results ultimately will be used to assess the impacts of the project on poverty reduction in the targeted rural areas of Morocco.

Application of METRIC for ET mapping at Landsat scale can be used to assess the impacts of climate change on future water consumption. Rates and spatial variation of ET are derived over large areas and at relatively fine resolution, providing substantial input to other hourly or daily land surface process models that can, in turn, be applied with climate projections. Because METRIC requires no a priori knowledge of soil water content, the ET estimates from METRIC are independent of biases or assumptions regarding vegetation physiology and phenology. This allows derivation of vegetation-related parameters by inverting components of the energy balance produced by METRIC with less bias and independent of the process models.

A METRIC-produced image from Landsat or MODIS satellites can be sampled using basic GIS analysis to provide numerous combinations of ET, vegetation amount, relative water availability, and ambient air and surface temperature. Analysis of these combinations can increase understanding of how various vegetation communities may behave under different levels of water, environmental, and management stressors. METRIC and other satellite-based analyses also provide the means to extend local studies and measurements of surface energy and CO_2 fluxes to much larger areas by confirming or bias-correcting model calibration and for particular vegetation types.

Acknowledgements Some contents in Sect. 4 describing the METRIC model are derived from Allen et al. (2011).

This work was funded by the World Bank under the guidance of Mr. Hassan Lamrani, the World Bank, Rabat. The authors recognize and thank the Tadla, Doukkala, and Haouz ORMVAs for providing data and insight into irrigation systems management and operations.

In addition to the authors, this study was conducted by a team of scientists and engineers from Morocco and USA (in alphabetical order): Graeme Aggett, Nils Babel, Omar Berkat, Mohammed Bourass, Jan Hendrickx, Said Ouattar, Claudio Schneider, and Ricardo Trezza. The views, opinions, and findings contained in this publication are those of the authors and should not be considered official position, policy, or decision.

References

ASCE – EWRI (2005) The ASCE Standardized reference evapotranspiration equation. ASCE-EWRI Standardization of reference evapotranspiration task comm. report, ASCE Bookstore, ISBN 078440805, Stock Number 40805, p 216

Agoumi A (2003) Vulnerability of North African countries to climatic changes: adaptation and implementation strategies for climate change, International Institute for Sustainable Development, Winnipeg, 14p

Allen R, Trezza R (2009) Combining MODIS vegetation indices to extend Landsat-based METRIC estimates in morocco. Report to Riverside Technology, Inc., Fort Collins

Allen RG, Pruitt WO, Businger JA, Fritschen LJ, Jensen ME, Quinn FH (1996) Chap. 4: Evaporation and transpiration. In: Wootton TP et al (eds) ASCE handbook of hydrology. ASCE, Reston, pp 125–252

Allen RG, Pereira LS, Raes D, Smith M (1998) Crop evapotranspiration: guidelines for computing crop water requirements. United Nations FAO, irrigation and drainage Paper 56, Rome, 1998, p 300. http://www.fao.org/docrep/X0490E/X0490E00.htm. Accessed 5 Feb 2007

Allen RG, Tasumi M, Trezza R (2005) Benefits from tying satellite-based energy balance to ground-based reference evapotranspiration. In: Earth observation for vegetation monitoring and water management. AIP conference proceedings, vol 852. ISBN 0-7354-0346-5, AIP, College Park, pp 127–137

Allen RG, Tasumi M, Morse A, Trezza R, Wright JL, Bastiaanssen W, Kramber W, Lorite I, Robison C (2007a) Satellite-based energy balance for mapping evapotranspiration with internalized calibration (METRIC) – applications. J Irrig Drain Eng (ASCE) 133:395–406

Allen RG, Tasumi M, Trezza R (2007b) Satellite-based energy balance for mapping evapotranspiration with internalized calibration (METRIC) – model. J Irrig Drain Eng (ASCE) 133:380–394

Allen R, Irmak A, Trezza R, Hendrickx JMH, Bastiaanssen W, Kjaersgaard J (2011) Satellite-based ET estimation in agriculture using SEBAL and METRIC. Hydrol Process 25:4011–4027. doi:10.1002/hyp. 8408

Anderson MC, Kustas WP, Dulaney W, Feng G, Summer D (2010) Integration of multi-scale thermal satellite imagery for evaluation of daily evapotranspiration at the sub-field scale. Remote sensing and hydrology symposium 2010. Jackson Hole, p 62

Arnell NW (1999) Climate change and global water resources. Glob Environ Chang 9:S31–S49

Bastiaanssen WGM (1995) Regionalization of surface flux densities and moisture indicators in composite terrain: a remote sensing approach under clear skies in Mediterranean climates. Ph.D. Diss., CIP Data Koninklijke Bibliotheek, Den Haag, p 273

Bastiaanssen WGM (2000) SEBAL-based sensible and latent heat fluxes in the irrigated gediz basin. Turkey J Hydrol 229:87–100

Bastiaanssen WGM, Menenti M, Feddes RA, Holtslag AAM (1998) A remote sensing surface energy balance algorithm for land (SEBAL): 1. Formulation. J Hydrol 212–213:198–212

Bastiaanssen WGM, Noordman EJM, Pelgrum H, Davids G, Thoreson BP, Allen RG (2005) SEBAL model with remotely sensed data to improve water-resources management under actual field conditions. J Irrig Drain Eng (ASCE) 131(1):85–93

Bennani A, Buret J, Senhaji F (2001) Communication Nationale Initiale a la Convention Cadre des Nations Unies sur les changements climatiques. Ministe're de l'Ame´nagement du Territoire, de l'Urbanisme de l'Habitat et de l'Environnement, 101pp, Royaume du Maroc

Born K, Christoph M, Fink A, Kinppertz P, Paeth H, Sperth P (2008a) Moroccan climate in the present and future: combined view from observational data and regional climate scenarios. In: Zereini F, Hoetzl H (eds) Climatic changes and water resources in the Middle East and in North Africa. Springer, Wien, pp 29–45. ISBN 978-3-540-85046-5

Born K, Fink A, Paeth H (2008b) Dry and wet periods in the northwestern Maghreb from present day and future climate conditions. Meteorol Zeit 17:533–551

Chaouki N, Stockton C, Myers D (1995) Spatio-temporal patterns of drought in morocco. Int J Climatol 15:187–205

Colaizzi PD, Evett SR, Howell TA, Tolk JA (2006) Comparison of five models to scale daily evapotranspiration from one-time-of-day measurements. Trans ASABE 49(5):1409–1417

Driouech F, Deque M, Sanchez-Gomez E (2010) Weather regimes – Moroccan precipitation link in the regional climate change simulation. Glob Planet Change 72(1–2):10

El Faiz, M, El Gouch M, El Gueroua A (2001) ISIIMM project: case studies synthesis Morocco, case of the Haouz of Marrakech and of the Aït Bougmez valley, Institutional and Social Innovations in Irrigation Mediterranean Management, Euro-Mediterranean Regional Programme for Local Water Management ME8/AIDCO/2001/0515/59763-P016, Agropolis International, 62p

El Ghissassi A (2005) Moroccan national committee reviews the press: favourable to dams! The Dams Newsletter – no. 4, p 11, ICOLD-CIGB, Paris

Gao F, Masek J, Schwaller M, Hall F (2006) On the blending of the landsat and modis surface reflectance: predicting daily landsat surface reflectance. IEEE Trans Geosci Remote Sens 44:2207–2218

Hong S (2008) Mapping regional distributions of energy balance components using optical remotely sensed imagery. Unpublished PhD Dissertation, New Mexico Institute of Mining and Technology, Department of Earth and Environmental Science, Socorro, New Mexico, 378p

Hulme M, Wigley T, Barrow E, Raper S, Centella A, Smith S, Chipanshi A (2000) Using a climate scenario generator for vulnerability and adaptation assessments. Climatic Research Unit, University of East Anglia, Norwich and the National Communications Support Programme, UNDP/GEF, New York, 51pp

IPCC (2007) Summary for policymakers. In: Solomon S, Qin D et al (See reference in Spain paper)

Jensen ME, Burman RD, Allen RG (eds) (1990) Evapotranspiration and irrigation water requirements, ASCE Manuals and Reports on Engineering Practice No. 70. ASCE, Reston, p 332. ISBN 0-87262-763-2

Jung M, Reichstein M, Ciais P, Seneviratne S, Sheffield J, Goulden M, Bonan G, Cescatti A, Chen J, de Jeu R, Dolman J et al (2010) Recent decline in the global land evapotranspiration trend due to limited moisture supply. Nature 467:951–954

Kselik RAL, Bos MG, Hammani A, Bellouti A (2008) Assessment of sustainable agriculture in the irrigated perimeter of Tadla, Morocco using the CRIWAR strategy module. IWRA conference paper 2008

Ministry of Agriculture Morocco (2008) Plan Maroc Vert: Premieres, perspectives sur la strategie agricole. Ministere de l'Agriculture, Rue Patrice Lumumba, Rabat, Morocco, Avril 2008

Morse A, Kramber WJ, Allen RG, Tasumi M (2005) Mapping evapotranspiration using Landsat and the METRIC evapotranspiration model. Idaho Department of Water Resources, Boise, ID and University of Idaho, Kimberly Research Center, Kimberly, ID

Patricola C, Cook K (2010) Northern African climate at the end of the twenty-first century: an integrated application of regional and global climate models. Clim Dyn 34:193–212

Ragab R, Prudhomme C (2002) Climate change and water resources management in arid and semi-arid regions: prospective and challenges for the 21st century. Biosyst Eng 1(1):3–34

Riverside Technology, Inc. (2010) Satellite based evapotranspiration mapping and water user by rural communes of Morocco. Final Report to The World Bank, TF056929 – BNPP Water Resources Management Program II (BNWPP), Rabat

Romero MG (2004) Daily evapotranspiration estimation by means of evaporative fraction and reference ET fraction. Ph.D. dissertation, Utah State Univ, Logan

Singh RK, Irmak A, Irmak S, Martin DL (2008) Application of SEBAL model for mapping evapotranspiration and estimating surface energy fluxes in South-Central Nebraska. J Irrig Drain Eng 134(3):273–285

Tasumi M, Allen RG, Trezza R, Wright JL (2005) Satellite-based energy balance to assess within-population variance of crop coefficient curves. ASCE J Irrig Drain Eng 131(1):94–109

Wright JL (1982) New evapotranspiration crop coefficients. J IrrigDrain Div (ASCE) 108:57–74

.

Chapter 14
Snow Cover

Peter Romanov

Abstract Satellites present an important component of the global snow observing system. Routine monitoring of the snow cover properties from space started in late 1960s. In this chapter, an overview is provided of techniques developed and used to identify snow cover in satellite images and to generate maps of snow cover distribution. The reviewed techniques include an interactive approach where snow maps are manually generated by human analysts through a visual examination of satellite imagery and automated algorithms that utilize satellite observations in multiple bands in the optical, infrared, and microwave spectral range. Satellite-based retrievals of the extent and the spatial distribution of snow cover are accurately and spatially detailed. Estimates of bulk snow pack properties such as the snow depth and the snow water equivalent are less reliable since they are strongly dependent on other snow pack features, particularly on the snow grain size and the snow pack stratification.

Keywords Snow cover extent • Satellite sensors • Remote sensing • Optical microwave

14.1 Introduction

Terrestrial snow has the largest geographic extent of the cryosphere components. It covers nearly 50 million km^2 of the Northern Hemisphere (NH) continent in winter, affecting heavily populated mid-latitude regions as well as higher latitudes. The extent of seasonal and perennial snow cover in the Southern Hemisphere is smaller, up to about 1 million km^2, but it still presents an important hydrological

P. Romanov (✉)
National Oceanic and Atmospheric Administration/National Environmental Satellite, Data, and Information Service, Office of Research and Applications, 5830 University Research Court, College Park, MD 20740, USA
e-mail: peter.romanov@noaa.gov

J.J. Qu et al. (eds.), *Satellite-based Applications on Climate Change*,
DOI 10.1007/978-94-007-5872-8_14,

factor controlling water budget and affecting pastoral farming in many mountain regions. The high sensitivity of snow to changes in temperature and precipitation makes it a primary indicator of climate change.

For over three decades, satellites have been actively used for large-scale monitoring of snow cover from regional to global scales. Owing to frequent scene revisits, wide-area coverage and high spatial resolution satellite observations can effectively supplement ground-based measurements and provide near-real-time spatially detailed information on the snow cover distribution. Different techniques both automated and interactive have been developed and applied to infer information on snow from satellite imagery. The developed snow mapping techniques utilize satellite measurements in the visible, near-IR, infrared (IR) and in the microwave spectral bands.

14.2 Interactive Snow Mapping Technique and Product

Since 1966 NOAA has been generating snow cover charts for the Northern Hemisphere. Maps are drawn interactively by analysts who rely primarily on the optical imagery from geostationary and polar-orbiting satellites (Ramsay 1998). Until 1997 snow maps were produced on a coarse grid with about 180 km cell size on a weekly basis. In 1998 the temporal and spatial resolution of the maps was increased to daily and 24 km, respectively, and in 2004 the spatial resolution of the product was further improved to 4 km (Helfrich et al. 2007) (see an example of the daily chart in Fig. 14.1). NOAA's interactive snow cover charts are the longest satellite-derived record of snow extent. This dataset has been used as the basis for many analyses of snow cover variability and change on a hemispheric and continental basis (e.g., Robinson et al. 1993; Dery and Brown 2007). At NOAA, the National Weather Service (NWS) interactive snow maps are used to initialize operational numerical weather prediction (NWP) models (Ek et al. 2003).

From the climatological point of view, a drawback of the NOAA interactive snow charts consists in the change of the temporal and, especially, of the spatial resolution of the product which introduced inhomogeneity in the snow extent time series. Although NOAA analysts are instructed to use a "50% coverage rule" when deciding whether the grid cell is snow covered or snow free, they typically follow an "aggressive" approach preferring commission errors in snow mapping to omission errors and therefore tend to overestimate the extent of a patchy and intermittent snow cover. D. A. Robinson (2006, personal communication) has found that at coarser spatial resolution, analysts map considerably more snow in the mountainous areas in fall and spring. Due to the same reason, the snow extent in coarser resolution maps may also be overestimated along the snow boundary.

Assessment of the Northern Hemisphere snow extent derived from the NOAA interactive snow and ice charts has revealed an above average coverage in the middle of 1970s and a substantial decline in the yearly average snow-covered area during 1980s and beginning of 1990s. Later in the second half of 1990s, the snow

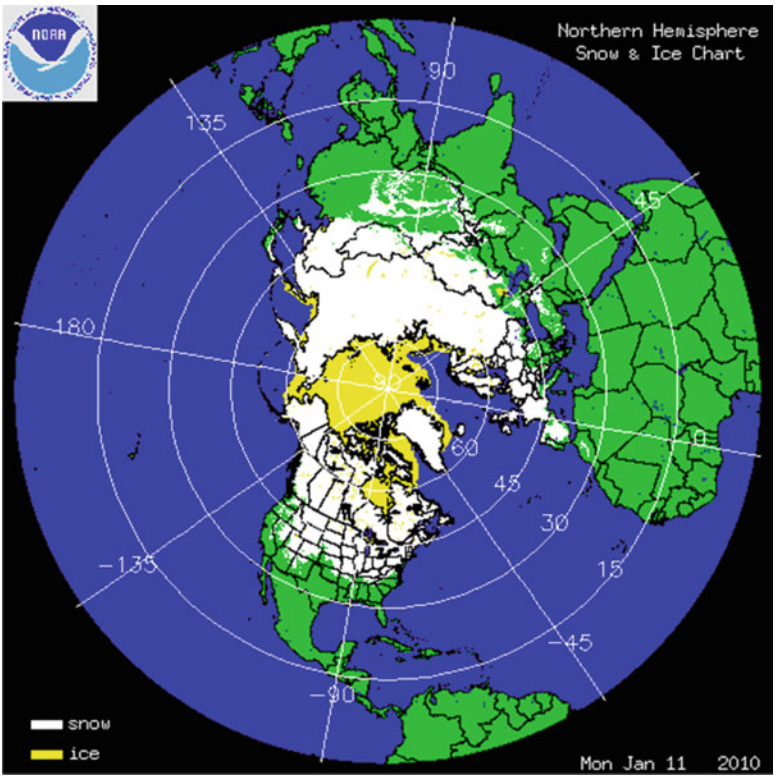

Fig. 14.1 Example of the daily snow and ice cover map for the Northern Hemisphere generated within NOAA interactive multisensor snow and ice mapping system (IMS). On the web at http://www.natice.noaa.gov/ims/

extent recovered and remained close to its average values from late 1990s into the beginning of the twenty-first century. Despite this recovery, the overall trend in the satellite-derived snow extent since early 1970s remains negative. Figure 14.2 illustrates the differences in NH springtime snow cover for the period 1988–2004 relative to the period 1967–1987 derived from NOAA interactive snow cover charts. While there are some areas where snow cover increased, overall the extent of snow cover in spring has declined.

14.3 Snow Retrievals with Microwave Sensors Data

Since 1978 global observations of the snow cover have been performed using microwave measurements from Nimbus-7 Scanning Multichannel Microwave Radiometer (SMMR) and later, since 1987, with the Special Sensor Microwave Imager (SSM/I) flown by the Defense Meteorological Satellite Program (DMSP)

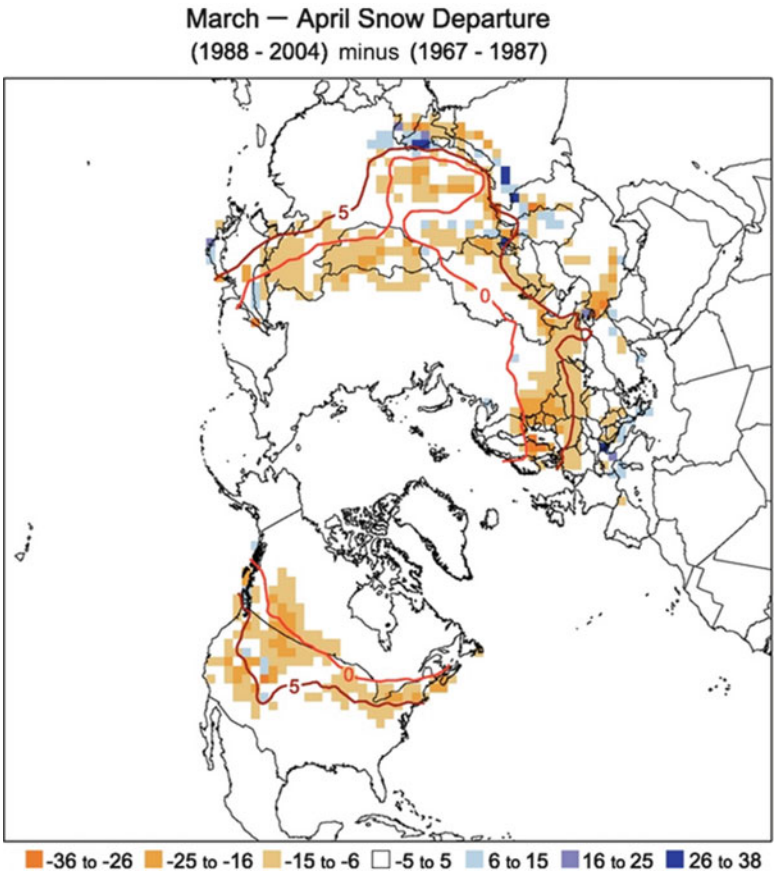

Fig. 14.2 Differences in the distribution of Northern Hemisphere March–April average snow cover between earlier (1967–1987) and later (1988–2004) portions of the satellite era (expressed in % coverage). *Negative values* indicate greater extent in the earlier portion of the record. Extents are derived from NOAA/NESDIS snow maps. *Red curves* show the 0 and 5°C isotherms averaged for March and April 1967–2004, from the Climatic Research Unit (CRU) gridded land surface temperature version 2 (CRUTEM2v) data (From IPCC 2007)

(e.g., Grody and Basist 1996). Snow cover products have been also generated from the Advanced Microwave Sounding Unit (AMSU) onboard NOAA polar-orbiting satellites (Kongoli et al. 2004) and from the Advanced Microwave Sounding Radiometer (AMSR-E) onboard the Aqua satellite (Kelly et al. 2003). Most clouds are transparent in the microwave which makes microwave snow remote sensing techniques practically weather independent. Microwave-based techniques also attract a lot of interest due to their ability (although rather limited) to provide information on physical properties of the snow pack, particularly on its depth and water equivalent. To identify snow in satellite imagery, most algorithms utilize observations of upwelling microwave radiance at two frequencies, typically 19 and 37 GHz. Algorithms to infer

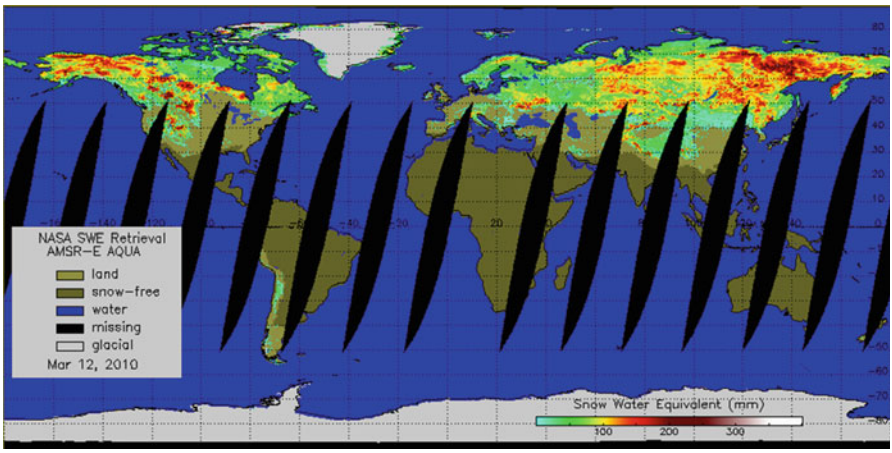

Fig. 14.3 Example of a global map of snow water equivalent (SWE) derived from observations of AMSR-E onboard Aqua satellite. SWE retrievals are not reliable and therefore are not performed over Antarctica and most of Greenland. AMSR-E SWE retrievals are available from National Snow and Ice Data Center (NSIDC) at http://nsidc.org/

snow depth (SD) or snow water equivalent (SWE) from observations in the microwave usually assume a linear relationship between SD or SWE and the difference of microwave brightness temperatures at 19 and 37 GHz. Figure 14.3 presents an example of a global SWE map derived from observations of AMSR-E instrument onboard Aqua. These maps have been generated at NASA daily since 2002 at the spatial resolution of 25 km.

The most notable limitations of microwave observations consist in their relatively coarse spatial resolution (currently 10–50 km) and in poor sensitivity to shallow and melting snow (Walker and Goodison 1993). Cold rocks exhibit a spectral response in the microwave similar to the one of snow (Grody and Basist 1996). As a result microwave algorithms tend to confuse cold rocks with snow cover and thus overestimate snow in the mountains. Because of a tendency to miss shallow and melting snow, microwave products typically underestimate the snow extent in the beginning and in the end of the snow season. Armstrong and Brodzik (2001) have found that the SSM/I and SMMR data-based algorithm maps consistently have less snow over the Northern Hemisphere as compared to NOAA interactive snow charts. The difference in the estimated snow-covered area ranges from 2% in early spring to 25% in late fall. In the same time, anomalies in the yearly average in the snow extent derived from SSM/I demonstrate a noticeable correlation with NOAA interactive charts.

Snow depth and snow water equivalent estimates from observations in the microwave are limited only to dry snow packs. The reported errors of the snow water equivalent range within 5–45 mm over non-forested areas and increase by 5–10 mm over forests (e.g., Singh and Gan 2000; Pulliainen et al. 1999; Tait 1998). This corresponds to 40–100% if the error is expressed as a percentage error of the total SWE. Kelly et al. (2003) put the estimate of the accuracy of microwave snow

depth retrievals at 50–70% for mostly forested locations. Much of uncertainty associated with SWE and snow depth retrievals from satellite observations in the microwave results from a strong dependence of the surface-emitted microwave radiation on other physical properties of the snow pack: its depth, the snow grain size, density, and stratification (Rosenfeld and Grody 2000). Uncertainty in the forest cover properties and its effect on the upwelling radiation complicate microwave snow depth and SWE retrievals even further. Currently the most accurate estimates are obtained from region-specific empirical algorithms, where limiting the geographic domain helps to reduce the variation of sensitive factors (e.g., Derksen et al. 2003).

As compared to passive microwave instruments, synthetic aperture radars (SAR) provide much higher, up to several meters spatial resolution imagery. However, current active microwave sensors operate at frequencies too low to derive information on the snow depth or SWE. They can be effectively used only to distinguish between dry and melting snow and thus can be applied to monitor seasonal snow freeze/thaw processes (e.g., Koskinen et al. 1997).

14.4 Automated Snow Remote Sensing in Optical Spectral Bands

As compared to satellite passive microwave measurements, observations in the optical spectral range allow for more accurate mapping of snow cover at higher spatial resolution. The reflectance of snow is high in the visible spectral band but drops to very low values in the shortwave and in the middle infrared. This specific spectral feature distinguishes snow from most other natural land surface cover types and clouds and therefore is actively used in automated algorithms to identify snow in satellite imagery.

Since 2000 NASA has produced snow cover maps from observations of the Moderate Resolution Imaging Spectroradiometer (MODIS) onboard Terra and Aqua satellites. A suite of MODIS snow products includes global maps of snow cover distribution generated at daily, 16-day, and monthly time steps at a spatial resolution ranging from 500 m to 20 km (Hall et al. 2002). Several algorithms have been developed and applied to identify and map snow cover from Advanced Very High Resolution Radiometer (AVHRR) sensor onboard NOAA polar-orbiting satellites (e.g., Simpson et al. 1998; Baum and Trepte 1999). In 2006, an automated algorithm to identify snow cover in AVHRR imagery was implemented at NOAA NESDIS. This technique is used to produce daily, global snow cover maps of snow cover at 4 km spatial resolution (http://www.star.nesdis.noaa.gov/smcd/emb/snow/HTML/snow.htm). Maps of snow cover distribution are also produced from a number of other instruments onboard polar-orbiting satellites including, in particular, VEGETATION from the Système Pour l'Observation de la Terre, literally translated as the "system for earth observation" (SPOT) and the Landsat Thematic Mapper (e.g., Xiao et al. 2004; Dozier and Painter 2004).

Clouds present the major problem for snow cover mapping from satellite observations in the optical spectral range. Estimates of Simic et al. (2004) show that in daily MODIS-based snow maps, clouds occupy about 40% of the area in the middle and high latitudes. Inability to distinguish between snow-free and snow-covered land beneath the clouds cause discontinuity both in the time series and in the derived spatial distribution of snow cover and therefore reduce the value of these products for model applications. Because of cloud gaps, optical snow maps do not allow for accurate estimation of the continental or hemispherical snow extent on a daily basis. Partial improvement in the map area coverage can be achieved with geostationary satellites which provide multiple observations per day and hence increase the chance to see the land surface clearly without cloud (Romanov and Tarpley 2006; de Wildt et al. 2007). With geostationary satellites, however, the map coverage is only regional and is limited to the area within ~ 65°N and S.

Snow maps derived from satellite observations in the visible and infrared generally demonstrate higher accuracy than corresponding microwave products. MODIS snow maps were found to correspond to surface observations of snow cover in 90–100% of cases over non-forested locations, deciduous forests, and in 80–90% over dense coniferous forests (Simic et al. 2004). Hall and Riggs (2007) estimated the average rate of agreement between MODIS 500 m resolution snow maps and in situ data equal to 93%. A slightly lower, 88%, agreement was reported by Romanov et al. (2000) for snow maps derived from observations of Geostationary Operational Environmental Satellite (GOES). All of the above estimates pertain to North America; however, there is no reason to expect substantially different accuracies of snow retrievals in Eurasia.

Continuous observations from AVHRR onboard different NOAA satellites have been available since the late 1970s. The Canadian Center for Remote Sensing (CCRS) has applied an automated technique to consistently reprocess historical AVHRR data for the time period from 1982 to 2005 and to establish the snow cover climatology over Canada at 1 km resolution (Khlopenkov and Trishchenko 2007). Expanding these efforts to the whole globe would lead to the development of a consistent long-term dataset suitable for snow climatology and climate change studies.

References

Armstrong RL, Brodzik MJ (2001) Recent Northern Hemisphere snow extent: a comparison of data derived from visible and microwave satellite sensors. Geophys Res Lett 28:3673–3676

Baum BA, Trepte Q (1999) A grouped threshold approach for scene identification in AVHRR imagery. J Atmos Ocean Technol 16:793–800

de Wildt MD, Gabriela S, Gruen A (2007) Operational snow mapping using multitemporal Meteosat SEVIRI imagery. Remote Sens Environ 109:29–41

Derksen C, Walker A, Goodison B (2003) A comparison of 18 winter seasons of in situ and passive microwave-derived snow water equivalent estimates in Western Canada. Remote Sens Environ 88:271–282

Dery SJ, Brown RD (2007) Recent Northern Hemisphere snow cover extent trends and implications for the snow-albedo feedback. Geophys Res Lett 34:l22504. doi:10.1029/2007gl031474

Dozier J, Painter TH (2004) Multispectral and hyperspectral remote sensing of alpine snow properties. Annu Rev Earth Planet Sci 32:465–494. doi:10.1146/annurev.earth.32.101802.120404

Ek MB, Mitchell KE, Lin Y, Rogers E, Grunmann P, Koren V, Gayno G, Tarpley JD (2003) Implementation of NOAH land surface model advances in the National Centers for Environmental Prediction operational mesoscale Eta model. J Geophys Res 108:8851. doi:10.1029/2002JD003296

Grody NC, Basist AN (1996) Global identification of snow cover using SSM/I measurements. IEEE Trans Geosci Remote Sens 34:237–249

Hall DK, Riggs GA (2007) Accuracy assessment of the MODIS snow-cover products. Hydrol Process 21:1534–1547

Hall DK, Riggs G, Salomonson V, DiGirolamo NE, Bayr KJ (2002) MODIS snow cover products. Remote Sens Environ 83:181–194

Helfrich SR, McNamara D, Ramsay BH, Baldwin T, Kasheta T (2007) Enhancements to, and forthcoming developments in the Interactive Multisensor Snow and Ice Mapping System (IMS). Hydrol Process 21:1576–1586

Kelly RE, Chang AT, Tsang L, Foster JL (2003) A prototype AMSR-E global snow area and snow depth algorithm. IEEE Trans Geosci Remote Sens 41(2):230–242

Khlopenkov KV, Trishchenko AP (2007) SPARC: new cloud, snow, and cloud shadow detection scheme for historical 1-km AVHHR data over Canada. J Atmos Ocean Technol 24:322–343

Kongoli C, Grody NC, Ferraro RR (2004) Interpretation of AMSU microwave measurements for the retrievals of snow water equivalent and snow depth. J Geophys Res 109:D24111. doi:10.1029/2004JD004836

Koskinen JT, Pulliainen JT, Hallikainen MT (1997) The use of ERS-1 SAR data in snow melt monitoring. IEEE Trans Geosci Remote Sens 35:601–610

Pulliainen JT, Grandell J, Hallikainen M (1999) HUT snow emission model and its applicability for snow water equivalent retrieval. IEEE Trans Geosci Remote Sens 37:1378–1390

Ramsay B (1998) The interactive multisensor snow and ice mapping system. Hydrol Process 12:1537–1546

Robinson DA, Dewey KF, Heim RR (1993) Global snow cover monitoring: an update. Bull Am Meteorol Soc 74:1689–1696

Romanov P, Tarpley D (2006) Monitoring snow cover over Europe with Meteosat SEVIRI. EUMETSAT P.46. In: Proceedings of the 2005 EUMETSAT meteorological satellite conference, Dubrovnik, 19–23 Sept 2005, pp 282–287

Romanov P, Gutman G, Csiszar I (2000) Automated monitoring of snow over North America with multispectral satellite data. J Appl Meteorol 39:1866–1880

Rosenfeld S, Grody N (2000) Anomalous microwave spectra of snow covered observed from Special Sensor Microwave/Imager measurements. J Geophys Res 105:14913–14925

Simic A, Fernandes R, Brown R, Romanov P, Park W (2004) Validation of VEGETATION, MODIS, and GOES C SSM/I snow-cover products over Canada based on surface snow depth observations. Hydrol Process 18(6):1089–1104

Simpson JJ, Stitt JR, Sienko M (1998) Improved estimates of the areal extent of snow cover from AVHRR data. J Hydrol 204:1–23

Singh P, Gan TY (2000) Retrieval of snow water equivalent using passive microwave brightness temperature data. Remote Sens Environ 74:275–286

Tait AB (1998) Estimation of snow water equivalent using passive microwave radiation data. Remote Sens Environ 64:286–291

Walker AE, Goodison BE (1993) Discrimination of a wet snow cover using passive microwave satellite data. Ann Glaciol 17:301–311

Xiao X, Zhang Q, Boles S, Rawlings M, Moore B III (2004) Mapping snow cover in the Pan-Arctic Zone, using multi-year (1998–2001) images from optical VEGETATION and SPOT sensor. Int J Remote Sens 25:5731–5744

Chapter 15
Climate-Scale Oceanic Rainfall Based on Passive Microwave Radiometry

Long S. Chiu, Si Gao, and Dong-Bin Shin

Abstract In the microwave regime, the relatively low and stable emissivity of the sea surface serves as an excellent background over which brightly emitting hydrometeors can be distinguished. Space/time oceanic rainfall has been estimated from microwave radiometry using a simple radiative transfer model of an atmospheric rain column, a rain rate distribution to account for sampling deficiencies, and an empirical correction of the nonuniformly filled field of view of the microwave sensor. The microwave emission-based brightness temperature histogram (METH) technique has been applied to the Defense Meteorological Satellite Program (DMSP) Special Sensor Microwave Imager (SSM/I) to produce over 25 years of monthly oceanic rainfall. The METH technique is described and the retrieved parameters are assessed. The inter-satellite calibration of microwave and DMSP SSM/I sensors provided a climate-scale oceanic rainfall time series capable of examining climate trends and variabilities.

Keywords Microwave radiometry • SSM/I • Oceanic rainfall • Rain frequency • Mixed lognormal distribution • Inter-satellite calibration • Climate trend

15.1 Introduction

Accurate measurements of global rainfall are crucial for advancing our understanding of the climate system such as the water and energy cycles. The lack of global gauge networks, especially over the ocean, in mountainous terrains, or in remote

L.S. Chiu (✉) • S. Gao
Department of Atmospheric, Oceanic and Atmospheric Sciences, College of Science, George Mason University, Fairfax, VA 22030, USA
e-mail: lchiu@gmu.edu; sgao2@gmu.edu

D.-B. Shin
Department of Atmospheric Science, Yonsei University, Seoul, South Korea
e-mail: dbshin@yonsei.ac.kr

J.J. Qu et al. (eds.), *Satellite-based Applications on Climate Change*,
DOI 10.1007/978-94-007-5872-8_15,

areas, points to satellite observation as the only viable mean for global-scale rainfall monitoring. Over the ocean, marine observations by ships and buoys have been the major source of rainfall observations. Efforts to document and analyze these marine observations have pointed to lack of standards of measurement, inadequate sampling as major sources of uncertainty. Major efforts, such as the International Comprehensive Ocean-Atmosphere Data Set (ICOADS), have been undertaken to collect, document, and quality control these observations (Woodruff et al. 1987, 2011). The advent of satellite and sensor technology that began in the late 1960s ushered in a new era of geophysical monitoring techniques for operational and climate applications (Acker et al. 2002).

Early work of oceanic rainfall relies on visible and infrared observations of cloud type and extent (see Barrett and Martin 1981; Acker et al. 2002; Chiu 2011). During the Global Atmospheric Research Experiment (GARP) Atlantic Tropical Experiment (GATE) conducted in 1974, Arkin (1979) found a tight relation between the total areal rainfall as estimated from shipborne radar data taken and the area of high clouds within the observation area. He developed a GOES Precipitation Index (GPI). The GPI expresses the total space/time rainfall as the total areas of high clouds (with cloud top temperature of $<$235 K) multiplied by a constant rain rate of 3 mm/day. This technique has been extended to other geosynchronous satellites and has proven to work well in the tropics if high non-raining cirrus clouds are excluded (Chiu et al. 1993). This observation is consistent with the so-called area-time integral in radar rainfall estimation and the threshold techniques in estimating space/time rainfall (Lovejoy and Austin 1979; Inoue 1987; Chiu 1988; Chiu and Kedem 1990). Follow-on development includes the partitioning of the cloud areas into convective and stratiform rain, technique to discriminate non-raining high cirrus, and their merging with microwave rainfall measurements to improve the space/time sampling (Acker et al. 2002; Chiu 2011; Chokngamwong and Chiu 2009; Huffman et al. 1997).

Microwave remote sensing of rain is especially suited over the ocean. In the microwave regime, the emissivity of the sea surface decreases with temperature; hence, the sea surface acts as a fairly constant dark background against which highly emissive raining hydrometeors can be distinguished. Since the first launch of the Electrically Scanning Microwave Radiometer onboard NASA's NIMBUS 5 satellite (Wilheit et al. 1977), our understanding on the use of microwave in rainfall estimation has greatly improved. This is propelled by a long record of the Special Sensor Microwave Imager (SSM/I) data taken on board the Defense Meteorological Satellite Program (DMSP) satellites and a focused international effect of the Tropical Rainfall Measuring Mission (TRMM, Kummerow et al. 2000).

While satellite observations provide snapshots of the raining conditions, the revisit time tends to be long compared to the timescale of rain cells. These small-scale rain events are likely to be under-sampled, thus leading to a bias in the estimation of space/time rainfall. This chapter describes a technique to estimate space/time oceanic rainfall from microwave radiometry that takes account of the interactions between the microwave radiation and the falling hydrometeors and the characteristics of the rain fields. The microwave emission-based brightness temperature histogram technique,

or (METH), is based on the use of histogram of brightness temperature over the time period, providing a characterization of the non-raining portion of the observations (Wilheit et al. 1991; Chiu et al. 2010). The technique is robust and is suited for examining rainfall estimates across different satellite platforms and sensors. Inter-sensor and inter-satellite calibrations are crucial for establishing multi-platform multi-sensor rainfall record for climate studies.

In Sect. 15.2, the model structure and the underlying theory is briefly described. Section 15.3 examines the product output parameters. Section 15.4 describes examples of the technique to climate studies, and Section 15.5 discusses future work and potential improvements to improving this product.

15.2 Background

SSM/I is a seven-channel, four-frequency (19.35, 22.235, 37, and 85.5 GHz) conically scanning microwave radiometer (Hollinger et al. 1990). The Special Sensor Microwave Imager/Sounder (SSMIS) is a 24-channel microwave radiometer and sounder with frequencies range from 19 to 183 GHz (Kunkee et al. 2008). It combines an SSM/I with a microwave sounder that provide temperature and moisture profile information. They are flown on board DMSP satellites. Description of the SSM/I and SSMIS sensors and their operations can be obtained from the National Snow and Ice Data Center (NSIDC)'s web site (http://nsidc.org/data/docs/daac/f8_platform.gd.html).

Given an atmospheric profile, the observed microwave radiation from a satellite can be calculated via radiative transfer. This is the forward problem. The inverse (or retrieval) problem is to estimate parameters of the atmospheric column from the observed radiance.

15.2.1 Atmospheric Model

The atmospheric model consists of a cloud layer on top of a rain column over the ocean surface (see Fig. 15.1 from Wilheit et al. 1977). A surface relative humidity (RH) of 80% is assumed which increases linearly to saturation (100%) at the freezing level (FL) (Wilheit et al. 1977, 1991). The FL is the height of the zero degree isotherm. A non-precipitating cloud layer with a density of 0.5 g/m^3 and 0.5 km in thickness is present near the freezing level. Underneath the FL is a rain column consisting of rain drops that follow a Marshall Palmer (M-P) distribution (Marshall and Palmer 1948).

With the assumption of the humidity and M-P rain drop distribution, the FL specifies the moisture condition of the rain column. A brightness temperature T, defined as twice the brightness temperature of the vertically polarized 19 GHz minus the 22 GHz ($T = 2T_{\mathrm{b\ 19V}} - T_{\mathrm{b\ 22V}}$), is used. This combination channel

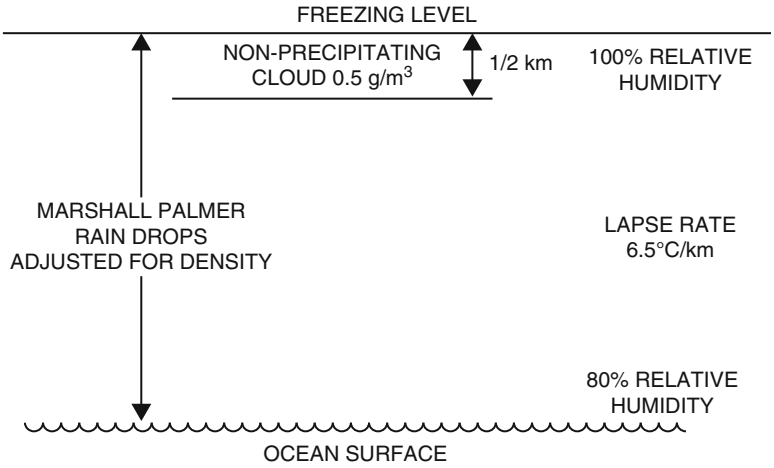

Fig. 15.1 Schematic showing the atmospheric model used in radiative transfer computations of the brightness temperature in the Wilheit et al. (1977) model

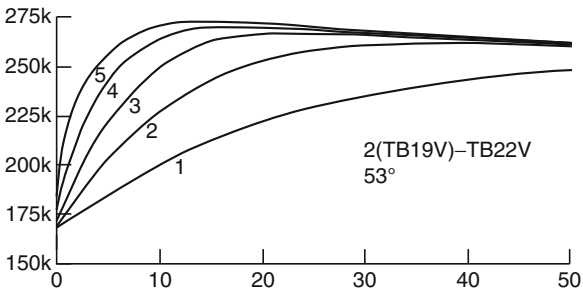

Fig. 15.2 Brightness temperature of the combination channel as a function of the rain rate (R, x-axis, in mm/h) at different freezing level heights (in km) (From Wilheit et al. 1977)

minimizes the effect of water vapor on the rain signal. Figure 15.2 (from Wilheit et al. 1977) shows the T–R relation for an earth incidence angle of 53° for various FL values. The T–R relation can be empirically approximated as

$$T(R, \mathrm{FL}) = T_0 + (285\ \mathrm{K} - T_0)(1 - e^{-R/R_C}) - 3.5R^{1/2} \tag{15.1}$$

where $R_C = 25/\mathrm{FL}^{1.2}$

Here T is the combination channel brightness temperature, R the rain rate in mm/h, T_0 the brightness temperature in non-raining conditions, and FL is the freezing level height, in km. The second term of the equation on the right represents the emission from the rain column, and the third term represents scattering effects. It can be seen that this is a double value problem, i.e., given a value of T, there are two solutions of R that satisfy this relation. With the resolution of the SSM/I, the high rain rate solutions are rarely observed.

15.2.2 Statistical Rain Field Model

The rainfall model used is a mixed distribution model, consisting of a no rain probability of $(1-p)$ at zero rain rate and a lognormal distribution for the rainy part (rain rate >0 mm/day) as follows (Kedem et al. 1990):

$$G(x) = (1-p)H(x) + pF(x) \tag{15.2}$$

where p is the rain probability (or frequency), x is rain rate, and $H(x)$ is the Heaviside step function

$$H(x) = \begin{cases} 0, & \text{if } x<0 \\ 1, & \text{if } x \geq 0 \end{cases}$$

And $F(x)$ is a Lognormal Distribution with parameters of μ and σ,

$$F(x)\mathrm{d}x = \frac{1}{\sigma\sqrt{2\pi}} \exp\left[\frac{-(\ln x - \mu)^2}{2\sigma^2}\right] \frac{\mathrm{d}x}{x} \tag{15.3}$$

The expected value of the mean of the mixed distribution is

$$E(x) = p \times \exp(\mu + \sigma^2/2) \tag{15.4}$$

Other statistical models have also been used to describe the rainy portion of the distribution (Kedem and Chiu 1987a; Kedem et al. 1990). The lognormal distributions have often been used to describe geophysical parameters which show skew distributions. Based on a simple model, Kedem and Chiu (1987a) argued that the lognormal distribution is not unreasonable for rain rate distributions.

15.2.3 Beamfilling Correction

One of the disadvantages of the use of passive remote sensors is the coarse resolution of the sensor field of view (FOV) compared to the spatial scale of rain clouds. The beamfilling error refers to a bias associated with the nonuniformly filled FOV coupled with a nonlinear relation between the observed and the estimated parameter, i.e., T–R relation (Eq. 15.1) (Short and North 1990). Chiu et al. (1990) examined radar rainfall observed at the GATE and derived an approximate formula for the beamfilling correction (BFC). The beamfilling bias depends on nonlinearity of T–R relation and rain rate variance within field of view

$$R_E - [R] = \frac{T''}{2T'}\left[(R-[R])^2\right] \tag{15.5}$$

where R_E is the estimated rain rate, $[R]$ is the true rain rate within the FOV, and T' and T'' are slope and curvature of T–R relation (Eq. 15.1), and $[x]$ represents area averaging. The first term on the right-hand side ($T''/2T'$) depends only on the atmospheric and radiative transfer model, the sensor response, and the orbital parameters of the satellite. The second part, $[(R - [R])^2]$, depends solely on the structure of the rain field. It is the coupling of these effects that comprise the beamfilling effect. Since the slope of the T–R relation is positive and the curvature negative, and the rain rate variance is always positive, the right-hand side of (15.5) is negative, i.e., a negative bias is incurred.

Ha and North (1995) examined different theoretical rain rate distributions and concluded that a climatological correction for the beamfilling error is appropriate. From theoretical considerations, Wang (1997) proposed a FL-dependent BFC. Cho et al. (2004) examined data collected by the TRMM Precipitation Radar and showed that both the gamma and lognormal distributions provide good fits to the observed data. However, the gamma (lognormal) distribution tends to better fit the observed distribution for wet (dry) conditions.

Kummerow (1998) provide a methodology to examine the BFC structure and Kummerow et al. (2004) showed the sensitivity of the slant path and rain rate inhomogeneity within the FOV on the BFC based on TRMM data. Methods to correct for the BFC have been investigated (Kubota et al. 2009; Lafont and Guillemet 2004).

15.3 Data Product

15.3.1 Data Processing

The processing of the data begins with the computation of the brightness temperature (T_b) histograms and the determination of the FL using the top one percentile of the vertically polarized T_b at 22 GHz ($T_{b\ 22V}$) and vertically polarized T_b ($T_{b\ 19V}$). This choice is an attempt to exclude non-raining pixel in the FL calculations. The method of moments is used. The mean of the combination channel ($T = 2T_{b\ 19V} - T_{b\ 22V}$) of the non-raining pixels and the first, second, and third moments of the T histogram are calculated. These moments of the T histogram are matched iteratively to the parameters of a mixed lognormal distribution via the T–R relation. The output parameters are RE, T_0, σ_0, p, μ, σ, and FL, where RE is the estimated rain rate, T_0 and σ_0 the mean and variance of the non-raining portion of the T_b histogram, p the rain fraction, and μ and σ are the estimated mean and variance of the logarithm of the rain rate. After the computation of the RE, a BFC is applied to get the BFC corrected rain rate (see Wilheit et al. 1991).

The METH technique has been applied to all SSM/I data on the DMSP satellites (F8, F10, F11, F13, F14, F15) and SSMIS on board F17 satellites. The data are available via the Global Precipitation Climatology Project-Polar Satellite Precipitation Data Center (GPCP-PSPDC) website (http://gpcp-pspdc.gmu.edu/).

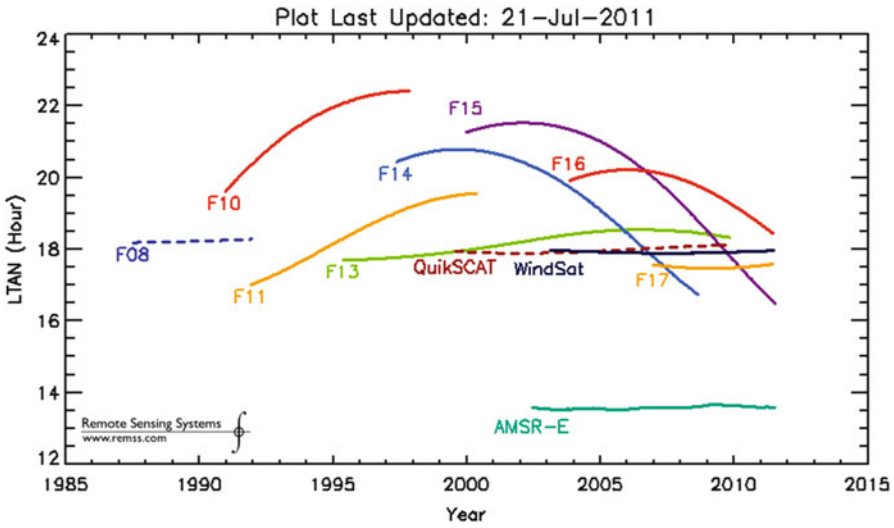

Fig. 15.3 Equatorial passing times of the DMSP satellites and other microwave sensor platforms. *Solid lines* represent ascending nodes, and *dotted lines* (for F8 and WindSat) represent descending nodes (From http://www.ssmi.com/support/crossing_times.html)

Figure 15.3 shows the mean equatorial passing time of the DMSP satellites, together with other spaceborne microwave radiometers – the wind sensing scatterometers QuikScat and WindSat and the Advanced Microwave Scanning Radiometer onboard NASA's EOS Aqua satellite (AMSR-E). These sensors are designed to have local satellite overpass times around early morning and evening (6 a.m. and 6 p.m.). However, there are substantial drifts in the orbital parameters during the satellite life.

Two types of products, 2.5 × 2.5° monthly and 5 ×5° monthly products, are available. The 5 × 5° products are produced by first computing the histograms for the morning (a.m.) and afternoon (p.m.) satellite passes separately, and the monthly mean is an average of the a.m. and p.m. rain rates. The 2.5° product is derived from combining all a.m. and p.m. satellite passes to form a monthly histogram, before computing the monthly average. The original monthly time series were processed using SSM/I version 4 (V4) T_b data provided by Remote Sensing Systems (RSS) (website: http://www.ssmi.com/).

A trend in the T_0 data was found in the version 4 products which may be related to differences in the orbital parameters of satellites (Chokngamwong and Chiu 2006). Trends in other oceanic water cycle products, in particular, surface latent heat fluxes, were also noted for satellite products that are mostly based on SSM/I (Chiu et al. 2008). Further analyses of the trends in the latent heat fluxes show that the trend in the NASA Goddard Satellite-based Sea Surface Turbulent Fluxes (GSSTF) product is associated with an increase in the wind speed and an increase in the sea-air humidity difference. These trends can be traced back to the brightness temperature data of the SSM/I (Chiu et al. 2012; Chap. 11, this book).

An improved version that removes the wind trend (version 6, V6) was made available by RSS in 2006. All data have been reprocessed using the V6 data. A comparison of the version 4 and version 6 products showed a reduced linear trend in the rain rate data (Chiu and Chokngamwong 2010). These products are labeled V4 and V6, respectively, corresponding to the RSS versions. In the following, we will restrict our discussion on the V6 2.5° product.

15.3.2 Sampling

The sampling errors associated with these products are examined using a simple error model and different satellite combinations of the monthly products. In general the error structure follows a power law of the form ERR $= aR - b$, where ERR is the sampling error, R the rain rate, and a and b are empirical constants. The value of b is between 0.25 and 0.33, while the constant a is determined by the particular sensor (Chang and Chiu 1999, 2001). Analyses also show that large errors are observed for grid boxes with insufficient sample. This threshold is approximately 2,500, compared to typical averages of 4,000–4,500 for the 2.5° boxes. These grid boxes are flagged in the output files.

15.3.3 Product Evaluation

Analyses of the early records have been presented elsewhere (Chang et al. 1993; Chiu and Chang 1994). Figure 15.4 shows the time series of the domain (65°N–65°S, ocean) average rain rates. Linear regression analyses show no significant trend.

15.3.3.1 Rainfall Rate (*R*) (Unconditional)

Equation 15.4 shows that the total (unconditional) rainfall rate is the product of the rain frequency (p) multiplied by the conditional rain rate (mean rain rate for the lognormal distribution). Figure 15.5 shows the annual and monthly average rainfall rates. Major features, such as that over the maritime continent, Intertropical Convergence Zone (ITCZ) in the Pacific and the Atlantic, the South Pacific and South Atlantic Convergence Zones (SPCZ, SACZ), and the storm tracks in the western oceans, are quite distinct. Seasonally, the Pacific ITCZ is strongest in the boreal summer to early fall (JJAS). During the JJA season, the SPCZ is extremely weak. It intensifies and acquires its maximum strength in January. The intensification of the Pacific ITCZ is accompanied by the decay of the SPCZ, and in March there is a separation of the SPCZ and the ITCZ as the SPCZ is attached to the southern branch of the double ITCZ. The double ITCZ is clearly present during the months of March

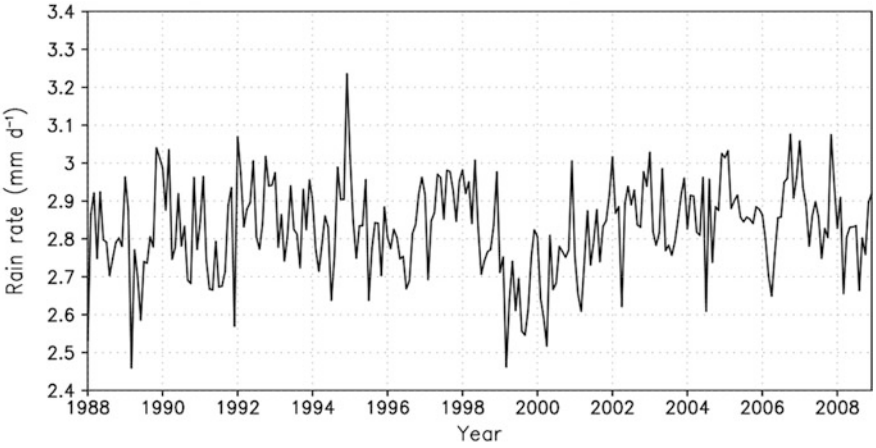

Fig. 15.4 Time series of the domain average rain rate. *Grid boxes* with insufficient samples are excluded in the compilation

and April in the Pacific, while there is only a slight hint in the Atlantic, probably due to the low product resolution (2.5°). It should be pointed out that during the warm phase of El Nino years, the two rainbands merge to form a huge rainband, and the double ITCZ disappears. The existence of a double ITCZ in the eastern Pacific has been suggested to be related to the existence of a cold tongue (low sea surface temperature), while the central and western portion is due to cold advection by the easterlies (Zhang 2001). While the existence of a double Atlantic ITCZ has been demonstrated by surface wind convergence derived from scatterometer data (Liu and Xie 2002), detail structure and intensity of these features pose challenges to the modeling community (Lin 2007).

The storm tracks intensify during June and fully develop during July and August. The rather wide band of rainfall in the western part of the north Pacific and north Atlantic oceans indicate the variability of the typhoon (hurricane) tracks. The high rain rates located off the western coast of India, in the Bay of Bengal, and off the eastern coast of China coincide with the monsoon on set in June. The heavy rain in the Bay of Bengal persists into August.

15.3.3.2 Conditional Rain Rate (r_{cond})

The conditional rain rate (r_{cond}), or the rain rate in rainy conditions, is computed using the formula $r_{cond} = \exp(\mu + \frac{1}{2}\sigma^2)$ (see Eq. 15.4) and shown in Fig. 15.6. The pattern of conditional rain rate follows that of total rainfall. The high conditional rain rates around Antarctic may be due to the inclusion of pixels that contain sea ice but was not detected in the algorithm.

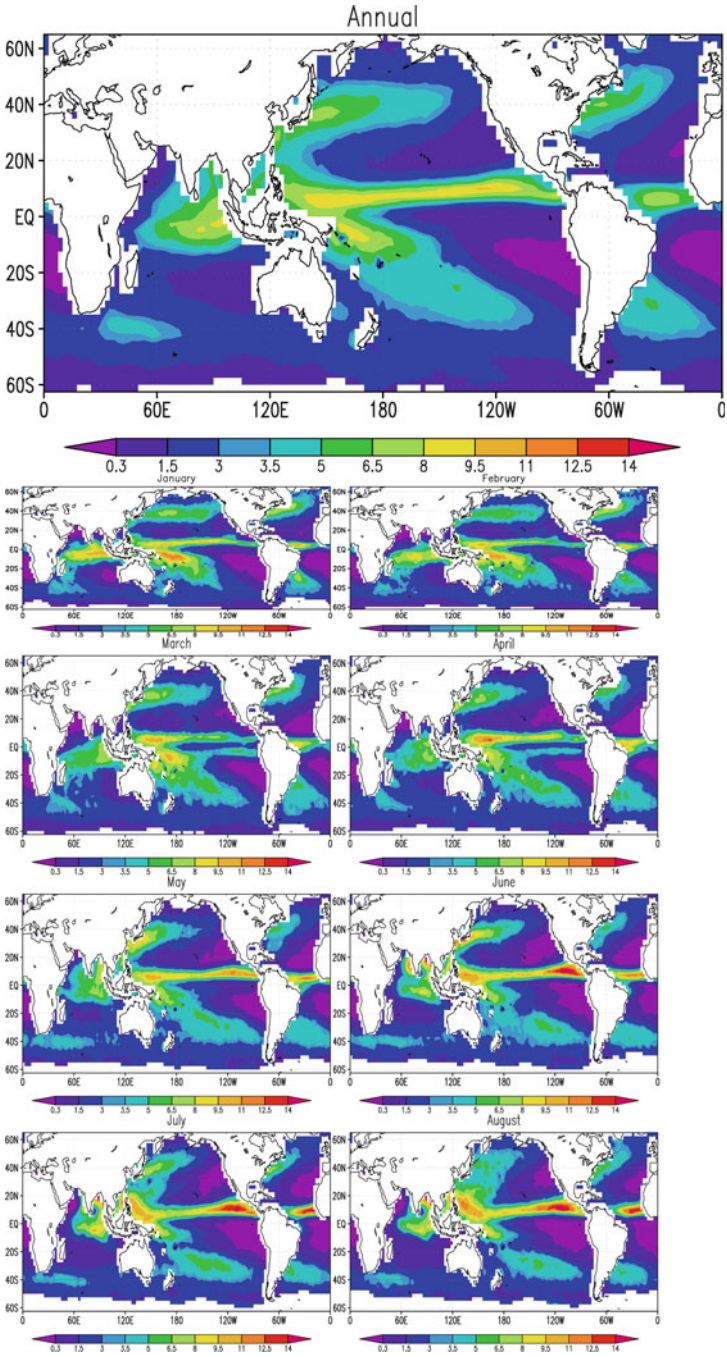

Fig. 15.5 Annual and monthly average rainfall rates from all SSM/I sensors

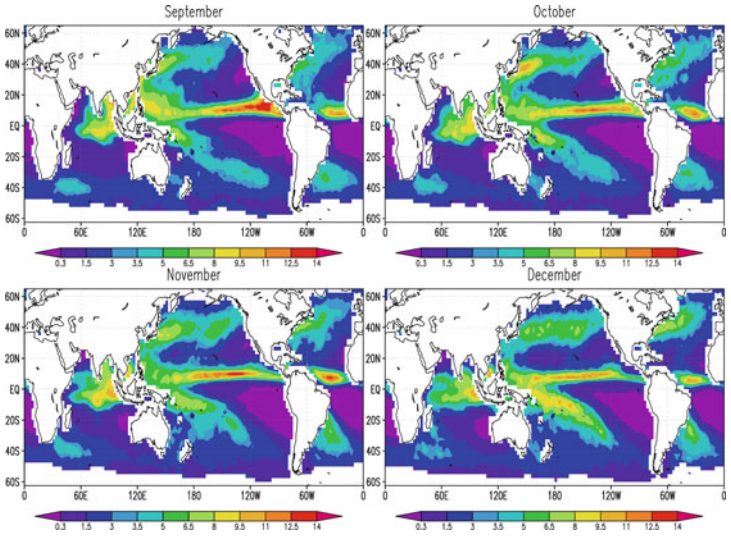

Fig. 15.5 (continued)

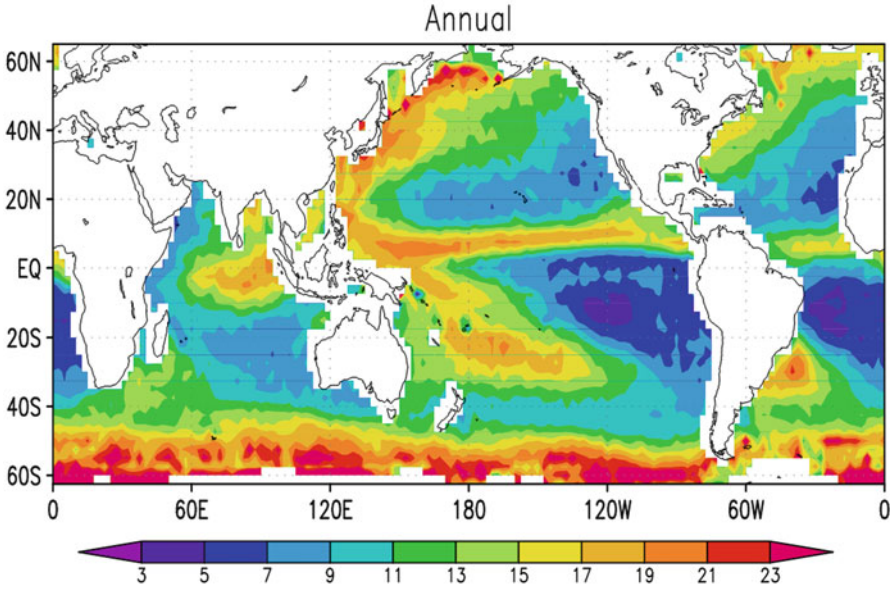

Fig. 15.6 Map of annual average conditional rain rates in mm day^{-1}

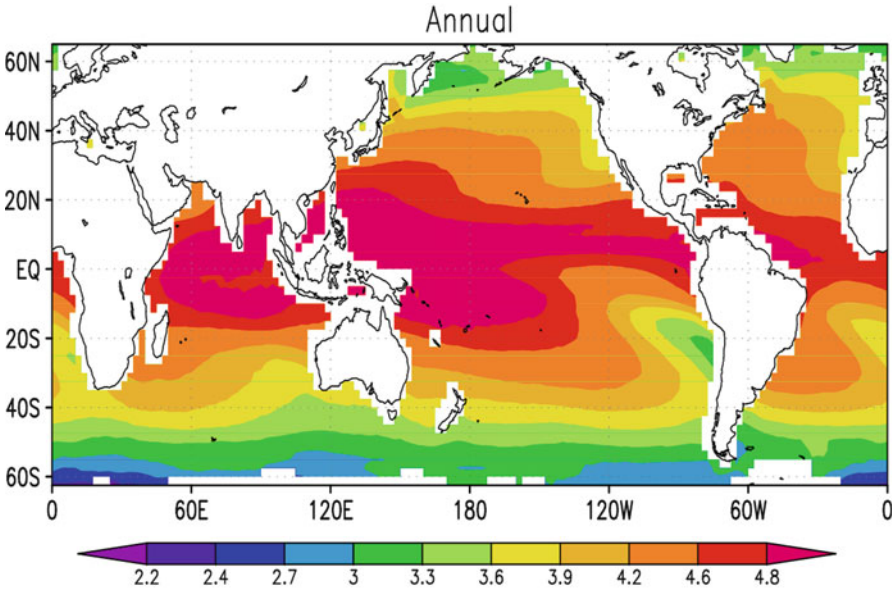

Fig. 15.7 Map of annual average freezing level height (FL) in km

15.3.3.3 Freezing Level Height (FL)

Chiu and Chang (2000) compared the SSM/I METH freezing height (FL) with results from general circulation models (GCMs). While there is a small bias between the FL and the freezing level derived from GCMs in the tropics, there are rather large discrepancies in the mid-latitudes. There is a relative weak but significant diurnal variation of the FL as computed from the DMSP morning and afternoon passes (Chang et al. 1995). As pointed out earlier, FL is a columnar moisture index. The retrieved quantity is a "rain volume", i.e., a product of the rain column height and the rain rate. Hence, errors in the FL will impact the rain rate inversely. Figure 15.7 indicated the annual average FL.

15.3.3.4 Rain Frequency (*p*)

An early climatology of the METH SSM/I rain frequency (p) showed maxima peaks that follows the thermal equator and at latitudes 45–50° in both hemispheres (Chiu and Chang 1994). Figure 15.8 shows that the equatorial and high latitude (~50°) maxima are about 50% and there are subtropical minima (~20° latitude) of about 30%.

Quantitative rainfall measurements were not included in the ship observations collected in ICOADS. However, meteorological observations of precipitation were

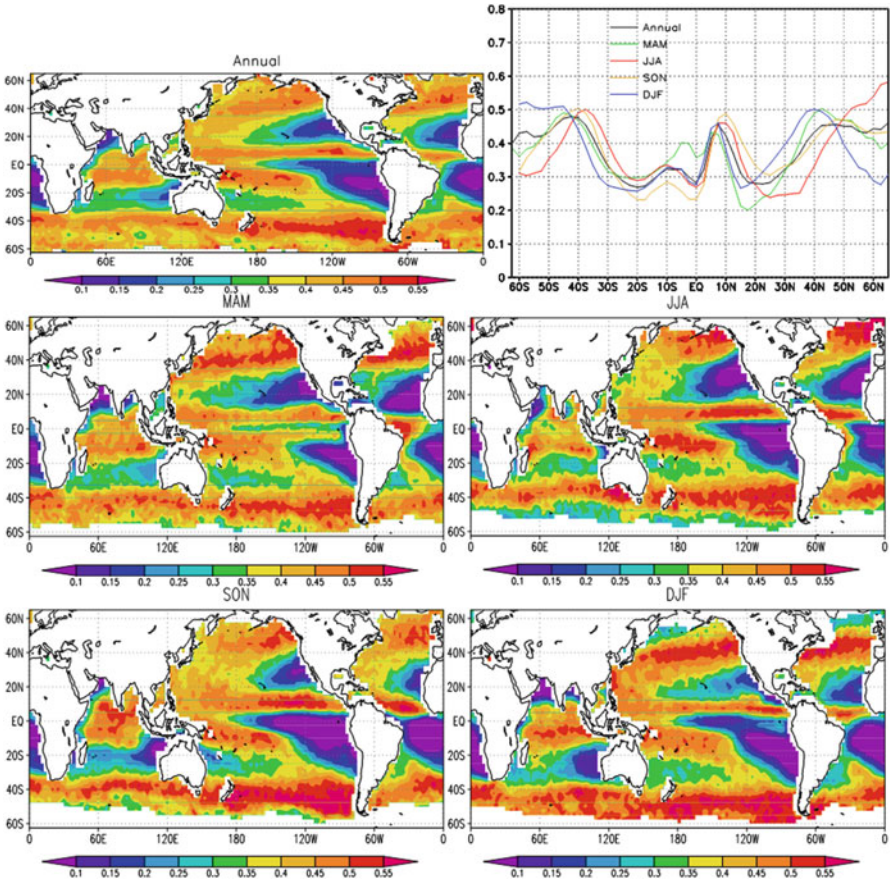

Fig. 15.8 Seasonal average (*middle panels*) and annual rain frequency (*bottom panel*). The zonal annual and seasonal average rain frequency appears in the *top panel*

coded and recorded. Analyses of meteorological observations in ICOADS show zonal bands of high rain frequency near the equator and at latitudes of 50–60° latitudes in both hemispheres (Petty 1995). This zonal pattern is consistent with the pattern derived from the limited GTS and marine observations (Dai 2001). Most satellite algorithms were able to correctly estimate the high rain frequency near the equator (Petty 1997) and for the Atlantic from TRMM precipitation radar data (Short 2003). However, the high rain frequency at the high latitudes is usually underestimated (Petty 1997). Ellis et al. (2009) compare rain frequency derived from the CloudSat radar for the period 2006–2007 and found that the CloudSat rain frequency is quite consistent with that derived from ICOADS data. While the zonal patterns are similar, the magnitudes are quite different. This is attributed to the different fields of view of the observations. The CloudSat radar has a resolution of about 1 km whereas that for the TRMM radar is 4–5 km. The FOV of the SSM/I

sensor is about 40–50 km. For ship observations, the field of view varies with the weather condition and can be as large as tens of kilometers for a clear day down to a few kilometers under misty or hazy conditions to less than a few 100 m in severe weather conditions. The probability of observing rain increases as the FOV increases. For GATE rainfall, the rain frequency increases from around 10% at a resolution of 4 km to 40% at a resolution of 40 km (Kedem and Chiu 1987b).

15.4 Applications

15.4.1 GPCP Merging

This product serves as input to GPCP rain maps (Huffman et al. 1997). This data set and derived products (Adler et al. 2003; Huffman et al. 2001; Xie et al. 2003) have been utilized rather extensively in climate and weather analyses.

15.4.2 Climate "Trend" and Variations

Trends in the data set have been examined. A trend is dependent on the length of the time record. The version 6 data showed a smaller trend than the version 4 data. Overall, the trends are consistent with the GPCP estimates and are generally lower than the other estimates (Chiu and Chokngamwong 2010). No significant trend in global oceanic rainfall is observed. The only significant trend in zonal mean is observed at the tropical Pacific between 0 and 10ºN. Figure 15.9 shows the linear trend pattern of global rainfall. The monthly rainfall data have been deseasonalized, i.e., monthly climatology removed.

An empirical orthogonal function (EOF) analysis was performed on the nonseasonal time series. Only the first two EOFs are judged to be significant and distinct according to the criteria of North et al. (1982) (see also Chiu et al. 2008).

Figure 15.10 shows the first two EOF patterns (with variance explained) and the associated time series (principal component, or PCs). A Southern Oscillation Index (SOI), scaled to match the time series, is also included in the figure. The first PC shows a correlation coefficient of 0.8, significant at the 95% level, while the contemporaneous correlation with the second PC (at −0.11) is insignificant. The major mode of nonseasonal rainfall variations is associated with the El Nino Southern Oscillation (ENSO) phenomena. This rather robust result is well established (Chang et al. 1993; Kafatos et al. 2001).

The second mode (EOF2) is similar to the first mode (EOF1). This pattern is characterized by an equatorial dipole. The overall wedge pattern is hinged in the central Pacific instead of the maritime continents as demonstrated in EOF1. There are recognitions of an ENSO pattern that has its origin in the central Pacific. This is termed the ENSO Modoki (Weng et al. 2007). Others have coined the canonical

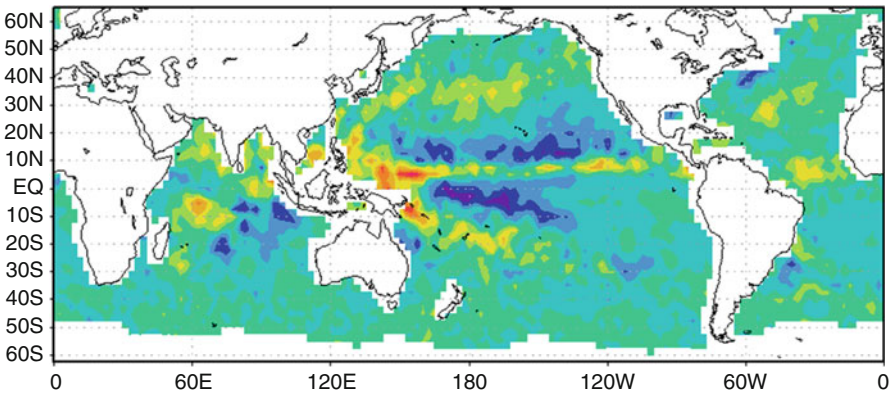

Fig. 15.9 Map of distribution of linear trends (mm day^{-1} decade^{-1}) of oceanic rain rates. The linear trends are computed from linear regression analysis of the nonseasonal (with climatology removed) data

ENSO as the eastern Pacific ENSO (EP ENSO) and central Pacific ENSO (CP ENSO) (Yeh et al. 2011). PC2 shows a significant correlation of 0.55 with an ENSO Modoki index (EMI, available at: http://www.jamstec.go.jp/frcgc/research/d1/iod/modoki_home.html).

15.4.3 TRMM Applications

A passive microwave imager was launched as part of TRMM instrument package. The TRMM Microwave Imager (TMI) has similar channels as the SSM/I, with an additional channel of 10 GHz. Early analysis of the METH rain rate demonstrated that microwave rainfall estimates can produce climate signals such as the El Nino/Southern Oscillation (Chang et al. 1993; Kafatos et al. 2001). The METH algorithm has been applied to TMI data (Chang et al. 1999; Kummerow et al. 2000). The strength of this product is its robustness and, when properly calibrated, is capable of detecting climate-scale signals.

15.4.4 TRMM Boost

The robustness of this technique is demonstrated when the TRMM satellite is boosted from an original altitude of 350 km to a higher altitude of 402 km in August 2001 to save fuel and prolong satellite and mission life. The change in the satellite altitude changes the TMI's earth's incidence angle and the atmospheric paths and introduces discontinuities in the retrieved radar rainfall and reflectivity (Shimizu et al. 2009; Short and Nakamura 2010). We perform a quick fix by

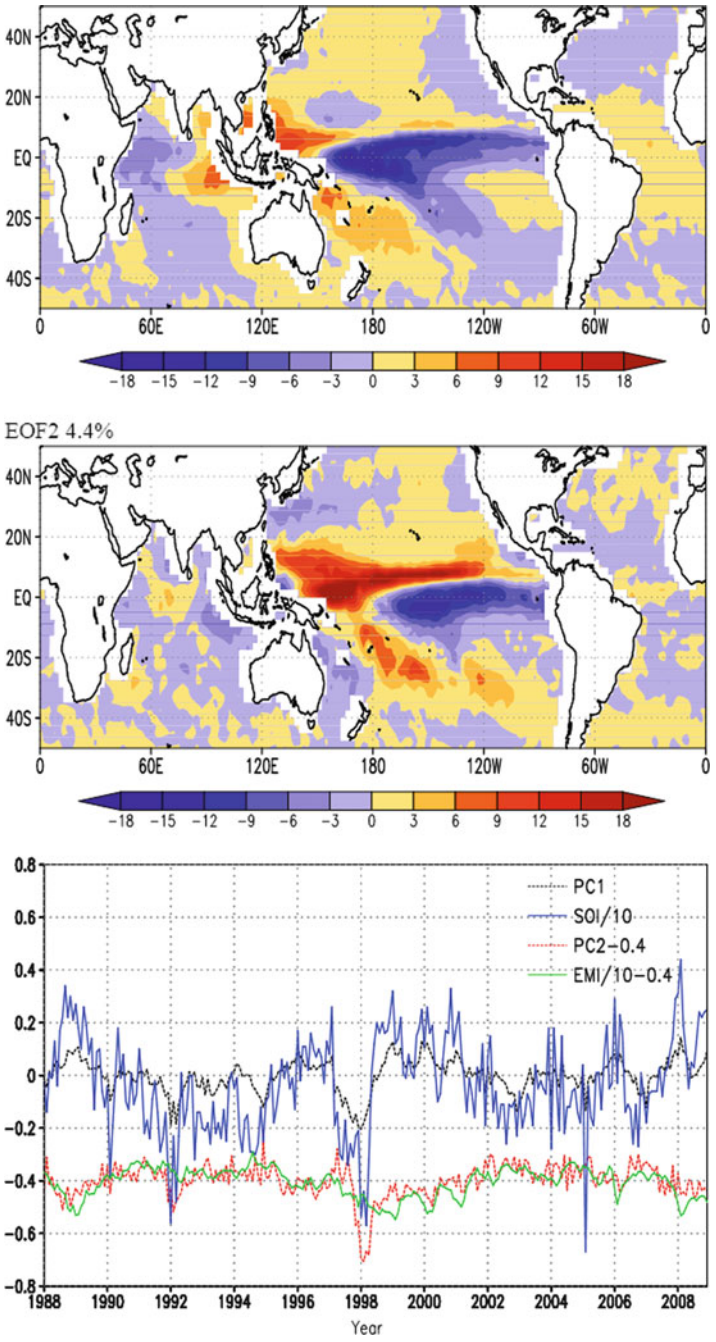

Fig. 15.10 First (*top panel*) and second (*middle panel*) EOF pattern of nonseasonal rainfall, explaining 6.9 and 4.4% of the nonseasonal variance, respectively. The *lower panel* shows the associated time series (PC1 and PC2). A scaled Southern Oscillation Index (*SOI*) is included for comparison. The correlations between SOI and PC1 and PC2 are 0.8 (significant at the 95%) and −0.11 (not significant), respectively. PC2 leads variations in SOI (correlation at 0.4) by 6 months. The correlation between PC2 and an index of the ENSO Modoki (or ENSO central Pacific) index is 0.55, significant at the 95%

adjusting the difference in the T_b for the pre- and post-boost T_bs in the TMI channel data (Shin and Chiu 2008) and by properly adjusting the *T–R* relation in the algorithm by changing the earth incidence angle and redoing the radiative transfer calculations (Chiu et al. 2010). During the transition period, another satellite, the DMSP F13, is in stable operations. We use the METH product derived from the F13 as a calibration point and compare the differences for the pre- and post-boost periods. The adjustment effectively eliminates the discontinuity introduced by the TRMM boost.

15.5 Summary and Discussions

In this chapter, we discuss the theoretical bases of the METH technique, describe the processing of the METH products, present the climatology of these parameters, and discuss their relevance to climate studies. The uniqueness of this technique is the determination of the background brightness temperature for the non-raining portion and fitting the brightness temperature histogram to a mixed lognormal rain rate distribution via a *T–R* relation derived from an atmospheric radiative transfer model. The so-called beamfilling error is corrected using empirical data.

We briefly examine the characteristics of the rain rate parameters including the unconditional rain rate, conditional rain rate, freezing level, and rain frequency. These parameters are consistent with more recent and detail estimates, such as the rain frequency computed from the CloudSat radar. Application to other microwave sensors is rather straightforward and has been applied to TMI rather successfully. The strength of this technique is well demonstrated in mitigating the discontinuity of the TMI data record by simply changing the *T–R* relation in the algorithm.

We found no significant trend in the global (domain) average rainfall; however, significant linear trends are detected in the equatorial belt 0–10ºN. Whether this pattern is due to an intensification of the Hadley circulation or a shift of the rain belts has yet to be determined. Two distinct modes of nonseasonal variations are detected from an empirical orthogonal function analysis. The first mode is the well-recognized ENSO mode, the associated time series of which show a correlation of 0.8 with a Southern Oscillation Index. The second mode is recognized as the ENSO Modoki mode (or the central Pacific ENSO mode) and shows a correlation of 0.55 with an index of the ENSO Modoki. The ENSO Modoki mode leads the ENSO mode by roughly 6 months.

This algorithm has been in operation for over 20 years and has served as an important input to the Global Precipitation Climatology Project rain maps. With improved understanding of the precipitation processes and the information collected during major international missions, some of the crude physics and model assumptions need to be revisited and improved so that uncertainties of climate-scale rainfall can be better quantified and the data better utilized.

Abbreviations

AMSR-E	Advanced Microwave Scanning Radiometer-Earth Observing System
BFC	Beamfilling correction
DMSP	Defense Meteorological Satellite Program
EMI	El Nino Southern Oscillation Modoki Index
ENSO	El Nino Southern Oscillation
EOF	Empirical Orthogonal Function
FOV	Field of view
GARP	Global Atmospheric Research Experiment
GATE	GARP Atlantic Tropical Experiment
GCM	General circulation model
GOES	Geostationary Operational Environmental Satellite
GPCP	Global Precipitation Climatology Project
GPI	Geostationary Operational Environmental Satellite Precipitation Index
GSSTF	Goddard Space Flight Center Satellite-based Sea surface Turbulent
ICOADS	International Comprehensive Ocean-Atmosphere Data Set
ITCZ	Intertropical Convergence Zone
METH	Microwave emission-based brightness temperature histogram
NASA	National Aeronautics and Space Administration
NSIDC	National Snow and Ice Data Center
PC	Principal component
PSPDC	Polar Satellite Precipitation Data Center
RSS	Remote Sensing Systems
SACZ	South Atlantic Convergence Zone
SOI	Southern Oscillation Index
SPCZ	South Pacific Convergence Zone
SSM/I	Special sensor microwave imager
SSMIS	Special Sensor Microwave Imager/Sounder
TMI	Tropical Rainfall Measuring Mission Microwave Imager
TRMM	Tropical Rainfall Measuring Mission

Acknowledgments Drs. T. Wilheit and A. T-C. Chang are codevelopers of this technique. Dr. Chang started the GPCP-PSPDC and was responsible for the initial development and operations. He passed away in May 2004. His leadership, perseverance, and mentoring would be sorely missed. Thanks are due to Drs. R. North, B. Kedem, D. Short, A. McConnell, R. Adler, and G. Huffman for their input throughout the course of development. Our work has been supported by NASA TRMM and NOAA Office of Global Programs during its various stages of development and processing. Drs. R. Adler, P. Arkin, A. Gruber, R. Kakar, S. Braun, and A. Hou are acknowledged for their support. DBS was supported by the Korea Meteorological Administration Research and Development Program under Grant CATER 2012–2063.

References

Acker J, Williams R, Chiu LS et al (2002) Remote sensing from satellites. In: Meyers R (ed) Encyclopedia in physical science and technology, 3rd edn. Academic, San Diego

Adler RF, Huffman GJ, Chang ATC, Ferraro A, Xie P, Janowiak J, Rudolf B, Schneider U, Curtis S, Bolvin D, Gruber A, Susskind J, Arkin P (2003) The version 2 global precipitation climatology project (GPCP) monthly precipitation analysis (1979–present). J Hydrometeorol 4:1147–1167

Arkin P (1979) The relationship between the fractional coverage of high cloud and rainfall accumulation during the GATE over the B–Scale array. Mon Weather Rev 107:1382–1387

Barrett E, Martin D (1981) The use of satellite data in rainfall monitoring. Academic, London

Chang ATC, Chiu LS (2001) Nonsystematic errors of oceanic monthly rainfall derived from microwave radiometry. Geophys Res Lett 28:1223–1226

Chang ATC, Chiu LS, Kummerow C, Meng J, Wilheit TT (1999) First results of the TRMM Microwave Imager (TMI) monthly oceanic rain rate: comparison with SSM/I. Geophys Res Lett 26:2379–2382

Chang ATC, Chiu LS, Wilheit TT (1993) Oceanic monthly rainfall derived from SSM/I. Eos Trans 74:505

Chang ATC, Chiu LS, Yang G (1995) Diurnal cycle of oceanic precipitation from SSM/I data. Mon Weather Rev 123:3371–3380

Chiu LS (1988) Estimating areal rainfall from rain area. In: Theon J, Fugono N (eds) Tropical precipitation measurements. Deepak, Hampton

Chiu LS (2011) Atmospheric remote sensing. In: Yang C, Wong D, Miao Q, Yang R (eds) Advanced geoinformation science. CRC, Boca Raton

Chiu LS, Chang ATC (1994) Oceanic rain rate parameters derived from SSM/I. U.R.S.I. commission F, Climate arameters in Radiowave Propagation Prediction, CLIMPARA'94, p11.3:1–5, Moscow, May 31–June 3 1994. (URL: http://www.scribd.com/doc/81459037/Climatic–Parameters–in–Radiowave–Propagation–Prediction–Climpara–94–Rutherford–Appleton–Laboratory–06–1994)

Chiu LS, Chang ATC (2000) Oceanic rain column height derived from SSM/I. J Climate 13:4125–4136

Chiu LS, Chokngamwong R (2010) Microwave emission brightness temperature histograms (METH) rain rates for climate studies: Remote Sensing Systems SSM/I version-6 results. J Appl Meteorol Clim 49:115

Chiu LS, Kedem B (1990) Estimating the exceedance probability of rain by logistic regression. J Geophys Res 95:2177–2227

Chiu LS, North G, Short D, McConnell A (1990) Rain estimation from satellite: effect of finite field of view. J Geophys Res 95(D3):2177–2185

Chiu LS, Chang ATC, Janowiak J (1993) Comparison of monthly rain rates derived from GPI and SSM/I using probability distribution functions. J Appl Meteorol 32:323–334

Chiu LS, Chokngamwong R, Xing Y, Shie C-L (2008) "Trends" and variations of global oceanic evaporation data set from remote sensing. Acta Oceanol Sin 24:127–135

Chiu LS, Chokngamwong R, Wilheit TT (2010) Modified monthly oceanic rain-rate algorithm to account for TRMM boost. IEEE Trans Geosci Remote Sens 48:3081–3086

Chiu LS, Gao S, Shie C-L (2012) Oceanic evaporation: trends and variabilities. In: Escalante-Ramírez B (ed) Remote sensing – applications. InTech, Rijeka

Cho H-K, Bowman KP, North GR (2004) A comparison of gamma and lognormal distributions for characterizing satellite rain rates from the Tropical Rainfall Measuring Mission. J Appl Meteorol 43:1586–1597

Chokngamwong R, Chiu LS (2006) Variation of oceanic rain rate parameters from SSM/I: mode of brightness temperature histogram, 14th conference in satellite meteorology and oceanography, AMS annual meeting, Atlanta, Jan 29–Feb 2 2006

Chokngamwong R, Chiu LS (2009) Development of the microwave calibrated infrared split-window technique (MIST) for rainfall estimation. Int J Remote Sens 30:3115–3131

Dai A (2001) Global precipitation and thunderstorm frequencies. Part I: seasonal and interannual variations. J Climate 14:1092–1111

Ellis TD, L'Ecuyer T, Haynes JM, Stephens GL (2009) How often does it rain over the global oceans? The perspective from CloudSat. Geophys Res Lett 36:L03815

Ha E, North GR (1995) Model study of the beam-filling error for rainfall retrieval with microwave radiometers. J Atmos Ocean Technol 12:268–281

Hollinger JP, Pierce JL, Poe GA (1990) SSM/I instrument evaluation. IEEE Trans Geosci Remote Sens 28:781–790

Huffman GJ, Adler RF, Arkin P, Chang ATC, Ferrero R, Gruber A, Janowiak J, McNab A, Rudolph B, Schneider U (1997) The global precipitation climatology project (GPCP) combined precipitation dataset. Bull Am Meteorol Soc 78:5–20

Huffman GJ, Adler RF, Morrissey M, Bolvin DT, Curtis S, Joyce R, McGavock B, Susskind J (2001) Global precipitation at one-degree daily resolution from multi-satellite observations. J Hydrometeorol 2:36–50

Inoue T (1987) An instantaneous delineation of convective rainfall area using split window data of NOAA-7 AVHRR. J Meteorol Soc Jpn 65:469–481

Kafatos M, Chiu LS, Yang RX et al (2001) Interannual variation of oceanic precipitation, IGARSS 2001: scanning the present and resolving the future, vol 1–7, Proceedings, in IEEE international symposium on geoscience and remote sensing (IGARSS), pp 1143–1145

Kedem B, Chiu LS (1987a) On the lognormality of rain rate. Proc Natl Acad Sci 84:901–905

Kedem B, Chiu LS (1987b) Are rain rate processes self–similar? Water Resour Res 23:1816–1818

Kedem B, Chiu LS, North G (1990) Estimation of mean rain rate: application to satellite observation. J Geophys Res 95:1965–1972

Kubota T, Shige S, Aonashi K, Okamoto K (2009) Development of nonuniform beamfilling correction method in rainfall retrievals for passive microwave radiometers over ocean using TRMM observations. J Meteorol Soc Jpn 87a:153–164

Kummerow C (1998) Beamfilling errors in passive microwave rainfall retrievals. J Appl Meteorol 37:356–370

Kummerow C et al (2000) The status of the tropical rainfall measuring mission (TRMM) after 2 years in orbit. J Appl Meteorol 39:1965–1982

Kummerow C, Poyner P, Berg W, Thomas-Stahle J (2004) The effects of rainfall inhomogeneity on climate variability of rainfall estimated from passive microwave sensors. J Atmos Ocean Technol 21:624–638

Kunkee DB, Poe GA, Boucher DJ, Swadley SD, Hong Y, Wessel JE, Uliana EA (2008) Design and evaluation of the first special sensor microwave imager/sounder. IEEE Trans Geosci Remote Sens 46:863–883

Lafont D, Guillemet B (2004) Subpixel fractional cloud cover and inhomogeneity effects on microwave beam-filling error. Atmos Res 72:149–168

Lin J-L (2007) The double-ITCZ problem in IPCC AR4 coupled GCMs: ocean-atmosphere feedback analysis. J Climate 20:4497–4525

Liu WT, Xie X (2002) Double intertropical convergence zones–a new look using scatterometer. Geophys Res Lett 29:2072

Lovejoy G, Austin G (1979) The delineation of rain areas from visible and IR satellite data for GATE and mid-latitudes. Atmos-Ocean 17:77–92

Marshall JS, Palmer W (1948) The distribution of raindrops with size. J Meteorol 5:165–166

North GR, Bell TL, Cahalan RF, Moeng FJ (1982) Sampling errors in the estimation of empirical orthogonal functions. Mon Weather Rev 110:699–706

Petty GW (1995) Frequencies and characteristics of global oceanic precipitation from shipboard present-weather reports. Bull Am Meteorol Soc 76:1593–1616

Petty G (1997) An intercomparison of oceanic precipitation frequencies from 10 special sensor microwave/imager rain rate algorithms and shipboard present weather reports. J Geophys Res 102:1757–1777

Shimizu S, Oki R, Tagawa T, Iguchi T, Hirose M (2009) Evaluation of the effects of the orbit boost of the TRMM satellite on PR rain estimates. J Meteorol Soc Jpn 87:83–92

Shin DB, Chiu LS (2008) Effects of TRMM boost on oceanic rainfall estimates based on microwave emission brightness temperature histograms (METH). J Atmos Ocean Technol 25:1888–1893

Short DA (2003) Equatorial Atlantic rain frequency: an intercentennial comparison. J Climate 16:2296–2301

Short DA, Nakamura K (2010) Effect of TRMM orbit boost on radar reflectivity distributions. J Atmos Ocean Technol 27:1247–1254

Short DA, North GR (1990) The beam-filling error in the NIMBUS 5 electrically scanning microwave radiometer observations of global tropical Atlantic tropical experiment rainfall. J Geophys Res 95:2187–2193

Wang A (1997) Modeling the beam filling correction for the microwave retrieval of oceanic rainfall. PhD dissertation, Texas A&M University

Weng H, Ashok K, Behera SK, Rao SA, Yamagata T (2007) Impacts of recent El Niño Modoki on dry/wet conditions in the Pacific rim during boreal summer. Climate Dyn 29:113–129

Wilheit TT, Chang ATC, Rao MSV, Rodgers EB, Theon JS (1977) A satellite technique for quantitatively mapping rainfall rates over the oceans. J Appl Meteorol 16:551–560

Wilheit TT, Chang ATC, Chiu LS (1991) Retrieval of monthly rainfall indices from microwave radiometric measurements using probability distribution functions. J Atmos Ocean Technol 8:118–136

Woodruff SD, Slutz RJ, Jenne RL, Steurer PM (1987) A comprehensive ocean-atmosphere data set. Bull Am Meteorol Soc 68:1239–1250

Woodruff SD, Worley SJ, Lubker SJ, Ji Z, Freeman JE, Berry DI, Brohan P, Kent EC, Reynolds RW, Smith SR, Wilkinson C (2011) ICOADS Release 2.5: extensions and enhancements to the surface marine meteorological archive. Int J Climatol 31:951–967

Xie P, Janowiak JE, Arkin PA, Adler RF, Gruber A, Ferraro RR, Huffman GJ, Curtis S (2003) GPCP pentad precipitation analyses: an experimental dataset based on gauge observations and satellite estimates. J Climate 16:2197–2214

Yeh S-W, Kirtman BP, Kug J-S, Park W, Latif M (2011) Natural variability of the central Pacific El Niño event on multi–centennial timescales. Geophys Res Lett 38:L02704

Zhang C (2001) Double ITCZs. J Geophys Res 106:11785–11792

Chapter 16
Integrating Landsat with MODIS Products for Vegetation Monitoring

Feng Gao

Abstract Satellite imagery provides a valuable data source for monitoring vegetation from space. In order to monitor vegetation dynamic and changes, high spatial resolution satellite imagery with frequent acquisition is required. However, current satellite systems cannot satisfy these requirements due to either technical or fiscal difficulties. In recent years, studies have been focused on integrating high spatial resolution Landsat and high temporal resolution MODIS data for vegetation monitoring. This chapter describes three categories of approach to integrate two data sources. The first category approach adopts MODIS algorithms for Landsat data processing. The second category approach blends Landsat and MODIS data through a data fusion approach. The third category approach normalizes Landsat data using standard MODIS data products. This chapter presents examples and recent applications on the integration of Landsat and MODIS data. Their advantages and limitations are discussed.

16.1 Introduction

The Landsat satellites have been providing earth observation data continuously since early 1970s and form a cornerstone for medium spatial resolution remote sensing. Landsat is the sole medium resolution satellite that provides continuous global coverage in nearly four decades. Though the failure of the scan-line corrector (SLC) mechanism on Landsat 7 in 2003 and the decommisioned Landsat 5 in 2012 have threatened this continuity, Landsat data are still the most widely used medium resolution remote sensing data especially after Landsat data become freely available from the US Geological Survey (USGS) Earth Resources Observation and Science (EROS) Center since October 2008 (www1).

F. Gao (✉)
USDA, Agricultural Research Service, Hydrology and Remote Sensing Laboratory,
104 BARC-West, Baltimore Avenue, 10300, Beltsville, MD 20705, USA
e-mail: Feng.Gao@ars.usda.gov

J.J. Qu et al. (eds.), *Satellite-based Applications on Climate Change*,
DOI 10.1007/978-94-007-5872-8_16,

Table 16.1 Corresponding bandwidths of Landsat TM/ETM+ and MODIS

Landsat TM/ETM+	TERRA/AQU MODIS
B1: 0.45–0.52	B3: 0.459–0.479
B2: 0.53–0.61	B4: 0.545–0.565
B3: 0.63–0.69	B1: 0.620–0.670
B4: 0.78–0.90	B2: 0.841–0.876
B5: 1.55–1.75	B6: 1.628–1.652
B7: 2.08–2.35	B7: 2.105–2.155

Landsat has been widely used in agriculture, geology, forestry, regional planning, education, mapping, and global change research (Townshend et al. 1991; Loveland and Shaw 1996). For example, the US Department of Agriculture (USDA) National Agricultural Statistics Service (NASS) uses Landsat and other medium resolution data to generate annual crop data layer (CDL) for each state in the United States (www2). The USGS EROS produced the National Land Cover Data (NLCD) on 2001 and 2006 based on Landsat TM and ETM+ data (www3). More recently, many time series data analysis approaches have been developed and applied to Landsat image stack for detecting surface changes such as mapping forest disturbance and regrowth in past four decades (Masek et al. 2008; Huang et al. 2009; Kennedy et al. 2010). Projects funded by different countries/agencies are using Landsat data to map land cover and land use changes at continental or global scale. More global Landsat data products and applications can be expected in upcoming years (Gong et al. 2013).

The Moderate-Resolution Imaging Spectroradiometer (MODIS) is a key instrument launched into Earth orbit by NASA on board the Terra satellite in 1999 and then onboard the Aqua satellite in 2002. MODIS instrument provides 36 spectral bands ranging from visible, near-infrared bands to thermal infrared bands in different spatial resolutions (red and near-infrared bands at 250 m, 5 spectral bands at 500 m, and 29 other bands at 1 km). Table 16.1 lists the similar bandwidths for Landsat and MODIS. Each Landsat band has a corresponding MODIS band except that MODIS bandwidths are narrower.

MODIS is designed to provide measurements in global dynamics for land, ocean, and atmosphere (Justice et al. 2002). MODIS data are well calibrated, and data products have been validated with independent field measurements (www4). MODIS products provide extensive quality assessment (QA) data layers to flag data quality associated with input data and algorithm. MODIS data products have been used in many applications and help to improve our understanding on climate changes, vegetation dynamics, weather forecasting, etc.

In general, Landsat data provide sufficient spatial details (30 m for TM/ETM+) for monitoring land surface and changes (Townshend and Justice 2002; Loveland et al. 2008; Gutman et al. 2008; Goward et al. 2008). However, the 16-day revisit cycle has limited its use for studying global biophysical processes, which evolve rapidly during the growing season. Meanwhile, MODIS sensors aboard the NASA EOS Terra and Aqua satellites provide daily global observations which are valuable for capturing rapid surface changes. However, the spatial resolutions of 250–1,000 m may not be

good enough for heterogeneous areas. A feasible and less expensive approach is to integrate Landsat and MODIS data for applications.

There are varieties of approaches to integrate Landsat and MODIS data. In this chapter, we limit our discussions on several selected examples and focus on three categories of integration. The first category focuses on the algorithm integration and tries to create consistent MODIS data product for Landsat using similar algorithm such as the Landsat Ecosystem Disturbance Adaptive Processing System (LEDAPS). The second category focuses on the data fusion approach and attempts to integrate high temporal information from MODIS with high spatial information from Landsat such as the Spatial and Temporal Adaptive Reflectance Fusion Model (STARFM). The third category focuses on producing consistent data products using MODIS data products as references.

16.2 Algorithm Integration

In order to integrate Landsat and MODIS data product, an intuitive idea is to use MODIS algorithm for Landsat and produces similar data products at Landsat spatial resolution. A first step of this effort is to produce surface reflectance using MODIS algorithm. The surface reflectance product strives to remove atmospheric effects (scattering and absorption) and is the basis for many high-level products and quantitative applications. The LEDAPS is a NASA project to map disturbance, regrowth, and permanent forest conversion across the continent (Masek et al. 2006). It processes Landsat imagery to surface reflectance, using atmospheric correction routines developed for the Terra MODIS instrument (Vermote et al. 2002).

The LEDAPS first calibrates Landsat data in digital number to the top-of-atmosphere (TOA) reflectance using calibration coefficients provided in the metadata file. TOA reflectance is then atmospherically corrected using the 6S radiative transfer code (Vermote et al. 1997) similar to the MODIS surface reflectance product. Atmosphere correction procedure needs ancillary information on ozone and water vapor, etc. Ozone concentrations are derived from Total Ozone Mapping Spectrometer (TOMS) data aboard the Nimbus-7, Meteor-3, and Earth Probe platforms. Column water vapor uses data from the NCEP reanalysis data. The ozone and water vapor data are downloaded and organized into daily ancillary data for LEDAPS processing. Digital topography and NCEP surface pressure data are used to adjust Rayleigh scattering to local conditions (Masek et al. 2006).

Similar to the atmospheric correction scheme in the MODIS surface reflectance product, LEDAPS retrieves aerosol optical thickness (AOT) from Landsat imagery using the dark and dense vegetation concept (Kaufman et al. 1997). Aerosol optical depth is retrieved at 1-km coarse spatial resolution first and then interpolated spatially between the dark targets. The 6S radiative transfer algorithm uses the interpolated AOT, ozone, atmospheric pressure, and water vapor to retrieve surface reflectance.

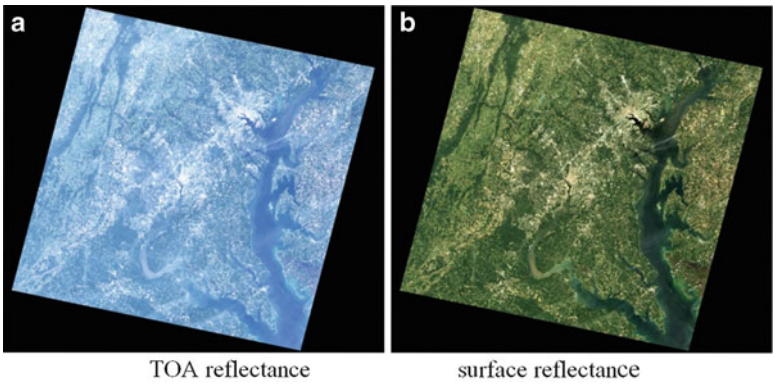

Fig. 16.1 True color composites of a Landsat-7 ETM+ scene (WRS-2 path 15 and row 33 acquired on September 6, 2002) show that the surface reflectance (**b**) removes atmosphere effect from TOA reflectance (**a**)

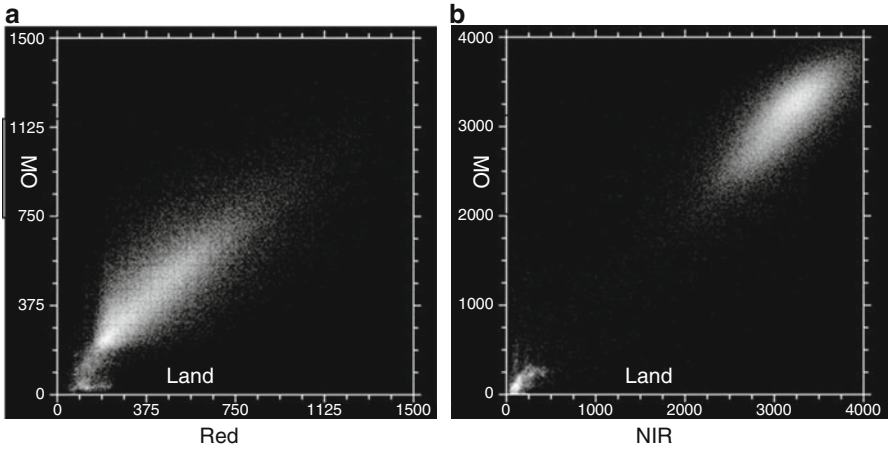

Fig. 16.2 Scattering plot of surface reflectance for red (**a**) and NIR (**b**) between MODIS and Landsat (in Fig. 16.1). Scale factor for reflectance is 0.0001

Figure 16.1 shows the true color composites of Landsat ETM+ reflectance produced from the LEDAPS system for a DC scene (WRS-2 path 15 and row 33) acquired on September 6, 2002. The TOA reflectance image looks hazier and brighter than surface reflectance.

Comparison of surface reflectance between Landsat and MODIS shows general good agreements. In Fig. 16.2, surface reflectance from Landsat in Fig. 16.1 are first aggregated to MODIS resolution (500 m) and then compared to MODIS surface reflectance. The scattering plot shows a general 1-to-1 relationship. Some disagreements may be caused by the geolocation mismatch and bandwidth differences.

A stand-alone LEDPAS software package extracted from the NASA LEDAPS system has been released to public for scientific uses. It is freely available from the NASA GSFC LEDAPS Web site (www5). The LEDAPS system has been adopted by

the USGS EROS to produce the next generation Landsat data product. The Global Land Survey Facility at the University of Maryland used LEDAPS approach and produced global Landsat surface reflectance from Global Land Survey (GLS) data. The extensive comparisons of surface reflectance between Landsat and MODIS show general good agreements with overall discrepancies (root-mean-squared deviation (RMSD)) between 1.0 and 2.5% reflectance for Landsat-7 ETM+ and between 1.6 and 3.2% reflectance for Landsat-5 TM (Feng et al. 2012, under review). The Web-enabled Landsat Data (WELD) project, a joint effort between South Dakota State University and the USGS EROS, uses same atmosphere correction approach (6S) but different ancillary data from MODIS atmosphere data products to generate 30-m composites of Landsat mosaics at weekly, monthly, seasonal, and annual periods for the conterminous United States (CONUS) and Alaska (Roy et al. 2010; www6).

Surface reflectance is the basis for generating high-level biophysical products such as Leaf Area Index (LAI). Using Landsat surface reflectance, NASA AMES has prototyped Landsat LAI product by adopting MODIS LAI algorithm (Ganguly et al. 2012).

16.3 Data Fusion Approach

The data fusion solution integrates the spatial resolution of Landsat with the temporal frequency of coarse-resolution MODIS sensor and thus produces fused data products for applications that require high resolution in both time and space (Gao et al. 2006; Hansen et al. 2008).

Traditional image fusion methods such as intensity-hue-saturation (IHS) transformation, principal component substitution (PCS), and wavelet decomposition focus on producing new multispectral images that combine high-resolution panchromatic data with multispectral observations acquired simultaneously at coarser resolution. They are useful for generating pan-sharpened images. However, they are not effective in fusing spatial resolution and temporal coverage when input data sources are acquired from different dates which may be affected by large geolocation errors, high ratio of coarse-to-fine resolution, and land surface changes.

16.3.1 STARFM Approach

The Spatial and Temporal Adaptive Reflectance Fusion Model (STARFM) was developed to combine high spatial Landsat and high temporal MODIS data (Gao et al. 2006). This approach requires input data pairs to be consistent. Observations from different platforms first need to be calibrated and atmospherically corrected to surface reflectance so that they are comparable spatially and temporally. Landsat data are calibrated and atmospherically corrected using the LEDAPS approach. Although MODIS and Landsat surface reflectance data are very consistent.

However, due to the differences in the acquisition time, bandwidth, and geolocation errors, bidirectional effect and small biases are expected. For a homogenous "pure" pixel at the coarser MODIS resolution, surface reflectance measured by Landsat data may be expressed as

$$L(x, y, t_k) = M(x, y, t_k) + \varepsilon_k \tag{16.1}$$

where (x, y) is a given pixel location for both Landsat (L) and MODIS (M) images, t_k is acquisition date for both MODIS and Landsat data, and ε_k represents the difference between the observed MODIS and Landsat surface reflectance (caused by differing bandwidth and solar geometry).

Supposing land cover type and system errors at pixel (x, y) do not change between prediction dates t_0 and t_k, we will have $\varepsilon_0 = \varepsilon_k$, and thus

$$L(x, y, t_0) = L(x, y, t_k) + (M(x, y, t_0) - M(x, y, t_k)) \tag{16.2}$$

However, this ideal situation cannot often be satisfied from MODIS and Landsat observations. In most cases, the MODIS observation is not a homogeneous pixel and may include mixed land cover types when considered at Landsat spatial resolution. To consider mixed pixels in the prediction, we introduce additional information from neighboring pixels and use spectrally similar pixels in the prediction. The predicted surface reflectance for the central pixel at date t_0 is then computed with a weighting function:

$$L(w/2, w/2, t_0) = \sum_{x=1}^{w} \sum_{y=1}^{w} \sum_{k=1}^{n} W_{ijk} \times (L(x, y, t_k) + (M(x, y, t_0) - M(x, y, t_k))) \tag{16.3}$$

where w is the searching window size and (w/2, w/2) is the central pixel of this moving window. To ensure the correct information from neighboring pixels is used, only spectrally similar (i.e., from the same spectral class) and cloud-free pixels from Landsat surface reflectance within the moving window are used to compute reflectance.

The weighting function W_{ijk} determines how much each neighboring pixel contributes to the estimated reflectance of the central pixel. It is determined by three measures based on (1) spectral difference between MODIS and ETM+ data at a given location, (2) temporal difference between input and the predicted MODIS data, and (3) geographic distance between the central pixel and the candidate pixel. These measures ensure that "pure" neighbor pixels get higher weights in the prediction.

The STARFM approach was tested for simulated data and real satellite observations (Gao et al. 2006). Figure 16.3 shows a simulation test for changing reflectance and linear objects. Linear objects such as roads and small rivers are normally visible in fine-resolution Landsat imagery but are not obvious in coarse-resolution MODIS imagery. Figure 16.3a–c represent simulated Landsat-like

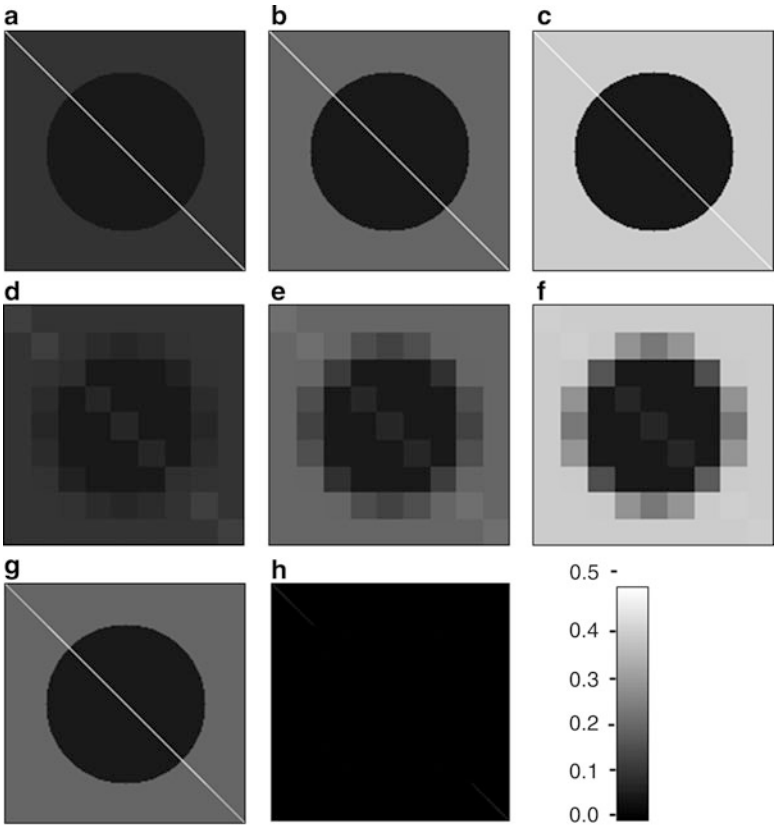

Fig. 16.3 A simulation test for changing reflectance and linear objects. The MODIS-like resolution data (**d–f**) are aggregated from the Landsat-like data (**a–c**), respectively. Imagery (**g**) is predicted from fine-resolution imageries (**a**) and (**c**) and coarse-resolution imageries (**d–f**). Imagery (**h**) is the absolute difference between prediction (**g**) and truth (**b**). In this test, the STARFM algorithm predicts constant reflectance, changing reflectance, and linear segment (*within circle*) well. Linear segments *outside circle* are predicted but not perfect value

images with background changing from 0.1 (Fig. 16.3a) to 0.2 (Fig. 16.3b) and then 0.4 (Fig. 16.3c). The simulated water body (circle) has a constant reflectance of 0.05. The simulated road (over background) and bridge (over water) have a constant reflectance of 0.5. The MODIS-like data (Fig. 16.3d–f) are aggregated from the Landsat-like data. Roads (over background) are still visible in Fig. 16.3d, e, but not in Fig. 16.3f due to the smaller contrast of roads and background in (Fig. 16.3c). Figure 16.3g is a predicted version of Fig. 16.3b using fine-resolution images (Fig. 16.3a, c) and coarse-resolution imageries (Fig. 16.3d–f). Figure 16.3h shows the absolute difference between prediction (Fig. 16.3g) and truth (Fig. 16.3b). In this test, constant reflectance, changing reflectance, and the bridge are predicted perfectly. Roads (segment outside circle) are predicted but not perfect value.

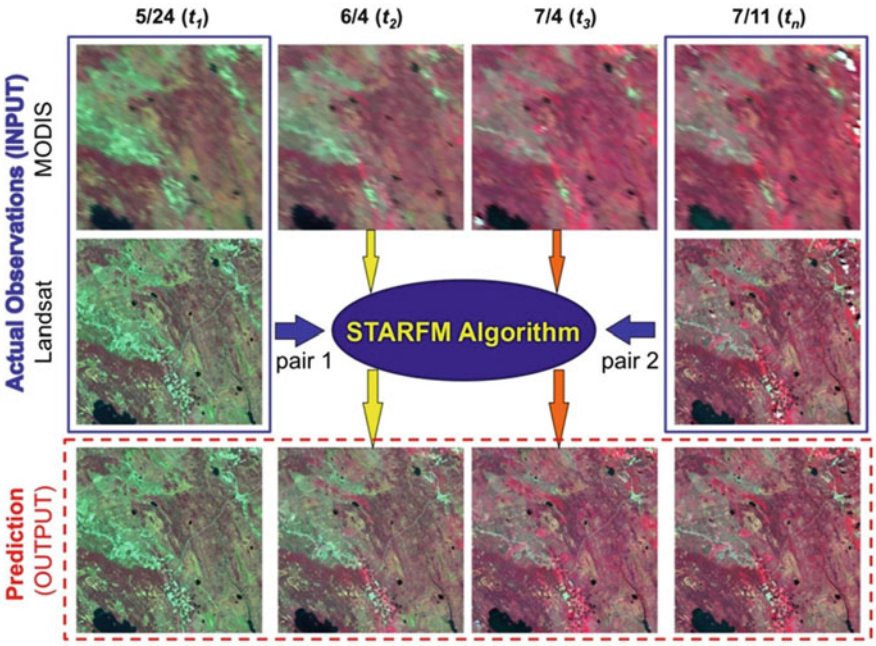

Fig. 16.4 Predicted Landsat surface reflectance (*bottom row*) from daily MODIS reflectance imagery (*top row*) and Landsat/MODIS imagery pairs (in *blue rectangles*) on the BOREAS Southern Study Area (54°N, 104°W). In this example, Landsat observations were not available on 6/4 (t_2) and 7/4 (t_3) in 2001 – the Landsat-resolution images at t_2 and t_3 are entirely synthesized from the simultaneous MODIS data and bracketing Landsat images using the STARFM algorithm

Figure 16.4 shows the STARFM predicted Landsat surface reflectance on 6/4 and 7/4 in 2001 for the BOREAS Southern Study Area using same-day MODIS images and ETM+/MODIS image pairs on 5/24 and 7/11 in 2001. In this example, Landsat observations are not available on 6/4 (t_2) and 7/4 (t_3). This process may also be thought of as using daily MODIS information to make a "time correction" to infrequent Landsat data. The predicted images (bottom row) capture rapid seasonal changes from MODIS data while retaining the Landsat spatial details. Clear land and water boundaries can be predicted. Linear objects such as roads can be observed in the predicted images.

Initial validation studies show that both mean differences and absolute differences of surface reflectance between predictions (i.e., synthesized Landsat-resolution data) and real Landsat observations are small. STARFM can preserve the high spatial resolution of Landsat and high temporal resolution of MODIS if "pure" coarse-resolution neighbor pixels can be found within the moving window. For complex mixtures of different land cover types, performance degrades somewhat, and the adjustment of algorithm parameters may be needed to improve prediction.

The original STARFM code has been released for public use since 2006. The STARFM and derived approaches have been tested and used for fusing Landsat and MODIS reflectance (Gao et al. 2006; Hilker et al. 2009a). Several ongoing researches are expanding STARFM approach to different biophysical parameters and use it for sensors other than Landsat and MODIS.

16.3.2 The Enhanced STARFM Approach

In order to better handle heterogeneous pixels even if no "pure" neighbor pixel exists, an enhanced STARFM approach was recently developed based on a pixel unmixing theory (Zhu et al. 2010). An additional assumption in the enhanced STARFM is that the percentages of land types contained in the mixed coarse-resolution pixel remain the same during the prediction period. Therefore, the reflectance of a mixed MODIS pixel can be described as the linear mixture of Landsat pixels for two input pairs with the same percentages of land cover types. The ESTARFM approach introduces a conversion coefficient into the prediction. The conversion coefficient indicates the ratio of the change of reflectance for the end-member to the change of reflectance for a mixed coarse-resolution pixel from input pairs. When the end-members are taken as fine-resolution pixels within a mixed coarse-resolution pixel, the conversion coefficient can be computed by linearly regressing the reflectance changes of fine-resolution pixels of the same end-member and coarse-resolution pixel. Taking into consideration the spectral similar pixels, the final prediction for the center pixel ($w/2$, $w/2$) in the moving window with end-member i can be revised to

$$L(w/2, w/2, t_0) = \sum_{x=1}^{w} \sum_{y=1}^{w} \sum_{k=1}^{n} W_{ijk}(L_i(x, y, t_k) + v_i(x, y) \times (M(x, y, t_0) - M(x, y, t_k))) \quad (16.4)$$

where $v_i(x, y)$ is the conversion coefficient for the ith end-member in the mixed pixel (x, y). It can be computed based on two acquisition pairs (t_m and t_n):

$$\nu_i(x, y) = \frac{L_i(x, y, t_n) - L_i(x, y, t_m)}{M(x, y, t_n) - M(x, y, t_m)} \quad (16.5)$$

Results from simulated data and real satellite data show that the enhanced STARFM can improve the accuracy of prediction, especially for complex heterogeneous landscapes, and preserve spatial details for small patches. In a homogeneous area, the prediction of ESTARFM is slightly better than STARFM with the average absolute difference of 0.0106 (vs. 0.0129) for the NIR band. In a complex mixed area, the prediction accuracy of ESTARFM is improved significantly when compared to the original STARFM (0.0135 vs. 0.0194) for NIR band (Zhu et al. 2010).

16.3.2.1 STAARCH for Mapping Reflectance Change

Hilker et al. (2009b) developed a new data fusion model STAARCH for detecting reflectance changes associated with land cover change and disturbance. STAARCH produces both a spatial change mask from two Landsat images as well as an image sequence from the MODIS time series which describes the temporal evolution of disturbance events. The algorithm includes functionality for the prediction of surface reflectance based on an extended version of STARFM. The STAARCH approach constrains the optimal image pair to be used in the STARFM prediction.

Hilker et al. (2009b) applied the STAARCH approach over a 185 × 185 km area in southern Alberta, Canada. Results show that STAARCH predictions agreed well with field-based observations (93% for spatial accuracy of the disturbed area). Temporal changes in the landscape were correctly predicted for 87–89% of instances for the total disturbed area (Hilker et al. 2009b). The change sequence derived from STAARCH was used to fuse Landsat images for each available date of MODIS imagery. The fused results were improved when compared to existing Landsat observations.

STAARCH requires a minimum of two image pairs to develop the change mask required as input to the algorithm. It focuses on detecting changes at Landsat scale from the MODIS time series. ESTARFM also requires two image pairs but focuses more on improving predictions for the mixed pixels.

16.3.3 Products Normalization

Remote sensing data products from different instruments may not consistent due to many factors such as the differences in spectral bandwidth, spectral response function, spatial resolution, and processing approach (Roy et al. 2008). Even using same algorithm, Landsat and MODIS data products may be different. The normalization approach produces a consistent data product using MODIS data products as references. Gao et al. (2010) developed a generalized reference-based approach to build a MODIS-consistent data set from multiple Landsat-like sensors. The generalized reference-based empirical approach was tested for converting medium resolution data product from digital number (DN) to a standard surface reflectance product. The globally available, consistent MODIS surface reflectance products were used as the reference. As opposed to a physically based atmosphere correction approach (e.g., LEDAPS), this empirical approach is a relative correction, and therefore, the corrected surface reflectance is a kind of "MODIS-like" surface reflectance. It provides a way to standardize satellite data from different medium resolution sensors to one standard and thus allow continuous time-series analysis and land cover change detection. This approach builds on a long history of regression-based image normalization procedures from the remote sensing literature (Schott et al. 1988; Du et al. 2001; Olthof et al. 2005) and provides a practical "operational" framework for merging information from multiple sensors.

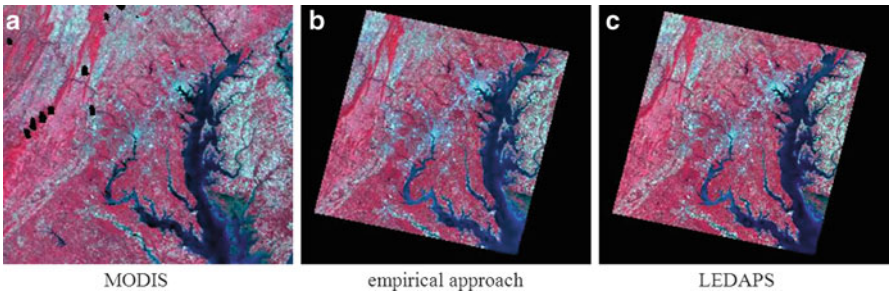

Fig. 16.5 MODIS surface reflectance (**a**) and Landsat ETM + surface reflectance derived from the reference-based approach (**b**) and LEDAPS physical approach (**c**) for Washington DC area (Landsat WRS-2 path 15 and row 33). *Black areas* represent clouds, cloud shadows, and missing or poor quality data

The basis of this approach is that homogeneous pixels of the same land cover type have the same surface reflectance regardless of patch size and that the seasonal and bidirectional reflectance changes of those pixels should also be the same for different patch sizes given each land cover type does not split into two or more types (1-to-*n*) during a short period. The relationship of each land cover type between acquisition date and target date remain approximately same for different resolution images. Therefore, the relationships built on the MODIS data and the aggregated medium resolution data can be applied to medium resolution data to produce surface reflectance at a target date (e.g., MODIS acquisition date).

Differing from traditional empirical approaches that need to measure surface reflectance on the ground, this approach takes ground "truth" from MODIS data. The high-quality MODIS data represent one of the most accurate data records we achieved today and are thus an appropriate data source to use as a reference data set. The approach uses the cluster-based pure homogeneous pixels as samples; this allows the approach to be generalized and deal with various seasonal changes from different surface types and can be extended to other biophysical parameters.

Figure 16.5 shows the Landsat surface reflectances derived from the physical-based LEDAPS approach (Fig. 16.5c) and the reference-based normalized approach (Fig. 16.5b). They are very similar in surface reflectance composition from near-infrared, red and green bands.

The normalization approach can be used to normalize satellite images from different acquisition dates to a close and clear MODIS acquisition date. Figure 16.6 illustrates the processing result over Chesapeake Bay. In the test, 14 Landsat Global Land Survey (GLS)-2000 data were used. Although the GLS-2000 Landsat scenes have been selected from growing seasons, the differences are inevitable due to the different acquisition dates. Figure 16.7a is the mosaic of Landsat surface reflectance produced by the LEDAPS system. The differences of seasonality are obvious on this map. However, those differences have been reduced in the mosaic map of the normalized Landsat images by using MODIS surface reflectance as a correction reference. The remaining differences in water body are due to the lack of samples from MODIS NBAR product.

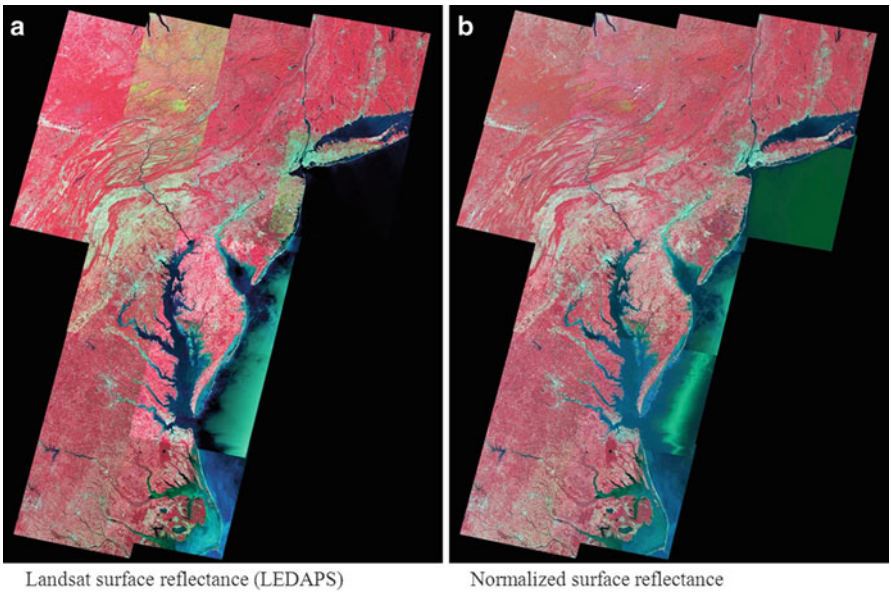

Fig. 16.6 Fourteen GLS-2000 Landsat scenes acquired from different dates are normalized to the MODIS-like surface reflectance by using MODIS Nadir BRDF-adjusted reflectance (September 21–October 6, 2000) as a reference. The normalized surface reflectance (**b**) reduced the seasonal variations in the original surface reflectance mosaic (**a**)

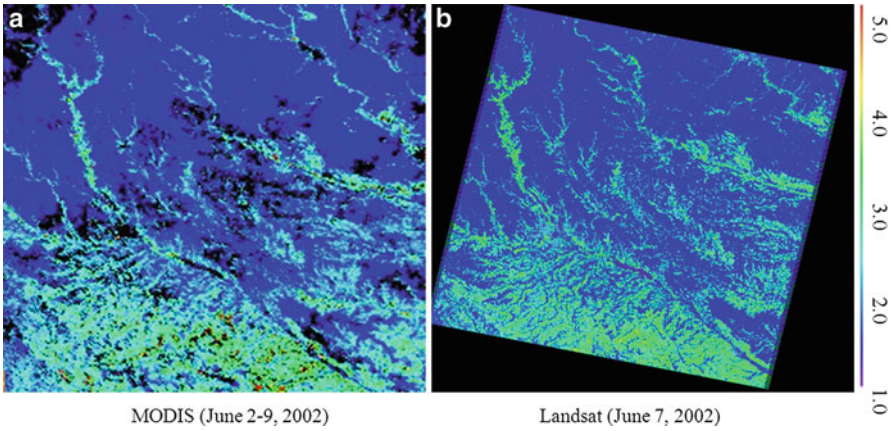

Fig. 16.7 Leaf Area Index (LAI) retrieved from Landsat (June 7, 2002) (**b**) using referenced-based approach shows consistent values to the MODIS LAI product (June 2–9, 2002) (**a**) during same period. *Black* represents the missing or low quality value

Similar normalization approach can be applied for retrieving biophysical parameters. In Fig. 16.7, MODIS Leaf Area Index (LAI) 8-day composite product (MOD15A2, Myneni et al. 2002) from June 2–9, 2002, was used as a reference to retrieve LAI from Landsat data (WRS-2 path 26 and row 31). The LAI from

Landsat and MODIS are consistent in the test. The accuracy of normalization approach depends on the data qualities of Landsat surface reflectance and MODIS data products. Well-distributed high-quality samples across the full range of data product values can help to reduce the variability.

The MODIS data products are the appropriate data sources for use as a reference for Landsat since (1) MODIS has similar bandwidth to medium resolution data sources, (2) MODIS provides daily global coverage data, (3) MODIS products have been validated in transparent validation exercises and provide comprehensive pixel level quality control flags, and (4) MODIS products are freely available online and easy to access. Other consistent coarse-resolution data sources can also be used as reference. When MODIS data products are utilized as references, the results will be limited to the MODIS era.

Different from other data fusion approaches such as the STARFM and the STAARCH, the normalization approach only requires one target MODIS data and thus simpler and faster. However, it assumes that land cover types do not change and split to 1-to-*n* relation between medium spatial resolution sensor and target MODIS acquisition date. Ideally, the medium spatial resolution data and MODIS data should be acquired from the same season in similar phenology stage.

References

Du Y, Cihlar J, Beaubien J, Latifovic R (2001) Radiometric normalization, compositing, and quality control for satellite high resolution image mosaics over large areas. IEEE Trans Geosci Remote Sens 39:623–634. doi:10.1109/36.911119

Feng M, Sexton JO, Huang C, Masek JG, Vermote EF, Gao F, R Narasimhan, Channan S, Wolfe RE, Townshend JR (2012) Global, long-term surface reflectance 1 records from Landsat. Remote Sens Environ (under review)

Ganguly S, Nemani R, Zhang G et al (2012) Generating global leaf area index from Landsat: algorithm formulation and demonstration. Remote Sens Environ 122:185–202. doi:10.1016/j.rse.2011.10.032

Gong P, Wang J, Yu L et al (2013) Finer resolution observation and monitoring of global land cover: first mapping results with Landsat TM and ETM+ data. Int J Remote Sens 34(7):2607–2654

Gao F, Masek J, Schwaller M, Hall F (2006) On the blending of the Landsat and MODIS surface reflectance: predict daily landsat surface reflectance. IEEE Trans Geosci Remote Sens 44(8):2207–2218

Gao F, Masek J, Wolfe R, Huang C (2010) Building consistent medium resolution satellite data set using moderate resolution imaging spectroradiometer products as reference. JAppl Remote Sens 4:043526. doi:10.1117/1.3430002

Goward SN, Masek JG, Cohen WB, Moisen G, Collatz G, Healey S, Houghton RA, Huang C, Kennedy R, Law B, Powell S, Turner D, Wulder MA (2008) Forest disturbance and North American carbon flux. EOS Trans 89:105–116, American Geophysical Union

Gutman G, Byrnes R, Masek J, Covington S, Justice C, Franks S, Headley R (2008) Towards monitoring land cover and land-use changes at a global scale: the Global Land Survey (2005). Photogrammetr Eng Remote Sens 74:6–10

Hansen MC, Roy DP, Lindquist E, Justice CO, Altstaat A (2008) A method for integrating MODIS and Landsat data for systematic monitoring of forest cover and change in Central Africa. Remote Sens Environ 112:2495–2513

Hilker T, Wulder MA, Coops NC, Seitz N, White JC, Gao F, Masek JG, Stenhouse G (2009a) Generation of dense time series synthetic Landsat data through data blending with MODIS using a spatial and temporal adaptive reflectance fusion model. Remote Sens Environ. doi:10.1016/j.rse.2009.05.011

Hilker T, Wulder MA, Coops NC, Linke J, McDermid G, Masek JG, Gao F, White JC (2009b) A new data fusion model for high spatial- and temporal- resolution mapping of forest disturbance based on Landsat and MODIS. Remote Sens Environ. doi:10.1016/j.rse.2009.03.007

Huang C, Goward SN, Masek JG, Gao F, Vermote EF, Thomas N, Schleeweis K, Kennedy RE, Zhu Z, Eidenshink JC, Townshend JRG (2009) Development of time series stacks of Landsat images for reconstructing forest disturbance history. Int J Digi Earth. doi:10.1080/17538940902801614

Justice CO, Townshend JRG, Vermote EF, Masuoka E, Wolfe RE, Saleous N, Roy DP, Morisette JT (2002) An overview of MODIS land processing and products status. Remote Sens Environ 83:3–15. doi:10.1016/S0034-4257(02)00084-6

Kaufman YJ, Wald AE, Remer LA, Gao B-C, Li R-R, Flynn L (1997) The MODIS 2.1 um channel – correlation with visible reflectance for use in remote sensing of aerosol. IEEE Trans Geosci Remote Sens 35:1286–1298

Kennedy RE, Yang Z, Cohen WB (2010) Detecting trends in forest disturbance and recovery using yearly Landsat time series: 1. LandTrendr – temporal segmentation algorithms. Remote Sens Environ 114:2897–2910

Loveland TR, Cochrane MA, Henebry GM (2008) Landsat still contributing to environmental research – response. Trends Ecol Evol 23(4):182–183

Loveland TR, Shaw DM (1996) Multi-resolution land characterization: building collaborative partnerships. In: Scott JM, Tear TH, Davis FW (eds) GAP analysis: a landscape approach to biodiversity planning. American Society for Photogrammetry and Remote Sensing, Bethesda, pp 79–85

Masek JG, Vermote EF, Saleous NE, Wolfe R, Hall FG, Huemmrich F, Gao F, Kutler J, Lim TK (2006) A Landsat surface reflectance data set for North America, 1990–2000. IEEE Geosci Remote Sens Lett 3(1):69–72

Masek JG, Huang C, Wolfe R, Cohen W, Hall F, Kutler J, Nelson P (2008) North American forest disturbance mapped from a decadal Landsat record. Remote Sens Environ 112:2914–2926

Myneni RB, Hoffman S, Knyazikhin Y et al (2002) Global products of vegetation leaf area and fraction absorbed PAR from year one of MODIS data. Remote Sens Environ 83:214–231

Olthof I, Pouliot D, Fernandes R, Latifovic R (2005) Landsat ETM + radiometric normalization comparison for northern mapping applications. Remote Sens Environ 95:388–398. doi:10.1016/j.rse.2004.06.024

Roy DP, Ju J, Lewis P, Schaaf C, Gao F, Hansen M, Lindquist E (2008) Multi-temporal MODIS-Landsat data fusion for relative radiometric normalization, gap filling, and prediction of Landsat data. Remote Sens Environ 112:3112–3130

Roy DP, Ju J, Kline K, Scaramuzza PL, Kovalskyy V, Hansen MC, Loveland TR, Vermote EF, Zhang C (2010) Web-enabled Landsat data (WELD): Landsat ETM + composited mosaics of the conterminous United States. Remote Sens Environ 114:35–49

Schott JR, Salvaggio C, Volchock WJ (1988) Radiometric scene normalization using pseudo invariant features. Remote Sens Environ 26:1–16. doi:10.1016/0034-4257(88)90116-2

Townshend J, Justice C, Li W, Gurney C, McManus J (1991) Global land cover classification by remote sensing: present capabilities and future possibilities. Remote Sens Environ 35:243–255

Townshend JRG, Justice CO (2002) Towards operational monitoring of terrestrial systems by moderate resolution imaging. Remote Sens Environ 83:351–359

Vermote EF et al (1997) Atmospheric correction of visible to middle-infrared EOS-MODIS data over land surfaces: background, operational algorithm, and validation. J Geophys Res 102:17131–17 141

Vermote EF, El Saleous N, Justice C (2002) Atmospheric correction of the MODIS data in the visible to middle infrared: first results. Remote Sens Environ 83:97–111

www1: U.S. Geological Survey (USGS) Earth Resources Observation and Science Center (EROS). Global Visualization Viewer web page. http://glovis.usgs.gov/. Accessed 31 Dec 2012
www2: U. S. Department of Agriculture (USDA) National Agricultural Statistics Service (NASS). Research and Science web page. http://www.nass.usda.gov/Research_and_Science/index.asp. Accessed 31 Dec 2012
www3: USGS National Land Cover Database web page. http://www.mrlc.gov/. Accessed 31 Dec 2012
www4: NASA Goddard Space Flight Center (GSFC): MODIS Land Validation web page. http://landval.gsfc.nasa.gov/. Accessed 31 Dec 2012
www5: NASA GSFC Landsat Ecosystem Disturbance Adaptive Processing System (LEDAPS) web page. http://ledaps.nascom.nasa.gov/. Accessed 31 Dec 2012
www6: The Web-Enabled Landsat Data (WELD) web page. http://weld.cr.usgs.gov/. Accessed 31 Dec 2012
Zhu X, Chen J, Gao F, Masek J (2010) An enhanced spatial and temporal adaptive reflectance fusion model for complex heterogeneous regions. Remote Sens Environ 114:2610–2623. Accessed 31 Dec 2012

Chapter 17
Satellite Applications for Detecting Vegetation Phenology

Min Li and John J. Qu

Abstract Vegetation phenology describing the seasonal cycle of plants is currently one of the main concerns in the study of climate change and carbon balance estimation in ecosystems. Satellite-derived information has been demonstrated to be an important source for detecting vegetation phenology. A variety of methods have been developed to generate phenological metrics from satellite measurements varying from empirically, simple threshold of vegetation index to automated, elaborate logistic model. Each method provides certain advantages and paves the way for the success of satellite-derived vegetation phenology. The vegetation phenology derived from satellite measurements has been utilized for tracking vegetation dynamics, invasive species, and land use changes as well as assessing crop conditions, drought severity, and wildfire risk. Satellite sensors have their specific characteristics of temporal and spatial resolution, spatial coverage, and data quality and archive history. Each satellite takes advantages of its respective strengths to provide certain phenological applications. Despite the insights gained form satellite observations of vegetation phenology, the scale problem brings a big challenge for comparing satellite-derived vegetation phenology and ground records. In the future, more detailed information of ground records together with phenophases of individual species could be integrated to reflect the canopy phenology and compared with the satellite-derived phenology. The well-validated vegetation phenology from satellite measurements will contribute to the improvement in ecosystem process models.

M. Li (✉)
I. M. Systems Group, Inc, 5830 University Research Court, College Park, MD 20740, USA
e-mail: Min.Li@noaa.gov

J.J. Qu
Department of Geography and GeoInformation Science, Environmental Science and Technology Center, George Mason University, 4400 University Drive, Fairfax, VA 22030, USA

J.J. Qu et al. (eds.), *Satellite-based Applications on Climate Change*,
DOI 10.1007/978-94-007-5872-8_17,

17.1 Introduction

Phenology, first introduced in 1853 by the Belgian botanist Charles Morren, is derived from the Greek words phainos, meaning "to appear, to come into view," and logos, meaning "to study" (Haggerty and Mazer 2008). The study of phenology ranges from the leafing, maturating, and defoliating times of plants to the molting, mating, and migration times of animals. Since this chapter focuses on the plant phenological events, the animal phenological events are not within the scope. The plant phenological events can be observed and measured at multiple levels, varying from individual and population to community and biome. Information from each of these levels provides fundamental knowledge about ecological interactions and process in nature. Conventional phenological studies are carried out by biologists and ecologists through botanical inventories. Such conventional approaches, which often include manual sampling, can track fine details of the phenology process; however, they are time-consuming and costly. A landscape-based approach using remote sensing techniques provides an efficient way to observe phenology at large scales, which can complement the site intensive information provided by conventional approaches. Plant phenology observed from satellites at landscape scales is called vegetation phenology, also referred as land surface phenology (Reed et al. 2009).

The vegetation phenology at landscape scales which is comparable with climate model-derived data (Botta et al. 2000) is an important signal of climate change and global environment variation. Global climate warming may advance the biological spring and delay the arrival of biological winter. The earlier presence of green land cover and the delay in leaf fall of deciduous canopies in turn alter the seasonal climate through the effects of biogeochemical process and physical properties (Peñuelas et al. 2009). Accurate assessment of phenological events, therefore, becomes increasingly vital for investigating vegetation–climate interactions. Satellite-derived information has been demonstrated to be an important source for detecting vegetation phenology. The advantages in high temporal frequency and large spatial scales make satellite data increasingly prevalent in determining leaf onset and offset dates (Botta et al. 2000; Kang et al. 2003; Zhang et al. 2003), developing phenological models (DeBeurs and Henebry 2005; Kim and Wang 2005; Stöckli et al. 2008; White et al. 1997; Zhang et al. 2004; Zhou et al. 2003), and quantifying effects of phenological changes on local, regional, and global scale (Myneni et al. 1997; Peckham et al. 2008; Schwartz et al. 2006; White et al. 1999, 2002). This chapter outlines the methods used to develop phenological metrics from satellite measurements and the applications of satellite-derived vegetation phenology.

17.2 Method

Vegetation phenology derived from satellite measurements is distinct from the individual plants or species phenology. The large view of satellite sensors captures the canopy reflectance over the pixel size which ranges from high resolution as 30 by 30 m to coarse resolution as 8 by 8 km. The pixel-sized canopy reflectance is an

aggregation of heterogeneous vegetation. This aggregated information stands for the overall development stage of various plants, species within a pixel. It is important for investigating biogeochemical process, such as water, energy exchange, and carbon fluxes between biosphere and atmosphere.

Validation is a significant challenge for the study of satellite-derived vegetation phenology. First of all, the reflectance reached to satellite sensors can be contaminated by soil background signal and atmospheric influences. The contamination must be discussed or identified during validation. Secondly, scaling from field observations to satellite image requires multiple simultaneously collected data at intensive field observation sites. Finally, the key phenological metrics that are often derived from satellite measurements refer to the onset of greenness and dormancy and length of the growing season. Although the meaning of these metrics in many ecosystems is clear, there are many environments in which the precise interpretation is needed, such as mixed forests, evergreen forests, and dry lands.

17.2.1 Physical Principles for Deriving Phenology from Satellite Measurements

Remote sensing techniques, which can capture canopy reflectance, allow vegetation photosynthetic capacity to be assessed. Reflected red energy decreases with plant development due to chlorophyll absorption within actively photosynthetic leaves. Reflected near infrared (NIR), on the other hand, will increase with plant development through scattering processes (reflection and transmission) in healthy, turgid leaves (Huete et al. 1999). However, the red and NIR radiation reflected from a plant canopy to a satellite sensor can be contaminated by the effects of atmospheric particles through absorption and scattering and soil background. A simple measure of reflected energy is not able to quantify plant biophysical parameters from satellite measurements. Many spectral combinations or transformations, referred as Vegetation Indices (VI), are utilized to circumvent the problems of solar irradiance, atmospheric aerosols, and canopy background. These VIs are designed to enhance spectral reflectance and emissive characteristics of vegetation that are related to phenological development.

Most of the studies have used satellite-derived VIs to exploit the seasonal changes in the spectral signature of vegetation photosynthetic activity. Normalized Difference Vegetation Index (NDVI), Enhanced Vegetation Index (EVI), and Leaf Area Index (LAI) are the most widely used indices in satellite monitoring of vegetation phenology (Ahl et al. 2006; Peckham et al. 2008; Reed et al. 1994; White et al. 1997; Zhang et al. 2004). The NDVI, computed from NIR reflectance and red reflectance Eq. 17.1, has been related to several biophysical parameters including the fraction of photosynthetically active radiation (fPAR) (Huete et al. 1997), chlorophyll density (Tucker et al. 2001), percent canopy cover (Yoder and Waring 1994), and productivity (Prince et al. 1995). The EVI Eq .17.2 is developed to optimize the vegetation signal with improved sensitivity in high biomass regions (Huete et al. 2002) and to reduce the canopy background signal and atmosphere

influences by utilizing the more atmosphere-sensitive blue band to correct the red band for aerosol influences (Kaufman and Tanre 1992). The EVI has been found to perform well in heavy aerosol, biomass burning conditions (Miura et al. 1998).

$$\mathrm{NDVI} = \frac{\mathrm{NIR} - \mathrm{Red}}{\mathrm{NIR} + \mathrm{Red}} \tag{17.1}$$

$$\mathrm{EVI} = G\frac{\mathrm{NIR} - \mathrm{Red}}{\mathrm{NIR} + C_1\mathrm{Red} - C_2\mathrm{Blue} + L} \tag{17.2}$$

where L (=1) is the coefficient for canopy background adjustment, $C1$ (=6) and $C2$ (=7.5) are aerosol resistance coefficients, and G (=2.5) is a gain factor (Huete et al. 2002).

LAI is broadly defined as the amount of leaf area (m^2) or the number of equivalent layers in a canopy per unit ground area (m^2) (Knyazikhin et al. 1999). The LAI is a state parameter needed by large-scale ecosystem models describing the exchange flux of water vapor and CO_2 across the global biosphere–atmosphere interface (McWilliam et al. 1993). The LAI product derived from the Moderate Resolution Imaging Spectroradiometer (MODIS) reflectance monitors seasonal variation in LAI at 1-km nadir resolution every 8 days. MODIS LAI provides a more physically meaningful threshold for defining phenology events (such as onset of greenness) than other vegetation indices (Kang et al. 2003).

Many validation efforts have been made to demonstrate the capability and accuracy of deriving vegetation phenology from satellite measurements. Schwartz et al. (2002) compared three satellite-derived start-of-season measures and matched the results to field data collected at the Harvard forest in Massachusetts. They concluded that each method does a modestly accurate job of tracking the general pattern of surface phenology. Ahl et al. (2006) compared field measurements of springtime forest canopy phenology onset and maturity with estimates calculated from the MODIS-derived vegetation products in northern Wisconsin forest. Their results showed that MODIS products captured the general phenological development of the canopy although they overestimated the leaf area during the over story leaf out period and predicted onset of greenness and maturity earlier than that from field observations.

17.2.2 Approaches for Deriving Phenology from Satellite Measurements

Many satellite phenology detection approaches have been addressed since early 90s (Table 17.1). The threshold for NDVI has been applied for phenological classification of terrestrial vegetation (Lloyd 1990), modeling seasonal variation of vegetation (Fischer 1994), and detecting characteristic of vegetation phenology (Markon et al. 1995). They assume that a single threshold is applicable across land covers. However, variation in background reflectance of different vegetation types makes this a tenuous assumption. Therefore, it is not possible to establish a single, meaningful threshold that signifies the onset (or end) of vegetative activity for the

Table 17.1 Summary of approaches for satellite-derived phenology

Approach	Reference	Advantage	Disadvantage
Vegetation index threshold	Lloyd (1990); Fischer (1994); Markon et al. (1995)	Easy to apply	Not applicable across land covers
Moving average of smoothed NDVI	Reed et al. (1994)	Independent of land cover types	Hard to determine the moving average time interval
Normalized NDVI ratio	White et al. (1997)	Ecologically meaningful	Dependent of land covers
Derivative of NDVI	Moulin et al. (1997)	Independent of land cover	Sensitive to the weight of the derivative term
Linear segments of NDVI time series	Duchemin et al. (1999)	Easy to apply	Sensitive to a change in the rate of NDVI variation
Curvature-change rate for vegetation indices	Zhang et al. (2003)	For multiple growth cycle Independent of land covers	Hard to determine the single growth and senescence periods

wide variety of cover types that occur in the continental United States. Reed et al. (1994) developed an automated, quantitative approach to derive phenological measures from multitemporal Advanced Very High Resolution Radiometer (AVHRR) NDVI observations. To identify the onset of the growing seasons, an auto-regressive moving average of previous smoothed nine NDVI biweekly composite values was compared to the smoothed NDVI value. Selecting the moving average time interval (the number of NDVI composite periods used to calculate the moving average) is a critical issue; a large time interval may miss natural vegetation changes, while a small interval may result in extremely noisy NDVI curves. White et al. (1997) provided a methodology which determined the start and the end of growing season by the threshold of the normalized NDVI ratio. Instead of original NDVI values, they normalized the NDVI to 0–1 by its maximum and minimum value. A new smoothed NDVI ratio curve was developed based on the method of Reed et al. (1994), and then the NDVI ratio threshold of 0.5 was used to identify growing season length. Moulin et al. (1997) used time derivative of NDVI to detect three transition dates of vegetation cycle: beginning, maximum, and end. The time derivative before beginning date should be zero and after beginning date should be positive; the end date was calculated similarly to the beginning date. The algorithm is sensitive of the weight of the derivative term. If the weight is too large, the detection may be confused by short-term signal variations due to residual noise (e.g., soil color, directional effects). If the weight is too small, the algorithm may fail for pixels, which remain partly green during the year. Duchemin et al. (1999) revealed that the temporal variation of NDVI during budburst and senescence was nearly linear. A line segment model was used to fit the effect of budburst and senescence. The method was sensitive to a change in the rate of NDVI variation, resulting, for instance, from a spring frost during budburst or from a severe drought in summer accelerating the senescence. Zhang et al. (2003) identified phenological transition dates based on the curvature-change rate of a logistic model for time series of MODIS vegetation indices. This method has been applied in many researches (Ahl et al. 2006; Peckham et al. 2008; Zhang et al. 2004) because it is able to handle multiple growth cycles and is not tied to a specific calendar period (e.g., January to December). The challenge for this method is to identify a single sustained increase (growth) and decrease (senescence) period before the MODIS measurements could be fit to the logistic model.

Li et al. (2010b) modified Zhang et al. (2003)'s approach by using the Fourier series to decompose the periodic vegetation indices instead of the moving average window Eq. 17.3.

$$y = a + b\cos(\omega x) + c\sin(\omega x) \tag{17.3}$$

where a, b, and c are fitting parameters; ω is the angular frequency which is equal to $2 \times \pi/T$; and T is period time of the growth cycle. For instance, the T for the single growth cycle is the number of data samples for 1 year. For multiple growth cycle, T equals to the number of data samples divided by the number of cycles for 1 year. The other parameters are solved by least square fitting. Local maximum and minimum points of the simulated data divided original data into a series of sustained increasing and decreasing trends (Fig. 17.1). Using Fourier series to

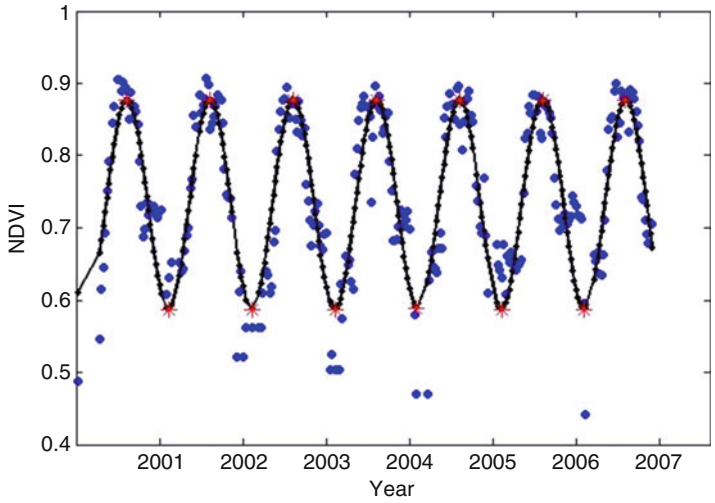

Fig. 17.1 Smoothed data by Fourier series. Original MODIS data are shown in *blue points* and simulated data in *black solid line*. The *red star* marks are local maximum and local minimum

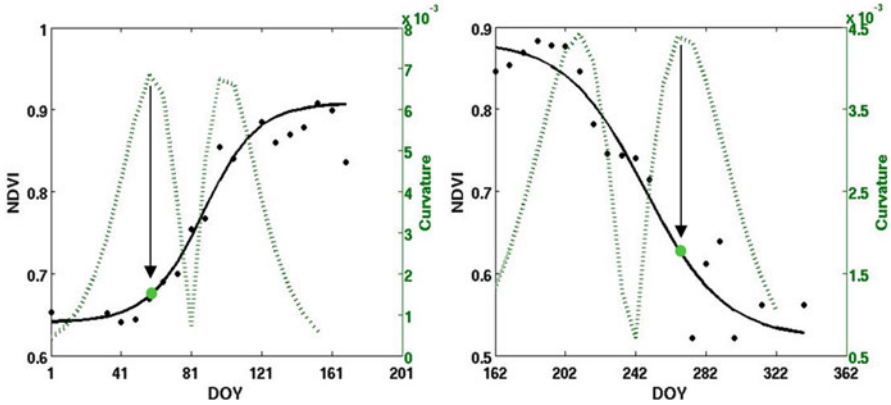

Fig. 17.2 Onset date detection. The *solid line* is fitted logistic model and the *dashed line* is the curvature of the NDVI time series. The *green point* indicates the greenup onset (*left figure*) and the dormancy onset (*right figure*)

identify the single growth or senescence period are independent of the data set temporal resolution and no empirical parameters settings. Based on the single growth or senescence period, the logistic model provided by Zhang et al. (2003) (Eq. 17.4) is used to identify phenological metrics, by determining the curvature of the fitted logistic models. The first point with largest curvature in increasing period corresponds to the greenup onset, and the second point with largest curvature in decreasing period corresponds to the dormancy onset (Fig. 17.2).

$$y(t) = \frac{c}{1 + e^{a+bt}} + d \tag{17.4}$$

17.3 Applications

The vegetation phenology derived from satellite-based sensors with a variety of spatial and temporal resolutions has been utilized for tracking vegetation dynamics, invasive species, and land cover changes as well as assessing crop conditions, drought severity, and wildfire risk. Since phenological events are sensitive to climate variation, satellite-derived phenology data also represent a powerful tool for detecting the response of terrestrial ecosystems to climate change at multiple scales. Satellite sensors have their own characteristics of temporal and spatial resolution, spatial coverage, and data quality and archive history. Each satellite takes advantages of its respective strengths to provide certain phenological applications.

17.3.1 Landsat-Derived Vegetation Phenology

For monitoring vegetation phenology at regional scale, the Landsat data offers three primary advantages. First, with more than 30 years of data archive, it provides the longest-running time series of systematically collected remote sensing data. Second, the 30-m spatial resolution facilitates landscape characterization. Third, the free-of-charge data through the US Geological Survey (USGS) make it possible to acquire by all researchers.

Landsat data have been translated into useful phenological behavior both on the methods and applications. A "temporal profile" model (Badhwar 1984a, b) that simulates phenological dynamics as a quadratic rise and exponential decay has been utilized to extract features to classify the agriculture crops. Goetz and Prince (1996) have used the species-specific foliar phenology to estimate the amount of incident photosynthetically active radiation (PAR) and further to estimate the net primary production (NPP) in boreal forest stands. Fisher et al. (2006) have provided an approach to bridge the in situ, plot-level phenological measurements and satellite-derived phenological metrics through Landsat data and quantified the accuracy by comparing the half-maximum leaf onset and offset. Although Landsat's 16-day repeat cycle does not provide readily available data for the rapidly changing phenological stages, application of Landsat data paved the way for remote sensing-based phenology, and the development of new methodologies can potentially overcome the shortcomings of Landsat series.

17.3.2 AVHRR-Derived Vegetation Phenology

Current research using satellite sensors with a more frequent repeat cycle dominates the study of remote sensing phenology. The AVHRR provides data globally with daily repeat cycle since the 1980s. A variety of AVHRR collections are available for phenology study. AVHRR vegetation index data are available in a consistently

processed database at 8-km resampling grid twice monthly from 1982 covering the globe and at 1-km resolution with biweekly intervals since 1989 covering the conterminous United States.

The high temporal resolution, moderate spatial resolution, and relatively long-term continuity make this sensor well suited for examining and monitoring phenological events for entire ecosystems on regional as well as on global scale. AVHRR-derived vegetation phenology has widely been used in research areas of vegetation activity, climate change, land use, and disaster. Vegetation phenology derived from AVHRR provides unique opportunities for monitoring vegetation activity trends at large scales. Myneni et al. (1997) have presented an increase in plant growth associated with a lengthening of the active growing season from the 1981 to 1991 for the north hemisphere, based on AVHRR Pathinder NDVI data set and the Global Inventory Monitoring and Modeling Studies (GIMMS) AVHRR NDVI data set. They have estimated an advance in the active growing season of 8 ± 3 days, a prolongation of the declining phase at 4 ± 2 days, and therefore, a longer active growing season of 12 ± 4 days over the 1980s. Zhou et al. (2001) have investigated the AVHRR-derived northern hemisphere vegetation activity and the land surface temperature records for the period from 1981 to 1999. Their results show a persistent increase in growing season NDVI over broad contiguous forests and woodlands for Europe, a larger increase in growing season NDVI magnitude and a longer active growing season for Eurasia and North America, and NDVI decreases due to temperature-induced drought in boreal zones.

In addition to the trend over long periods captured by AVHRR-derived vegetation phenology, interannual anomalies of phenological dynamics also contain meaningful information on the response of vegetation to climate change. Asner et al. (2000) has revealed that the seasonal NDVI amplitude provided by AVHRR measurements increased throughout Amazon forest during EI Niño periods when rainfall was anomalously low. Based on vegetation phenology data set created from Pathfinder NDVI, European spring phenology has been shown to correlate particularly well with anomalies in winter temperature and winter North Atlantic Oscillation Index for 20 years from 1982 to 2001 (Stöckli and Vidale 2004).

The phenological changes and attributes have been used as an indicator of land use changes and land use classification. Reed (2006) shows that changes in agricultural practices result in a trend toward long duration of season in Saskatchewan, Canada, based on 8-km AVHRR data set. Wessels et al. (2009) have used AVHRR-derived phenology data in a fully supervised decision-tree classification based on the new biome map of South Africa to identify the phenological attributes that distinguish between the different biomes.

Furthermore, extensive research has shown the important contribution of vegetation phenology to the monitoring of environmental disaster. Peckham et al. (2008) demonstrates that fire has a significant effect on the phenological dates of the Canadian boreal forest derived from AVHRR–NDVI. They state that the most recently burned areas have later greenup dates. Brown et al. (2008) has integrated the 1-km AVHRR-derived phenological metrics, with climate-based drought index data and other biophysical information into a vegetation drought response model (VegDRI) to generate higher resolution drought monitoring information in near real time.

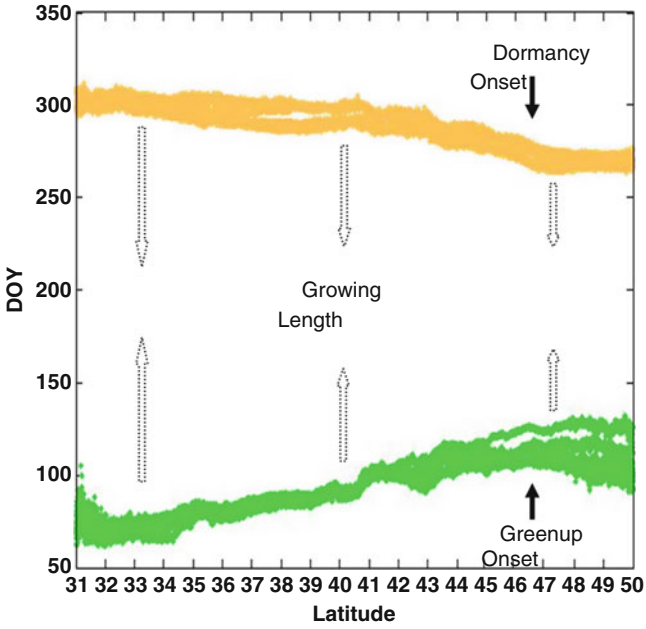

Fig. 17.3 The variation of MODIS-derived phenology in DBF along latitudes over the Eastern US

17.3.3 MODIS-Derived Vegetation Phenology

The newer generation of sensor MODIS was launched in December 1999. Improved geometry, radiometry, and overall data quality of MODIS, combined with its free-of-charge data policy, provide readily available high-quality data for phenology studies. MODIS onboard NASA's Terra and Aqua satellites collect daily reflectance data at spatial resolution of 250 m, 500 m, and 1 km globally. One of the standard MODIS land products is the Land Cover Dynamics product (MOD12Q2), distributed from the Land Processes Distributed Active Archive Center, which includes several phenology metrics at 1-km spatial resolution (Zhang et al. 2003). The MODIS-derived phenology can be used in the similar research areas of AVHRR-derived phenology, such as trends of vegetation dynamics, response to climate change, land cover change, and disaster monitoring (Ahl et al. 2006; Kang et al. 2003; Kim and Wang 2005; Peckham et al. 2008; Zhang et al. 2004).

Besides these research areas, the higher spatial and temporal resolution has enabled MODIS-derived vegetation phenology to develop a stronger understanding of how environmental conditions affect phenological patterns among regional and broad scales. Li et al. (2010a) have quantified the effects of latitude, elevation, and ecoregions on MODIS-derived vegetation phenology in Deciduous Broadleaf Forest (DBF) over continental USA during 2000–2008. Figure 17.3 shows an obvious phenological pattern dependent on latitude. The rate of change for greenup onset and dormancy onset is about 2 days per degree latitude. They also have

pointed out that the variation of greenness onset is not only dependent on latitude but also associated with elevation and ecoregions. When the elevation is higher than 1 km, mountain area tends to green up latter than other ecoregions.

17.3.4 Applications of Other Sensors

The SPOT Vegetation optical instrument launched in March 1998 operates in four spectral bands: blue, red, NIR, and shortwave infrared (SWIR). Delbarta et al. (2005) have provided an accurate and precise determination of the dates of greenness onset based on the Normalized Difference Water Index (NDWI) which generated from SPOT Vegetation NIR and SWIR bands. Their detection algorithm relies on the fact that NDWI first decreases with snowmelt and then increases during the vegetation greening. The Medium Resolution Image Spectrometer Instrument (MERIS) is one of the sensors on Environmental Satellite (ENVISAT) which was launched by the European Space Agency (ESA) in 2002. Although MERIS was primarily dedicated to ocean color, its band configuration broadens its application to vegetation monitoring (Dente et al. 2008). The MERIS collect global data every 3 days in 15 wavebands at 300-m spatial resolution. The Terrestrial Chlorophyll Index (MTCI), one of the MERIS products, has enabled researchers to provide temporally continuous phenological variables at a much finer spatial resolution more accurately and precisely (Lankester et al. 2010). The SeaWiFS carried on SeaStar spacecraft was launched in 1997. The sensor records information in eight optical bands with 1.1-km spatial resolution for Local Area Coverage (LAC) and 4.5-km resolution for Global Area Coverage (GAC). Verstraete et al. (2008) have described a method to define the start, end, and length of growing season based on the statistical analysis of time series of the biogeophysical quantity known as the fraction of absorbed photosythetically active radiation (FAPAR) derived from SeaWiFS data for various biomes.

17.4 Summary

Satellite measurements have gained the insights about phenological behavior both on the methods and applications. The method for satellite-derived vegetation phenology has been developed from empirically, simple threshold of vegetation index to automated, elaborate logistic model. Some methods are carried on specific satellite data or specific land cover types, while some methods are independent of data set and can be utilized on different land cover types. Each method provides certain advantages and helps lay the way open for the success of satellite-derived vegetation phenology. A variety of satellite sensors have been used to detect vegetation phenology varying from instruments designed for land application purpose such as Landsat, AVHRR, MODIS, and SPOT Vegetation to instruments not for land application such as MERIS and SeaWiFS. The application of satellite-derived vegetation phenology

varies among sensors due to their specific advantages. The majority of studies have taken advantages of the moderate spatial resolution and long-term continuity of AVHRR data to investigate the influence of climate change and disaster on terrestrial ecosystems. More recent and much better calibrated sensor MODIS has additional spectral bands besides maintain the visible and near-infrared wavelengths which are important for phenological studies. The EVI based on multiple MOIDS bands has been successfully used to assess environmental effects on phenological patterns. However, the coarse scale of AVHRR and MODIS measurements render ground validations difficult. The 30-m Landsat spatial resolution offers an appropriate scale to bridge the ground-based observations and satellite-derived phenological metrics. Other sensors although was not primarily designed for vegetation applications, its multiple optical bands have broadened their application to vegetation phenology, such as MERIS and SeaWiFS.

Despite the achievement obtained from satellite observations of vegetation seasonal cycle, efforts to validate the accuracy of satellite-derived vegetation phenology have had a low success rate. It is a big challenge to compare the two sources (satellite and ground) of phenological data more effectively. Partially, this is a scale problem. The satellite-derived vegetation phenology is based on pixel level, while the ground records usually measure phenology at individual species level. How to integrate the species-level phenology to pixel level is key issue in validating satellite-derived vegetation phenology. In the further, more detailed information of ground records should be collected, such as the area of field plots, the composition, and the structure in vegetation community. The information together with phenophases of individual species could be integrated to reflect the canopy phenology and compared the results with satellite-derived phenology. There is also a strong need to investigate the relationship between growing season length and the concentration of atmospheric carbon dioxide. Increased knowledge about the net ecosystem exchange of carbon dioxide between forest and atmosphere would lead to regulate seasonal and interannual fluctuations of carbon uptake.

References

Ahl DE, Gower ST, Burrows SN, Shabanov NV, Myneni RB, Knyazikhin Y (2006) Monitoring spring canopy phenology of a deciduous broadleaf forest using MODIS. Remote Sens Environ 104:88–95

Asner GP, Townsend AR, Braswell BH (2000) Satellite observation of El Nino effects on Amazon forest phenology and productivity. Geophys Res Lett 27:981–984

Badhwar GD (1984a) Classification of corn and soybeans using multitemporal thematic mapper data. Remote Sens Environ 16:175–182

Badhwar GD (1984b) Use of Landsat-derived profile features for spring small-grains classification. Int J Remote Sens 5:783–897

Botta A, Viony N, Ciais P, Friedlingstein P, Monfray P (2000) A global prognostic scheme of leaf onset using satellite data. Glob Chang Biol 6:709–725

Brown JF, Wardlow BD, Tadesse T, Hayes MJ, Reed BC (2008) The Vegetation Drought Response Index (VegDRI): a new integrated approach for monitoring drought stress in vegetation. GIScience Remote Sens 45:16–46

DeBeurs KM, Henebry GM (2005) Land surface phenology and temperature variation in the International Geosphere-Bioshpere program high-latitude transects. Glob Chang Biol 11:779–790

Delbarta N, Kergoat L, Toan TL, Lhermitte J, Picard G (2005) Determination of phenological dates in boreal regions using normalized difference water index. Remote Sens Environ 97:26–38

Dente L, Satalino G, Mattia F, Rinaldi M (2008) Assimilation of leaf area index derived from ASAR and MERIS data into CERES-wheat model to map wheat yield. Remote Sens Environ 112:1395–1407

Duchemin B, Goulbier J, Courrier G (1999) Monitoring phenological key stages and cycle duration of temperate deciduous forest ecosystems with NOAA/AVHRR data. Remote Sens Environ 67:68–82

Fischer A (1994) A model for the seasonal variations of vegetation indices in coarse resolution data and its inversion to extract crop parameters. Remote Sens Environ 48:220–230

Fisher JI, Mustard JF, Vadeboncoeur MA (2006) Green leaf phenology at Landsat resolution: scaling from the field to the satellite. Remote Sens Environ 100:265–279

Goetz SJ, Prince SD (1996) Remote sensing of net primary production in boreal forest stands. Agr Forest Meteorol 17:149–179

Haggerty BP, Mazer SJ (2008) The phenology handbook. A guide to phenological monitoring for students, teachers, families, and nature enthusiasts. In: UCSB Phenology Stewardship program. http://plantingtheseed.colostate.edu/WebContent/WS/plantingtheseed/links/Phenology_Handbook_2nd_ed_Abridged.pdf

Huete AR, Liu HQ, Batchily K, van Leeuwen W (1997) A comparison of vegetation indices over a global set of TM images for EOS-MODIS. Remote Sens Environ 59:440–451

Huete A, Justice C, van Leeuwen W (1999) MODIS Vegetation Index (MOD 13) algorithm theoretical basis document, University of Arizona Version 3, 30 Apr 1999. http://modis.gsfc.nasa.gov/data/atbd/atbd_mod13.pdf

Huete AR, Didan K, Miura T, Rodriguez EP, Gao X, Ferreira LG (2002) Overview of the radiometric and biophysical performance of the MODIS vegetation indices. Remote Sens Environ 83:195–213

Kang S, Running SW, Lim J-H, Zhao M, Park C-R, Loehman R (2003) A regional phenology model for detecting onset of greenness in temperate mixed forests, Korea: an application of MODIS leaf area index. Remote Sens Environ 86:232–242

Kaufman YJ, Tanre D (1992) Atmospherically resistant vegetation index (ARVI) for EOS MODIS. IEEE Trans Geosci Remote Sens 30:261–270

Kim Y, Wang G (2005) Modeling seasonal vegetation variation and its validation against moderate resolution imaging spectroradiometer (MODIS) observations over North America. J Geophys Res 110:D04106

Knyazikhin Y, Glassy J, Privette JL, Tian Y, Lotsch A, Zhang Y, Wang Y, Morisette JT, Votava P, Myneni RB, Nemani RR, Running SW (1999) MODIS Leaf Area Index (LAI) and fraction of photosynthetically active radiation absorbed by vegetation (FPAR) product (MOD15) algorithm, Theoretical Basis Document, NASA Goddard Space Flight Center, Greenbelt. http://cybele.bu.edu/download/manuscripts/ytian03.pdf

Lankester T, Dash J, Baret F, Hubbard S (2010) Introduction of the PHenology And Vegetation Earth Observation Service (PHAVEOS). In: The remote sensing and photogrammetry society conference remote sensing and the carbon cycle. Burlington House, London

Li M, Qu JJ, Hao X (2010a) Investigating phenological changes using MODIS vegetation indices in deciduous broadleaf forest over continental U.S. During 2000–2008. Ecol Inform 5:410–417

Li M, Qu JJ, Hao X (2010b) Monitoring temporal and spatial variations of vegetation phenology from space. SPIE Newsroom. doi:10.1117/2.1201009.003242. http://spie.org/documents/Newsroom/Imported/003242/003242_10.pdf

Lloyd D (1990) A phenological classification of terrestrial vegetation cover using shortwave vegetation imagery. Int J Remote Sens 11:2269–2279

Markon CJ, Fleming MD, Binnian EF (1995) Characteristic of vegetation phenology over the Alaskan landscape using AVHRR time-series data. Polar Rec 31:179–190

McWilliam ALC, Roberts JM, Cabral OMR, Leitao MVBR, de Costa ACL, Maitelli GT, Zamparoni CAGP (1993) Leaf-area index and aboveground biomass of terra-firme rainforest and adjacent clearings in Amazonia. Funct Ecol 7:310–317

Miura T, Huete AR, van Leeuwen WJD, Didan K (1998) Vegetation detection through smoke-filled AVIRIS images: an assessment using MODIS band passes. J Geophys Res 103:32001–32011

Moulin S, Kergoat L, VIiovy N, Dedieu G (1997) Global-scale assessment of vegetation phenology using NOAA/AVHRR satellite measurements. J Climate 10:1154–1170
Myneni RB, Keeling CD, Tucker CJ, Asrar G, Nemanl RR (1997) Increased plant growth in the northern high latitudes from 1981 to 1991. Nature 386:698–702
Peckham SD, Ahl DE, Serbin SP, Gower ST (2008) Fire-induced changes in green-up and leaf maturity of the Canadian boreal forest. Remote Sens Environ 112:3594–3603
Peñuelas J, Rutishauser T, Filella I (2009) Phenology feedbacks on climate change. Science 324:887–888
Prince SD, Goetz SJ, Goward SN (1995) Monitoring primary productivity from Earth observing satellites. Water Air Soil Pollut 82:509–522
Reed BC (2006) Trend analysis of time-series phenology of North America derived from satellite data. GIScience Remote Sens 43:24–38
Reed BC, Brown JF, VanderZee D, Loveland TR, Merchant JW, Ohlen DO (1994) Measuring phenological variability from satellite imagery. J Veg Sci 5:703–714
Reed BC, Schwartz MD, Xiao X (2009) Remote sensing phenology: status and the way forward. In: Noormets A (ed) Phenology of ecosystem processes. Springer, New York, pp 231–246
Schwartz MD, Reed BC, White MA (2002) Assessing satellite-derived start-of-season measures in the conterminous USA. Int J Climatol 22:1793–1805
Schwartz MD, Ahas R, Aasa A (2006) Onset of spring starting earlier across the Northern hemisphere. Glob Chang Biol 12:343–351
Stöckli R, Vidale PL (2004) European plant phenology and climate as seen in a 20-year AVHRR land-surface parameter dataset. Int J Remote Sens 25:3303–3330
Stöckli R, Rutishauser T, Dragoni D, O'Keefe J, Thornton PE, Jolly M, Lu L, Denning AS (2008) Remote sensing data assimilation for a prognostic phenology model. J Geophys Res 113:G04021
Tucker CJ, Slayback DA, Pinzon JE, Los SO, Myneni RB, Taylor MG (2001) Higher northern latitude normalized difference vegetation index and growing season trends from 1982 to1999. Int J Biometeorol 45:184–190
Verstraete MM, Gobron N, Aussedat O, Robustelli M, Pinty B, Widlowski J-L, Taberner M (2008) An automatic procedure to identify key vegetation phenology events using the JRC-FAPAR products. Adv Space Res 41:1773–1783
Wessels KJ, Steenkamp K, Maltitz GV, Archibald S, Scholes RJ, Miteff S, Bachoo A (2009) Remotely sensed phenology for mapping biomes and vegetation functional types. In: Geoscience and remote sensing symposium, 2009 IEEE international, IGARSS 2009, vol 4, Cape Town, pp 1034–1037. doi:10.1109/IGARSS.2009.5417564
White MA, Thornton PE, Runing SW (1997) A continental phenology model for monitoring vegetation responses to interannual climate variability. Global Biogeochem Cycles 11:217–234
White MA, Running SW, Thoronton PE (1999) The impact of growing-season length variability on carbon assimilation and evapotranspiration over 88 years in the eastern US deciduous forest. Int J Biometeorol 42:139–145
White MA, Nemani RR, Thornton PE, Runing SW (2002) Satellite evidence of phenological differences between urbanized and rural areas of the eastern United States deciduous broadleaf forest. Ecosystems 5:260–277
Yoder BJ, Waring RH (1994) The normalized difference vegetation index of small Douglas-Fir canopies with varying chlorophyll concentrations. Remote Sens Environ 49:81–91
Zhang X, Friedl MA, Schaaf CB, Strahler AH, Hodges JCF, Gao F, Reed BC, Huete A (2003) Monitoring vegetation phenology using MODIS. Remote Sens Environ 84:471–475
Zhang X, Friedl MA, Schaaf CB, Strahler AH (2004) Climate controls on vegetation phenological patterns in northern mid- and high latitudes inferred from MODIS data. Glob Chang Biol 10:1133–1145
Zhou L, Tucker CJ, Kaufmann RK, Slayback D, Shabanov NV, Myneni RB (2001) Variations in northern vegetation activity inferred from satellite data of vegetation index during 1981 to 1999. J Geophys Res 106:20069–20083
Zhou L, Kaufmann RK, Tian Y, Myneni RB, Tucker CJ (2003) Relation between interannual variations in satellite measures of northern forest greenness and climate between 1982 and 1999. J Geophys Res 108:D14004

Chapter 18
Monitoring a Sentinel Species from Satellites: Detecting *Emiliania huxleyi* in 25 Years of AVHRR Imagery

Stephanie Schollaert Uz, Christopher W. Brown, Andrew K. Heidinger, Tim J. Smyth, and Raghu Murtugudde

Abstract Blooms of the coccolithophore *Emiliania huxleyi* were detected around the world from 1982 through 2006 using Advanced Very High Resolution Radiometer (AVHRR) remote sensing reflectances. The annually averaged surface area of these blooms has decreased over the past 25 years in regions where *E. huxleyi* blooms are most prevalent – the Bering Sea, the North Atlantic south of Iceland, the Norwegian and Barents Sea, and the Patagonian Shelf. Though less sensitive than satellite ocean color sensors, AVHRR offers the longest continuous global dataset of visible reflectances and has been used previously to identify regional *E. huxleyi* blooms. This declining long-term trend in bloom surface area was correlated to warm sea-surface temperature anomalies. The trend was weakly correlated to increased mixed-layer depths. There were mixed results when comparing bloom surface area to climate indices. Previous studies associated individual *E. huxleyi* blooms to warmer temperatures and increased stratification. This apparently contrary result may indicate that the dynamics of large-scale changes are different from those of individual, local blooms. The decreased extent of blooms could also mean that *E. huxleyi* respond to additional factors over the long term, such as ocean chemistry.

Keywords Coccolithophore • *Emiliania huxleyi* • Phytoplankton bloom • SeaWiFS • AVHRR • Remote sensing reflectance • Stratification • Warming

S. Schollaert Uz (✉) • R. Murtugudde
ESSIC, University of Maryland, 5825 University Research Court, College Park, MD 20740, USA
e-mail: ses@essic.umd.edu

C.W. Brown
NOAA NESDIS STAR, 5830 University Research Court, College Park, MD 20740, USA

A.K. Heidinger
UW/CIMSS/NOAA, 1225 West Dayton St, Madison, WI 53706, USA

T.J. Smyth
Plymouth Marine Laboratory, Plymouth, UK

J.J. Qu et al. (eds.), *Satellite-based Applications on Climate Change*,
DOI 10.1007/978-94-007-5872-8_18,

18.1 Introduction

Marine phytoplankton are ideal indicators of environmental change. These microscopic algae form the base of the oceanic food web and respond rapidly to changes in their environment. Individuals of most phytoplankton species are short-lived and react quickly to varying ambient conditions caused by both short-term weather and long-term climate (Hays et al. 2005). As the cells essentially function as an integrated, nonlinear sensor of environmental conditions, they may be more sensitive to change than mechanical sensors measuring only one environmental variable. Also, because phytoplankton are not commercially important, any observed changes can be attributed to changes in the environment and not to harvesting.

Excluding physiological change and adaptation, the response by phytoplankton and other organisms to environmental changes can be manifested by alterations in both their spatial distribution pattern and their phenology, i.e., the timing of events in seasonal life cycle (Hughes 2000). Recent studies have begun to explore the observed variability in marine phytoplankton phenology and its effect on higher trophic levels (Platt and Sathyendranath 2008; Platt et al. 2009, 2010; Vargas et al. 2009; Sapiano et al. 2012). An examination of the spatial distribution pattern was conducted for the cosmopolitan species *Emiliania huxleyi* (Fig. 18.1), an important member of the phytoplankton group that generates calcareous plates called coccoliths, for which they are known as coccolithophorids.

Coccolithophorids are an abundant and widely distributed type of marine phytoplankton and play an important role in the oceanic carbon and sulfur cycles through their production of $CaCO_3$ coccoliths and dimethyl sulfide (DMS), the dominant precursor for cloud condensation nuclei in the maritime atmosphere. As one of the principal producers of DMS among phytoplankton, coccolithophorids act as a significant biogenic source of sulfur to the atmosphere and may influence regional albedo via increased cloud formation. Coccolithophorids generate as much as two-thirds of open ocean calcification through their generation of calcareous coccoliths, and *E. huxleyi* is considered to be the largest current producer of calcite (Westbroek et al. 1989, 1993).

Blooms of *E. huxleyi* profoundly affect the biogeochemical and optical properties of the waters they occupy. For example, generation and export of their calcareous coccoliths alter the equilibrium of the regional ocean carbonate system and the sea-air flux of carbon dioxide. The influence of *E. huxleyi* blooms also cascades to upper trophic levels of the food chain, including fish and marine mammals (Napp and Hunt 2001; Tynan et al. 2001). As a consequence, documenting the seasonal to decadal variability of these blooms is important to assess climate variability and environmental conditions and to better understand their potential impact on the carbon cycle and regional ecosystems.

Several environmental conditions appear to be favorable to *E. huxleyi* bloom development, including increased stratification of the upper ocean (Tyrrell and Merico 2004). Smyth et al. (2004) found a strong correlation between bloom presence with warm sea-surface temperatures and reduced salinities in the Barents Sea.

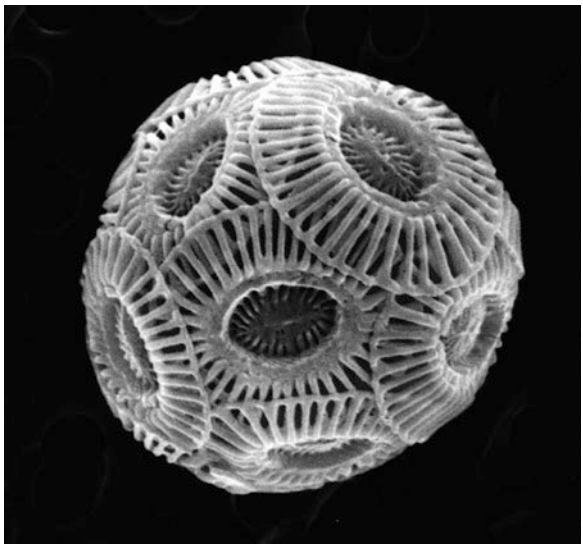

Fig. 18.1 Scanning electron photomicrograph of the coccolithophorid *Emiliania huxleyi*. The diameter of the cell is approximately 12 μm

In the subarctic North Atlantic, Raitsos et al. (2006) noted that coccolithophore abundance could be explained by increased stratification. There are predictions for warming and large-scale freshening by increased precipitation and river outflow in the subpolar seas (Delworth and Dixon 2000). Understanding whether and how *E. huxleyi* blooms respond to changes in these and other environmental conditions is critical to our understanding of their ecology and effect on the subpolar ecosystem. Furthermore, although the response by *E. huxleyi* to ocean acidification is not yet clear (Riebesell et al. 2008; Iglesias-Rodriguez et al. 2008), the uptake of atmospheric CO_2 by the upper ocean is generally expected to adversely impact calcifying taxa, such as *E. huxleyi* (Doney et al. 2009).

Blooms of *E. huxleyi* occupying the surface layer are identifiable in visible satellite observations due to their high ocean volume reflectance caused principally by the presence of detached coccoliths (Holligan et al. 1983). The blooms and their associated high concentrations of calcite have been identified in ocean color imagery from the Coastal Zone Color Scanner (CZCS) (Brown and Yoder 1994), Sea-viewing Wide Field-of-view Sensor (SeaWiFS) (Iglesias-Rodriguez et al. 2002), and Moderate Resolution Imaging Spectroradiometer (MODIS) (Balch et al. 2005). Though a general description of the distribution of *E. huxleyi* blooms was gleaned from the proof-of-concept CZCS mission that extended from 1978 to 1986, a more complete understanding of their spatial and temporal variability awaited the launch of the dedicated SeaWiFS in 1997. Satellite ocean color data, however, provide a limited time series to document *E. huxleyi* blooms. Although not as sensitive as these ocean color sensors, Advanced Very High Resolution Radiometer (AVHRR) imagery can also be used to detect *E. huxleyi* blooms and extend the time series of their distribution back to the early 1980s.

The areal extent of *E. huxleyi* blooms is documented in a 25-year time series from AVHRR in four regions around the world where *E. huxleyi* are prevalent and

have been observed in situ, using a satellite method similar to that employed by another study (Smyth et al. 2004). We examine these results in relation to physical processes and climatic indices.

18.2 Methods

Blooms of *E. huxleyi* were identified in global AVHRR and SeaWiFS imagery as described in the following sections.

18.2.1 AVHRR Imagery

Daily global, 1/4° resolution remote sensing reflectances (R_{rs}), derived from Rayleigh-corrected radiances of the AVHRR visible and near-infrared channels, were acquired from the Clouds from AVHRR Extended (CLAVR-X) Project (Heidinger et al. 2002). Input radiances from the different AVHRR platforms had been intercalibrated to ensure a reliable and comparable time series of R_{rs}. CLAVR-X was developed specifically to separate the cloud and sea-surface signals. To separate the effect of atmospheric contamination, R_{rs} was estimated using a method for detecting *E. huxleyi* blooms developed by Smyth et al. (2004):

$$R_{rs} = (R1 - R2)/(\exp((-0.057/2) \times p1)$$

where *R1* and *R2* are Rayleigh-corrected channel 1 (0.580–0.680 μm) and channel 2 (0.725–1.1 μm) reflectances and pl is the optical path length, a function of the satellite and solar zenith angle. The factor of −0.057 is the calculated value of the Rayleigh optical depth in channel 1 for a *p*l of unity and a standard atmosphere.

18.2.2 SeaWiFS Imagery

SeaWiFS Global Area Coverage Level 1a data were acquired from the SeaWiFS Project and Distributed Active Archive Center, processed to Level 2 radiances while retaining the coccolith-flagged pixels normally masked during standard processing, and spatially binned to 9-km resolution. SeaWiFS classification of pixels into *E. huxleyi* bloom and non-bloom was based on 8-day mean normalized water-leaving radiances using the supervised, multispectral classification scheme of Iglesias-Rodriguez et al. (2002). The spectral signature of *E. huxleyi* blooms was empirically ascertained to distinguish them from other oceanic conditions and has been well validated.

18.2.3 Detecting E. huxleyi Blooms

E. huxleyi blooms were classified in AVHRR daily imagery by applying an R_{rs} threshold tuned to the well-validated SeaWiFS maps. Whenever two AVHRR sensors were flying, daily composites were created incorporating both sensors. A threshold of 1.0 was established for R_{rs} so the spatial extent of *E. huxleyi* from AVHRR was similar to maps derived from SeaWiFS for blooms in the Barents Sea (Smyth et al. 2004) and North Atlantic Ocean south of Iceland (Raitsos et al. 2006), where in situ samples had confirmed *E. huxleyi* presence at high numbers. For each AVHRR scene, pixels of $R_{rs} > 1.0$ were assigned a value of 1; pixels of $R_{rs} < 1.0$ were assigned 0. An R_{rs} threshold of 1.5 was applied for pixels with solar zenith angles between 50° and 70° after observing several false-positive results correlated to high solar zenith angles. Weekly composite AVHRR *E. huxleyi* maps were created by summing these binary data over 8 days for each pixel, such that pixel values could range from 0 (*E. huxleyi* absent) to 8 (*E. huxleyi* always present), then dividing by the number of valid observations in the weekly composite to estimate the percentage of time a pixel possessed *E. huxleyi* during the period. Fractions were averaged over the entire region for a final value ranging between 0 (no *E. huxleyi* in the region) and 1 (a bloom covered the whole region for the 8-day period). Only pixels with a minimum of 25% valid data, or 2 days out of eight, were included in the final area average. Repeating our analyses with more stringent cloud and aerosol screening criteria yielded nearly identical patterns, albeit fewer data, suggesting that this *E. huxleyi* classification method is not biased by nearby clouds.

In order to minimize false-positives in both AVHRR and SeaWiFS data, we excluded imagery collected during winter months (i.e., October–March in the Northern Hemisphere, vice versa in the Southern) when materials such as diatom frustules are resuspended by high winds and spectrally mimic *E. huxleyi* blooms (Broerse et al. 2003). We applied a bathymetric threshold (depth >150 m) between 45ºS and 45ºN to avoid the incorrect classification of shallow carbonate shelves as coccolithophore blooms.

The number of times *E. huxleyi* blooms were identified in a pixel of both AVHRR and SeaWiFS (± 1 week) was summed as was the number of times either AVHRR or SeaWiFS detected a bloom when the other did not. From this map, four open ocean and coastal regions were selected where *E. huxleyi* was frequently present and the matchups of blooms derived from both sensors were most consistent as well as being locations where blooms had been sampled during cruises (Fig. 18.2): the Bering Sea west of Alaska, the North Atlantic south of Iceland, the North and Norwegian Seas, and the Patagonian Shelf east of Argentina. Over 216 coincident weeks, the correlation between AVHRR and SeaWiFS *E. huxleyi* detection was significant: $r = 0.46$ (Bering Sea), $r = 0.63$ (south of Iceland), $r = 0.39$ (North and Norwegian Seas), and $r = 0.30$ (Patagonian Shelf). Although the Black Sea had an abundance of blooms consistently identified by both sensors, it was excluded because the focus of this study was on open ocean systems.

The areal extent of blooms in each region was estimated by averaging bloom pixels. After integrating over each year, the maximum bloom area was normalized

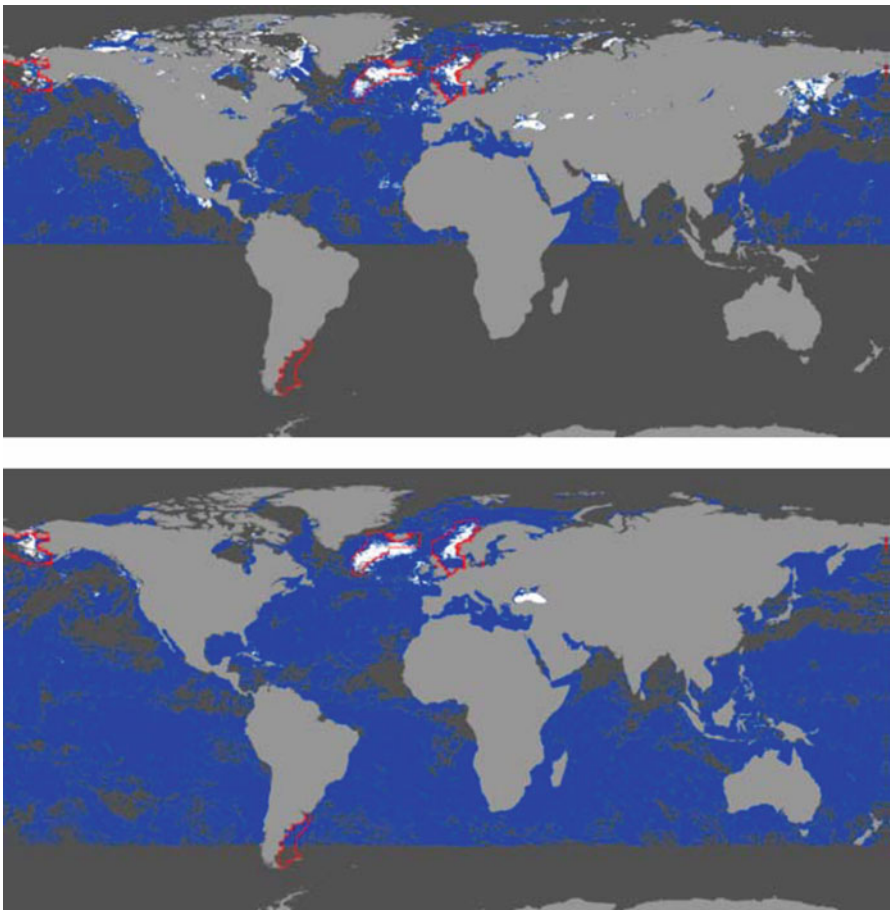

Fig. 18.2 AVHRR (*top panel*) and SeaWiFS (*bottom*) *E. huxleyi* composites for June 10–17, 1998. *White* pixels indicate *E. huxleyi* bloom; *blue* pixels, no bloom; *gray* pixels are missing data; the four regions we highlight in this study are outlined in *red*

over the 25-year period. The seasonal cycle in the coverage of *E. huxleyi* was calculated by averaging coincident periods for all years and performing a 5-week running box car filter. Anomalies were not found useful for this analysis due to the annual variability in bloom onset; therefore, this analysis focused on the original time series and annual cumulative values.

18.2.4 Geophysical Data and Climate Indices

The areal extent of *E. huxleyi* blooms were compared to sea-surface temperature (SST) and mixed-layer depth. Optimally interpolated weekly and monthly 1° resolution SST (NOAA OI.v2) were created from in situ and satellite-derived

SST (Reynolds and Smith 1994). Mixed-layer depths were acquired from Simple Ocean Data Assimilation Reanalysis (SODA) Version 2.0.2 (Carton and Giese 2008). This blended ocean product combines the advantages of ground-truth observations with the uniformly mapped regularity of numerical simulation.

The annual bloom extent was also compared to several climate indices which have been linked to ecosystem changes: El Niño Southern Oscillation (ENSO) (Wolter and Timlin 1998), Pacific Decadal Oscillation (PDO) (Trenberth and Hurrell 1994), and North Atlantic Oscillation (NAO) (Hurrell 1995). The trend toward more positive NAO values over the past 30 years coincides with changes in marine and terrestrial ecosystems (Hurrell and Deser 2009). Over short time scales, warm PDO eras have been linked to enhanced coastal ocean productivity near Alaska and inhibited productivity to the south, with the opposite patterns during cold eras (Mantua et al. 1997).

18.3 Results and Discussion

18.3.1 Extent of E. huxleyi Blooms

The timing of *E. huxleyi* blooms detected in AVHRR showed good correspondence to those identified in SeaWiFS (Fig. 18.3). Some discrepancies in magnitudes were evident, but were expected due to differences in sensor sensitivity and image coverage between the two satellites. During 10 years of overlapping data, the Bering Sea had the greatest fraction of bloom coverage, followed by the Norwegian Sea and the area south of Iceland. Our AVHRR bloom detection method did not match SeaWiFS as well on the Patagonian Shelf; there was some disparity in magnitudes, and many times SeaWiFS detected a bloom but AVHRR did not. In general, using AVHRR, *E. huxleyi* blooms were detected more frequently in Bering and Norwegian Seas. Using SeaWiFS, blooms were detected more frequently in the Patagonian Shelf and south of Iceland.

For the entire AVHRR series (Fig. 18.4), some years show greater bloom coverage over a week or two, while some smaller fractional bloom areas are maintained over several weeks. Normalized annual cumulative bloom coverage values account for this effect. *E. huxleyi* blooms in all regions achieved their annual cumulative maxima around 1992 and 1996 (Fig. 18.4). Since then, annual values clearly show a trend toward less bloom area. Blooms in all regions increased slightly in 2006 after decreasing over the last decade. A linear fit to the annual values shows a marked decrease in all regions; this trend is highly statistically significant for the Northern Hemisphere regions and to 94% confidence for the Patagonian Shelf (Table 18.1). *E. huxleyi* blooms were identified in the Bering Sea in 1997 with the advent of SeaWiFS ocean color, although they had been present prior to that as evidenced in AVHRR as well as in situ data collected during field studies in the early 1990s (Merico et al. 2003). The Patagonian Shelf had the smallest area covered by *E. huxleyi* blooms which were drastically reduced since 2000, suggesting a possible regime shift. For all regions, there was no evidence for any poleward shift by the species.

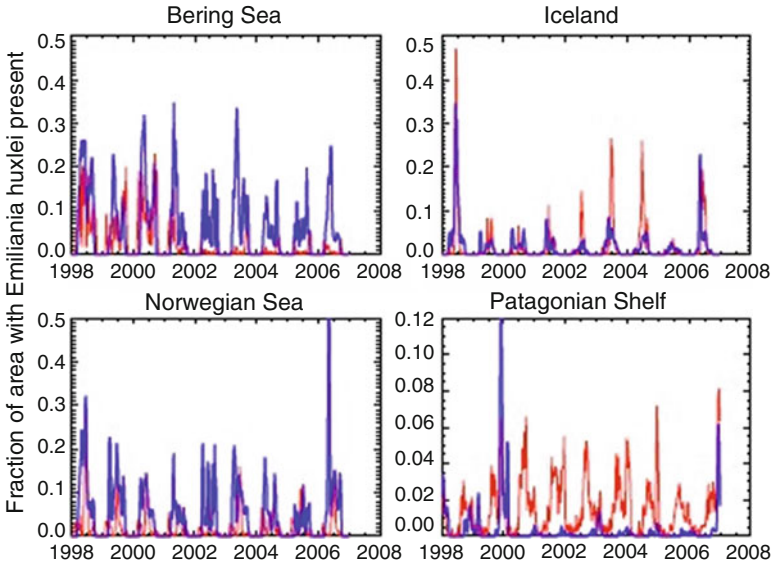

Fig. 18.3 Fraction of area covered by *E. huxleyi* blooms each week detected by AVHRR (*blue*) and SeaWiFS (*red*) between 1998 and 2006 in the four regions with a 2-week smoothing

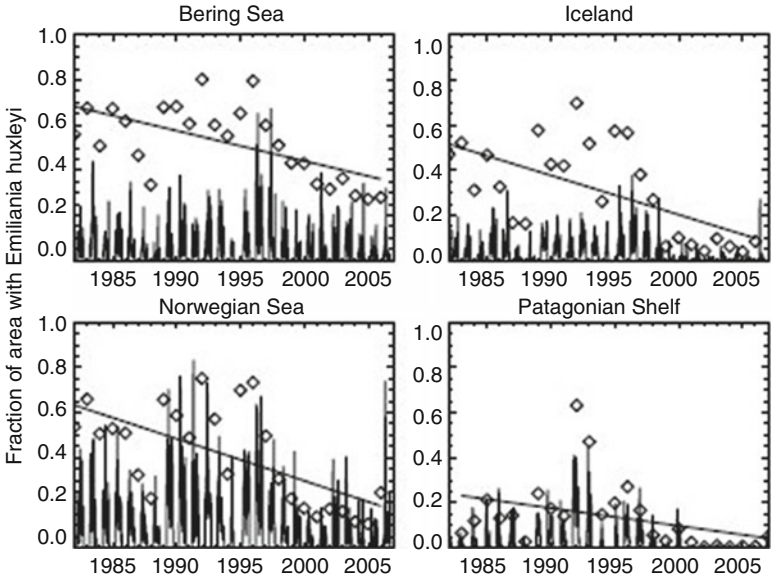

Fig. 18.4 Fraction of area covered by *E. huxleyi* blooms from 1982 to 2006 in the four regions. Weekly bloom episodes are plotted as lines as in Fig. 18.3; *diamonds* (◇) show integrated annual amounts normalized by the maximum for the time series. *Regression lines* for the annual values are superimposed with slopes, standard errors, correlation coefficients, and probabilities itemized in Table 18.1

Table 18.1 The trend in annual cumulative amounts during 1982–2006 as shown in Fig. 18.4

Region	β_1	se (β_1)	r_{xy}	p
Bering Sea	−0.013	0.0036	−0.61	0.001
Iceland	−0.017	0.0046	−0.62	0.0009
Norwegian Sea	−0.019	0.0046	−0.64	0.0009
Patagonian Shelf	−0.008	0.0039	−0.39	0.054

Draper and Smith (1981)
β_1 is the slope of the regression line, se is the standard error of β_1, r_{xy} is the autocorrelation coefficient, and p is the probability where $p < 0.05$ is considered statistically significant

Table 18.2 The cross correlations between the annual cumulative fraction of area covered by *E. huxleyi* bloom with SST and MLD anomalies, as well as ENSO, PDO, and NAO climate indices

Region	SST r_{xy}	MLD r_{xy}	ENSO r_{xy}	PDO r_{xy}	NAO r_{xy}
Bering Sea	−0.35	−0.21	0.20	0.22	0.33
Iceland	−0.64	−0.11	0.26	0.25	0.38
Norwegian Sea	−0.59	−0.48	0.23	0.22	0.35
Patagonian Shelf	−0.50	−0.59	0.07	−0.21	0.32

18.3.2 Relationship to Environmental Variables and Climatic Indices

Sea-surface temperatures during bloom events were highly variable between the regions. The Bering Sea had the coolest temperatures, generally less than 10°C, without any correspondence to the fraction of area covered by *E. huxleyi* blooms. The Patagonian Shelf was the warmest, ranging from 10 to18°C. The regions south of Iceland and in the Norwegian Seas ranged from 5°C to 12 and 16°C, respectively. Annual *E. huxleyi* fractions were anti-correlated to sea-surface temperature anomalies (Table 18.2). Other studies have found a correlation between warm temperature anomalies and bloom episodes (Smyth et al. 2004; Raitsos et al. 2006), so we interpret our opposite result to indicate that the warming trend is not driving the long-term decrease in *E. huxleyi* bloom extent.

Correlations with mixed-layer depths confirm the importance of stratification to bloom development (Table 18.2): shallower mixed layers corresponded to a higher fraction of area covered by bloom, albeit weakly. The highest correlation was for the Patagonian Shelf with mixed layers shallower than 20 m; the most variability was seen off Alaska where mixed layer depths ranging 10–50 m showed variable bloom coverage, while less than 20 m corresponded to the greatest areas of bloom. For the North Atlantic, typical bloom size increased for shallower mixed layers, while some atypical blooms were associated with mixed layers deeper than 100 m.

Comparison with the three climate indices examined did not produce a significant relationship. ENSO had a large warm peak in 1997, following the maximum bloom area; the warm ENSO peak in 2006 corresponded to a slightly increased

bloom area in all regions, but there was generally no consistent relationship between the ENSO indices and the fraction of area covered by *E. huxleyi*. The monthly and annual PDO indices were also not significantly correlated to *E. huxleyi* blooms over the 25-year time series, although it is worth noting that the summertime PDO had a higher correlation for all regions (0.2–0.3) compared to wintertime PDO (0.05–0.06). Although the NAO wintertime index was correlated with a 2-year lag in bloom fractional area between 0.3 and 0.4 for all regions, they were not statistically significant.

The lack of significant correlations between bloom fractional area and the relevant environmental variables and climatic indices examined above suggest that a nonlinear combination of these or others factors, such as changing ocean chemistry, are responsible for the decreasing trend in the surface area of *E. huxleyi* blooms documented in the four regions of our study. For example, recent studies suggest that decreasing alkalinity in ocean surface layers could lead to changes in coccolith size, shell thickness, species distribution, calcification rate, and carbon fixation (Barcelos e Ramos et al. 2010; Charalampopoulou et al. 2010) which could conceivably decrease the calcite concentration within blooms and impair our ability to detect them in AVHRR imagery. Further study, especially with in situ data, is required to ascertain the factors responsible for this decreasing trend in the *E. huxleyi* bloom surface area.

18.4 Conclusion

The well-established ocean color satellite measurements of *E. huxleyi* blooms around the world were extended back to 1982 by identifying them in AVHRR imagery. The observed trend over 25 years toward decreasing bloom areal extent in the four regions examined at the same time that temperatures have been rising suggests that the hypothesized relationship between *E. huxleyi* bloom events and warming temperatures does not hold over the long term. Other than the weak relationship between bloom fractional area and mixed layer depth, the paucity of robust correlations with physical variables and climate indices suggest a nonlinear combination of those or other factors are responsible for the decreasing trend in the surface area of *E. huxleyi* blooms documented here. Other possible factors, such as ocean acidification or salinity anomalies, need to be studied further.

Acknowledgments This study benefited from many discussions with Mete Uz. The AVHRR data were specially processed for R_{rs} by Aleksander Jelenak and William Straka. This research was supported by the Office of Global Program's NOAA Climate and Global Change Program. The views, opinions, and findings contained in this paper are those of the authors and should not be construed as an official National Oceanic and Atmospheric Administration or US Government position or decision.

References

Balch WM, Gordon HR, Bowler BC, Drapeau DT, Booth ES (2005) Calcium carbonate measurements in the surface global ocean based on Moderate-Resolution Imaging Spectroradiometer data. J Geophys Res 110. doi:10.1029/2004JC002560

Barcelos e Ramos J, Muller MN, Riebesell U (2010) Short-term response of the coccolithophore Emiliania huxleyi to an abrupt change in seawater carbon dioxide concentrations. Biogeosciences 7:177–186

Broerse ATC, Tyrrell T, Young JR, Poulton AJ, Merico A, Balch WM, Miller PI (2003) The cause of bright waters in the Bering Sea in winter. Cont Shelf Res 23:1579–1596. doi:10.1016/j.csr.2003.07.001

Brown CW, Yoder JA (1994) Coccolithophorid blooms in the global ocean. J Geophys Res 99:7467–7482

Carton JA, Giese BS (2008) A reanalysis of ocean climate using simple ocean data assimilation (SODA). Mon Wea Rev 136:2999–3017

Charalampopoulou A, Tyrrell T, Poulton A, Lucas M (2010) Investigating the response of coccolithophores to variable carbonate chemistry between UK and Svalbard, AGU 2010 Ocean Science Meeting, Portland, OR. BO15A-07

Delworth TL, Dixon KW (2000) Implications of the recent trend in the Arctic/North Atlantic Oscillation for the North Atlantic thermohaline circulation. J Climate 13:3721–3727

Doney SC, Fabry VJ, Feely RA, Kleypas JA (2009) Ocean acidification: the other CO2 problem. Ann Rev Mar Sci 1:169–192. doi:10.1146/annurev.marine.010908.163834

Draper NR, Smith H (1981) Applied regression analysis. Wiley, New York

Hays GC, Richardson AJ, Robinson C (2005) Climate change and marine plankton. Trends Ecol Evol 20:337–344

Heidinger AK, Cao C, Sullivan JT (2002) Using Moderate Resolution Imaging Spectrometer (MODIS) to calibrate advanced very high resolution radiometer reflectance channels. J Geophys Res 107. doi:10.1029/2001JD002035

Holligan PM, Viollier M, Harbour DS, Camus P, Champagne-Philippe M (1983) Satellite and ship studies of coccolithophore production along a continental shelf edge. Nature 304:339–342

Hughes L (2000) Biological consequences of global warming: is the signal already apparent? Trends Ecol Evol 15:56–61

Hurrell JW (1995) Decadal trends in the North Atlantic Oscillation regional temperatures and precipitation. Science 269:676–679

Hurrell JW, Deser C (2009) North Atlantic climate variability: the role of the North Atlantic Oscillation. J Mar Syst 78(1):28–41. doi:10.1016/j.jmarsys.2008.11.026

Iglesias-Rodriguez MD, Brown CW, Doney SC, Kleypas J, Kolber D, Kolber Z, Hayes PK, Falkowski PG (2002) Representing key phytoplankton functional groups in ocean carbon cycle models: coccolithophorids. Global Biogeochem Cycles 16(4):1100. doi:10.1029/2001GB001454

Iglesias-Rodriguez MD, Halloran PR, Rickaby REM, Hall IR, Colmenero-Hidalgo E, Gittins JR, Green DRH, Tyrrell T, Gibbs SJ, von Dassow P, Rehm E, Armbrust EV, Boessenkool KP (2008) Phytoplankton calcification in a high-CO2 world. Science 320:336–340. doi:10.112/science.1154122

Mantua NJ, Hare SR, Zhang Y, Wallace JM, Francis RC (1997) A Pacific interdecadal oscillation with impacts on salmon production. Bull Am Meteor Soc 78:1069–1079

Merico A, Tyrrell T, Brown CW, Groom SB, Miller PI (2003) Analysis of satellite imagery for Emiliania huxleyi blooms in the Bering Sea before 1997. Geophys Res Lett 30(6):1337. doi:10.1029/2002GL016648

Napp JM, Hunt GL (2001) Anomalous conditions in the south-eastern Bering Sea 1997: linkages among climate, weather, ocean, and biology. Fish Oceanogr 10(1):61–68

Platt T, Sathyendranath S (2008) Ecological indicators for the pelagic zone of the ocean from remote sensing. Remote Sens Environ 112(8):3426–3436

Platt T et al (2009) The phenology of phytoplankton blooms: ecosystem indicators from remote sensing. Ecol Model 220(21):3057–3069

Platt T et al (2010) Diagnostic properties of phytoplankton time series from remote sensing. Estuaries Coasts 33(2):428–439

Raitsos DE, Lavender SJ, Pradhan Y, Tyrell T, Reid PC, Edwards M (2006) Coccolithophore bloom size variation in response to the regional environment of the subarctic North Atlantic. Limnol Oceanogr 51(5):2122–2130

Reynolds RW, Smith TM (1994) Improved global sea surface temperature analyses. J Climate 7:929–948

Riebesell U, Bellerby RGJ, Engel A, Fabry VJ, Hutchins DA, Reusch TBH, Schulz KG, Morel FMM (2008) Comment on "phytoplankton calcification in a high-CO2 world". Science 322:1466b. doi:10.112/science.1161096

Sapiano MRP, Brown CW, Schollaert Uz S, Vargas M (2012) Establishing a global climatology of marine phytoplankton phonological characteristics. J Geophys Res. doi:10.1029/2012JC007958

Smyth TJ, Tyrrell T, Tarrant B (2004) Time series of coccolithophore activity in the Barents Sea, from twenty years of satellite imagery. Geophys Res Lett 31:L11302. doi:10.1029/2004GL019725

Trenberth KE, Hurrell JW (1994) Decadal atmosphere–ocean variations in the Pacific. Clim Dyn 9:303–319

Tynan CT et al (2001) Endangered right whales on the southeastern Bering Sea shelf. Science 294 (5548):1894

Tyrrell T, Merico A (2004) Emiliania huxleyi: bloom observations and the conditions that induce them. In: Thiertein HR, Young J (eds) Coccolithophores: from molecular processes to global impact. Springer, Heidelberg, pp 75–97

Vargas M, Brown CW, Sapiano MRP (2009) Phenology of marine phytoplankton from satellite ocean color measurements. Geophys Res Lett 36:L01608. doi:10.1029/2008GL036006

Westbroek P, Young JR, Linschooten K (1989) Coccolith production (biomineralization) in the marine alga Emiliania huxleyi. J Protozool 36:368–373

Westbroek P, Brown CW, van Bleijswijk J, Brownlee C, Brummer GJ, Conte M, Egge J, Fernandez E, Jordan R, Knappertsbusch M, Stefels J, Veldhuis M, van der Wal P, Young J (1993) A model system approach to biological climate forcing: the example of Emiliania huxleyi. Global Planet Change 8(1–2):27–46

Wolter K, Timlin MS (1998) Measuring the strength of ENSO events – how does 1997/98 rank? Weather 53:315–324

Chapter 19
Land Surface Temperature (LST) Retrieval from GOES Satellite Observations

Donglian Sun and Yunyue Yu

Abstract This chapter includes recent advances on the retrieval of land surface temperature (LST) from satellite observations. Special attention has been paid to the LST retrieval from GOES satellites. Detailed introduction is given about the literature review, the existing problems and challenges, and the advantages of geostationary satellites and GOES instruments. Algorithm theoretical basis (both physical and mathematical) has been provided. The simulation test and error analysis are enclosed. The chapter gives a complete coverage on the LST retrieval from GOES observations, including the physical problem, mathematical description of the theoretical basis, forward model simulations, and algorithm coefficient derivation, validation against ground observations, and error estimate and analysis.

Keywords Land surface temperature (LST) • GOES • LST product • Validation

19.1 Introduction

Surface skin temperature, which is the temperature at the interface between the land surface and atmosphere, is an important climate parameter due to its control of the upward terrestrial radiation, and hence, the surface sensible heat and latent heat flux exchange with the atmosphere. The importance of land surface processes for climate and weather modeling has increasingly been recognized. Many general circulation and climate models are now coupled with land surface schemes. For example, the community climate model (CCM) is coupled with the biosphere-atmosphere transfer scheme (BATS); the National Environmental Prediction

D. Sun (✉)
Department of Geography and Geoinformation Science, George Mason University, Fairfax, VA 22030, USA

Y. Yu
NOAA/NESDIS/STAR, College Park, MD 20740, USA

J.J. Qu et al. (eds.), *Satellite-based Applications on Climate Change*,
DOI 10.1007/978-94-007-5872-8_19,

Center (NCEP) mesoscale Eta model is coupled with Oregon State University (OSU) land surface scheme and with the simple biosphere (SIB) scheme. The inclusion of detailed land surface schemes into the general circulation models (GCMs) and numerical weather prediction (NWP) models is motivated by the realization that the surface plays an important role, in regulating the exchange of heat, momentum, and energy between the Earth's surface and the atmosphere. Skin temperature is a key parameter for land surface process parameterization. At present, information on surface skin temperature is available only from few field experiments, such as the First International Satellite Land Surface Climatology Project (ISLSCP) Field Experiment (FIFE) (Sellers et al. 1992), Boreal Ecosystem-Atmosphere Study (BOREAS) Experiment (Sellers et al. 1995, 1997), the Atmospheric Radiation Measurement Program (ARM) Experiment (http://www.arm.gov), the MONSOON experiment (Kustas and Goodrich 1994), the Oklahoma Mesonet Network (http://okmesonet.ocs.ou.edu), the CASES experiment (http://www.mmm.ucar.edu/cases), and many more shorter field observations. Till now, surface shelter temperature was used as proxy to skin surface temperature, even though; these are known to differ. Observations from satellites have been proven to be useful for inferring surface skin temperature. However, not all satellites have the necessary capabilities to derive surface temperature at high accuracy; some do not have sufficient number of channels to derive surface emissivity, while others do not observe the Earth's surface frequently enough to represent the diurnal cycle.

Deriving accurate land surface temperature (LST) from satellites is both attractive and challenging. It is attractive because LST is a highly variable quantity in both space and time. Satellites provide efficient and practical means of capturing this variability. It is challenging because the land surface is very heterogeneous, LST is generally not homogeneous within one pixel, and land surface emissivities may be quite different from unity and spectrally variable (Lyon 1965; Nerry et al. 1990).

There are three main sources of error in the determination of LST from satellites. First, the satellite instruments have sensor noise and calibration errors that transfer into errors in brightness temperature. Next, algorithms may have errors in the determination of the atmospheric effect, and lack of knowledge of spectral emissivities of the land surface. The third source of error is the evaluation process itself. Ground observations are limited in scope and measurements are taken at a point, while satellites measure a pixel average. For example, for GOES, it is a 4 km $\times$ 4 km area, and it is well known that land surface temperature is not homogeneous on such scale.

While surface temperature retrievals from satellites utilize atmospheric windows (where absorption is minimum), the influence of atmospheric absorption and emission is not negligible. Water vapor is the major absorbing gas in the window channels; it varies with season and latitude.

The effect of surface emissivity is twofold. Since the land surface emissivity is generally less than one, part of the atmospheric downward radiation is reflected by the surface and has to be accounted for (Lorenz 1986). The emitted radiation by the surface is modified in each channel, yielding different values for the brightness temperature.

19.1.1 Literature Review

19.1.1.1 Importance of Skin Temperature

Land surface temperature (LST), a key indicator of the Earth's surface energy budget, plays an important role in land surface processes on regional as well as on global scales. It combines the surface-atmosphere interactions and energy fluxes between the atmosphere and the ground (Mannstein 1987). It is of fundamental importance to the net radiation budget at the Earth's surface and to monitoring the state of crops and vegetation (Norman and Becker 1995; Li and Becker 1993; Sellers et al. 1998). Therefore, it is required for a wide variety of climate, hydrological, ecological, and biogeochemical studies (Camillo 1991; Schmugge and Becker 1991; Running 1991; Zhang et al. 1995; Running et al. 1994).

Skin temperatures at the Earth's surface are important for the study of global warming (Knox 1999; Jin and Dickerson 2002). Typically, global temperature change is assessed by in situ surface air temperature (SAT) measurements at 2 m height at weather stations. However, weather stations are usually located in relatively densely populated regions where anthropogenic impacts may affect measurements, and thus the temperature record may not be representative of global change. Moreover, station observations are sparse and unevenly distributed, and suffer from differences in elevation and time of observation (Peterson 2003). The use of satellite-derived data could contribute to a large-area consistent measurement (Gallo et al. 1999). Satellite LST can also be assimilated into climate, mesoscale atmospheric, and land surface models to estimate sensible heat flux and latent heat flux. It can also be applied for analyzing climate change due to its rich archive from being routinely produced from imagery data of geostationary and polar-orbiting satellites.

A long-term data set of satellite-derived land surface temperature can be used as an index of greenhouse effect and climate change. For example, accurate Arctic snow and ice surface temperature is needed to improve estimates of the heat budget in the polar region and our understanding of its link to the global climate change (Yu et al. 1995). Canopy temperature may be used to estimate evapotranspiration and sensible heat flux (Vining and Blad 1992), to evaluate water requirements of wheat (Jackson et al. 1977), and sensible and latent heat fluxes (Kimura and Shimiru 1994). Satellite-measured surface temperature may be used to improve models and methods for evaluating land surface energy balance (Diak and Whipple 1993; Crago et al. 1995). Furthermore, atmospheric general circulation model (GCM) simulations indicate that stronger summer monsoons are associated with higher land temperatures (Meehl 1994).

19.1.1.2 LST Derivation from Satellites Under Clear Conditions

The first effort to retrieve LST from satellites was made by Price (1984), by adopting the AVHRR sea surface temperature (SST) split-window algorithm over

agricultural land. After a careful analysis of the relevant error sources, he showed that the split-window method for SST could be adopted with an accuracy of 3°C. Since most land surface emissivities are not close to unity, Becker (1987) pointed out that if emissivities in the two split-window channels are assumed to be 1, the error ΔT in LST by the SST split-window method is significant and is of the order of

$$\Delta T = 50\frac{(1-\varepsilon)}{\varepsilon} - 300\frac{(\varepsilon_1 - \varepsilon_2)}{\varepsilon} \qquad \varepsilon = \frac{(\varepsilon_1 + \varepsilon_2)}{2} \tag{19.1}$$

Becker and Li (1990) extended the split-window method for SST to LST and accounted for land surface emissivity. Again, surface temperature is expressed as a linear combination of the brightness temperature in the two split-window channels, in a form similar to SST, but with coefficients varying with spectral emissivites. They show that more accurate LST can be retrieved with this local split-window method, once the surface emissivities are known with sufficient accuracy. This approach, the so-called local split-window LST algorithm, has been widely used. As yet, information on surface emissivities is lacking. In some algorithms (Vidal 1991; Ulivieri et al. 1992), the land surface emissivity correction term derived by Becker (1987) is added to the SST split-window equation, to obtain a split-window equation for LST.

The coefficients of the above LST split-window algorithms depend on spectral emissivities but not on atmospheric conditions. The corrections for atmospheric effects are limited to the use of the differential absorption of water vapor continuum inside the atmospheric window 10.5–12.5 μm. Prata (1993) introduced a split-window algorithm with coefficients that not only depend on surface emissivity but also on atmospheric transmittance. Sobrino et al. (1994) also developed an LST split-window algorithm with coefficients that vary with both surface emissivity and atmospheric transmittance. However, it is difficult to obtain information on atmospheric transmittance.

Since water vapor is the major absorbing gas in the split-window channels, Becker and Li (1995) introduced a new split-window algorithm with coefficients depending on surface emissivity and the atmospheric water vapor content. Francois and Ottle (1996) introduced another LST split-window algorithm with coefficients being quadratic functions of the water vapor content and tabulated for different emissivity values. Coll and Caselles (1997) developed an LST algorithm with nonlinear brightness temperature difference term, with coefficients of emissivity correction terms changing with atmospheric transmittance and water vapor content. The problem with these algorithms is that the error of precipitable water itself may become another source for LST retrieval error. Although precipitable water can be estimated from satellites (Jedlovec 1989; Kleespies and McMillin 1990), errors are unavoidable.

The algorithms discussed above are physically based, starting from a theoretical description of the important radiative transfer processes at the surface and in the atmosphere and ending in a regression relation with coefficients that are adjustable, or at least, changing with surface and atmospheric parameters. All of these split-window approaches utilize the 11- and 12-μm window channels and assume constant surface emissivities.

Bates and Smith (1985) included the 3.9-μm channel of GOES-5 in SST retrieval from the split-window channels, and were able to reduce the SST retrieval error. May (1993) introduced three-channel nighttime SST algorithm to retrieve SST from the NOAA/AVHRR imager during nighttime and demonstrated improved accuracy relative to the split-window algorithm. The transmittance of radiant energy from the surface through the atmosphere is greater for AVHRR channel 3 (3.75 μm) than for channels 4 and 5. This fact results in less atmospheric attenuation effects in channel 3 data, providing a more accurate SST retrieval when all the three thermal channels are used. However, this channel has not been used to retrieve LST and as yet no three-channel LST algorithm has been developed. Channel 3 can be used only at night because this wavelength contains reflected solar energy during the daytime, unless a correction to the solar contamination is adopted. Brown et al. (1996) investigated the possibility of correcting the solar contamination existing in the MID-IR channels during daytime for the bands of MODIS (Moderate-resolution Imaging Spectroradiometer). These studies are in progress and results are being evaluated.

Most studies on LST have focused on the use of polar-orbiting satellite systems, such as EOS/MODIS and NOAA/AVHRR. The temporal measurement frequency of the polar-orbiting satellite instruments is approximately two times per day. This sparse temporal sampling is inadequate to capture the LST diurnal cycle. Moreover, the NOAA satellites are not strictly sun-synchronous, implying that a drift in time of measurement may exist at a given location (Gutman 1992; Gleason et al. 2002).

Less work has been done with geostationary satellites. Prata (1999) investigated LST retrieval from the Japanese Geostationary Meteorological Satellite 5 (GMS-5) using a split-window LST algorithm. However, the GMS have only two window channels available for LST retrieval. Faysash and Smith (1999, 2000) proposed a simultaneous retrieval of LST and surface emissivity using MODTRAN; however, radiative transfer models (RTM) are very time consuming, and therefore, not well suited for large data sets and operational use. Several studies of LST retrieval from METEOSAT of the European Meteorological Satellite Programme (EUMETSAT) have been performed (Morcrette 1991; Olesen et al. 1995; Hay and Lennon 1999; Cresswell et al. 1999; Schadlich et al. 2001; Gottsche and Olesen 2001; Dash et al. 2002). They deal with modeling the brightness temperature of METEOSAT, studying ground height effects on LST, estimating air temperature from LST, and applications of LST in disease studies. Recently, a four-channel LST algorithm has been developed by Sun and Pinker (2007) for the METEOSAT second-generation imager SEVIRI.

19.1.2 LST Derivation from Satellites Under Cloudy Conditions

All of the algorithms described above are limited to clear sky conditions, while in reality, most of the sky is covered with clouds. Clouds affect surface temperature by reflecting solar radiation and by emitting longwave radiation.

Most LST retrievals under cloudy conditions use microwave observations since microwave channels have better transparency for clouds (McFarland et al. 1990; Chahine and Suskind 1991; Givri 1997; Plokhenko 1997; Weng and Grody 1998; Basist et al. 1998; Peterson et al. 2000; Williams et al. 2000; Aires et al. 2001; Dash et al. 2002). McFarland et al. (1990) derived surface temperature over crops, moist soils, and dry soils areas in the Central Plains of the United States from the DMSP Special Sensor Microwave/Imager (SSM/I) data. A regression analysis of all of the SSM/I channels and air temperatures (representing the surface temperatures assumed) showed a correlation with a root mean square error of 3 K. It was also determined that snow-surface temperature retrieval is very difficult, because snow emissivity varies with depth, density, and grain size.

Weng et al. (1998) developed a physical algorithm to retrieve land surface temperature from the microwave imager (SSM/I). However, as indicated by Ulaby et al. (1986) while satellite microwave radiometers have provided information about atmospheric and oceanic parameters for several years, they have not provided information on land parameters. The spatial resolution of the satellite microwave measurements (about 50 km) is more compatible with the dimensions associated with the spatial variation of oceanic parameters, and the mechanisms responsible for microwave emission from land surfaces are not well understood. Because of the much higher variations of the land surface emissivities in the microwave range and the dependence of microwave brightness temperature on surface roughness and structures (Eyre and Woolf 1988), it is not possible to retrieve global land surface temperature at accuracy of 1–2 K by microwave techniques alone. Since the visible and infrared data have no direct information on the surface temperature under overcast conditions, it is difficult to derive LST under such conditions from the imager data.

19.1.3 Ill-Posed Problem

Since surface emissivities change spectrally, the total number of unknowns (N emissivity values plus LST, $N + 1$) is always larger than the number (N band observations) of radiative transfer equations to be solved regardless how many thermal channels a sensor has. This is a typical ill-posed problem. A number of alternative methods have been proposed to simultaneously retrieve LST and band emissivity such as the temperature and emissivity separation method of Kealy and Hook (1993) as applied to the thermal infrared bands from TIMS (Thermal Infrared Multispectral Scanner) and ASTER (Advanced Spaceborne Thermal Emission

Reflectance Radiometer). This method utilizes six thermal bands from TIMS and five thermal bands from ASTER, focusing on emissivity retrieval. The MODIS team (Wan et al. 1996) proposes a day/night algorithm that uses day and night measurements in N MODIS bands with $2N$ observations. The unknown parameters include N band emissivities, daytime surface temperature, nighttime surface temperature, and four atmospheric parameters (air temperature and water vapor content at two times). The total number of unknowns $N + 7$ needs to be smaller than or equal to the $2N$ observations, $(N + 7) \leq 2N$, which requires $N \geq 7$. Seven MODIS thermal bands (12.91, 12.25, 11.98, 8.6, 4.70, 4.11, and 3.74) are used to solve a 14-equation set. The problem of this approach is that the pixel during nighttime may not be the same as during daytime, and seven infrared window bands are required to solve the equations. The alternative approach is to use Lookup Tables (LUT) generated from radiative transfer model simulations. This will introduce errors due to interpolation. Liang (2001) proposed an optimized algorithm for separating land surface temperature and emissivity from MODIS and Advanced Spaceborne Thermal Emission and Reflection Radiometer (ASTER). This method also needs five (ASTER) and six (MODIS) thermal window bands, and emphasize emissivity retrieval. Ma et al. (2002) proposed a physical algorithm for MODIS to retrieve LST and surface emissivity simultaneously. This algorithm uses nine channels and is computationally intensive.

19.1.4 Validation Issues

The evaluation of LST retrievals from satellites has been difficult since satellites measure skin temperature while global scale ground observations are from shelters. The difficulty in obtaining ground truth has been addressed by Prata (1994) and others. Weng and Grody (1998) tried to use shelter temperature in the early morning (when the difference between surface skin temperature and shelter temperature is the lowest) to validate LST retrieval from satellite SSM/I data.

Sugita and Brutsaert (1993) compared the land surface temperature derived from the AVHRR and TOVS instruments on NOAA-9 and NOAA-10, the TM instruments on Landsat-5, and VISSR instrument aboard GOES-7 with ground truth from the First ISLSCP Filed Experiment (FIFE) (Sellers et al. 1992). For clear condition, the root mean square differences from TOVS, TM, and VISSR data are about 1–2 K; for AVHRR, it is of the order of 2–3 K. Prince et al. (1998) compared surface temperature retrieved from the AVHRR with the BOREAS, HAPEX-Sahel (Hydrological and Atmospheric Pilot Experiment in the Sahel), and FIFE and showed RMS error of 3.5 K.

Existing approaches show that root mean square accuracy of 1–3 K can be reached from the current operational and research satellite-borne visible/infrared radiometers. While accuracy of 3 K is of marginal use, accuracy of 1 K or less is desired for many applications. A main objective of this study is to develop new algorithms to improve the accuracy of LST estimation from satellites.

Due to the lack of ground observations, all relevant sources of information on surface skin temperature, directly, including the skin temperature observation from the Atmospheric Radiation Measurement (ARM) and Mesonet networks, and indirectly, such as the surface upwelling and downwelling longwave radiation, and even soil temperature observations, had been used in the evaluations of retrieved LSTs from GOES by Sun and Pinker (2003, 2004, 2006 a, b, 2007) and Yu et al. (2009a, b, c).

19.2 LST Retrieval from Geostationary Satellites

Most surface temperature retrievals from satellites are based on polar orbiters. Surface temperature, especially land surface temperature, has a strong diurnal cycle, which cannot be captured at the temporal resolution (approximately two views per day) of such satellites. Geostationary satellites with high temporal resolution, on the other hand, provide good diurnal coverage, making them attractive for deriving information on the diurnal LST cycle and diurnal temperature range (DTR) (Sun et al. 2006), which is an important climate change index (Karl et al. 1993).

Satellite retrievals of LST have been conducted for over 40 years from a variety of polar-orbiting and geostationary satellites. For producing an LST climate data record from those programs, consistency of the LST products from different satellite mission is of importance. The GOES-Imager LST algorithm should have a good historical heritage for consistency among other satellite products.

The GOES imager is a multichannel instrument designed to sense emitted and reflected energy from sampled areas of the Earth. The multielement spectral channels simultaneously sweep east–west and west–east along a north to south path using a two-axis mirror scan system.

Accuracy of the satellite LST measurement is limited by the atmospheric correction, the complexity of surface emission characteristics, and sensor performance. Among those, variation of surface emissivity is the biggest difficulty in the satellite LST measurement.

Currently, surface emissivity variation is still the biggest impediment in satellite LST retrieval. The remote sensing community has been working for years to obtain a time series of accurate global land surface emissivity maps (e.g., Borbas et al. 2008). The GOES-Imager LST algorithm should potentially benefit from such improvement of emissivity measurement.

19.2.1 GOES Instrument Characteristics

The Geostationary Operational Environmental Satellite (GOES) system, operated by the United States National Environmental Satellite, Data, and Information Service

(NESDIS), supports weather forecasting, severe storm, tracking, and meteorology research. Spacecraft and ground system work together to provide a continuous stream of environmental data. The National Weather Service (NWS) uses the GOES system for its United States operational weather forecasting and monitoring, and scientific researchers use the data to better understand land, atmosphere, ocean, and climate.

The GOES system uses geosynchronous satellites which—since the launch in 1974—have been a basic element of US weather monitoring and forecasting. Designed to operate in geostationary orbit, 35,790 km (22,240 statute miles) above the Earth, thereby remaining stationary with respect to a point on the ground, the advanced GOES I–M spacecraft continuously view the continental United States, observing environments of the Pacific and Atlantic Oceans, Central, South America, and southern Canada. The three-axis, body-stabilized spacecraft design enables the sensors to "stare" at the Earth and thus more frequently image clouds, monitor Earth's surface temperature and water vapor fields, and sound the atmosphere for its vertical thermal and vapor structures. Before being launched, GOES satellites are designated by letters (-A, -B, -C. . .). Once a GOES satellite is launched successfully, it is redesignated with a number (-1, -2, -3. . .). So, GOES-A to GOES-F became GOES-1 to GOES-6. Because GOES-G was a launch failure, it never received a number. Since then, GOES-H to GOES-N became GOES-7 to GOES-13.

In this chapter, we mainly focus our efforts to derive the LST products from the imager of the GOES satellites currently available for operational use:

- GOES-12 is designated GOES-South, currently located at 75°W over the Amazon River.
- GOES-13 is designated GOES-East, currently located at 105°W. It provides most of the U.S. weather information.
- GOES 14 was placed in orbit on 7 July 2009, underwent Post-Launch Testing until December 2009 and then was placed in on-orbit storage.

The GOES imager is a multichannel instrument designed to sense emitted and reflected energy from sampled areas of the Earth. The multielement spectral channels simultaneously sweep east–west and west–east along a north to south path using a two-axis mirror scan system.

The GOES imager before GOES-12 had five channels centered at 0.67, 3.9, 6.7, 11, and 12 μm, respectively. The 3.9-, 11-, and 12-μm channels are infrared windows with little water vapor absorption, while the 6.7-μm band is a water vapor band that can be used to detect atmospheric water vapor in the upper troposphere. The 0.67 μm is a visible band that can be used to detect clouds during daytime.

The transmittance of the four thermal channels of GOES 8-11 vs. surface skin temperature distribution is shown in Fig. 19.1a. The transmittance at the 6.7-μm water vapor band is almost zero for skin temperature above 240 K. The surface radiation is almost totally absorbed by water vapor, so this band can be used to detect atmospheric water vapor distribution, but not for retrieving surface skin

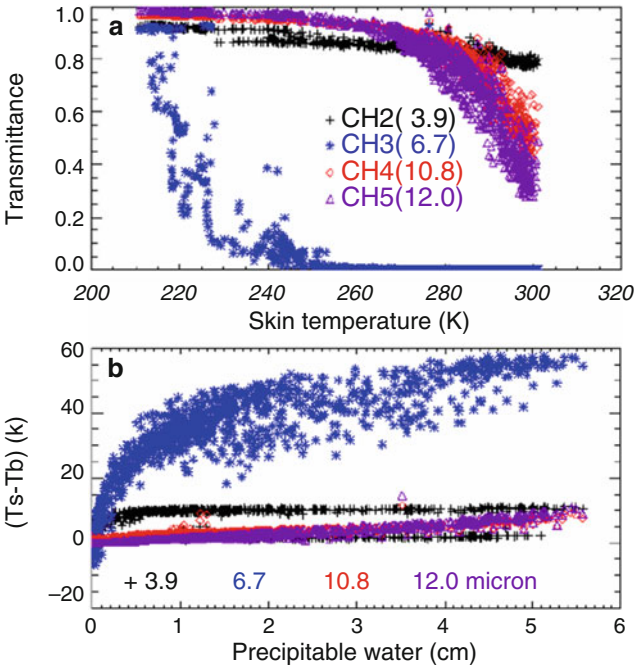

Fig. 19.1 The transmittance (**a**) and temperature deficits ($T_s - T_b$) (**b**) for the four infrared channels of the GOES 8–11

temperature. The transmittances of the 11- and 12-μm channels decrease significantly at high temperature (285–305 K); most values are below 0.8. This is why most existing split-window algorithms that use the 11- and 12-μm channels get larger errors at the warmer temperature range of 285–305 K. The transmittance for MIR channel 3.9 μm is more stable, with less sensitivity to the surface skin temperature most values being above 0.8. Therefore, the MIR 3.9-μm channel is a more appropriate window channel for retrieving LST than IR 11- and 12-μm channels. Moreover, temperature deficit between skin temperature T_s and brightness temperature T_b, ($T_s - T_b$) as shown in Fig. 19.1b, increases quickly at water vapor channel 6.7 μm, and it can be as large as 60 K. Temperature deficit is relatively stable at window channels, it increases with water vapor at IR channels, but it almost doesn't change with water vapor amount at MIR channel. Therefore, it is best to use the MIR 3.9-μm channel combined with the split-window 11- and 12-μm channels during nighttime, when the MIR channel does not contain solar energy reflected by surface.

The imagers on board the GOES M (12)-Q series, including the current operational GOES-13, don't have the 12-μm channel (Fig. 19.2), so it would not be possible to use the brightness temperature difference in the 11- and 12-μm channels to correct for atmospheric effects. Attempts have been made to use ancillary data

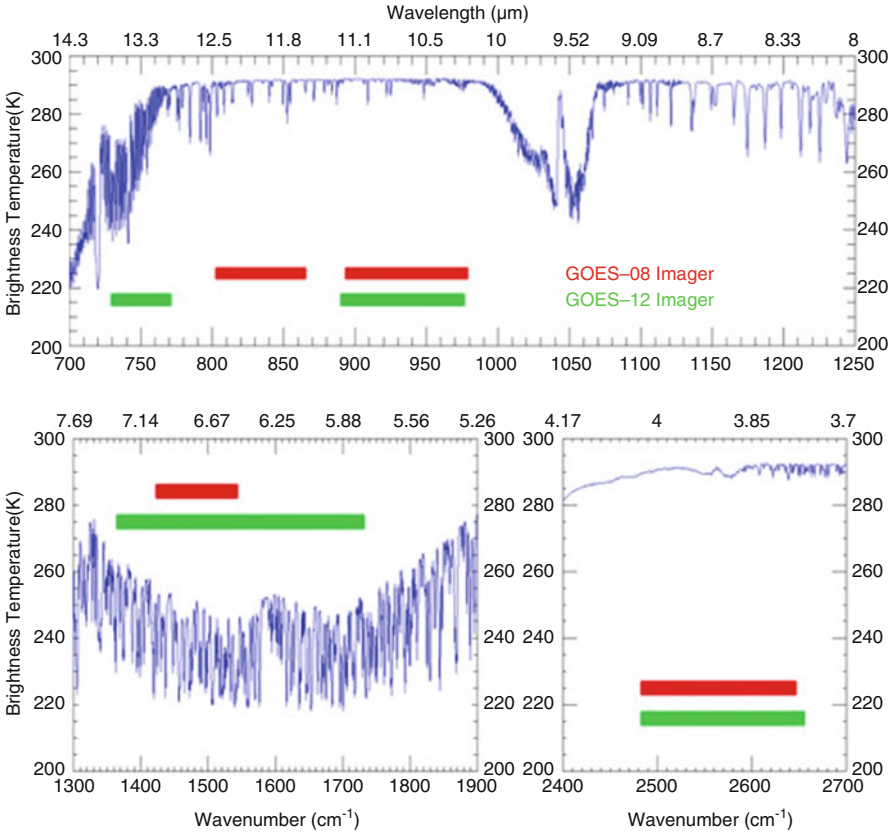

Fig. 19.2 Spectral distribution of the GOES-8 and GOES-12 imager channels

such as the total precipitable water and the characteristics of the middle-infrared channel of 3.9 μm to correct for atmospheric effects.

The land surface temperature can be produced for each cloud-free land pixel observed by the GOES sensor. The spectral characters of GOES-12 through 15 imager are listed in Table 19.1.

19.3 Theoretical Description

The GOES-LST algorithm development is based on a scientific research conducted by Sun and Pinker (2004) and Yu et al. (2008, 2009a, b, c). Theoretical details of the research are provided in this section.

Table 19.1 Spectral characters of GOES-12 through GOES-15 imager

Channels	Central wavelength (μm)	Resolution (km)
1 (visible)	0.65	1
2 (infrared)	3.9	4
3 (infrared)	6.48	4
4 (infrared)	10.7	4
6 (infrared)	13.3	8 (GOES-12/13) 4 (GOES-14/15)

Shaded channels are used for LST retrieval

19.3.1 Physical Description

Under clear sky conditions, the outgoing spectral radiance at the top of the atmosphere can be represented as

$$R(\lambda, \mu) = \varepsilon_0(\lambda, \mu)B(\lambda, T_s)\,\tau_0(\lambda,\mu) + R_a(\lambda, \mu) + R_s(\lambda, \mu, \mu_0, \varphi_0) + R_d(\lambda, \mu, \mu_0, \varphi_0) + R_r(\lambda, \mu) \tag{19.2}$$

where ε_0 is the surface spectral emissivity, B is the Planck function, τ_0 is the transmittance from the Earth's surface to the top of atmosphere, R_a is the thermal path radiance, R_s is the path radiance resulting from scattering of solar radiation, R_d is the solar diffuse radiance, and R_r is the atmospheric thermal radiation reflected by the surface. T_s is the skin temperature, λ is the wavelength, $\mu = \cos(\theta)$, and $\mu_0 = \cos(\psi)$, where θ is the satellite zenith angle, ψ is the solar zenith angle, and φ_0 is the azimuth angle.

The wavelength λ is actually the wavelength center of a narrow interval because there is no way to measure the exact monochromatic signal as a continuous function of wavelength by satellite sensors. For the far-IR bands, solar contributions can be negligible, so the outgoing infrared spectral radiance at the top of atmosphere can be represented by

$$R(\lambda, \mu) = \varepsilon_0(\lambda, \mu)B(\lambda, T_s)\,\tau_0(\lambda,\mu) + R_a(\lambda, \mu) \tag{19.3}$$

The purpose of the LST algorithm is to retrieve the land surface skin temperature T_s from the satellite sensor measured radiance $R(\lambda, \mu)$. Physically, in this problem, the surface temperature is basically coupled with two other factors: surface emissivity and the atmospheric absorptions. Developing an LST algorithm means to find a solution of decoupling the emissivity and the atmospheric absorption effects from satellite received radiance.

As shown from Fig. 19.3, in order to retrieve surface information from satellite observations, we need to select window channels with no or less atmospheric absorption. Some bands, such as 3–4, 8–9, and 10–12 μm, are some typical atmospheric windows.

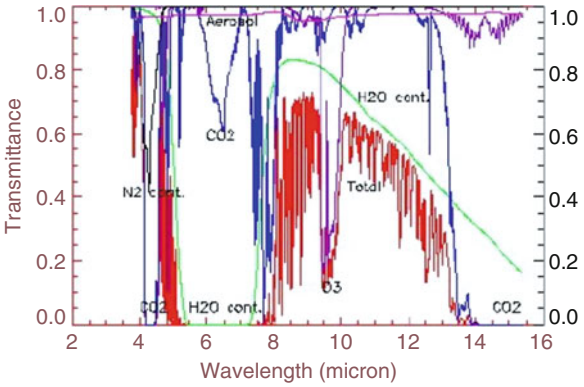

Fig. 19.3 Atmospheric transmittance vs. wavelength for some typical absorbing gases

Harris and Mason (1992) found that for a given change in surface temperature ΔT_0, the resulting changes in brightness temperatures in the two wavebands has the following relationship:

$$\frac{\Delta T_2}{\Delta T_1} = \frac{\varepsilon_2}{\varepsilon_1} \frac{\tau_2(0, p_0)}{\tau_1(0, p_0)} \tag{19.4}$$

where ε is the surface emissivity, τ is the atmospheric transmittance, and subscripts 1 and 2 refer to the index of the two channels. The absorbing gases can be divided into water vapor and other gases as follows:

$$\tau_\lambda(0, p_0) = \exp(-k_{w\lambda} U_w(0, p_0)) \exp(-k_{o\lambda} U_o(0, p_0)) \tag{19.5}$$

where $k_{W\lambda}$ and $k_{o\lambda}$ are the band-averaged absorption coefficients for water vapor and other gases, respectively; $U_w\,(0, p_0)$ and $U_o\,(0, p_0)$ are the total column contents of water vapor and other gases, respectively. Apply this to Eq. 19.4, yields

$$\frac{\Delta T_2}{\Delta T_1} = \frac{\varepsilon_2}{\varepsilon_1} \exp((k_{w1} - k_{w2}) U_w(0, p_0)) \exp(((k_{o1} - k_{o2}) U_o(0, p_0)) \tag{19.6}$$

Assuming the magnitude $(k_{w1} - k_{w2})$ and $U_w\,(0, p_0)$ is small, and it is reasonable to take the first-order expansion. As $U_w\,(0, p_0)$ is the total column water or precipitable water W, we get

$$\frac{\Delta T_2}{\Delta T_1} \approx \frac{\varepsilon_2}{\varepsilon_1} (1 + KW + \text{const.}) \tag{19.7}$$

Namely, the surface emissivity and atmospheric total column water vapor cause the brightness temperature change and therefore, cause LST retrieval error.

19.3.2 Mathematical Description of the LST Algorithm

An analytic solution to Eq. 19.1 is not easy, because the integration of the terms requires good knowledge of the atmospheric profiles which is not available in real time. In addition, land surface emissivity is coupled with the surface temperature in the equation, so the number of unknowns is always larger than the number of equations and this is the so-called ill-posed problem, even multiple channels of information are available. In the past 35 years, many approaches, by using the two split-window (SW) channels (11.0 and 12.0 μm) to the solution, have been suggested (e.g., McMillin 1975; Walton et al. 1998) and widely used for producing the LST product (e.g., Prata 1993, 1994; Wan 1999; Caselles et al. 1997), as listed in Table 19.2.

Most split-window algorithms explicitly use land surface emissivity values, while Sun and Pinker (2003, 2004) and Sikorsky et al. (2002) proposed emissivity information indirectly incorporated through the use of different coefficient sets determined by different land surface types. The latter approach must be tolerant to within-class emissivity variability and assume the land cover maps can be updated frequently; however, most available land cover products can only be available annually from EOS/MODIS and NOAA/AVHRR or seasonally from NPOESS/VIIRS, meanwhile emissivity maps that accommodate within-class variability (Yu et al. 2005) can be available more frequently from MODIS product. We expect that other emissivity map developments will be significantly improved by the launch of GOES-R in 2014.

Since the operational GOES-LST retrieval will be from current GOES sensors, including GOES-12 and GOES-13, there will be no 12.0-μm channel. Therefore, split-window channels cannot be used to correct atmospheric effect. Due to the lack of split-window channels for the imager of GOES M (12)-Q series, Sun and Pinker (2004) proposed a dual-window algorithm by using the characteristics of the mid-infrared channel (3.9 μm) with less atmospheric (water vapor) absorption (Fig. 19.1), and one-channel (11 μm) plus water vapor correction algorithm.

19.3.2.1 GOES Split-Window Algorithm

For far-IR bands, terms R_d, R_s, and R_r in Eq. 19.1 are negligible. Therefore, only the first two terms on the right side are important. The first term represents the surface contribution term, and it is the gray-body radiance emitted by the Earth's surface. The second term is the atmospheric contribution term, referred to as path thermal radiance in Eq. 19.5, and is the vertically integrated effect of emission from every

Table 19.2 List of some split window LST algorithms

No.	Formula[a]	Reference
1.	$T_s = C + \left(A_1 + A_2\frac{1-\varepsilon}{\varepsilon} + A_3\frac{\Delta\varepsilon}{\varepsilon^2}\right)(T_{11}+T_{12}) + \left(A_4 + A_5\frac{1-\varepsilon}{\varepsilon} + A_6\frac{\Delta\varepsilon}{\varepsilon^2}\right)(T_{11}-T_{12}) + D(T_{11}-T_{12})(\sec\theta - 1)$	Wan and Dozier (1996), Becker and Li (1990)
2.	$T_s = C + A_1\frac{T_{11}}{\varepsilon} + A_2\frac{T_{12}}{\varepsilon} + A_3\frac{1-\varepsilon}{\varepsilon} + D(T_{11}-T_{12})(\sec\theta - 1)$	Prata and Platt (1991), modified by Caselles et al. (1997)
3.	$T_s = C + A_1T_{11} + A_2(T_{11}-T_{12}) + A_3(1-\varepsilon_{11}) + A_4\Delta\varepsilon + D(T_{11}-T_{12})(\sec\theta - 1)$	Coll and Valor (1997)
4.	$T_s = C + A_1T_{11} + A_2(T_{11}-T_{12}) + A_3\frac{1-\varepsilon}{\varepsilon} + A_4\frac{\Delta\varepsilon}{\varepsilon^2} + D(T_{11}-T_{12})(\sec\theta - 1)$	Vidal (1991)
5.	$T_s = C + A_1T_{11} + A_2(T_{11}-T_{12}) + A_3(T_{11}-T_{12})\varepsilon_{11} + A_4T_{12}\Delta\varepsilon + D(T_{11}-T_{12})(\sec\theta - 1)$	Price (1984)
6.	$T_s = C + A_1T_{11} + A_2(T_{11}-T_{12}) + A_3\varepsilon + D(T_{11}-T_{12})(\sec\theta - 1)$	Uliveri and Cannizzaro (1985)
7.	$T_s = C + A_1T_{11} + A_2(T_{11}-T_{12}) + A_3\varepsilon + A_4\frac{\Delta\varepsilon}{\varepsilon} + D(T_{11}-T_{12})(\sec\theta - 1)$	Sobrino et al. (1994)
8.	$T_s = C + A_1T_{11} + A_2(T_{11}-T_{12}) + A_3(1-\varepsilon) + A_4\Delta\varepsilon + D(T_{11}-T_{12})(\sec\theta - 1)$	Ulivieri et al. (1992)
9.	$T_s = C + A_1T_{11} + A_2(T_{11}-T_{12}) + A_3(T_{11}-T_{12})(T_{11}-T_{12}) + A_4(1-\varepsilon_{11}) + A_5\Delta\varepsilon + D(T_{11}-T_{12})(\sec\theta - 1)$	Sobrino et al. (1993)

Each algorithm is composed of two parts: the base split window algorithm and path length correction (the last term in each algorithm). The base split window algorithms are adapted from these published split window algorithms as referred in the references, while the path length term is particularly added for additional atmospheric correction

[a]Note: T_{11} and T_{12} represent the top-of-atmosphere brightness temperatures of GOES Imager channels 14 and 15, respectively; $\varepsilon = (\varepsilon_{11} + \varepsilon_{12})/2$ and $\Delta\varepsilon = (\varepsilon_{11} - \varepsilon_{12})$, where ε_{11} and ε_{12} are the spectral emissivity values of the land surface at GOES Imager channels 14 and 15, respectively; and θ is the satellite view zenith angle

atmospheric layer modulated by the transmittance of the air above that emitting layer:

$$L(\lambda,\mu) = \varepsilon_0(\lambda,\mu)B(\lambda,T_\mathrm{s})\tau_0(\lambda,\mu) + \int_{\tau_0}^{1} B\big(\lambda,T_\mathrm{p}\big)\mathrm{d}\tau(\lambda,\mu,p) \tag{19.8}$$

where T_p is the air temperature at vertical layer p and p is the pressure of the vertical emitting layer.

For a specific land surface type with surface emissivity close to unity, the radiance error introduced by the atmosphere ΔL can be represented as

$$\begin{aligned}\Delta L = B(\lambda,T_\mathrm{s}) - L(\lambda,\mu) &= B(\lambda,T_\mathrm{s}) - B(\lambda,T_\mathrm{s})\,\tau_0(\lambda,\mu) - \int_{\tau_0}^{1} B\big(\lambda,T_\mathrm{p}\big)\mathrm{d}\tau(\lambda,\mu,p)\\ &= \int_{\tau_0}^{1} B(\lambda,T_\mathrm{s})\mathrm{d}\tau(\lambda,\mu,p) - \int_{\tau_0}^{1} B\big(\lambda,T_\mathrm{p}\big)\mathrm{d}\tau(\lambda,\mu,p)\\ &= \int_{\tau_0}^{1} \left(B(\lambda,T_\mathrm{s}) - B\big(\lambda,T_\mathrm{p}\big)\right)\mathrm{d}\tau(\lambda,\mu,p)\end{aligned} \tag{19.9}$$

From the Planck function, we find

$$\Delta L = B(\lambda,T_\mathrm{s}) - L(\lambda,\mu) = B(\lambda,T_\mathrm{s}) - B(\lambda,T_\lambda) \approx \left.\frac{\partial B}{\partial T}\right|_{T_\mathrm{s}} (T_\mathrm{s} - T_\lambda) \tag{19.10}$$

where T_λ is brightness temperature at wavelength λ.

For an optically thin gas, the following approximations can be made:

$$\mathrm{d}\tau = \mathrm{d}\{\exp(-k_\lambda l)\} \approx \mathrm{d}(1 - k_\lambda l) = -k_\lambda \mathrm{d}l \tag{19.11a}$$

where k_λ is the absorption coefficient and l is the optical path length:

$$\mathrm{d}l = \rho \mathrm{d}z \approx \rho_0 \exp(-z/H)\mathrm{d}z \tag{19.11b}$$

ρ is the density of the absorption gas, ρ_0 is the density at 0 km, H is the atmospheric scale height, and z is the height. If we assume that the Planck function is adequately represented by a first-order Taylor series expansion in each window channel, then

$$B(\lambda,T_\mathrm{s}) - B\big(\lambda,T_\mathrm{p}\big) \approx \left.\frac{\partial B}{\partial T}\right|_{T_\mathrm{s}} \big(T_\mathrm{s} - T_\mathrm{p}\big) \tag{19.12}$$

Substituting Eqs. 19.10, 19.11a, 19.11b, and 19.12 into Eq. 19.9, we obtain

$$T_s - T_\lambda = K_\lambda \int_0^{l_0} (T_s - T_p) \mathrm{d}l \tag{19.13a}$$

Here, l_0 is the optical depth from the Earth's surface to top of the atmosphere:

$$l_0 = \int_0^{\infty} \rho \mathrm{d}z \approx \int_0^{\infty} \rho_0 \exp(-z/H) \mathrm{d}z \tag{19.13b}$$

If two close spectral channels are selected to give equal values of T_p, such as the split-window channels 11 and 12 μm, we will have two equations with different absorption coefficient k_λ to solve simultaneously:

$$\frac{T_s - T_{11}}{T_s - T_{12}} = \frac{k_{11}}{k_{12}} \text{ or } T_s - T_{11} = \left(\frac{k_{11}}{k_{12} - k_{11}}\right)(T_{11} - T_{12}) \tag{19.14}$$

Here, T_{11} and T_{12} are brightness temperature of 11- and 12-μm channel; k_{11} and k_{12} are the absorption coefficients of 11- and 12-μm channel. This equation is frequently used as a basis for split-window SST algorithms (McClain et al. 1985). In our case, Eq. 19.14 can be used for any surface type, land or water, as long as the surface emissivities in the split-window channels are close to unity.

Sun and Pinker (2003) introduced a split-window algorithm by using surface type information instead of traditional surface emissivity:

$$T_s(i) = a_0(i) + a_1(i)T_{11} + a_2(i)(T_{11} - T_{12}) + a_3(i)(T_{11} - T_{12})^2 + a_4(i)(\sec\theta - 1) \tag{19.15}$$

where i is the surface type index, θ is the satellite-viewing angle, T_{11} and T_{12} are the brightness temperatures at 10.8 and 12.0 mm channels, a_0–a_4 are coefficients, and T_s is the derived skin temperature.

19.3.2.2 Some Other Traditional Split-Window-Type LST Algorithms

For GOES 8-11, we can use split-window algorithms. Since several split-window LST algorithms have been developed in the past, we compared our algorithms with these split-window-type algorithms in our previous publications (Sun and Pinker 2004; Pinker et al. 2009). In Sect. 4.3 about simulation analysis, some comparison will be made for these split-window-type algorithms and their modified forms with additional path correction term.

19.3.2.3 Triple-Window LST Algorithm

Starting from the radiative transfer equation, the radiance measured by channel i of a satellite sensor can be written as

$$B_i(T_i) = \left[\varepsilon_i B_i(T_s) + \rho_i R_i^{\downarrow}\right] \tau_i + R_i^{\uparrow} \tag{19.16}$$

where B_i is the Planck function weighted for channel i; T_i is the brightness temperature measured at satellite level in the channel i; τ_i is the atmospheric transmittance for channel i; $R_i\downarrow$ is the hemispheric downward atmospheric radiance for the waveband of channel i; ρ_i is the channel bidirectional reflectivity of the surface; $\rho_i R_i^{\downarrow}$ is referred to term R_r in Eq. 19.2; and $R_i^{\uparrow}$ is the upward radiance emitted by the atmosphere in the waveband of channel i; it corresponds to the thermal path radiance term R_a in Eq. 19.2. Equation 19.16 is a simplification of Eq. 19.2, considering channel values instead of spectral values and accounting for part of the atmospheric downward radiation reflected by the surface. For simplicity, we assume Lambertian reflection $\rho_i = (1 - \varepsilon_i)$ and define brightness temperature at surface level T_i*:

$$B_i(T_i^*) = \varepsilon_i B_i(T_s) + (1 - \varepsilon_i) R_i^{\downarrow} \tag{19.17}$$

McMillin (1975) used the mean value theorem to define the mean radiative temperature of the atmosphere in the upward direction $T_a\uparrow$:

$$B_i\left(T_a{}^{\uparrow}\right) = \frac{R_i^{\uparrow}}{1 - \tau_i} \tag{19.18a}$$

We can introduce a similar mean radiative temperature of the atmosphere in the downward direction according to McMillin (1975) approach:

$$B_i\left(T_a{}^{\downarrow}\right) = \frac{R_i^{\downarrow}}{1 - \tau_i} \tag{19.18b}$$

By inserting Eqs. 19.17, 19.18a, and 19.18b into Eq. 19.16,

$$B_i(T_i) = \tau_i B_i(T_i^*) + (1 - \tau_i) B_i\left(T^{\uparrow}{}_a\right) \tag{19.19}$$

Linearizing the Planck function in (19.19) around T_i yields

$$\begin{aligned} \frac{\partial B}{\partial T}|_{T_i} L(T_i) = \tau_i \frac{\partial B}{\partial T}|_{T_i} (T_i^* - T_i + L(T_i)) \\ + (1 - \tau_i) \frac{\partial B}{\partial T}|_{T_i} \left(T_a{}^{\uparrow} - T_i + L(T_i)\right) \end{aligned} \tag{19.20a}$$

$$\text{with} \quad L(T_i) = B_i(T_i) / \frac{\partial B}{\partial T}|_{T_i} \tag{19.20b}$$

The Planck function can be well approximated using a simple power function (Price 1989):

$$B_i(T_i) \approx \alpha_i T^{n_i} \tag{19.21}$$

Parameters α_i and n_i are constants obtained by a least-square regression fitting. In order to have the best approximation of the Planck function, we divide the temperature range into two parts, (a) less than 285 K, and (b) more than 285 K. The parameter n_i is given in Table 19.3 for each case.

The power law approximation is very useful for analyses involving the Planck function, with this approximation:

$$L(T_i) = B_i(T_i) / \frac{\partial B}{\partial T}|_{T_i} \approx \frac{\alpha_i T_i^{n_i}}{\alpha_i n_i T_i^{n_i - 1}} = \frac{T_i}{n_i} \tag{19.22}$$

Inserting Eqs. 19.21 and 19.22 into Eqs. 19.20a and 19.20b, the atmospheric correction for brightness temperature can be written as

$$T_i^* - T_i = \frac{1 - \tau_i}{\tau_i} \left(T_i - T_a^{\uparrow} \right) \tag{19.23}$$

We linearize Planck function in (19.17) around T_i* and obtain the emissivity correction:

$$T_s - T_i^* = \frac{(1 - \varepsilon_i)}{\varepsilon_i} \left[\frac{T_i^*}{n_i} + \frac{(n_i - 1)}{n_i} (1 - \tau_i) T_i^* - (1 - \tau_i) T_a^{\downarrow} \right] \tag{19.24}$$

Inserting (19.23) into (19.24), we get

$$T_s = C_{1i} T_i - C_{2i} T_a^{\uparrow} - C_{3i} T_a^{\downarrow}$$

where

$$\begin{aligned} C_{1i} &= \frac{1}{\tau_i} \left[1 + \frac{(1 - \varepsilon_i)}{n_i \varepsilon_i} + \frac{(1 - \varepsilon_i)(1 - \tau_i)(n_i - 1)}{n_i \varepsilon_i} \right] \\ C_{2i} &= \frac{(1 - \tau_i)}{\tau_i} \left[1 + \frac{(1 - \varepsilon_i)}{n_i \varepsilon_i} + \frac{(1 - \varepsilon_i)(1 - \tau_i)(n_i - 1)}{n_i \varepsilon_i} \right] \\ C_{3i} &= \frac{(1 - \varepsilon_i)}{\varepsilon_i} (1 - \tau_i) \end{aligned} \tag{19.25}$$

Table 19.3 Parameter n_i for approximate Planck function (power function) for GOES window channels

Channel (μm)	n_i ($T_i < 285$ K)	n_i ($T_i > 285$ K)
3.9	13.88	12.90
10.8	4.99	4.57
12.0	4.51	4.15

Table 19.4 Atmospheric transmittance for standard atmosphere profiles

Atmosphere	Precipitable water (g/cm-2)	$\tau_{10.8}$	τ_{12}
US standard	1.13	0.8552	0.8014
Tropical	3.32	0.5574	0.4159
Midlatitude summer	2.36	0.6915	0.5786
Midlatitude winter	0.69	0.8993	0.8646
Subarctic summer	1.65	0.7847	0.7011
Subarctic winter	0.33	0.9336	0.9147

Suppose that surface emissivity and the atmospheric transmittance are known, and n_i is a constant that depends on the spectral channel. Now we have the three unknown parameters: T_s, $T_a{}^{\uparrow}$, and $T_a{}^{\downarrow}$, and we can use the information of the three channels to obtain the surface temperature. In order to take advantage of all the available information, we choose three channels to solve the equations. Assuming the channel indexes are i_1, i_2, and i_3, we get

$$\begin{aligned}
T_s &= C_{1i_1}T_{i_1} - C_{2i_1}T_a{}^{\uparrow} - C_{3i_1}T_a{}^{\downarrow} \\
T_s &= C_{1i_2}T_{i_2} - C_{2i_2}T_a{}^{\uparrow} - C_{3i_2}T_a{}^{\downarrow} \\
T_s &= C_{1i_3}T_{i_3} - C_{2i_3}T_a{}^{\uparrow} - C_{3i_3}T_a{}^{\downarrow} \\
T_a{}^{\uparrow} &= \frac{(C_{3i_3} - C_{3i_2})(C_{1i_3}T_{i_3} - C_{1i_2}T_{i_2}) - (C_{3i_2} - C_{3i_1})(C_{1i_2}T_{i_2} - C_{1i_1}T_{i_1})}{(C_{2i_3} - C_{2i_2})(C_{3i_3} - C_{3i_2}) - (C_{3i_2} - C_{3i_1})(C_{2i_2} - C_{2i_1})} \\
T_s &= C_{1i}T_i - C_{2i}T_a{}^{\uparrow} - C_{3i}T_a{}^{\downarrow}
\end{aligned} \tag{19.26}$$

For standard MODTRAN atmospheric profiles, we can calculate their atmospheric transmittance, as shown in Table 19.4.

In the event that the atmospheric transmittance is not available, we can use regression methods to find the appropriate coefficients for each term in Eqs. 19.25 and 19.26.

T_s can then be written as

$$\begin{aligned}
T_s &= a_0 + a_1T_{i_1} + a_2T_{i_2} + a_3T_{i_3} + a_4\frac{(1-\varepsilon_{i_1})}{\varepsilon_{i_1}}T_{i_1} + a_5\frac{(1-\varepsilon_{i_2})}{\varepsilon_{i_2}}T_{i_2} + a_6\frac{(1-\varepsilon_{i_3})}{\varepsilon_{i_3}}T_{i_3} \\
C_{ji} &= a_0(j) + a_1(j)\frac{(1-\varepsilon_i)}{\varepsilon_i}, \quad j = i_1,\ i_2,\ i_3
\end{aligned} \tag{19.27}$$

19.3.2.4 LST Algorithms for GOES M (12)-Q Series

In the absence of the 12-μm channel for the GOES M (12)-Q series, we proposed two candidate approaches:

- Dual-window algorithm combining 3.9- and 11.0-μm channels
- One-channel algorithm using total precipitable water (TPW)

Dual-Window Algorithm

The path thermal radiance in radiative transfer Eq. 19.2 is the vertically integrated effect of emission from every atmospheric layer modulated by the transmittance of the air above that emitting layer. It can be represented in spectral form as

$$R_{\mathrm{a}}(\lambda,\mu) = \int_{\tau_0}^{1} B\left(\lambda, T_{\mathrm{p}}\right)\mathrm{d}\tau(\lambda,\mu,p) \tag{19.28}$$

where B, λ, and μ are as given in Eq. 19.3, T_{p} is the air temperature (K) at vertical layer p, p is the pressure of the vertical emitting layer (mb). Therefore, for the thermal infrared channel like 11.0 μm, the outgoing infrared spectral radiance at the top of atmosphere can be represented in spectral form as

$$R(\lambda,\,\mu) = \varepsilon_0(\lambda,\,\mu)B(\lambda,\,T_{\mathrm{s}})\,\tau_0(\lambda,\mu) + \int_{\tau_0}^{1} B\left(\lambda, T_{\mathrm{p}}\right)\mathrm{d}\tau(\lambda,\mu,p) \tag{19.29}$$

However, for the middle-infrared (MIR) 3.9-μm channel, during nighttime, the MIR radiance can be represented as the one in Eq. 19.29. But during daytime, the solar radiation reflected by the Earth's surface needs to be accounted for, and therefore, the outgoing infrared spectral radiance at the top of atmosphere is represented as

$$\begin{aligned} R(\lambda,\,\mu) = {} & \varepsilon_0(\lambda,\,\mu)B(\lambda,\,T_{\mathrm{s}})\,\tau_0(\lambda,\mu) + \int_{\tau_0}^{1} B(\lambda,T_{\mathrm{p}})\mathrm{d}\tau(\lambda,\mu,p) \\ & + E_{solar}\frac{{d_0}^2}{d^2}\cos\theta_{\mathrm{s}}\,\rho_{\mathrm{b}}(\theta_{\mathrm{s}},\theta)\tau_0(\lambda,\mu) \end{aligned} \tag{19.30}$$

where d_0 is the Earth-sun distance, E_{solar} is the solar constant, d is the Earth-sun distance, θ_{s} is solar zenith angle, and ρ_{b} is the bidirectional reflectivity of the surface. During nighttime, the outgoing infrared spectral radiance at the top of atmosphere in both of the 11- and 3.9-μm channels can be represented by Eq. 19.28.

For a specific land surface type with surface emissivity close to unity, based on Eq. 19.28, the radiance error introduced by the atmosphere, ΔR, can be represented as

$$\begin{aligned}\Delta R &= B(\lambda, T_s) - R(\lambda, \mu) = B(\lambda, T_s) - B(\lambda, T_s)\,\tau_0(\lambda, \mu) - \int_{\tau_0}^{1} B\big(\lambda, T_p\big)\mathrm{d}\tau(\lambda, \mu, p) \\ &= \int_{\tau_0}^{1} B(\lambda, T_s)\mathrm{d}\tau(\lambda, \mu, p) - \int_{\tau_0}^{1} B\big(\lambda, T_p\big)\mathrm{d}\tau(\lambda, \mu, p) \\ &= \int_{\tau_0}^{1} \big(B(\lambda, T_s) - B\big(\lambda, T_p\big)\big)\mathrm{d}\tau(\lambda, \mu, p) \end{aligned} \tag{19.31}$$

In the atmospheric window regions, the absorption is weak, so that

$$\tau = e^{-k_\lambda u} \approx 1 - k_\lambda u \tag{19.32}$$

where k_λ is the absorption coefficients at wavelength λ and u is absorption gas optical path (mainly water vapor in window channel). Under this assumption, Eq. 19.31 can be rewritten as

$$u_s = \int_0^{\infty} \rho\,\mathrm{d}s = \int_0^{\infty} \rho\,\sec\theta\,\mathrm{d}z \tag{19.33}$$

u_s is the total optical depth from the surface to the top of atmosphere. From the Planck function, we get

$$\Delta R = B(\lambda, T_s) - R(\lambda, \mu) = B(\lambda, T_s) - B(\lambda, T_\lambda) \approx \left.\frac{\partial B}{\partial T}\right|_{T_s} (T_s - T_\lambda) \tag{19.34}$$

From (19.33) and (19.34), it follows that

$$T_s - T_\lambda = k_\lambda \int_0^{u_s} \big(T_s - T_p\big)\mathrm{d}l \tag{19.35}$$

Using the two window channels 11.0 and 3.9 μm (night), two such equations with different absorption coefficient k_λ can be solved simultaneously to yield

$$T_s - T_{11} = \left(\frac{k_{11}}{k_{3.9} - k_{11}}\right)(T_{11} - T_{3.9}) \tag{19.36}$$

Equation 19.35 is derived based on the assumption that surface emissivity is close to unity, and therefore it can be applied to any surface type, land as well as water, as long as the assumption is valid. However, the surface emissivities for some land surface types are not close to unity, in particular, in the 3.9-μm channel. As shown in Fig. 19.4, the relationship between the deficit of surface skin temperature and brightness temperature at 11 μm ($T_s - T_{11}$) and brightness temperature difference ($T_{11} - T_{3.9}$) is unlinear, so we propose to add an unlinear term $(T_{11} - T_{3.9})^2$.

Moreover, we need to add some emissivity correction term. If the satellite-viewing correction term ($\sec\theta - 1$) proposed by McClain et al. (1985) is added to the LST retrieval equation, during nighttime, we can get

$$LST = a_0 + a_1\, T_{11} + a_2(T_{11} - T_{3.9}) + a_3(T_{11} - T_{3.9})^2 + a_4(1 - \varepsilon) + a_5\,(\sec\theta - 1) \tag{19.37}$$

However, during daytime, as shown in Fig. 19.5, the brightness temperature deficits ($T_{11} - T_{3.9}$) have large negative values. During daytime, the brightness temperature in the middle-infrared channel contains the solar radiation reflected by the Earth's surface, which makes $T_{3.9}$ increase. To reduce the solar signal contamination in the brightness temperature, the solar contribution should be subtracted from the observed middle-infrared signal:

$$T'_{3.9} = T_{3.9} - f^{-1}\left(E_{solar}\frac{{d_0}^2}{d^2}\cos\theta_s\,\rho_b(\theta_s,\theta)\tau_0(\lambda,\mu)\right) \tag{19.38}$$

As the solar constant E solar and sun-Earth distance d are constant, for a specific surface type, the bidirectional effect depends on the solar zenith angle θ_s and the satellite-viewing angle θ. From Eq. 19.32, the surface transmittance τ_0 can be approximated as

$$\tau_0(\lambda,\mu) \approx 1 - k_\lambda u_s \tag{19.39}$$

u_s is the atmospheric total optical path,

$$u_s = \int_0^\infty \rho\,\mathrm{d}s = \int_0^\infty \rho\,\sec\theta\,\mathrm{d}z \tag{19.40}$$

ρ is density of the atmospheric absorption gas, s is the geometry path, and z is the height. Therefore, the solar correction term in Eq. 19.38 is a function of atmospheric total optical path us, satellite zenith angle θ, and solar zenith angle θs, given as

$$\begin{aligned} T'_{3.9} &= T_{3.9} - f^{-1}\left(E_{\text{solar}}\frac{{d_0}^2}{d^2}\cos\theta_s\,\rho_b(\theta_s,\theta)\,\tau_0(\lambda,\mu)\right) \\ &\approx T_{3.9} - (c_0 + c_1\,\rho_b(\theta_s,\theta)u_s\cos\theta_s) \end{aligned} \tag{19.41}$$

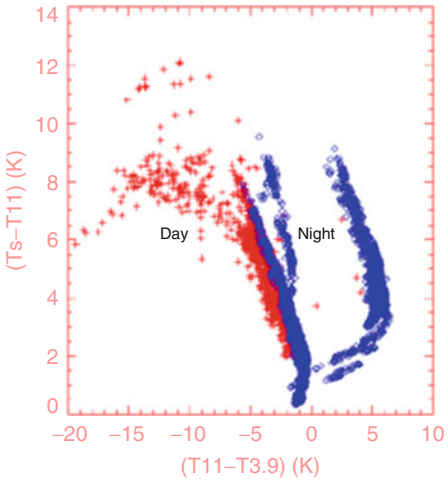

Fig. 19.4 $(T_s - T_{11})$ vs. $(T_{11} - T_{3.9})$ distribution, where T_{11} and $T_{3.9}$ are the GOES brightness temperature at channels 4 and 2 and T_s is the skin temperature

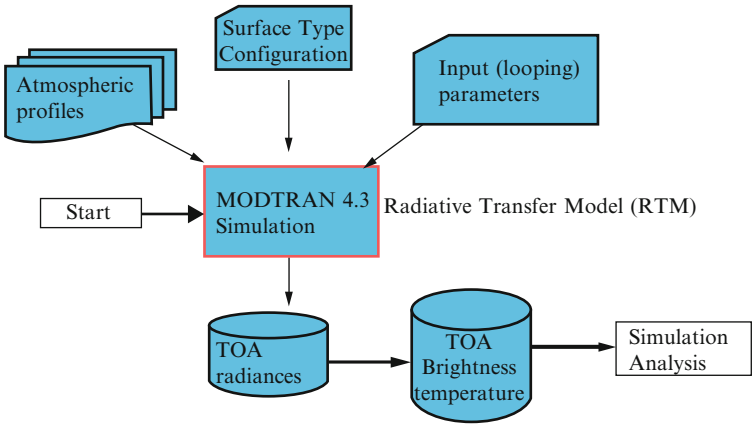

Fig. 19.5 Radiative transfer simulation procedure

The coefficients in (19.41) may depend on surface type or emissivity, since the surface bidirectional reflectivity is related to it. In the window channels, the major absorbing gas is the water vapor, but neglect of absorption from CH_4 and N_2O in the GOES 3.9-μm channel can contribute to additional errors. Estimating atmospheric CH_4 and N_2O amounts is difficult. To allow for the effect of all absorbers in this channel, we propose to use the brightness temperature $T_{3.9}$ to replace $\rho_b(\theta_s, \theta)$ us in (19.41), by modifying the coefficients in this equation as follows:

$$T'_{3.9} \approx T_{3.9} - \left(c_0'(l) + c'_1(l) T_{3.9} \cos\theta_s\right) \tag{19.42}$$

During daytime, $T_{3.9}$ in Eq. 19.37 should be replaced by $T'_{3.9}$, therefore, we have

$$LST = a_0 + a_1 T_{11} + a_2(T_{11} - T_{3.9}) + a_3(T_{11} - T_{3.9})^2 + a_4\ T_{3.9}\ \cos\theta_s + a_5(1-\varepsilon) + a_6(\sec\theta - 1) \tag{19.43}$$

One-Channel Algorithm

In the atmospheric window channels, the water vapor absorption is weak. Therefore,

$$\tau_i = \exp(-k_i w \sec\theta) \approx 1 - k_i w \sec\theta \tag{19.44}$$

where i denotes the channel index, k_i is the absorption coefficient at channel i, θ is the satellite viewing angle, and w is the column water vapor. Hence,

$$\mathrm{d}\tau_i \approx -k_i \sec\theta\, \mathrm{d}w \tag{19.45}$$

The measured radiance in the thermal window region can be expressed with respect to channel value from the radiative transfer equation (RTE) as

$$\begin{aligned} R_i &= \varepsilon_i B_i(T_s)\tau_i + \int_0^{\tau} B_i(T_p)\mathrm{d}\tau \\ &\approx \varepsilon_i B_i(T_s)(1 - k_i W \sec\theta) + k_i \sec\theta \int_0^{W} B_i(T_p)\mathrm{d}w \end{aligned} \tag{19.46}$$

where B_i is the Planck function weighted for channel i, T_i is the brightness temperature (K), measured at the satellite level in channel i, T_s is the surface skin temperature (K), ε_i and τ_i are the surface emissivity and atmospheric transmittance in channel i, T_p is the air temperature (K) at vertical layer p, p is the pressure of the vertical emitting layer (mb), and W represents the total precipitable water (TPW) (cm). Equation 19.46 is a simplification of Eq. 19.2, considering channel values instead of spectral values. Defining an atmospheric mean Planck radiance

$$B_i(T_a) = \frac{\int_0^{W} B(T_p)\mathrm{d}w}{\int_0^{W} \mathrm{d}w} \tag{19.47}$$

T_a is the atmospheric mean temperature. Inserting Eq. 19.47 into Eq. 19.46 will yield

$$R_i \approx \varepsilon_i B_i(T_s)(1 - k_i W \sec\theta) + k_i \sec\theta\, W\, B_i(T_a) \tag{19.48}$$

The Planck function can be expanded into a Taylor series about the brightness temperature T_i in the form of

$$\begin{aligned} R_i = B_i(T_i) &= \frac{DB}{DT}|_{T_i} \frac{B(T_{ii})}{\frac{DB}{DT}|_{T_i}} = \frac{DB}{DT}|_{T_i} L(T_i) \\ B_i(T_s) &\approx B_i(T_i) + \frac{DB}{DT}|_{T_i}(T_s - T) = \frac{DB}{DT}|_{T_i}(T_s - T_i + L(T_i)) \\ B_i(T_a) &\approx B_i(T_i) + \frac{DB}{DT}|_{T_i}(T_a - T_i) = \frac{DB}{DT}|_{T_i}(T_a - T_i + L(T_i)) \end{aligned} \tag{19.49}$$

Inserting Eq. 19.49 into Eq. 19.48 will linearize the RTE with respect to temperature:

$$L(T_i) \approx \varepsilon_i(1 - k_i w \sec\theta)(T_s - T_i + L(T_i)) + k_i w \sec\theta(T_a - T_i + L(T_i)) \tag{19.50}$$

Several approximations have been proposed for $L\,(T_i)$. Sun and Pinker (2003) use

$$L(T_i) \approx T_i / n_i \tag{19.51}$$

By inserting Eq. 19.51 into Eq. 19.50,

$$(C_{i1} T_i - \varepsilon_i T_s) = (T_a - \varepsilon_i T_s - C_{i2} T_i)\, k_i W \sec\theta \tag{19.52a}$$

where

$$C_{i1} = \frac{1 + (n_i - 1)\varepsilon_i}{n_i},\ C_{i2} = \frac{(n_i - 1)(1 - \varepsilon_i)}{n_i} \tag{19.52b}$$

Let i represent the 11.0-μm channel. For most land surfaces and the ocean, the emissivity at 11.0 μm is essentially unity.

In order to reduce the number of unknown variables, we assume that the atmospheric mean temperature T_a is proportional to the surface temperature T_s:

$$T_a \approx a_w T_s \tag{19.53}$$

It needs to be stated that assumption (19.53) may introduce errors if the surface emissivity at 11.0-μm channel is not close to unity. A solution for T_s can be obtained as follows:

$$T_s \approx \frac{T_i}{[(a_w - 1)k_i W \sec\theta + 1]} = \frac{T_{11}}{cW \sec\theta + 1} \tag{19.54}$$

If we adopt emissivity correction to this equation, then

$$LST = c_1 + c_2 T_{11} + c_3 W \sec\theta + c_4 (1 - \varepsilon_{11}) \tag{19.55}$$

19.4 Forward Simulations and Regression Coefficients

19.4.1 Forward Simulations

In order to derive regression coefficients in our algorithms and test and compare algorithm accuracy, forward simulations using radiative transfer model, such as the MODerate-resolution atmospheric TRANsmission (MODTRAN), are performed to generate a comprehensive simulation dataset.

The MODTRAN atmospheric radiative transfer model (Berk et al. 2000) has been widely used in satellite remote sensing studies for about three decades. It is a moderate spectral resolution model, up to cm-1 in frequency. The radiative transfer simulation procedure is illustrated in Fig. 19.5.

In order to account for the wide range of different atmospheric and surface conditions, a large number of simulations for each season need to be performed with variations in:

- Geometry of the problem (solar zenith angle, viewing, and azimuth angles).
- Atmospheric conditions (profiles of ozone, water vapor, aerosols).
- Surface conditions (spectral characteristics of the surface).
- Characteristics of the instrument (spectral response of the satellite sensors); the GOES spectral response functions can be obtained from the NOAA/NESDIS (http://www.oso.noaa.gov/goes/goes-calibration/goes-imager-srfs.htm).

To make the simulations applicable to all possible conditions, the atmospheric (height, temperature, and relative humidity) profiles with the matched surface height, pressure, temperature, and relative humidity from the Global NCEP Reanalysis (NRA) climatology (long-term mean) are used as the input.

In order to represent the variability in solar geometry, the solar zenith angel (SZA) are calculated according to the latitude, longitude, Julian day, GMT time; thus, the values at global coverage may vary from 0° to 180°.

To consider the effects of satellite zenith angles, simulations were performed for five zenith angle bins as satellite viewing zenith angle (VZA: 0, 2, 4, 6, 8), which is equal to satellite zenith angle (SZA: 0, 12.8, 26.38, 41.75, 62.44).

In order to make the GOES forward simulations applicable to different sensors with different spectral response functions (SRF), we performed simulations to a wide spectral range from 3 to 14 μm with 10 cm-1 resolution. Therefore, the input surface reflectance/emissivity was not for a specific channel, but was for full spectra. We used

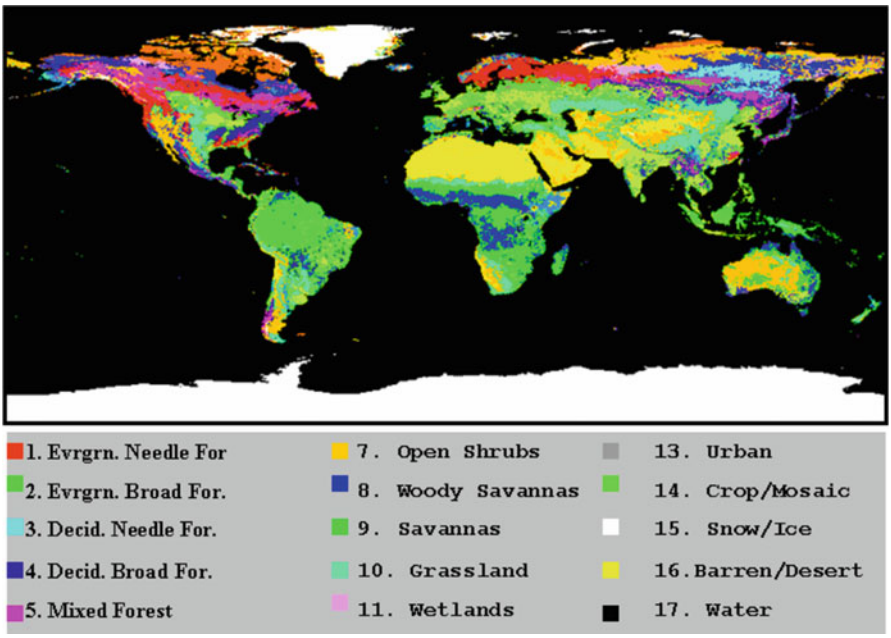

Fig. 19.6 The 18 IGBP surface types used to match the full spectra of surface reflectance for forward GOES simulations

spectral IR emissivity with full spectra for IGBP types, including the 17 MODIS IGBP types plus one surface type (Tundra). The total 18 IGBP types are shown in Fig. 19.6.

The full spectra from 0.2 and 15 um at high spectral resolution (0.02 um) for these 18 IGBP surface types were modified and immigrated from the latest MODTRAN and MOSART emissivity database.

We have completed this simulation database for testing and evaluation of LST algorithms. A total of 144 (cols) × 73 (rows) × 5 (satellite zenith angles) × 4 (seasons) simulation datasets were generated from the simulation process. The simulated datasets cover a wide range of spectrum from 3 to 14 μm, with 10 cm-1 spectral resolution which can be used to simulate satellite sensor received radiances in different infrared channels.

The narrowband outgoing radiances at the TOA are obtained by convoluting the spectral radiances with the response function of the specific instrument.

$$I(\mu_0, \mu, \varphi) = \int_{\lambda_1}^{\lambda_2} L(\lambda) I_\lambda(\mu_0, \mu, \varphi) \mathrm{d}\lambda \tag{19.56}$$

The radiance is then converted to reflectance. We first determined the mean channel radiance by integrating over the sensor spectral response function (SRF). For example, the current GOES-13 spectral response functions from NOAA/NESDIS

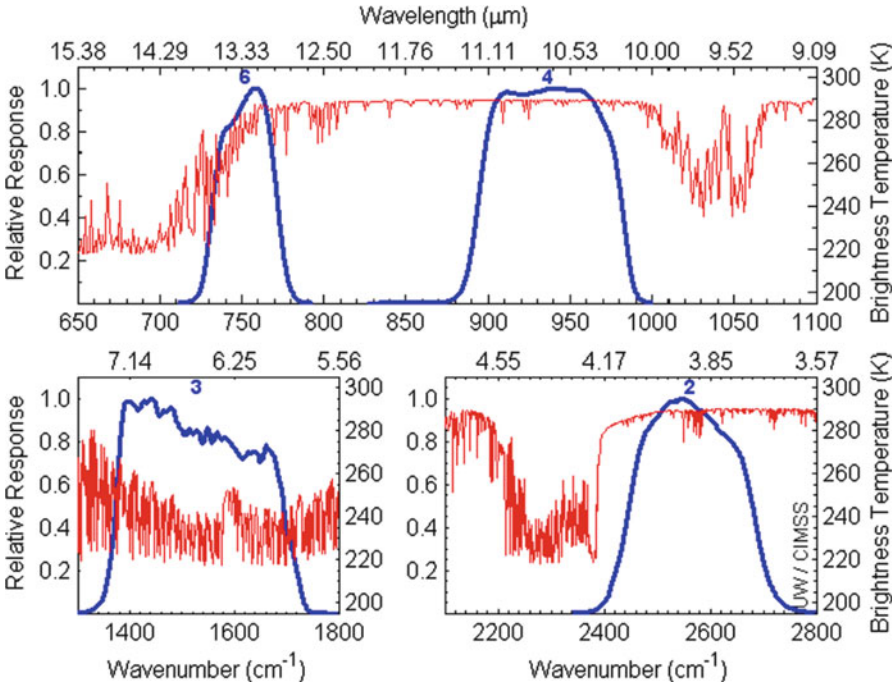

Fig. 19.7 The four GOES-13 imager infrared band spectral response functions superimposed over the calculated high-res Earth-emitted US Standard Atmosphere spectrum

(http://www.oso.noaa.gov/goes/goes-calibration/goes-imager-srfs.htm) are shown in Fig. 19.7. The channel radiances were then converted into corresponding brightness temperatures.

Absorption due to carbon dioxide (CO_2), water vapor (H_2O), and other gases are evident in the high-spectral resolution Earth-emitted spectrum.

19.4.2 Coefficients Derivation

Upon simulating the top-of-atmosphere radiances, we then conducted regression analyses and coefficients derivation for the algorithm development. The regression procedure and coefficients derivation process is illustrated in Fig. 19.8.

We first perform convolution to calculate the mean channel radiance by integrating over the sensor spectral response function (SRF). The channel radiances are then converted into corresponding brightness temperatures using the Planck function.

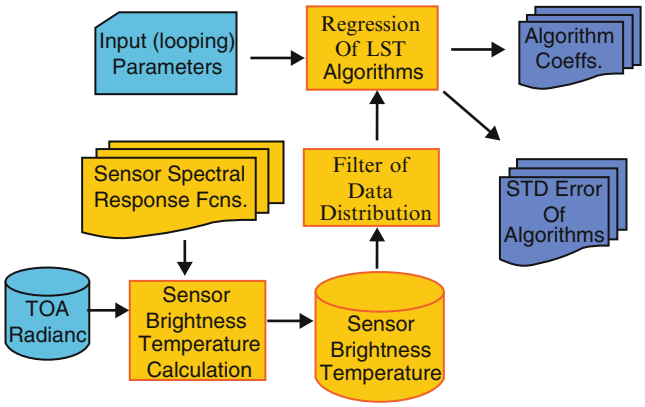

Fig. 19.8 Procedure of the algorithm regression analyses

19.4.3 Simulation Analyses

One season (summer) has been tested for nine previously published split-window-type algorithms and their modified (with zenith angle correction term) forms, totally 18 SW algorithms and two proposed algorithms for GOES M (12)-Q.

For each of the tested algorithms, we calculated the bias and standard deviation of the regressions. Due to the high water vapor amount during summer, the LST retrieval errors are usually larger than in other seasons. As shown in Fig. 19.9, it is found that the largest errors always appear at warm surface temperature above 280 K, and viewing zenith angle larger than 4° or satellite zenith angle greater than 41.75°, and the following algorithms gave better performance than other split-window algorithms:

The modified Becker and Li (1990) algorithm, which was a local split-window algorithm, and later modified by Wan and Dozier (1996) to make the coefficients varying with different conditions as the generalized split-window algorithm. The maximum standard deviation is only 0.75 K for this algorithm.

The modified Vidal 1991 algorithm (Vidal 1991; Yu et al. 2008). The maximum standard deviation is less than 1.0 K for this algorithm.

The modified Sobrino 1993 algorithm (Sobrino et al. 1993; Yu et al. 2008). The maximum standard deviation is only 0.75 K for this algorithm.

The modified Sobrino 1994 algorithm (Sobrino 1994; Yu et al. 2008). The maximum standard deviation is less than 1.0 K for this algorithm.

Meanwhile, it is found that the modified Sobrino et al. (1993) algorithm with nonlinear term gave better performance than the modified Sobrino (1994) algorithm without nonlinear term.

Nevertheless, Yu et al. (2008) found that the modified Ulivieri-1985 algorithm showed the least sensitivity to the emissivity variation, so they suggest this algorithm as the baseline GOES-R LST algorithm (Yu et al. 2010).

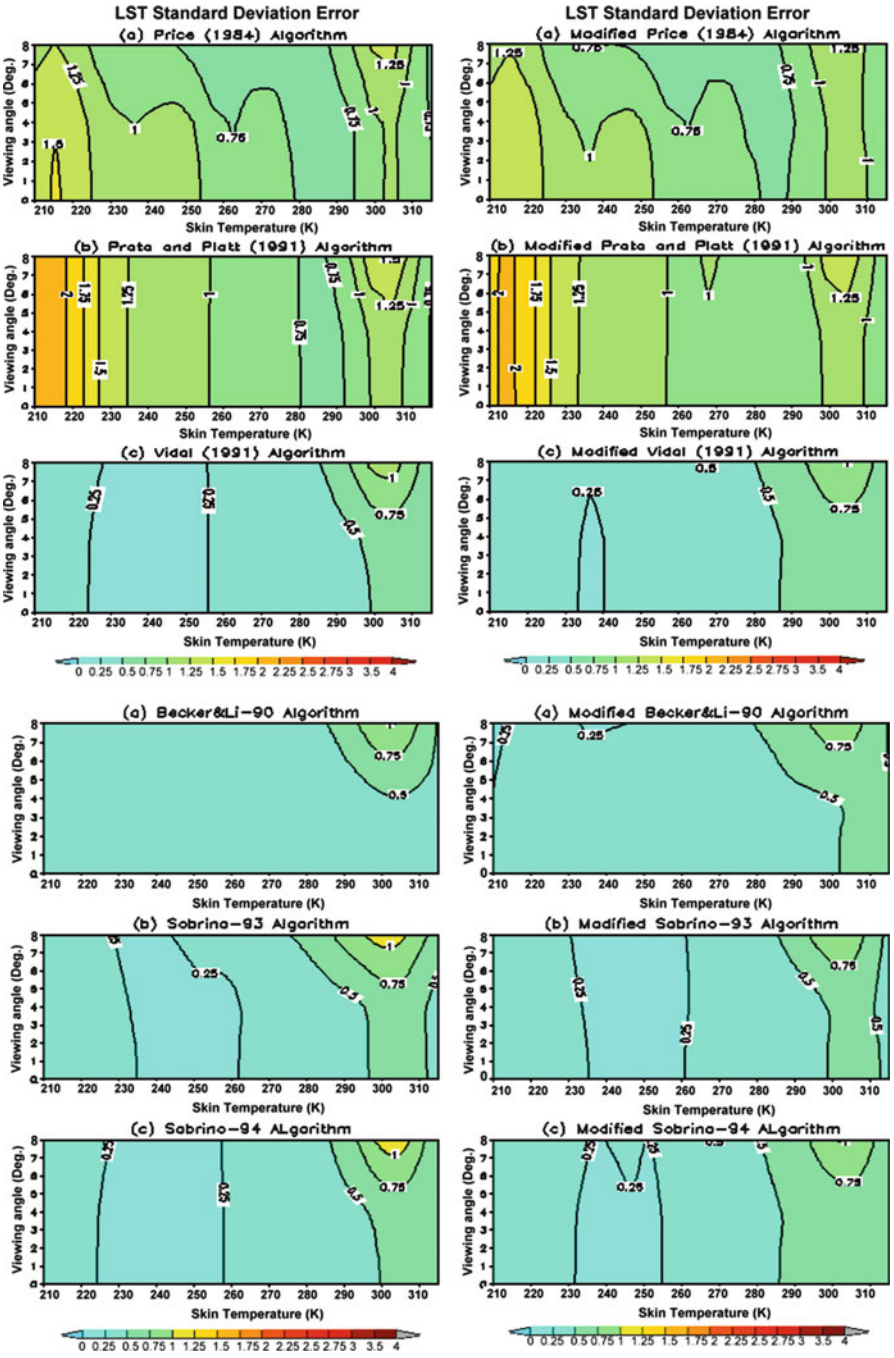

Fig. 19.9 The standard deviation errors of LST retrieval from the forward GOES simulations for the nine inherited SW algorithms and their modified forms

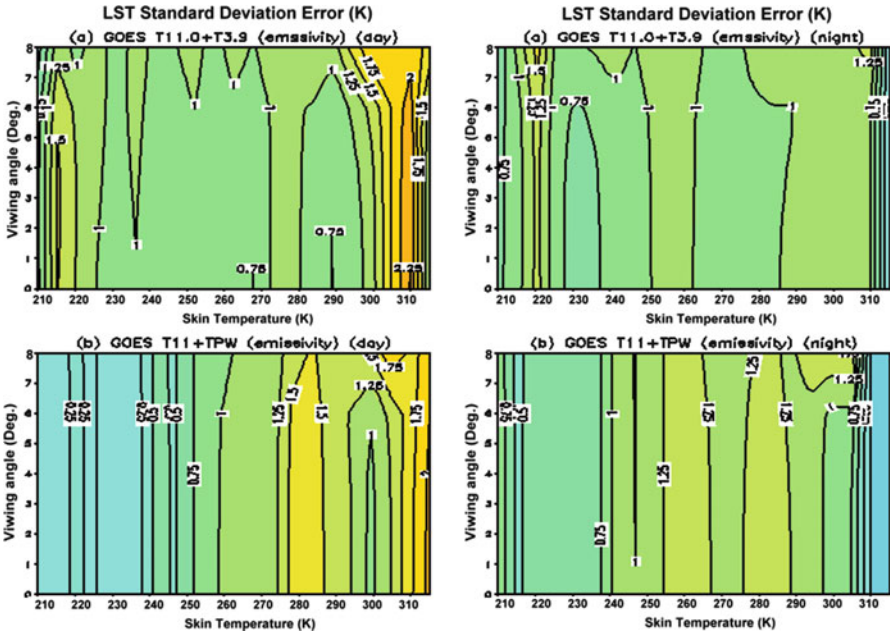

Fig. 19.10 The standard deviation errors of LST retrieval from the GOES-13 simulations for the two proposed GOES M (12)-Q algorithms for daytime (*left*) and nighttime (*right*)

To have a closer look at error distributions, we produced errors vs. viewing angles and skin temperature distributions of the regression fits for the two proposed GOES M (12)-Q algorithms in Figs. 19.10, 19.11, 19.12, and 19.13 for daytime and nighttime results, respectively. Figure 19.9 shows the standard deviation error is usually larger during daytime than those during nighttime. Compared to split-window-type algorithms as shown in Fig. 19.9, we can see both dual-window (3.9 + 11 μm) algorithm and one-channel ($T_{11} + T_{PW}$) algorithms show worse performance than the split-window-type algorithms (Fig. 19.9). Meanwhile, Fig. 19.10 shows that the bias errors from dual-window algorithm are smaller than those from one-channel algorithm. If we stratify LST retrieval according to water vapor intervals of 2.0 g/cm^2, then both standard deviation and bias errors show improvements than those without water vapor stratification. But one-channel algorithm still shows worse performance than dual-window algorithm. Both dual-window and one-channel algorithms still show worse performance than split-window-type algorithms.

Compared to the daytime algorithm performance, the standard deviation and bias errors of the nighttime are usually better than that during daytime for each algorithm. This is because there is no or less solar contamination and less water vapor during nighttime.

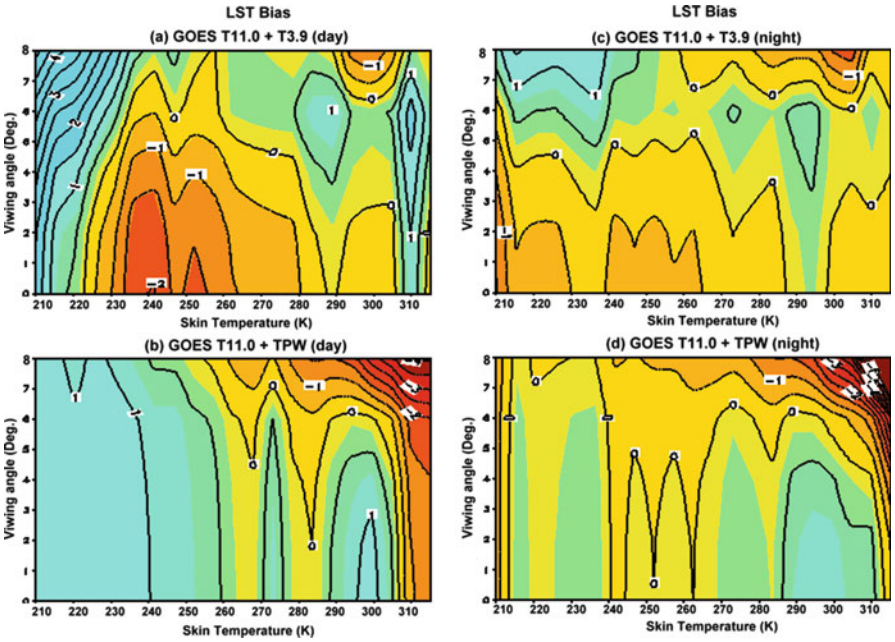

Fig. 19.11 Bias errors (*K*) of the regression analysis for daytime (*left*) and nighttime (*right*)

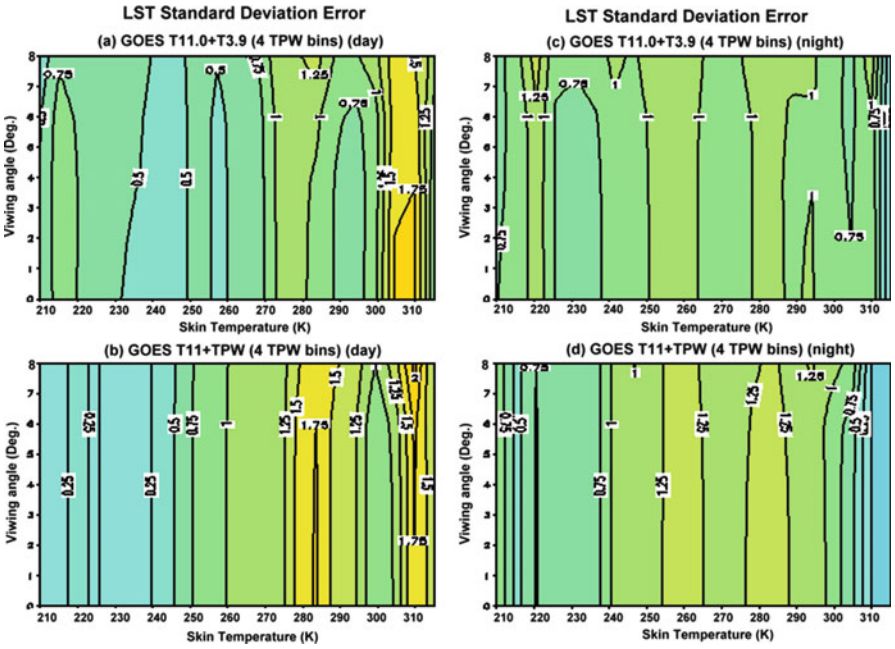

Fig. 19.12 Standard deviation (STD) with water vapor bins are given for daytime (*left*) and nighttime (*right*)

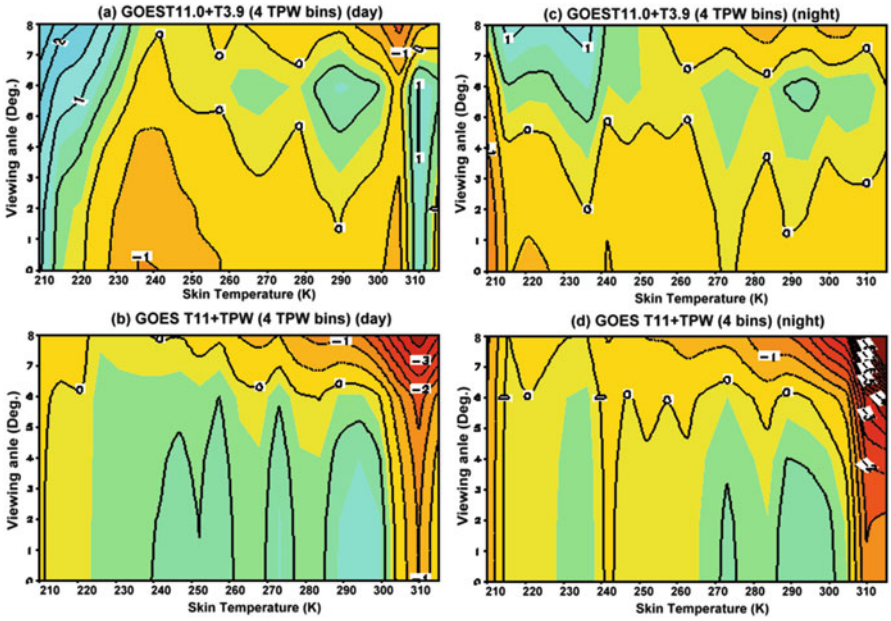

Fig. 19.13 Bias errors of the regression analysis with water vapor bins are given for daytime (*left*) and nighttime (*right*)

19.5 Tests and Applications with Real GOES Observations

19.5.1 Diurnal Temperature Range Derivation and Studies

Diurnal temperature range (DTR) is an important index of climate change (Karl et al. 1984) and is susceptible to urban effects (IPCC 2001). As stressed by Braganza et al. (2004), mean surface temperature alone is not as useful an indicator of climate change as the change in daily maximum and minimum temperatures. Trends in mean surface temperature are due to changes in either maximum or minimum temperature, or relative changes in both. The recently reported surface warming over land is associated with relatively larger increase in daily minimum temperature rather than in maximum temperature (Karl et al. 1993; Easterling et al. 1996). Most information on DTR came from station observations of surface air temperature (SAT) or from numerical model simulations. Station observations are sparse, unevenly distributed, and suffer from differences in elevation, time of observation, and nonstandard sitting (Peterson 2003). The use of satellite-based estimates of DTR can provide consistent information over large areas (Gallo and Owen 1999). The high temporal resolution of geostationary satellites like GOES

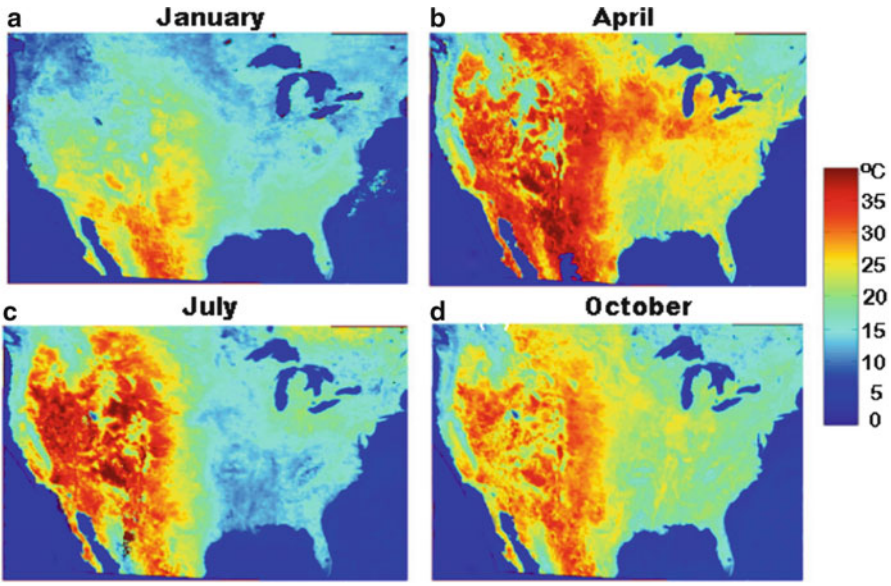

Fig. 19.14 Spatial distribution of DTR derived from the GOES-8 observations for different months as averaged from 1996 to 2000 (**a**) January, (**b**) April, (**c**) July, and (**d**) October

make them very attractive for derivation of DTR. Recently, Sun et al. (2007) applied the split-window algorithm developed by Sun and Pinker in 2003 to GOES-8 observations. For the first time, a satellite view of continuous spatial distribution of DTR over the continental United States was shown (Fig. 19.14). The 5-year average DTRs for the four mid-seasons show geographical differences, with western and central USA being systematically higher than those of the eastern USA or the northwestern coast (Fig. 19.14). Over the western USA, DTR is larger in spring and summer than fall and winter. Over the eastern part, DTR is larger in spring and fall than in summer and winter (dividing line between west and east is about 100° W). As shown in Fig. 19.15, which illustrates the 5-year average meridional mean DTR in July for the following selected LC/LU types: cropland, forest, grassland, and urban. There exists distinct difference in DTR between the west and east for each surface type, the DTRs being much larger over the west than over the east. In general, the DTR of urban area is usually smaller than those of other surface types.

A remarkable resemblance between high vegetation (Fig. 19.16) and low DTR can be seen for all four mid-season months. Evapotranspiration from vegetation contributes significantly to the decrease in DTR during summer in the eastern United States (Durre and Wallace 2001). Moreover, the smaller DTR areas over the eastern United States are found to have higher sulfate aerosol emissions than the western USA (Chin et al. 2000). Sulfate aerosols scatter solar radiation back to space and tend to cool the surface during daytime and may result in a decreased DTR (Stone and Weaver 2003).

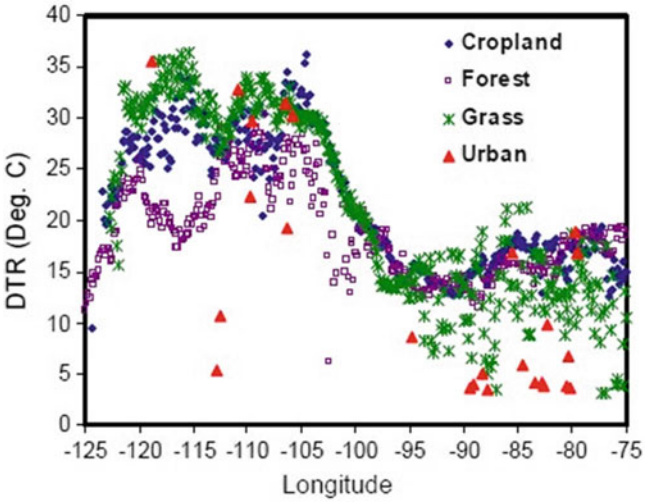

Fig. 19.15 Meridional mean DTR derived from GOES-8 for cropland, forests, grassland, and urban surfaces for a 5-year average July

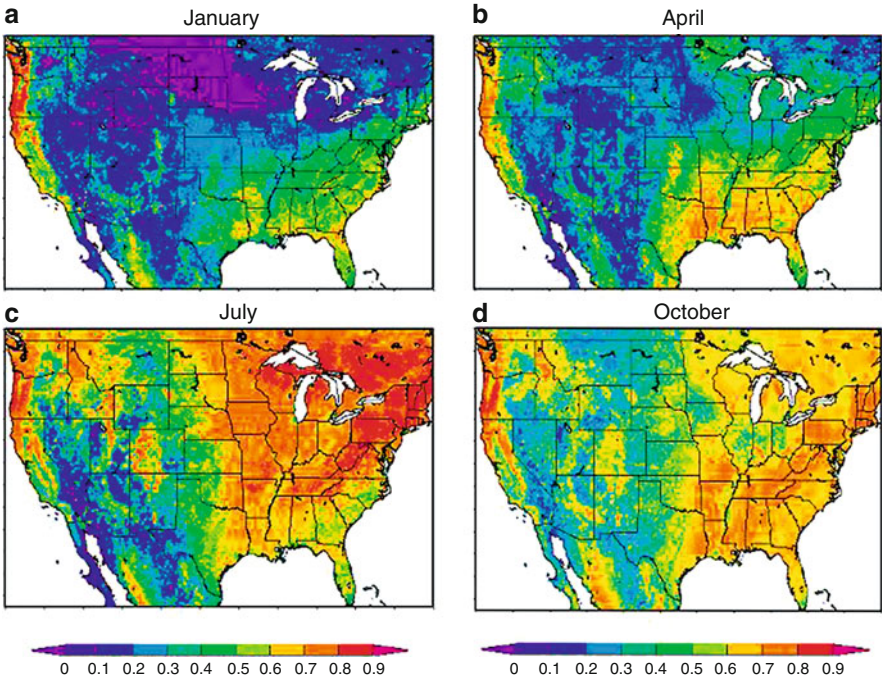

Fig. 19.16 Spatial distribution of NDVI derived from AVHRR observations for different months as averaged from 1996 to 2000 (**a**) January, (**b**) April, (**c**) July, and (**d**) October

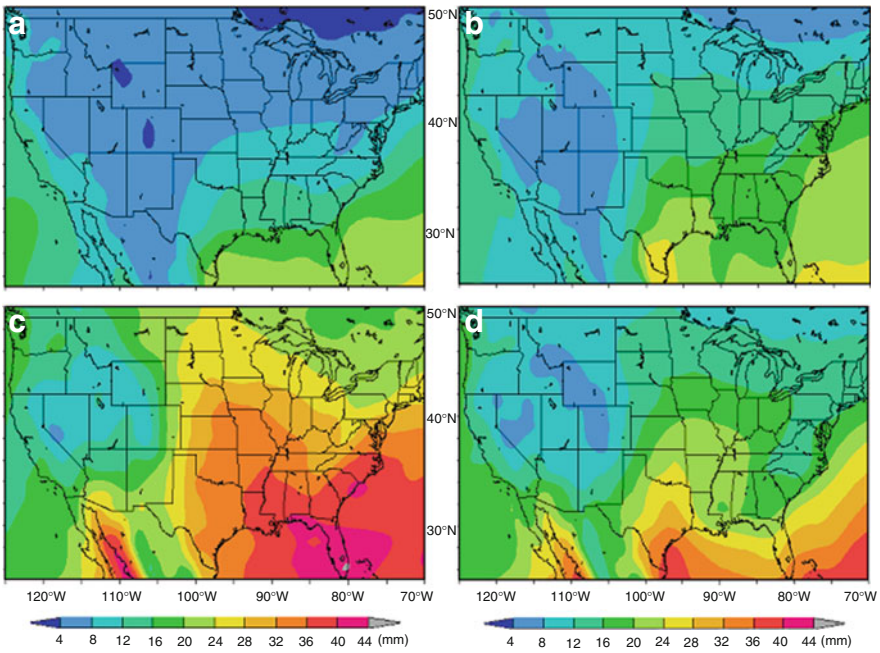

Fig. 19.17 Spatial distribution of water vapor amount during: (**a**) winter, (**b**) spring, (**c**) summer, and (**d**) fall as available from the ETA model

Further analysis shows that the effects of water vapor radiative forcing may be another important factor for the decrease in DTR in summer over the southeastern United States (Sun et al. 2006). As shown in Fig. 19.17, water vapor amount is higher over the eastern USA than in the western part; it is highest over the southeastern part during summer.

19.5.2 Comparison of Dual-Window and Split-Window Algorithms

It is appropriate here to examine whether the LST retrieved from the dual-window (3.9 + 11 μm) algorithm is comparable to LST derived from the split-window channels (viz., two far-infrared channels, 11 + 12 μm) that has never been compared before, for ensuring the applicability of the dual-window algorithm in the future. For each of the two algorithms, we calculated the bias, standard deviation (STD), and root mean square (RMS) errors in the satellite LST retrieval as evaluated against the in situ observations (Fig. 19.18).

The scatter plots shown in Fig. 19.18 indicate that both algorithms perform well, since they have fairly good correlation with the ground observations, though the scatter distribution of the dual-window (3.9 + 11 μm) algorithm is worse than the split-window (11 + 12 μm) algorithm, bringing about the STD error of 2.53 K from

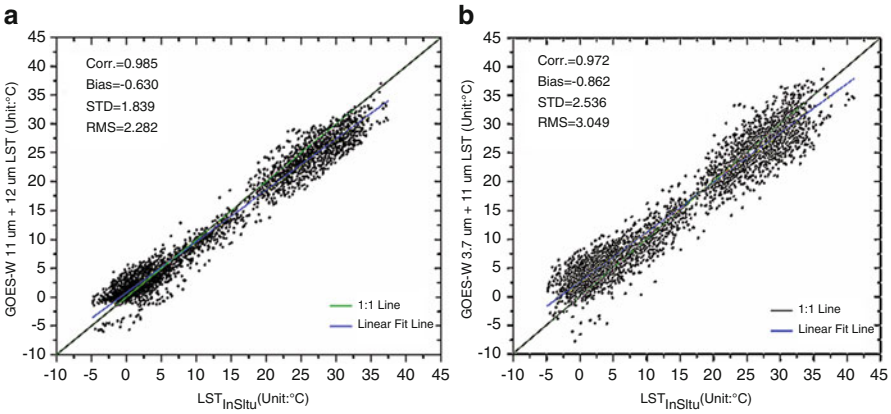

Fig. 19.18 Scatter plots of LST derived from the GOES vs. in situ observations for (**a**) split-window algorithm and (**b**) dual-window algorithm

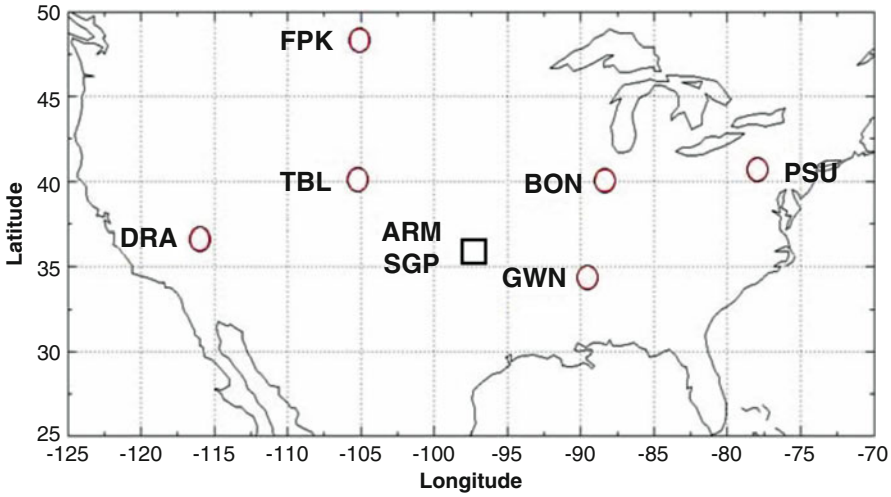

Fig. 19.19 Distribution of the SURFRAD and ARM sites

the dual-window algorithm, as compared to 1.83 K from the split-window algorithm.

However, in general, all of accuracy comparisons show that using the dual-window to derive LST is fairly feasible, though its total accuracy is slightly worse than those from the split-window algorithm. These results show that the lack of split-window channels on the GOES M-Q series may degrade the performance of GOES-LST retrieval.

Table 19.5 Accuracy/precision estimations of four seasons from GOES-12 LST retrieval

	January			April			July			October		
Site	*N*	ACC	PREC	*N*	ACC	PREC	*N*	ACC	PREC	*N*	ACC	PREC
1	164	−1.64	1.46	120	−1.83	1.93	151	−2.18	1.49	121	−0.32	1.75
2	188	−1.27	2.28	71	−2.88	1.54	146	−2.94	1.48	74	−0.38	2.57
3	208	−1.13	1.64	183	−1.53	1.89	104	−2.89	1.43	163	0.12	1.81
4	206	−0.53	2.15	145	−0.02	2.28	209	0.11	1.95	192	−1.01	1.85
5	182	−1.33	2.00	127	−1.42	2.49	167	−1.41	2.08	135	−0.13	2.65
6	133	−1.68	2.34	99	−1.46	2.23	169	−1.08	2.30	133	1.56	2.65

19.5.3 Precision and Accuracy Estimates

Table 19.5 shows the evaluation results of the GOES-12 LST from the dual-window algorithm with emissivity approach against the SURFRAD observations at the six stations. The accuracy (ACC) represents the mean bias (difference) error between GOES-LST and SURFRAD observations. The precision (PREC) represents the standard deviation error between GOES-LST and SURFRAD observations. *N* indicates the total sample numbers. The station ID (STAID) is:

STAID = 1, Bondville, IL
STAID = 2, Fort Peck, MT
STAID = 3, Goodwin Creek, MS
STAID = 4, Table Mountain, CO
STAID = 5, Desert Rock, NV
STAID = 6, Penn State, PA

Shown in Table 19.5 are the accuracy (ACC) and precision (PREC) values for the four seasons, respectively. It is worth of noting that the seasonal precision values are still around 2.5 K. But the seasonal accuracy patterns vary from site to site. It is unsure whether such distinct seasonal patterns might be related to the different surface covers and regional climates. All these statistical features will be further studied in the future.

19.5.4 Error Sources

19.5.4.1 Large Viewing Angle

The GOES sensor view geometry may have significant impact on the variation of atmospheric absorption due to the radiative transfer path length increase from nadir to the edge of the scan. Considering that altitude of GOES satellite is about 36,000 km and the Earth radius is about 6,700 km, the relationship between the satellite zenith angle (θ) and the satellite viewing angle (θ_v) is (Sun and Pinker 2004)

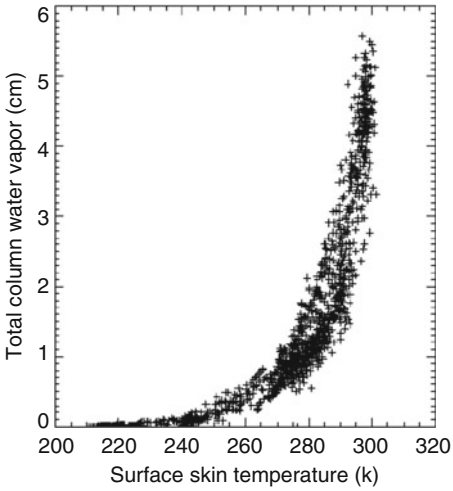

Fig. 19.20 Distributions of total column water vs. surface skin temperatures of the atmospheric profiles used in simulation analyses (From Sun and Pinker 2003)

$$\sin\theta = \frac{\text{Satellite Altitude} + \text{Earth Radius}}{\text{Earth Radius}} \sin\theta_v \approx 6.37 \sin\theta_v \tag{19.57}$$

Therefore, the maximum satellite viewing angle (about 8.7°) corresponds to 74.48° of view zenith angle. Such a large view zenith angle may have great impact on LST retrieval since, for instance, when the zenith angle is increased from 0° to 60°, the atmospheric path length is doubled. As shown in Figs. 19.9, 19.10, 19.11, 19.12, and 19.13, we can see the algorithm error distributions with satellite zenith angle indicate, for the moist atmospheric conditions, the errors become significantly worse when the viewing zenith angle is larger than 6 or satellite zenith angle (SZA) is larger than 42°. For dry atmospheric conditions, the LST errors are less sensitive to viewing geometry.

Two other important error sources in LST retrieval are the surface emissivity uncertainty and the atmospheric water vapor absorption.

19.5.4.2 Water Vapor Uncertainty

Figure 19.20 shows total column water vapor vs. LST distribution. As can be seen, most water vapor is concentrated at the warmer temperature range of 280–305 K and can vary from 0.25 to 7 cm due to increased evaporation from warmer surfaces, except for rocks, sand, and desert areas. This is why bigger errors occurred at temperature above 280 K, especially bias error, show significant underestimate at warmer temperature. Furthermore, for the LST larger than 280 K with moist atmospheric conditions, such water vapor sensitivity increases when the satellite zenith angle increases. This is because the atmosphere is getting moister when the total column water

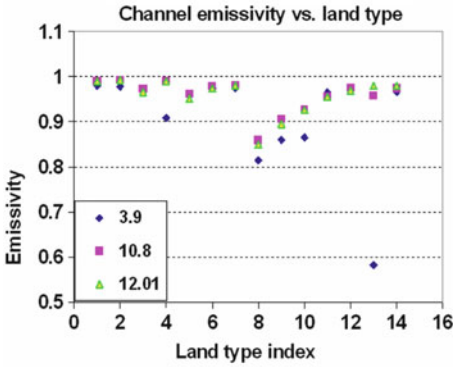

Fig. 19.21 Spectral variation in surface emissivity for different surface types (From MOSART)

vapor along the view path increases with the increase of satellite zenith angle. For the lower LST cases (LST less than 280 K) with dry atmospheric conditions, the STD and bias errors are not significantly sensitive to the view zenith angle.

Stratifying our regressions by water vapor regime, we assume that water vapor content can be well estimated as a priori. In practice, water vapor information is usually available from satellite soundings, in situ radiosondes and/or operational numerical weather prediction model forecasts. Nevertheless, two errors may occur. First, the water vapor value may be mismeasured due to a variety of error sources. Second, due to spatial resolution differences between the GOES observations and water vapor data, both "dry" and "moist" atmospheric conditions may occur within the unit spatial area over which the water vapor was estimated.

19.5.4.3 Emissivity Uncertainty

An emissivity error can cause errors in the simulated brightness temperature and therefore an LST retrieval error. As shown in Fig. 19.21, the brightness temperature error increases with the increase in the emissivity error and is larger in the split-window channels at 11.0 and 12.0 μm and smaller in the middle-infrared (MIR) 3.9 μm band. The brightness temperature error due to emissivity error in Fig. 19.10 is the average of all global data points over the entire temperature range. For a specific temperature, the error may be larger. As shown in Fig. 19.21, emissivity variations are fairly small in the thermal IR bands (11.0 and 12.0 mm) but somewhat larger in the MIR band (3.9 mm); however, an emissivity error causes a smaller brightness temperature error in the MIR band than in the thermal IR bands (Fig. 19.22). This is another reason for us to introduce the dual-window algorithm.

Analytically, the maximum LST uncertainty T_s due to the emissivity uncertainty can be described as

$$\delta T_s = \sqrt{\delta T_1{}^2 + \delta T_2{}^2} \tag{19.58}$$

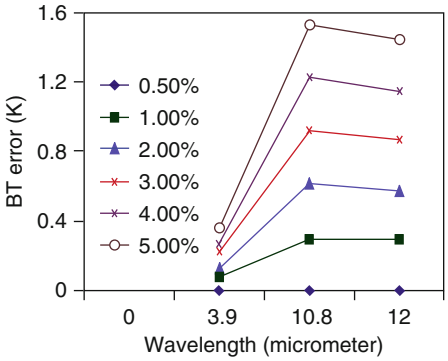

Fig. 19.22 Distributions of brightness temperature (*BT*) errors due to errors in surface emissivity from GOES forward simulations

where T_1 and T_2 represent the 3.9 and 11 μm band uncertainties resulting from the uncertainties of the mean emissivity (ε) and emissivity difference ($\Delta\varepsilon$), respectively. Using the Sobrino et al. (1994) split-window algorithm as an example, these two components are

$$\delta T_1 = \left(A_3 - \frac{A_4}{\varepsilon^2}\right)\delta\varepsilon \text{ and } \delta T_2 = \frac{A_4}{\varepsilon}\delta(\Delta\varepsilon) \tag{19.59}$$

Therefore, the maximum LST uncertainty is

$$\delta T_s = \sqrt{\left(\left(A_3 - \frac{A_4}{\varepsilon^2}\right)\delta\varepsilon\right)^2 + \left(\frac{A_4}{\varepsilon}\delta(\Delta\varepsilon)\right)^2} \tag{19.60}$$

Considering that $\varepsilon = (\varepsilon_{11} + \varepsilon_{12})/2$ and $\Delta\varepsilon = (\varepsilon_{11} - \varepsilon_{12})$, and assuming the emissivity uncertainties in each band are the same, i.e., $\delta\varepsilon = \delta\varepsilon_{11} = \delta\varepsilon_{12}$, the maximum uncertainty of the emissivity difference is $\delta(\Delta\varepsilon) = |\delta\varepsilon_{11}| + |\delta\varepsilon_{12}| = 2\delta\varepsilon$. Thus, the LST uncertainty, Ts, due to the emissivity uncertainty can be calculated using the above equation.

From the above equations, we can see, in order to reduce the LST algorithm sensitivity to the emissivity error, the emissivity difference should not be included in the algorithm formulation.

19.6 Summary and Discussion

In recent years, LST products have been successfully generated from polar-orbiting instruments, such as MODIS and ASTER. The polar-orbiting system has the advantage of global coverage. Surface temperature, especially land surface temperature, has a strong diurnal cycle, which cannot be captured by the temporal

resolution (approximately two views per day) of polar-orbiting satellites. Geostationary satellites with high temporal resolution provide good diurnal coverage, making them attractive for deriving information on the diurnal LST cycle and diurnal temperature range (DTR), which is an important climate change index. In this chapter, special attention has been paid to LST retrieval from geostationary GOES satellites. Algorithm theoretical basis (both physical and mathematical) has been provided. LST product is generated from current GOES satellites from our proposed dual-window algorithm.

References

Aminou D et al (2003) Meteosat second generation: a comparison of on-ground and on-flight imaging and radiometric performances of SEVIRI on MSG-1. Proceedings of 'the 2003 EUMETSAT meteorological satellite conference', Weimar, Germany, 29 Sept–3 Oct 2003, pp 236–243

Augustine JA, DeLuisi JJ, Long CN (2000) SURFRAD- a national surface radiation budget network for atmospheric research. Bull Am Meteorol Soc 81:2341–2357

Augustine JA, Hodges GB, Cornwall CR, Michalsky JJ, Medina CI (2005) An update on SURFRAD- the GCOS surface radiation budget network for the continental United States. J Atmos Oceanic Technol 22:1460–1472

Becker F, Li ZL (1990) Towards a local split window method over land surfaces. Int J Remote Sens 11:369–393

Berk A, Anderson GP, Acharya PK, Chetwynd JH, Hoke ML, Bernstein LS, Shettle EP, Matthew MW, Alder-Golden SM (2000) MODTRAN4 version 2 users's manual, space vehicles directorate, Hanscom AFB, MA 01731-3010, Apr 2000

Borbas EE, Moy L, Seemann SW, Knuteson RO, Antonelli P, Li J, Huang HL, Trigo I, de Meteorologia I, Zhou L (2008) A global infrared land surface emissivity database and its validation. P2.7, AMS annual meeting, New Orleans, Jan 2008

Braganza K, Karoly DJ, Arblaster JM (2004) Diurnal temperature range as an index of global climate change during the twentieth century. Geophys Res Lett 31:L13217. doi:10.1029/2004GL019998

Brown OB, Monnett PJ (1996) MODIS infrared sea surface temperature, Algorithm theoretical basis document (ATBD), version 2.0, Available at: http://oceancolor.gsfc.nasa.gov/DOCS/atbd_mod25.pdf

Caselles V, Coll C, Valor E (1997) Land surface temperature determination in the whole Hapex Sahell area from AVHRR data. Int J Remote Sens 18:1009–1027

Chin M, Rood RB, Lin SJ, Muller JF, Thomspon AM (2000) Atmospheric sulfur cycle in the global model GOCART: model description and global properties. J Geophys Res 105:24,671–24,687

Intergovernmental Panel on Climate Change (2001) In: Houghton JT, Ding Y, Griggs DJ, Noguer M, van der Linden PJ, Dai X, Maskell K, Johnson CA (eds) Climate change (2001) the scientific basis. Cambridge Univ. Press, Cambridge

Coll C, Valor E, Schmugge T, Caselles V (1997) A procedure for estimating the land surface emissivity difference in the AVHRR channels 4 and 5. Remote sensing application to the valencian area, Spain

Durre I, Wallace JM (2001) The warm season dip in diurnal temperature range over the eastern United States. J Climate 14:354–360

Easterling DR, Peterson TC, Karl TR (1996) On the development and use of homogenized climate datasets. J Climate 9:1429–1434

Ellrod GP (1998) Detection and analysis of fog at night using GOES multispectral infrared imagery. NOAA Tech Rep NESDIS 75:22

EUMETSAT homepage, http://www.eumetsat.int/groups/ops/documents/document/pdf_ten_052562_msg1_spctrsp.pdf

Faysash DA, Smith EA (1999) Simultaneous land surface temperature-emissivity retrieval in the infrared split window. J Atmos Ocean Tech 16(11):1673–1689

Faysash DA, Smith EA (2000) Simultaneous retrieval of diurnal to seasonal surface temperatures and emissivities over SGP ARM-CART site using GOES split window. J Appl Meteorol 39(7):971–982

Flynn L (2006) Comparisons two sets of noisy measurements. NOAA technical report, NESDIS office of research and applications

Francois C, Ottle C (1996) Atmospheric corrections in the Thermal Infrared: Global and Water Vapor Dependent Split-Window Algorithms-Applications to ATSR and AVHRR data. IEEE Trans Geosci Remote Sens 34(2):457–470

Gallo KP, Owen TW (1999) Satellite-based adjustments for the urban heat island temperature bias. J Appl Meteorol 38(6):806–813

Gallo KP, Owen TW, Easterling DR (1999) Temperature trends of the U.S. historical climatology network based on satellite-designated land use/land cover. J Clim 12:1344–1348

Hansen M, Reed B (2000) A comparison of the IGBP DISCover and University of Maryland 1 km global land cover products. Int J Remote Sens 21:1365–1373

Harris AR, Mason IM (1992) An extension to the split-window technique giving improved atmospheric correction and total water vapor. Int J Remote Sens 13:881–892

Hillger D, Ellrod W, Gary P (2003) Detection of important atmospheric and surface features by employing principal component image transformation of GOES imagery. J Appl Meteorol 42:611–629

Karl TR, Kukla G, Gavin J (1984) Decreasing diurnal temperature range in the United States and Canada from 1941-1980. J Clim Appl Meteor 23:1489–1504

Karl TR, Jones PD, Knight RW, Kukla G, Plummer N, Razuvayev V, Gallo KP, Lindseay J, Charlson RJ, Peterson TC (1993) A new perspective on recent global warming. Bull Am Meteorol Soc 74:1007–1023

Kealy PS, Hook SJ (1993) Separating temperature and emissivity in thermal infrared multispectral scanner data: implications for recovering land surface temperature. IEEE Trans Geosci Remote Sens 31:1155–1164

Li ZL, Becker F (1993) Feasibility of land surface temperature and emissivity determination from AVHRR data. Remote Sens Environ 43:67–85

Liang S (2001) An optimization algorithm for separating land surface temperature and emissivity from multispectral thermal infrared imagery. IEEE Trans Geosci Remote Sens 39:264–274

Ma XL, Wan Z, Moeller CC, Menzel WP, Gumley LE (2002) Simultaneous retrieval of atmospheric profiles, land surface temperature, and surface emissivity from Moderate Resolution Imaging Spectroradiometer thermal infrared data: extension of a two-step physical algorithm. Appl Opt 41:909–924

May DA (1993) Global and regional comparative performance of linear and non-linear satellite multichannel sea surface temperature algorithms, Tech. Rep. NRL/MR/7240-93-7049, Nav. Res. Lab., Stennis Space Cent., Miss., Washington, D.C.

McClain EP, Pichel WG, Walton CC (1985) Comparative performance of AVHRR-based multichannel sea surface temperatures. J Geophys Res 90:11587–11601

McFarland MJ, Miller RL, Neale CMU (1990) Land surface temperature derived from the SSM/I passive microwave brightness temperatures. IEEE Trans Geosci Remote Sens 28:839–845

McMillin LM (1975) Estimation of sea surface temperatures from two infrared window measurements with different absorption. J Geophys Res 80:5113–5117

McMillin LM, Crosby DS (1984) Theory and validation of multiple window sea surface temperature technique. J Geophys Res 89:3655–3661

Menzel WP, Purdom JFW (1994) Introducing GOES-I: the first of a new generation of geostationary operational environmental satellites. Bull Am Meteorol Soc 75:757–781

Norman JM, Becker F (1995) Terminology in thermal infrared remote sensing of natural surfaces. Remote Sens Rev 12:159–173
Peterson TC (2003) Assessment of urban versus rural in situ surface temperature in the contiguous United States: no difference found. J Clim 16:2941–2959
Prata AJ (1993) Land surface temperatures derived from the AVHRR and the ATSR, 1, theory. J Geophys Res 98:16,689–16,702
Prata AJ (1994) Land surface temperatures derived from the AVHRR and the ATSR, 2, experimental results and validation of AVHRR algorithms. J Geophys Res 99:13,025–13,058
Prata AJ, Platt CMR (1991) Land surface temperature measurements from the AVHRR. In: Proceedings of the 5th AVHRR data users conference, Tromso, Norway, 25–28 Jun, pp 438–443. EUM P09, 1991
Price JC (1984) Land surface temperature measurements from the split window channels of the NOAA-7/AVHRR. J Geophys Res 89:7231–7237
Schmetz J, Pili P, Tjemkes S, Just D, Kerkmann J, Rota S, Ratier A (2002) An introduction to meteosat second generation (MSG). Bull Am Meteorol Soc 83:977–992
Schmid J (2000) The SEVIRI instrument. Proceedings of the 2000 EUMETSAT meteorological satellite data user's conference, Bologna, Italy, 29 May–2 Jun 2000
Schmit TJ, Feltz WF, Menzel WP, Jung J, Noel AP, Heil JN, Nelson JP III, Wade GS (2002) Validation and use of GOES sounder moisture information. Weather Forecast 17:139–154
Schmit TJ, Li J, Gunshor MM, Schmidt CC, Menzel WP, Gurka J, Sieglaff J (2004) Study of the advanced baseline imager (GOES IMAGER) on the GOES-R and beyond. 84th AMS annual meeting, Seattle, WA
Schmit TJ, Menzel WP, Gurka J, Gunshor M (2007) The GOES IMAGER on GOES-R. 3rd annual symposium future national operational environmental satellite systems, San Antonio, 16 Jan 2007
Schumann W, Stark H, McMullan K, Aminou D, Luhmann H-J (2002) The MSG system ESA bulletin. 111
Sellers PJ, Hall FG, Asrar G, Strebel DE, Murphy RE (1998) The first ISLSEP field experiment (FIFE). Bull Am Meteorol Soc 69:22–27
Sikorski RJ, Kealy PS, Emery WJ (2002) Land surface temperature. Visible/infrared imager. Radiometer suite algorithm theoretical basis document, version 5, Raytheon Systems Company. Available at: http://npoesslib.ipo.noaa.gov/atbd/viirs/
Snyder WC, Wan Z, Feng YZ (1998) Classification-based emissivity for land surface temperature measurement from space. Int J Remote Sens 19:2753–2774
Sobrino JA, Li ZL, Stoll MP, Becker F (1993) Determination of the surface temperature from ATSR data. In: Proc. 25th int. symp. remote sens. Environ., Graz, Austria, 4–8 Apr, pp II-19–II-109
Sobrino JA, Li ZL, Stoll MP, Becker F (1994) Improvements in the split-window technique for land surface temperature determination. IEEE Trans Geosci Remote Sens 32:243–253
Stone DA, Weaver AJ (2003) Factors contributing to diurnal temperature range trends in twentieth and twenty-first century simulations of the CCCma coupled model. Clim Dynam 20:435–445
Sugita M, Brutsaert W (1993) Comparison of land surface temperature derived from satellite observations with ground truth during FI FE. Int J Remote Sens 14:1659–1676
Sun D, Pinker RT (2003) Estimation of land surface temperature from a geostationary operational environmental satellite (GOES-8). J Geophys Res 108. doi:10.1029/2002JD002422
Sun DL, Pinker RT (2004) Case study of soil moisture's effect on land surface temperature retrieval. IEEE Trans Geosci Remote Sens Lett 1:127–130
Sun DL, Pinker RT, Basara JB (2004) Land surface temperature estimation from the next generation of geostationary operational environmental satellites: GOES M-Q. J Appl Meteorol 43:363–372
Sun DL, Pinker RT, Kafatos M (2006a) Diurnal temperature range over the United States: a satellite view. Geophys Res Lett 33. doi:10.1029/2005GL024780
Sun DL, Kafatos M, Pinker RT, Easterling D (2006b) Seasonal variations in diurnal temperature range from satellite and surface observations. IEEE Trans Geosci Remote Sens 44:2779–2785

Ulaby FT, Moore RK, Fung AK (1986) Microwave remote sensing-active and passive, vol 111, From theory to applications. Artech, Norwood

Ulivieri C, Cannizzaro G (1985) Land surface temperature retrievals from satellite measurements. Acta Astronaut 12:985–997

Ulivieri C, Castronouvo MM, Francioni R, Cardillo A (1992) A SW algorithm for estimating land surface temperature from satellites. Adv Space Res 14:59–65

Vidal A (1991) Atmospheric and emissivity correction of land surface temperature measured from satellite using ground measurements or satellite data. Int J Remote Sens 12:2449–2460

Vinnikov KY, Yu Y, Rama Varna Raja MK, Tarpley D, Goldberg M (2008) Diurnal-seasonal and weather-related variations of land surface temperature observed from geostationary satellites. Geophys Res Lett. doi:10.1029/2008GL035759, 2008

Walton CC, Pichel WG, Sapper JF, May DA (1998) The development and operational application of non-linear algorithms for the measurement of sea surface temperatures with the NOAA polar-orbiting environmental satellites. J Geophys Res 103:27999–28012

Wan Z (1999) MODIS land-surface temperature algorithm basis document (LST ATBD): version 3.3

Wan Z, Dozier J (1996) A generalized split-window algorithm for retrieving land-surface temperature measurement from space. IEEE Trans Geosci Remote Sens 34:892–905

Weng F, Grody N (1998) Physical retrieval of land surface temperature using the special sensor microwave imager. J Geophys Res 103:8839–8848

Yu Y, Barton IJ (1994) A non-regression-coefficients method of sea surface temperature retrieval from space. Int J Remote Sens 15:1189–1206

Yu Y, Privette JL, Pinheiro AC (2005) Analysis of the NPOESS VIIRS land surface temperature algorithm using MODIS data. IEEE Trans Geosci Remote Sens 43:2340–2350

Yu Y, Pinheiro AC, Privette JL (2006) Correcting land surface temperature measurements for directional emissivity over 3-D structured vegetation. SPIE, San Diego

Yu Y, Privette JP, Pinheiro AC (2008) Evaluation of split window land surface temperature algorithms for generating climate data records. IEEE Trans Geosci Remote Sens 46:179–192

Yu Y, Tarpley D, Privette JL, Rama Varna Raja MK, Vinnikov K, Xue H (2009a) Developing algorithm for operational GOES-R land surface temperature product. IEEE Trans Geosci Remote Sens 47:936–951

Yu Y, Chen M, Vinnikov K, Tarpley D, Xu H (2009b) A three-measurement model developed for evaluating satellite land surface temperature product. SPIE 2009, San Diego

Yu Y, Xu H, Tarpley D, Goldberg M (2009c) A Simplified method for measuring land surface temperature and emissivity using thermal infrared split-window channels. IGARSS 2009, Proc., Cape Town

Yu Y, Tarpley D, Prrivette JL, Flynn L, Xu H, Chen M, Vinnikov K, Sun D (2012) Towards satellite land surface temperature validation using SURFRAD ground measurements. IEEE Trans Geosci Remote Sens 50:704–713

Chapter 20
Remote Sensing of Leaf, Canopy, and Vegetation Water Contents for Satellite Environmental Data Records

E. Raymond Hunt Jr., Susan L. Ustin, and David Riaño

Abstract The absorption features of liquid water in plant leaves are readily detectable, and the amount of leaf water content may be determined by spectroscopy. Spectral reflectances at about 1240 and 1650 nm are the basis of numerous remote-sensing indices that could be used to estimate liquid water content of leaves and canopies. Two applications of remotely sensed water content are estimation of fuel moisture content for wildfire potential and estimation of vegetation water content for improving retrievals of soil moisture content from microwave sensors. The temporal record of MODIS, SPOT Vegetation, and AVHRR/3 sensors and the future record from VIIRS will create a global environmental data record of canopy water content for climate change studies.

Keywords Drought • Soil moisture content • Plant water stress • Wildfire potential • Fuel moisture content • Spectroscopy • Vegetation indices • Model inversion

E.R. Hunt Jr. (✉)
USDA-ARS Hydrology and Remote Sensing Laboratory, Bldg 007 Room 104 BARC-West, 10300 Baltimore Avenue, Beltsville, MD 20705, USA
e-mail: Raymond.Hunt@ars.usda.gov

S.L. Ustin
Department of Land, Air and Water Resources, University of California, Davis, CA 95616, USA
e-mail: SLUstin@ucdavis.edu

D. Riaño
Department of Land, Air and Water Resources, University of California, Davis, CA 95616, USA

Centro de Ciencias Humanas y Sociales, Consejo Superior de Investigaciones Científicas (CSIC), Madrid 28037, Spain
e-mail: driano@ucdavis.edu

J.J. Qu et al. (eds.), *Satellite-based Applications on Climate Change*,
DOI 10.1007/978-94-007-5872-8_20,

20.1 Introduction

The long time series of Normalized Difference Vegetation Index (NDVI) acquired from the Advanced Very High Resolution Radiometer (AVHRR), the Moderate Resolution Imaging Spectroradiometer (MODIS), and the System Pour l'Observation de la Terre (SPOT) Vegetation sensors enabled the development of environmental data records for the study of climatic change (NRC 2004; Tucker et al. 2005). Liquid water has absorption features at near-infrared and shortwave-infrared wavelengths (Curcio and Petty 1951; Palmer and Williams 1974) which are readily identified in leaf spectral reflectance (Gates et al. 1965; Tucker 1980). MODIS, SPOT Vegetation, and AVHRR/3 data cover a relatively short time period for climate data records; with the recently launched Visible Infrared Imaging Radiometer Suite (VIIRS), global measurements will continue into the foreseeable future. Standardized data products of canopy water content could be the start of a satellite environmental data record that would provide important information for assessing global climatic change.

Landsat Thematic Mapper, MODIS, AVHRR/3, SPOT Vegetation, and other sensors have bands at about 1650-nm wavelength, which is at a local absorption minimum for liquid water (Fig. 20.1). Because the water absorption coefficient at this wavelength is relatively small, differences in the amount of leaf water are detectable by changes in leaf reflectance (Olsen 1967; Tucker 1980; Hunt and Rock 1989). Imaging spectrometers have many more bands and potentially have better algorithms for the retrieval of water content (Ustin et al. 1998, 2004, 2012).

One of the large uncertainties about future climatic change is about changes in precipitation frequency and amount (Christensen et al. 2007; Allan and Soden 2008). Drought will cause changes in leaf water content for many vegetation types, so remotely sensed data products are important for assessing the impact and helping to mitigate the effects of climatic change on vegetation. Furthermore, climate change is expected to increase the potential for wildfire (Liu et al. 2010); thus, a water content data product may help manage efforts for disaster prevention and recovery. The objective of this chapter is to review remote sensing for the retrieval of water content in vegetation canopies for remotely sensed data products and to show how these data products could be used for various applications.

20.2 Quantifying the Amount of Water in Vegetation

Different quantities and methods are used to measure the amount of water in foliage (Table 20.1). The basic measurements are leaf fresh and dry weights; the difference is the amount of water in a leaf. However, these basic data have little value because of variation in leaf size, dry weight, and morphology. Plant physiological responses to drought and water stress usually depend on relative water content (RWC) and water potential (Ψ), which are defined in thermodynamics by reference to the maximum amount of water a plant cell may hold (Nobel 2009). Cells with the maximum amount of water (i.e., RWC = 100%) also have the maximum turgor

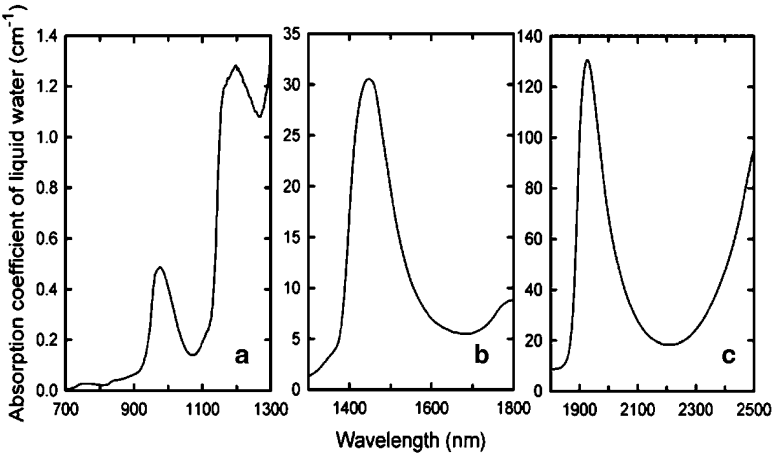

Fig. 20.1 Absorption coefficients for water from 700- to 2,500-nm wavelength. The y-axis scales are different for panels (**a**) near-infrared, (**b**) shortwave-infrared 1, and (**c**) shortwave-infrared 2. The coefficients are from the PROSPECT model (Jacquemoud and Baret 1990; Féret et al. 2008)

Table 20.1 Quantities to express vegetation biophysical parameters

Term	Abbreviation or symbol	Formula	Units
Weight: fresh, dry, and at full turgor[a]	W_f, W_d, and W_t, respectively	Measured	kg
Area: ground and leaf	A_g & A_{lf}, respectively	Measured	m^2
Leaf Area Index	LAI	A_{lf}/A_g	Dimensionless
Leaf dry matter content[b]	C_m	W_d/A_{lf}	kg m^{-2}
Leaf water potential[a]	Ψ	Measured	MJ m^{-3} = MPa
Relative water content[a]	RWC	$(W_f - W_d)/(W_t - W_d)$	Dimensionless
Leaf water content[c]	LWC (or C_w)	$(W_f - W_d)/A_{lf}$	kg m^{-2}
Canopy water content[c]	CWC	LWC × LAI	kg m^{-2}
Vegetation water content	VWC	CWC+ stem water content	kg m^{-2}
Fuel moisture content	FMC	LWC/C_m	Dimensionless

[a]By definition, leaves at full turgor have Ψ = 0 MPa and RWC = 100%
[b]C_m is also known as the leaf mass to area ratio (LMA) and $1/C_m$ is known as the specific leaf area (SLA)
[c]LWC and CWC are also known as the leaf and canopy equivalent water thickness (EWT), respectively (volume/area, 1 mm = 1 kg m^{-2})

potential (i.e., full turgor), which offsets the cellular osmotic potential so that Ψ is 0 MPa (Nobel 2009). Leaf wilting is a visible sign of water stress, which occurs when the turgor pressure is 0 MPa and Ψ is equal to the osmotic potential. RWC and Ψ for leaves are approximately the RWC and Ψ of the leaf mesophyll cells and are unrelated to leaf area (A_{lf}), fresh weight (W_f), or dry weight (W_d). For a given leaf, there is a one-to-one relationship between RWC and Ψ known as a "pressure-volume curve," which is determined by measurement (Lenz et al. 2006; Nobel 2009).

The Beer-Lambert law states that the amount of radiation either absorbed by or transmitted through a homogeneous substance depends on the path length through that substance. Leaves are not homogeneous; however, the effective path length of water in a leaf, called the equivalent water thickness (EWT), may be calculated from leaf transmittances using the Beer-Lambert law (Gausman et al. 1970). Leaf water content (LWC, Table 20.1) is a slightly more accurate term compared to EWT, because water volume is determined by the difference of leaf fresh and dry weights, and the density of water has a small dependency on temperature. Leaf Area Index (LAI) of x may be thought of as a stack of x leaves (Miller et al. 1992); LWC multiplied by LAI is the canopy water content (CWC, Table 20.1). Reflectance parallels transmittance through leaves (Gates et al. 1965), so leaf and canopy reflectances may be used to estimate LWC and CWC.

There are two terms (Table 20.1) that are often used interchangeably with LWC and CWC; these are the vegetation water content (VWC) and fuel moisture content (FMC). Except for grass species and very small plants, there is usually more liquid water in stems compared to leaves, and there is some water in flowers and fruits. Active and passive remote sensing at microwave wavelengths is sensitive to all of the water in plants (Jackson et al. 2004; Entekhabi et al. 2010). VWC is a term which better describes the total amount of water in vegetation aboveground, approximately equal to the sum of LWC and stem water content (Table 20.1).

Leaves from different species, or from the same species but under different growth conditions, have different leaf thicknesses and LWC (Abrams and Kubiske 1990). Leaf dry matter content (C_m, Table 20.1) is the leaf dry weight per leaf area and may vary up to 100-fold for different species (Poorter et al. 2009). FMC is the ratio of LWC/C_m and is used to estimate the potential for wildfire ignition and spread (Burgan 1988; Chuvieco et al. 2002, 2010; Yebra et al. 2008). Canopy FMC is equal to leaf FMC because LAI cancels out from the numerator and denominator. FMC and RWC are both expressed as percentages; occasionally, studies will measure FMC or LWC/W_f but report the data as RWC.

20.3 Multi-temporal NDVI and Drought Stress

NDVI (Rouse et al. 1974; Tucker 1979) distinguishes vegetation and soils based on the high reflectance of foliage at near-infrared wavelengths and the low reflectance of foliage at red wavelengths. The low reflectance of red light by vegetation is caused by a very large chlorophyll absorption coefficient; so changes in red reflectance are small for large changes of chlorophyll content. Therefore, NDVI cannot be used to estimate foliar chlorophyll concentration under most conditions (Lichtenthaler et al. 1996). Depending on the plant species, dehydration may increase leaf reflectance at visible and red-edge wavelengths (Fig. 20.2), due to some chlorophyll degradation (Carter 1991, 1993; Govender et al. 2009). However, many different stresses also affect leaf chlorophyll content (Carter 1993), so if a decrease in chlorophyll content is detected by remote sensing, the cause of the stress cannot be determined.

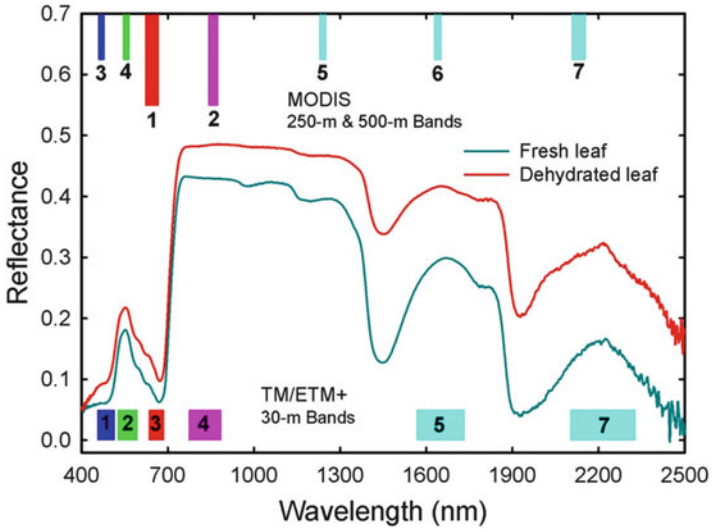

Fig. 20.2 Spectral reflectances for fresh and dehydrated leaves of corn (*Zea mays*). Along the top are the wavelength positions of the Moderate Resolution Imaging Spectroradiometer (*MODIS*) land/cloud/aerosol bands (250 and 500-m pixels) and along the bottom are the wavelength positions of the Thematic Mapper (*TM*) and Enhanced Thematic Mapper Plus (*ETM+*) bands. MODIS ocean color and water vapor bands (1,000-m pixels) are not shown

Many vegetation types respond to changes in the season by growth of new leaves and senescence of old leaves. Different vegetation types have different seasonality defined by either temperature or precipitation (Tucker et al. 1985). By analysis of multi-temporal NDVI, phenological events such as the start of spring may be determined (Schwarz et al. 2002). As a response to stress, many vegetation types lose some or all of their leaves, so differences in NDVI compared to the annual maximum and minimum NDVI become powerful indicators of vegetation stress (Kogan et al. 2003; Brown et al. 2008). Changes in LAI will proportionately affect CWC (Table 20.1), so annual changes in remotely sensed CWC should be similar to the annual changes in NDVI or other red/near-infrared index.

If changes in remotely sensed CWC simply mirrored changes in NDVI, there would be no use for CWC data products. From the previous section, single measurements of LWC and CWC values cannot indicate physiological measures of stress (RWC or Ψ). However, reductions in LWC and CWC occur with drought stress before changes in LAI, so a high frequency of CWC observations may yield more reliable estimates of drought stress than NDVI. Quantifying physiological water stress accurately over time would then become an important environmental data record.

20.4 Spectroscopic Retrieval of Leaf and Canopy Liquid Water Contents

Olsen (1967) published the first spectral measurements of leaves drying in the laboratory, and the data look similar to Fig. 20.2. Typically, dehydration initially increases near-infrared reflectance, indicating changes in the cellular structure of a leaf (Aldakheel and Danson 1997). Relative to the near-infrared wavelengths (Fig. 20.1a), leaf dehydration causes increased reflectance at longer near-infrared and shortwave-infrared wavelengths (Fig. 20.2). The largest percent changes in reflectance occur at wavelengths around 1495 and 1950 nm; however, water vapor strongly absorbs near these wavelengths, making the atmosphere opaque to solar radiation (Green et al. 2006). Thus, the 1495- and 1950-nm liquid water absorption features can be used only to estimate LWC under an artificial light source. At wavelengths greater than 2000 nm, there are strong biochemical absorption features from lignin and cellulose (Daughtry and Hunt 2008), so the reflectance spectrum of dehydrated leaves becomes more complex. Therefore, the three regions that have potential for routinely monitoring changes in LWC and CWC are the local absorption maxima around 970 and 1240 nm (Fig. 20.1a) and the local absorption minimum around 1650 nm (Fig. 20.1b). Below, spectroscopic retrieval of LWC and CWC are discussed. In the next section, remote-sensing indices using these three regions are described.

Allen et al. (1969) showed that LWC could be estimated by comparing the leaf reflectance spectrum with the expected spectrum determined from different equivalent thicknesses of pure liquid water; however, calculators or personal computers were not available so the comparisons were qualitative. If the reflectances from leaves and canopies are assumed to follow the Beer-Lambert law (Downing et al. 1993; Gao and Goetz 1990, 1995; Roberts et al. 1998, and Sims and Gamon 2003), then:

$$-ln(R_\lambda) = \alpha_\lambda l \tag{20.1}$$

where R_λ is the reflectance at wavelength λ, ln is the natural logarithm operation, α_λ is the absorption coefficient at wavelength λ, and l is the optical path length of liquid water. The path length l, that is, the LWC or CWC, is determined from the slope of a linear regression between $\ln(R_\lambda)$ and α_λ over some wavelength region. The regression intercept is supposed to account for fixed effects from errors in the assumptions (Roberts et al. 2004; Sims and Gamon 2003). Gao and Goetz (1990, 1995) use predicted CWC to estimate the amount of water vapor for atmospheric correction of imaging spectrometer data (Gao et al. 2009).

Gao and Goetz (1995) showed that the retrieved CWC at 1,000 nm was greater than the retrieved CWC at 1600 nm. Using the two spectra in Fig. 20.2, regressions of $\ln(R_\lambda)$ versus α_λ around 970, 1240, and 1650 nm were made according to Eq. 20.1. The measured LWC for the fresh leaf and dehydrated leaf were 0.14 and 0.04 kg m^{-2}, respectively. The retrieved LWC for the fresh leaf were 0.70, 0.59, and 0.45 kg m^{-2} for 970, 1240, and 1650 nm, respectively, whereas the retrieved LWC for the dehydrated leaf were 0.24, 0.19, and 0.16 kg m^{-2},

respectively. There were highly significant linear relationships between measured and retrieved LWC and CWC for the three wavelength regions (Hunt et al. 2011a). Larger values of retrieved parameters are regularly observed in the analytical procedures of near-infrared spectroscopy, which are attributed to multiple scattering (Zhang et al. 2011).

Because it is difficult to account for multiple scattering without additional terms in Eq. 20.1, the retrieved values of LWC and CWC probably should not be used, except when the actual values of LWC or CWC are not relevant, such as with atmospheric correction (Gao et al. 2009) or water-spectrum removal (Gao and Goetz 1994, 1995; Schlerf et al. 2010; Ramoelo et al. 2011; Wang et al. 2011a).

Alternative methods for retrieving LWC or CWC with spectroscopy may be insensitive to multiple scattering within a leaf and other confounding factors (Asner and Martin 2008; Zhang et al. 2011). Li et al. (2008) used a genetic algorithm-partial least squares regression and obtained very low root mean square errors (RMSE), but the results did not scale between leaves and canopies. Cheng et al. (2011b) used wavelet transforms to obtain similar results. While the recent research is promising for the spectroscopic retrieval of LWC and CWC, the results are not yet applicable for imaging spectroscopy.

20.5 Remotely Sensed Foliar Water Indices

Initially, vegetation indices such as NDVI were utilized because satellite multispectral imagery was acquired as digitized radiances (digital numbers), whereas ground data were usually measured reflectances. Jackson et al. (1983) wrote that an ideal vegetation index should be sensitive to vegetation amount and insensitive to the following: (1) soil background, (2) surface topography, (3) atmospheric effects, and (4) solar zenith angle. Furthermore, an ideal vegetation index should be insensitive to the bidirectional reflectance distribution functions of vegetation and soils (Huete et al. 2002). Today, satellite imagery is frequently corrected for atmospheric effects and solar-target-sensor geometry to obtain apparent land-surface reflectance (Gao et al. 2009). Even with apparent land-surface reflectances, however, vegetation indices are still a practical method for monitoring vegetation because (1) atmospheric corrections usually assume a standard atmosphere and (2) surface topography and soil background create variation in the apparent reflectances.

Hardisky et al. (1983) proposed that a normalized difference index using Landsat Thematic Mapper (TM) bands 4 and 5 was related to the amount of water in vegetation (Fig. 20.2). Kimes et al. (1981) studied this index but found TM band 3 and TM band 5 reflectances were very highly correlated ($r = 0.97$), so there was no added benefit for using TM band 5 to monitor agronomic variables. Hardisky et al. (1983) called NDVI simply the Vegetation Index and called the normalized difference of TM bands 4 and 5 the Infrared Index. Hunt and Rock (1989) and Ji et al. (2011) recommended that the Infrared Index be called instead the Normalized Difference Infrared Index (NDII, Table 20.2) parallel to the universally accepted NDVI. Hunt et al. (1987) and Hunt and Rock (1989) developed and

Table 20.2 Multispectral indices related to leaf and canopy water content

Index	Abbreviation	Equation[a]	Author	Comments
Normalized Difference Vegetation Index	NDVI	$(R_{850} - R_{680})/(R_{850} + R_{680})$	Rouse et al. (1974), Tucker (1979)	–
Normalized Difference Infrared Index	NDII	$(R_{850} - R_{1650})/(R_{850} + R_{1650})$	Hardisky et al. (1983)	Also see Ji et al. (2011)
Leaf Water Stress Index	LWSI	$-\log[1 - (R_{850} - R_{1650})]/$ $-\log[1 - (R_{850} - R'_{1650})]$	Hunt et al. (1987)	R'_{1650} is the reflectance at full turgor (RWC = 100%)
Moisture Stress Index	MSI	R_{1650}/R_{850}	Hunt and Rock (1989)	Defined for Thematic Mapper Bands 5 and 4
Global Vegetation Moisture Index	GVMI	$[(R_{850} + 0.1) - (R_{1650} + 0.02)]/$ $[(R_{850} + 0.1) + (R_{1650} + 0.02)]$	Ceccato et al. (2002a, b)	See also Dasgupta and Qu (2009)
Shortwave Infrared Water Stress Index	(a) SIWSI (6,2)	(a) $(R_{1650} - R_{850})/(R_{1650} + R_{850})$	Fensholt and Sandholt (2003)	(a) SIWSI (6,2) = −NDII
	(b) SIWSI (5,2)	(b) $(R_{1240} - R_{850})/(R_{1240} + R_{850})$		(b) SIWSI(5,2) = −NDWI
Normalized Difference Water Index	NDWI	$(R_{850} - R_{1240})/(R_{850} + R_{1240})$	Gao (1996)	Designed for MODIS bands 2 and 5
Simple Ratio Water Index	SRWI	R_{850}/R_{1240}	Zarco-Tejada et al. (2003)	–
Water Index	WI	R_{900}/R_{970}	Peñuelas et al. (1993, 1997)	–
Maximum Difference Water Index	MDWI	$(R_{1650} - R_{1500})/(R_{1650} + R_{1500})$	Eitel et al. (2006)	R_{1650} and R_{1500} are about the max and min R between 1500 and 1750 nm
Shortwave Angle Slope Index	SASI	$(R_{850}, R_{1650}, R_{2200})$	Khanna et al. (2007)	Angle formed at R_{1650} between R_{850} and R_{2200}
Vegetation Water Stress Index	VWSI	$1 - [(M_1 - M)(R_{850} - M_2R_{1650} - I_2)/$ $(M_1 - M_2)(R_{850} - M\,R_{1650})]$ $- [I_2(M_1 - M) + I_1(M_2 - M)]$	Ghulam et al. (2008)	M_1, M_2, I_1, I_2 are points bounding a trapezoid in NIR-SWIR image feature space

[a] R_λ is the reflectance at λ nanometers wavelength

tested a Leaf Water Stress Index (LWSI, Table 20.2), which was derived from the Beer-Lambert law to be equal to leaf RWC. However, Hunt and Rock (1989) and Cohen (1991a, b) showed that LWSI was not practical, because of the requirements to measure reflectances of fully turgid and dry leaves. Furthermore, Hunt and Rock (1989) showed there is a log-linear relationship between the Moisture Stress Index (MSI, Table 20.2) with LWC for different species from crops to desert succulents. Because there is a one-to-one relationship between a ratio index and the corresponding normalized difference index, there is a strong relationship between NDII and CWC (Yilmaz et al. 2008a, b).

NDII is also an important index for the remote sensing of snow cover and flooded areas. NDII time series in the northern latitudes show both snow and vegetation dynamics, so estimating the start of spring for phenological studies may be difficult (Xiao et al. 2002b; Delbart et al. 2005, 2006). Xiao et al. (2002a) used NDII to detect flooded rice paddy fields in China.

The design for MODIS defined a band 5 located at 1240 nm (Fig. 20.2), thus Gao (1996) defined the Normalized Difference Water Index (NDWI; Table 20.2). Similar to other NIR wavelengths, radiation at MODIS band 5 is highly scattered by leaf cellular structure and multiple leaves, so the two bands of NDWI sample the same amount of canopy (Gao 1996). Furthermore, NDWI does not saturate at low LAI as does NDVI or NDII. Zarco-Tejada et al. (2003) recommended the Simple Ratio Water Index (SRWI, Table 20.2) which also uses the apparent reflectance at 1240 nm.

The water absorption feature at 970 nm is interesting for remote sensing because reflectances at this wavelength may be measured using low-cost silicon detectors. Peñuelas et al. (1993, 1997) designed the Water Index (WI, Table 20.2) and compared it to FMC and measures of plant water stress. To date, WI can only be measured over larger areas with airborne or satellite imaging spectrometers. There are no current or planned satellite multispectral sensors with a 970-nm band for calculating WI.

The variety of foliar water indices based on the wavelengths of 970, 1240, and 1650 nm indicates there may not be a single index that outperforms the others for estimating CWC under all conditions. This situation should be expected simply from the history of red-NIR indices, such as NDVI and the simple ratio of R_{850}/R_{680}. One of the first alternative red-NIR indices was the Soil-Adjusted Vegetation Index (SAVI, Huete 1988), which corrected for numerical offsets between the red and NIR bands at low LAI. Using the method of Huete (1988), Cecatto et al. (2002a, b) developed the Global Vegetation Moisture Index (GVMI, Table 20.2) to adjust the NIR and SWIR reflectances so zero vegetation would have zero GVMI (also see Dasgupta and Qu 2009).

New paradigms may be needed for development of effective vegetation water indices. The Maximum Difference Water Index uses maximum reflectance and minimum reflectance between 1500 and 1750 nm to estimate the depth of this water absorption feature (Eitel et al. 2006), which were assumed to be at 1500 and 1650 nm in Table 20.2. Khanna et al. (2007) created the Shortwave Angle Slope Index (SASI, Table 20.2), which is calculated from the angle between the three points: (850 nm, R_{850}), (1650 nm, R_{1650}), and (2200 nm, R_{2200}). Ghulam et al. (2008) created a statistical approach based on a scatter plot of R_{850} versus R_{1650} called the Vegetation Water Stress Index (VWSI, Table 20.2). A trapezoid is

created to surround the data in order to determine the amount of water stress of one pixel compared to the other pixels in the scatter plot (Ghulam et al. 2008). Another line of research is the development of multiband indices, such as the ratio of WI/NDVI (Peñuelas et al. 1997), and the ratio of MSI with the Normalized Multiband Drought Index (Wang and Qu 2007).

The Soil Moisture Experiments 2004 and 2005 were conducted in Southeastern Arizona and Central Iowa, respectively, to test microwave radiometer retrievals of soil moisture. During these experiments, extensive data for CWC were measured and related to Landsat NDII (Yilmaz et al. 2008a, b) and MODIS and AVIRIS data (Cheng et al. 2006, 2008). A single linear relationship was found between NDII and CWC (Fig. 20.3); RMSE of the regression equation was 0.091 kg m^{-2} (Hunt et al. 2011b). Féret et al. (2011) surveyed a large number of leaves from different species and obtained a median LWC equal to 0.11 kg m^{-2}. The RMSE from Fig. 20.3 is 83% of the median LWC value from Féret et al. (2011), so NDII can estimate LAI to an accuracy of ± 0.83 for a land-cover type with known LWC. Asner et al. (2004) used NASA Earth-Observing-1 Hyperion data to show there was a significant reduction in CWC during an imposed drought from rainfall exclusion in an Amazon forest. However, Asner et al. (2004) also showed that LAI decreased, so the amount of CWC decrease attributed to either water stress or LAI is not known.

The individual data sets are not significantly different from the overall regression equation. Comparison of the RMSE in Fig. 20.3 to the median LWC value (Féret et al. 2011) indicates that there may be a limit to the accuracy of CWC achievable from foliar water indices. Therefore, in the next three sections, we discuss three applications for remotely sensed CWC in order to determine the accuracy requirements for a CWC data product.

20.6 Estimation of Vegetation Water Content for Soil Moisture Retrievals

VWC is one of the important parameters required for the retrieval of soil moisture content using microwave sensors (Jackson et al. 2004; Entekhabi et al. 2010). VWC may be estimated directly from the microwave data, but having independent data of VWC from AVHRR/3, MODIS, or VIIRS would help to improve accuracy of the retrieved soil moisture content. The central problem is that VWC is not estimated directly from vegetation moisture indices such as NDII, because of the amount of water in plant stems and other organs (Fig. 20.3).

Two of the Soil Moisture Experiments, 2002 and 2005, were conducted in central Iowa, USA, where 70% of the area are agricultural fields planted in either corn or soybean (Alan K. Stern, personal communication). Because stems support the leaves, biophysical allometric relationships should exist between the amount of water in stems and the amount of water in the foliage (Yilmaz et al. 2008b). Unlike the relationship between NDII and CWC (Fig. 20.3), corn and soybeans have very different relationships between NDII and VWC, because proportionally more stem mass is required to support the larger leaves of corn (Fig. 20.4a).

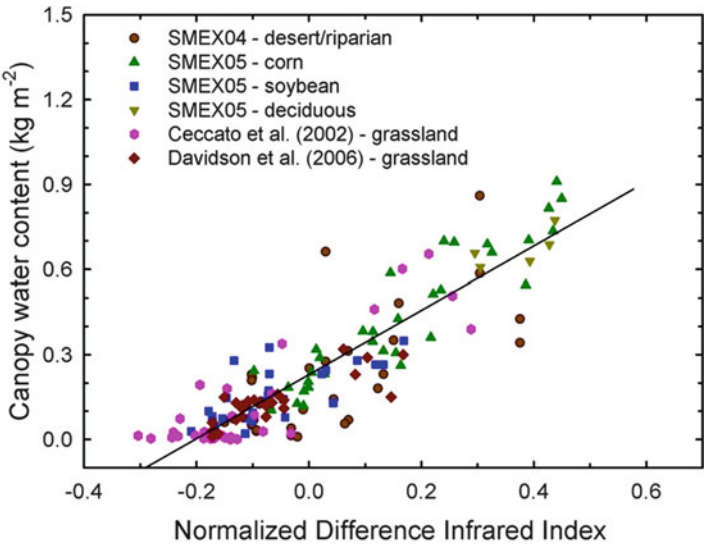

Fig. 20.3 Relationship between canopy water content (*CWC*) and the Normalized Difference Infrared Index (*NDII*) from different data sets (Hunt et al. 2011b). The Soil Moisture Experiment 2004 (*SMEX04*) was conducted in Arizona, USA, and Sonora, Mexico (Yilmaz et al. 2008a), and the Soil Moisture Experiment 2005 (*SMEX05*) was conducted in central Iowa (Yilmaz et al. 2008b). Grassland data sets were kindly provided by (Ceccato et al. 2002b) and (Davidson et al. 2006)

WindSat is a multifrequency polarimetric passive microwave spaceborne radiometer built by the US Naval Research Laboratory for measuring wind speed and direction over the oceans. Li et al. (2010) developed a biophysically based algorithm for estimating VWC and soil moisture content for WindSat. Hunt et al. (2011b) upscaled the NDII-VWC relationship using MODIS to the 50-km diameter WindSat footprint for the 2003–2005 growing seasons. The estimated VWC from MODIS and WindSat were linearly related, but the WindSat VWC was about twice the MODIS VWC (Fig. 20.4b). The lowest frequency on Windsat was 6.9 GHz (C-band), which had strong radio frequency interference, so the lowest frequency used for the WindSat retrievals was 10.7 GHz (Li et al. 2004). Much lower frequencies, such as 1.26–1.41 GHz (L-band), are considerably more sensitive to soil and vegetation water content and thus are being used for the Soil Moisture Active Passive (SMAP) mission (Entekhabi et al. 2010). The merger of the optical and microwave domains for remote sensing of liquid water in vegetation and soil will enable new and better methodologies for the study of water stress and drought.

20.7 Detection of Water Stress

Plant water stress is a general term that encompasses different phenomena at different temporal scales, from short-term leaf wilting to long-term drought (Jones 2007; Passioura 2007). Low water content in the soil causes plants to close

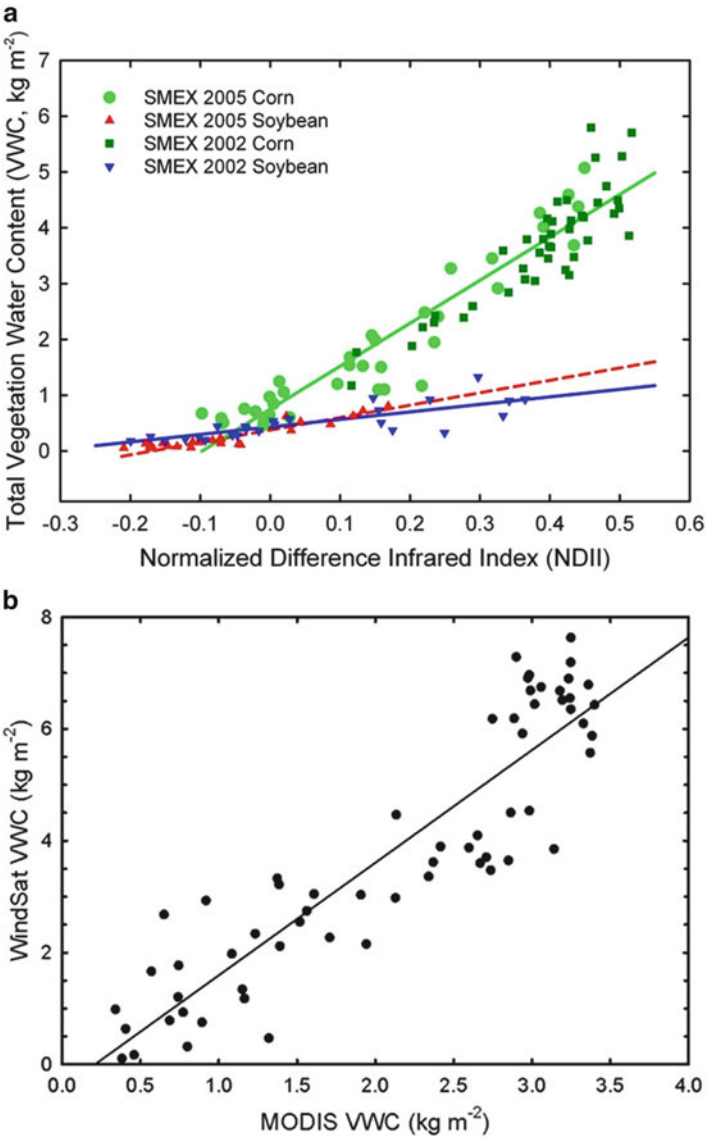

Fig. 20.4 (**a**) Landsat Thematic Mapper NDII and VWC for corn and soybeans during the Soil Moisture Experiments (*SMEX*) 2002 and 2005 in Ames, Iowa (Yilmaz et al. 2008b). (**b**) A comparison between VWC estimated from MODIS and WindSat (circular footprint of 25-km radius) for agricultural areas in central Iowa 2003–2005 (Hunt et al. 2011b)

their stomata (Jones 2007; Passioura 2007; Waring and Landsberg 2011), which decreases latent heat loss and increases canopy temperatures detectable in the thermal infrared (Anderson et al. 2003; Kustas and Anderson 2009). Some species avoid

drought by losing leaves and going dormant, which is detectable using NDVI and other red/near-infrared vegetation indices (see Sect. 20.3). However, plants that tolerate drought will continue to lose water at a slow rate through the leaf cuticle. Therefore, can repeated estimates of LWC or CWC be used to detect plant water stress?

Lenz et al. (2006) determined the pressure-volume curves for different species of trees from different ecosystems in Australia. When the turgor potential was 0 MPa, the mean RWC was 85.7 and 76.9% for species from high- and low-rainfall areas, respectively (Lenz et al. 2006). Using the median LWC value from Féret et al. (2011) of 0.11 kg m^{-2}, the LWC difference required to detect water stress is about 0.016–0.025 kg m^{-2} for repeated measurements on a single leaf. Because of multiplicative effect of LAI, the difference in CWC between stressed and non-stressed plants is larger, which leads to a somewhat ironic result that it may be easier to detect water stress from satellites than it would be in a laboratory.

There have been several studies examining the effect of water stress on leaf and canopy reflectances, but the data reported were either LWC, FMC, or LWC/W_f (Table 20.1), all of which cannot be related unambiguously to the amount of plant water stress. Early studies suggested that water stress could not be detected using reflectances at about 1650-nm wavelength (Jackson et al. 1986; Bowman 1989; Hunt and Rock 1989; Pierce et al. 1990; Riggs and Running 1991, but see Collier 1989). Later studies used more spectral channels and found significant correlations between Ψ (or measures of soil water content) and vegetation water indices (Serrano et al. 2000; Fensholt and Sandholt 2003; Stimson et al. 2005; Elsayed et al. 2011). Rodríguez-Pérez et al. (2007) found that vegetation water indices could not be used to detect stress in grape vineyards, but spectroscopic methods were significant.

During the night, plants draw water from the soil and reach the highest Ψ just before dawn. During the day, water loss from the foliage lowers Ψ. In 2010, Cheng et al. (2011a) used MODIS/ASTER Airborne Simulator (MASTER) morning and afternoon flights over almond and pistachio orchards in the southern San Joaquin Valley, California. Changes in NDII were related to the small changes in CWC (mean difference = 0.021 kg m^{-2}) between the morning and afternoon MASTER overflights, and the RMSE of an NDII-LWC regression was 0.035 kg m^{-2}. Several areas in the orchards had LWC differences greater than 0.04 kg m^{-2} (Cheng et al. 2011b). Therefore, it is possible that water stress may be detected with remote sensing if the LAI of the canopy is sufficiently large. From the numerous studies above, however, detection of water stress using foliar water indices may be problematic for routine applications.

20.8 Estimating Fuel Moisture Content

Another major application for monitoring CWC is to estimate FMC, because it is directly correlated with risk of wildfire. Field crews regularly sample FMC in order to estimate fire danger ratings, which are assumed to be representative over large

areas (Burgan 1988). Burgan (1988) used AVHRR-NDVI data to estimate the spatial extent of vegetation dryness (Burgan and Hartford 1993; Hardy and Burgan 1999). The estimated FMC data are used in fire potential models that include weather, topography, vegetation type, and other variables (Keane et al. 2001, 2010; Dennison et al. 2008; Rollins et al. 2004; Rollins 2009; Chuvieco et al. 2010). However, NDVI is only indirectly correlated to FMC, so remotely sensed CWC has the potential to be more accurate for estimating wildfire risk.

FMC depends on the accurate estimation of both CWC and dry matter (C_m). Because there is a large variation in C_m among different habitats, from thin mesic leaves to thick succulent leaves in xeric habitats, C_m is hard to predict. Further, differences in leaf thickness, dry weight, and morphology cause large variation in FMC for leaves at full turgor. LWC or CWC are linearly related to FMC when vegetation types with similar C_m are considered (Chuvieco et al. 2002, 2003; Zarco-Tejada et al. 2003; Maki et al. 2004; Dennison et al. 2005; Roberts et al. 2006; Dasgupta et al. 2007; Verbesselt et al. 2007). According to Shipley and Vu (2002), differences in C_m among species accounts for 95% of total intraspecies variation. The use of a constant C_m throughout the year could be considered, but an overall decrease is expected during the drought season (Garnier et al. 2001).

Remote sensing C_m directly is difficult because absorption features associated with dry matter are obscured by liquid water in the leaves (Fourty and Baret 1997). With imaging spectrometers that have very high signal to noise, C_m could be estimated at about 1722-nm wavelength, because C_m has an average absorption coefficient somewhat greater than that of liquid water. On the other hand, there is much more water than dry matter so that the 1722-nm absorption feature is not plainly visible in green-leaf reflectance spectra. To uncover the spectrum of dry matter, effects of liquid water "may be removed" by fitting the absorption coefficients of water (Fig. 20.1) to the foliar reflectance spectrum (Gao and Goetz 1994, 1995; Schlerf et al. 2010; Ramoelo et al. 2011; Wang et al. 2011a). The residuals between the foliar reflectance spectrum and the fitted equation show the absorption features associated with dry matter, particularly at the 1,722-nm wavelength (Gao and Goetz 1994, 1995; Wang et al. 2011a). The depth of the residual absorption feature is directly related to C_m (Wang et al. 2011a).

Even for fresh green leaves, C_m subtly influences the foliar reflectance spectrum, so that narrow-band indices are useful for estimating FMC (Wang et al. 2011b, c; Romero et al. 2012). Wang et al. (2011b, c) developed the Normalized Dry Matter Index (NDMI) based on the absorption at 1722-nm wavelength. Because FMC is the ratio of LWC/C_m (Table 20.1), Wang et al. (2011b) hypothesized that the ratio of a foliar water index and the NDMI should be related to FMC. The results are promising (Fig. 20.5), but use of this index will require imaging spectrometers, which probably will not be available for routine monitoring of FMC for another decade.

FMC changes dramatically over a growing season, so data need to be acquired much more frequently than may be possible with imaging spectrometers. Daily weather sensors such as MODIS and VIIRS, however, do not have narrow bands useful for the detection of dry matter. As discussed in the next section, inversion of

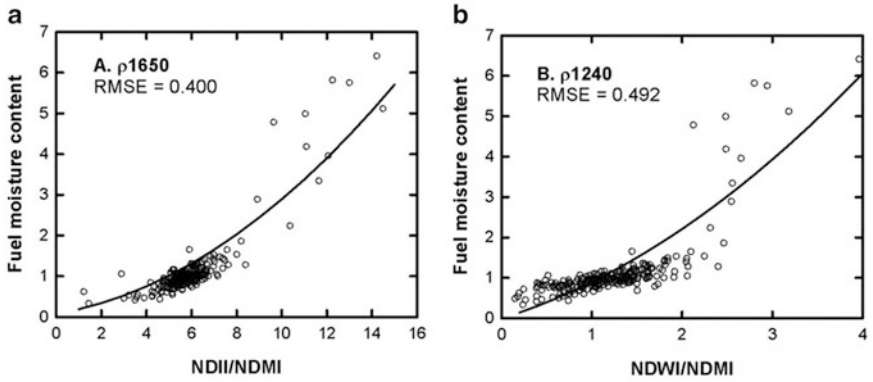

Fig. 20.5 Leaf fuel moisture content (kg H_2O/kg dry matter) predicted by narrow-band indices. (**a**) NDII and (**b**) NDWI are based on the water absorption features at 1650 and 1240 nm, respectively (Table 20.2). NDMI is the Normalized Dry Matter Index [= $(R_{1650} - R_{1722})/(R_{1650} + R_{1722})$, Wang et al. (2011b, c)]. The leaf data were from *Acer rubrum*, *Quercus alba*, and *Zea mays*

radiative transfer models may be the only reliable method to estimate both LWC and C_m with MODIS or VIIRS (Riaño et al. 2005; Hao and Qu 2007; Yebra et al. 2008).

20.9 Robust Inversion Algorithms for Canopy Water Content

The interaction between the incoming radiative energy from the sun and the vegetation canopy and its soil background can be modeled to obtain canopy reflectance (Jacquemoud et al. 2009). Input parameters to the models include LWC, C_m, leaf chlorophyll content, and variables to characterize the canopy structure such as LAI, leaf angle distribution, and sun-target-sensor angles (Jacquemoud et al. 2009). Model inversion starts with canopy reflectances to estimate the input parameters that would result in the same canopy reflectances (Jacquemoud et al. 2000; Zarco-Tejada et al. 2003). Other data sources may be used to narrow down the possible range of solutions for the inversion, for example, land-cover type or LAI (Riaño et al. 2005; Trombetti et al. 2008; Yebra and Chuvieco 2009a, b).

There are several different algorithms that can be used to invert radiative transfer models. A drawback is that the model inversions are computationally very expensive (Fang and Liang 2003), so inversions require optimization techniques to allow the calculation of CWC and other parameters for large data sets. For example, lookup tables can speed the inversion process (Champagne et al. 2003; Yebra et al. 2008). Using the PROSAIL model to train an artificial neural network for the inversion, Trombetti et al. (2008) estimated CWC for the continental USA from

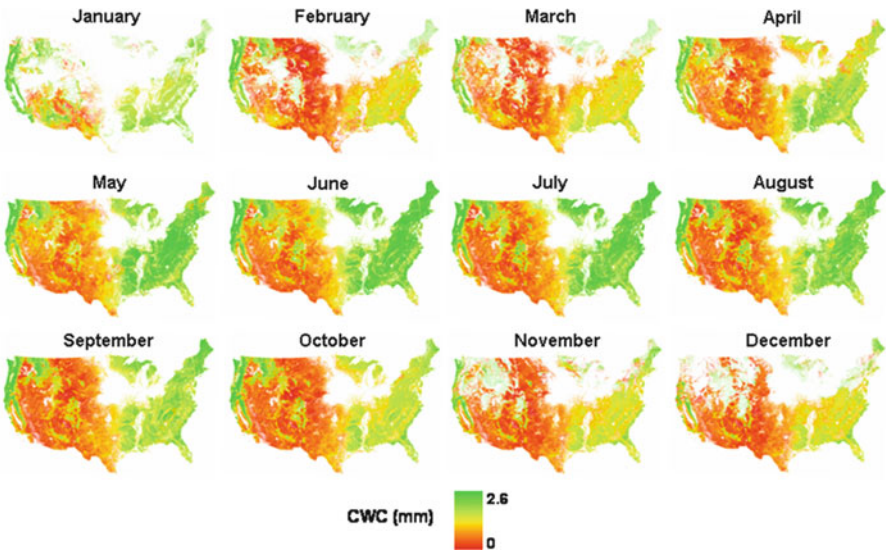

Fig. 20.6 Monthly changes in CWC during 2005 for natural vegetated areas in the USA. Each month is depicted by a single image composite after areas covered by snow, clouds, water, and agricultural land-cover types were masked out (Trombetti et al. 2008)

MODIS, which were put in relation to rainfall and temperature patterns on each eco-region (Fig. 20.6).

20.10 Conclusions

While more research needs to be done to develop and validate inversion algorithms for CWC, it must be realized that much more effort over a longer time period was expended for environmental data records based on NDVI (Tucker et al. 2005). NDVI data collection began in 1982, so the data record can be used to distinguish the contributions of local and global drivers for changing vegetation dynamics (Neigh et al. 2008). The availability of global imagery with shortwave-infrared bands began in 1998 with SPOT Vegetation and AVHRR/3. These sensors have one band in the shortwave infrared, so NDII could be used as a start for a CWC data product. Given the relationships among NDII, CWC, and VWC, NDII could be quickly assimilated into microwave data products for soil moisture.

On the other hand, MODIS and VIIRS have multiple bands at wavelengths at which liquid water absorbs solar radiation, so CWC data products are not limited to NDII or NDWI. Inversions of radiative transfer models have potentially the highest accuracies for retrieval of most vegetation parameters, which are required for applications detecting water stress and monitoring FMC (Riaño et al. 2005). CWC data products are nearing maturity in part by using the synergy between

imaging spectrometers and polar-orbiting environmental satellites for algorithm development (Cheng et al. 2008). As the NASA Terra and Aqua missions are nearing their end, retrieval algorithms are being developed mindful of the capabilities of VIIRS. Most of all, the development of CWC data products had a major advantage by following the examples set during the development and testing of the standard MODIS data products and NDVI environmental data records.

Acknowledgements Funding for this work was provided by the NASA Terrestrial Hydrology Program (Grants NAG5-11260 and NNX09AN51G) and MODIS Science Team (Grant NNX11AF93G).

References

Abrams MD, Kubiske ME (1990) Leaf structural characteristics of 31 hardwood and conifer tree species in central Wisconsin: influence of light regime and shade-tolerance rank. Forest Ecol Manag 31:245–253

Aldakheel YY, Danson FM (1997) Spectral reflectances of dehydrating leaves: measurements and modelling. Int J Remote Sens 18:3683–3690

Allan RP, Soden BJ (2008) Atmospheric warming and the amplification of precipitation extremes. Science 321:1481–1484

Allen WA, Gausman HW, Richardson AJ (1969) Interaction of isotropic light with a compact plant leaf. J Opt Soc Am 59:1376–1379

Anderson MC, Kustas WP, Norman JM (2003) Upscaling and downscaling – a regional view of the soil-plant-air continuum. Agron J 95:1408–1423

Asner GP, Martin RE (2008) Spectral and chemical analysis of tropical forests: scaling from leaf to canopy levels. Remote Sens Environ 112:3958–3970

Asner GP, Nepstad D, Cardinot G, Ray D (2004) Drought stress and carbon uptake in an Amazon forest measured with spaceborne imaging spectroscopy. Proc Natl Acad Sci 101:6039–6044

Bowman WD (1989) The relationship between leaf water status, gas exchange, and spectral reflectance in cotton leaves. Remote Sens Environ 30:249–255

Brown JF, Wardlow BD, Tadesse T, Hayes MJ, Reed BC (2008) The vegetation drought response index (VegDRI): a new integrated approach for monitoring drought stress in vegetation. GISci Remote Sens 45:16–46

Burgan RE (1988) 1988 Revisions to the 1978 national fire danger rating system. Res Pap SE-273. USDA Forest Service, Southeastern Forest Experiment Station, Asheville

Burgan RE, Hartford RA (1993) Monitoring vegetation greenness with satellite data. Gen Tech Rep INT-297. USDA Forest Service, Intermountain Research Station, Ogden

Carter GA (1991) Primary and secondary effects of water content on the spectral reflectance of leaves. Am J Bot 78:916–924

Carter GA (1993) Responses of leaf spectral reflectances to plant stress. Am J Bot 80:239–243

Ceccato P, Gobron N, Flasse S, Pinty B, Tarantola S (2002a) Designing a spectral index to estimate vegetation water content from remote sensing data: part 1 theoretical approach. Remote Sens Environ 82:188–197

Ceccato P, Flasse S, Grégoire JM (2002b) Designing a spectral index to estimate vegetation water content from remote sensing data: part 2 validation and applications. Remote Sens Environ 82:198–207

Champagne CM, Staenz K, Bannari A, McNairn H, Deguise JC (2003) Validation of a hyperspectral curve-fitting model for estimation of plant water content of agricultural canopies. Remote Sens Environ 87:148–160

Cheng T, Riaño D, Koltunov A, Whiting ML, Ustin SL (2011a) Remote detection of water stress in orchard canopies using MODIS/ASTER airborne simulator (MASTER) data. In: Gao W et al (eds) Remote sensing and modeling of ecosystems for sustainability VIII, Proc SPIE, vol 8156. SPIE, Bellingham

Cheng T, Rivard B, Sánchez-Azofeifa A (2011b) Spectroscopic determination of leaf water content using continuous wavelet analysis. Remote Sens Environ 115:659–670

Cheng YB, Ustin SL, Riaño D, Vanderbilt VC (2008) Water content estimation from hyperspectral images and MODIS indexes in Southeastern Arizona. Remote Sens Environ 112:363–374

Cheng YB, Zarco-Tejada PJ, Riaño D, Rueda CA, Ustin SL (2006) Estimating vegetation water content with hyperspectral data for different canopy scenarios: relationships between AVIRIS and MODIS indexes. Remote Sens Environ 105:354–366

Christensen JH, Hewitson B, Busuioc WA, Chen A, Gao X et al (2007) Regional climate projections. In: Solomon S et al (eds) Climate change 2007: the physical science basis. Contribution of working group 1 to the fourth assessment report of the intergovernmental panel on climate change. Cambridge University Press, Cambridge

Chuvieco E, Aguado I, Cocero D, Riaño D (2003) Design of an empirical index to estimate fuel moisture content from NOAA-AVHRR analysis in forest fire danger studies. Int J Remote Sens 24:1621–1637

Chuvieco E, Aguado I, Yebra M, Nieto H, Salas J, Martín MP, Vilar L, Martínez J, Martín S, Ibarra P, Herrera MA, Zamora R (2010) Development of a framework for fire risk assessment using remote sensing and geographic information system technologies. Ecol Model 221:46–58

Chuvieco E, Riaño D, Aguado I, Cocero D (2002) Estimation of fuel moisture content from multitemporal analysis of landsat thematic mapper reflectance data: applications in fire danger assessment. Int J Remote Sens 23:2145–2162

Cohen WB (1991a) Temporal versus spatial variation in leaf reflectance under changing water stress conditions. Int J Remote Sens 12:1865–1876

Cohen WB (1991b) Chaparral vegetation reflectance and its potential utility for assessment of fire hazard. Photogramm Eng Remote Sens 57:203–207

Collier P (1989) Radiometric monitoring of moisture stress in irrigated cotton. Int J Remote Sens 10:1445–1450

Curcio JA, Petty CC (1951) The near infrared absorption spectrum of liquid water. J Opt Soc Am 41:302–304

Dasgupta S, Qu JJ (2009) Soil adjusted water content retrievals in grasslands. Int J Remote Sens 30:1019–1043

Dasgupta S, Qu JJ, Hao X, Bhoi S (2007) Evaluating remotely sensed live fuel moisture estimation for fire behavior predictions in Georgia, USA. Remote Sens Environ 108:138–150

Daughtry CST, Hunt ER (2008) Mitigating the effects of soil and residue water contents on remotely sensed estimates of crop residue cover. Remote Sens Environ 112:1647–1657

Davidson A, Wang S, Wilmhurst J (2006) Remote sensing of grassland-shrubland vegetation water content in the shortwave domain. Int J Appl Earth Observ GeoInform 8:225–236

Delbart N, Kergoat L, Le Toan T, Lhermitte J, Picard G (2005) Determination of phenological dates in boreal regions using normalized difference water index. Remote Sens Environ 97:26–38

Delbart N, Le Toan T, Kergoat L, Fedotova V (2006) Remote sensing of spring phenology in boreal regions: a free of snow-effect method using NOAA-AVHRR and SPOT-VGT data (1982-2004). Remote Sens Environ 101:53–62

Dennison PE, Moritz MA, Taylor RS (2008) Evaluating predictive models of critical live fuel moisture in the Santa Monica Mountains, California. Int J Wildland Fire 17:18–27

Dennison PE, Roberts DA, Peterson SH, Rechel J (2005) Use of normalized difference water index for monitoring live fuel moisture. Int J Remote Sens 26:1035–1042

Downing HG, Carter GA, Holladay KW, Cibula WG (1993) The radiative-equivalent water thickness of leaves. Remote Sens Environ 46:103–107

Eitel JUH, Gessler PE, Smith AMS, Robberecht R (2006) Suitability of existing and novel spectral indices to remotely detect water stress in Populus spp. Forest Ecol Manag 229:170–182

Elsayed S, Mistele B, Schmidhalter U (2011) Can changes in leaf water potential be assessed spectrally? Funct Plant Biol 38:523–533

Entekhabi D, Njoku EG, O'Neill PE, Kellogg KH, Crow WT et al (2010) The soil moisture active passive mission. Proc IEEE 98:704–716

Fang HL, Liang SL (2003) Retrieving leaf area index with a neural network method: simulation and validation. IEEE Trans Geosci Remote Sens 41:2052–2062

Fensholt R, Sandholt I (2003) Derivation of a shortwave infrared water stress index from MODIS near- and shortwave infrared data in a semiarid environment. Remote Sens Environ 87:111–121

Féret JB, François C, Asner GP, Gitelson AA, Martin RE, Bidel LPR, Ustin SL, le Maire G, Jacquemoud S (2008) PROSPECT-4 and -5: advances in the leaf optical properties model separating photosynthetic pigments. Remote Sens Environ 112:3030–3042

Féret JB, François C, Gitelson A, Asner GP, Barry KM, Panigada C, Richardson AD, Jacquemoud S (2011) Optimizing spectral indices and chemometric analysis of leaf chemical properties using radiative transfer modeling. Remote Sens Environ 115:2742–2750

Fourty T, Baret F (1997) Vegetation water and dry matter contents estimated from top-of-the atmosphere reflectance data: a simulation study. Remote Sens Environ 61:34–45

Gao BC (1996) NDWI. A normalized difference water index for remote sensing of vegetation liquid water from space. Remote Sens Environ 58:257–266

Gao BC, Goetz AFH (1990) Column atmospheric water vapor and vegetation liquid water retrievals from airborne imaging spectrometer data. J Geophys Res 95:3549–3564

Gao BC, Goetz AFH (1994) Extraction of dry leaf spectral features from reflectance spectra of green vegetation. Remote Sens Environ 47:369–374

Gao BC, Goetz AFH (1995) Retrieval of equivalent water thickness and information related to biochemical components of vegetation canopies from AVIRIS data. Remote Sens Environ 52:155–162

Gao BC, Montes MJ, Davis CO, Goetz AFH (2009) Atmospheric correction algorithms for hyperspectral remote sensing data of land and ocean. Remote Sens Environ 113:S17–S24

Garnier E, Laurent G, Bellmann A, Debain S, Berthelier P, Ducout B, Roumet C, Navas ML (2001) Consistency of species ranking based on functional leaf traits. New Phytol 152:69–83

Gates DM, Keegan HJ, Schleter JC, Weidner VR (1965) Spectral properties of plants. Appl Optic 4:11–20

Gausman HW, Allen WA, Cardenas R, Richardson AJ (1970) Relation of light reflectance to histological and physical evaluations of cotton leaf maturity. Appl Opt 9:545–552

Govender M, Dye PJ, Weiersbye IM, Witkowski ETF, Ahmed F (2009) Review of commonly used remote sensing and ground-based technologies to measure plant water stress. Water SA 35:741–752

Green RO, Painter TH, Roberts DA, Dozier J (2006) Measuring the expressed abundance of the three phases of water with an imaging spectrometer over snow. Water Resour Res. doi:10.1029/2005WR004509

Ghulam A, Li ZL, Qin Q, Yimit H, Wang J (2008) Estimating crop water stress with ETM+ NIR and SWIR data. Agr Forest Meteorol 148:1679–1695

Hao X, Qu JJ (2007) Retrieval of real-time live fuel moisture content using MODIS measurements. Remote Sens Environ 108:130–137

Hardisky MA, Klemas V, Smart RM (1983) The influence of soil-salinity, growth form, and leaf moisture on the spectral radiance of Spartina alterniflora canopies. Photogramm Eng Remote Sens 49:77–83

Hardy CC, Burgan RE (1999) Evaluation of NDVI for monitoring live moisture in three vegetation types of the Western U.S. Photogramm Eng Remote Sens 65:603–610

Huete AR (1988) A soil-adjusted vegetation index (SAVI). Remote Sens Environ 25:295–309

Huete A, Didan K, Miura T, Rodriguez EP, Gao X, Ferreira LG (2002) Overview of the radiometric and biophysical performance of the MODIS vegetation indices. Remote Sens Environ 83:195–213

Hunt ER, Daughtry CST, Qu JJ, Wang L, Hao X (2011a) Comparison of hyperspectral retrievals with vegetation water indices for leaf and canopy water content. In: Gao W et al (eds) Remote sensing and modeling of ecosystems for sustainability VIII, Proc SPIE, vol 8156. SPIE, Bellingham

Hunt ER, Li L, Yilmaz MT, Jackson TJ (2011b) Comparison of vegetation water contents derived from shortwave-infrared and passive microwave sensors over central Iowa. Remote Sens Environ 115:2376–2383

Hunt ER, Rock BN (1989) Detection of changes in leaf water content using near- and middle-infrared reflectances. Remote Sens Environ 30:43–54

Hunt ER, Rock BN, Nobel PS (1987) Measurement of leaf relative water content by infrared reflectance. Remote Sens Environ 22:429–435

Jacquemoud S, Bacour C, Poilve H, Frangi JP (2000) Comparison of four radiative transfer models to simulate plant canopies reflectance: direct and inverse mode. Remote Sens Environ 74:471–481

Jacquemoud S, Baret F (1990) Prospect – a model of leaf optical-properties spectra. Remote Sens Environ 34:75–91

Jacquemoud S, Verhoef W, Baret F, Bacour C, Zarco-Tejada PJ, Asner GP, Francois C, Ustin SL (2009) PROSPECT plus SAIL models: a review of use for vegetation characterization. Remote Sens Environ 113:S56–S66

Jackson RD, Slater PN, Pinter PJ (1983) Discrimination of growth and water stress in wheat by various vegetation indices through clear and turbid atmospheres. Remote Sens Environ 13:187–208

Jackson RD, Pinter PJ, Reginato RJ, Idso SB (1986) Detection and evaluation of plant stresses for crop management decisions. IEEE Trans Geosci Remote Sens 24:99–106

Jackson TJ, Chen D, Cosh M, Li F, Anderson M, Walthall C, Doraiswamy PC, Hunt ER (2004) Vegetation water content mapping using landsat data derived normalized difference water index for corn and soybeans. Remote Sens Environ 92:475–482

Ji L, Zhang L, Wylie BK, Rover J (2011) On the terminology of the spectral vegetation index (NIR-SWIR)/(NIR+SWIR). Int J Remote Sens 32:6901–6909

Jones HG (2007) Monitoring plant and soil water status: established and novel methods revisited and their relevance to studies of drought tolerance. J Exp Bot 58:119–130

Keane RE, Burgan R, van Wagtendonk J (2001) Mapping wildland fuels for fire management across multiple scales: integrating remote sensing, GIS, and biophysical modeling. Int J Wildland Fire 10:301–319

Keane RE, Drury SA, Karau EC, Hessburg PF, Reynolds KM (2010) A method for mapping fire hazard and risk across multiple scales and its application in fire management. Ecol Model 221:2–18

Khanna S, Palacios-Orueta A, Whiting ML, Ustin SL, Riaño D, Litago J (2007) Development of angle indexes for soil moisture estimation, dry matter detection and land-cover discrimination. Remote Sens Environ 109:154–165

Kimes DS, Markham BL, Tucker CJ, McMurtrey JE (1981) Temporal relationships between spectral response and agronomic variables of a corn canopy. Remote Sens Environ 11:401–411

Kogan F, Gitelson A, Zakarin E, Spivak L, Lebed L (2003) AVHRR-based spectral vegetation index for quantitative assessment of vegetation state and productivity: calibration and validation. Photogramm Eng Remote Sens 69:899–906

Kustas WP, Anderson MC (2009) Advances in thermal infrared remote sensing for land surface modeling. Agr Forest Meteorol 149:2071–2081

Lenz TI, Wright IJ, Westoby M (2006) Interrelations among pressure-volume curve traits across species and water availability gradients. Physiol Plant 127:423–433

Li L, Cheng YB, Ustin SL, Hua XT, Riaño D (2008) Retrieval of vegetation equivalent water thickness from reflectance using genetic algorithm (GA)-partial least squares (PLS) regression. Adv Space Res 41:1755–1763

Li L, Gaiser PW, Gao BC, Bevilacqua RM, Jackson TJ, Njoku EG, Rëdiger C, Calvet JC, Bindlish R (2010) WindSat global soil moisture retrieval and validation. IEEE Trans Geosci Remote Sens 48:2224–2241

Li L, Njoku EG, Im E, Chang PS, St. Germain K (2004) A preliminary survey of radio-frequency interference over the U.S. In AQUA AMSR-E data. IEEE Trans Geosci Remote Sens 42:380–390

Lichtenthaler HK, Gitelson A, Lang M (1996) Non-destructive determination of chlorophyll content of a green and an aurea mutant of tobacco by reflectance measurements. J Plant Physiol 148:483–493

Liu Y, Stanturf J, Goodrick S (2010) Trends in global wildfire potential in a changing climate. Forest Ecol Manag 259:685–697

Maki M, Ishiahra M, Tamura M (2004) Estimation of leaf water status to monitor the risk of forest fires by using remotely sensed data. Remote Sens Environ 90:441–450

Miller JR, Steven MD, Demetriades-Shah TH (1992) Reflection of layered bean leaves over different soil backgrounds: measured and simulated spectra. Int J Remote Sens 13:3273–3286

Neigh CSR, Tucker CJ, Townshend JRG (2008) North American vegetation dynamics observed with multi-resolution satellite data. Remote Sens Environ 112:1749–1772

Nobel PS (2009) Physicochemical and environmental plant physiology, 4th edn. Academic, San Diego

NRC (2004) Climate data records from environmental satellites: interim report. National research council committee on climate data records from NOAA operational satellites. National Academies Press, Washington

Olsen CE (1967) Optical sensing the moisture content in fine forest fuels: final report. Willow Run Laboratories, University of Michigan, Ann Arbor

Palmer KF, Williams D (1974) Optical properties of water in the near infrared. J Opt Soc Am 64:107–111

Passioura J (2007) The drought environment: physical, biological and agricultural perspectives. J Exp Bot 58:113–117

Peñuelas J, Filella I, Biel C, Serrano L, Savé R (1993) The reflectance at the 950–970 nm region as an indicator of plant water status. Int J Remote Sens 14:1887–1905

Peñuelas J, Piñol J, Ogaya R, Filella I (1997) Estimation of plant water concentration by the reflectance water index WI (R900/R970). Int J Remote Sens 18:2869–2875

Pierce LL, Running SW, Riggs GA (1990) Remote detection of canopy water stress in coniferous forests using the NS001 thematic mapper simulator and the thermal infrared multispectral scanner. Photogramm Eng Remote Sens 56:579–586

Poorter H, Niimenets Ü, Poorter L, Wright IJ, Villar R (2009) Causes and consequences of variation in leaf mass per area (LMA): a meta-analysis. New Phytol 182:565–588

Ramoelo A, Skidmore AK, Schlerf M, Mathieu R, Heitkönig IMA (2011) Water-removed spectra increase the retrieval accuracy when estimating savanna grass nitrogen and phosphorus concentrations. ISPRS J Photogramm Remote Sens 66:408–417

Riaño D, Vaughan P, Chuvieco E, Zarco-Tejada PJ, Ustin SL (2005) Estimation of fuel moisture content by inversion of radiative transfer models to simulate equivalent water thickness and dry matter content: analysis at leaf and canopy level. IEEE Trans Geosci Remote Sens 43:819–826

Riggs GA, Running SW (1991) Detection of canopy water stress in conifers using the Airborne Imaging Spectrometer. Remote Sens Environ 35:51–68

Roberts DA, Brown K, Green R, Ustin SL, Hinckley T (1998) Investigating the relationship between liquid water and leaf area in clonal populus. In: Summaries of the 7th annual JPL earth science workshop. Jet Propulsion Laboratory, Pasadena

Roberts DA, Dennison PE, Peterson S, Sweeny S, Rechel J (2006) Evaluation of Airborne Visible/Infrared Imaging Spectrometer (AVIRIS) and Moderate Resolution Imaging Spectrometer (MODIS) measures of live fuel moisture and fuel condition in a shrubland ecosystem in southern California. J Geophys Res. doi:10.1029/2005JG000113

Roberts DA, Ustin SL, Ogenjemiyo S, Greenberg J, Dobrowski SZ, Chen J, Hinckley TM (2004) Spectral and structural measures of northwest forest vegetation at leaf to landscape scales. Ecosystems 7:545–562

Rodríguez-Pérez JR, Riaño D, Carlisle E, Ustin S, Smart DR (2007) Evaluation of hyperspectral reflectance indexes to detect grapevine water status in vineyards. Am J Enol Viticult 58:302–317

Rollins MG (2009) LANDFIRE: a nationally consistent vegetation, wildland fire, and fuel assessment. Int J Wildland Fire 18:235–249

Rollins MG, Keane RE, Parsons RA (2004) Mapping fuels and fire regimes using remote sensing, ecosystem simulation, and gradient modeling. Ecol Appl 14:75–95

Romero A, Aguado I, Yebra M (2012) Estimation of dry matter content in leaves using normalized indexes and PROSPECT model inversions. Int J Remote Sens 33:396–414

Rouse JW, Haas RW, Schell JA, Deering DH, Harlan JC (1974) Monitoring the vernal advancement and retrogradation (greenwave effect) of natural vegetation. NASA GSFC, Greenbelt

Schlerf M, Atzberger C, Hill J, Buddenbaum H, Werner W, Schüler G (2010) Retrieval of chlorophyll and nitrogen in Norway spruce (Picea abies L. Karst.) using imaging spectroscopy. Int J Appl Earth Observ Geoinform 12:17–26

Schwarz MD, Reed BC, White MA (2002) Assessing satellite-derived start-of-season measures in the conterminous USA. Int J Clim 22:1793–1805

Serrano L, Ustin SL, Roberts DA, Gamon JA, Peñuelas J (2000) Deriving water content of chaparral vegetation from AVIRIS data. Remote Sens Environ 74:570–581

Shipley B, Vu TT (2002) Dry matter content as a measure of dry matter concentration in plants and their parts. New Phytol 153:359–364

Sims DA, Gamon JA (2003) Estimation of vegetation water content and photosynthetic tissue area from spectral reflectance: a comparison of indices based on liquid water and chlorophyll absorption features. Remote Sens Environ 84:526–537

Stimson HC, Breshears DD, Ustin SL, Kefauver SC (2005) Spectral sensing of foliar water conditions in two co-occurring conifer species: pinus edulis and Juniperus monosperma. Remote Sens Environ 96:108–118

Trombetti M, Riaño D, Rubio MA, Cheng YB, Ustin SL (2008) Multitemporal vegetation canopy water content retrieval using artificial neural networks for the USA. Remote Sens Environ 112:203–215

Tucker CJ (1979) Red and photographic infrared linear combinations for monitoring vegetation. Remote Sens Environ 8:127–150

Tucker CJ (1980) Remote sensing of leaf water content in the near infrared. Remote Sens Environ 10:23–32

Tucker CJ, Pinzon JE, Brown ME, Slayback DA, Pak EW, Mahoney R, Vermote EF, Saleous NE (2005) An extended AVHRR 8-km NDVI dataset compatible with MODIS and SPOT vegetation NDVI data. Int J Remote Sens 26:4485–4498

Tucker CJ, Townshend JRG, Goff TE (1985) African land-cover classification using satellite data. Science 227:369–375

Ustin SL, Riaño D, Hunt ER (2012) Estimating canopy water content from spectroscopy. Israel J Plant Sci 60:9–23

Ustin SL, Roberts DA, Gamon JA, Asner GP, Green RO (2004) Using imaging spectroscopy to study ecosystem processes and properties. Bioscience 54:523–534

Ustin SL, Roberts DA, Pinzón J, Jacquemoud S, Gardner M, Scheer B, Castañeda CM, Palacios-Orueta A (1998) Estimating canopy water content of chaparral shrubs using optical methods. Remote Sens Environ 65:280–291

Verbesselt J, Somers B, Lhermitte S, Jonckheere I, van Aardt J, Coppin P (2007) Monitoring herbaceous fuel moisture content with SPOT VEGETATION time-series for fire risk prediction in savanna ecosystems. Remote Sens Environ 108:357–368

Wang L, Hunt ER, Qu JJ, Hao X, Daughtry CST (2011a) Estimating the dry matter content of leaves from the residuals between leaf and water reflectance. Remote Sens Lett 2:137–145

Wang L, Hunt ER, Qu JJ, Hao X, Daughtry CST (2011b) Towards estimation of canopy foliar biomass with spectral reflectance measurements. Remote Sens Environ 115:836–840

Wang L, Qu JJ, Hao X, Hunt ER (2011c) Estimating dry matter content from spectral reflectances for green leaves of different species. Int J Remote Sens 32:7097–7109

Wang L, Qu JJ (2007) NMDI: a normalized multi-band drought index for monitoring soil and vegetation moisture with satellite remote sensing. Geophys Res Lett. doi:10.1029/2007GL031021

Waring RH, Landsberg JJ (2011) Generalizing plant-water relations to landscapes. J Plant Ecol 4:101–113

Xiao X, Boles S, Frolking S, Salas W, Moore B, Li C (2002a) Observation of flooding and rice transplanting of paddy rice fields at site to landscape scales in China using VEGETATION sensor data. Int J Remote Sens 23:3009–3022

Xiao X, Boles S, Liu J, Zhaung D, Liu M (2002b) Characterization of forest types in Northeastern China, using multi-temporal SPOT-4 VEGETATION sensor data. Remote Sens Environ 82:335–348

Yebra M, Chuvieco E (2009a) Generalization of a species-specific look-up table for fuel moisture content assessment. IEEE J Select Topic Appl Earth Observ Remote Sens 2:21–26

Yebra M, Chuvieco E (2009b) Linking ecological information and radiative transfer models to estimate fuel moisture content in the Mediterranean region of Spain: solving the ill-posed inverse problem. Remote Sens Environ 113:2403–2411

Yebra M, Chuvieco E, Riaño D (2008) Estimation of live fuel moisture content from MODIS images for fire risk assessment. Agr Forest Meteorol 148:523–536

Yilmaz MT, Hunt ER, Goins LD, Ustin SL, Vanderbilt VC, Jackson TJ (2008a) Vegetation water content during SMEX04 from ground data and landsat 5 thematic mapper imagery. Remote Sens Environ 112:350–362

Yilmaz MT, Hunt ER, Jackson TJ (2008b) Remote sensing of vegetation water content from equivalent water thickness using satellite imagery. Remote Sens Environ 112:2514–2522

Zarco-Tejada PJ, Rueda CA, Ustin SL (2003) Water content estimation in vegetation with MODIS reflectance data and model inversion methods. Remote Sens Environ 85:109–124

Zhang QX, Li QB, Zhang GJ (2011) Scattering impact analysis and correction for leaf biochemical parameter estimation using VIS-NIR spectroscopy. Spectroscopy 26:28–39

Chapter 21
Recent Advances and Challenges of Monitoring Climate Change from Space

John J. Qu, Alfred M. Powell Jr., and Mannava V.K. Sivakumar

Abstract Extreme weather and climate events have over the years impacted human society and have currently become a more complex challenge with the changing climate. Many more climate change consequences have been recognized due to various environmental and social stresses in the last few decades. One way to assess the impacts of observed climate change is by viewing the Earth from space. Monitoring climate change from space is one of the most important and challenging responsibilities. Satellite remote sensing measurements can make the task of monitoring the entire Earth relatively easy with low costs; thus, environment and weather satellite measurements provide the ability to observe and predict the Earth's environment and weather while improving the accuracy. Satellite observations make a significant contribution to the Essential Climate Variables (ECVs) and their associated data sets and products of the Global Climate Observing System (GCOS) which was established to ensure that all users have access to the climate observations, data records, and information which they require to address pressing climate-related concerns. Generating climate data records with multi-mission and multi-instrument measurements is difficult and complex because of the spectral spatial, temporal, and angular coverage issues. Cross-sensor calibration and

J.J. Qu (✉)
Department of GGS/College of Science (COS), Environmental Science and Technology Center (ESTC), George Mason University (GMU), MS 6A2, Fairfax, VA 22030, USA
e-mail: jqu@gmu.edu

A.M. Powell Jr.
Center for Satellite Applications and Research (STAR)/NOAA/NESDIS, World Weather Building, 5830 University Research Court, College Park, MD 20746, USA
e-mail: Al.Powell@noaa.gov

M.V.K. Sivakumar
Climate Prediction and Adaptation Branch (CLPA), Climate and Water Department (CLW), World Meteorological Organization, 7 bis Avenue de la Paix, Case Postale No. 2300, Geneva 2 CH-1211, Switzerland
e-mail: msivakumar@wmo.int

J.J. Qu et al. (eds.), *Satellite-based Applications on Climate Change*,
DOI 10.1007/978-94-007-5872-8_21,

validation play a pivotal role relative to understanding the climate and its trends—an important issue. The applications of satellite data for climate change are summarized based on the 20 chapters in this book, and recent advances of climate change monitoring from space are discussed. Monitoring climate change from space presents major challenges that will be briefly summarized. The era of collecting satellite images from space is rapidly being replaced by the era of "Satellite Climatology" as the time series of satellite measurements has reached over 30 years of extended applications and use.

21.1 Introduction

Monitoring climate change from space is one of most important and challenging responsibilities. Satellite remote sensing measurements can make the task of monitoring the entire Earth relatively easy with low costs. Satellite measurements provide the ability to observe and predict the Earth's environment and weather more reliably. Accurate, reliable, and consistent measurements from multiple satellite sensors are critical for weather prediction and climate change studies. However, each satellite instrument has different spectral, spatial, and temporal specifications and is usually calibrated separately with different methodologies. There is often bias between different satellite measurements which will impact trend assessments and induce errors if not corrected. Satellite observations make a significant contribution to the Essential Climate Variables (ECVs) and their associated data sets and products of the Global Climate Observing System (GCOS) which was established to ensure that all users have access to the climate observations, data records, and information which they require to address pressing climate-related concerns. The recent advances and challenges of monitoring climate change with multi-instrument measurements from space will be discussed. The state of the art of collecting satellite images from space is rapidly being replaced by the era of "Satellite Climatology" as the time series of satellite measurements has reached over 30 years of extended applications and use. A discussion of recent satellite application advances from the previous 20 chapters will be summarized.

21.2 Summary of This Book

The summary of the previous 20 chapters includes different climate zones including the tropical, middle-latitude, high-latitude, and Arctic climates. This book was organized in four sections: (1) overview of satellite-based measurements and applications, (2) atmospheric and climate applications, (3) hydrological and cryospheric applications, and (4) land surface and ecological applications. Because the long-term climate monitoring system from space is very complex, only a small but important subset of satellite progress was presented. In Chap. 1, an introduction to satellite-based applications and research for understanding climate change is given by the book editors (Powell et al. 2013). The background information highlights the early

efforts and major objectives of satellite monitoring and applications. As the use of satellites advanced, the objectives for their use changed from tracking cloud patterns to specialized products like snow cover, precipitation, and vegetation indices. As satellite monitoring progressed, it became evident that new challenges associated with using satellite data for long-term monitoring of climate change require better approaches for calibration, derived products, trend uncertainty, and measurement quality. As the global satellite constellation continues to expand and our knowledge base matures, future satellite measurement issues will center on calibration techniques as the foundation for all the derived products and services. To monitor climate change effectively requires a stable and consistent baseline from which to judge the change with significantly reduced uncertainties.

In Chap. 2, Drs. Cao et al. (2013) present the fundamental issues in satellite instrument calibration and provide an overview of the current status, challenges, and latest developments in inter-satellite calibration.

MODIS is a key instrument of the NASA Earth Observing System (EOS) with 36 spectral bands covering wavelengths from 0.41 to 14.4 μm and three nadir spatial resolutions: 250 m, 500 m, and 1 km. Terra and Aqua MODIS have produced more than 10 years of global data sets that have significantly helped scientists to better understand the Earth system. In Chap. 3, Drs. Salomonson and Xiong (2013) discuss the MODIS instrument characterization and performance. Potential applications of MODIS data products for climate studies are illustrated, and the follow-on instrument, VIIRS, is briefly introduced.

In Chap. 4, Drs. Powell and Xu (2013) compare the temperature responses to climate forcings in winter (December–February) between the pre- (1958–1978) and post- (1979–2002) periods of satellite data assimilation using multiple linear regression analysis for the lower stratospheric and the middle tropospheric temperature changes associated with key climate forcings: solar variability, ENSO, QBO, and stratospheric aerosols for the two periods based on three temperature data sets. The analysis reaffirms the core forcing parameters for atmospheric temperature trends, such as solar radiation, ENSO, QBO, and stratospheric aerosols, and demonstrates similar features and trends of approximately the same magnitude. The discrepancies between the pre- and post-satellite era analyses are also discussed.

Long-term high-quality consistent fundamental climate data records (FCDRs) are critical in understanding the complicated changes of the Earth system. Although there have been many satellite instruments available for Earth observation, the integration of remote sensing measurements from different sensors is necessary for constructing consistent long-term climate data records. In Chap. 5, Drs. Hao and Qu (2013) introduce the band mapping approach for FCDR generation and demonstrate results for the thermal infrared bands of AVHRR and MODIS. Quantitative relationships between thermal emissive measurements of different sensors are investigated towards the construction of thermal emissive FCDRs.

In Chap. 6, Drs. Ferraro and Smith (2013) discuss various satellite precipitation retrieval methods and applications of global precipitation data sets. Various precipitation retrieval algorithms are reviewed, and the strengths and weaknesses of these algorithms are discussed. In addition, the emerging techniques and products using integrated multiple satellite measurements for the best possible historical precipitation estimation are presented.

Global historical precipitation record is very important for climate change studies and climate model evaluations. In Chap. 7, Dr. Smith (2013) reviews approaches for reconstructing the historical precipitation record, and demonstrates the feasibility of reconstructing large-scale features of oceanic precipitation variations from 1900. Possible improvements in the long-term reconstruction using data assimilation and integration of longer satellite-based observations are discussed.

In Chap. 8, Dr. Zou (2013) reviews the simultaneous nadir overpass (SNO) method for developing a fundamental climate data record (FCDR) from the Microwave Sounding Unit (MSU) and the Advanced MSU observations onboard NOAA polar orbiting satellite series. Various residual bias correction algorithms, including antenna pattern corrections, limb adjustments, diurnal drift corrections, geolocation-dependent bias removal, and channel frequency differences, are discussed. The effects of an improved inter-calibrated FCDR on the reanalysis bias correction are demonstrated. The atmospheric temperature TCDR and applications are also described.

Arctic change is of considerable interest for climate change studies, and satellite remote sensing measurements are critical for monitoring and evaluating changes in the Arctic. Dr. Key (2013) discusses satellite-based approaches for monitoring Arctic climate characteristics in Chap. 9. Methods and applications for retrieving physical variables of the Arctic climate system, such as winds, clouds, surface temperature and albedo, and sea ice, are summarized. Applications of satellite remote sensing data products for climate change detection are discussed.

Considerable societal and economic importance can be associated with reliably monitoring the intensity of tropical cyclones and investigating the impacts of global climate change on hurricane tracks and characteristics. In Chap. 10, Drs. DeMaria et al. (2013) review methods for estimating tropical cyclone intensity with satellite remote sensing techniques, including visible, infrared, and microwave instruments. Integrated solutions for TC forecasting and monitoring based on multiple instruments are suggested. Possible improvements in the next generation of satellites for TC monitoring are also discussed.

A changing climate impacts human lives. The impacts are derived from process interactions between the Earth system components: the atmosphere, hydrosphere, lithosphere, biosphere, and anthrosphere. In Chap. 11, Drs. Chiu and Gao addressed the satellite-based ocean surface turbulent flux, which is one of the important parameters for monitoring and predicting global climate change. The ocean processes interact with the Earth's key cycles: the energy cycle, water cycle, and other biogeochemical cycles. The authors discuss the transfer mechanisms occurring at the air-sea interface, present the bulk formulae for estimating the flux transfers and introduce the bulk parameters from satellite observations, describe various research or operational products that integrate the bulk parameters to produce surface flux products, and present an assessment of these products. The use of these products in climate research and operational applications is also discussed in Chap. 11 (Chiu and Gao 2013).

Snow cover is an important indicator of global climate change and plays a key role in the climate system. Satellite remote sensing provides an excellent method to observe the snow cover, both in visible and passive microwave regions of the spectrum. In Chap. 12, Dr. Li Xu introduces satellite-based applications of snow cover. The role of snow in the climate system, satellite snow observations and

monitoring, snow-climate interaction, and snow-atmosphere coupling strength was reviewed in this chapter (Xu 2013).

Evapotranspiration is a crucial variable for understanding the impact of the climate on vegetation health and is an important indicator for monitoring global and regional climate changes. It is directly associated with energy and water cycles and has critical impacts on irrigated crops, ecosystem services, and water resource management. In Chap. 13, Drs. Martin, Allen, and Brazil estimate evapotranspiration with satellite remote sensing for irrigation water management. MODIS and Landsat data products and the METRIC surface energy method were used to estimate crop evapotranspiration in three Moroccan irrigation sectors. They found that the satellite remote sensing data analysis delivered useful results for large irrigated areas with little information on crop consumptive use and irrigation efficiency, and almost no information on groundwater abstraction (Martin et al. 2013).

Satellite measurements are an important component of the global snow observing system. In Chap. 14, Dr. Romanov presents an overview of the satellite-based applications of snow cover. The reviewed techniques include an interactive approach where snow maps are manually generated by human analysts through a visual examination of satellite imagery. The most recent fully automated algorithms that utilize satellite observations in multiple bands in the optical, infrared, and microwave spectral range are discussed. The author concluded that satellite-based retrievals of the snow extent and the spatial distribution of snow cover are accurately and spatially detailed (Romanov 2013).

Accurate measurements of global rainfall are crucial for better understanding the water and energy cycles of the climate system. The lack of global gauge networks, especially over the ocean, in mountainous terrains, or in remote areas, points to satellite observation as the only viable method for global scale rainfall monitoring. In Chap. 15, Drs. Chiu, Gao, and Shi discuss the recent advances of climate-scale oceanic rainfall based on passive microwave radiometry. The authors describe the model structure and the underlying theory, examine the product output parameters, and discuss example techniques related to climate studies, future work, and potential product improvements.

Vegetation monitoring is crucial for understanding the sustainability of our planet and represents an important approach to monitor climate change. Satellite remote sensing measurements provide a valuable data source for monitoring vegetation from space. In Chap. 16, Dr. Gao discusses recent studies using integrated high spatial resolution Landsat and high temporal resolution MODIS data for vegetation monitoring. Dr. Gao describes three categories of approach to integrate the two satellite data sources. The data fusion approach synthesizes Landsat and MODIS data to produce the fused data products with high spatial and temporal resolution. Each approach has its advantages and limitations. These approaches can be applied to other similar sensors. Their advantages and limitations are also discussed (Gao 2013).

Vegetation phenology describing the seasonal cycle of plants is currently one of the main concerns in the study of climate change and carbon balance estimation in ecosystems. Monitoring phenology from space is another recent advance in satellite-based applications. Satellite-derived information has been demonstrated

to be an important source for detecting vegetation phenology. In Chap. 17, Drs. Li and Qu show that satellite-derived information has demonstrated the value of vegetation phenology observations from space. The advances and challenges and future applications are discussed. The well-validated vegetation phenology from satellite measurements will contribute to the improvement in ecosystem process models (Li and Qu 2013).

Marine phytoplankton is another ideal indicator of environment and climate change. In Chap. 18, Uz et al. (2013) describe monitoring a sentinel species from satellites, i.e., detecting *Emiliania huxleyi* using 25 years of AVHRR data products. They found that AVHRR offers the longest continuous global data set of visible reflectance which can be used to identify regional *E. huxleyi* blooms. The declining long-term trend in bloom surface area was correlated to warm sea-surface temperature anomalies. The trend was weakly correlated to increased mixed layer depths. They analyzed the well-established ocean color satellite measurements of *E. huxleyi* blooms around the world via a data set extension back to 1982 by identifying them in AVHRR imagery. The authors concluded the hypothesized relationship between *E. huxleyi* bloom events and warming temperatures does not hold over the long term.

In Chap. 19, Drs. Sun and Yu give an overview of the recent advances on the retrieval of land surface temperature (LST) from satellite observations. Special attention has been paid to the LST retrieval from GOES satellites. A detailed introduction is given about the literature review, the existing problems and challenges, and the advantages of geostationary satellites and the GOES instrument. Special attention was paid to the LST retrieval from geostationary GOES satellites. Algorithm theoretical basis (both physical and mathematical) has been provided. LST product is going to be generated from current GOES satellites from their proposed dual window algorithm (Sun and Yu 2013).

Remote sensing of leaf, canopy, and vegetation water content for satellite environmental data records (EDRs) is discussed by Dr. Hunt in Chap. 20. Those EDRs can be used to generate CDRs. The temporal record of multiple instruments, such as MODIS, SPOT Vegetation, and AVHRR/3 sensors, and the future record from VIIRS will create a global environmental data record of canopy water content for climate change studies (Hunt et al. 2013). Measurement continuity with multi-mission and multisensor measurements is also discussed this chapter.

21.3 Challenges of Monitoring Climate Change from Space

One of the most challenging and critical issues facing climatologists during the next century is related to the operation of a long-term climate monitoring system capable of delivering continuous and reliable data and information (Karl 1996). The operation of environmental data services is an important and challenging responsibility. The growing needs for environmental data are coupled with opportunities for more effective environmental information services, for a few new types of satellite

observations. Better information services will result in improvements in prediction capabilities and in the products offered by advances in technology (both hardware and software). Research will bring new insights via an improved understanding and use of the data (National Research Council, 2003). There are many challenges related to generating climate data records (CDRs) from international multi-mission and multi-satellite measurements. First, because each satellite instrument has different spectral, spatial, angular, and temporal measurements, cross-sensor calibration and validation has become a critical issue. Second, because there are many satellites in space, international collaboration is needed. Third, satellites provide the best spatial and temporal coverage; even so, satellite measurements should be combined with in situ observations and model simulations to monitor and forecast climate changes. Fourth, in situ ground measurements are essential for monitoring climate change. Integrating satellite, in situ measurements, model simulation, GIS, and decision support system (DSS) is the future direction of the Global Earth Observing System (GEOS) and the GCOS that will span the era of "Satellite Climatology."

References

Cao C, Chen R, Uprety S (2013) Calibrating a system of satellites. In: Qu JJ, Powell A, Sivakumar MVK (eds) Satellite-based applications to climate change. Springer, New York

Chiu L, Gao S (2013) Satellite-based ocean surface turbulent fluxes. In: Qu JJ, Powell A, Sivakumar MVK (eds) Satellite-based applications to climate change. Springer, New York

Chiu L, Gao S. and Shin D-B (2013) Climate-Scale Oceanic Rainfall Based on Passive Microwave Radiometry. In: Qu JJ, Powell A, Sivakumar MVK (eds) Satellite-based applications to climate change. Springer, New York

DeMaria M, Knaff JA, Zehr R (2013) Assessing hurricane intensity using satellites. In: Qu JJ, Powell A, Sivakumar MVK (eds) Satellite-based applications to climate change. Springer, New York

Ferraro R, Smith T (2013) Global precipitation monitoring. In: Qu JJ, Powell A, Sivakumar MVK (eds) Satellite-based applications to climate change. Springer, New York

Gao F (2013) Integrating landsat with MODIS products for climate study. In: Qu JJ, Powell A, Sivakumar MVK (eds) Satellite-based applications to climate change. Springer, New York

Hao X, Qu JJ (2013) Development of the global multispectral imager thermal emissive FCDRs. In: Qu JJ, Powell A, Sivakumar MVK (eds) Satellite-based applications to climate change. Springer, New York

Hunt ER Jr, Ustin SL, Riaño D (2013) Remote sensing of leaf, canopy and vegetation water contents for satellite climate data records. In: Qu JJ, Powell A, Sivakumar MVK (eds) Satellite-based applications to climate change. Springer, New York

Karl TR (1996) Long-term climate monitoring by the Global Climate Observing System. Kluwer Academic Publishers, London, p 518

Key J (2013) Monitoring change in the arctic. In: Qu JJ, Powell A, Sivakumar MVK (eds) Satellite-based applications to climate change. Springer, New York

Li M, Qu JJ (2013) Satellite applications for detecting vegetation phenology. In: Qu JJ, Powell A, Sivakumar MVK (eds) Satellite-based applications to climate change. Springer, New York

Martin TC, Brazil LE, Allen RG (2013) Applications of remote sensing derived evapotranspiration for water. In: Qu JJ, Powell A, Sivakumar MVK (eds) Satellite-based applications to climate change. Springer, New York

National Research Council (2003) Satellite observations of the earth's environment: accelerating the transition of research to operation, The National Academies Press, Washington, D.C, pp 1–163

Powell A, Xu J (2013) Evaluation of the temperature trend and climate forcing in the pre- and post periods of satellite data assimilation. In: Qu JJ, Powell A, Sivakumar MVK (eds) Satellite-based applications to climate change. Springer, New York

Powell A, Qu JJ, Sivakumar MVK (2013) Introduction to "satellite remote sensing of climate". In: Qu JJ, Powell A, Sivakumar MVK (eds) Satellite-based applications to climate change. Springer, New York

Romanov P (2013) Snow cover. In: Qu JJ, Powell A, Sivakumar MVK (eds) Satellite-based applications to climate change. Springer, New York

Salomonson V, Xiong J (2013) MODIS ten year performance to support climate change study. In: Qu JJ, Powell A, Sivakumar MVK (eds) Satellite-based applications to climate change. Springer, New York

Smith TM (2013) Developing a historical precipitation record Thomas M. Smith. In: Qu JJ, Powell A, Sivakumar MVK (eds) Satellite-based applications to climate change. Springer, New York

Sun D, Yu Y (2013) Land surface temperature monitoring with multi-instrument measurements. In: Qu JJ, Powell A, Sivakumar MVK (eds) Satellite-based applications to climate change. Springer, New York

Uz SS, Brown CW, Heidinger AK, Smyth TJ, Murtugudde R (2013) Monitoring a sentinel species from satellites: detecting *emiliania huxleyi* in 25 years of AVHRR imagery. In: Qu JJ, Powell A, Sivakumar MVK (eds) Satellite-based applications to climate change. Springer, New York

Xu L (2013) Satellite monitored snow cover in the climate system. In: Qu JJ, Powell A, Sivakumar MVK (eds) Satellite-based applications to climate change. Springer, New York

Zou C-Z (2013) Atmospheric temperature climate data records from satellite microwave sounders. In: Qu JJ, Powell A, Sivakumar MVK (eds) Satellite-based applications to climate change. Springer, New York

Index

J.J. Qu et al. (eds.), *Satellite-based Applications on Climate Change*,
DOI 10.1007/978-94-007-5872-8,